Multipolar scattering expansion for the Casimir effect in the sphere-plane geometry.

Antoine Canaguier-Durand

THÈSE DE DOCTORAT
DE L'UNIVERSITÉ PIERRE ET MARIE CURIE

Spécialité : Physique

École doctorale : La Physique de la Particule à la Matière Condensée (ED P2MC 389)

réalisée au

Laboratoire Kastler Brossel (UPMC, ENS)

présentée par

Antoine CANAGUIER-DURAND

pour obtenir le grade de :

DOCTEUR DE L'UNIVERSITÉ PIERRE ET MARIE CURIE

Sujet de la thèse :

Multipolar scattering expansion for the Casimir effect in the sphere-plane geometry.

soutenue le 30 septembre 2011

devant le jury composé de :

M.	Daniel BLOCH	Rapporteur
M.	Holger GIES	Rapporteur
Mme	Marie-Christine ANGONIN	Examinateur
M.	Georges PALASANTZAS	Examinateur
M.	Cyriaque GENET	Examinateur
Mme	Astrid LAMBRECHT	Directrice de thèse
M.	Serge REYNAUD	Invité

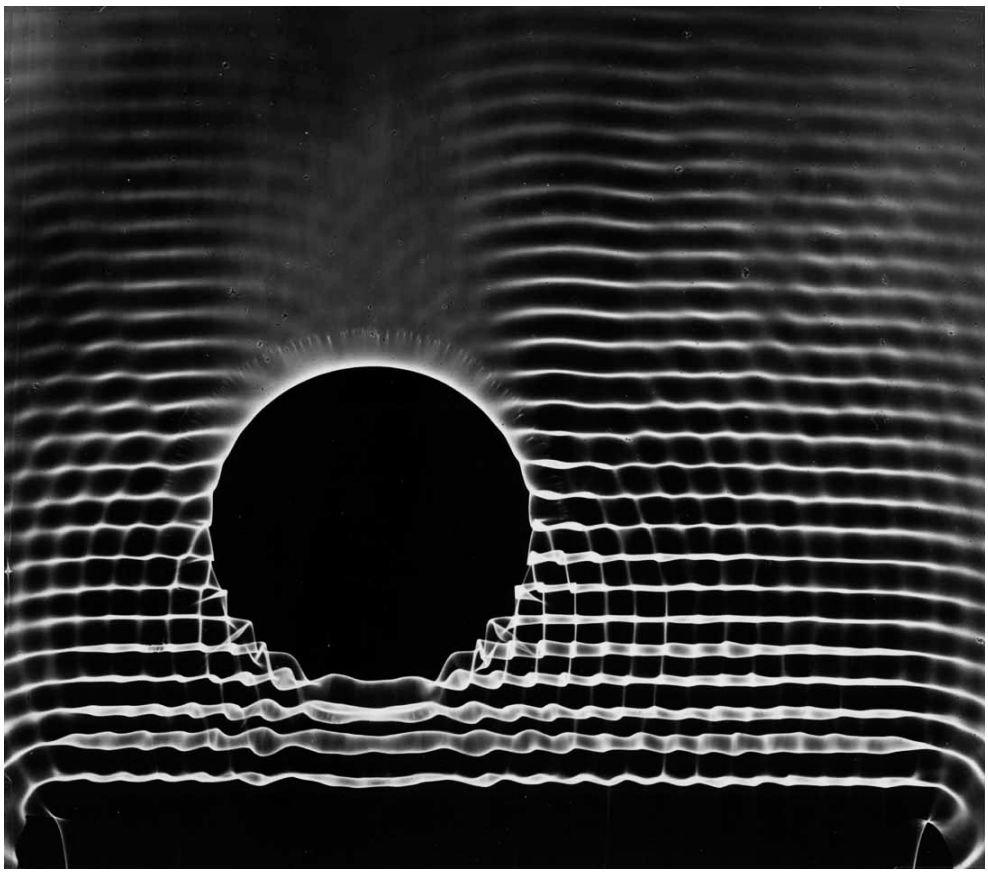

Behavior of waves, Berenice Abbott (1962).[1]

[1]Published in *Documenting science*, Steidler; Reprint edition (February 12, 2012). Reproduced with kind permission of the editors.

Remerciements

Arrivé au terme de la rédaction de ce manuscrit de thèse, il m'est particulièrement agréable d'exprimer ma gratitude et mes remerciements à tous ceux qui, par leur aide, leur soutien ou leur simple présence, ont participé de près ou de loin à sa réalisation.

J'adresse tout d'abord ma reconnaissance à Astrid Lambrecht et Serge Reynaud pour leur encadrement pendant ces trois années de thèse, notamment pour leur grande disponibilité, leur soutien constant, ainsi que pour la confiance témoignée à mon égard. Je les remercie également pour les nombreuses et minutieuses relectures de mon manuscrit, qui ont même occupé leurs trajets en RER ces derniers mois.

Je voudrais également remercier les différents chercheurs avec qui j'ai eu la chance de travailler, rencontrés lors de séjours, de visites, ou lors de conférences. Collaborer avec chacun d'entre eux fut pour moi très enrichissant et m'a permis de mieux comprendre comment s'accomplit la recherche à travers le monde. Merci tout d'abord à Paulo Maia Neto qui m'a fait découvrir Rio et les fonctions de Bessel, à Gert-Ludwig Ingold pour son accueil à Augsburg, ainsi qu'à Diego Dalvit et Markus Arndt pour l'intérêt manifesté pour mon travail, et pour leur aide.

Je remercie Daniel Bloch, Holger Gies, Marie-Christine Angonin, George Palasantzas et Cyriaque Genet d'avoir accepté de participer à mon jury de thèse, et d'avoir contribué à l'élaboration de ce manuscrit par leurs nombreuses suggestions, discussions et remarques, tant avant que pendant la soutenance. Je remercie particulièrement Daniel Bloch et Holger Gies d'avoir accepté d'être rapporteurs de ce manuscrit de thèse, et leur suis infiniment reconnaissant pour le temps et l'attention qu'ils ont accordés à la lecture de mon manuscrit.

J'ai effectué ma thèse au Laboratoire Kastler Brossel entre octobre 2008 et septembre 2011, où j'ai trouvé un cadre particulièrement favorable à l'apprentissage du monde de la recherche et à la conduite de mes travaux de thèse. Ceci résulte à la fois d'un espace scientifique et intellectuel extrêmement stimulant et d'une organisation exceptionnelle. Merci donc à Jean-Michel Courty, à Dominique Delande, à Brahim Lamine d'avoir pris le temps pour répondre à mes questions, et d'avoir stimulé ma curiosité scientifique. Merci aux doctorants et post-doctorants de mon équipe, Riccardo Messina, Ines Cavero-Pelaez, Romain Guérout, Johan Lussange et Antoine Gérardin, pour la richesse de nos échanges et la passion qui les anime. Merci également à Monique Granon, Lætitia Morel, Annick Lamarck, Serge Begon et Corinne Poisson de faire de ce laboratoire un endroit où il fait bon vivre et travailler. Merci enfin à Alexandre, Ferrucio, Godefroy, Piernicola, Oxana, Virginia, Alberto, Chiara et Giuseppe, avec qui j'ai partagé tant de bons moments d'échange, de détente et d'entraide, même si je n'ai jamais réellement compris sur quoi ils travaillaient.

Parallèlement à ma thèse, j'ai effectué un monitorat au sein de l'Unité de Formation et de Recherche (UFR 929) de mathématiques de l'Université Pierre et Marie Curie - Paris VI. Je remercie Elisha Falbel de m'y avoir encadré, ainsi que les autres professeurs avec qui j'ai partagé mes enseignements : Stanislaw Szarek, Jan Nekovář et Thérèse Merlier.

Alors que ce doctorat en physique marque l'aboutissement de mes études, mes pensées se portent aussi vers les différents enseignants qui, au long de mon cursus, m'ont transmis leur passion pour la science et m'ont guidé dans mon sinueux parcours étudiant. Je pense d'abord à Jean-Marie Mercier et à Philippe Gaillard du lycée Pierre-de-Fermat à Toulouse, qui m'ont inspiré le goût de la physique "propre", de la rigueur mathématique, et l'envie de faire de la recherche. Je remercie également Patrick Ciarlet, Daniel Bouche, Marc Lenoir et Jérôme Perez de l'ENSTA à Paris, pour

leur aide précieuse dans mon orientation, et lors de ma recherche de thèse. Je remercie enfin Anne-Sophie Bonnet-BenDhia, Éric Lunéville et Christophe Hazard du groupe POEMS à l'ENSTA, ainsi que Frédéric Nataf du Laboratoire Jacques-Louis Lions pour leur encadrement et leur aide lors de mes stages de Master.

J'exprime enfin ma reconnaissance à tous mes proches, qui par leur soutien, leur présence et les moments partagés m'ont permis de traverser ces années dans les meilleures conditions. Merci donc à tous mes amis parisiens, qu'ils soient de l'ENSTA, de Nanterre ou d'ailleurs, pour les petits bonheurs quotidiens, aux perchistes fous de Charléty avec qui j'ai partagé cette passion lors des séances, compétitions et stages, aux Kavettes pour ces joyeux mercredis soir passés dans un caveau à jouer du rock fort, à Nina, ses colocs, et toute la bande des brunchs du dimanche, aux habitants du Pilok pour les goûters et leur canap'. Merci à mes amis d'enfance rochelais, pour avoir préservé ce lien entre nous malgré les années et les kilomètres. Des remerciements particuliers à Daniel pour sa patience et ses fromages, à Thomas, Élise, Julien et Jérémanon pour tout ce qu'ils m'apportent et représentent pour moi. Merci enfin aux membres de ma famille, pour leur confiance indéfectible dans mes choix, et pour leur soutien permanent et inconditionnel. Merci Marie.

Contents

Résumé

Introduction

L'effet Casimir est une force attractive apparaissant entre deux objets neutres et réfléchissants, placés dans le vide. Cet effet a été découvert par Hendrik Casimir en 1948 à la suite de travaux sur les colloïdes et la force de van der Waals. Le vide quantique est le siège de fluctuations du champ électromagnétique, associées à une énergie $\frac{\hbar\omega}{2}$ pour le mode de fréquence ω. Lorsque l'on considère le vide quantique entre deux objets réfléchissant, des effets de résonance apparaissent, et la distribution en fréquence des fluctuations est modifiée. La pression radiative associée au champ électromagnétique est donc différente à l'intérieur et à l'extérieur de la cavité, et il en résulte une force attractive entre les deux objets. Pour deux miroirs plans, infinis, parallèles, et parfaitement réfléchissants à température nulle, Casimir donne l'expression de cette force par unité de surface en fonction de la distance L entre les deux miroirs :

$$\frac{F}{A} = -\frac{\hbar c \pi^2}{240 L^4} \ . \tag{0.1}$$

Si les premiers travaux expérimentaux n'ont pas réussi à confirmer cet effet de manière précise, à cause de nombreuses difficultés techniques, une seconde série d'expériences beaucoup plus performantes a vu le jour à la fin des années 90, avec notamment les travaux de Lamoreaux en 1997 et 2011 utilisant un pendule de torsion, ceux de Mohideen en 1998 utilisant un microscope à force atomique, et ceux de Decca en 2003 utilisant un micro-résonnateur. Toutes ces expériences sont réalisées dans la géométrie d'une sphère face à plan, de manière à éviter le problème du maintient du parallélisme entre deux plaques planes.

De nombreux travaux théoriques ont vu le jour, afin de modifier le résultat original (0.1) calculé par Casimir dans une configuration très idéalisée, par la prise en compte de conditions plus réalistes. La réflexion imparfaite des miroirs est incorporée dans les calculs théoriques dès 1956 grâce à Lifshitz et l'utilisation de la fonction diélectrique $\varepsilon(\omega)$ pour décrire la conductivité des matériaux. L'effet de la température non-nulle est également prise en compte quelques années plus tard, en ajoutant aux fluctuations du vide les fluctuations thermiques, exprimées grâce à la formule de Planck :

$$\hbar\omega \longrightarrow \hbar\omega \left(\frac{1}{2} + \overline{n_\omega}\right) \qquad \text{avec} \quad \overline{n_\omega} = \frac{1}{e^{\frac{\hbar\omega}{k_B T}} - 1} \ . \tag{0.2}$$

Enfin la géométrie sphère-plan des expériences est habituellement traitée grâce à l'approximation de proximité (PFA). Le domaine de validité de cette approximation est la limite des courtes distances, qui est réaliste au vue des paramètres utilisés dans les expériences, cependant l'erreur de cette approximation n'est pas maîtrisée. De plus, cette méthode utilise l'évaluation de l'effet Casimir dans la géométrie plan-plan afin d'introduire les effets de la température et de la conductivité finie, ce qui empêche de voir de possible couplages entre ces effets et ceux de la géométrie.

Cette thèse présente une évaluation de l'effet Casimir dans la géométrie sphère-plan, basée sur la méthode de diffusion, avec un traitement multipolaire permettant d'obtenir des résultats très précis, et dont l'erreur est maîtrisable. Les descriptions de la réflexion imparfaite et de la température non-nulle sont directement incorporées dans l'évaluation faite pour la géométrie correcte. Les résultats numériques et analytiques permettent d'estimer l'erreur faite par l'approximation PFA, d'observer des couplages entre les effets de température, de conductivité finie, de dissipation, et de géométrie. Les travaux réalisés lors de cette thèse permettent donc à la fois une meilleure compréhension des résultats expérimentaux, mais aussi une étude, plus théorique, de la riche dépendance de l'effet Casimir à la géométrie.

1. Rappels sur la méthode de diffusion pour l'effet Casimir et exemple de la géométrie plan-plan

Dans cette première partie nous introduisons la méthode de diffusion, qui permet d'exprimer l'effet Casimir en fonction des opérateurs de réflexion sur les objets, et rappelons comment cette méthode permet la prise en compte de propriétés optiques réalistes pour les matériaux et de la température arbitraire. La géométrie plan-plan est montré comme exemple d'application de cette méthode, et les principaux résultats obtenus dans cette configuration sont rappelés. Enfin, la méthode d'approximation de proximité (PFA), communément utilisée pour calculer l'effet Casimir dans la géométrie sphère-plan, est rappelée.

La méthode de diffusion

La formule de diffusion est une méthode générale pour évaluer l'interaction Casimir entre deux objets séparables par un plan. Elle utilise la théorie de l'optique des réseaux pour exprimer l'effet Casimir en fonction des propriétés diffusives des objets. Son expression, donnée en Eq.(0.3), utilise les opérateurs de réflexion $\mathcal{R}_i$ sur l'objet i, évalués à la fréquence imaginaire $\omega = \imath\xi$:

$$E = \hbar \int_0^\infty \frac{\mathrm{d}\xi}{2\pi} \ln\det \mathcal{D}(\imath\xi) \quad \text{avec} \quad \mathcal{D} = \mathcal{I} - \mathcal{R}_1 \mathcal{T}_{1\leftarrow 2} \mathcal{R}_2 \mathcal{T}_{2\leftarrow 1} \ , \tag{0.3}$$

où les opérateurs de translation $\mathcal{T}$ permettent d'exprimer les opérateurs de réflexion dans le repère associé à chaque objet.

La formule (0.3) prend une forme particulièrement simple dans le cas de deux miroirs plans infinis parallèles, séparés d'une distance L dans la direction z. Les opérateurs ont alors une expression très simple lorsqu'on les exprime dans la base des modes plans de fréquence ω, notés $\mid \mathbf{k}, p, \phi\rangle$, où $\mathbf{k} = (k_x, k_y)$ est la partie transversale du vecteur d'onde, $p = \mathrm{TE}, \mathrm{TM}$ est la polarisation, et $\phi = \pm$ est le sens de propagation, permettant de déterminer la partie longitudinale du vecteur d'onde $k_z = \phi\sqrt{\frac{\omega^2}{c^2} - \mathbf{k}^2}$. Après le passage aux fréquences imaginaires $\omega = \imath\xi$, l'opérateur $\mathcal{D}$ a pour éléments:

$$\begin{aligned} &\mathcal{D}(\imath\xi) \mid \mathbf{k}, p, +\rangle = (1 - \rho_p(\xi, \mathbf{k})) \mid \mathbf{k}, p, +\rangle \quad \text{avec} \quad \rho_p(\xi, \mathbf{k}) = r_p^{(1)}(\xi, \mathbf{k}) r_p^{(2)}(\xi, \mathbf{k}) e^{-2\kappa L} \\ &\mathcal{D}(\imath\xi) \mid \mathbf{k}, p, -\rangle = \mid \mathbf{k}, p, -\rangle \end{aligned} \tag{0.4}$$

où $r_{\mathrm{TE}}, r_{\mathrm{TM}}$ sont les coefficients de Fresnel pour chaque miroir plan, et $\kappa = \sqrt{\frac{\xi^2}{c^2} + \mathbf{k}^2}$. En insérant ces éléments dans la formule de diffusion (0.3), et en utilisant la condition des miroirs parfaitement réfléchissants $r_{\mathrm{TE}} = r_{\mathrm{TM}} = 1$, on retrouve l'expression originale (0.1) calculée par Casimir.

Prise-en-compte des propriétés optiques des matériaux

La méthode de diffusion permet de décrire les propriétés optiques des objets par l'intermédiaire de l'opérateur de réflexion, et en particulier de prendre en compte la conductivité finie des matériaux. L'imperfection de la réflexion peut par exemple être décrite pour les métaux par les modèles de plasma et de Drude pour la fonction diélectrique $\varepsilon(\omega)$, ce dernier modèle se différenciant par l'ajout de la description de la dissipation dans les métaux:

$$\varepsilon^{\mathrm{plas}}(\omega) = 1 - \frac{\omega_P^2}{\omega^2} \qquad \varepsilon^{\mathrm{Drud}}(\omega) = 1 - \frac{\omega_P^2}{\omega\,(\omega + \imath\gamma)} \ . \tag{0.5}$$

Ces deux fonctions diélectriques sont illustrés par le graphique de gauche de la figure 1, où l'on peut voir que ces modèles permettent de recréer la transparence des métaux à haute fréquence.

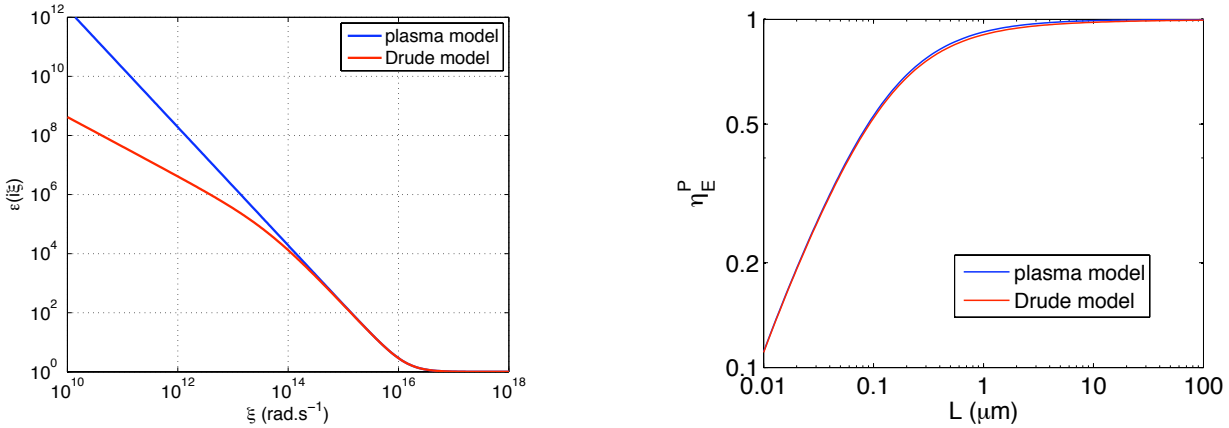

Figure 1: (gauche) Fonction diélectrique $\varepsilon(\xi)$ pour les modèles de plasma de et Drude en fonction de la fréquence imaginaire $\imath\xi$. (droite) Facteur de correction $\eta_E^P = \frac{E^{\text{metal}}}{E^{\text{perf}}}$ pour la conductivité finie avec les modèles de plasma et de Drude, en fonction de la distance L entre les deux plans.

Ces deux modèles diffèrent uniquement pour les basses fréquences, où la divergence est en ξ^{-2} pour le modèle plasma et en ξ^{-1} pour le modèle de Drude.

Dans le cas particulier de la géométrie plan-plan, la méthode de diffusion offre un cadre permettant de prendre en compte facilement la fonction diélectrique $\varepsilon(\imath\xi)$ modélisant la réponse optique des matériaux, par l'intermédiaire des coefficients de Fresnel $r_{\text{TE}}, r_{\text{TM}}$. Le changement de l'énergie et de la force de Casimir par rapport au cas des miroirs parfait peut alors être exprimé par les facteurs correctif $\eta_E^P = \frac{E^{\text{metal}}}{E^{\text{perf}}}$ et $\eta_F^P = \frac{F^{\text{metal}}}{F^{\text{perf}}}$, qui ont pour expressions :

$$\eta_E^P = \frac{E^{\text{metal}}}{E^{\text{perf}}} = -\frac{180L^3}{c\pi^4}\int_0^\infty \mathrm{d}\xi \int_{\xi/c}^\infty \kappa \mathrm{d}\kappa \ln\left[(1-\rho_{\text{TE}}(\xi,\kappa))(1-\rho_{\text{TM}}(\xi,\kappa))\right]$$
$$\eta_F^P = \frac{F^{\text{metal}}}{F^{\text{perf}}} = \frac{120L^4}{c\pi^4}\int_0^\infty \mathrm{d}\xi \int_{\xi/c}^\infty \kappa^2 \mathrm{d}\kappa \left[\frac{\rho_{\text{TE}}(\xi,\kappa)}{1-\rho_{\text{TE}}(\xi,\kappa)} + \frac{\rho_{\text{TM}}(\xi,\kappa)}{1-\rho_{\text{TM}}(\xi,\kappa)}\right] . \qquad (0.6)$$

L'évaluation numérique de ces expressions est présentée en fonction de la distance L séparant les deux miroirs par le graphique de droite de la figure 1, où l'on peut observer que la réflexion imparfaite diminue l'effet Casimir pour les distances courtes, mais n'a aucune influence à longue distance ($L \gtrsim 1$ μm). Les facteurs η_E^P et η_F^P deviennent proportionnels à L à courte distance, un régime asymptotique qui peut être quantifié analytiquement :

$$\eta_E^P = \frac{3\alpha}{2}\frac{L}{\lambda_P} \quad \text{et} \quad \eta_F^P = \alpha\frac{L}{\lambda_P} \text{avec} \quad \alpha = \frac{30}{\sqrt{2}\pi^2}\sum_{n=1}^{\infty}\frac{1}{n^3}\frac{(4n-3)!!}{(4n-2)!!} \simeq 1.1933 \qquad (0.7)$$

où λ_P est la longueur d'onde plasma, associée à la fréquence plasma par la relation $\lambda_P = \frac{2\pi c}{\omega_P}$.

La méthode de diffusion à température non-nulle

La formule de diffusion (0.3) peut être modifiée afin de prendre en compte les fluctuations thermiques en plus des fluctuations du vide, apparaissant dès que la température est non-nulle. L'énergie de chaque mode du vide $\frac{\hbar\omega}{2}$ est donc transformée selon (0.2), utilisant le nombre moyen de photons thermiques $\overline{n_\omega}$ donné par la formule de Planck. Lorsque cette modification est introduite dans la formule de diffusion (0.3), qui donne maintenant l'énergie libre de Casimir $\mathcal{F}$, on peut montrer

mathématiquement que l'intégrale sur les fréquences est remplacée par une somme discrète sur les fréquences $(\xi_n)_{n\in\mathbb{N}}$ dites de Matsubara:

$$\mathcal{F} = k_B T \sum_n{}' \ln\det \mathcal{D}(\imath\xi_n) \quad \text{avec} \quad \xi_n = n\omega_T = n\frac{2\pi k_B T}{\hbar} \tag{0.8}$$

où l'apostrophe sur le symbole $\sum$ indique une somme sur $\mathbb{N}$ avec un facteur $\frac{1}{2}$ pour le terme 0. Pour des températures basses, les fréquences de Matsubara se rapprochent et la somme discrète tend vers l'intégrale de l'expression (0.3). Pour des températures hautes, seule la fréquence nulle intervient dans cette somme.

Dans l'exemple de la géométrie plan-plan, cette modification entraîne une modification de l'énergie libre de Casimir, qui peut être mesurée à l'aide du facteur correctif thermique $\eta_{\mathcal{F}}^T = \frac{\mathcal{F}(T)}{\mathcal{F}(0)}$. Pour les miroirs parfaits, ce facteur est une fonction croissante de la distance et de la température, toujours supérieur à 1, comme illustré par le trait noir dans le graphique gauche de la figure 2. L'entropie de Casimir est alors une quantité toujours positive.

Lorsque les effets de la température et de la réflexion imparfaite sont pris en compte simultanément, il apparaît une différence fondamentale entre les résultats obtenus à partir des modèles de plasma et de Drude. Pour le premier, les effets des deux corrections sont très légèrement corrélées, et la correction totale est proche du produit des deux corrections considérées séparément, comme illustré par le trait bleu dans le graphique gauche de la figure 2. Pour le modèle dissipatif de Drude en revanche, de fortes corrélations apparaissent entre les effets thermiques et de conductivité finie, comme illustré par le trait rouge dans le même graphique. Ces corrélations entraînent l'apparition de valeurs négatives pour l'entropie de Casimir aux distances intermédiaires, et aux grandes distances un facteur 2 de réduction de l'effet Casimir par rapport aux métaux sans dissipation.

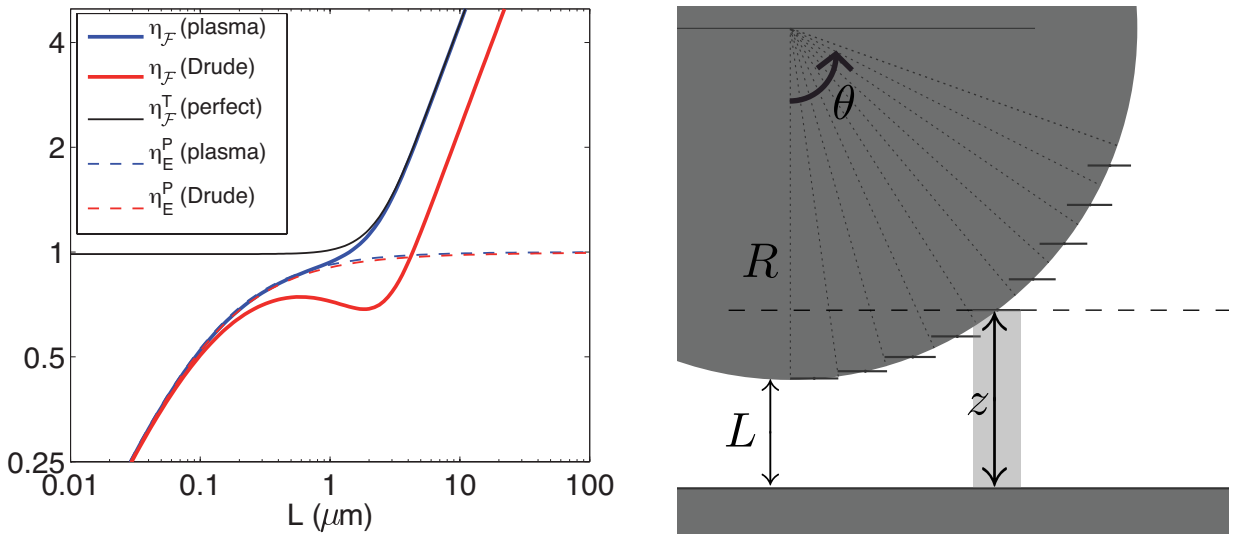

Figure 2: (gauche) Facteurs de correction de conductivité η_E^P à température nulle (tirets), de température η_E^T (trait continu noir) et prenant en compte les deux effets simultanément, pour le modèle plasma (trait continu bleu) et la modèle de Drude (trait continu rouge). (droite) Schéma reprenant la processus d'intégration des contributions à la force de Casimir fait par l'approximation de proximité (PFA).

L'approximation de proximité (PFA)

Afin de comparer les résultats des expériences, réalisées dans la configuration sphère-plan, aux prédictions théoriques, l'approximation de proximité est communément utilisée. Celle-ci repose sur l'hypothèse que la sphère est "proche" du plan ; en notant R le rayon de la sphère et L la distance entre le plan et la partie de la sphère la plus proche du plan, le domaine de validité de cette approximation s'écrit ($L \ll R$). Son principe est illustré par le schéma de droite de la figure 2 : la sphère est découpé en parties infinitésimales de surface $\mathrm{d}^2\sigma$, pour lesquelles on considère que la force d'interaction est la même que pour la partie d'un plan infini situé à la même distance z. En intégrant sur la sphère toutes ces contributions on obtient la force totale F_{PFA} (ou de manière similaire le gradient de la force G_{PFA}) :

$$F_{\mathrm{PFA}}(L,R) = 2\pi R \frac{E_{\mathrm{PP}}(L)}{A} \qquad\qquad G_{\mathrm{PFA}}(L,R) = 2\pi R \frac{F_{\mathrm{PP}}(L)}{A} \tag{0.9}$$

exprimé grâce à l'énergie par unité de surface $\frac{E_{\mathrm{PP}}}{A}$ entre deux plans, évaluée à la distance L.

Le premier inconvénient de cette approximation est que son erreur n'est pas maîtrisée lorsque l'on s'éloigne de son domaine limite de validité ($L \ll R$). On considère habituellement que cette erreur est linéaire en $\frac{L}{R}$, le rapport d'aspect, et l'on cherchera donc à caractériser le coefficient linéaire β_E de la correction géométrique pour l'énergie, en l'exprimant sous la forme d'un développement de Taylor en $\frac{L}{R}$:

$$\rho_E = \frac{E}{E_{\mathrm{PFA}}} = 1 + \beta_E \frac{L}{R} + \gamma_E \left(\frac{L}{R}\right)^2 + \cdots \ . \tag{0.10}$$

Un raisonnement similaire permet de définir les coefficients linéaires β_F, β_G pour le facteur correctif de la force F, et du gradient de la force G. Le second handicap de cette approximation est qu'elle introduit les propriétés optiques des matériaux et la température par l'intermédiaire du terme calculé dans la géométrie plan-plan, et donc de manière découplée par rapport aux effets géométriques. Toute corrélation entre les effets de la géométrie et ceux de la température ou de la conductivité finie est donc impossible à observer avec cette approximation.

2. Application de la méthode de diffusion au cas de la géométrie sphère-plan

Dans cette partie nous décrivons comment le formule de diffusion précédemment introduite peut être appliquée à la géométrie sphère-plan à l'aide de l'utilisation conjointe des bases des ondes planes et sphériques, débouchant sur un développement multipolaire. Nous évoquons ensuite la mise-en-œuvre numérique pour l'évaluation de l'effet Casimir grâce aux expressions obtenues.

Calcul des opérateurs de réflexion

La formule de diffusion est ici appliquée à la géométrie d'une sphère de rayon R placée à une distance L d'un plan, ($L = 0$) indiquant le contact entre les deux objets. L'opérateur de réflexion sur le plan $\mathcal{R}_P$ s'exprime aisément dans la base des ondes planes de fréquence imaginaire $\imath\xi$ introduite plus haut, à l'aide des coefficients de Fresnel $r_p(\xi, \mathbf{k})$:

$$\mathcal{R}_P \mid \mathbf{k}, p, - \rangle = r_p(\xi, \mathbf{k}) \mid \mathbf{k}, p, + \rangle \qquad\qquad \mathcal{R}_P \mid \mathbf{k}, p, + \rangle = 0 \ . \tag{0.11}$$

L'opérateur de réflexion sur la sphère $\mathcal{R}_S$ est quant à lui mieux exprimé à l'aide des ondes sphériques $\mid \ell, m, P \rangle$, où ℓ et m sont les indices azimutal et magnétique, et $P = E, M$ la polarisation. Afin d'exprimer l'opérateur $\mathcal{D}$ pour calculer son déterminant, il est également nécessaire de disposer de transformations entre la base des ondes planes et celle des ondes sphériques. Le schéma présenté

en figure 3 illustre le cheminement du calcul pour l'aller-retour dans la cavité : on considère une onde sphérique $|\ \ell_2, m_2, P_2\rangle$ s'éloignant de la sphère, que l'on transforme en ondes planes $|\ \mathbf{k}, p, -\rangle$ descendant vers le plan. L'expression (0.11) est alors utilisée pour la réflexion sur le plan, puis la réflexion sur la sphère de l'onde plane sortante $|\ \mathbf{k}, p, +\rangle$ est écrite grâce aux coefficients de Mie sous la forme d'ondes sphériques $|\ \ell_1, m_1, P_1\rangle$.

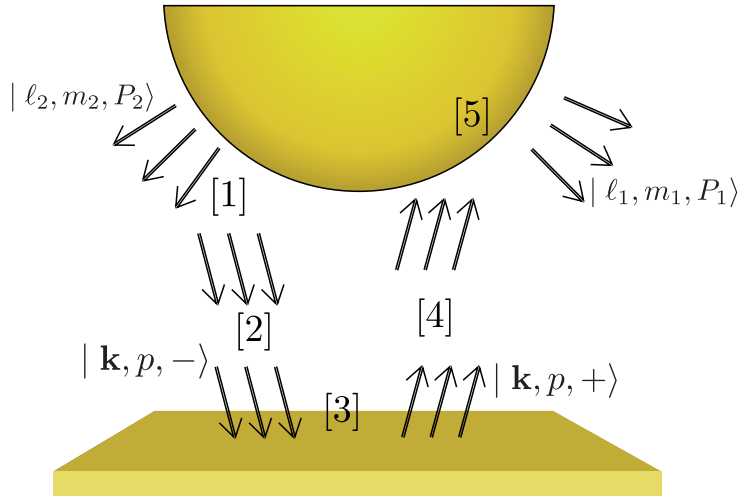

Figure 3: Schéma de l'utilisation conjointe des bases d'ondes planes et sphériques afin d'exprimer la formule de diffusion dans la géométrie sphère-plan. La réflexion sur le plan, ainsi que les deux translations utilisent les ondes planes, la réflexion sur la sphère est décomposée en ondes sphériques.

Quand toutes ces étapes sont écrites, et que leurs expressions sont regroupées, on peut les simplifier jusqu'à obtenir l'expression finale :

$$\begin{aligned} E &= \frac{\hbar c}{\pi R}\int_0^\infty \mathrm{d}\tilde{\xi}\ {\sum_m}' \ln\det\left[I - \mathcal{N}^{(m)}(\tilde{\xi})\right] \\ \mathcal{F} &= 2k_BT {\sum_n}' {\sum_m}' \ln\det\left[I - \mathcal{N}^{(m)}(\tilde{\xi}_n)\right] \end{aligned} \tag{0.12}$$

où les $\tilde{\xi}_n = n\frac{2\pi R}{\lambda_T}$ sont les fréquences réduites de Matsubara, et l'opérateur réel $\mathcal{N}$ s'écrit :

$$\mathcal{N}^{(m)}(\tilde{\xi}) = \begin{pmatrix} \mathcal{N}^{(m)}_{EE}(\tilde{\xi}) & \mathcal{N}^{(m)}_{EM}(\tilde{\xi}) \\ \\ \mathcal{N}^{(m)}_{ME}(\tilde{\xi}) & \mathcal{N}^{(m)}_{MM}(\tilde{\xi}) \end{pmatrix} \tag{0.13}$$

avec les quatre blocs correspondant aux différentes polarisations P_1 et P_2, et contenant les coefficients de Mie a_ℓ et b_ℓ :

$$\begin{aligned} \left(\mathcal{N}^{(m)}_{EE}(\tilde{\xi})\right)_{\ell_1,\ell_2} &= \sqrt{\tfrac{(2\ell_1+1)\pi}{\ell_2(\ell_2+1)}}a_{\ell_1}(i\tilde{\xi})\left(A^{(m)}_{\ell_1,\ell_2,\mathrm{TE}}(\tilde{\xi}) + B^{(m)}_{\ell_1,\ell_2,\mathrm{TM}}(\tilde{\xi})\right) \\ \left(\mathcal{N}^{(m)}_{EM}(\tilde{\xi})\right)_{\ell_1,\ell_2} &= \sqrt{\tfrac{(2\ell_1+1)\pi}{\ell_2(\ell_2+1)}}a_{\ell_1}(i\tilde{\xi})\left(C^{(m)}_{\ell_1,\ell_2,\mathrm{TE}}(\tilde{\xi}) + D^{(m)}_{\ell_1,\ell_2,\mathrm{TM}}(\tilde{\xi})\right) \\ \left(\mathcal{N}^{(m)}_{ME}(\tilde{\xi})\right)_{\ell_1,\ell_2} &= \sqrt{\tfrac{(2\ell_1+1)\pi}{\ell_2(\ell_2+1)}}b_{\ell_1}(i\tilde{\xi})\left(C^{(m)}_{\ell_1,\ell_2,\mathrm{TM}}(\tilde{\xi}) + D^{(m)}_{\ell_1,\ell_2,\mathrm{TE}}(\tilde{\xi})\right) \\ \left(\mathcal{N}^{(m)}_{MM}(\tilde{\xi})\right)_{\ell_1,\ell_2} &= \sqrt{\tfrac{(2\ell_1+1)\pi}{\ell_2(\ell_2+1)}}b_{\ell_1}(i\tilde{\xi})\left(A^{(m)}_{\ell_1,\ell_2,\mathrm{TM}}(\tilde{\xi}) + B^{(m)}_{\ell_1,\ell_2,\mathrm{TE}}(\tilde{\xi})\right)\ . \end{aligned} \tag{0.14}$$

Les blocks A, B, C, D contenus dans ces expressions s'écrivent, pour $m \geq 0$:

$$
\begin{aligned}
A^{(m)}_{\ell_1,\ell_2,p} &= m(-1)^{\ell_2} \int_1^\infty \frac{\mathrm{d}\cos\theta}{s(\theta)} d_m^{\ell_1,s}[\mathrm{sum}]\ Y^s_{\ell_2 m}(\theta)\ r_p(\imath\xi,k)\ e^{-2\hat{\xi}\mathcal{L}\cos\theta} \\
B^{(m)}_{\ell_1,\ell_2,p} &= (-1)^{\ell_2+1} \int_1^\infty \mathrm{d}\cos\theta\ d_m^{\ell_1,s}[\mathrm{dif}]\ \partial_\theta Y^s_{\ell_2 m}(\theta)\ r_p(\imath\xi,k)\ e^{-2\hat{\xi}\mathcal{L}\cos\theta} \\
C^{(m)}_{\ell_1,\ell_2,p} &= (-1)^{\ell_2} \int_1^\infty \mathrm{d}\cos\theta\ d_m^{\ell_1,s}[\mathrm{sum}]\ \partial_\theta Y^s_{\ell_2 m}(\theta)\ r_p(\imath\xi,k)\ e^{-2\hat{\xi}\mathcal{L}\cos\theta} \\
D^{(m)}_{\ell_1,\ell_2,p} &= m(-1)^{\ell_2+1} \int_1^\infty \frac{\mathrm{d}\cos\theta}{s(\theta)} d_m^{\ell_1,s}[\mathrm{dif}]\ Y^s_{\ell_2 m}(\theta)\ r_p(\imath\xi,k)\ e^{-2\hat{\xi}\mathcal{L}\cos\theta}
\end{aligned}
\tag{0.15}
$$

où l'on a utilisé une forme modifiée des harmoniques sphériques $Y_{\ell m}$, ainsi que deux combinaisons de rotations finies :

$$
\begin{aligned}
d_m^{\ell,s}[\mathrm{sum}] &= d_{m,1}^{\ell,s}(\theta) + (-1)^{\ell+m} d_{m,1}^{\ell,s}(\pi-\theta) \\
d_m^{\ell,s}[\mathrm{dif}] &= d_{m,1}^{\ell,s}(\theta) - (-1)^{\ell+m} d_{m,1}^{\ell,s}(\pi-\theta)\ .
\end{aligned}
\tag{0.16}
$$

Mise-en-œuvre numérique

L'opérateur $\mathcal{D}$ ayant une dimension infinie, due à l'infinité de couples d'indices possibles pour ℓ et m, l'évaluation numérique nécessite une troncation préalable des indices de cet opérateur. Ceci est possible dans la base des ondes sphériques, en introduisant une coupure $\ell_{\max}$ pour ces deux indices. Cette troncation ne modifie le résultat de l'évaluation du déterminant que pour de petites valeurs du rapport d'aspect $\frac{L}{R}$, pour lesquels de nombreux multipoles contribuent à l'effet Casimir. Ceci est illustré par le graphique de gauche de la figure 4, où la convergence du résultat est obtenu pour une troncation d'autant plus élevée que $\frac{L}{R}$ est petit. Ainsi, plus on repousse la troncation numérique $\ell_{\max}$ à des grandes valeurs, plus il est possible d'atteindre de petites valeurs du rapport d'aspect $\frac{L}{R}$. Lors de nos calculs numériques, nous avons pu réaliser des évaluations avec $\ell_{\max} = 520$, permettant d'obtenir des résultats précis pour $\frac{L}{R} \gtrsim 0.01$.

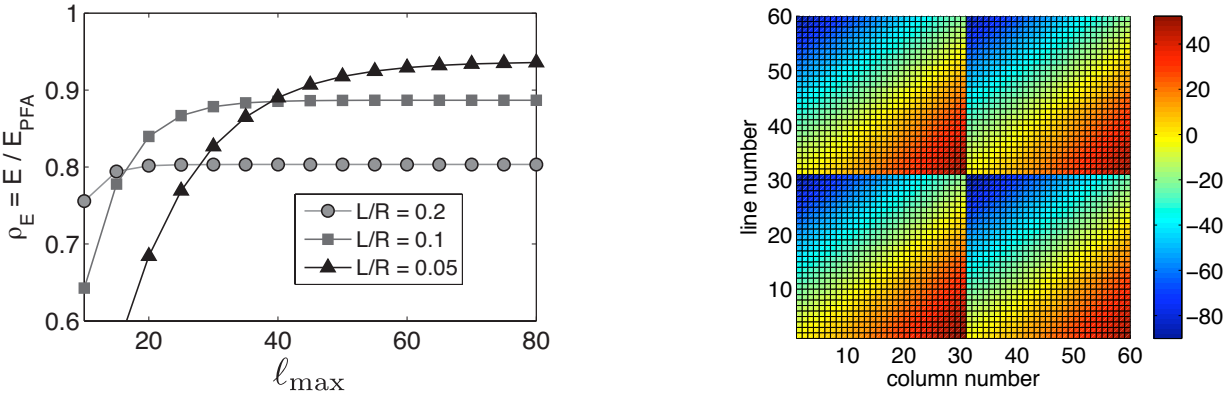

Figure 4: (gauche) Energie de Casimir normalisée par l'estimation de PFA $\rho_E = \frac{E}{E_{\mathrm{PFA}}}$ dans la géométrie sphère-plan, en fonction de la troncation $\ell_{\max}$, pour différentes valeurs du rapport d'aspect $\frac{L}{R}$. (droite) Magnitude, en puissances de 10, des éléments de la matrice $\mathcal{N}^{(1)}$. Le cas étudié est $\tilde{\xi} = 0.1$, $\ell_{\max} = 30$, $\frac{L}{R} = 1$.

La problématique de la stabilité numérique est cruciale avec une telle méthode, à cause de l'utilisation des fréquences imaginaires, qui transforment une fonction oscillante en une exponentielle dans l'expression (0.15). Cela entraîne l'apparition de nombres très grands et très petits dans la matrice $\mathcal{N}$, comme illustré dans le graphique de droite de la figure 4. Il y a donc le risque d'obtenir

des nombres extérieurs au domaine représentable numériquement, ce qui est peut être évité en utilisant des représentations plus riches pour les nombres flottants, de type double (64 bits) ou quadruple (128 bits). D'autre part, ces nombres rendent la matrice très mal conditionnée, ce qui peut également être la source d'instabilité numériques. Ce problème peut être traité en appliquant des procédures de régularisation à la matrice, qui laissent son déterminant inchangé.

3. Résultats analytiques

Dans cette partie, on étudie deux régimes limites dans lesquels l'expression de la formule de diffusion obtenue dans la partie précédente peut être traitée analytiquement. Ces résultats analytiques seront utiles à la fois pour vérifier les évaluations numériques, mais aussi pour mieux comprendre les résultats obtenus.

Limite basse fréquence

On considère dans un premier temps la limite basse-fréquence ($\tilde{\xi} \to 0$) pour l'opérateur $\mathcal{D}(\imath\xi)$. Cette limite est utile pour la détermination de la contribution de la première fréquence de Matsubara dans l'expression (0.12) donnant l'énergie libre de Casimir. Elle permet en outre d'obtenir la limite haute-température ($T \to \infty$) de l'énergie libre, qui s'écrit :

$$\mathcal{F}^{\mathrm{HT}} = \frac{k_B T}{2}\Phi(0) \quad \text{où} \quad \Phi(\imath\xi) = \ln\det \mathcal{D}(\imath\xi)\ . \tag{0.17}$$

L'étude de la limite basse-fréquence pour les coefficients de Mie et de Fresnel mettent en évidence une différence fondamentale entre les cas des miroirs parfaits, décrits par le modèle de plasma, et par le modèle de Drude. Après un calcul asymptotique permettant d'extraire les termes dominants de la limite étudiée, on obtient les résultats suivants pour les miroirs parfaits et ceux décrits par le modèle de Drude :

$$\begin{aligned}
\Phi^{\mathrm{perf}}(0) &= 2{\sum_m}' \left[\ln\det\left(\mathbb{D}^{(m)}_{a,\mathrm{TM}}(\tilde{\mathcal{L}})\right) + \ln\det\left(\mathbb{D}^{(m)}_{b,\mathrm{TE}}(\tilde{\mathcal{L}})\right)\right] \\
\Phi^{\mathrm{Drud}}(0) &= 2{\sum_m}' \ln\det\left(\mathbb{D}^{(m)}_{a,\mathrm{TM}}(\tilde{\mathcal{L}})\right)
\end{aligned} \tag{0.18}$$

où l'on utilise les matrices $\mathbb{D}^{(m)}_{a,\mathrm{TM}}$ et $\mathbb{D}^{(m)}_{b,\mathrm{TE}}$ qui ne dépendant que de $\tilde{\mathcal{L}} = \frac{L}{R} + 1$:

$$\begin{aligned}
\mathbb{D}^{(m)}_{a,\mathrm{TM}}(\tilde{\mathcal{L}}) &= \delta_{\ell_1,\ell_2} - \frac{1}{\left(2\tilde{\mathcal{L}}\right)^{\ell_1+\ell_2+1}} \frac{(\ell_1+\ell_2)!}{\sqrt{(\ell_1-m)!}\sqrt{(\ell_1+m)!}\sqrt{(\ell_2-m)!}\sqrt{(\ell_2+m)!}} \\
\mathbb{D}^{(m)}_{b,\mathrm{TE}}(\tilde{\mathcal{L}}) &= \delta_{\ell_1,\ell_2} - \frac{1}{\left(2\tilde{\mathcal{L}}\right)^{\ell_1+\ell_2+1}} \frac{\ell_1}{\ell_1+1} \frac{(\ell_1+\ell_2)!}{\sqrt{(\ell_1-m)!}\sqrt{(\ell_1+m)!}\sqrt{(\ell_2-m)!}\sqrt{(\ell_2+m)!}}\ .
\end{aligned} \tag{0.19}$$

Pour le modèle de plasma, à cause de la limite à basse fréquence du coefficient de Fresnel r_{TE}, l'expression analytique est plus compliquée et contient encore une intégrale sur la variable $\cos\theta$.

Limite grande distance

On considère ensuite la limite grande distance ($L \gg R$), pour laquelle il est possible de montrer que l'on peut tronquer le développement multipolaire à $\ell_{\max} = 1$ sans modifier le résultats de la formule de diffusion. En outre, à grande distance la réflexion simple dans la cavité donne une

contribution beaucoup plus grande que les réflexion multiples, on peut donc remplacer $\ln\det\mathcal{D}$ par $-\mathrm{Tr}\mathcal{N}$, l'intégrant pour la formule de diffusion devient alors :

$$\begin{aligned}\Phi(\imath\xi) &= 2{\sum_m}' \ln\det\mathcal{D}^{(m)}\left(\tilde{\xi}\right)\\ &\simeq -\left(\mathcal{N}^{(0)}_{EE}(\tilde{\xi})\right)_{(1,1)} - \left(\mathcal{N}^{(0)}_{MM}(\tilde{\xi})\right)_{(1,1)} - 2\left(\mathcal{N}^{(1)}_{EE}(\tilde{\xi})\right)_{(1,1)} - 2\left(\mathcal{N}^{(1)}_{MM}(\tilde{\xi})\right)_{(1,1)} .\end{aligned} \tag{0.20}$$

Le régime grande distance permet donc une approximation dipolaire avec réflexion simple du développement multipolaire mulitdiffusif. En explicitant chaque terme dans les matrices $\mathcal{N}$, et en observant que $(L \gg R)$ entraîne $\tilde{\xi} \ll 1$ dans les coefficients de Mie, on obtient finalement, selon le modèle utilisé pour décrire les miroirs :

$$\begin{aligned}\Phi^{\mathrm{perf}}_{\mathrm{LD}}(\tilde{\xi}) &= -\frac{3}{4}\frac{1}{\tilde{\mathcal{L}}^3}\left(1+2\tilde{\xi}\tilde{\mathcal{L}}+2\left(\tilde{\xi}\tilde{\mathcal{L}}\right)^2\right)e^{-2\tilde{\xi}\tilde{\mathcal{L}}}\\ \Phi^{\mathrm{plas}}_{\mathrm{LD}}(\tilde{\xi}) &= \left(1+\frac{1}{\alpha^2}-\frac{\coth\alpha}{\alpha}\right)\Phi^{\mathrm{perf}}_{\mathrm{LD}}(\tilde{\xi})\\ \Phi^{\mathrm{Drud}}_{\mathrm{LD}}(\tilde{\xi}) &= \frac{2}{3}\Phi^{\mathrm{perf}}_{\mathrm{LD}}(\tilde{\xi})\end{aligned} \tag{0.21}$$

où $\alpha = 2\pi\frac{R}{\lambda_P}$, et l'on a fait l'hypothèse supplémentaire que $(R \ll \lambda_P)$ pour le modèle de plasma, et les deux hypothèses $\left(L \gg \frac{\lambda_P^2}{\lambda_\gamma}\right)$ et $\left(L \gg \frac{R^2\lambda_\gamma}{\lambda_P^2}\right)$ pour le modèle de Drude. Ces résultats montrent que la limite asymptotique à grande distance a la même forme, et donc les mêmes propriétés, pour les trois modèles de miroirs, moyennant une multiplication par un facteur $\frac{2}{3}$ pour le modèle de Drude, et par $f(\alpha) = 1 + \frac{1}{\alpha^2} - \frac{\coth\alpha}{\alpha}$ pour le modèle plasma, fonction croissante de α prenant des valeurs entre $\frac{2}{3}$ et 1, comme illustré par le graphique de gauche de la figure 5.

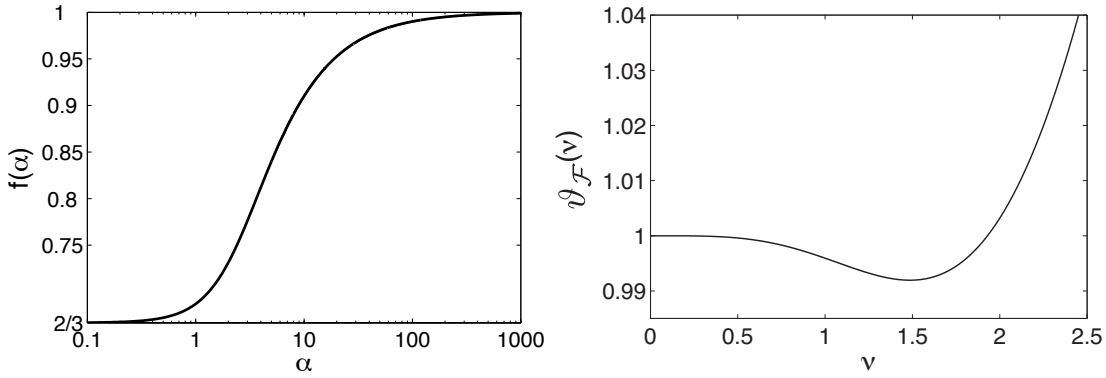

Figure 5: (gauche) Fonction $f(\alpha) = 1 + \frac{1}{\alpha^2} - \frac{\coth\alpha}{\alpha}$. (droite) Facteur correctif thermique $\vartheta_{\mathcal{F}}$ pour l'énergie libre de Casimir, en fonction de $\nu = 2\pi\frac{\mathcal{L}}{\lambda_T}$.

À température nulle l'intégration de $\Phi(\tilde{\xi})$ donné par les équations 0.21 donne l'énergie de Casimir E_{LD}, tandis qu'à température non-nulle, une somme sur les fréquences de Matsubara permet d'obtenir l'énergie libre $\mathcal{F}_{\mathrm{LD}}$. Dans le cas des miroirs parfaits, on obtient alors :

$$\begin{aligned}E^{\mathrm{perf}}_{\mathrm{LD}} &= -\frac{9\hbar c R^3}{16\pi\mathcal{L}^4}\\ \mathcal{F}^{\mathrm{perf}}_{\mathrm{LD}} &= -\frac{3\hbar c R^3}{4\lambda_T\mathcal{L}^3}\phi\left(\frac{2\pi\mathcal{L}}{\lambda_T}\right) \quad \text{avec} \quad \phi(\nu) = \frac{\nu\sinh\nu+\cosh\nu\left(\nu^2+\sinh^2\nu\right)}{2\sinh^3\nu} .\end{aligned} \tag{0.22}$$

On retrouve alors bien $\mathcal{F}_{\mathrm{LD}}^{\mathrm{perf}}(T=0) = E_{\mathrm{LD}}^{\mathrm{perf}}$, et le changement en l'énergie dû à la température peut être mesuré grâce au facteur correctif thermique $\vartheta_{\mathcal{F}} = \frac{\mathcal{F}(T)}{\mathcal{F}(0)}$, qui est présenté dans le graphique de droite de la figure 5. On observe en particulier que ce ratio passe par un minimum inférieur à 1 pour des distances intermédiaires, ce qui implique pour certaines valeurs des paramètres une contribution répulsive des photons thermiques à la force de Casimir, ainsi que des valeurs négatives pour l'entropie de Casimir.

4. Résultats à température nulle

Miroirs parfaits

Nous étudions d'abord le cas le plus simple où la température est nulle et les miroirs parfaitement réfléchissants. L'effet Casimir ne dépend alors que du rayon R de la sphère et de la distance L entre le plan et le sommet de la sphère le plus proche du plan, et peut donc s'écrire comme une fonction du rapport d'aspect $\frac{L}{R}$. Nous vérifions dans un premier temps que les quantités calculées par la méthode PFA sont obtenues à la limite des petits rapports d'aspect, tandis que dans l'autre limite, les résultats convergent vers la formule analytique calculée plus haut. Ceci est illustré par le graphique de gauche de la figure 6, et l'on voit que pour des valeurs intermédiaires de $\frac{L}{R}$, un traitement multipolaire complet est nécessaire.

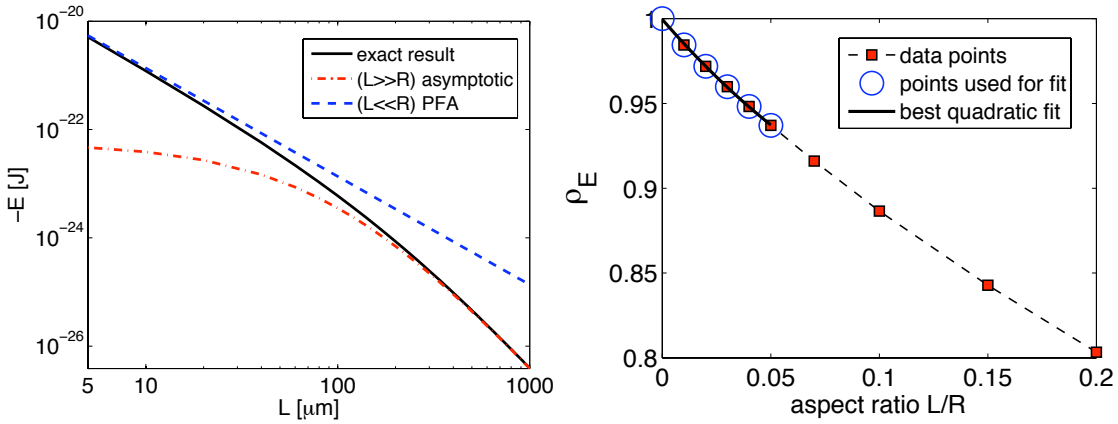

Figure 6: (gauche) Énergie de Casimir à température nulle pour des miroirs parfaits, en fonction de la distance L. Les résultats numériques obtenus avec notre méthode sont présentés en noir, l'approximation PFA est présentée en tirets bleus, et la formule analytique à grande distance est présentée en tirets rouges. Le rayon de la sphère est $R = 100$ μm. (droite) Méthode d'extrapolation du ratio ρ_E aux courtes distances. Les carrées rouges représentent les données calculées numériquement, les cercles bleus indiquent les points utilisés pour la détermination du fit polynomial, et ce dernier est présenté en noir.

Dans un second temps, nous utilisons ces résultats pour estimer l'erreur de l'approximation PFA, à l'aide du ratio $\rho_E = \frac{E}{E_{\mathrm{PFA}}}$ de l'énergie de Casimir E obtenue numériquement, normalisée par la quantité correspondante calculée avec l'approximation PFA. Les résultats obtenus pour les plus petites valeurs de $\frac{L}{R} \geq 0.01$ sont ensuite extrapolées à la limite des courtes distances à 1 grâce à un fit polynomial, comme illustré dans le graphique de droite dans la figure 6. La pente du fit polynomial à l'origine est le terme linéaire β_E du développement de Taylor pour ρ_E aux petites distances décrit dans l'équation (0.10). Nous obtenons alors la valeur $\beta_E = -1.47$, correspondant à $\beta_G = \frac{\beta_E}{3} = -0.49$ pour le gradient de la force de Casimir, ce qui semble être en contradiction avec la borne $|\beta_G| < 0.4$ obtenue par des travaux expérimentaux.

Miroirs métalliques

Sont ensuite étudiés les miroirs métalliques à température nulle, à l'aide des modèles de plasma et de Drude. Afin de mesurer l'effet de la réflexion imparfaite sur l'effet Casimir, on utilise le facteur de correction $\eta_E^P = \frac{E^{\text{metal}}}{E^{\text{perf}}}$. Dans la géométrie plan-plan, et pour les deux modèles métalliques, celui-ci est croissant avec la distance, et tend vers 1 à la limite des grandes distances, comme illustré par le graphique de droite dans la figure 1. Les résultats dans la géométrie sphère-plan sont qualitativement différents, comme illustré par la figure 7. Pour le modèle plasma (graphique de gauche), la limite du facteur de correction η_E^P aux grandes distances est proche de 1 pour les grandes sphères, mais diminue progressivement jusqu'à $\frac{2}{3}$ pour des sphères plus petites. Cette observation est en accord avec la fonction $f(\alpha)$ calculée analytiquement dans la partie précédente. Pour le modèle de Drude, le facteur de correction η_E^P n'est plus monotone, et présente un maximum avant de tendre vers la valeur $\frac{2}{3}$, quelque soit la valeur du rayon. Ce résultat est lui aussi en accord avec les calculs analytiques aux grandes distances. Ces différences du comportement du facteur η_E^P quand la géométrie change sont la signature de l'existence de corrélations entre les effets de la géométrie et de la réflexion imparfaite sur l'effet Casimir.

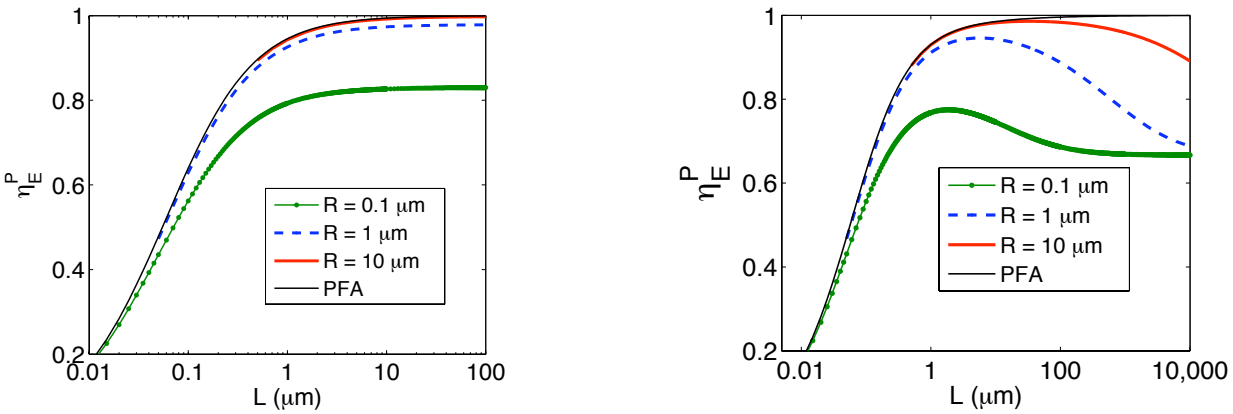

Figure 7: Facteur correctif η_E^P pour la réflexion imparfaite en fonction de la distance L pour plusieurs tailles de sphères, avec l'utilisation d'un modèle plasma à gauche, et d'un modèle de Drude à droite.

Ces corrélations ont une influence sur la précision de l'approximation PFA, comme illustré par le graphique de gauche de la figure 8, représentant le ratio ρ_E pour plusieurs tailles de sphères, quand le modèle de Drude est utilisé. Pour l'énergie de Casimir E, ce facteur est plus petit que pour des miroirs parfaits, et l'erreur de l'approximation PFA est donc augmentée par la prise en compte de la conductivité finie des métaux. Pour le gradient de la force G en revanche, le ratio ρ_G n'a plus la même forme et une inflexion apparaît aux courtes distances, ce qui a pour effet de diminuer considérablement la valeur absolue de la pente initiale ($\beta_G \simeq -0.2$) par rapport au cas des miroirs parfaits. Cette inflexion est illustrée sur le graphique de droite de la figure 8, et permet de résoudre le désaccord entre la borne expérimentale et la valeur obtenue précédemment pour des miroirs parfaits.

5. Résultats à température non-nulle

Miroirs parfaits

On introduit ensuite l'effet de la température non-nulle grâce à la formule de Matsubara. On considère dans un premier temps le cas des miroirs parfaits uniquement, afin de simplifier l'étude de l'influence thermique sur l'effet Casimir. Cette influence est mesurée par le facteur de correction

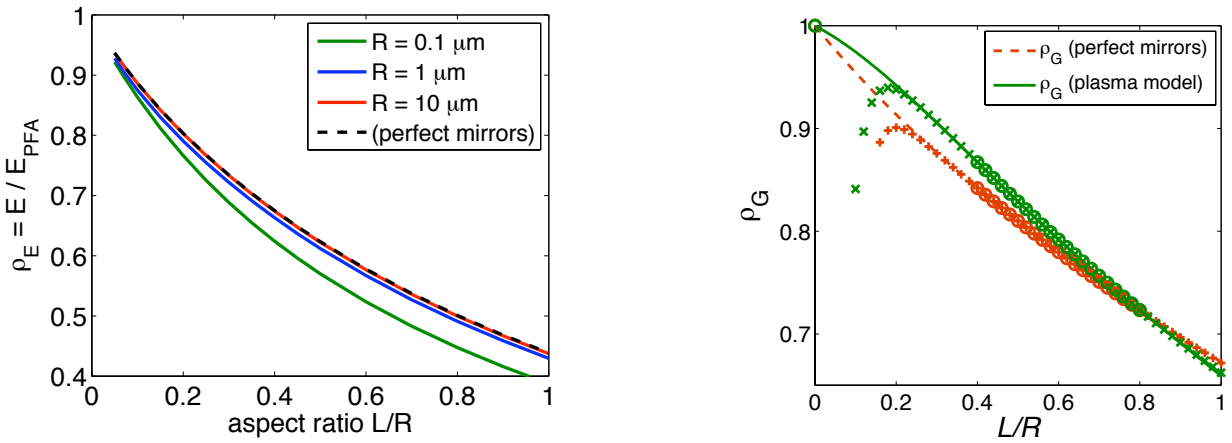

Figure 8: (gauche) Ratio $\rho_E = \frac{E}{E_{\mathrm{PFA}}}$ pour différentes tailles de sphères, en fonction du rapport d'aspect $\frac{L}{R}$. Les matériaux sont décrits par le modèle de Drude, le résultat obtenu avec des miroirs parfaits est présenté en tirets noirs. (droite) Ratio $\rho_G = \frac{G}{G_{\mathrm{PFA}}}$ en fonction du rapport d'aspect $\frac{L}{R}$, et son extrapolation polynomiale aux courtes distances. Les courbes rouges représentent le cas des miroirs parfaits, les courbes vertes celui d'un miroir métallique.

thermique $\vartheta_F = \frac{F(T)}{F(0)}$ qui compare la force à température T à celle à température nulle. Dans la géométrie plan-plan, ce facteur est croissant avec la distance, tendant vers l'unité à courte distance, et divergent en L pour les grandes distances. Les résultats obtenus dans la géométrie sphère-plan, présentés dans le graphique de gauche de la figure 9, sont qualitativement différents : le facteur correctif ϑ_F est toujours inférieur à celui obtenu par l'approximation PFA, dépend du rayon de la sphère R, et pour des petites sphères il présente même un minimum inférieur à 1. Cette dernière observation est confirmée par le calcul analytique à grande distance ($R \ll L$), qui permet d'obtenir le même comportement, comme illustré par le graphique de droite dans la figure 5.

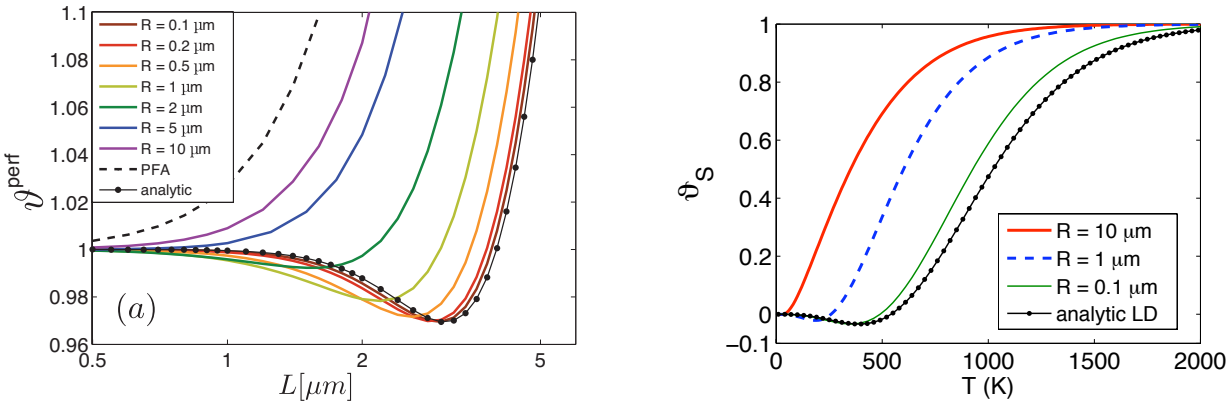

Figure 9: (gauche) Facteur de correction thermique ϑ_F pour la force de Casimir en fonction de la distance L. Le résultat PFA est indiqué en tirets, la formule analytique pour les grandes distances est représentée par la ligne avec points, le résultat exact est présenté pour plusieurs tailles de rayon par des traits pleins de différentes couleurs. (droite) Entropie de l'interaction de Casimir en fonction de la température, normalisée par l'entropie à température infinie.

Les photons thermiques ont alors une contribution répulsive à la force de Casimir, ce qui constitue

une observation inédite dans le cas des miroirs parfaits, et est la signature d'une corrélation non-triviale entre les effets de la température et de la géométrie. Ce phénomène peut être également mis en évidence avec l'étude de l'entropie d'interaction de Casimir $S = -\frac{\partial \mathcal{F}}{\partial T}$, qui peut prendre des valeurs négatives pour des températures suffisamment basses, comme illustré dans le graphique de droite de la figure 9. Dans la géométrie plan-plan, ces valeurs négatives pour l'entropie n'apparaissent qu'avec l'utilisation d'un modèle de Drude pour la description des miroirs, ce qui a donné lieu à des discussions sur la validité de ce modèle. Avec la géométrie sphère-plan, nous montrons que l'apparition de valeurs négatives pour l'entropie est également possible avec des miroirs parfaits, où ils sont un effet de la géométrie et non de la dissipation.

Ces corrélations entre les effets de la température et de la géométrie ont une influence sur la précision de l'approximation PFA. En effet, comme illustré par le graphique de gauche de la figure 10, le ratio ρ_E dépend du régime thermique, qui est caractérisé par le paramètre $\alpha_T = \frac{2\pi L}{\lambda_T}$. Les petites valeurs de α_T correspondent à la limite basse température, les grandes valeurs à la limite haute-température. Les valeurs de $\rho_{\mathcal{F}}$ décroissent avec la température, ce qui signifie que l'erreur de l'approximation PFA est aggravée lorsque la température augmente. Cette aggravation sature dans le régime des hautes températures, lorsque $\alpha_T \gtrsim 5$. Cette dépendance du ratio $\rho_{\mathcal{F}}$ au

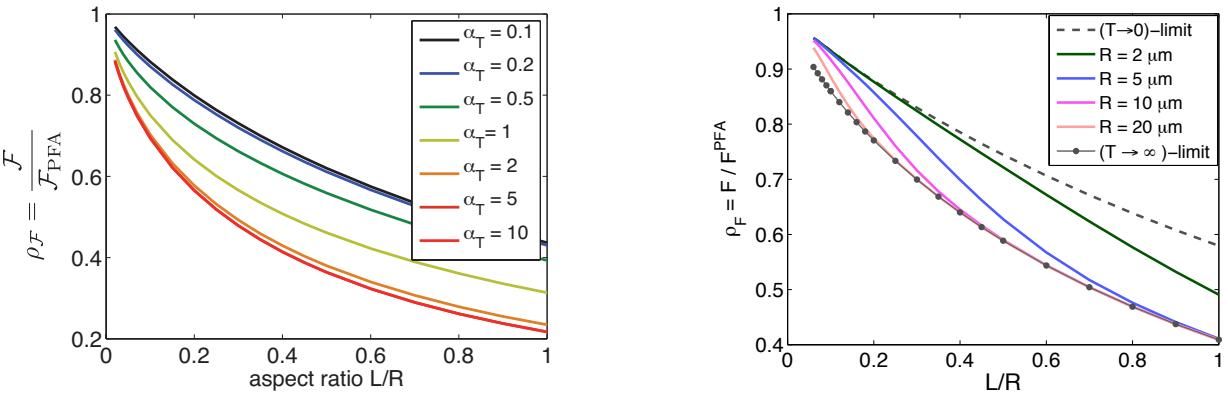

Figure 10: (gauche) Ratio $\rho_{\mathcal{F}} = \frac{\mathcal{F}}{\mathcal{F}_{\rm PFA}}$ en fonction du rapport d'aspect $\frac{L}{R}$. Les différentes valeur de $\alpha_T = 2\pi\frac{L}{\lambda_T}$ représentent différent régimes thermiques. (droite) Ratio $\rho_F = \frac{F}{F_{\rm PFA}}$ en fonction du rapport d'aspect $\frac{L}{R}$, pour différentes valeurs du rayon R de la sphère.

régime thermique empêche d'avoir une détermination simple du terme linéaire β de la correction à courtes distances. En effet, comme illustré par le graphique de droite de la figure 10, pour un rayon R fixé de la sphère, lorsque le rapport d'aspect diminue, la distance diminue, et le régime thermique change pour se rapprocher du régime des basses températures.

Miroirs métalliques

On étudie ensuite l'effet Casimir pour des miroirs métalliques à température non-nulle. On regarde tout d'abord l'effet de la température sur l'énergie libre, à l'aide du facteur de correction thermique $\vartheta_{\mathcal{F}} = \frac{\mathcal{F}(T)}{\mathcal{F}(0)}$, pour des miroirs parfaits et décrits par un modèle de Drude. L'étude de ce paramètre, présentée sur le graphique de gauche de la figure 11 pour une sphère de rayon $R = 1$ μm en fonction de la distance L, montre que ces deux modèles de miroirs, parfait et imparfaits, donnent des résultats très différents. Ceci est la signature de couplages apparaissant entre les effets thermiques et de conductivité finie. En comparaison avec le cas plan-plan, donné ici en tirets par l'intermédiaire du résultat de l'approximation PFA, les courbes correspondant aux miroirs parfaits et imparfaits sont plus proches, ceci étant particulièrement visible aux distances courtes.

Un autre angle de vue est d'étudier l'effet de la réflexion imparfaite sur les miroirs, grâce au

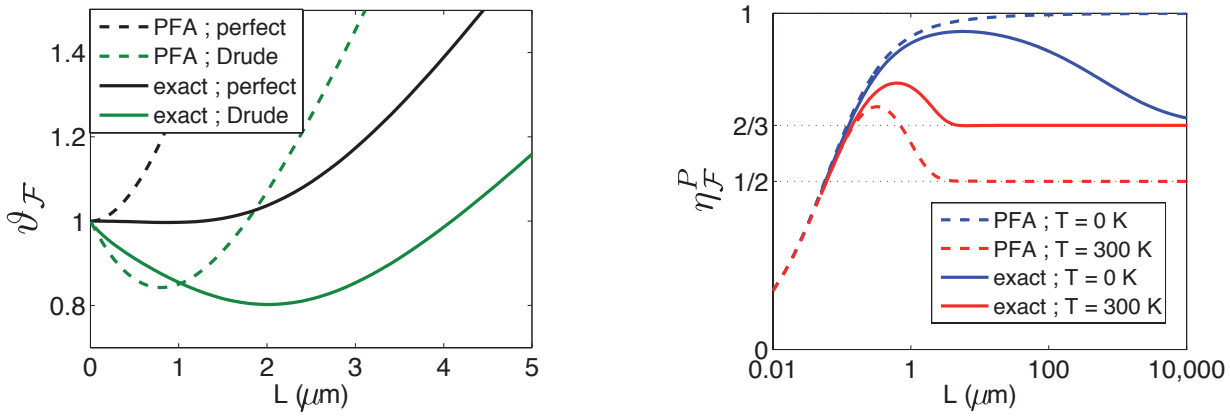

Figure 11: (gauche) Facteur correctif thermique $\vartheta_{\mathcal{F}}$ en fonction de la distance L, pour les résultats de l'approximation PFA (tirets) et de notre calcul numérique (traits pleins). Le cas des miroirs décrits par un modèle de réflecteurs parfaits est présenté en noir, celui des miroirs décrits par un modèle de Drude en vert. Le rayon de la sphère est $R = 1\mu$m, la température ambiante est $T = 300$ K. (droite) Facteur correctif $\eta^P_{\mathcal{F}}$ pour les effets de conductivité finie en fonction de la distance L, pour les résultats de l'approximation PFA (tirets) et de notre calcul numérique (traits pleins). Le cas à température nulle est présenté en bleu, le cas à température ambiante en rouge. Le rayon de la sphère est $R = 1\mu$m, la température ambiante est $T = 300$ K.

facteur correctif de conductivité $\eta^P_{\mathcal{F}}(T) = \frac{\mathcal{F}^{\mathrm{Drud}}(T)}{\mathcal{F}^{\mathrm{perf}}(T)}$, à température nulle et ambiante. L'étude de ce paramètre, présentée sur le graphique de droite de la figure 11 pour une sphère de rayon $R = 1$ μm en fonction de la distance L, montre que ces deux courbes, à températures nulle et ambiante, sont différentes, comme c'était le cas pour la géométrie plan-plan, rappelée par l'intermédiaire du résultat PFA en tirets. Ceci est à nouveau la signature de couplages entre les effets thermiques et de conductivité finie. Dans la géométrie sphère-plan, la limite à grande distance du facteur $\eta^P_{\mathcal{F}}(T)$ est la même $\left(\frac{2}{3}\right)$ pour les deux températures, alors qu'elles diffèrent dans la configuration plan-plan, avec les valeurs 1 à température nulle et $\frac{1}{2}$ à température ambiante.

Cette différence à grande distance a un effet sur la comparaison de la force de Casimir obtenue pour un modèle de plasma sans dissipation, et de celle pour un modèle de Drude dissipatif. À température ambiante, le rapport de ces deux quantités dans la géométrie plane-plan tend vers la valeur 2 à la limite des grandes distances, ce qui a donné lieu à d'importantes discussions au cours des dix dernières années. Nous montrons que dans la géométrie sphère-plan, ce rapport tend vers une valeur proche de $\frac{3}{2}$ pour des grandes sphères, et peut être encore plus faible pour des sphères de tailles intermédiaires et plus petites. Cette différence est illustrée pour différentes tailles de sphères par la figure 12.

Conclusion

Dans cette thèse nous avons étudié l'interaction de Casimir entre une sphère et un plan infini, pour une température arbitraire et avec une description optique des miroirs permettant de rendre compte de la conductivité finie des matériaux. L'évaluation de l'effet Casimir, nécessaire à cette étude, a été réalisé grâce à la formule de diffusion, basée sur la théorie des réseaux optiques, adaptée à la configuration sphère-plan. Cette adaptation prend la forme d'un développement multipolaire, en utilisant les ondes électromagnétiques sphériques pour décrire la réflexion sur la sphère. Numériquement, ce développement doit être tronqué à un valeur maximale $\ell_{\max}$, ce qui rend cette méthode particulièrement bien adaptée aux valeurs intermédiaires et grandes du rapport

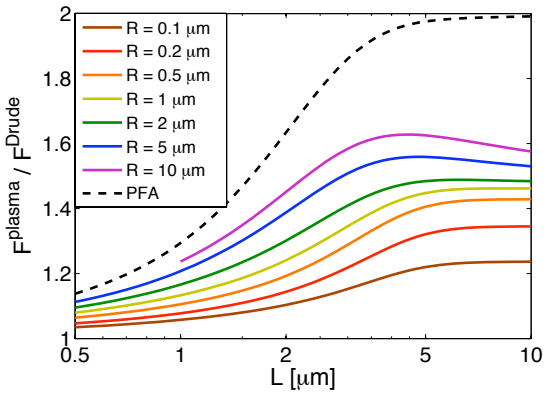

Figure 12: Rapport de la force de Casimir calculée avec un modèle plasma non-dissipatif pour les deux miroirs, par la force calculée avec un modèle de Drude dissipatif, en fonction de la distance L. Le résultat de l'approximation PFA est indépendant du rayon R et est présenté en tirets. Le résultat de nos évaluations numériques est présenté sous différentes couleurs selon la valeur du rayon de la sphère.

d'aspect ($\frac{L}{R} \gtrsim 1$). Grâce à des efforts numériques, nous somme néanmoins arrivés à atteindre des rapports d'aspect de 0.01 en repoussant la troncation jusqu'à $\ell_{\max} = 520$. Ces évaluations permettent d'estimer l'erreur commise par les méthodes d'approximation, comme par exemple l'approximation de proximité (PFA), mais aussi de sonder la dépendance de l'effet Casimir à la géométrie dans des conditions variées de température et de nature des matériaux.

À température nulle, nous mesurons l'erreur commise par l'approximation de proximité dans le cas des miroirs parfaits et obtenons des résultats différents de ceux calculés avec un champ scalaire, ce qui montre l'importance d'un traitement électromagnétique dans cette géométrie où les polarisations sont couplées. Pour des miroirs métalliques nous observons des corrélations entre les effets de la géométrie et de la conductivité finie, qui modifient considérablement l'erreur commise par l'approximation de proximité. Il en résulte une modification du terme linéaire de la correction géométrique pour le gradient de la force β_G, qui redevient en accord avec la borne expérimentale.

Pour un plan et une sphère parfaitement réfléchissants à température ambiante, nous observons de fortes corrélations entre les effets de la géométrie et de la température, pouvant changer qualitativement la dépendance de l'effet Casimir à la température. En effet, pour de petites sphères, nous montrons pour certaines distances une contribution répulsive des photons thermiques à la force de Casimir, ainsi que des valeurs négatives de l'entropie. Ces résultats sont corroborés par un calcul analytique dans le régime des grandes distances ($R \ll L$), et montrent que les valeurs négatives de l'entropie ne sont pas seulement causées par la dissipation, mais peuvent également apparaître comme effets de la géométrie.

Dans le cas des miroirs métalliques à température ambiante, de nombreuses corrélations apparaissent entre les effets de la géométrie, de la température et de la conductivité finie. Une des conséquences est le changement du ratio $\frac{F^{\text{plas}}}{F^{\text{Drud}}}$ dans la limite des grandes distances par rapport à la configuration plan-plan, qui passe de 2 à une valeur dépendante de R comprise entre 1 et $\frac{2}{3}$.

Cette étude montre qu'un traitement électromagnétique complet, incluant de manière directe et simultanée la géométrie exacte, la température et la description des miroirs, est nécessaire pour obtenir une prédiction théorique fiable de l'effet Casimir entre une sphère et un plan. Cette configuration constitue en effet un bon exemple de situation où des changements importants de la dépendance de l'effet Casimir aux conditions physiques apparaissent à cause de la géométrie.

Introduction

The classical vacuum

In the history of sciences, the concept of vacuum has often been a matter of debate [1, 2], mainly because of its philosophical, religious, and metaphysical implications. Already in the beginning of the 5$^{\text{th}}$ century BCE, the atomists Leucippus and Democritus hold that everything is composed by atoms, and that between them lies the vacuum (or nothingness), in which movement takes place [3, 4]. In the same century, Parmenides defines the vacuum as a lack of being. Using an ontological argument, he shows that vacuum cannot exist [5, 6]. Plato adds to this idea that, as all physical things are instantiations of an ideal in the sensible world, the existence of vacuum would need an ideal form of vacuum, which he cannot conceive as reasonable. As for him, Aristotle considers the vacuum as impossible to be created, arguing that nothing cannot be obtained from something.

In medieval Europe the concept of vacuum itself was considered as heretic, as it implies the absence of God [7]. In the beginning of the 17$^{\text{th}}$ century, Galileo nevertheless introduced the vacuum in its mechanical laws, as the limit of a non-frictious medium, when studying the acceleration of falling objects [8]. Descartes [9, II; 16] in 1644 rejects the theory of vacuum: as he refuses the distinction between object and space, and states that the existence of the object implies the existence of space, he deduces the impossibility of vacuum. The same year Toricelli [10] remarked that mercury only goes up by 760 mm when pumped in a tube, a phenomenon that Pascal [11, 12] explained a few years later by the existence of an atmospheric pressure. Against the common idea that "matter hates vacuum", he shows that vacuum appears in the upper space of the tube when the liquid is pumped.

In 1801, while Newtonian physics had successfully described light as tiny particles moving in vacuum for years, the appearance of interference effects in Young's diffraction experiment [13] gives evidence of the wave nature of light, already predicted by Hooke [14] and Huygens [15] in the 17$^{\text{th}}$ century, and foreseen by Euler [16] in the 18$^{\text{th}}$ century. Sound is a vibration of the air, and light propagates in the vacuum, the scientist therefore assume that light must have a proper vibrating media, which they call the luminiferous aether [17].

In 1887, the Michelson-Morley experiment [18, 19] aiming at measuring the speed of the aether with respect to the earth turned out to be inconclusive. The solution came from Einstein special relativity [20], which disproves the existence of an aether. The light is then described as a wave of the electromagnetic field $(\mathbf{E}, \mathbf{B})$, travelling in vacuum at an equal velocity c for any direction, and in any unaccelerated frame, following the Maxwell equations [21]. Finally, the classical vacuum can be defined as space when all matter has been removed and when the electromagnetic field is zero:

$$\text{Classical vacuum:} \quad \mathbf{E} = \mathbf{B} = \mathbf{0} \ .$$

The quantum vacuum

The advent of Quantum Theory has deeply changed our understanding of many basic physical concepts such as light, matter, and movement. One example of a new idea brought by Quantum Theory is the Heisenberg uncertainty[2] principle [22], stating the impossibility of measuring the position x and the momentum p_x of a particle with an unlimited accuracy:

$$\Delta x \cdot \Delta p_x \geq \frac{\hbar}{2}$$

where Δx and Δp_x are the indetermination of x and p_x, respectively, and $\hbar$ is the reduced Planck's constant. For the simple case of a harmonic oscillator model, such as a mass attached to a spring,

[2] The Heisenberg principle can also be called the *indeterminacy* principle. In [22], Heisenberg used the word *Unbestimmtheit*, which has then been translated to *uncertainty* in [23], wrongfully according to many epistemologists [24, 25].

this leads to the impossibility for the objet to stand still in a lower position with no oscillations. The configuration with the minimum of movement is then a tiny rocking, associated to a non-zero energy $E_0 > 0$.

In Quantum Field Theory, each mode of frequency ω of the electromagnetic field can be described as a harmonic oscillators [26, 27, 28]. The Heisenberg uncertainty principle can then be applied, and yields that the electromagnetic field must undergo unavoidable fluctuations around zero, and that the electromagnetic energy cannot decrease below a zero-point energy $E_0 = \frac{\hbar\omega}{2}$. In opposition to the classic vacuum, the electromagnetic fields are not zero anymore, but rather fluctuate around 0:

$$\text{Quantum vacuum:} \quad \overline{\mathbf{E}} = \overline{\mathbf{B}} = \mathbf{0} \qquad \text{but} \qquad \overline{\mathbf{E}^2}, \overline{\mathbf{B}^2} > 0$$

where $\overline{\mathbf{E}}$ is the average of $\mathbf{E}$ over time. Quantum Theory has changed dramatically our conception of vacuum, as an active and dynamic media, undergoing fluctuations of the electromagnetic field and creation of particle pairs. The discontinuity between matter (or light) and vacuum has been removed, and philosophically speaking, the concept of vacuum now lies much closer to the being than to the nothingness.

The Casimir effect

The van der Waals force [29] describes the interaction between neutral atoms or molecules, and plays a crucial role in colloid chemistry, nanotechnologies and surface science. An important contribution to this interaction is done by the London dispersion forces [30, 31, 32, 33], arising from quantum induced instantaneous polarization multipoles in molecules.

Studying the stability of colloids, Verwey and Overbeek observed [34] that the van der Waals-London interaction seems to decrease at long range more rapidly than the L^{-6} predicted power-law. Overbeek pointed out that forces need time to propagate, while van der Waals-London forces were derived by considering instantaneous interactions. In 1946 Casimir and Polder manage to include the effects of retardation [35], which becomes non-negligible for large distances and change the power-law in the distance from L^{-6} to L^{-7}. In their work they also include the situation of an atom facing a perfectly reflecting surface, taken "as a preliminary exercice" [36], bearing the famous Casimir-Polder potential:

$$E_{\text{CP}} = -\frac{3\hbar c\alpha}{8\pi L^4}$$

where α is the atomic polarizability. The obtained formula are simple and elegant and Casimir was sure that there should be an elegant way to derive them. Advised by Bohr [36], Casimir interpreted the retarded van der Waals-London interaction as an effect of the quantum vacuum zero-point energy [37]. He also realised in 1948 that his founding could be applied to the case of two perfectly reflecting parallel mirrors [38], and obtained the energy per unit area:

$$\frac{E_{\text{Cas}}}{A} = -\frac{\hbar c\pi^2}{720L^3} \ ,$$

giving birth to the famous Casimir effect, an observable manifestation of quantum vacuum fluctuations in the macroscopic world [39]. In this formula, the mixture of Maxwell's electromagnetism and Quantum Theory in the Casimir effect is clearly illustrated by the two terms c and $\hbar$.

Applications

The Casimir force is the most accessible experimental effect of vacuum fluctuations in the macroscopic world. As the non-zero vacuum energy is known to raise serious difficulties at the interface

of quantum theory and gravitational effects, it is worth investigating the Casimir effect with the greatest care and highest accuracy, in order to test the predictions of Quantum Field Theory [40, 41, 42, 43, 44, 45, 46, 47, 48, 49] and its connection with the problem of zero-point energy [50, 44, 51, 52].

Moreover, in various accurate force measurements in the nanometer to micrometer range, the Casimir effect becomes the dominant force and a precise knowledge of its magnitude is often a key point. The most obvious case are the tests of Newtonian gravity [53, 54, 55, 56, 57, 58, 59, 60, 61, 62], and the search for new weak forces predicted in theoretical unification models in the nanometric to millimetric range [63, 64, 65, 66, 67, 68, 69, 70]. Assuming a corrective term to the Newtonian gravity in the Yukawa form:

$$U(L) = G\frac{m_1 m_2}{L}\left(1 + \alpha e^{-\frac{L}{\lambda}}\right) \ ,$$

those studies aim at giving constraints on the possible range λ and relative amplitude α.

Various other experiments have their results "contaminated" by the Casimir effect. For molecular interferometry [71, 72, 73, 74, 75, 76], because of the increased size and the reduced speed of the molecules, the Casimir attraction to the grating deviates the molecules when it passes through the grating, leading to an effective smaller slit width. In some cases, the Casimir interaction is too strong [77, 78] and has to be avoided, for instance with the use of light gratings [79]. In **Section 12** (p.158) we will mention the study the intriguing phenomenon of small heating of ultracold neutrons (UCNs) in traps [80, 81, 82], for which an accurate knowledge of the quantum states of nanospheres interacting with surfaces is needed. As we will see, this has to be done through a careful treatment of the Casimir potential undergone by the nanospheres.

Finally, because the Casimir and van der Waals forces are dominant at the scale of the micrometer and below, they enter various important domains such as atomic and molecular physics, condensed matter and surface physics, chemical and biological physics, and micro and nanotechnologies [83]. For the latter they are important in the architecture of micro and nano-oscillators (NEMS and MEMS), not only to avoid stiction [84, 85, 86, 87], but also to be used as an actuator [49, chap.8].

Experimental works

The first experiment to measure qualitatively the Casimir force is performed in 1958 by Sparnaay [88], using a spring balance to measure the force between two flat neutral metallic plates. The measurements were carried out for distances between 0.5 and 2 μm, and the poor experimental accuracy led the author to the conclusion that "the observed attractions do not contradict Casimir's theoretical prediction".

A major difficulty in the former experiment being to keep a good parallelism between the two plates, a first unambiguous measurement of the Casimir force could only be achieved twenty years later by van Blockland and Overbeek [89], by using a lens and a flat plate covered with chromium layers. The measurements were carried out for distances between 132 to 760 nm and led to an agreement with the theory that can be estimated around 25% [55]. Other early experimental efforts have measured the Casimir force in those years, such as [90, 91, 92, 93], the reader is referred to detailed and systematic reviews that may be found in [94, 40, 95, 41, 42, 55].

In the past years, a series of new measurements with improved accuracy have been possible thanks to new techniques. In 1997 Lamoreaux measured the Casimir force between a metallized sphere and a flat metallic plate, using a torsion pendulum [96, 97, 98, 99, 100] for distances between 0.6 and 6 μm with an agreement to theory that can be evaluated to 10% for the shortest distances [55]. For the largest distances, the weak magnitude of the force prevented the observation of temperature corrections.

A second precise measurement of the Casimir effect has been done in 1998 by Mohideen [101, 102, 103]. The experimental setup, presented in the left part of **Fig. 13**, consists on a

metallized sphere attached to the cantilever of an atomic force microscope (AFM), brought close to a metallic plate. The Casimir attraction between the sphere and the flat plate yields a bent of the cantilever, which is measured by the deflection of a laser beam on the top of the cantilever. The distance range, from 0.1 to 0.9 μm, is smaller than in the previous experiment, enabling an experimental accuracy at the level of 1%.

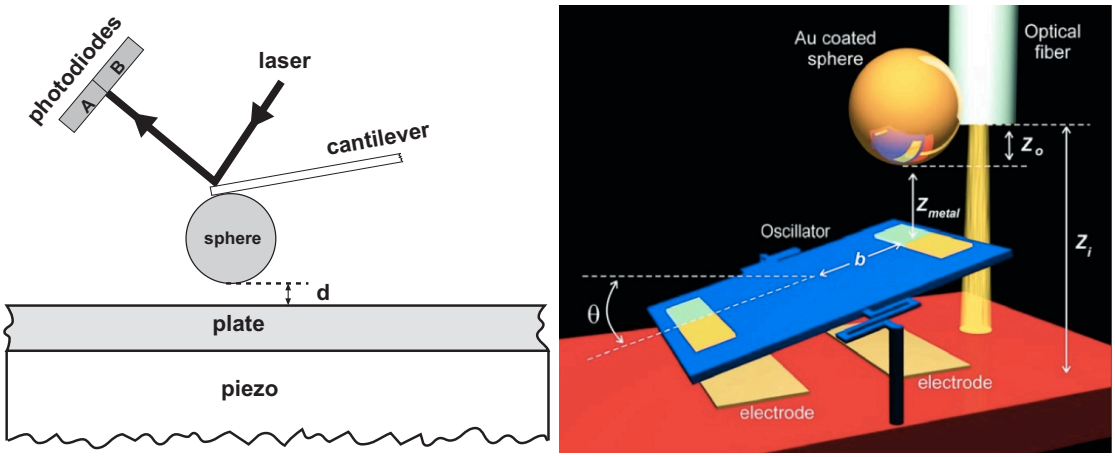

Figure 13: (left) Sketch of Mohideen's experiment. (right) Sketch of Decca's experiment.

In 2001 Capasso and his group measured the Casimir force gradient using a microelectromechanical system (MEMS) [85, 104] for distances between 0.1 and 1 μm. The presence of a polystyrene sphere with metallic coating close to a polysilicon plate, also with metallic coating, changes its oscillation frequency in agreement with the prediction from the Casimir effect.

With a similar technique, presented in the right part of **Fig. 13**, Decca carried out in 2003 one of the most precise experiment on the Casimir effect [105, 46, 106, 107, 60, 108], for distances between 0.2 and 2 μm. The experimental accuracy, below the percent level for small distances, enable to observe a discrepancy with the theory that the author attribute to a poor characterisation of the optical properties of the chosen materials. Moreover, the experimental data surprisingly seem to favour a description of metals by the loss-less plasma model, with respect to a description with the dissipative Drude model [107, 109]: the experimental points are closer to theoretical curves derived with the plasma model (see **Fig. 14**), and no thermal effect is observed at short distances as it should with the Drude model.

Very recently, Lamoreaux conducted another experiment [110, 111] with a torsion pendulum attached to a very large spherical lens, in order to measure the Casimir force for larger distances from 0.7 to 7 μm. The conclusions are opposite to the ones in [107], as the author reported that "the experimental results are in excellent agreement with the Casimir force calculated using the Drude model" and that "plasma model result is excluded in the measured separation range". Moreover, thermal effect in the Casimir force is clearly observed, thanks to the larger distance range.

With this review of experiments dedicated to the Casimir effect, we observe that the sphere-plane geometry is the configuration of the most precise measurements, and therefore the important one in the prospect of gravity tests. Some other configurations have been studied, such as non-parallel cylinders [112], corrugated plates [113, 114], or even the original Casimir configuration of two flat plates [115, 116, 117], for which an experimental accuracy of the order of 15% could be achieved for distances between 0.5 and 3 μm. This remark stresses the importance of the theoretical investigation of the sphere-plane configuration for accurate comparison between theory and experiments.

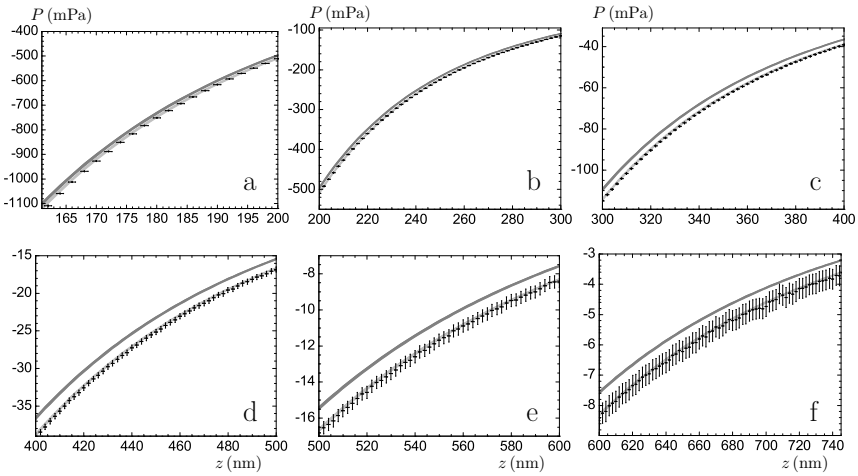

Figure 14: Comparison in [107] of the experimental data with theoretical predictions emerging from both the plasma model and the Drude model. The theoretical curve from the Drude model (upper grey line) is outside the experimental errors bars, while the theoretical curve from the plasma model is always within them.

Theoretical works

The original derivation of Casimir presented previously is done for the ideal situation of two perfectly reflecting infinite plates at zero temperature. In order to obtain reliable theoretical predictions to be compared with Casimir force measurements discussed above, one must then take into account realistic experimental conditions of various kinds.

The first imperfection in the experiments is the finite conductivity of the metallic plates used for the measurements, leading to an imperfect reflection. In 1956 Lifshitz [118, 119, 120] developed a theory of the Casimir effect for materials whose optical properties are described by a frequency-dependent permittivity $\varepsilon(\omega)$. For metals, this function can be found by fitting the optical data, obtained experimentally, with a plasma or a Drude model:

$$\varepsilon^{\text{plas}}(\omega) = 1 - \frac{\omega_P^2}{\omega^2} \qquad\qquad \varepsilon^{\text{Drud}}(\omega) = 1 - \frac{\omega_P^2}{\omega(\omega + \imath\gamma)}$$

where ω_P is the plasma frequency, accounting for high-frequency transparency, and γ is the relaxation frequency, accounting for dissipation in the metal. The plasma model is obtained when the dissipation is set to zero ($\gamma \to 0$), and the Drude model is considered as more realistic, as it meets the important property of finite static conductivity $\sigma_0 = \frac{\omega_P^2}{\gamma}$, and yields better fits of tabulated optical data [121, 122]. This improvement of the theory revealed itself crucial when comparing theory and experiments [94, 96, 101, 103, 112, 117, 105, 107, 123, 124, 125, 126, 127, 128, 129].

Another correction to the Casimir effect comes to the effect of thermal fluctuations, as experiments are performed at room temperature. The contribution of thermal fluctuations can be taken into account [130, 131, 132, 133] by changing the zero-point energy as:

$$E_0(T) = \hbar\omega\left(\frac{1}{2} + \overline{n}_\omega\right) \qquad\qquad \overline{n}_\omega = \frac{1}{e^{\frac{\hbar\omega}{k_B T}} - 1}$$

where the mean number of photons $\overline{n}_\omega$ is given by the Planck's law [134, 135, 136], and k_B is the Boltzmann's constant. Boström and Sernelius [137] were the first to notice in 2000 that a small but non-zero value of γ on the dielectric function $\varepsilon(\omega)$ of the material has a significant effect

on the Casimir energy evaluated at ambient temperature between two plates: the ratio between the predictions with perfect and imperfect reflectors reaches a factor 2 in the long-distance limit, because of the vanishing contribution of TE-polarized modes at zero frequency for dissipative metals. This remark, together with the fact that the Drude model leads to negative values of the Casimir entropy [138, 139, 140], led to a series of studies about the thermal effect on the Casimir force [141, 142, 143, 144, 145].

Finally, while the Casimir original formula describes the Casimir interaction of two infinite plates, most of the experiments described previously involve the geometry of a sphere in front of a plane. The proximity force approximation (PFA) [146, 147, 148] is commonly used to estimate the Casimir force in the sphere-plane geometry, and amounts to averaging the force calculated in the simpler plane-plane configuration over the distribution of local inter-plate distances. Its most common form reads: $F_{\rm PFA}(L,R) = 2\pi R \times E_{\rm PP}(L)$. This approximation is valid [149, 150, 151, 152] when the distance between the surfaces is much smaller than the sphere radius ($L \ll R$), but it is not expected to reproduce the complex dependance of the Casimir effect on geometry [153, 154, 155]. Moreover, PFA gives no information about its accuracy for a given non-zero aspect ratio $\frac{L}{R} > 0$. Numerous theoretical efforts have then been pushed beyond-PFA [149, 156, 157, 158, 159, 151, 160, 161, 162, 163, 164, 165, 166, 167, 168] in order to try to assess this accuracy. These works will be reviewed in **Section 9** (p.137).

In the past years, a great variety of numerical techniques have been developed [49, chap. 6] in order to evaluate the Casimir effect for various and complex configurations. Among them, let us mention:

- Worldline numerics [156, 169, 170, 157, 158, 171, 159, 172, 173, 174, 175] obtained by a Monte-Carlo simulation of path-integrals.

- The scattering approach [47] [49, chap.4] and equivalent $\mathbb{T}$-matrix formulations [166, 176] (for a complete review see [177]), which derives the Casimir interaction from the scattering operators of the objects in vaccum, and has been used in the plane-plane configuration to study the roughness [178, 179], the lateral Casimir force [180, 181, 182] and torque [183], or with corrugated plates [184, 185, 186, 187], to compare with experiments.

- And more recently, adaptations of classical methods for electromagnetism calculations to the Casimir problem [188, 189, 190, 191, 192, 193, 194, 195, 196, 197, 198, 199, 200, 201, 202, 203, 204, 205, 206].

Outline

This manuscript presents a theoretical investigation of the Casimir effect between a sphere and a plane, using the scattering approach. This geometry is the one of the most accurate experimental measurements, and a realistic theoretical evaluation – at non-zero temperature and which takes into account the finite conductivity of the objects – is an important step in the theory-experiments comparison topic. The aim of this study is also to investigate the rich dependence of the Casimir effect with the geometry: compared to the original plan-plane geometry, the sphere-plane configuration is a simple situation with finite size, curvature, non-specular scattering, and coupling of polarizations. All this features have an impact on the Casimir effect and its dependence to the thermal fluctuations and the finite conductivity, which will be explored.

In **part I**, we will recall the scattering approach in its most general form, and explicit its connection to the Casimir effect through the radiation pressure. The modelling of the imperfect refection of the objects and the inclusion of thermal fluctuations are also discussed. Finally, we will recall the main results obtained when applying it to the situation of two planes, and in particular the correlations appearing between the effects of temperature and of finite conductivity.

The scattering formula in the sphere-plane configuration is derived in **part II**, and the method to get all the quantities involved in the expression is given. The numerical difficulties when evaluating the Casimir energy are treated, and the choice of numerical methods are discussed and tested.

An analytical expansion is performed in **part III**, in order to express the Casimir interaction without any numerical evaluation for some limiting cases. The high-temperature regime is first tackled, with the help of a low-frequency expansion of the scattering formula. The long-distance regime is then analyzed, and found to exhibit an unexpected dependance of the Casimir effect on temperature.

The results of numerical evaluations for the general situation are given in **part IV** and **V**, organised by steps of more and more complex and realistic situations. **Part IV** is dedicated to the zero temperature case, and investigate the dependance of Casimir effect with the geometry, first for perfect reflectors, then with metallic mirrors for which the interplay between the effects of finite conductivity and geometry are studied. Information on the beyond-PFA correction and in the dependance of the energy with respect to the distance L and the radius R of the sphere are also given. The zero-temperature study closes with the application of dielectric nanospheres, in the prospect of studying their interaction with ultracold neutrons. In **part V** we switch to the non-zero temperature case, for perfect mirrors first, in order to study the effect of temperature on the Casimir effect and its correlations with the sphere-plane geometry. The complete picture with the inclusion of temperature, finite conductivity and dissipation in the material is finally presented, with a systematic study of the different correlations and its implication for theory-experiments comparison. A high-temperature numerical study closes the manuscript.

Part I.
Reminder on the use of the scattering formalism for Casimir computations, and example of the plane-plane geometry

Table of Contents

This first part is an introduction on the scattering approach for Casimir computations, which relates the Casimir energy to the scattering properties of the objects lying in vacuum. This method allow for a realistic description, with the inclusion of temperature and of finite conductivity in the materials. The scope of this introduction is not specific to the sphere-plane configuration and is rather general to the situation of any pair of facing objects. The plane-plane configuration is used as a simple example along this part, while the application to the sphere-plane geometry will be treated more specifically in the next part.

The scattering formalism for the Casimir energy is introduced in **Section 1** and an idea of its derivation is given through the radiation pressure. To do so, we will first introduce the electromagnetic modes of vacuum and the scattering operators in the cavity. At the end of this first section, we show how this formalism recovers the famous Casimir's expression [38] between two perfectly reflecting parallel mirrors at zero temperature.

The inclusion of a realistic description for the optical properties of the scatterers, with the help of a frequency dependent dielectric function $\varepsilon(\omega)$, is discussed in **Section 2**. For metallic materials, we present two models: the plasma one, which accounts for high-frequency transparency, and the Drude one, which additionally takes into account dissipation in the material. The case of dielectric materials is also treated. The effect of the finite conductivity on the Casimir effect is illustrated by a reminder of the results obtained in the plane-plane geometry [207, 208].

The inclusion of a non-zero temperature T in the scattering formula is treated in **Section 3**. Here we assume thermal equilibrium in the system, the temperature must then be uniformly the same for the two objects and the vacuum. The Matsubara formula is derived from the zero-temeprature scattering formula in the mathematical context of distribution theory. Again, the influence of temperature in the Casimir effect is illustrated by the plane-plane configuration, where the correlations between the effects of temperature and of finite conductivity are investigated.

Finally, in **Section 4**, we describe how the results obtained in the plane-plane configuration can be used to calculate the Casimir energy in the sphere-plane geometry, through the Proximity-Force Approximation (PFA). We will comment on the drawbacks of this method, its accuracy, and the way to measure it.

1 The Scattering formula

We are interested in the study of the Casimir interaction between two stationary objects, labelled 1 and 2, lying in vacuum, at thermal equilibrium. The two objects are not touching each other, and can be separated by a plane between them. The optical properties of object i is contained in the reflection operator $\mathcal{R}_i$ that expresses the scattered electromagnetic wave $|\text{ out}\rangle$ corresponding to an incoming wave $|\text{ in}\rangle$:

$$|\text{ out}\rangle = \mathcal{R}_i \,|\text{ in}\rangle \ . \tag{1.1}$$

The reflection operator $\mathcal{R}_i$ for the object i is written with respect to a reference point M_i, that is assumed to lie inside or at the border of object i. We define $\mathcal{T}$ the translation operator from one reference point to the other. For practical purpose the direction of the translation will be taken as the z-axis of Cartesian coordinates. As the objects are assumed to be separated, the translation will always be over a distance $\mathcal{L} > 0$. We restrict the relative displacement of the objects to the z-direction, and therefore the Casimir force F to its component in the z-direction, as an effect of the change of the Casimir free-energy $\mathcal{F}$ when $\mathcal{L}$ varies.

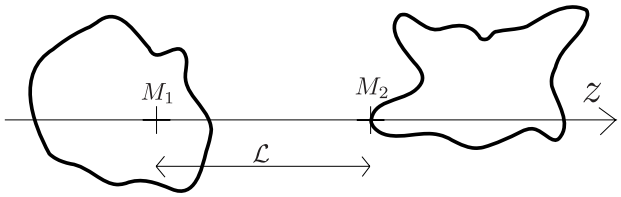

Figure 15: Scheme of the studied situation. The two objects have the reference point M_1 and M_2 inside or at their border. This two points are separated by a distance $\mathcal{L}$ in the z-direction.

In this section, we first introduce the electromagnetic planar modes which form a complete set of solutions to the Maxwell equations in vacuum, then use the anticommutators of those modes to express the radiation pressure exerted inside and outside the cavity formed by the two objects. This aims at giving an idea of the origin of the scattering formula, however not a proper mathematical derivation. For a full study of the scattering theory, the reader might refer to [47]. The scattering formalism is then rewritten in imaginary frequencies for practical purpose, and the complete derivation is carried out with the example of the plane-plane geometry[3].

1.1 The planar electromagnetic modes

In order to specify the vector space for the incoming and outgoing waves appearing in eq. (1.1) as well as for the reflection operator, we introduce in this section the electromagnetic planar modes, which are a complete set of solutions to the Maxwell equations for the fields $(\mathbf{E}, \mathbf{B})$ in vacuum.

1.1.1 The Maxwell equations in vacuum in reciprocal space

In ordinary space (the one where we live) the position vector $\mathbf{r}$ has components (x, y, z) in Cartesian coordinates and (r, θ, φ) in spherical coordinates, r being the radius, θ the polar angle (origin on the z-axis), and φ the azimuthal angle (origin along the x-axis). The unit vectors are written as $(\hat{\mathbf{x}}, \hat{\mathbf{y}}, \hat{\mathbf{z}})$ in Cartesian coordinates and $(\hat{\mathbf{r}}, \hat{\theta}, \hat{\varphi})$ in spherical coordinates. We then define the reciprocal space, where the wavevector $\mathbf{K}$ lies and has components (k_x, k_y, k_z) in Cartesian coordinates and

[3] The scattering formula and its application to the plane-plane geometry is specially and greatly described in [207, 208], therefore a lot of notations and derivations are inspired by these works.

(K, θ_K, φ_K) in spherical coordinates, with the same convention for the radius and angles. The unit vectors are written as $(\hat{\mathbf{K}}, \hat{\theta}_K, \hat{\varphi}_K)$ in spherical coordinates. We use non-bold version of vectors for their modulus, and hatted version to represent the unit vector in the same direction: $K = |\mathbf{K}|$ and $\hat{\mathbf{K}} = \frac{\mathbf{K}}{K}$.

The two spaces are connected through the spatial Fourier transform[4], which transforms an integrable function A, whose argument lies in the ordinary space, to an integrable function $\mathcal{A}$, acting on the reciprocal space:

$$\mathcal{A}(\mathbf{K}) = \int_{\mathbb{R}^3} \mathrm{d}^3\mathbf{r}\; e^{-\imath\mathbf{K}\cdot\mathbf{r}} A(\mathbf{r}) \tag{1.2}$$

$$A(\mathbf{r}) = \frac{1}{(2\pi)^3} \int_{\mathbb{R}^3} \mathrm{d}^3\mathbf{K}\; e^{\imath\mathbf{K}\cdot\mathbf{r}} \mathcal{A}(\mathbf{K}) \tag{1.3}$$

where A can be a scalar function, as well as a vector function. The Maxwell equations in vacuum for the electromagnetic field read in ordinary space:

$$\begin{aligned} \nabla\cdot\mathbf{E}(\mathbf{r},t) &= 0 & \nabla\cdot\mathbf{B}(\mathbf{r},t) &= 0 \\ \nabla\times\mathbf{E}(\mathbf{r},t) &= -\frac{\partial\mathbf{B}(\mathbf{r},t)}{\partial t} & \nabla\times\mathbf{B}(\mathbf{r},t) &= \frac{1}{c^2}\frac{\partial\mathbf{E}(\mathbf{r},t)}{\partial t} \end{aligned} \tag{1.4}$$

where $\mathbf{E}$ and $\mathbf{B}$ are the electric and magnetic fields, respectively, and c is the speed of light. Defining $\mathcal{E}(\mathbf{K},t)$ and $\mathcal{B}(\mathbf{K},t)$ the results of their spatial Fourier transformations (1.2), the Maxwell equations in vacuum write in reciprocal space:

$$\begin{aligned} \imath\mathbf{K}\cdot\mathcal{E}(\mathbf{K},t) &= 0 & \imath\mathbf{K}\cdot\mathcal{B}(\mathbf{K},t) &= 0 \\ \imath\mathbf{K}\times\mathcal{E}(\mathbf{K},t) &= -\frac{\partial\mathcal{B}(\mathbf{K},t)}{\partial t} & \imath\mathbf{K}\times\mathcal{B}(\mathbf{K},t) &= \frac{1}{c^2}\frac{\partial\mathcal{E}(\mathbf{K},t)}{\partial t} \end{aligned} \tag{1.5}$$

where the first line shows that the electromagnetic field is purely transverse in the reciprocal space, which means that the two vector fields $\mathcal{E}(\mathbf{K},t)$ and $\mathcal{B}(\mathbf{K},t)$ are in the plane perpendicular to $\mathbf{K}$. Moreover, we remark that it yields $\mathbf{K}\times(\mathbf{K}\times\mathcal{E}) = -\mathcal{E}$, and similarly for $\mathcal{B}$. Then the second line of Eq.(1.5) , eliminating either of the fields, shows that both $\mathcal{E}$ and $\mathcal{B}$ fulfill the wave equation in reciprocal space:

$$\left(\frac{\partial^2}{\partial t^2} + c^2K^2\right)\mathcal{E}(\mathbf{K},t) = \mathbf{0} \qquad \left(\frac{\partial^2}{\partial t^2} + c^2K^2\right)\mathcal{B}(\mathbf{K},t) = \mathbf{0} \tag{1.6}$$

which are six independent scalar wave equations, and the system can even be reduced to only four independent scalar wave equations if we decompose the fields in the spherical coordinates $\mathcal{E} = (\mathcal{E}_K, \mathcal{E}_{\theta_K}, \mathcal{E}_{\varphi_K})$, as their radial component $\mathcal{E}_K$ must be zero:

$$\left(\frac{\partial^2}{\partial t^2} + c^2K^2\right) f(\mathbf{K},t) = 0 \tag{1.7}$$

where $f = \mathcal{E}_{\theta_K}, \mathcal{B}_{\theta_K}, \mathcal{E}_{\varphi_K}$ or $\mathcal{E}_{\varphi_K}$. When looking for a solution of the form $f(\mathbf{K},t) = g(\mathbf{K})h(t)$, the scalar wave equation (1.7) yields that $h(t) = e^{\pm\imath\omega t}$, with $\omega = cK \geq 0$ the frequency[5] and the scalar solutions have the general form:

$$f(\mathbf{K},t) = g_+(\mathbf{K})e^{\imath\omega t} + g_-(\mathbf{K})e^{-\imath\omega t}\ . \tag{1.8}$$

The reality of the electromagnetic fields $(\mathbf{E},\mathbf{B})$ implies that $\mathcal{E}(-\mathbf{K},t) = (\mathcal{E}(\mathbf{K},t))^*$ and $\mathcal{B}(-\mathbf{K},t) = (\mathcal{B}(\mathbf{K},t))^*$, which yields that in (1.8) the functions $g_+(\mathbf{K})$ and $g_-(\mathbf{K})$ are the complex conjugate

[4] Here we choose the convention of the non-unitary Fourier transform for an angular frequency ω.

[5] Strictly speaking, ω is an angular frequency, in $\mathrm{rad}\cdot s^{-1}$, but it will be referred to as a frequency thereafter.

of each other. From now on, we will only consider the second term $g(\mathbf{K})e^{-\imath\omega t}$ in Eq.(1.8), keeping in mind that the complex conjugate (also called negative frequency component) must be added at the end to obtain the correct solution. The four components of the electromagnetic field in reciprocal space are:

$$\begin{aligned} \mathcal{E}_{\theta_K}(\mathbf{K},t) &= g^{\mathcal{E}}_{\theta_K}(\mathbf{K})e^{-\imath\omega t} + \text{C.C.} & \mathcal{E}_{\varphi_K}(\mathbf{K},t) &= g^{\mathcal{E}}_{\varphi_K}(\mathbf{K})e^{-\imath\omega t} + \text{C.C.} \\ \mathcal{B}_{\theta_K}(\mathbf{K},t) &= g^{\mathcal{B}}_{\theta_K}(\mathbf{K})e^{-\imath\omega t} + \text{C.C.} & \mathcal{B}_{\varphi_K}(\mathbf{K},t) &= g^{\mathcal{B}}_{\varphi_K}(\mathbf{K})e^{-\imath\omega t} + \text{C.C.} \end{aligned} \tag{1.9}$$

Coming back to the Maxwell equations in reciprocal space (1.5), with the time-dependance $e^{-\imath\omega t}$ the second line now implies that $\mathbf{K}\times\mathcal{E} = \omega\mathcal{B}$ and $\mathbf{K}\times\mathcal{B} = -\frac{\omega}{c^2}\mathcal{E}$. The two fields are thus orthogonal, with the triplet $(\mathbf{K},\mathcal{E},\mathcal{B})$ having a right-handed orientation, and the field transverse components obey the relations $\mathcal{B}_{\varphi_K} = \mathcal{E}_{\theta_K}/c$ and $\mathcal{B}_{\theta_K} = -\mathcal{E}_{\varphi_K}/c$. It is then possible to express $\mathcal{B}$ from $\mathcal{E}$, and we are left in the end with only two scalar functions to be chosen instead of four, which we call the TE and TM polarizations:

$$\mathcal{E}(\mathbf{K},t) = \begin{pmatrix} 0 \\ \mathcal{E}_{\theta_K}(\mathbf{K},t) \\ \mathcal{E}_{\varphi_K}(\mathbf{K},t) \end{pmatrix} = \begin{pmatrix} 0 \\ g_{\text{TM}}(\mathbf{K}) \\ g_{\text{TE}}(\mathbf{K}) \end{pmatrix} e^{-\imath\omega t} + \text{C.C.}$$

$$\mathcal{B}(\mathbf{K},t) = \begin{pmatrix} 0 \\ \mathcal{B}_{\theta_K}(\mathbf{K},t) \\ \mathcal{B}_{\varphi_K}(\mathbf{K},t) \end{pmatrix} = \begin{pmatrix} 0 \\ -g_{\text{TE}}(\mathbf{K}) \\ g_{\text{TM}}(\mathbf{K}) \end{pmatrix} \frac{e^{-\imath\omega t}}{c} + \text{C.C.} \quad .$$

We associate to the TE and TM polarizations the unit electric vectors $\hat{\epsilon}$ for $\mathcal{E}$ and the unit magnetic vectors $\hat{\beta}$ for $\mathcal{B}$:

$$\begin{aligned} \hat{\epsilon}_{\mathbf{K},\text{TE}} &= \hat{\varphi}_K & \hat{\beta}_{\mathbf{K},\text{TE}} &= -\hat{\epsilon}_{\text{TM}} = -\hat{\theta}_K \\ \hat{\epsilon}_{\mathbf{K},\text{TM}} &= \hat{\epsilon}_{\text{TE}}\times\hat{\mathbf{K}} = \hat{\theta}_K & \hat{\beta}_{\mathbf{K},\text{TM}} &= \hat{\epsilon}_{\text{TE}} = \hat{\varphi}_K \ . \end{aligned} \tag{1.10}$$

such that the fields $\mathcal{E}$ and $\mathcal{B}$ could be written in a unified manner:

$$\begin{aligned} \mathcal{E}(\mathbf{K},t) &= \left(g_{\text{TE}}(\mathbf{K})\hat{\epsilon}_{\mathbf{K},\text{TE}} + g_{\text{TM}}(\mathbf{K})\hat{\epsilon}_{\mathbf{K},\text{TM}}\right)e^{-\imath\omega t} + \text{C.C.} \\ \mathcal{B}(\mathbf{K},t) &= \left(g_{\text{TE}}(\mathbf{K})\hat{\beta}_{\mathbf{K},\text{TE}} + g_{\text{TM}}(\mathbf{K})\hat{\beta}_{\mathbf{K},\text{TM}}\right)\frac{e^{-\imath\omega t}}{c} + \text{C.C.} \end{aligned} \tag{1.11}$$

where the two functions $g_{\text{TE}}, g_{\text{TM}}$ can be freely chosen.

1.1.2 Description of the planar electromagnetic modes

The planar modes are here chosen as a basis for the electromagnetic solutions for their relative simplicity and illustrative virtue, and will be well adapted for the plane-plane geometry. This is however not the only possibility, and for the sphere-plane configuration we will see that the basis of spherical vector waves will be better adapted.

To get the planar electromagnetic modes, we just have to take as a basis of the set of all possible functions $g_{\text{TE}}, g_{\text{TM}}$ a delta function $\delta_{\mathbf{K}_0}(\mathbf{K}) = (2\pi)^3\delta^3(\mathbf{K}_0 - \mathbf{K})$ for one of them (polarization p). The planar modes $\mid \mathbf{K}_0, p\rangle$ are then labelled by their wavevector $\mathbf{K}_0 \in \mathbb{R}^3$ and their polarization $p \in \{\text{TE},\text{TM}\}$. They are associated with a frequency $\omega = cK_0$, c being the speed of light in vacuum. Their representation in the reciprocal space is, for example for the electric field:

$$\mathcal{E}(\mathbf{K},t) = \langle \mathbf{K} \mid \mathbf{K_0}, p\rangle = (2\pi)^3\delta^3(\mathbf{K}-\mathbf{K}_0)\hat{\epsilon}_{\mathbf{K}_0,p} + \text{C.C.} \quad . \tag{1.12}$$

In the ordinary space, using the inverse Fourier transformation (1.3), the corresponding electric field takes the form of a propagative wave:

$$\mathbf{E}(\mathbf{r},t) = \langle \mathbf{r} \mid \mathbf{K}_0, p\rangle = e^{\imath(\mathbf{K}_0\cdot\mathbf{r}-\omega t)}\hat{\epsilon}_{\mathbf{K}_0,p} + \text{C.C.} \quad . \tag{1.13}$$

For simplicity, we will call m a planar mode, with $m = (\mathbf{K}, p)$. We accordingly define the coefficients e_m that refers to the two functions $(g_{\text{TE}}, g_{\text{TM}})$ of $\mathbf{K}$, with:

$$e_m = \sqrt{\frac{2\varepsilon_0}{\hbar\omega}} g_p(\mathbf{K}) \quad , \quad m = (\mathbf{K}, p)$$

where ε_0 is the vacuum permittivity, $\hbar$ the reduced Planck constant (or Dirac constant), $\omega = cK$ the frequency of the mode, and the square root factor is introduced in order for the coefficients e_m to have simple commutation rules in quantum theory. Finally the planar electromagnetic modes are the set of $\mid \mathbf{K}, p\rangle$, and the general form of the solution can be decomposed into these modes as:

$$\begin{aligned}
\mathbf{E}(\mathbf{r},t) &= \frac{1}{\sqrt{\varepsilon_0}} \sum_{m\in\{|\mathbf{K},p\rangle\}} \sqrt{\frac{\hbar\omega}{2}}\hat{\epsilon}_m \left(e_m e^{-\imath(\omega t - \mathbf{K}\cdot\mathbf{r})} + (e_m)^\dagger e^{\imath(\omega t-\mathbf{K}\cdot\mathbf{r})}\right) \\
\mathbf{B}(\mathbf{r},t) &= \frac{1}{c\sqrt{\varepsilon_0}} \sum_{m\in\{|\mathbf{K},p\rangle\}} \sqrt{\frac{\hbar\omega}{2}}\hat{\beta}_m \left(e_m e^{-\imath(\omega t - \mathbf{K}\cdot\mathbf{r})} + (e_m)^\dagger e^{\imath(\omega t-\mathbf{K}\cdot\mathbf{r})}\right)
\end{aligned} \tag{1.14}$$

where $\hat{\epsilon}_m$ (resp. $\hat{\beta}_m$) are the unit electric (resp. magnetic) vectors defined in Eq.(1.10) for the mode $m =\mid \mathbf{K}, p\rangle$, and the coefficients $e_m, e_m^\dagger$ correspond to positive and negative frequency components for the mode m. In quantum field theory [209], those operators become operators of creation and annihilation and obey canonical commutation relations:

$$\begin{aligned}
\left[e_{m'}, e_m^\dagger\right] &= \delta_{mm'} = (2\pi)^3\delta^{(3)}(\mathbf{K}-\mathbf{K}')\delta_{pp'} \\
[e_{m'}, e_m] &= \left[e_{m'}^\dagger, e_m^\dagger\right] = 0 \ .
\end{aligned} \tag{1.15}$$

1.1.3 Including evanescent planar waves

Because the z-direction has a special role in the description, we will separate the 3-dimensional wavevector $\mathbf{K} = (k_x, k_y, k_z)$ in a 2-dimensional transverse part $\mathbf{k} = (k_x, k_y)$ and a longitudinal part k_z, such as $\mathbf{K} = \mathbf{k} + k_z\hat{\mathbf{z}}$. The three Cartesians components of the wavevector $\mathbf{K}$ can then be written from its associated frequency $\omega = cK$ and orientation (θ_K, φ_K):

$$\begin{aligned}
k &= \frac{\omega}{c}\sin\theta_K \qquad k_z = \frac{\omega}{c}\cos\theta_K \\
k_x &= k\cos\varphi_K \qquad k_y = k\sin\varphi_K \ .
\end{aligned} \tag{1.16}$$

We remark that a physical solution in vacuum only contains modes with real wavevectors $(k_x, k_y, k_z \in \mathbb{R})$, in order to avoid diverging quantities at large $|x|$,$|y|$ or $|z|$. Nevertheless, in the situation where scattering objects are placed in the vacuum, we must consider also the case of a complex longitudinal component $k_z \in \mathbb{C}$ for the field around the objects, as evanescent waves can exist around the two objects. The transverse components k_x and k_y have to remain real, as there is still the possibility of a diverging field on the sides of the objects. From $\frac{\omega^2}{c^2} = k_z^2 + k^2$, we deduce that k_z^2 has to be real, and k_z is either real or purely imaginary.

To include evanescent waves in the z-direction ($k_z^2 < 0$), we change the labeling of the modes, using the relation $\frac{\omega^2}{c^2} = \mathbf{K}^2 = k_z^2 + k^2$ to replace the wavevector $\mathbf{K}$ by the frequency ω and the transverse wavevector $\mathbf{k}$. The set of all modes including evanescent ones is covered with $\omega \in \mathbb{R}^+$, $\mathbf{k} \in \mathbb{R}^2$. The longitudinal part is then obtained as a solution to $k_z^2 = \frac{\omega^2}{c^2} - k_x^2 - k_y^2$. When the latter is positive, k_z is real and the wave is propagative, when it is negative, k_z is purely imaginary[6] and

[6]Here we take the convention that $\sqrt{z} = \sqrt{|z|}e^{\imath\arg(z)/2}$, with $\arg(z) \in]-\pi, \pi]$, giving for example $\sqrt{-1} = +\imath$.

the wave is evanescent. The longitudinal component k_z of the wave vector for propagative and evanescent waves are then obtained as:

$$\begin{aligned} &\text{[propagative]} \quad k_z = \phi\sqrt{\frac{\omega^2}{c^2} - k^2} \quad , \quad \phi = \pm 1 \\ &\text{[evanescent]} \quad k_z = \imath\phi\sqrt{k^2 - \frac{\omega^2}{c^2}} \quad , \quad \phi = \pm 1 \end{aligned} \tag{1.17}$$

where ($\phi = 1$) corresponds to a wave with upward propagation (z-positive direction) and ($\phi = -1$) to a wave with downward propagation (z-negative direction) for the first case $\frac{\omega^2}{c^2} \geq k^2$. This notation will turn out to be very practical in the scattering formalism, as it will enable one to distinguish between incoming and outgoing waves for every object. We have a bijection between the two representations and $\mathbf{K}$ can be equivalently replaced by $(\omega, \mathbf{k}, \phi)$. The new set of modes is then $\mid \omega, \mathbf{k}, p, \phi\rangle$, with $\omega \in \mathbb{R}^+$ the frequency, $\mathbf{k} \in \mathbb{R}^2$ the transverse wavevector, $p \in \{\text{TE}, \text{TM}\}$ the polarization, and $\phi = \pm 1$ the longitudinal direction.

1.1.4 Summing over the planar modes

When considering the total Casimir effect, we will study independently the contribution of the modes of frequency ω, then gather everything in a summation. The sum over all modes can thus be firstly done for the frequency:

$$\sum_{m \in \{|\omega, \mathbf{k}, p, \phi\rangle\}} = \int_0^\infty \frac{\mathrm{d}\omega}{2\pi} \sum_{\mathbf{k}, p, \phi} \frac{\omega}{c^2 k_z} \tag{1.18}$$

where the Jacobian $\frac{\omega}{c^2 k_z}$ comes from the change of variable $k_z \to \omega$. The summation on the right hand of Eq.(1.18) is a non-trivial procedure, as its labels are not discrete variables, and an integration $\int \mathrm{d}^2\mathbf{k}$ for example would yield a change in the dimensionality. Following [47], it can be done by considering virtual quantization boxes along x and y of size L_x, L_y and surface $A = L_x L_y$. The transverse wavevector then take discrete values ($k_x = \frac{2\pi n_x}{L_x}, k_y = \frac{2\pi n_y}{L_y}$). When the size of the box becomes infinite (the continuum limit), the discrete sum becomes:

$$\sum_{\mathbf{k}} = \sum_{n_x \in \mathbb{Z}} \sum_{n_y \in \mathbb{Z}} \longrightarrow A \int_{-\infty}^{+\infty} \frac{\mathrm{d}k_x}{2\pi} \int_{-\infty}^{+\infty} \frac{\mathrm{d}k_y}{2\pi} \ . \tag{1.19}$$

Doing so, we get for the remaining summation in expression (1.18) over all modes of frequency ω an adimensional quantity:

$$\sum_{\mathbf{k}, p, \phi} = A \sum_{\phi} \sum_{p} \int_{-\infty}^{+\infty} \frac{\mathrm{d}k_x}{2\pi} \int_{-\infty}^{+\infty} \frac{\mathrm{d}k_y}{2\pi} \tag{1.20}$$

and finally the summation over all modes can be written as:

$$\sum_{m \in \{|\omega, \mathbf{k}, p, \phi\rangle\}} = A \sum_{\phi} \sum_{p} \int_0^\infty \frac{\mathrm{d}\omega}{2\pi} \int \frac{\mathrm{d}^2\mathbf{k}}{(2\pi)^2} \frac{\omega}{c^2 k_z} \tag{1.21}$$

where $A = L_x L_y$ is the surface of the quantization box. The presence of this factor means that this summation is well-adapted to the situation of two infinite objects, such as two planes or two corrugated planes, as the Casimir quantity per unit area will emerge after division by the factor A. For finite-size objects however, the choice of planar waves does not seem to be suitable. In the sphere-plane geometry, we will choose the spherical vector wave, which are labelled with a frequency and discrete quantum numbers (ℓ, m). The factor A will then disappear and extensive Casimir quantities will be computed.

1.2 The cavity operator

The two objects form a cavity, or 'quasi-cavity', as an electromagnetic wave can be successively scattered by the two objects, and resonances can emerge. To characterize them, we define the round-trip operator $\mathcal{M}$:

$$\mathcal{M} = \mathcal{R}_1 \mathcal{T}_{1\leftarrow 2} \mathcal{R}_2 \mathcal{T}_{2\leftarrow 1} \tag{1.22}$$

that describes the transformation for an incoming wave after a single round-trip between the two objects inside the cavity (open loop). The operator $\mathcal{M}$ contains the two operators $\mathcal{R}_1$ and $\mathcal{R}_2$, which describe the reflection on each object, and the translation operators $\mathcal{T}_{1\leftarrow 2}$ and $\mathcal{T}_{2\leftarrow 1}$, to account for the change of phase when changing the reference point from one object to the other.

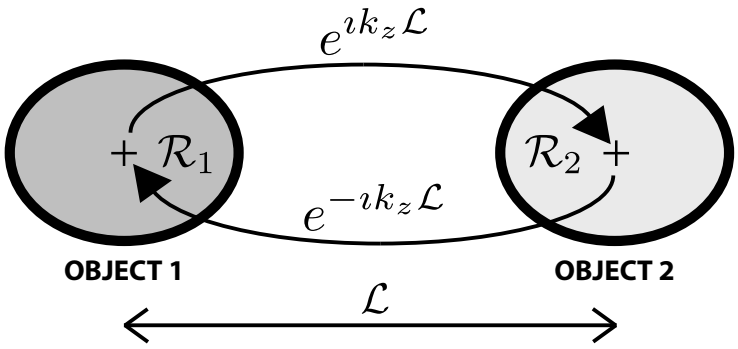

Figure 16: Translations $\mathcal{T}_{2\leftarrow 1}$ (top) and $\mathcal{T}_{1\leftarrow 2}$ (bottom) between the reference points for the two reflections ($\mathcal{R}_1$ and $\mathcal{R}_2$).

The two reference points are separated by a distance $\mathcal{L}$ along the z-axis (object one on the left, two on the right), and the chosen basis for the electromagnetic fields is the set of the planar waves $|\,\omega, \mathbf{k}, p, \phi\rangle$, the translation operators are thus diagonal with elements:

$$\mathcal{T}_{2\leftarrow 1} = e^{\imath k_z \mathcal{L}} \qquad\qquad \mathcal{T}_{1\leftarrow 2} = e^{-\imath k_z \mathcal{L}}\ . \tag{1.23}$$

Before the reflection on object 2, we will only consider modes with ($\phi = 1$) for $\mathcal{T}_{2\leftarrow 1}$, as they are the only one to hit object 2. Likewise, after the reflection on object 2, we will only consider modes with ($\phi = -1$) for $\mathcal{T}_{1\leftarrow 2}$, as they are headed to object 1. With this restriction, we can write in a unified manner the diagonal elements of the translation operators as they will appear in (1.22) for a mode $|\,\omega, \mathbf{k}, p, +\rangle$ before applying the operator $\mathcal{M}$:

$$\begin{aligned}
\mathcal{T}_{2\leftarrow 1}\,|\,\omega, \mathbf{k}, p, +\rangle &= e^{i\mathcal{L}\sqrt{\frac{\omega^2}{c^2} - \mathbf{k}^2}}\,|\,\omega, \mathbf{k}, p, +\rangle = e^{ik_z\mathcal{L}}\,|\,\omega, \mathbf{k}, p, +\rangle \\
\mathcal{T}_{1\leftarrow 2}\,|\,\omega, \mathbf{k}, p, -\rangle &= e^{i\mathcal{L}\sqrt{\frac{\omega^2}{c^2} - \mathbf{k}^2}}\,|\,\omega, \mathbf{k}, p, -\rangle = e^{ik_z\mathcal{L}}\,|\,\omega, \mathbf{k}, p, -\rangle
\end{aligned} \tag{1.24}$$

if we redefine k_z as $\sqrt{\frac{\omega^2}{c^2} - \mathbf{k}^2}$ during the whole roundtrip in the cavity. The complete scattering process inside the cavity is made of all multiples of $\mathcal{M}$ and is obtained by the infinite series:

$$\sum_{k=1}^{\infty} \mathcal{M}^k = \mathcal{M} \sum_{k=0}^{\infty} \mathcal{M}^k = \mathcal{M}\,(I - \mathcal{M})^{-1} \tag{1.25}$$

which builds the closed-loop operator, in opposition to the open-loop operator $\mathcal{M}$.

The studies [208, 47] of the specular scattering in a Fabry-Perot cavity exhibit a scalar cavity function g_m that is the ratio of the commutators of the intracavity fields with those of the input and output external fields:

$$\begin{aligned} \left[e_{m'}, e_m^\dagger\right]_{\text{ext}} &= \delta_{mm'} & \left[e_{m'}, e_m^\dagger\right]_{\text{cav}} &= g_m \delta_{mm'} \\ g_m &= 1 + f_m + f_m^* & f_m &= \frac{r_1 r_2 e^{2ik_z\mathcal{L}}}{1 - r_1 r_2 e^{2ik_z\mathcal{L}}} \end{aligned} \tag{1.26}$$

where r_1 and r_2 are the reflection amplitudes of objects 1 and 2 inside the cavity for the mode m, $\mathcal{L}$ is the distance between the two reference points used to express the former amplitudes, and k_z is defined as $\sqrt{\frac{\omega^2}{c^2} - \mathbf{k}^2}$ like in the unified expression for the translation operators (1.24). This cavity function g_m gives the ratio between the energy inside the cavity and the energy outside the cavity for each mode $m =\mid \omega, \mathbf{k}, p, \phi\rangle$, and can be decomposed with the function f_m, which can be seen as the scalar counterpart of the infinite series (1.25).

We then introduce the generalization of the cavity function g_m to the cavity operator $\mathcal{G}$ for all modes:

$$\mathcal{G} = \mathcal{I} + \mathcal{M}\left(\mathcal{I} - \mathcal{M}\right)^{-1} + \left[\mathcal{M}\left(\mathcal{I} - \mathcal{M}\right)^{-1}\right]^\dagger = \mathcal{I} + \sum_{k=1}^{\infty} \mathcal{M}^k + \sum_{k=1}^{\infty} \left(\mathcal{M}^\dagger\right)^k \tag{1.27}$$

which can also be understood as the addition of all terms in the total scattering: zero scattering, loops in one direction, loops in the other direction.

Because the configuration is time-invariant, the frequency ω will be preserved through the scattering process on an object or inside the cavity, and we can therefore define all the previous operators for a given ω. The vector space in which the operators $\mathcal{M}(\omega)$ and $\mathcal{G}(\omega)$ act will then be the set of all planar modes $(\mid \mathbf{k}, p, \phi\rangle)_\omega$ for a fixed frequency ω. We define for the latter operators the adimensional trace over this vector space Tr_ω, following the summation presented in Eq.(1.20):

$$\begin{aligned} \text{Tr}_\omega \mathcal{G}(\omega) &= \sum_{\mathbf{k},p,\phi} \left[\mathcal{G}(\omega)\right]_{(\mathbf{k}p\phi,\mathbf{k}p\phi)} \\ &= A \sum_{\phi} \sum_{p} \int \frac{\mathrm{d}^2\mathbf{k}}{(2\pi)^2} \left[\mathcal{G}(\omega)\right]_{(\mathbf{k}p\phi,\mathbf{k}p\phi)} \ . \end{aligned} \tag{1.28}$$

The cavity operator will be useful to compare the canonical commutation relations inside and outside the cavity, and obtain Casimir quantities. Outside the cavity, the vacuum state has the following anticommutators at zero temperature:

$$\begin{aligned} \left\langle e_{m'} \cdot e_m^\dagger \right\rangle_{\text{ext}} &= \frac{1}{2}\left(e_{m'} e_m^\dagger + e_m^\dagger e_{m'}\right) = \frac{1}{2}\delta_{mm'} \\ \left\langle e_{m'} \cdot e_m \right\rangle_{\text{ext}} &= \left\langle e_{m'}^\dagger \cdot e_m^\dagger \right\rangle_{\text{ext}} = 0 \end{aligned} \tag{1.29}$$

where the dot symbolizes the symmetrized product. Inside the cavity, the anticommutators are the same, but multiplied by the diagonal elements of the cavity operator:

$$\begin{aligned} \left\langle e_{m'} \cdot e_m^\dagger \right\rangle_{\text{cav}} &= \mathcal{G}_{(m',m)} \left\langle e_{m'} \cdot e_m^\dagger \right\rangle_{\text{ext}} = \frac{1}{2}\mathcal{G}_{(m,m)}\delta_{mm'} \\ \left\langle e_{m'} \cdot e_m \right\rangle_{\text{cav}} &= \left\langle e_{m'}^\dagger \cdot e_m^\dagger \right\rangle_{\text{cav}} = 0 \ . \end{aligned} \tag{1.30}$$

1.3 The Casimir energy from the radiation pressure

The z-component of the radiation pressure exerted by the fields on one object is determined by the component T_{zz} of the Maxwell stress tensor:

$$T_{zz}(\mathbf{r},t) = \frac{1}{2\mu_0 c}\left(E_x^2 + E_y^2 - E_z^2 + c^2B_x^2 + c^2B_y^2 - c^2B_z^2\right) \ . \tag{1.31}$$

Averaging T_{zz} with the expressions (1.14) for the fields and (1.29) for the anticommutators outside the cavity leads to:

$$\begin{aligned}\langle T_{zz}(\mathbf{r},t)\rangle_{\text{ext}} &= \sum_m \frac{\hbar\omega}{2}\cos^2\theta \\ &= \sum_m \frac{\hbar k_z^2 c^2}{2\omega} \\ &= \int_0^\infty \frac{d\omega}{2\pi}\sum_{\mathbf{k},p,\phi}\frac{\hbar k_z}{2}\end{aligned} \tag{1.32}$$

using (1.18) for the sum over the modes m. The same derivation can be done for the field inside the cavity for which the diagonal elements of the cavity operator $\mathcal{G}$ must be taken into account through the anticommutators (1.30):

$$\langle T_{zz}(\mathbf{r},t)\rangle_{\text{cav}} = \int_0^\infty \frac{\mathrm{d}\omega}{2\pi}\sum_{\mathbf{k},p,\phi}\frac{\hbar k_z}{2}\left[\mathcal{G}(\omega)\right]_{(\mathbf{k}p\phi,\mathbf{k}p\phi)} \ . \tag{1.33}$$

The force exerted on one object is the difference of inside and outside radiation pressures. In order to have $F<0$ for an attractive force and $F>0$ for a repulsive force between the two objects, we define the force as follows:

$$\begin{aligned}F &= F_{\text{inside}} - F_{\text{outside}} \\ &= \langle T_{zz}(\mathbf{r},t)\rangle_{cav} - \langle T_{zz}(\mathbf{r},t)\rangle_{ext} \\ &= \int_0^\infty \frac{\mathrm{d}\omega}{2\pi}\sum_{\mathbf{k},p,\phi}\hbar k_z\left(\left[\mathcal{G}(\omega)\right]_{(\mathbf{k}p\phi,\mathbf{k}p\phi)} - 1\right) \\ &= \int_0^\infty \frac{\mathrm{d}\omega}{2\pi}\,\mathrm{Tr}_\omega\,\hbar k_z\left[\mathcal{M}(\omega)\left(\mathcal{I}-\mathcal{M}(\omega)\right)^{-1} + \mathcal{M}^\dagger(\omega)\left(\mathcal{I}-\mathcal{M}^\dagger(\omega)\right)^{-1}\right] \ .\end{aligned}$$

As the distance $\mathcal{L}$ between the two objects only appears in $\mathcal{M}$ through $e^{\imath k_z\mathcal{L}}$ in the two translations operators $\mathcal{T}$, as seen in Eq.(1.24), we have:

$$-\frac{\partial}{\partial\mathcal{L}}\left[\ln(I-\mathcal{M}(\omega)) - \ln(I-\mathcal{M}^\dagger(\omega))\right] = 2\imath k_z\left[\mathcal{M}(\omega)\left(I-\mathcal{M}(\omega)\right)^{-1} + \mathcal{M}^\dagger(\omega)\left(I-\mathcal{M}^\dagger(\omega)\right)^{-1}\right]$$

then, by identification with $F=-\frac{\partial E}{\partial\mathcal{L}}$, we get the energy:

$$\begin{aligned}E =& \hbar\int_0^\infty \frac{\mathrm{d}\omega}{2\pi}\mathrm{Tr}_\omega\left[\frac{1}{2\imath}\ln(\mathcal{I}-\mathcal{M}(\omega)) - \frac{1}{2\imath}\ln(I-\mathcal{M}^\dagger(\omega))\right] \\ =& \hbar\int_0^\infty \frac{\mathrm{d}\omega}{2\pi}\left[\left(-\frac{\imath}{2}\right)\mathrm{Tr}_\omega\ln\left(\mathcal{D}(\omega)\right) + \text{C.C.}\right] \\ =& \hbar\int_0^\infty \frac{\mathrm{d}\omega}{2\pi}\left[\left(-\frac{\imath}{2}\right)\ln\det_\omega\left(\mathcal{D}(\omega)\right) + \text{C.C.}\right]\end{aligned} \tag{1.34}$$

with $\mathcal{D}(\omega) = \mathcal{I} - \mathcal{M}(\omega)$ the scattering operator of the cavity that contains all the information of the geometric configuration and the optical properties of the objects. In some sense, $\mathcal{D}$ can be interpreted as applying to a wave a measure of the difference between doing a round trip in the cavity and not doing it. The resulting energy E can then be understood as the energy contained in the electromagnetic modes when the two objects are placed in the vacuum, minus the energy contained in the electromagnetic modes when the objects are not here. Doing this difference, we take away the infiniteness of the quantity $\sum_m \frac{\hbar\omega}{2}$ which can be theoretically problematic and needs renormalization procedures.

The final expression (1.34) is the scattering formula at real frequencies. It can be transform by a Wick rotation to an integration over complex frequencies ($\omega = \imath\xi$):

$$E = \hbar \int_0^\infty \frac{\mathrm{d}\xi}{2\pi} \mathrm{Tr} \ln \left(\mathcal{D}(i\xi)\right) = \hbar \int_0^\infty \frac{\mathrm{d}\xi}{2\pi} \ln \det \mathcal{D}(i\xi) \tag{1.35}$$

where we dropped the index ω in the notation for the trace, as it is valid with other basis for the electromagnetic modes, but keeping in mind that this trace must be adimensional.

Moreover, the procedure of the Wick rotation for the frequency has the advantage of expressing propagative and evanescent wave in the same manner, as the longitudinal wavevector is transformed into:

$$\begin{aligned} &\text{[propagative]} \quad k_z = \phi\sqrt{\frac{\omega^2}{c^2} - k^2} = \phi\sqrt{-\frac{\xi^2}{c^2} - k^2} = \imath\phi\sqrt{\frac{\xi^2}{c^2} + k^2} = \imath\phi\kappa \\ &\text{[evanescent]} \quad k_z = \imath\phi\sqrt{k^2 - \frac{\omega^2}{c^2}} = \imath\phi\sqrt{k^2 + \frac{\xi^2}{c^2}} = \imath\phi\kappa \end{aligned} \tag{1.36}$$

with $\kappa = \sqrt{k^2 + \frac{\xi^2}{c^2}} > 0$ the Wick rotated counterpart of the longitudinal component k_z of the wavevector. Then the reflection operators $(\mathcal{R}_1, \mathcal{R}_2)$ in $\mathcal{M}(i\xi)$ have to be evaluated at imaginary frequencies, and the translation operators common expression (1.24) becomes:

$$\begin{aligned} \mathcal{T}_{2\leftarrow 1} \mid \imath\xi, \mathbf{k}, p, + \rangle &= e^{\imath\mathcal{L}\sqrt{-\frac{\xi^2}{c^2} - \mathbf{k}^2}} \mid \imath\xi, \mathbf{k}, p, + \rangle = e^{-\kappa\mathcal{L}} \mid \imath\xi, \mathbf{k}, p, + \rangle \\ \mathcal{T}_{1\leftarrow 2} \mid \imath\xi, \mathbf{k}, p, - \rangle &= e^{\imath\mathcal{L}\sqrt{-\frac{\xi^2}{c^2} - \mathbf{k}^2}} \mid \imath\xi, \mathbf{k}, p, - \rangle = e^{-\kappa\mathcal{L}} \mid \imath\xi, \mathbf{k}, p, - \rangle \ . \end{aligned} \tag{1.37}$$

From this exponential decrease with respect to the Wick-rotated longitudinal component of wavevector κ, we know that the integrand function in the scattering formula (1.35) at imaginary frequencies is quickly decreasing for high frequencies. Indeed, as $\kappa^2 = \frac{\xi^2}{c^2} + k^2$, $\kappa > \frac{\xi}{c}$, and the translation operators bring a factor:

$$e^{-2\kappa\mathcal{L}} \leq e^{-\frac{\xi\mathcal{L}}{c}} \ , \tag{1.38}$$

meaning that all frequencies $\xi \gg \frac{c}{\mathcal{L}}$ will give a negligible contribution to the Casimir effect in the ξ-integration.

1.4 The example of the plane-plane geometry

As an illustrative example, we apply the scattering formalism (1.35) introduced above in the simple situation where the two objects are parallel planes, the first with its surface at $(z = 0)$, the second at $(z = \mathcal{L})$, as presented in **Fig. 17**. The two planes are assumed to be infinite in the x and y-directions, and to be thick enough to be considered as a bulk. For a more complete study of this situation the reader is reported to [207] which focus on this plane-plane geometry. The translational invariance in the x and y-directions makes the planar modes $\mid \omega, \mathbf{k}, p, \phi \rangle$ introduced

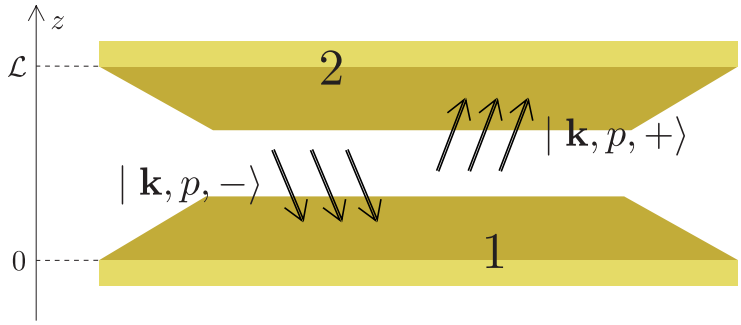

Figure 17: Schema of the plane-plane configuration. The two planes are infinite in the x and y-directions, and are separated by a distance $\mathcal{L}$ in the z-direction.

in **Section 1.1** very well suited to express the scattering. We recall that $\omega \in \mathbb{R}^+$ is the frequency of the mode, $\mathbf{k} = (k_x, k_y) \in \mathbb{R}^2$ the transverse component of the wavevector $\mathbf{K}$, $p \in \{\mathrm{TE}, \mathrm{TM}\}$ the polarization, and $\phi = \pm 1$ chooses between the two possibilities for the longitudinal part of the wavevector $k_z = \phi\sqrt{\frac{\omega^2}{c^2} - k^2}$.

When switching to imaginary frequencies $\omega = \imath\xi$, the longitudinal wavevector becomes $k_z = \imath\phi\kappa$, with $\kappa = \sqrt{\frac{\xi^2}{c^2} + k^2} \in \mathbb{R}^+$. The optical response of the planes is described through the Fresnel coefficients, which will be derived at imaginary frequencies in **Section 5.2.1** (p.70) and read for the two transverse polarizations:

$$\begin{aligned} r_{\mathrm{TE}}(\xi,\kappa) &= \frac{c\kappa - \sqrt{\xi^2(\varepsilon(\imath\xi)-1)+c^2\kappa^2}}{c\kappa + \sqrt{\xi^2(\varepsilon(\imath\xi)-1)+c^2\kappa^2}} \\ r_{\mathrm{TM}}(\xi,\kappa) &= \frac{c\kappa\varepsilon(\imath\xi) - \sqrt{\xi^2(\varepsilon(\imath\xi)-1)+c^2\kappa^2}}{c\kappa\varepsilon(\imath\xi) + \sqrt{\xi^2(\varepsilon(\imath\xi)-1)+c^2\kappa^2}} \end{aligned} \tag{1.39}$$

where $\varepsilon(\imath\xi)$ is the dielectric function of the material, which enables to describe the optical properties of the material and will be discussed more thoughfully in **Section 2**. A perfectly reflecting material has an infinite dielectric function and its Fresnel coefficients go the limits ($r_{\mathrm{TE}} \to -1$) and ($r_{\mathrm{TM}} \to 1$), an imperfect mirror always has $r_{\mathrm{TE}}, r_{\mathrm{TM}} \in [-1, 1]$.

The point of reference for the first plate will be the origin $(0,0,0)$ while the reference point for the second plate will be $(\mathcal{L}, 0, 0)$. The reflection operators $\mathcal{R}_1, \mathcal{R}_2$ on the planar surfaces for planar modes introduced in a previous section, are given by Fresnel coefficients:

$$\begin{aligned} \mathcal{R}_1(\imath\xi)\,|\,\mathbf{k},p,+\rangle &= 0 & \mathcal{R}_2(\imath\xi)\,|\,\mathbf{k},p,+\rangle &= r_p^{(2)}(\xi,\kappa)\,|\,\mathbf{k},p,-\rangle \\ \mathcal{R}_1(\imath\xi)\,|\,\mathbf{k},p,-\rangle &= r_p^{(1)}(\xi,\kappa)\,|\,\mathbf{k},p,+\rangle & \mathcal{R}_2(\imath\xi)\,|\,\mathbf{k},p,-\rangle &= 0 \end{aligned} \tag{1.40}$$

and the translation operators $T_{1\leftarrow 2}, T_{2\leftarrow 1}$ give:

$$\begin{aligned} \mathcal{T}_{1\leftarrow 2}(\imath\xi)\,|\,\mathbf{k},p,+\rangle &= e^{\kappa\mathcal{L}}\,|\,\mathbf{k},p,+\rangle & T_{2\leftarrow 1}(\imath\xi)\,|\,\mathbf{k},p,+\rangle &= e^{-\kappa\mathcal{L}}\,|\,\mathbf{k},p,+\rangle \\ \mathcal{T}_{1\leftarrow 2}(\imath\xi)\,|\,\mathbf{k},p,-\rangle &= e^{-\kappa\mathcal{L}}\,|\,\mathbf{k},p,-\rangle & T_{2\leftarrow 1}(\imath\xi)\,|\,\mathbf{k},p,-\rangle &= e^{\kappa\mathcal{L}}\,|\,\mathbf{k},p,-\rangle\ . \end{aligned} \tag{1.41}$$

Using the two last sets of equations, we can obtain the image of a wave $|\,\mathbf{k},p,\phi\rangle$ of frequency ω by

the round-trip operator defined by Eq.(1.22):

$$\begin{aligned}
\mathcal{M}(\imath\xi) \mid \mathbf{k}, p, -\rangle &= \mathcal{R}_1(\imath\xi)\mathcal{T}_{1\leftarrow 2}(\imath\xi)\mathcal{R}_2(\imath\xi)\mathcal{T}_{2\leftarrow 1}(\imath\xi) \mid \mathbf{k}, p, -\rangle = 0 \\
\mathcal{M}(\imath\xi) \mid \mathbf{k}, p, +\rangle &= \mathcal{R}_1(\imath\xi)\mathcal{T}_{1\leftarrow 2}(\imath\xi)\mathcal{R}_2(\imath\xi)\mathcal{T}_{2\leftarrow 1}(\imath\xi) \mid \mathbf{k}, p, +\rangle \\
&= e^{-\kappa\mathcal{L}}\ \mathcal{R}_1(\imath\xi)\mathcal{T}_{1\leftarrow 2}(\imath\xi)\mathcal{R}_2(\imath\xi) \mid \mathbf{k}, p, +\rangle \\
&= e^{-\kappa\mathcal{L}} r_p^{(2)}(\xi,\kappa)\ \mathcal{R}_1(\imath\xi)\mathcal{T}_{1\leftarrow 2}(\imath\xi) \mid \mathbf{k}, p, -\rangle \\
&= e^{-\kappa\mathcal{L}} r_p^{(2)}(\xi,\kappa) e^{-\kappa\mathcal{L}}\ \mathcal{R}_1(\imath\xi) \mid \mathbf{k}, p, -\rangle \\
&= e^{-\kappa\mathcal{L}} r_p^{(2)}(\xi,\kappa) e^{-\kappa\mathcal{L}} r_p^{(1)}(\xi,\mathbf{k})\ \mid \mathbf{k}, p, +\rangle \\
&= \rho_p(\xi,\mathbf{k}) \mid \mathbf{k}, p, +\rangle \quad \text{with } \rho_p(\xi,\mathbf{k}) = r_p^{(1)}(\xi,\kappa) r_p^{(2)}(\xi,\kappa) e^{-2\kappa\mathcal{L}}
\end{aligned}$$

where we see that only the block for $\phi = \phi' = 1$ has non-zero entries. Moreover, the operator $\mathcal{M}(\imath\xi)$ is diagonal in the basis of planar electromagnetic modes, which comes from the fact that planar reflection is specular. It would not be the case for general non-specular reflections, and $\mathcal{M}$ can contain non-diagonal elements that couple the different modes in the cavity. It follows that in this simple case the determinant of the cavity operator $\mathcal{D}(\imath\xi) = \mathcal{I} - \mathcal{M}(\imath\xi)$ reduces to a product of the diagonal elements for $(\phi = 1)$:

$$\det \mathcal{D}(\imath\xi) = \prod_{\mathbf{k},p} (1 - \rho_p(\xi,\mathbf{k})) \tag{1.42}$$

so that, when taking the logarithm, the integrand for the Casimir energy is:

$$\begin{aligned}
\ln\det \mathcal{D}(\imath\xi) &= \ln \prod_{\mathbf{k},p} (1 - \rho_p(\xi,\mathbf{k})) = \sum_{\mathbf{k},p} \ln(1 - \rho_p(\xi,\mathbf{k})) \\
&= A \sum_p \int \frac{d^2\mathbf{k}}{(2\pi)^2} \ln(1 - \rho_p(\xi,\mathbf{k})) \\
&= A \int_0^\infty \frac{k\mathrm{d}k}{2\pi} \int_0^{2\pi} \frac{\mathrm{d}\theta_K}{2\pi} \sum_p \ln(1 - \rho_p(\xi,\mathbf{k})) \\
&= A \int_{\xi/c}^\infty \frac{\kappa\mathrm{d}\kappa}{2\pi} \ln\left[(1 - \rho_{\mathrm{TE}}(\xi,\kappa))(1 - \rho_{\mathrm{TM}}(\xi,\kappa))\right] \ .
\end{aligned} \tag{1.43}$$

Finally the Casimir energy per unit area is given by a double integral:

$$E/A = \frac{\hbar}{2\pi} \int_0^\infty \frac{\mathrm{d}\xi}{2\pi} \int_{\xi/c}^\infty \kappa\mathrm{d}\kappa \ln\left[(1 - \rho_{\mathrm{TE}}(\xi,\kappa))(1 - \rho_{\mathrm{TM}}(\xi,\kappa))\right] \ . \tag{1.44}$$

As the distance between the two objects $\mathcal{L}$ only appears in the translation operator as $e^{-\kappa\mathcal{L}}$, remarking that:

$$\begin{aligned}
\frac{\partial}{\partial\mathcal{L}} \rho_p(\xi,\kappa) &= -2\kappa\rho_p(\xi,\kappa) \\
\frac{\partial}{\partial\mathcal{L}} \ln\left(1 - \rho_p(\xi,\kappa)\right) &= \frac{2\kappa\rho_p(\xi,\kappa)}{1 - \rho_p(\xi,\kappa)}
\end{aligned}$$

it is easy in to obtain a similar expression for the Casimir force per unit area from (1.44):

$$F/A = -\frac{\partial E/A}{\partial\mathcal{L}} = -\frac{\hbar}{2\pi} \int_0^\infty \frac{\mathrm{d}\xi}{2\pi} \int_{\xi/c}^\infty 2\kappa^2\mathrm{d}\kappa \left[\frac{\rho_{\mathrm{TE}}(\xi,\kappa)}{1 - \rho_{\mathrm{TE}}(\xi,\kappa)} + \frac{\rho_{\mathrm{TM}}(\xi,\kappa)}{1 - \rho_{\mathrm{TM}}(\xi,\kappa)}\right] \ . \tag{1.45}$$

In the case of perfect mirrors, the Fresnel coefficients are $r_{\mathrm{TE}} = -1$, $r_{\mathrm{TM}} = 1$, and the Casimir energy per unit area becomes:

$$\begin{aligned} E/A &= \frac{\hbar}{2\pi}\int_0^\infty \frac{\mathrm{d}\xi}{2\pi}\int_{\xi/c}^\infty \kappa \mathrm{d}\kappa \ln\left[(1-e^{-2\kappa\mathcal{L}})^2\right] \\ &= \frac{\hbar}{\pi}\int_0^\infty \frac{\mathrm{d}\xi}{2\pi}\int_{\xi/c}^\infty \kappa \mathrm{d}\kappa \ln\left[1-e^{-2\kappa\mathcal{L}}\right] \\ &= \frac{\hbar}{\pi}\int_0^\infty \kappa \mathrm{d}\kappa \int_0^{c\kappa} \frac{\mathrm{d}\xi}{2\pi} \ln\left[1-e^{-2\kappa\mathcal{L}}\right] \\ &= \frac{\hbar c}{2\pi^2}\int_0^\infty \kappa^2 \mathrm{d}\kappa \ln\left[1-e^{-2\kappa\mathcal{L}}\right] \\ &= \frac{\hbar c}{16\pi^2\mathcal{L}^3}\int_0^\infty \mathrm{d}t\ t^2 \ln\left(1-e^{-t}\right) \\ &= \frac{\hbar c}{16\pi^2\mathcal{L}^3}\left(-2\zeta(4)\right) \\ &= -\frac{\hbar c\pi^2}{720\mathcal{L}^3} \end{aligned} \tag{1.46}$$

which reproduces the original result derived by Casimir in [38]. Taking the derivative with respect to the distance $\mathcal{L}$, we get the Casimir force per unit area for perfect mirrors:

$$F/A = = -\frac{\hbar c\pi^2}{240\mathcal{L}^4} \tag{1.47}$$

2 Optical properties of materials

In order to write the reflection operators $\mathcal{R}$ on the objects, defined in Eq.(1.1), one needs a realistic description of the optical response of materials. In particular in the experimental situations, objects are usually made of metallic or dielectric materials, and an accurate modeling of the material often turns out to be crucial [94, 96, 101, 103, 112, 117, 105, 107, 123, 124, 125, 126, 127, 128, 129]. Moreover, as discussed in the introduction, the model used for metallic reflectors has been a matter of debate in the past years, as some experimental work seem to be in better agreement with the lossless plasma model than with the dissipative Drude model [107, 109].

In this section, we first introduce the frequency-dependant relative permittivity $\varepsilon(\omega)$ of the material, also called dielectric function, which will be used to account for imperfect reflection on the objects. Then several models for metals and for dielectrics will be presented, along with their corresponding dielectric function.

2.1 The dielectric function

In this section we will present models for a linear, time-invariant, homogeneous and isotropic dielectric medium. We start from the general Maxwell equations:

$$\nabla \times \mathbf{E} = -\frac{\partial \mathbf{B}}{\partial t} \qquad \nabla \times \mathbf{H} = \mathbf{j} + \frac{\partial \mathbf{D}}{\partial t}$$
$$\nabla \cdot \mathbf{D} = \rho \qquad \nabla \cdot \mathbf{B} = 0$$

with $\mathbf{E}$ and $\mathbf{B}$ the electric and magnetic fields, $\mathbf{D} = \varepsilon_0 \mathbf{E} + \mathbf{P}$ the electric displacement field, and $\mathbf{H} = \frac{\mathbf{B}}{\mu_0} + \mathbf{M}$ the magnetizing field. $\mathbf{P}$ and $\mathbf{M}$ are respectively the polarization and magnetization density fields, $\mathbf{j}$ and ρ represent the free current and charge densities, also called $\mathbf{j}_f$ and ρ_f in the literature, that don't take into account bound current and charge.

The assumption of linear, time-invariant, homogeneous and isotropic dielectric medium leads to $\mathbf{P} = \varepsilon_0 \chi \mathbf{E}$ and $\mathbf{M} = \mathbf{0}$, where the electric susceptibility of the material χ is a homogeneous and real function. It yields that the electric displacement field linearly depends on the electric field: $\mathbf{D} = \varepsilon_0(1+\chi)\mathbf{E}$ and that the magnetizing field linearly depends on the magnetic field: $\mathbf{H} = \frac{\mathbf{B}}{\mu_0}$. Thus, replacing $\mathbf{D}$ and $\mathbf{H}$ by the latter expressions, the Maxwell equations can be written the same way as in vacuum, with the replacement $\varepsilon_0 \to \varepsilon_0(1+\chi) = \varepsilon$:

$$\nabla \times \mathbf{E} = -\frac{\partial \mathbf{B}}{\partial t} \qquad \nabla \times \mathbf{B} = \mu_0 \left(\mathbf{j} + \varepsilon \frac{\partial \mathbf{E}}{\partial t} \right)$$
$$\nabla \cdot \mathbf{E} = \frac{\rho}{\varepsilon} \qquad \nabla \cdot \mathbf{B} = 0 \ .$$

The relative permittivity $\varepsilon_r = \frac{\varepsilon}{\varepsilon_0} = 1 + \chi$, also called dielectric function, will be first derived from a simple physical model for the medium, then the general results of electromagnetism in optical media can be used to study physical properties of the dielectric medium. From now on, ε will be used to represent the relative permittivity ε_r, for simplicity.

2.2 The plasma model

The plasma model is the simplest way to take into account the high-frequency transparency, which is a common properties of metals. The fact that they are poor reflectors at high frequencies can be understood from the point of view of the electrons inside the material: when an incoming wave hits the material, the electrons move due to the electromagnetic field, and this movement creates the reflected wave. When the frequency increases, their inertia is too large for them to follow the incoming wave and they do not move fast enough, resulting in a deterioration in the energy

of the outgoing reflected wave. The presented model will give the opportunity to represent this phenomena with a very simple modeling of the electron's movement.

The plasma model consists in assuming the valence electrons to have their mutual electrostatic influences neglected. The only remaining force acting on them is the effect of external field (in the present case, the incident electromagnetic wave), as the influence of the crystal lattice made of positive ions does not need to be explicitly taken into account: Bloch's Theorem describes the movement of an unbound electron in a periodic potential to be quite similar to a free electron in vacuum, except for the electron mass m_e becoming an effective mass m_e^*. The movement of the electron and the positive ions is then steered by the following equation:

$$m_e^* \dot{\mathbf{v}}_e = -e\mathbf{E} \qquad\qquad m_i^* \dot{\mathbf{v}}_i = e\mathbf{E} \tag{2.1}$$

where m_e^* (resp. m_i^*) is the effective mass of the electron (resp. of the positive ion), and $(-e)$ is the charge of the electron. Using time-Fourier transformation, this equation can be rewritten as:

$$\mathbf{v}_e = -\imath \frac{e}{m_e^* \omega}\mathbf{E} \qquad\qquad \mathbf{v}_i = \imath \frac{e}{m_i^* \omega}\mathbf{E}$$

where ω is the frequency of the incoming wave, generating the movement of the electrons. The total current $\mathbf{j}$ comes from both movements:

$$\mathbf{j} = n_e \mathbf{v}_e (-e) + n_i \mathbf{v}_i e = \imath \frac{ne^2}{\omega}\left(\frac{1}{m_e^*} + \frac{1}{m_i^*}\right)\mathbf{E}$$

where n_e (resp. n_i) is the number of electrons (resp. positive ions) per unit volume. This expression can be simplified, observing that $m_e^* \ll m_i^*$ (or equivalently assuming the ions to be static) to:

$$\mathbf{j} = \imath \frac{ne^2}{\omega m_e^*}\mathbf{E} = \imath \varepsilon_0 \frac{\omega_P^2}{\omega}\mathbf{E} \tag{2.2}$$

defining the plasma frequency $\omega_P = \sqrt{\frac{ne^2}{\varepsilon_0 m_e^*}}$, associated to a plasma wavelength $\lambda_P = \frac{2\pi c}{\omega_P}$. Incorporating (2.2) in Maxwell equation in reciprocal space[209], it yields the following identity for the transverse part of the magnetic field:

$$\mathbf{k} \times \left(\mathbf{k} \times \hat{\mathbf{B}}_\perp\right) = \mu_0 \varepsilon_0 \left(\omega_P^2 - \omega^2\right) \hat{\mathbf{B}}_\perp \tag{2.3}$$

which gives $\mathbf{k}^2 = \frac{\omega^2 n^2}{c^2}$ with the media index $n = \sqrt{\varepsilon_0 \left(1 - \frac{\omega_P^2}{\omega^2}\right)}$. $\varepsilon = n^2$ is the permittivity, and finally the dielectric function for the plasma model is:

$$\varepsilon^{\text{plas}}(\omega) = 1 - \frac{\omega_P^2}{\omega^2}\ . \tag{2.4}$$

For an imaginary frequency $\omega = i\xi$, it becomes a positive function:

$$\varepsilon^{\text{plas}}(\imath\xi) = 1 + \frac{\omega_P^2}{\xi^2} \tag{2.5}$$

which is presented in **Fig. 18** with a blue curve on a log-log scale. At the limit of very low frequencies, the dielectric function diverges and the material becomes perfectly reflecting. The slope is 2, as $\varepsilon^{\text{plas}}$ diverges with ξ^{-2}. On the contrary at high frequencies it goes to one, which is the dielectric function of vacuum, and the material does not reflect anything.

It is important to notice that this description of the electron's movement is valid for a bulk material. For finite-size object, and particularly for very small sphere in our case, it would be necessary to take into account the confinement effect for conduction electrons [210, 211]. For that reason, in the following we will restrict the application of the plasma and Drude models to bulk materials, and in the case of spheres, to radii large enough ($R \gtrsim \lambda_P$).

2.3 The Drude model

The Drude model is an extension of the formerly introduced plasma model, which accounts for dissipation in the metal. Indeed the relation (2.2) between the flux and the electric field yield a conductivity $\sigma(\omega) = \imath\varepsilon_0\frac{\omega_P^2}{\omega}$ which becomes infinite when the frequency ω goes to zero. Metals are however known to have a finite DC-conductivity, and thus the plasma dielectric function (2.4,2.5) is not a correct description of the optical response for low frequencies.

To account for dissipation we add to the equation of motion for the electron (2.1) a friction term:

$$m_e^*\dot{\mathbf{v}}_e = -e\mathbf{E} - m_e^*\gamma\mathbf{v}_e$$

where $\gamma > 0$ is called the relaxation frequency. The equation (2.2) then becomes $\mathbf{j} = \imath\frac{ne^2}{\omega m_e^* + im_e^*\gamma}\mathbf{E}$ and for the same reason as above, one finds $\mathbf{k}^2 = \frac{\omega^2 n^2}{c^2}$ with the media index $n = \sqrt{\varepsilon_0\left(1 - \frac{\omega_P^2}{\omega(\omega+\imath\gamma)}\right)}$. It results in a dielectric function for the Drude model:

$$\varepsilon^{\text{Drud}}(\omega) = 1 - \frac{\omega_P^2}{\omega(\omega + \imath\gamma)} \tag{2.6}$$

which becomes at imaginary frequency $\omega = i\xi$ a real-valued function:

$$\varepsilon^{\text{Drud}}(\imath\xi) = 1 + \frac{\omega_P^2}{\xi(\xi + \gamma)}\ . \tag{2.7}$$

This function is presented in **Fig. 18** with a red curve on a log-log scale. For high and intermediate frequencies, the dielectric function $\varepsilon^{\text{Drud}}$ for the Drude model is similar to $\varepsilon^{\text{plas}}$ from the plasma model (blue curve). At the limit of very low frequencies, the dielectric function diverges and the material becomes perfectly reflecting, but the slope is now 1, as $\varepsilon^{\text{Drud}}$ diverges with ξ^{-1}.

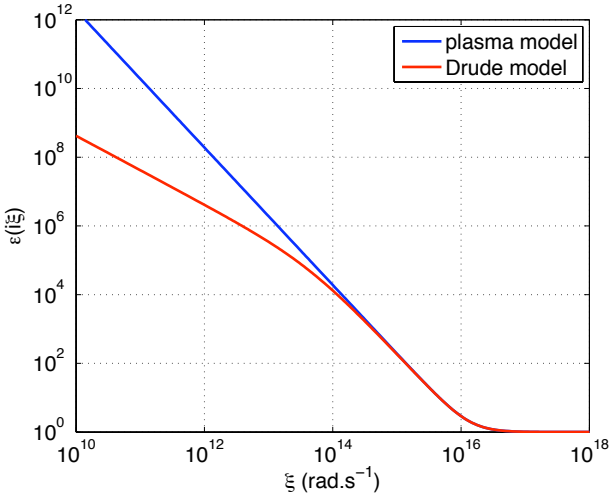

Figure 18: Dielectric function $\varepsilon(i\xi)$ as a function of the imaginary frequency ξ for the plasma (blue curve) or Drude model (red curve). The parameters are those for gold ($\lambda_P = 136$ nm ; $\delta = 0.0033$).

With the Drude model, the conductivity $\sigma(\omega) = \imath\varepsilon_0\frac{\omega_P^2}{\omega+\imath\gamma}$ yields at the limit of zero frequency a finite DC-conductivity. The plasma dielectric function (2.5) is recovered from the Drude one (2.7) in the limit $\gamma \to 0$. But, as it will be discussed later on, this does not imply that there must be a continuity in the Casimir effect from the Drude to the plasma model in this limit [140].

	Au	Cu	Al
λ_P	136 nm	136 nm	107 nm
$\delta = \frac{\gamma}{\omega_P}$	0.0038	0.0033	0.0044

Table 1: Values of the parameters for plasma and Drude models for some metals

In **Table 1** are presented parameters of the plasma and Drude models for some metals. It is also possible to improve plasma and Drude models for the permittivity with additional oscillators [107] in order to better describe the interband transitions:

$$\varepsilon(\imath\xi) = 1 + \frac{\omega_P^2}{\xi(\xi+\gamma)} + \sum_{j=1}^{J} \frac{f_j}{\omega_j^2 + \xi^2 + g_j\xi} \tag{2.8}$$

but this sophistication will not be studied here, as we will focus on the qualitative influence of finite conductivity and dissipation in the Casimir effect.

2.4 Dielectrics

Dielectric materials, like silica or diamond, are not very good reflectors at low frequencies. Unlike metals, their relative permittivity goes to a constant $\varepsilon^{\text{diel}}(0)$ when $\omega \to 0$, and a different model for the dielectric function is thus needed. A pragmatic approach for such a dielectric function is the Sellmeier model [212]:

$$\varepsilon^{\text{diel}}(\omega) = 1 + \sum_i \frac{B_i\omega_i^2}{\omega_i^2 - \omega^2} \tag{2.9}$$

where the $(\omega_i)_i$ are the resonance frequencies, associated with coefficient B_i. From the $(\omega_i)_i$ we can define corresponding lengthscales $\lambda_i = \frac{2\pi c}{\omega_i}$. At imaginary frequencies, the dielectric function becomes:

$$\varepsilon^{\text{diel}}(\imath\xi) = 1 + \sum_i \frac{B_i\omega_i^2}{\omega_i^2 + \omega^2} \tag{2.10}$$

which is presented in **Fig. 19** for various dielectric materials. Like for metals, the dielectric function $\varepsilon^{\text{diel}}$ enables to model the high-frequency transparency of the materials, as it goes to unity at the limit ($\xi \to \infty$). For lower frequencies however, it converges to a constant value $\varepsilon^{\text{diel}}(0) = 1 + \sum_i B_i$. At intermediate frequencies, the dielectric function undergoes plateaus if there is enough space between the oscillators frequencies.

For simplicity, only a few oscillators are kept in the Sellmeier equation, and we give the example of two-oscillators parameters values for diamond, silica and bromobenzene in **Table 2**.

2.5 The example of the plane-plane geometry

The reflection operator $\mathcal{R}_{\text{P}}$ for a plane is diagonal in the basis of planar modes introduced in **Section 1.1**, with its elements being the Fresnel coefficients, whose expression at imaginary

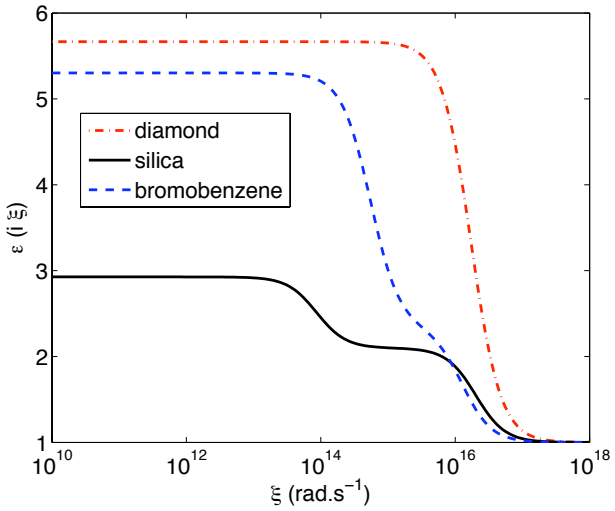

Figure 19: Dielectric function $\varepsilon(i\xi)$ as a function of the imaginary frequency for some materials using a Sellmeier model. Upper red dashed curve represents diamond, lower blue dashed curve bromobenzene, and solid black curve is for silica. The value of the parameters for the Sellmeier equation (2.10) are given in **Table 2**.

	diamond	Silica	Bromobenzene
$\lambda_1(\mu\text{m})$	0.106	0.093	0.147
B_1	4.3356	1.098	1.335
$\lambda_2(\mu\text{m})$	0.175	21.726	3.444
B_2	0.3306	0.829	2.967

Table 2: Values of the parameters for Sellmeier models for some dielectrics. Data for diamond are derived from [213], for Silica from [214], and for Bromobenzene from [215].

frequencies is, for the two polarizations:

$$\begin{aligned} r_{\text{TE}}(\xi,\kappa) &= -\frac{\sqrt{\xi^2(\varepsilon(\imath\xi)-1)+c^2\kappa^2}-c\kappa}{\sqrt{\xi^2(\varepsilon(\imath\xi)-1)+c^2\kappa^2}+c\kappa} \\ r_{\text{TM}}(\xi,\kappa) &= -\frac{\sqrt{\xi^2(\varepsilon(\imath\xi)-1)+c^2\kappa^2}-c\kappa\varepsilon(\imath\xi)}{\sqrt{\xi^2(\varepsilon(\imath\xi)-1)+c^2\kappa^2}+c\kappa\varepsilon(\imath\xi)} \end{aligned} \tag{2.11}$$

The dielectric function is incorporated in the scattering formula (1.44) for the Casimir energy per unit area through those Fresnel coefficients. A finite value of this dielectric function will give $r_{\text{TE}}, r_{\text{TM}} \in [-1,1]$, but a perfectly reflecting material, for which $\varepsilon(\imath\xi) = +\infty$ at all frequencies, has the Fresnel coefficients:

$$\begin{aligned} r_{\text{TE}}^{\text{perf}}(\xi,\kappa) &= \lim_{\varepsilon\to+\infty} -\frac{\sqrt{\xi^2(\varepsilon(\imath\xi)-1)+c^2\kappa^2}-c\kappa}{\sqrt{\xi^2(\varepsilon(\imath\xi)-1)+c^2\kappa^2}+c\kappa} = -1 \\ r_{\text{TM}}^{\text{perf}}(\xi,\kappa) &= \lim_{\varepsilon\to+\infty} -\frac{\sqrt{\xi^2(\varepsilon(\imath\xi)-1)+c^2\kappa^2}-c\kappa\varepsilon(\imath\xi)}{\sqrt{\xi^2(\varepsilon(\imath\xi)-1)+c^2\kappa^2}+c\kappa\varepsilon(\imath\xi)} = 1 \end{aligned} \tag{2.12}$$

To study the effect of the model for the reflection on the objects, we introduce the finite conductivity correction factor η_E^P for the Casimir energy, as the energy with imperfect reflectors normalized by the one for perfect mirrors, and a similar factor η_F^P for the Casimir force. From the expressions (1.44,1.45) (p.37) obtained from the scattering formula, we get the following expressions for the two factors:

$$\eta_E^P = \frac{E}{E_{\text{perf}}} = -\frac{180\mathcal{L}^3}{c\pi^4}\int_0^\infty \mathrm{d}\xi \int_{\xi/c}^\infty \kappa \mathrm{d}\kappa \ln\left[(1-\rho_{\text{TE}}(\xi,\kappa))(1-\rho_{\text{TM}}(\xi,\kappa))\right]$$
$$\eta_F^P = \frac{F}{F_{\text{perf}}} = \frac{120\mathcal{L}^4}{c\pi^4}\int_0^\infty \mathrm{d}\xi \int_{\xi/c}^\infty \kappa^2 \mathrm{d}\kappa \left[\frac{\rho_{\text{TE}}(\xi,\kappa)}{1-\rho_{\text{TE}}(\xi,\kappa)} + \frac{\rho_{\text{TM}}(\xi,\kappa)}{1-\rho_{\text{TM}}(\xi,\kappa)}\right] . \tag{2.13}$$

The results of numerical evaluation for the correction factor η_E^P for the Casimir energy are presented in **Fig. 20** for plasma and Drude models with parameters for gold, and in **Fig. 21** for various dielectrics using Sellmeier equation (2.10) for their dielectric function.

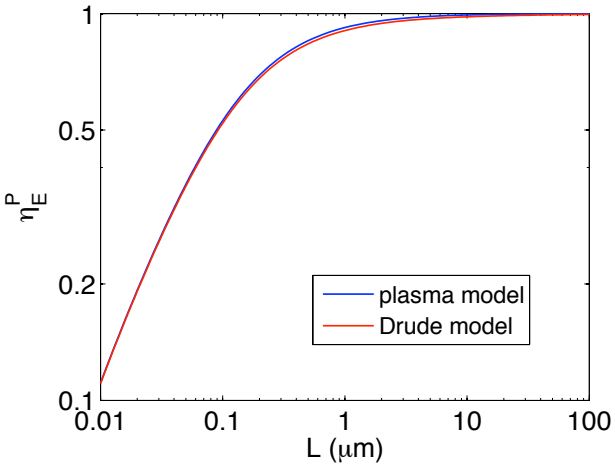

Figure 20: Finite conductivity correction factor η_E^P in the plane-plane geometry. The lossless plasma model is presented by a blue curve, the dissipative Drude model by a red curve. The values of the parameters are those of gold in **Table 1**.

The curves for plasma (blue solid curve) and Drude model (red solid curve) are very close, their relative difference is always smaller than 0.02 for the values of the parameters here considered, and vanishes at the limits of short and large separation. This will no longer be the case for non-zero temperature, as we will see in the next section. For both plasma and Drude model, at the limit of large distances we get $\eta_E^P \to 1$, meaning that imperfect reflection does not have influence in this regime. This can be understood by the fact that at large separation ($\mathcal{L} \gg \lambda_P$), only frequencies lower than the plasma frequency ω_P contribute to the Casimir energy, and both metallic models represent very good reflectors for low frequencies. At short separations, the conductivity correction factor η_E^P decreases below one and becomes linear in $\mathcal{L}$, meaning that imperfect reflection reduces the magnitude of the Casimir energy. The highly-imperfect reflection regime ($\mathcal{L} \ll \lambda_P$) gives [216, 217] the following asymptotic result:

$$\eta_E^P = \frac{3\alpha}{2}\frac{\mathcal{L}}{\lambda_P} \quad \text{and} \quad \eta_F^P = \alpha\frac{\mathcal{L}}{\lambda_P} \quad \text{with} \quad \alpha = \frac{30}{\sqrt{2}\pi^2}\sum_{n=1}^{\infty}\frac{1}{n^3}\frac{(4n-3)!!}{(4n-2)!!} \simeq 1.1933 \tag{2.14}$$

which shows that the imperfect reflection, at the limit of short distances, changes the power law from the perfect mirrors expression, replacing a $\mathcal{L}$ by a λ_P and changing the coefficient by a factor $\alpha \simeq 1.1933$.

For dielectric materials, the shape of the conductivity correction factor η_E^P depends on the oscillators frequencies. For diamond (upper red dashed curve) and bromobenzene (intermediate blue dashed curve) the function is quite monotonic, but for silica (lower black solid curve), the curve undergoes a plateau, just as does its dielectric function presented in **Fig. 19**.

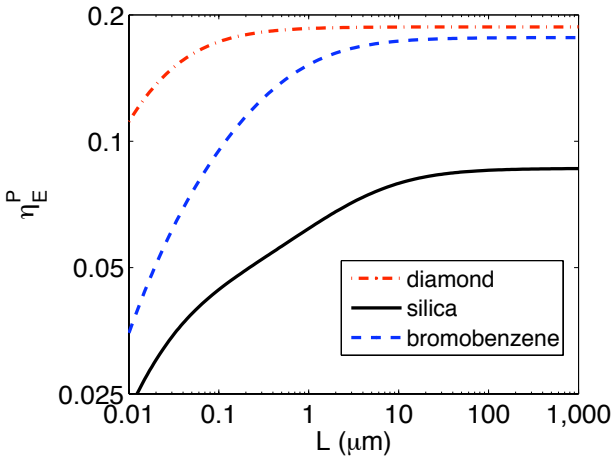

Figure 21: Finite conductivity correction factor η_E^P in the plane-plane geometry. Upper red dashed curve represents diamond, lower blue dashed curve bromobenzene, and solid black curve is for silica. The value of the parameters for the Sellmeier model are given in **Table 2**.

At the limit of large separation, unlike for metals, the conductivity correction factor η_E^P does not go to unity and is much smaller, as the materials are not very good reflectors at small frequencies. In this regime then, imperfect reflection still has an influence for dielectric materials. At the limit of small separations, like for metals a linear regime appears, which can also be computed analytically [218].

3 The scattering formula at non-zero temperature

At zero temperature, the Casimir effect is due to the quantum fluctuations of the vacuum only, and thus to its zero-point energy $E_0 = \frac{\hbar\omega}{2}$ per frequency mode. When the temperature is non-zero, the contribution of the thermal fluctuations of the electromagnetic field have to be added, and the energy of the vacuum follows Planck's law [136]:

$$E = \left(\frac{1}{2} + \overline{n}_\omega\right)\hbar\omega \qquad \text{with} \qquad \overline{n}_\omega = \frac{1}{e^{\frac{\hbar\omega}{k_B T}} - 1} = \frac{1}{e^{2\pi\frac{\omega}{\omega_T}} - 1}$$

where $\overline{n}_\omega$ is the mean number of photons per frequency mode, and $\omega_T = \frac{2\pi k_B T}{\hbar}$ is called the thermal frequency. The associated thermal wavelength is $\lambda_T = \frac{2\pi c}{\omega_T} = \frac{\hbar c}{k_B T} \simeq 7.6\mu m$ at ambiant temperature. In the latter expression of the vacuum energy, one clearly separates the vacuum energy between the contribution of "virtual photons" accounting for the quantum fluctuations of vacuum, and of "thermal photons" accounting for the classical thermal fluctuations.

As discussed in the introduction, the inclusion of temperature in the Casimir effect has been the subject of many theoretical works, among which we may cite the famous prediction of a ratio 2 appearing between the results of dissipative and non-dissipative metals at the limit of large distances when the temperature is non-zero [137]. The thermal effects in the Casimir force are also important in the discussion of the experimental measurements, as they are not observed in [107, 109] as they should if one uses the Drude model for the mirrors, but they are in a recent experiment [110, 111] performed at larger distances.

In [165], it is shown that the change from zero temperature to non-zero temperature can be mastered by introducing the multiplicative factor $1 + 2\bar{n}_\omega = \coth(\pi\frac{\omega}{\omega_T})$ in the trace over modes, and yields the following change in the scattering formula for the Casimir free energy:

$$\mathcal{F} = \frac{\hbar}{2\pi}\int_0^\infty \mathrm{d}\omega \left[\left(-\frac{\imath}{2}\right)\coth\left(\pi\frac{\omega}{\omega_T}\right)\mathrm{Tr}\ln\left(\mathcal{D}(\omega)\right) + \text{C.C.}\right] . \tag{3.1}$$

In [219], the rotation to imaginary frequencies is done from (3.1) with the thermal factor and yields:

$$\mathcal{F} = \frac{\hbar}{2\pi}\sum_{n\in\mathbb{Z}}\int_0^\infty \mathrm{d}\xi \cos\left(2\pi n\frac{\xi}{\omega_T}\right)\ln\det\mathcal{D}(\imath\xi) . \tag{3.2}$$

Expression (3.2) for the Casimir free-energy at ambient temperature seems more complex to handle than the corresponding expression (1.35) at zero-temperature, as it involves both a sum and an integral. Nevertheless, as will be discussed in **Section 3.1**, it can be reduced to a discrete sum over the Matsubara frequencies only. With this simplification, we will then recall in **Section 3.2** some results in the plane-plane configuration, particularly on the correlations between the effects of finite conductivity and temperature.

3.1 The Matsubara sum

The quantity $\mathcal{F}$ has the generic form :

$$Q = \frac{\hbar}{2\pi}\sum_{n\in\mathbb{Z}}\int_0^\infty \mathrm{d}x\cos(n\alpha x)\Phi(x) \tag{3.3}$$

$$\text{with} \quad \Phi(x) = \ln\det\mathcal{D}(\imath x) \quad \text{and} \quad \alpha = \frac{2\pi}{\omega_T}$$

where $\alpha > 0$ at $T > 0$. As this quantity uses both infinite series and integrals over $\mathbb{R}$, it is of great interest to manipulate it as a precise mathematical object. In the following is explained how the distribution theory offers a framework that allows to simplify the expressions for the case $T \neq 0$.

Definition 1 ***Schwarz Space*** $\boxed{\mathcal{S}(\mathbb{R})}$

The Schwarz Space is the set of all infinitely differentiable functions, whose derivatives are continuous and decrease faster than any polynomial at infinity. They are also called "rapidly decreasing functions". Formally this set is defined as :

$$\mathcal{S}(\mathbb{R}) = \left\{ \phi \in \mathcal{C}^\infty(\mathbb{R}) \,\middle|\, |x|^j \phi^{(k)}(x) \longrightarrow 0 \text{ when } |x| \to +\infty \ \forall j,k \in \mathbb{N} \right\} .$$

As $\kappa^2 = \hat{\xi}^2 + k^2$ for planar modes, all elements of matrix $\mathcal{M}$ contain a factor $e^{-2\kappa\mathcal{L}} < e^{-2\frac{\mathcal{L}}{c}\xi}$ from the translation operators, which is exponentially decreasing for $\xi \to +\infty$, as seen in Eq.(1.38). The integrand $\Phi(\xi) = \ln\det\mathcal{D}(\imath\xi) \simeq \ln(1 - \mathrm{Tr}\mathcal{M}(\imath\xi)) \simeq -\mathrm{Tr}\mathcal{M}(\imath\xi)$ for $\xi \to +\infty$, and thus lies in the Schwarz space for the variable ξ.

Definition 2 ***The space of tempered distributions*** $\boxed{\mathcal{S}'(\mathbb{R})}$

$\mathcal{S}'(\mathbb{R})$ *is the dual of the Schwarz space, thus the set of continuous linear form acting on* $\mathcal{S}(\mathbb{R})$*. As a result,* T *is a tempered distribution if only* $\exists K \in \mathbb{N}, C \in \mathbb{R}$*, such that :*

$$\forall \phi \in \mathcal{S}(\mathbb{R}), \quad |< T, \phi >| \leq C \sup_{0\leq j,k\leq K} \sup_{x\in\mathbb{R}} \left(|x|^j |\phi^{(k)}(x)| \right) .$$

Prop. 1 *Any bounded function on* $\mathbb{R}$ *defines a tempered distribution.*

This mathematical frame allows to use the Fourier Transform (FT) on both spaces.

Definition 3 ***Fourier transform in*** $\mathcal{S}(\mathbb{R})$

We define the FT of $\phi \in \mathcal{S}(\mathbb{R})$ *in angular-frequency domain by:*

$$\hat{\phi}(k) = \frac{1}{\sqrt{2\pi}} \int_{\mathbb{R}} \mathrm{d}x \ e^{-ikx} \phi(x) .$$

With this convention, the FT is almost an involution:

$$\phi(x) = \frac{1}{\sqrt{2\pi}} \int_{\mathbb{R}} \mathrm{d}k \ e^{ikx} \hat{\phi}(k) .$$

Prop. 2 *The Fourier Transform is a continuous linear application from* $\mathcal{S}(\mathbb{R})$ *to itself.*

Definition 4 ***Fourier transform of a tempered distribution***

If $T \in \mathcal{S}'(\mathbb{R})$*, one can define* $\hat{T} \in \mathcal{S}'(\mathbb{R})$ *as :*

$$< \hat{T}, \phi > = < T, \hat{\phi} > \ \ \forall \phi \in \mathcal{S}(\mathbb{R}) .$$

Prop. 3 *The Fourier Transform is a continuous linear application from* $\mathcal{S}'(\mathbb{R})$ *to itself.*

Within this formalism, one can write :

$$\begin{aligned} Q &= \frac{\hbar}{2\pi} \lim_{N\to+\infty} Q_N \\ Q_N &= \frac{\hbar}{2\pi} \sum_{n=-N}^{N} \int_0^\infty \mathrm{d}x \ \cos(n\alpha x)\Phi(x) = \frac{\hbar}{2\pi} \int_0^\infty \mathrm{d}x \left[\sum_{n=-N}^{N} \cos(n\alpha x) \right] \Phi(x) \\ &= \frac{\hbar}{4\pi} \int_{\mathbb{R}} \mathrm{d}x \left[\sum_{n=-N}^{N} \cos(n\alpha x) \right] \Phi(x) = \frac{\hbar}{4\pi} < S_N, \Phi > \end{aligned}$$

with $S_N(x) = \sum_{n=-N}^{N} \cos(n\alpha x) = \sum_{n=-N}^{N} e^{in\alpha x}$ a bounded function, thus defining a tempered distribution thanks to **Prop. 1**, and Φ extended on $\mathbb{R}$ by parity ($\Phi(x) = \Phi(-x)$ for $x < 0$).

Lemma 1 $\forall \alpha > 0, \forall \phi \in \mathcal{S}(\mathbb{R}), \forall x \in \mathbb{R}, \quad \sum_{n\in\mathbb{Z}} \phi(x+n\alpha) = \frac{\sqrt{2\pi}}{\alpha} \sum_{m\in\mathbb{Z}} \hat{\phi}\left(2\pi\frac{m}{\alpha}\right) e^{\imath 2\pi \frac{mx}{\alpha}}$

(For proof, see Appendix A.1 p.212)

Lemma 2 *The Dirac comb* $T = \sqrt{2\pi}\sum_{n\in\mathbb{Z}} \delta(x-n\alpha)$ *is in* $\mathcal{S}'(\mathbb{R})$ *and its inverse Fourier transform is* $\mathrm{TF}^{-1}(T) = \frac{2\pi}{\alpha}\sum_{n\in\mathbb{Z}} \delta\left(x - n\frac{2\pi}{\alpha}\right)$.

(For proof, see Appendix A.2 p.212)

Prop. 4

- $S_N \longrightarrow \mathrm{TF}^{-1}(T)$.
- *The computation of the quantity* Q *reduces to :* $Q = \frac{\hbar}{\alpha}{\sum_n}' \Phi\left(n\frac{2\pi}{\alpha}\right)$, *where the primed sum represents a sum over* $\mathbb{N}$ *with a coefficient* $\frac{1}{2}$ *for the zeroth term.*

(For proof, see Appendix A.3 p.213)

The scattering formula for the Casimir free-energy, with $\Phi(x) = \ln\det\mathcal{D}(\imath x)$ and $\alpha = \frac{2\pi}{\omega_T} = \frac{\lambda_T}{c} = \frac{\hbar}{k_B T}$, then takes the form of a discrete sum over the Matsubara frequencies $(\xi_n)_{n\in\mathbb{N}} = n\omega_T$:

$$\mathcal{F} = k_B T {\sum_n}' \ln\det\mathcal{D}(\imath\xi_n) \ . \tag{3.4}$$

The scattering formula (3.4) at non-zero temperatures replaces a continuous integration over all frequencies to a discrete sum over regularly spaced frequencies $\xi_n = n\omega_T$. This change goes with a multiplication by $\frac{2\pi k_B T}{\hbar} = \omega_T$, which is the spacing between the Matsubara frequencies. It follow that the non-zero formula (3.4) can be interpreted as an approximated evaluation of the integral involved in the zero-temperature formula (1.35) with a rectangle rule, involving rectangles of width ω_T, centered at the Matsubara frequencies $(n\omega_T)$. This interpretation is illustrated in **Fig. 22** where the rectangles are drawn for the first Matsubara frequencies, the first one being twice narrower.

When the temperature goes to 0, the width of the rectangles goes to zero and the discrete sum goes to the continuous integral. From this point of view, the scattering formula (3.4) containing the thermal fluctuations is both simpler and more general as it contains the zero-temperature formula as a limiting case. This regime can be characterized with the distance $\mathcal{L}$ between the two objects: because of the exponential decrease at high frequencies $e^{-2\frac{\xi\mathcal{L}}{c}}$, only frequencies with $\xi \lesssim \frac{c}{\mathcal{L}}$ give an important contribution to the Casimir effect. In order to have $N \gg 1$ Matsubara frequencies inside the interval $[0, \frac{c}{\mathcal{L}}]$, the N^{th} Matsubara term must be $\xi_N = N\omega_T \sim \frac{c}{\mathcal{L}}$. It follows that the distance must verify $\mathcal{L} \ll \frac{\lambda_T}{2\pi}$ in order to have a dense quadrature of the interval $[0, \frac{c}{\mathcal{L}}]$ which makes the discrete sum tending to the continuous integral and yields the low-temperature regime:

$$[\mathcal{L} \ll \lambda_T] \qquad \mathcal{F} \longrightarrow E = \frac{\hbar}{2\pi}\int_0^\infty \mathrm{d}\xi\ \Phi(\xi) \quad , \qquad \text{with} \quad \Phi(\xi) = \ln\det\mathcal{D}(\imath\xi) \ . \tag{3.5}$$

As the frequency-step between the Matsubara frequencies is proportional to the temperature T, we can expect in the limit of very large temperatures from the observation of **Fig. 22** this spacing to be large enough so that only the zeroth term in (3.4) has a non-negligible contribution to the Matsubara sum. Indeed, as the integrand exponentially decreases for large frequencies $\xi \gg \frac{c}{\mathcal{L}}$, as seen in Eq.(1.38), the second Matsubara frequency $\xi_1 = \omega_T$ gives a negligible contribution as soon

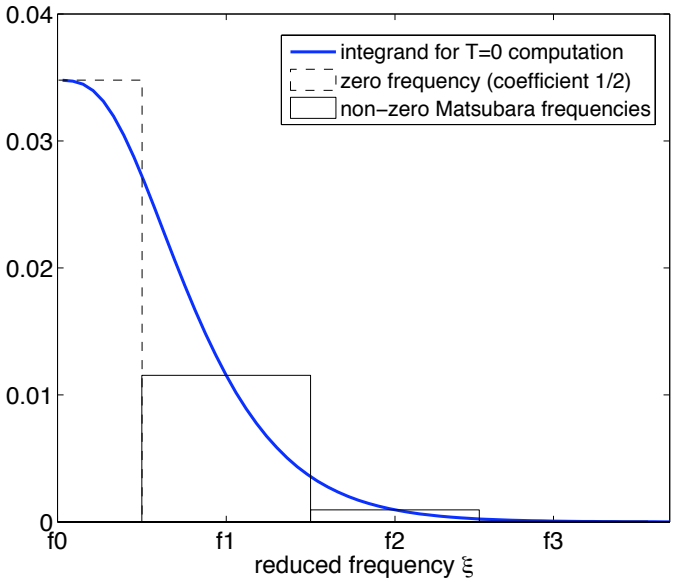

Figure 22: Comparison of the summation over frequencies ξ for the scattering formula at zero and non-zero temperature. The blue curves represents the integrand $\Phi(\xi)$. The zero temperature scattering formula (1.35) is obtained through continuous integration over all frequencies. The non-zero temperature scattering formula (3.4) involves a discrete sum of the integrand function, evaluated on a discrete set of frequencies $n\omega_T$.

as $\omega_T \gg \frac{c}{\mathcal{L}}$. With $\omega_T = \frac{2\pi c}{\lambda_T}$, the high-temperature regime can be written as ($\mathcal{L} \gg \frac{\lambda_T}{2\pi}$), or more simply ($\mathcal{L} \gg \lambda_T$), and in this limit the scattering formula (3.4) takes the simpler form:

$$[\mathcal{L} \gg \lambda_T] \qquad \mathcal{F} \longrightarrow \mathcal{F}^{\rm HT} = \frac{k_B T}{2}\Phi(0) \quad , \qquad \text{with} \quad \Phi(0) = \ln\det \mathcal{D}(0) \ . \tag{3.6}$$

that only involves the scattering operator $\mathcal{D}$ at zero frequency. This high-temperature (HT) limit is proportional to the temperature T and does not involves the number $\hbar$ anymore. As a consequence the Casimir effect only comes from classical thermal fluctuations in this limit.

3.2 The example of the plane-plane geometry

3.2.1 Expressions for the thermal Casimir effect and high-temperature regimes

To include the thermal fluctuations in the simple geometry of two planes, we extract the integrands Φ_E and Φ_F from the zero-temperature expression (1.44) for the Casimir energy and force per unit area:

$$\begin{aligned}
\Phi_E(\xi) &= \int_{\xi/c}^{\infty} \frac{\kappa {\rm d}\kappa}{2\pi} \ln\left[(1-\rho_{\rm TE}(\xi,\kappa))(1-\rho_{\rm TM}(\xi,\kappa))\right] \\
\Phi_F(\xi) &= -\int_{\xi/c}^{\infty} \frac{2\kappa^2 {\rm d}\kappa}{2\pi} \left[\frac{\rho_{\rm TE}(\xi,\kappa)}{1-\rho_{\rm TE}(\xi,\kappa)} + \frac{\rho_{\rm TM}(\xi,\kappa)}{1-\rho_{\rm TM}(\xi,\kappa)}\right]
\end{aligned} \tag{3.7}$$

then the Casimir free-energy $\mathcal{F}$ and force F at non-zero temperature is given by:

$$\begin{aligned}
\mathcal{F}/A &= k_B T {\sum_n}' \int_{\xi_n/c}^{\infty} \frac{\kappa {\rm d}\kappa}{2\pi} \ln\left[(1-\rho_{\rm TE}(\xi_n,\kappa))(1-\rho_{\rm TM}(\xi_n,\kappa))\right] \\
F/A &= -k_B T {\sum_n}' \int_{\xi_n/c}^{\infty} \frac{2\kappa^2 {\rm d}\kappa}{2\pi} \left[\frac{\rho_{\rm TE}(\xi_n,\kappa)}{1-\rho_{\rm TE}(\xi_n,\kappa)} + \frac{\rho_{\rm TM}(\xi_n,\kappa)}{1-\rho_{\rm TM}(\xi_n,\kappa)}\right] \ .
\end{aligned} \tag{3.8}$$

The high-temperature regime ($\mathcal{L} \gg \lambda_T$) can be analytically computed for perfect mirrors, as their Fresnel coefficients (2.12) are ± 1, and their open-loop functions ρ_p then reduce to $e^{-2\kappa\mathcal{L}}$:

$$\begin{aligned}\mathcal{F}^{\rm HT}_{\rm perf}/A &= \frac{k_B T}{2}\int_0^\infty \frac{\kappa \mathrm{d}\kappa}{2\pi}\ln\left[(1-e^{-2\kappa\mathcal{L}})(1-e^{-2\kappa\mathcal{L}})\right] \\ &= \frac{k_B T}{8\pi\mathcal{L}^2}\int_0^\infty t\mathrm{d}t\ln(1-e^{-t}) \\ &= -\frac{\zeta(3)k_B T}{8\pi\mathcal{L}^2}\end{aligned} \tag{3.9}$$

where ζ is Riemann's zeta function ($\zeta(3) \simeq 1.202057$). For planar mirrors described by the Drude model (resp. dielectrics), we will see in **Section 7.2** (p.111) that the zero-frequency limits of the Fresnel coefficients are 0 for TE modes and 1 (resp. $\frac{\varepsilon(0)-1}{\varepsilon(0)+1}$) for TM modes. With a similar derivation, we deduce the high-temperature regime ($\mathcal{L} \gg \lambda_T$) for the Casimir free-energy between two planes with Drude model for metals, or for dielectrics:

$$\mathcal{F}^{\rm HT}_{\rm Drud}/A = -\frac{\zeta(3)k_B T}{16\pi\mathcal{L}^2} \qquad\qquad \mathcal{F}^{\rm HT}_{\rm diel}/A = -\frac{\zeta(3)k_B T}{16\pi\mathcal{L}^2}\frac{\varepsilon(0)}{\varepsilon(0)+1} \tag{3.10}$$

where we remark that the result for Drude metals is half the expression (3.9) derived for perfect mirrors. This can be understood from the fact that both polarization TE and TM have the same role for perfect mirrors, and at the limit of low-frequencies one is turned off for Drude metals.

For plasma model, the situation is a bit more complex, however, as will be derived in **Section 7.2** (p.111), we can show that in the limiting case where ($\mathcal{L} \gg \lambda_P$), the plasma case recovers the Fresnel coefficients of perfect mirrors, which gives a high-temperature regime similar to (3.9), whereas in the opposite case where ($\mathcal{L} \ll \lambda_P$), the Fresnel coefficients of the Drude model at low frequency are recovered, leading to a high-temperature regime similar to the left part of (3.10). As a consequence, the ratio of the high-temperature long-distance ($\mathcal{L} \gg \lambda_T, \lambda_P$) limits of the Casimir free-energies obtained when using the lossless plasma and dissipative Drude models goes to 2, in agreement with [137].

The high-temperature regime of the Casimir free-energy of two planes with the plasma model is not universal, unlike with the Drude model, as it depends on the parameter λ_P of the material. This feature is important, and will be discussed also in the sphere-plane configuration. We remark that in common situation (usual materials and ambient temperature) we have ($\lambda_T \gtrsim \lambda_P$), and the high-temperature regime ($\mathcal{L} \gg \lambda_T$) entails the first condition ($\mathcal{L} \gg \lambda_P$). It means that the Drude high-temperature regime is usually different from the plasma one. Moreover, the fact that Drude result at high-temperatures does not depend on the material parameters (λ_P, δ) means that it does no tend to recover the plasma result when we take $\delta \to 0$ at the end. Consequently, this is a case where the limits $\mathcal{L} \to \infty$ and $\delta \to 0$ do not commute.

3.2.2 Observation of thermal effects

To study the influence of non-zero temperature on the Casimir effect, we introduce the thermal correction factor $\eta^T_{\mathcal{F}} = \frac{\mathcal{F}(T)}{\mathcal{F}(0)}$ for the free-energy as the Casimir free-energy at temperature T, normalized by the energy at zero temperature. A similar factor can be defined for the force and reads $\eta^T_F = \frac{F(T)}{F(0)}$. In **Fig. 23** we present the result of numerical evaluations for the thermal correction factor $\eta^T_{\mathcal{F}}$ for the free-energy, as a function of the distance. This is done for perfect mirrors, but also for metallic mirrors modelled by the plasma and Drude models.

For small distances we observe that $\eta^T_{\mathcal{F}} \simeq 1$ in all cases, meaning that temperature does not have influence in this regime. For large distances, for perfect mirrors and plasma model the factor increases and becomes linear in $\mathcal{L}$, meaning that thermal photons have an attractive contribution

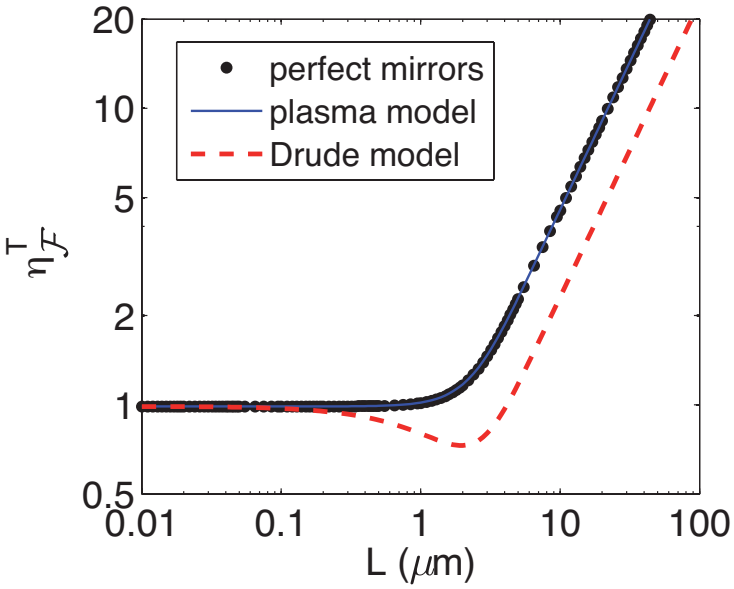

Figure 23: Thermal correction factor $\eta^T_{\mathcal{F}} = \frac{\mathcal{F}(T)}{\mathcal{F}(0)}$ for the Casimir free-energy between two planes as a function of the distance $\mathcal{L}$, with a log-log scale. The optical properties of the materials are described either by perfect mirrors (black dots), plasma (thin blue line), or Drude (lower red dashed curve) models. The two first curves are almost superimposed. The temperature is $T = 300$ K, which corresponds to a thermal length $\lambda_T = 7.6$ μm. The chosen parameters for the metal are those of gold ($\lambda_P = 136$ nm ; $\delta = 0.004$).

to the Casimir energy. This is consistent with the high-temperature ($L \gg \lambda_T$) regime for $\eta^T_{\mathcal{F}}$, derived from expressions at zero (1.46) and high (3.9) temperatures for perfect mirrors:

$$\eta^T_{\mathcal{F}} = \frac{\mathcal{F}_{\rm perf}(T \to \infty)}{\mathcal{F}_{\rm perf}(0)} = \frac{90\zeta(3)\mathcal{L}}{\pi^3 \lambda_T} \ . \tag{3.11}$$

For materials described by the Drude model however, the factor first decreases to a minimum below unity at intermediate distances, meaning that the thermal contribution to the Casimir free-energy is repulsive. The curve increases to a high-temperature regime for large distance, with a constant gap that reproduces the factor $\frac{1}{2}$ observed in the high-temperature regimes (3.9) and (3.10).

3.2.3 Correlations between the effects of imperfect reflection and temperature

We define the total correction factor $\eta^{TP}_{\mathcal{F}}$ as the ratio of the free-energy at ambient temperature with plasma or Drude model for the reflection, and the energy at zero temperature with perfect mirrors:

$$\eta^{TP}_{\mathcal{F}} = \frac{\mathcal{F}(T)}{\mathcal{F}^{\rm perf}(0)} = -\frac{360\mathcal{L}^3}{\lambda_T \pi^3} {\sum_n}' \int_{\xi_n/c}^{\infty} \kappa {\rm d}\kappa \ln\left[(1-\rho_{\rm TE}(\xi_n,\kappa))(1-\rho_{\rm TM}(\xi_n,\kappa))\right] \tag{3.12}$$

The numerical evaluations for this total correction factor are presented for plasma (resp. Drude) model in **Fig. 24** with a thick blue (resp. red) curve with respect to the distance $\mathcal{L}$. The simple thermal correction $\eta^T_{\mathcal{F}}$ for perfect mirrors and the simple finite-conductivity correction $\eta^P_{\mathcal{F}}$ at zero temperature are presented for reference with a thin black line and thin dashed curves, respectively.

At small distances, for both model, only the imperfect reflection has an influence and the curve for $\eta^{TP}_{\mathcal{F}}$ joins the one for $\eta^P_{\mathcal{F}}$. At large distances for the plasma model, only temperature has an

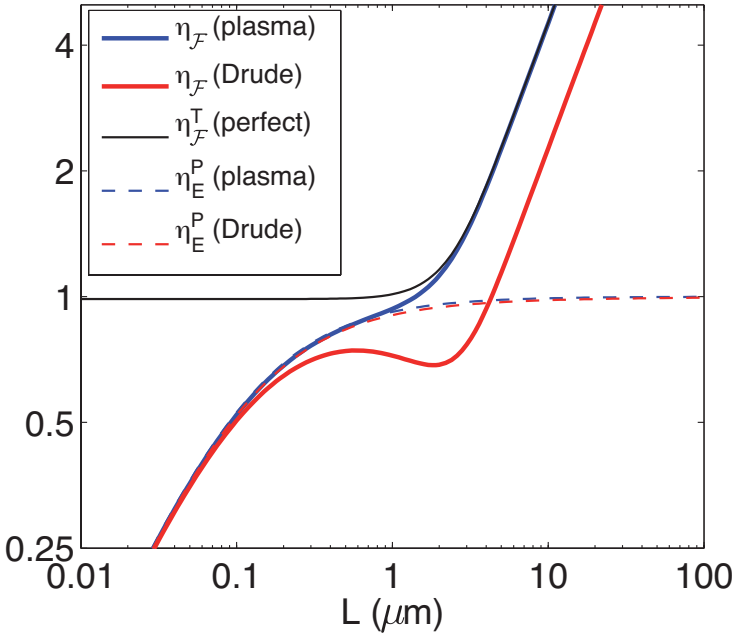

Figure 24: Total correction factor $\eta_{\mathcal{F}}^{TP}$ for the Casimir free-energy between two planes. The thick blue (resp. red) curve is obtained when using the plasma (resp. Drude) model for the description of optical properties of the materials. As a reminder, the simple thermal correction $\eta_{\mathcal{F}}^{T}$ for perfect mirrors is drawn with a thin black curve, and the simple finite-conductivity correction $\eta_{\mathcal{F}}^{P}$ is represented with dashed curves. The temperature is $T = 300$ K, which corresponds to a thermal length $\lambda_T = 7.6$ μm. The chosen parameters for the metal are those of gold ($\lambda_P = 136$ nm ; $\delta = 0.004$).

effect on the correction, and the curve catches up with the one for $\eta_{\mathcal{F}}^{T}$. For Drude model at large distances however, the high-temperature regime is obtained with a different multiplicative factor, as discussed in the previous section.

If the effects of temperature and finite conductivity were uncoupled, the thermal correction factor would not depend on the model of reflection and the finite conductivity correction factor would not depend on the temperature. The total correction factor $\eta_{\mathcal{F}}^{TP}$ would then reduce to the product of the two simple correction factors $\eta_{\mathcal{F}}^{P}$ and $\eta_{\mathcal{F}}^{T}$. Thus the observations, first that the curves are different in **Fig 23** for plasma and Drude models, but also that $\eta_{\mathcal{F}}^{TP} \neq (\eta_{\mathcal{F}}^{P}\eta_{\mathcal{F}}^{T})$ for Drude in **Fig. 24**, are clear signature of the existence of correlations between the effects of temperature and imperfect reflection. To measure how they interact with each other, we follow Eq.(4-24) in [207] and define the correlation number $\delta_{\mathcal{F}}^{TP}$ for the Casimir free-energy $\mathcal{F}$, which must be zero when the two effects are uncoupled:

$$\delta_{\mathcal{F}}^{TP} = \frac{\eta_{\mathcal{F}}^{TP}}{\eta_{\mathcal{F}}^{T}\eta_{\mathcal{F}}^{P}} - 1 = \frac{\mathcal{F}^{\mathrm{Drud}}(T)\mathcal{F}^{\mathrm{perf}}(0)}{\mathcal{F}^{\mathrm{perf}}(T)\mathcal{F}^{\mathrm{Drud}}(0)} - 1 \tag{3.13}$$

$$= \frac{\eta_{\mathcal{F}}^{T}[\mathrm{Drud}]}{\eta_{\mathcal{F}}^{T}[\mathrm{perf}]} - 1 \tag{3.14}$$

$$= \frac{\eta_{\mathcal{F}}^{P}(T)}{\eta_{\mathcal{F}}^{P}(0)} - 1 \tag{3.15}$$

The two last reformulations show that this correlation number can also be seen as the relative difference between the thermal correction factors with Drude and perfect mirrors thanks to Eq.(3.14), or from Eq.(3.15) as the relative difference between the finite conductivity correction factors at zero and ambient temperature. This parameter is presented in **Fig. 25** with respect to the distance $\mathcal{L}$, for both plasma and Drude models with blue and red curves, respectively.

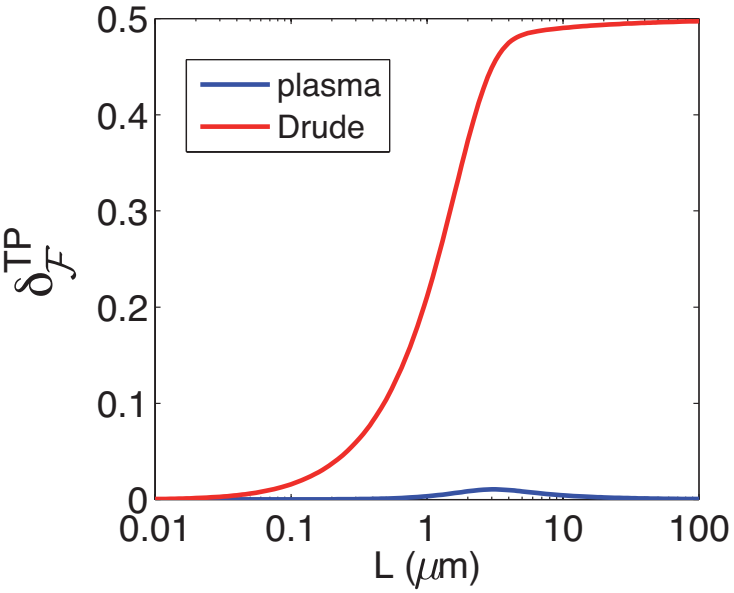

Figure 25: Correlation number $\delta_{\mathcal{F}}^{TP}$ for the Casimir free-energy between the effects of finite conductivity and temperature, in the plane-plane configuration. The temperature is $T = 300$ K, which corresponds to a thermal length $\lambda_T = 7.6\mu$m. The chosen parameters for the metal are those of gold ($\lambda_P = 136$ nm ; $\delta = 0.004$).

For materials described by the lossless plasma model, the correlation number $\delta_{\mathcal{F}}^{TP}$ remains small with a maximum value of $1.05e-2$ at intermediate distances, and vanishes in both short and large

separation limits. The shape of this curve and its dependance upon the scaling parameter $\frac{\lambda_P}{\lambda_T}$ has been studied in [207]. For the Drude model, the correlation is much more important, and does not vanish in the limit of large distances but rather goes to the value $\frac{1}{2}$.

4 The proximity force approximation (PFA)

We now consider a sphere of radius R, made of a material with a dielectric function $\varepsilon(i\xi)$, in front of an infinite plane of the same material. The surface-surface distance between the two objects will be noted L and the center-to-plate distance will be $\mathcal{L} = L + R$. The derivatives with respect to L and $\mathcal{L}$ are thus equivalent. We define the aspect ratio $\frac{L}{R}$, which will play a central role in this geometry. To produce theoretical predictions for the Casimir effect, the Proximity Force Approximation (PFA) has been commonly used [146, 147, 148] to handle that geometry. Its domain of validity is when the sphere is very close to the plane ($L \ll R$), and allows to derive simply the Casimir effect from the quantity computed in the plane-plane geometry, as in the previous sections.

We will first introduce the general idea of this approximation method and derive it in the sphere-plane geometry in **Section 4.1**. Then, we will introduce in **Section 4.2** what we call the primo-potential D, a quantity that will enable us to compute the Casimir energy from the PFA method. Finally, we will discuss the numerous limitations of this approximation, and how we can assess its accuracy in **Section 4.3**.

4.1 The PFA formula in the sphere-plane geometry

The Proximity Force Approximation relies on the assumption that when the sphere comes close to the surface of the plane ($L \ll R$), the main contribution to the Casimir interaction comes from the cap of the sphere facing the plane.

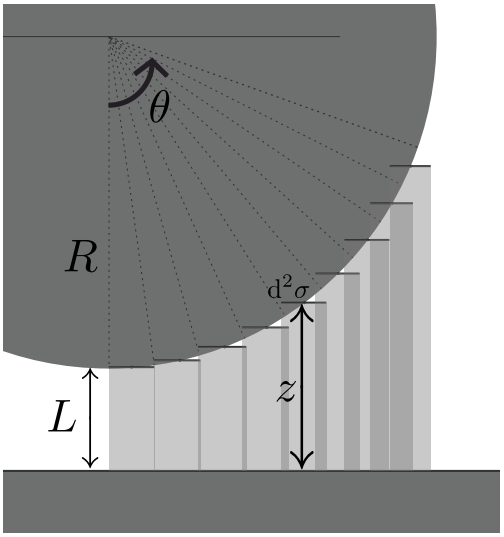

The surface Σ of the half-sphere closer to the plane is then decomposed in infinitesimal elements $\mathrm{d}^2\sigma$, which are considered to only interact with their corresponding infinitesimal element at the plane's surface, as if they were both part of two infinite parallel plates:

$$\mathcal{F}_{\mathrm{PFA}} = \iint_{\Sigma} \frac{\mathcal{F}_{\mathrm{PP}}(z)}{A} \mathrm{d}^2\sigma \ . \tag{4.1}$$

$\mathrm{d}^2\sigma = R^2 \sin\theta \mathrm{d}\theta \mathrm{d}\varphi$ is the infinitesimal surface element in spherical coordinates, $z = L + R(1 - \cos\theta)$ is the local distance between the two facing infinitesimal surfaces, and $\mathcal{F}_{\mathrm{PP}}/A$ is the Casimir free-energy per unit area in the plane-plane geometry given by Eq.(3.8).

As z only depends on θ, the integral can be simplified to a sum over z:

$$\begin{aligned} \mathcal{F}_{\mathrm{PFA}} &= 2\pi R \int_0^{\pi/2} \frac{\mathcal{F}_{\mathrm{PP}}(z(\theta))}{A} R \sin\theta \mathrm{d}\theta \\ &= 2\pi R \int_L^{L+R} \frac{\mathcal{F}_{\mathrm{PP}}(z)}{A} \mathrm{d}z \ . \end{aligned}$$

Taking the derivative of it, and multiplying by (-1), one obtains the force:

$$F_{\mathrm{PFA}}(L,R) = -2\pi R \left(\frac{\mathcal{F}_{\mathrm{PP}}(L+R)}{A} - \frac{\mathcal{F}_{\mathrm{PP}}(L)}{A} \right) \simeq 2\pi R \frac{\mathcal{F}_{\mathrm{PP}}(L)}{A} \tag{4.2}$$

when for a sufficiently fast decreasing amplitude of the free-energy with respect to the distance, we can neglect $\frac{\mathcal{F}_{\mathrm{PP}}(L+R)}{A}$ with respect to $\frac{\mathcal{F}_{\mathrm{PP}}(L)}{A}$. The same procedure can be followed to get

the approximated force gradient $G_{\text{PFA}} = -\frac{\partial F_{\text{PFA}}}{\partial L}$ in the sphere-plane configuration from the plane-plane force per unit area:

$$G_{\text{PFA}}(L,R) = 2\pi R \frac{F_{\text{PP}}(L)}{A} \tag{4.3}$$

The general method of splitting the sphere's surface in small parts, consider the Casimir interaction for each one with the plane, and then integrate over the whole sphere surface, as illustrated in Eq.(4.1), can be done in several ways, depending on the choice of the corresponding infinitesimal surfaces, and on the way one computes the Casimir interaction between the two infinitesimal surfaces. Alternative formulations of this general method are described in **Appendix B.1** (p.219), but we will keep the usual formulation here derived, leading to the simplest and most commonly used expressions (4.2, 4.3).

4.2 The primo-potential D

For the special case of perfectly reflecting materials at zero temperature, we obtain from the explicit expressions (1.46) and (1.47) in the plane-plane configuration, the PFA results for the force and the force gradient:

$$F_{\text{PFA}}(L,R) = -\frac{\hbar c \pi^3 R}{360 L^3} \qquad\qquad G_{\text{PFA}}(L,R) = -\frac{\hbar c \pi^3 R}{120 L^4} \ . \tag{4.4}$$

It is then simple to integrate this expression for the force and obtain the PFA result for the energy:

$$E_{\text{PFA}}(L,R) = -\frac{\hbar c \pi^3 R}{720 L^2} \ . \tag{4.5}$$

In order to obtain a similar result in the general case, a first possibility is to compute the force with (4.2) and then integrate it numerically over the distance L, as done analytically to obtain (4.5). For convenience, we introduce here a second possibility, in order to compute directly the Casimir free-energy. Observing the expressions (4.2) and (4.3), we can deduce that for this we need a function whose derivative would be the free-energy in the plane-plane configuration.

Definition 5 (primo-potential D) *The primo-potential $D(L,T)$ is a function such as*

$$-\frac{\partial D}{\partial L} = \mathcal{F}(L,T)$$

Once this function is known, the free energy $\mathcal{F}_{\text{PFA}}$ from the PFA method simply writes:

$$\mathcal{F}_{\text{PFA}}(L,R) = 2\pi R \ \frac{D_{\text{PP}}(L)}{A} \tag{4.6}$$

where D_{PP}/A denotes the Casimir primo-potential per unit area in the plane-plane configuration. For perfect mirrors at zero temperature, it is easily obtained by integrating the expression (1.46) for the energy in this configuration:

$$D_{\text{PP}}(L)/A = -\frac{\hbar c \pi^2}{1440 L^2} \qquad\qquad E_{\text{PFA}}(L,R) = -\frac{\hbar c \pi^3 R}{720 L^2} \ . \tag{4.7}$$

which is of course consistent with expression (4.5). In the general case, the expression of D_{PP}/A can be obtained from the expressions (1.44) and (3.8) for the energy and free-energy, thanks to the properties of the polylogarithm.

First let us remark that the function of $\rho_p(\xi,\kappa)$ to be integrated in (1.44) and (3.8) to get the energy and the force are polylogarithms of indices 0 and 1, respectively:

$$\mathrm{Li}_0(\rho) = \frac{\rho}{1-\rho} \qquad\qquad \mathrm{Li}_1(\rho) = -\ln(1-\rho)\ . \tag{4.8}$$

The polylogarithms of nearby order are related by derivation through $\rho\frac{\partial \mathrm{Li}_n(\rho)}{\partial\rho} = \mathrm{Li}_{n-1}(\rho)$. It follows that each time we take the derivative of $\mathrm{Li}(\rho)$ with respect to $\mathcal{L}$, the index is decreased by 1 and a factor (-2κ) appears:

$$\frac{\partial\rho}{\partial\mathcal{L}} = -2\kappa\rho$$
$$\frac{\partial \mathrm{Li}_n(\rho)}{\partial\mathcal{L}} = \frac{\partial \mathrm{Li}_n(\rho)}{\partial\rho}\frac{\partial\rho}{\partial\mathcal{L}} = (-2\kappa)\mathrm{Li}_{n-1}(\rho)$$

At zero temperature, the primo-potential, energy and force can be thus written in a similar manner as the following functions of polylogarithms:

$$D_{\mathrm{PP}}(L)/A = -\frac{\hbar}{8\pi^2}\int_0^\infty d\xi \int_{\xi/c}^\infty d\kappa\,[\mathrm{Li}_2(\rho_{\mathrm{TE}}(\xi,\kappa)+\mathrm{Li}_2(\rho_{\mathrm{TM}}(\xi,\kappa)] \tag{4.9}$$

$$E_{\mathrm{PP}}(L)/A = -\frac{\hbar}{4\pi^2}\int_0^\infty d\xi \int_{\xi/c}^\infty \kappa d\kappa\,[\mathrm{Li}_1(\rho_{\mathrm{TE}}(\xi,\kappa)+\mathrm{Li}_1(\rho_{\mathrm{TM}}(\xi,\kappa)] \tag{4.10}$$

$$F_{\mathrm{PP}}(L)/A = -\frac{\hbar}{2\pi^2}\int_0^\infty d\xi \int_{\xi/c}^\infty \kappa^2 d\kappa\,[\mathrm{Li}_0(\rho_{\mathrm{TE}}(\xi,\kappa)+\mathrm{Li}_0(\rho_{\mathrm{TM}}(\xi,\kappa)]\ . \tag{4.11}$$

where L is the distance between the two planes' surfaces. At non-zero temperature, these functions become:

$$D_{\mathrm{PP}}(L,T)/A = -\frac{k_BT}{4\pi}{\sum_n}' \int_{\xi_n/c}^\infty d\kappa\,[\mathrm{Li}_2(\rho_{\mathrm{TE}}(\xi_n,\kappa)+\mathrm{Li}_2(\rho_{\mathrm{TM}}(\xi_n,\kappa)] \tag{4.12}$$

$$\mathcal{F}_{\mathrm{PP}}(L,T)/A = -\frac{k_BT}{2\pi}{\sum_n}' \int_{\xi_n/c}^\infty \kappa d\kappa\,[\mathrm{Li}_1(\rho_{\mathrm{TE}}(\xi_n,\kappa)+\mathrm{Li}_1(\rho_{\mathrm{TM}}(\xi_n,\kappa)] \tag{4.13}$$

$$F_{\mathrm{PP}}(L,T)/A = -\frac{k_BT}{\pi}{\sum_n}' \int_{\xi_n/c}^\infty \kappa^2 d\kappa\,[\mathrm{Li}_0(\rho_{\mathrm{TE}}(\xi_n,\kappa)+\mathrm{Li}_0(\rho_{\mathrm{TM}}(\xi_n,\kappa)]\ . \tag{4.14}$$

We will use those expressions later on, in order to obtain the Casimir energy and free-energy from PFA.

4.3 Beyond the PFA method

4.3.1 Limitations of the PFA method

A major drawback of the PFA method is that the error is not mastered. While the approximation should be reasonably valid at the limit of small aspect ratios $\frac{L}{R}\to 0$, although not proven in the general case, there is no self-contained information on how well is reproduces the exact quantity at a non-zero value of $\frac{L}{R}$. A first utility of an exact result for the plane-sphere configuration would then be to assess quantitatively this error.

To do so, for instance for the Casimir energy E in the sphere-plane configuration, we write the ratio ρ_E of the two results, exact and PFA, and assume a Taylor expansion for small values of the aspect ratio $\frac{L}{R}$:

$$\rho_E = \frac{E}{E_{\mathrm{PFA}}} = 1 + \beta_E\frac{L}{R} + \gamma_E\left(\frac{L}{R}\right)^2 + ... \tag{4.15}$$

where the zeroth order term must be 1, to be consistent with the fact a sphere with an infinite radius is a plane. It would be very useful to have an estimate for the coefficients β_E and its successors, in order to assess the error made by PFA for small values of the aspect ratio $\frac{L}{R}$ encountered in experiments. An analogous expansion can be performed for the force F or the force gradient G, implying coefficients β_F, β_G for first order corrections, and γ_F, γ_G for second order terms.

The error made by PFA is of course dependent on the PFA formulation one chooses, and from the example of an alternative formulation of the plane-based PFA discussed in **Appendix B.1.1** (p.220), we see that, in the case of perfect mirrors at zero temperature, for a β_E obtained with E_{PFA}, $\beta_E^{(2)} = \beta_E - 1$ will be obtained for $E_{\mathrm{PFA}}^{(2)}$. The same remark holds for the force and the force gradient, with $\beta_F^{(2)} = \beta_F - \frac{1}{2}$ and $\beta_G^{(2)} = \beta_G - \frac{1}{3}$. In the discussion of the error made by PFA, we will restrict ourselves to the usual PFA formula (4.2), and thus to the usual coefficients such as those appearing in Eq.(4.15).

A second problem with the PFA method is that it reduces the physics in the sphere-plane geometry to the one of the plane-plane geometry, while both geometries are conceptually different:

- The sphere has a finite size, defined by its radius R, a feature that is absent with the two infinite planes. The PFA formula might thus miss finite-size effects such as resonances inside the sphere or along its surface.
- The sphere brings in the cavity a surface with curvature, which changes drastically the way waves are scattered. Indeed, considering each infinitesimal part of the sphere as a some straight plate parallel to the plane, a lot of field will be resonant while they should be scattered around with a curved and convex surface. As we will see, this is the main reason why PFA methods usually overestimate the magnitude of the Casimir effect.
- In a plane-plane cavity, the different polarizations TE and TM are uncoupled and can be considered separately. This is still the case in the cylinder-plane geometry, as this uncoupling emerges as soon as there is a direction in which the geometry is invariant. With a sphere this translational symmetry disappears, and the two polarizations are coupled.

Finally, in the PFA formula (4.2), all effects of temperature and finite conductivity are given by terms calculated in the plane-plane geometry, hiding thus any correlation due to the different geometry. In other words, the coefficient β_E in (4.15) could be modified by the introduction of finite conductivity, temperature, roughness, or any other refinement of the model. An exact computation of the plane-sphere geometry is thus the only way to study those possible correlations.

4.3.2 Beyond-PFA corrections coefficients

If we assume a Taylor expansion at small $\frac{L}{R}$ of the ratios ρ_E, ρ_F, ρ_G for the Casimir energy, force and force gradient, such as (4.15), we can give some relationships between the constitutive coefficients β, γ for the three quantities. A simple derivation with respect to the distance L of the supposed expansion of the Casimir energy:

$$E = E_{\mathrm{PFA}}\left[1 + \beta_E \frac{L}{R} + \gamma_E \left(\frac{L}{R}\right)^2 + \mathcal{O}\left(\left(\frac{L}{R}\right)^3\right)\right]$$

$$F = F_{\mathrm{PFA}}\left[1 + \beta_E \frac{L}{R}\left(1 - \frac{E_{\mathrm{PFA}}}{LF_{\mathrm{PFA}}}\right) + \gamma_E \left(\frac{L}{R}\right)^2 \left(1 - 2\frac{E_{\mathrm{PFA}}}{LF_{\mathrm{PFA}}}\right) + \mathcal{O}\left(\left(\frac{L}{R}\right)^3\right)\right]$$

which makes the important parameter $\nu_E = \frac{LF_{\mathrm{PFA}}}{E_{\mathrm{PFA}}} = -\frac{\partial \ln |E_{\mathrm{PFA}}|}{\partial \ln L}$ appear. A similar derivation can be done for the quantities F and G, and give the same relations, with the parameter $\nu_F =$

$\frac{LG_{\mathrm{PFA}}}{F_{\mathrm{PFA}}} = -\frac{\partial \ln|F_{\mathrm{PFA}}|}{\partial \ln L}$. We thus obtain the following relations between the beyond-PFA coefficients:

$$\beta_F = \frac{\nu_E - 1}{\nu_E}\beta_E \qquad \gamma_F = \frac{\nu_E - 2}{\nu_E}\gamma_E \tag{4.16}$$

$$\beta_G = \frac{\nu_F - 1}{\nu_F}\beta_F \qquad \gamma_G = \frac{\nu_F - 2}{\nu_F}\gamma_F \ . \tag{4.17}$$

The parameters ν_E, ν_F make particularly sense for functions that depend on L as a power law: if $E_{\mathrm{PFA}} = -\frac{a}{L^\alpha}$ with $\alpha > 0$, $F_{\mathrm{PFA}} = -\frac{a\alpha}{L^{\alpha+1}}$ and we obtain $\nu_E = \alpha$, $\nu_F = \alpha + 1$. Therefore, we can give examples of the relations (4.16) in some particular cases:

- For perfect mirrors at zero temperature $\nu_E = 2$ and $\nu_F = 3$, which yield:

$$\beta_F = \frac{1}{2}\beta_E \qquad \gamma_F = 0 \tag{4.18}$$

$$\beta_G = \frac{2}{3}\beta_F \qquad \gamma_G = \frac{1}{3}\gamma_F = 0 \ . \tag{4.19}$$

- For perfect or Drude-modeled mirrors at infinite temperature $\nu_E = 1$ and $\nu_F = 2$, which yield:

$$\beta_F = 0 \qquad \gamma_F = -\gamma_E \tag{4.20}$$

$$\beta_G = \frac{1}{2}\beta_F = 0 \qquad \gamma_G = 0 \ . \tag{4.21}$$

- For plasma-modeled mirrors at zero temperature $\nu_E = 1$ and $\nu_F = 2$, which yield the same relations.

Part II.
Method for the Casimir effect in the sphere-plane geometry

Table of Contents

After the general introduction of the scattering approach in the last part, we here focus on its application to the sphere-plane configuration. The only difference with respect to the plane-plane case is the appearance of the reflection operator on the sphere, but the loss of the two longitudinal symmetries will have a great impact on the derivation of the scattering operator. In the sphere-plane geometry this operator is no more diagonal in the basis of planar electromagnetic modes, and the coupling of waves with different wavevectors and polarizations has to be taken into account.

In **Section 5** we derive an expression for the scattering operator $\mathcal{D}$, with the help of spherical electromagnetic modes to express the reflection on the sphere, and planar electromagnetic modes for the rest of the scattering process. The quantities involved in the expression for $\mathcal{D}$ are then discussed and simplified to prepare for numerical evaluations. **Section 5.4** contains the final expressions that will be used in the continuation of the study.

The method for the numerical evaluation is described in details in **Section 6**, where all steps are discussed, from the computation of special functions to the integration methods and the stability issue.

5 The scattering formula in the sphere-plane geometry

In this section we apply the scattering formula, introduced in **Section 1** (p.27), in the configuration of a sphere and an infinite plane. The sphere has a radius R and its closest point to the plane lies at a distance L to the plane. To express later on its scattering operator, the origin of the reference frame of the sphere is its center, while for the plane it is on the surface, the distance between the two reference points is then the center-to-plate distance $\mathcal{L} = L + R$.

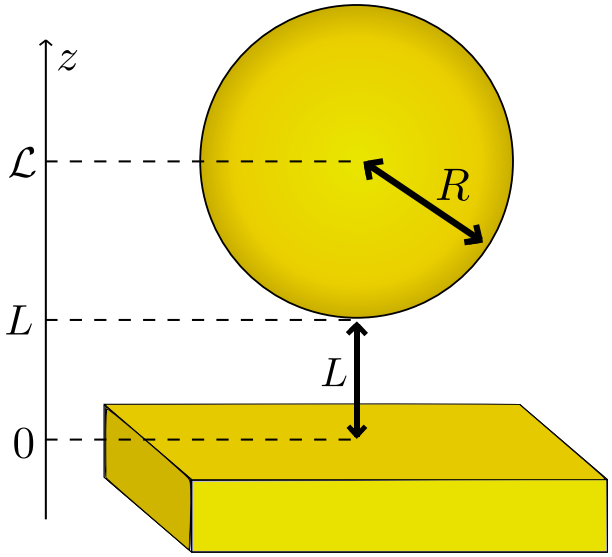

Figure 26: Scheme of the sphere-plane configuration. The plane is infinite in the x and y-directions, and lies in the $(z \leq 0)$-region. The sphere has a radius R and its center is located at $(0, 0, \mathcal{L})$, with $\mathcal{L} = L + R$.

The motivation for this configuration is double: as discussed in the introduction, the sphere-plane geometry is the configuration employed in the most precise experiments. Moreover, compared to the situation of two planes, it enables to study the dependance of the Casimir on nontrivial geometrical effects, as it introduces curvature, finite-size object, non-specular reflection, and coupling between the polarizations.

The scattering formula, introduced in Eq.(1.35) (p.35) at zero temperature, and in Eq.(3.4) (p.48) at non-zero temperature, expresses the Casimir energy from the scattering operator $\mathcal{D}$ at imaginary frequency $\omega = \imath\xi$. We recall here its expressions for the Casimir energy E at $(T = 0)$ and the free-energy $\mathcal{F}$ at $(T > 0)$:

$$E = \frac{\hbar}{2\pi} \int_0^\infty \mathrm{d}\xi \ln\det \mathcal{D}(\imath\xi) \qquad\qquad \mathcal{F} = k_B T \sum_n{}' \ln\det \mathcal{D}(\imath\xi_n) \tag{5.1}$$

Here we aim at giving an explicit expression for the scattering operator $\mathcal{D}(\imath\xi)$ in this sphere-plane geometry, that we will use in the future to compute the energy E and free-energy $\mathcal{F}$ from Eq.(5.1). The numerical evaluation will be tackled in a separate forthcoming section.

In **Section 5.1** we introduce the basis of spherical vector waves and express the elements of $\mathcal{D}$ for the present geometry in this basis. It involves various new quantities, because of the curvature introduced by the sphere, which are discussed in **Section 5.2** then simplified in **Section 5.3** to be prepared for future numerical evaluations and analytical derivations. Finally, we conclude in **Section 5.4** by summing up all the formulas that will be used to compute the Casimir interaction.

5.1 Derivation of the scattering operator $\mathcal{D}(\imath\xi)$

The physical configuration is assumed to be time-invariant, the frequency of an incoming wave is then preserved during any scattering process, and the scattering operator $\mathcal{D}$ is block-diagonal with respect to the variable ω. We can thus study independently the extracted block $\mathcal{D}(\omega)$ for the scattering of waves with frequency ω. This frequency-dependant scattering operator is defined from the round-trip operator $\mathcal{M}(\omega)$:

$$\mathcal{D}(\omega) = \mathcal{I} - \mathcal{M}(\omega) \qquad \mathcal{M}(\omega) = \mathcal{R}_{\mathrm{S}}(\omega)\mathcal{T}_{\mathrm{S}\leftarrow\mathrm{P}}(\omega)\mathcal{R}_{\mathrm{P}}(\omega)\mathcal{T}_{\mathrm{P}\leftarrow\mathrm{S}}(\omega) \tag{5.2}$$

where $\mathcal{R}_{\mathrm{S}}(\omega)$ (resp. $\mathcal{R}_{\mathrm{P}}(\omega)$) is the reflection operator on the sphere (resp. on the plane) for waves with frequency ω, and $\mathcal{T}(\omega)$ are the translation operators from one object to the other. The obtained expressions for the elements of $\mathcal{M}(\omega)$ will then be transformed to imaginary frequencies with the substitution $\omega = \imath\xi$, in order to obtain the scattering operator $\mathcal{D}(\imath\xi)$.

The planar modes for the electromagnetic field, introduced in **Section 1.1** (p.27), are well adapted to express the reflection on the plane and the translation operators, as we have seen in **Section 1.4** (p.35), with the example of the plane-plane geometry, that these operators were diagonal in this basis. For the operator describing the reflection on the sphere however, it is not true anymore, as the reflection is non-specular on this object, and the set of spherical electromagnetic modes will be more adapted to the geometry.

In this section, we will first introduce the planar and spherical electromagnetic modes, then we will express the reflection operators with the adapted basis for incoming and outgoing waves. The round-trip operator $\mathcal{M}(\omega)$ will be constructed at real frequencies with the appropriate transformation of basis, and finally the expressions will be transformed for imaginary frequencies.

5.1.1 Planar and spherical wave basis

In **Section 1.1.1** (p.27) we have shown from the Maxwell equations in reciprocal space that the Fourier transform of the electromagnetic field can be written as:

$$\begin{aligned}\mathcal{E}(\mathbf{K},t) &= \left(g_{\mathrm{TE}}(\mathbf{K})\hat{\epsilon}_{\mathbf{K},\mathrm{TE}} + g_{\mathrm{TM}}(\mathbf{K})\hat{\epsilon}_{\mathbf{K},\mathrm{TM}}\right) e^{-\imath\omega t} + \mathrm{C.C.}\\ \mathcal{B}(\mathbf{K},t) &= \left(g_{\mathrm{TE}}(\mathbf{K})\hat{\beta}_{\mathbf{K},\mathrm{TE}} + g_{\mathrm{TM}}(\mathbf{K})\hat{\beta}_{\mathbf{K},\mathrm{TM}}\right)\frac{e^{-\imath\omega t}}{c} + \mathrm{C.C.}\end{aligned}$$

where $\hat{\epsilon}$ (resp. $\hat{\beta}$) are the unit electric (resp. magnetic) vector defined in Eq.(1.10) (p.29), and the transverse electric and magnetic scalar functions $g_{\mathrm{TE}}(\mathbf{K}), g_{\mathrm{TM}}(\mathbf{K})$ can be freely chosen.

The planar electromagnetic modes $|\,\mathbf{K}_0, p\rangle$ have be obtained in **Section 1.1.2** (p.29) by taking delta functions for g_{TM} and g_{TE} as a basis for the set of all vacuum solutions:

$$\langle \mathbf{K} \mid \mathbf{K_0}, p\rangle = (2\pi)^3\delta(\mathbf{K}-\mathbf{K}_0)\hat{\epsilon}_p \quad \text{ with } \mathbf{K_0} \in \mathbb{R}^3,\ p \in \{\mathrm{TE},\mathrm{TM}\}\ . \tag{5.3}$$

We recall that for practical reasons, as introduced in **Section 1.1.3** (p.30), we label the planar modes of wavevector $\mathbf{K} = (k_x, k_y, k_z)$ and polarization p with the labels $|\,\omega, \mathbf{k}, p, \phi\rangle$, where $\omega = cK$ is the frequency, $\mathbf{k} = (k_x, k_y)$ the transverse part of the total wavevector $\mathbf{K}$, $p \in \{\mathrm{TE},\mathrm{TM}\}$ the polarization, and $\phi = \pm 1$ the direction of propagation, with $(\phi = 1)$ for upwards propagation and $(\phi = -1)$ for downward propagation. The remaining lateral component k_z of the wavevector $\mathbf{K}$ can then be obtained through: $k_z = \phi\sqrt{\frac{\omega^2}{c^2} - \mathbf{k}^2}$, which enables to account for evanescent waves in the z-direction when $\omega^2 < c^2\mathbf{k}^2$.

The planar modes have revealed themselves well adapted to study the Casimir effect in the plane-plane geometry. This comes mainly from the fact that this geometry is translational-invariant in the two transverse directions x and y. Replacing one of the planes with a sphere, we loose the

two translation symmetries, but we still have a rotational symmetry around the z-axis. This is the motivation to take for the functions g_{TM} and g_{TE} a basis made of eigenvectors for the operators $\mathbf{J}^2$ and $\mathbf{J}_z$, $\mathbf{J} = \mathbf{L} + \mathbf{S}$ being the total angular momentum operator, $\mathbf{L}$ and $\mathbf{S}$ the orbital and spin angular momentum operators, respectively. This choice leads to the spherical electromagnetic modes.

They can be constructed [209, chap. B_1.3] from the scalar eigenstates of the operators $\mathbf{L}^2$ and $\mathbf{L}_z$, which are the spherical harmonics $Y_{\ell,m}(\hat{\mathbf{K}})$ that we will present in more detail in **Section 5.2.3**. Here the indices ℓ and m are such that $\ell(\ell+1)$ and m correspond to the eigenvalues of $\mathbf{J}^2/\hbar^2$ and $\mathbf{J}_z/\hbar$, respectively. Then we can look for solutions in the form $(\mathbf{V}Y_{\ell,m})(\hat{\mathbf{K}})$ to be eigenvectors of $\mathbf{J}^2$ and $\mathbf{J}_z$, where $\mathbf{V}(\hat{\mathbf{K}})$ is an orbital vector field acting on the spherical harmonics (and any scalar function defined on the unit sphere). The case $\mathbf{V}(\hat{\mathbf{K}}) = \hat{\mathbf{K}}$ gives for example the longitudinal eigenvectors of $\mathbf{J}^2$ and $\mathbf{J}_z$. For the electromagnetic modes, which must be transverse, two solutions are $\mathbf{V} = \nabla_{\hat{\mathbf{K}}}$ and $\mathbf{V} = \hat{\mathbf{K}} \times \nabla_{\hat{\mathbf{K}}}$, with $\nabla_{\hat{\mathbf{K}}}$ the orbital part of the gradient $\nabla_{\mathbf{K}}$ in reciprocal space for spherical coordinates (K, θ_K, φ_K):

$$\nabla_{\mathbf{K}} = \hat{\mathbf{K}}\frac{\partial}{\partial K} + \hat{\theta}_K \frac{1}{K}\frac{\partial}{\partial \theta_K} + \hat{\varphi}_K \frac{1}{K\sin\theta_K}\frac{\partial}{\partial \varphi_K} = \hat{\mathbf{K}}\frac{\partial}{\partial K} + \frac{1}{K}\nabla_{\hat{\mathbf{K}}}$$

With those solutions for $\mathbf{V}$ we obtain the two transverse fields $\mathbf{Z}, \mathbf{X}$:

$$\begin{aligned}
\mathbf{Z}_{\ell,m}(\hat{\mathbf{K}}) &= \frac{\nabla_{\hat{\mathbf{K}}} Y_{\ell,m}(\hat{\mathbf{K}})}{\sqrt{\ell(\ell+1)}} \\
\mathbf{X}_{\ell,m}(\hat{\mathbf{K}}) &= \frac{\left(\hat{\mathbf{K}} \times \nabla_{\hat{\mathbf{K}}}\right) Y_{\ell,m}(\hat{\mathbf{K}})}{\sqrt{\ell(\ell+1)}}
\end{aligned} \tag{5.4}$$

which we will refer to as electric (E) and magnetic (M) multipole, respectively. Those two polarizations will be accounted for with the variable $P \in \{E, M\}$. Let us remark that the spherical harmonics with $\ell = 0$ must be removed, since $\nabla_{\hat{\mathbf{K}}} Y_{0,0} = \mathbf{0}$. The modes in Eq.(5.4) are thus defined for $\ell \geq 1$, and the coefficient $\sqrt{\ell(\ell+1)}$ accounting for the normalization[7] is never zero.

As these spherical modes are only a basis for the dependance on $\hat{\mathbf{K}}$ (orientation on the unit sphere), we take delta functions for the dependance on the radial part $K = \frac{\omega}{c}$ and obtain the electromagnetic spherical modes $|\,\omega, \ell, m, P\rangle$, which representation in reciprocal space is:

$$\begin{aligned}
\langle \mathbf{K} \mid \omega, \ell, m, E\rangle &= -\imath(2\pi)^2 \frac{\delta(K - \omega/c)}{\omega/c} \frac{\nabla_{\hat{\mathbf{K}}} Y_{\ell,m}(\hat{\mathbf{K}})}{\sqrt{\ell(\ell+1)}} \\
&= -\hat{\mathbf{K}} \times \langle \mathbf{K} \mid \omega, \ell, m, M\rangle
\end{aligned} \tag{5.5}$$

$$\begin{aligned}
\langle \mathbf{K} \mid \omega, \ell, m, M\rangle &= -\imath(2\pi)^2 \frac{\delta(K - \omega/c)}{\omega/c} \frac{\left(\hat{\mathbf{K}} \times \nabla_{\hat{\mathbf{K}}}\right) Y_{\ell,m}(\hat{\mathbf{K}})}{\sqrt{\ell(\ell+1)}} \\
&= \hat{\mathbf{K}} \times \langle \mathbf{K} \mid \omega, \ell, m, E\rangle \ .
\end{aligned} \tag{5.6}$$

The summation over all the spherical modes (5.5) is discrete, except for the frequency ω:

$$\sum_{m \in \{|\omega,\ell,m,P\rangle\}} = \int_0^\infty \frac{\mathrm{d}\omega}{2\pi} \sum_{\ell,m,P} \tag{5.7}$$

[7] With the present convention for the spherical harmonics, we have the normalization over the unit sphere: $\int \mathrm{d}^2\hat{\mathbf{K}}\ \mathbf{Z}^*_{\ell,m}(\hat{\mathbf{K}}) \cdot \mathbf{Z}_{\ell',m'}(\hat{\mathbf{K}}) = \delta_{\ell,\ell'}\delta_{m,m'}$.

and thus yields an adimensional trace over all modes $\mid \ell, m, P\rangle$ of frequency ω:

$$\sum_{\ell,m,P} = \mathrm{Tr}_\omega = \sum_{P\in\{E,M\}} \sum_{\ell=1}^{\infty} \sum_{m=-\ell}^{\ell} \ . \tag{5.8}$$

We remark that, unlike for the planar basis, the ω-trace for spherical modes is naturally adimensional and thus leads to an extensive quantity. The scattering formula then does not give an energy per unit area any more, but rather the energy itself. This is consistent with the fact that the present geometry does not have a translational invariance, and then defining a quantity per unit area does not have any physical sense.

It will be useful in the writing of the round-trip operator $\mathcal{M}(\omega)$ in the next section to have at our disposal the decomposition of those multipoles onto planar modes $\mid \mathbf{k}, p, -\rangle$ going downward. They give the following coefficients, for a similar frequency ω on both sides:

$$\begin{aligned}
\langle \mathbf{k}, \mathrm{TE}, - \mid \ell, m, E\rangle &= \frac{2\pi m\sqrt{\omega/c}}{k\sqrt{-k_z}} \frac{Y_{\ell,m}(\hat{\mathbf{K}})}{\sqrt{\ell(\ell+1)}} \\
\langle \mathbf{k}, \mathrm{TE}, - \mid \ell, m, M\rangle &= -\frac{2\pi\imath}{\sqrt{-k_z\omega/c}} \frac{\partial_{\theta_K} Y_{\ell,m}(\hat{\mathbf{K}})}{\sqrt{\ell(\ell+1)}} \\
\langle \mathbf{k}, \mathrm{TM}, - \mid \ell, m, E\rangle &= \langle \mathbf{k}, \mathrm{TE}, - \mid \ell, m, M\rangle \\
\langle \mathbf{k}, \mathrm{TM}, - \mid \ell, m, M\rangle &= -\langle \mathbf{k}, \mathrm{TE}, - \mid \ell, m, E\rangle
\end{aligned} \tag{5.9}$$

where $k_z = -\sqrt{\frac{\omega^2}{c^2} - k^2}$, and the normalization constants are such that $\langle \ell_1, m_1, P_1 \mid \ell_2, m_2, P_2\rangle = \delta_{\ell_1\ell_2}\delta_{m_1m_2}\delta_{P_1P_2}$ when inserting the representation:

$$Id = \sum_{p\in\{\mathrm{TE},\mathrm{TM}\}} \sum_{\phi=\pm 1} \int_{\mathbb{R}^2} \frac{\mathrm{d}^2\mathbf{k}}{(2\pi)^2} \mid \mathbf{k}, p, \phi\rangle\langle \mathbf{k}, p, \phi \mid \ . \tag{5.10}$$

5.1.2 The round-trip operator $\mathcal{M}(\omega)$

The physical nature of the action of the round-trip operator $\mathcal{M} = \mathcal{R}_\mathrm{S}\mathcal{T}_{\mathrm{S}\leftarrow\mathrm{P}}\mathcal{R}_\mathrm{P}\mathcal{T}_{\mathrm{P}\leftarrow\mathrm{S}}$ on an incoming wave of frequency ω can be understood by reading its constituents from right to left: the wave is first translated from the reference frame of the sphere to the one of the plane, then its reflection on the plane is taken, it is translated back to the reference frame of the sphere and finally it is reflected on the sphere. As we have chosen to use an adimensional trace (5.8) (p.65) for the operator, we will take the components of the round-trip operator on the basis of the spherical modes $\mid \ell, m, P\rangle$ of frequency ω:

$$\mathcal{M}_{1;2}(\omega) = \langle \ell_1, m_1, P_1 \mid \mathcal{R}_\mathrm{S}\mathcal{T}_{\mathrm{S}\leftarrow\mathrm{P}}\mathcal{R}_\mathrm{P}\mathcal{T}_{\mathrm{P}\leftarrow\mathrm{S}} \mid \ell_2, m_2, P_2\rangle \ .$$

Because of the axial symmetry of the geometry around the z-axis, the z-component of the angular momentum $\mathbf{J}_z$ is conserved, and m, like the frequency ω, is conserved through the scattering process. The operator $\mathcal{M}(\omega)$ is then diagonal with m, as elements with $(m_1 \neq m_2)$ are zero. We can thus reduce the study of the $\mathcal{M}(\omega)$ components to the diagonal blocks for m, keeping in mind that $|m| \leq \min(\ell_1, \ell_2)$:

$$\mathcal{M}^{(m)}_{1;2}(\omega) = \langle \ell_1, m, P_1 \mid \mathcal{R}_\mathrm{S}\mathcal{T}_{\mathrm{S}\leftarrow\mathrm{P}}\mathcal{R}_\mathrm{P}\mathcal{T}_{\mathrm{P}\leftarrow\mathrm{S}} \mid \ell_2, m, P_2\rangle \ . \tag{5.11}$$

The planar modes $\mid \mathbf{k}, p, \phi\rangle$ are better adapted than the spherical ones to express the reflection on the plane and the translations, as seen in **Section 1.4** (p.35) with the example of the plane-plane geometry. To take advantage of this fact, we insert the representation (5.10) (p.65) on the

immediate left of the ket $\mid \ell_2, m, P\rangle$ in the expression (5.11):

$$\mathcal{M}_{1;2}^{(m)}(\omega) = \sum_{p,\phi} \int_{\mathbb{R}^2} \frac{\mathrm{d}^2\mathbf{k}}{(2\pi)^2} \langle \ell_1, m, P_1 \mid \mathcal{R}_\mathrm{S}\mathcal{T}_{\mathrm{S}\leftarrow\mathrm{P}}\mathcal{R}_\mathrm{P}\mathcal{T}_{\mathrm{P}\leftarrow\mathrm{S}} \mid \mathbf{k}, p, \phi\rangle\langle \mathbf{k}, p, \phi \mid \ell_2, m, P_2\rangle \ . \tag{5.12}$$

where the infinitesimal transverse vector is $\mathrm{d}^2\mathbf{k} = \mathrm{d}k_x\mathrm{d}k_y = k\mathrm{d}k\mathrm{d}\varphi_K$.

The translation operators are diagonal in the plane wave basis and their coefficients are in the sphere-plane case:

$$\begin{aligned} \mathcal{T}_{\mathrm{P}\leftarrow\mathrm{S}} \mid \mathbf{k}, p, \phi\rangle &= e^{-\imath k_z \mathcal{L}} \mid \mathbf{k}, p, \phi\rangle \\ \mathcal{T}_{\mathrm{S}\leftarrow\mathrm{P}} \mid \mathbf{k}, p, \phi\rangle &= e^{\imath k_z \mathcal{L}} \mid \mathbf{k}, p, \phi\rangle \ . \end{aligned} \tag{5.13}$$

The reflection on the plane $\mathcal{R}_\mathrm{P}$ is also diagonal for the variables $\mathbf{k}$ and p, as the reflection is specular, but not for ϕ, the z-direction of the wave. The plane being here below the sphere, it only reflects downward incoming planar waves ($\phi = -1$) into upward outgoing planar waves ($\phi = 1$), and its coefficients read:

$$\begin{aligned} \mathcal{R}_\mathrm{P} \mid \mathbf{k}, p, +\rangle &= 0 \\ \mathcal{R}_\mathrm{P} \mid \mathbf{k}, p, -\rangle &= r_p(\omega, \mathbf{k}) \mid \mathbf{k}, p, +\rangle \end{aligned} \tag{5.14}$$

where $r_p(\omega, \mathbf{k})$ are the scalar Fresnel coefficients that will be discussed in more details in **Section 5.2.1**. We remark that because of the first line in Eq.(5.14), we can reduce the sum over ϕ in the expression (5.12) to the only value $\phi = -1$ and make the following transformations:

$$\begin{aligned} \mathcal{T}_{\mathrm{S}\leftarrow\mathrm{P}}\mathcal{R}_\mathrm{P}\mathcal{T}_{\mathrm{P}\leftarrow\mathrm{S}} \mid \mathbf{k}, p, -\rangle &= e^{\imath\mathcal{L}\sqrt{\frac{\omega^2}{c^2}-\mathbf{k}^2}} \mathcal{T}_{\mathrm{S}\leftarrow\mathrm{P}}\mathcal{R}_\mathrm{P} \mid \mathbf{k}, p, -\rangle \\ &= e^{\imath\mathcal{L}\sqrt{\frac{\omega^2}{c^2}-\mathbf{k}^2}} r_p(\omega, \mathbf{k}) \mathcal{T}_{\mathrm{S}\leftarrow\mathrm{P}} \mid \mathbf{k}, p, +\rangle \\ &= e^{2\imath\mathcal{L}\sqrt{\frac{\omega^2}{c^2}-\mathbf{k}^2}} r_p(\omega, \mathbf{k}) \mid \mathbf{k}, p, +\rangle \end{aligned}$$

using $k_z = \phi\sqrt{\frac{\omega^2}{c^2} - \mathbf{k}^2}$. The expression (5.12) for the coefficients of the round-trip operator then simplifies to:

$$\begin{aligned} \mathcal{M}_{1;2}^{(m)}(\omega) &= \sum_{p=\mathrm{TE,TM}} \int_{\mathbb{R}^2} \frac{\mathrm{d}^2\mathbf{k}}{(2\pi)^2} \langle \ell_1, m, P_1 \mid \mathcal{R}_\mathrm{S} \mid \mathbf{k}, p, +\rangle r_p(\omega, \mathbf{k}) e^{2\imath\mathcal{L}\sqrt{\frac{\omega^2}{c^2}-\mathbf{k}^2}} \langle \mathbf{k}, p, - \mid \ell_2, m, P_2\rangle \\ &= \sum_{p=\mathrm{TE,TM}} \int_0^\infty \frac{k\mathrm{d}k}{2\pi} \langle \ell_1, m, P_1 \mid \mathcal{R}_\mathrm{S} \mid \mathbf{k}, p, +\rangle r_p(\omega, \mathbf{k}) e^{2\imath\mathcal{L}\sqrt{\frac{\omega^2}{c^2}-\mathbf{k}^2}} \langle \mathbf{k}, p, - \mid \ell_2, m, P_2\rangle \end{aligned} \tag{5.15}$$

by simple integration over the azimuthal angle φ_K, because of the axial symmetry. The quantities that depend on φ_K, such as the spherical harmonics in Eq.(5.9) (p.65) for instance, will be taken at $\varphi_K = 0$ for simplicity. In the latter expression, we observe that the round-trip operator $\mathcal{M}(\omega)$ is simply expressed as a sum over planar polarizations and an integration over the norm of the transverse vector $\mathbf{k}$ of an integrand function made of three parts. The first on the right is a transformation from spherical waves to downward going planar waves, and is given in Eq.(5.9) (p.65). The second, in the middle, is just a scalar coefficient accounting for the two translations and the planar reflection. The last one remains to be computed and describes with outgoing spherical waves how an incoming planar wave reflects on the sphere.

The term $\langle \ell_1, m, P_1 \mid \mathcal{R}_S \mid \mathbf{k}, p, + \rangle$ can be derived using the Mie coefficients $a_\ell(\omega)$ and $b_\ell(\omega)$, that describe the scattering on the sphere for a planar wave with $\mathbf{k} = 0$. Finally, the reflection on the sphere can be written with the following coefficients, for $(\varphi_K = 0)$:

$$\begin{aligned}
\langle \ell, m, E \mid \mathcal{R}_S \mid \mathbf{k}, \mathrm{TE}, + \rangle &= \sqrt{\frac{\pi(2\ell+1)}{k_z \omega/c}} a_\ell\left(\frac{\omega R}{c}\right)\left[d^\ell_{m,1}(\theta) + d^\ell_{m,-1}(\theta)\right] \\
\langle \ell, m, M \mid \mathcal{R}_S \mid \mathbf{k}, \mathrm{TE}, + \rangle &= \imath\sqrt{\frac{\pi(2\ell+1)}{k_z \omega/c}} b_\ell\left(\frac{\omega R}{c}\right)\left[d^\ell_{m,1}(\theta) - d^\ell_{m,-1}(\theta)\right] \\
\langle \ell, m, E \mid \mathcal{R}_S \mid \mathbf{k}, \mathrm{TM}, + \rangle &= \imath\sqrt{\frac{\pi(2\ell+1)}{k_z \omega/c}} a_\ell\left(\frac{\omega R}{c}\right)\left[d^\ell_{m,1}(\theta) - d^\ell_{m,-1}(\theta)\right] \\
\langle \ell, m, M \mid \mathcal{R}_S \mid \mathbf{k}, \mathrm{TM}, + \rangle &= -\sqrt{\frac{\pi(2\ell+1)}{k_z \omega/c}} b_\ell\left(\frac{\omega R}{c}\right)\left[d^\ell_{m,1}(\theta) + d^\ell_{m,-1}(\theta)\right]
\end{aligned} \tag{5.16}$$

where $k_z = \sqrt{\frac{\omega^2}{c^2} - k^2}$, $a_\ell\left(\frac{\omega R}{c}\right)$ and $b_\ell\left(\frac{\omega R}{c}\right)$ are the Mie coefficients and $d^\ell_{m,1}(\theta)$ are the finite rotations. The two latter quantities will be studied in more details in **Section 5.2.2** (p.70) and **Section 5.2.4** (p.73).

In conclusion, the **Fig. 27** illustrates the chosen method to describe the round-trip inside the cavity:

[1] A spherical wave $\mid \ell_2, m_2, P_2 \rangle$ is first decomposed into planar waves going downward $\mid \mathbf{k}, p, - \rangle$. It results in a coefficient $\langle \mathbf{k}, p, - \mid \ell_2, m, P_2 \rangle$ appearing in Eq.(5.15).

[2] The translation over a distance $\mathcal{L}$ in the direction of negative z is applied to all waves $\mid \mathbf{k}, p, - \rangle$,to change the reference frame from the one of the sphere (its center) to the one of the plane (the $(z = 0)$ upper surface).

[3] The downward propagating waves are reflected on the plane, resulting in corresponding upward outgoing waves $\mid \mathbf{k}, p, + \rangle$, with the same transverse part of the wavevector $\mathbf{k} = (k_x, k_y)$ and polarization p, as the reflection is specular, multiplied by the Fresnel coefficient $r_p(\omega, \mathbf{k})$.

[4] The translation over a distance $\mathcal{L}$ in the direction of positive z is then applied to all waves $\mid \mathbf{k}, p, + \rangle$, to come back to the reference frame of the sphere.

[5] The planar waves $\mid \mathbf{k}, p, + \rangle$ hit the sphere, and their reflections are decomposed into spherical modes. It results in a coefficient $\langle \ell_1, m, P_1 \mid \mathcal{R}_S \mid \mathbf{k}, p, + \rangle$ appearing in Eq.(5.15).

5.1.3 Wick rotation to imaginary frequencies

When the scattering formula is rotated to the axis of imaginary frequencies $\omega = \imath\xi, \xi \in \mathbb{R}$, the longitudinal wavevector k_z must also be imaginary from $k_z^2 = \frac{\omega^2}{c^2} - k^2 = -\hat{\xi}^2 - k^2$. We thus define $\kappa = \sqrt{\frac{\omega^2}{c^2} + k^2} \in \mathbb{R}$, such that $k_z = \imath\phi\kappa$, as described in Eq.(1.36) (p.35). Meanwhile, the polar angle θ_K becomes imaginary, as it relates the frequency ω to the transverse and longitudinal part of the wavevector. Defining $\hat{\xi} = \frac{\xi}{c}$, for the frequency to have the dimension of a wavevector, the equations at real frequency (1.16) (p.30) here become:

$$\cos\theta_K = \frac{k_z}{\omega/c} = \phi\frac{\kappa}{\hat{\xi}} \quad , \quad \kappa = \sqrt{\hat{\xi}^2 + k^2} \tag{5.17}$$

$$\sin\theta_K = \frac{k}{\omega/c} = -\imath\frac{k}{\hat{\xi}} \in \Im^- \tag{5.18}$$

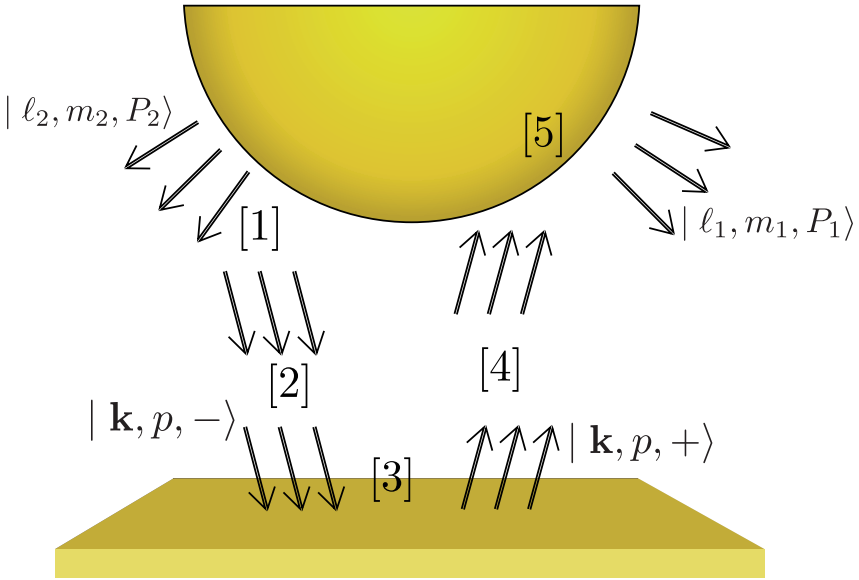

Figure 27: Schema of the wave basis used to express the scattering formula in the sphere-plane geometry. The reflection on the plane and the two translations are expressed with planar waves, the reflection on the sphere is expressed with spherical waves.

the second line shows that θ_K is now also purely imaginary, and can be written $\theta_K = \imath\upsilon$, with $\upsilon \leq 0$. Keeping this remark in mind, we will transform slightly the θ-notation, dropping the index K for implicit reference to the reciprocal space, and defining the two angles $\theta^{\pm}$ in terms of the cosine, to include the information on the value of ϕ:

$$\cos\theta^{\pm} = \pm\frac{\kappa}{\hat{\xi}} = \pm\sqrt{1+\frac{k^2}{\hat{\xi}^2}} = \pm\cosh\upsilon = -\cos\theta^{\mp}\ . \tag{5.19}$$

The sinus is not altered by the change of notation: $\sin\theta^+ = \sin\theta^-$. We recall that $\cos\theta^+ \geq 1$ and $\cos\theta^- \leq -1$.

The transformation from real to imaginary frequencies of the expression (5.15) for the elements of the round-trip operator $\mathcal{M}(\omega)$ is then straightforward:

$$\mathcal{M}^{(m)}_{1;2}(\imath\xi) = \sum_{p=\mathrm{TE,TM}} \int_0^\infty \frac{k\mathrm{d}k}{2\pi} \langle \ell_1, m, P_1 \mid \mathcal{R}_{\mathrm{S}} \mid \mathbf{k}, p, +\rangle r_p(\imath\xi, \mathbf{k}) e^{-2\kappa\mathcal{L}} \langle \mathbf{k}, p, - \mid \ell_2, m, P_2\rangle \tag{5.20}$$

where, in the term $\langle \ell_1, m, P_1 \mid \mathcal{R}_{\mathrm{S}} \mid \mathbf{k}, p, +\rangle$ expressed in Eqs.(5.16), the Mie coefficients are now expressed for imaginary frequency $\left(a_\ell\left(\imath\frac{\xi R}{c}\right), b_\ell\left(\imath\frac{\xi R}{c}\right)\right)$, and the product $k_z\omega = -\phi\kappa\xi = -\kappa\xi$ here (only planar waves with $\phi = 1$ are here considered). In the second term $\langle \mathbf{k}, p, - \mid \ell_2, m, P_2\rangle$ of conversion from one basis to the other, described in Eqs.(5.9) (p.65), there is no frequency dependance, except for the normalization coefficients which contain $-k_z\omega = \phi\kappa\xi = -\kappa\xi$, and $\frac{\omega}{-k_z} = -\phi\frac{\xi}{\kappa} = \frac{\xi}{\kappa}$ in this case.

5.1.4 Summary of the results

The expressions of the Casimir energy and free-energy in the scattering formula (5.1) both involve the logarithm of the determinant of the scattering operator $\mathcal{D}(\imath\xi)$ at imaginary frequencies. Let us

first remark that in the sphere-plane geometry, the fact that this operator is block-diagonal with the parameter m, when expressed on the spherical modes basis, implies that the determinant can be separated into a discrete sum:

$$\ln\det\mathcal{D}(\imath\xi) = \ln\prod_{m\in\mathbb{Z}}\det\mathcal{D}^{(m)}(\imath\xi) = \sum_{m\in\mathbb{Z}}\ln\det\mathcal{D}^{(m)}(\imath\xi)$$

where $\mathcal{D}^{(m)}(\imath\xi)$ denotes the extracted diagonal block from $\mathcal{D}(\imath\xi)$ with $m_1 = m_2 = m$. Hence, each block $\mathcal{D}^{(m)}(\imath\xi)$ (corresponding to a given subspace m) yields an independent contribution to the Casimir energy, and the scattering formula (5.1) can be written as:

$$\begin{aligned} E &= \sum_{m\in\mathbb{Z}}\frac{\hbar}{2\pi}\int_0^\infty \mathrm{d}\xi\,\ln\det\left(\mathcal{I}-\mathcal{M}^{(m)}(\imath\xi)\right) \\ \mathcal{F} &= k_B T\sum_{m\in\mathbb{Z}}{\sum_n}'\ln\det\left(\mathcal{I}-\mathcal{M}^{(m)}(\imath\xi)\right) \end{aligned} \tag{5.21}$$

where the prime denotes the sum for $n\in\mathbb{N}$ with a coefficient $\frac{1}{2}$ for the $(n=0)$-term. When expressing the operator $\mathcal{M}^{(m)}(\imath\xi)$ on the spherical modes $|\,\ell,m,P\rangle$, we can organize the operator with blocks corresponding to the input and output polarizations P_1, P_2:

$$\mathcal{M}^{(m)}(\imath\xi) = \begin{pmatrix} \mathcal{M}^{(m)}_{EE}(\imath\xi) & \mathcal{M}^{(m)}_{EM}(\imath\xi) \\ \\ \mathcal{M}^{(m)}_{ME}(\imath\xi) & \mathcal{M}^{(m)}_{MM}(\imath\xi) \end{pmatrix}. \tag{5.22}$$

Its elements (ℓ_1,ℓ_2) are then obtained from Eq.(5.20), with the inclusion of expressions (5.16) and (5.9), transformed to imaginary frequencies:

$$\left(\mathcal{M}^{(m)}_{EE}(\xi)\right)_{\ell_1,\ell_2} = \sqrt{\tfrac{(2\ell_1+1)\pi}{\ell_2(\ell_2+1)}}a_{\ell_1}(\imath\hat{\xi}R)\left(A^{(m)}_{\ell_1,\ell_2,\mathrm{TE}}+B^{(m)}_{\ell_1,\ell_2,\mathrm{TM}}\right) \tag{5.23}$$

$$\left(\mathcal{M}^{(m)}_{EM}(\xi)\right)_{\ell_1,\ell_2} = \imath\sqrt{\tfrac{(2\ell_1+1)\pi}{\ell_2(\ell_2+1)}}a_{\ell_1}(\imath\hat{\xi}R)\left(C^{(m)}_{\ell_1,\ell_2,\mathrm{TE}}+D^{(m)}_{\ell_1,\ell_2,\mathrm{TM}}\right) \tag{5.24}$$

$$\left(\mathcal{M}^{(m)}_{ME}(\xi)\right)_{\ell_1,\ell_2} = -\imath\sqrt{\tfrac{(2\ell_1+1)\pi}{\ell_2(\ell_2+1)}}b_{\ell_1}(\imath\hat{\xi}R)\left(C^{(m)}_{\ell_1,\ell_2,\mathrm{TM}}+D^{(m)}_{\ell_1,\ell_2,\mathrm{TE}}\right) \tag{5.25}$$

$$\left(\mathcal{M}^{(m)}_{MM}(\xi)\right)_{\ell_1,\ell_2} = \sqrt{\tfrac{(2\ell_1+1)\pi}{\ell_2(\ell_2+1)}}b_{\ell_1}(\imath\hat{\xi}R)\left(A^{(m)}_{\ell_1,\ell_2,\mathrm{TM}}+B^{(m)}_{\ell_1,\ell_2,\mathrm{TE}}\right) \tag{5.26}$$

where $\hat{\xi} = \frac{\xi}{c}$ and the terms $A^{(m)}$, $B^{(m)}$, $C^{(m)}$, and $D^{(m)}$ do neither depend on the radius R nor on the optical properties of the sphere. These terms write:

$$\begin{aligned} A^{(m)}_{\ell_1,\ell_2,p} &= -\imath m\int_0^\infty\frac{\mathrm{d}k}{\kappa}[d^{\ell_1}_{m,1}(\theta^+)+d^{\ell_1}_{m,-1}(\theta^+)]\;Y_{\ell_2 m}(\theta^-)\;r_p(\imath\xi,k)\;e^{-2\kappa\mathcal{L}} \\ B^{(m)}_{\ell_1,\ell_2,p} &= -\frac{1}{\hat{\xi}}\int_0^\infty\frac{k\mathrm{d}k}{\kappa}[d^{\ell_1}_{m,1}(\theta^+)-d^{\ell_1}_{m,-1}(\theta^+)]\;\partial_\theta Y_{\ell_2 m}(\theta^-)\;r_p(\imath\xi,k)\;e^{-2\kappa\mathcal{L}} \\ C^{(m)}_{\ell_1,\ell_2,p} &= \frac{1}{\hat{\xi}}\int_0^\infty\frac{k\mathrm{d}k}{\kappa}[d^{\ell_1}_{m,1}(\theta^+)+d^{\ell_1}_{m,-1}(\theta^+)]\;\partial_\theta Y_{\ell_2 m}(\theta^-)\;r_p(\imath\xi,k)\;e^{-2\kappa\mathcal{L}} \\ D^{(m)}_{\ell_1,\ell_2,p} &= \imath m\int_0^\infty\frac{\mathrm{d}k}{\kappa}[d^{\ell_1}_{m,1}(\theta^+)-d^{\ell_1}_{m,-1}(\theta^+)]\;Y_{\ell_2 m}(\theta^-)\;r_p(\imath\xi,k)\;e^{-2\kappa\mathcal{L}} \end{aligned} \tag{5.27}$$

where the angles $\theta^\pm$ are defined through their cosine in Eq.(5.19) and the spherical harmonics are evaluated at $\varphi_K = 0$. By using the two successive changes of variable $(k\to\kappa\to\cos\theta^+)$ in the

integral, with $k\mathrm{d}k = \kappa\mathrm{d}\kappa = \kappa\hat{\xi}\mathrm{d}\cos\theta^+$, they can be written without any reference to k nor to κ:

$$\begin{aligned}
A^{(m)}_{\ell_1,\ell_2,p} &= -m\int_1^\infty \frac{\mathrm{d}\cos\theta^+}{\sin\theta}[d^{\ell_1}_{m,1}(\theta^+) + d^{\ell_1}_{m,-1}(\theta^+)]\; Y_{\ell_2 m}(\theta^-)\; r_p(\imath\xi,k)\; e^{-2\hat{\xi}\mathcal{L}\cos\theta^+}\\
B^{(m)}_{\ell_1,\ell_2,p} &= -\int_1^\infty \mathrm{d}\cos\theta^+\; [d^{\ell_1}_{m,1}(\theta^+) - d^{\ell_1}_{m,-1}(\theta^+)]\; \partial_\theta Y_{\ell_2 m}(\theta^-)\; r_p(\imath\xi,k)\; e^{-2\hat{\xi}\mathcal{L}\cos\theta^+}\\
C^{(m)}_{\ell_1,\ell_2,p} &= \int_1^\infty \mathrm{d}\cos\theta^+\; [d^{\ell_1}_{m,1}(\theta^+) + d^{\ell_1}_{m,-1}(\theta^+)]\; \partial_\theta Y_{\ell_2 m}(\theta^-)\; r_p(\imath\xi,k)\; e^{-2\hat{\xi}\mathcal{L}\cos\theta^+}\\
D^{(m)}_{\ell_1,\ell_2,p} &= m\int_1^\infty \frac{\mathrm{d}\cos\theta^+}{\sin\theta}[d^{\ell_1}_{m,1}(\theta^+) - d^{\ell_1}_{m,-1}(\theta^+)]\; Y_{\ell_2 m}(\theta^-)\; r_p(\imath\xi,k)\; e^{-2\hat{\xi}\mathcal{L}\cos\theta^+}\;.
\end{aligned} \tag{5.28}$$

5.2 Explicit form of the various involved quantities

5.2.1 Fresnel coefficients

When considering an interface between two media (labelled 1 and 2), with refractive indices n_1 and n_2, the Fresnel coefficients give the reflection amplitudes for a TE or TM-polarized planar electromagnetic wave coming across the interface from media 1:

$$r_{\mathrm{TE}} = \frac{n_1\cos\theta_1 - n_2\cos\theta_2}{n_1\cos\theta_1 + n_2\cos\theta_2} \qquad r_{\mathrm{TM}} = \frac{n_2\cos\theta_1 - n_1\cos\theta_2}{n_2\cos\theta_1 + n_1\cos\theta_2} \tag{5.29}$$

where θ_1 and θ_2 are angle made by the wavevector with the normal direction of the interface, in each media. For a plane in vacuum, whose normal is along the z-axis, made of a material with dielectric function $\varepsilon(\omega)$ as introduced in **Section 2.1** (p.39), the Fresnel coefficients (5.29) become, for an incident planar mode $|\,\mathbf{K},p\rangle$:

$$r_{\mathrm{TE}} = \frac{1-\sqrt{1+\frac{\epsilon(\omega)-1}{\cos^2\theta_K}}}{1+\sqrt{1+\frac{\epsilon(\omega)-1}{\cos^2\theta_K}}} \qquad r_{\mathrm{TM}} = \frac{1+(\epsilon(\omega)-1)-\sqrt{1+\frac{\epsilon(\omega)-1}{\cos^2\theta_K}}}{1+(\epsilon(\omega)-1)+\sqrt{1+\frac{\epsilon(\omega)-1}{\cos^2\theta_K}}} \tag{5.30}$$

where $\cos\theta_K = \frac{k_z}{\omega/c}$. When switching to imaginary frequencies $\omega = \imath\xi$, they simply transform into:

$$r_{\mathrm{TE}} = \frac{1-\sqrt{1+\frac{\epsilon(\imath\xi)-1}{\cos^2\theta^+}}}{1+\sqrt{1+\frac{\epsilon(\imath\xi)-1}{\cos^2\theta^+}}} \qquad r_{\mathrm{TM}} = \frac{1+(\epsilon(\imath\xi)-1)-\sqrt{1+\frac{\epsilon(\imath\xi)-1}{\cos^2\theta^+}}}{1+(\epsilon(\imath\xi)-1)+\sqrt{1+\frac{\epsilon(\imath\xi)-1}{\cos^2\theta^+}}} \tag{5.31}$$

where $\cos^2\theta^+$ is now equal to $\frac{\kappa^2}{\hat{\xi}^2}$, with $\hat{\xi} = \frac{\xi}{c}$. For perfectly reflecting mirrors, the dielectric function is infinite at all frequencies and when taking the $(\varepsilon\to+\infty)$-limit in the expressions (5.30) or (5.31), we obtain that $r_{\mathrm{TE}}\to-1$ and $r_{\mathrm{TM}}\to+1$.

At imaginary frequencies, it is easy to see the sign of the Fresnel coefficients for general materials, since the dielectric function is real with $\varepsilon(\imath\xi)\geq 1$. For transverse electric modes, we easily see that $-1\leq r_{\mathrm{TE}}\leq 0$ because the numerator is negative, for transverse magnetic modes, we have $0\leq r_{\mathrm{TM}}\leq 1$, as $\cos\theta^+\geq 1$ enables us to write:

$$1+(\epsilon(\imath\xi)-1) \quge 1+\frac{\epsilon(\imath\xi)-1}{\cos^2\theta} \quge \sqrt{1+\frac{\epsilon(\imath\xi)-1}{\cos^2\theta}}$$

5.2.2 Mie coefficients

The Mie coefficients [220, chap.4] of order ℓ of a sphere of radius R in vacuum, the material of which is homogeneous and isotropic with a relative permittivity ε_S, a relative permeability μ_S and

a refractive index $n_S = \sqrt{\varepsilon_S \mu_S}$ read:

$$a_\ell(x) = \frac{n_S^2 s_\ell^{(a)}(x) - \mu_S s_\ell^{(b)}(x)}{n_S^2 s_\ell^{(c)}(x) - \mu_S s_\ell^{(d)}(x)} \qquad b_\ell(x) = \frac{\mu_S s_\ell^{(a)}(x) - s_\ell^{(b)}(x)}{\mu_S s_\ell^{(c)}(x) - s_\ell^{(d)}(x)}$$

$$\begin{aligned} s_\ell^{(a)}(x) &= j_\ell(n_S x)[x j_\ell(x)]' & s_\ell^{(b)}(x) &= j_\ell(x)[n_S x j_\ell(n_S x)]' \\ s_\ell^{(c)}(x) &= j_\ell(n_S x)[x h_\ell(x)]' & s_\ell^{(d)}(x) &= h_\ell(x)[n_S x j_\ell(n_S x)]' \end{aligned} \tag{5.32}$$

where $x = \frac{\omega R}{c}$ is the size parameter, $j_\ell(x)$ and $h_\ell(x) = j_\ell(x) + i y_\ell(x)$ are the spherical Bessel and Hankel functions of the first kind, and the prime indicates a differentiation with respect to the argument used in the brackets. The special case of a sphere with $\mu_S = 1$ will be the one of interest for the materials studied in the following. The derivatives in the expressions can be removed by using the downward derivative formula:

$$z_\ell^{'}(x) = z_{\ell-1}(x) - \frac{\ell+1}{x} z_\ell(x) \tag{5.33}$$

which is valid for $z = y, h$. The coefficients can now be described by spherical Bessel and Hankel functions with coefficients ℓ and $(\ell - 1)$:

$$\begin{aligned} s_\ell^{(a)}(x) &= j_\ell(n_S x)[x j_{\ell-1}(x) - \ell j_\ell(x)] & s_\ell^{(b)}(x) &= j_\ell(x)[n_S x j_{\ell-1}(n_S x) - \ell j_\ell(n_S x)] \\ s_\ell^{(c)}(x) &= j_\ell(n_S x)[x h_{\ell-1}(x) - \ell h_\ell(x)] & s_\ell^{(d)}(x) &= h_\ell(x)[n_S x j_{\ell-1}(n_S x) - \ell j_\ell(n_S x)] \; . \end{aligned} \tag{5.34}$$

The Mie coefficients can also be written in term of the Bessel and Hankel function of the first kind J, H with half-integer order $(\ell + 1/2)$ from the relation to spherical Bessel and Hankel functions j, h:

$$j_\ell(x) = \sqrt{\frac{\pi}{2x}} J_{\ell+1/2}(x) \qquad h_\ell(x) = \sqrt{\frac{\pi}{2x}} H_{\ell+1/2}(x) \; . \tag{5.35}$$

After a simplification by $\frac{\pi}{2x\sqrt{n_S}}$, the coefficients then become:

$$\begin{aligned} s_\ell^{(a)}(x) &= J_{\ell+1/2}(n_S x)[x J_{\ell-1/2}(x) - \ell J_{\ell+1/2}(x)] \\ s_\ell^{(b)}(x) &= J_{\ell+1/2}(x)[n_S x J_{\ell-1/2}(n_S x) - \ell J_{\ell+1/2}(n_S x)] \\ s_\ell^{(c)}(x) &= J_{\ell+1/2}(n_S x)[x H_{\ell-1/2}(x) - \ell H_{\ell+1/2}(x)] \\ s_\ell^{(d)}(x) &= H_{\ell+1/2}(x)[n_S x J_{\ell-1/2}(n_S x) - \ell J_{\ell+1/2}(n_S x)] \; . \end{aligned} \tag{5.36}$$

Finally, to prepare the Wick rotation to imaginary frequencies $\omega = \imath\xi$, it is of great use to express the Mie coefficients for an imaginary argument, with the help of the modified Bessel functions of the first and second kind, noted I and K, respectively. They are related to the Bessel and Hankel functions by:

$$I_\nu(x) = \imath^{-\nu} J_\nu(\imath x) \qquad K_\nu(x) = \frac{\pi}{2} \imath^{\nu+1} H_\nu(\imath x) \; . \tag{5.37}$$

After a few manipulations, this leads to the following expression for the Mie coefficients as functions

of an imaginary size parameter $(\imath x)$:

$$a_\ell(\imath x) = (-1)^{\ell+1}\frac{\pi}{2}\frac{n_S^2 s_\ell^{(a)}(x) - \mu_S s_\ell^{(b)}(x)}{n_S^2 s_\ell^{(c)}(x) - \mu_S s_\ell^{(d)}(x)}$$
$$b_\ell(\imath x) = (-1)^{\ell+1}\frac{\pi}{2}\frac{\mu_S s_\ell^{(a)}(x) - s_\ell^{(b)}(x)}{\mu_S s_\ell^{(c)}(x) - s_\ell^{(d)}(x)}$$

$$\begin{aligned}
s_\ell^{(a)}(x) &= I_{\ell+1/2}(n_S x)[xI_{\ell-1/2}(x) - \ell I_{\ell+1/2}(x)] \\
s_\ell^{(b)}(x) &= I_{\ell+1/2}(x)[n_S x I_{\ell-1/2}(n_S x) - \ell I_{\ell+1/2}(n_S x)] \\
s_\ell^{(c)}(x) &= I_{\ell+1/2}(n_S x)[-xK_{\ell-1/2}(x) - \ell K_{\ell+1/2}(x)] \\
s_\ell^{(d)}(x) &= K_{\ell+1/2}(x)[n_S x I_{\ell-1/2}(n_S x) - \ell I_{\ell+1/2}(n_S x)] \ .
\end{aligned} \tag{5.38}$$

In the special case of a perfectly reflecting sphere, the latter expressions can be simplified by taking the $(\varepsilon_S \to +\infty)$-limit together with $\mu_S = 1$. To do so, we need the asymptotic expansions for the modified Bessel functions:

$$I_\alpha(n_S x) \simeq \frac{e^{n_S x}}{\sqrt{2\pi n_S x}} \quad \text{when} \quad n_S \to +\infty \tag{5.39}$$

from which it follows that a_ℓ and b_ℓ are described by only one dominant term in the numerator and denominator:

$$\begin{aligned}
n_S^2 s_\ell^{(a)}(x) - s_\ell^{(b)}(x) &\simeq n_S^2 s_\ell^{(a)}(x) \\
n_S^2 s_\ell^{(c)}(x) - s_\ell^{(d)}(x) &\simeq n_S^2 s_\ell^{(c)}(x) \\
s_\ell^{(a)}(x) - s_\ell^{(b)}(x) &\simeq -s_\ell^{(b)}(x) \\
s_\ell^{(c)}(x) - s_\ell^{(d)}(x) &\simeq -s_\ell^{(d)}(x)
\end{aligned}$$

and the Mie coefficients finally take the simpler form:

$$\begin{aligned}
a_\ell(\imath x) &= (-1)^{\ell+1}\frac{\pi}{2}\frac{\ell I_{\ell+1/2}(x) - xI_{\ell-1/2}(x)}{\ell K_{\ell+1/2}(x) + xK_{\ell-1/2}(x)} \\
b_\ell(\imath x) &= (-1)^{\ell+1}\frac{\pi}{2}\frac{I_{\ell+1/2}(x)}{K_{\ell+1/2}(x)} \ .
\end{aligned} \tag{5.40}$$

5.2.3 Spherical harmonics

The expressions (5.27) for the blocks involved in the scattering formula contain spherical harmonics and their $\theta-$*derivatives*, evaluated at $\varphi = 0$. In this subsection we derive a recurrence relation for those quantities, in the prospect of numerical evaluation. We restrict ourselves to the cases where $m \geq 0$, the negative m will be obtained through symmetry at the end of the subsection.

Definition 6 ***Spherical harmonics*** $\boxed{Y_{\ell,m}(\theta,\phi)}$

The spherical harmonics $(Y_{\ell,m}(\theta,\phi))$ *are the angular portion of an orthogonal set of solutions to Laplace's equation* $(\Delta f = 0)$ *represented in a system of spherical coordinates. Those corresponding to* $m \in \mathbb{N}$ *can be written in terms of associated Legendre functions :*

$$Y_{\ell,m}(\theta,\phi) = \sqrt{\frac{2\ell+1}{4\pi}}\sqrt{\frac{(\ell-m)!}{(\ell+m)!}}P_\ell^m(\cos\theta)e^{im\phi} \tag{5.41}$$

From the properties of the associated Legendre polynomials, one can derive a recurrence law for the spherical harmonics which will be useful in order to construct them explicitly:

$$\boxed{m=0} \quad \begin{cases} Y_{1,0}(\theta) &= \sqrt{\frac{3}{4\pi}}\cos\theta & (\ell=1) \\ Y_{2,0}(\theta) &= \sqrt{\frac{5}{16\pi}}(3\cos^2\theta-1) & (\ell=2) \\ Y_{\ell,0}(\theta) &= \frac{\sqrt{4\ell^2-1}}{\ell}\cos\theta\ Y_{\ell-1,0}(\theta) - \frac{\ell-1}{\ell}\sqrt{\frac{2\ell+1}{2\ell-3}}\ Y_{l-2,0} & \forall \ell \geq 3 \end{cases}$$

$$\boxed{m>0} \quad \begin{cases} Y_{m,m}(\theta) &= (-1)^m\sqrt{\frac{2m+1}{4\pi(2m)!}}(2m-1)!!\ (1-\cos^2\theta)^{m/2} & (\ell=m) \\ Y_{m+1,m}(\theta) &= \sqrt{2m+3}\cos\theta\ Y_{m,m}(\theta) & (\ell=m+1) \\ Y_{\ell,m}(\theta) &= \sqrt{\frac{2\ell+1}{\ell^2-m^2}}\left(\sqrt{2\ell-1}\cos\theta\ Y_{\ell-1,m}(\theta)\right. & \\ & \qquad \left. -\sqrt{\frac{(\ell-1)^2-m^2}{2\ell-3}}\ Y_{\ell-2,m}(\theta)\right) & \forall \ell \geq m+2 \end{cases}$$

Then, to construct the θ-derivative of spherical harmonics, we will use the following relation for the derivative of associated Legendre functions :

$$x^2\frac{dP_\ell^m(x)}{dx} = \ell x P_\ell^m(x) - (\ell+m)P_{\ell-1}^m(x) \tag{5.42}$$

We still need the expression for the first term, which will be easily computed analytically. Using the latter equation to compute the θ-derivative of spherical harmonics after the first term, we find :

$$\boxed{m=0} \quad \begin{cases} \partial_\theta Y_{1,0}(\theta) &= -\sqrt{\frac{3}{4\pi}}\sin\theta & (\ell=1) \\ \partial_\theta Y_{\ell,0}(\theta) &= \frac{\ell}{\sin\theta}\left(\cos\theta\ Y_{\ell,0}(\theta) - \sqrt{\frac{2\ell+1}{2\ell-1}}\ Y_{\ell-1,0}\right) & \forall \ell \geq 2 \end{cases}$$

$$\boxed{m>0} \quad \begin{cases} \partial_\theta Y_{m,m}(\theta) &= (-1)^m\sqrt{\frac{2m+1}{4\pi(2m)!}}(2m-1)!!\ m & \\ & \qquad \times \sin\theta\cos\theta(1-\cos^2\theta)^{m/2-1} & (\ell=m) \\ \partial_\theta Y_{\ell,m}(\theta) &= \frac{1}{\sin\theta}\left(\ell\cos\theta\ Y_{\ell,m}(\theta)\right. & \\ & \qquad \left. -\sqrt{\ell^2-m^2}\sqrt{\frac{2\ell+1}{2\ell-1}}\ Y_{\ell-1,m}\right) & \forall \ell \geq m+1 \end{cases}$$

Finally, the terms with $m<0$ can be obtained from the relations:

$$Y_{\ell,m}^*(\theta,\varphi) = (-1)^m Y_{\ell,-m}(\theta,\varphi) \qquad \partial_\theta Y_{\ell,m}^*(\theta,\varphi) = (-1)^m \partial_\theta Y_{\ell,-m}(\theta,\varphi) \tag{5.43}$$

which mean, when $\varphi=0$, that they acquire a phase $(-1)^m$ when we apply the change $(m\to -m)$.

5.2.4 Finite rotations

To adapt the theory of Mie scattering to our case in **Section 5.1.2**, we had to rotate the reference frame of the planar waves coming into the sphere, bringing in coefficients $d^\ell_{m,\pm1}(\theta)$, called finite rotations, in the expression of the scattering formula. This subsection introduces the physical meaning of these terms, and give recurrence relations for them, in the prospect of their numerical evaluation. Like in the previous subsection, we restrict ourselves to the case when $m\geq 0$, and will obtain the remaining coefficient for negative m by symmetry at the end of the subsection.

Definition 7 ***Jacobi polynomials*** $\boxed{P_n^{(\alpha,\beta)}(x)}$

The Jacobi polynomials $P_n^{(\alpha,\beta)}(x)$ form a class of orthogonal polynomials and are solutions of the equations :

$$(1-x^2)y'' + (\beta - \alpha - (\alpha+\beta+2)x)\,y' + n(n+\alpha+\beta+1)y = 0 \tag{5.44}$$

As a class of orthogonal polynomials, they obey a second-order recurrence relation

$$P_{n+1}^{(\alpha,\beta)}(x) = (a_n x + b_n)P_n^{(\alpha,\beta)}(x) + c_n P_{n-1}^{(\alpha,\beta)}(x)$$

with coefficients :

$$\begin{cases} a_n &= \dfrac{(2n+1+\alpha+\beta)(2n+2+\alpha+\beta)}{2(n+1)(n+1+\alpha+\beta)} \\ b_n &= \dfrac{(\alpha^2-\beta^2)(2n+1+\alpha+\beta)}{2(n+1)(2n+\alpha+\beta)(n+1+\alpha+\beta)} \\ c_n &= \dfrac{(n+\alpha)(n+\beta)(2n+2+\alpha+\beta)}{(n+1)(2n+\alpha+\beta)(n+1+\alpha+\beta)} \end{cases} \tag{5.45}$$

Definition 8 ***Wigner D-functions*** $\boxed{D^{\ell}_{m,m'}(\alpha,\beta,\gamma)}$

The functions $D^{\ell}_{m,m'}(\alpha,\beta,\gamma)$ can be seen as matrix elements of the rotation operator $\hat{D}(\alpha,\beta,\gamma)$ in $\mathbb{R}^3$, with the $\mid \ell m\rangle$ representation basis. The three angles are the Euler angles which characterize the rotation $\hat{D}(\alpha,\beta,\gamma)$.

$$\langle \ell m \mid \hat{D}(\alpha,\beta,\gamma) \mid \ell' m' \rangle = \delta_{\ell,\ell'} D^{\ell}_{m,m'}(\alpha,\beta,\gamma) \tag{5.46}$$

Definition 9 ***Finite rotations*** $\boxed{d^{\ell}_{m,m'}(\beta)}$

As the first and last Euler angles (α and γ) are related to rotations around the last axis, they are each represented by a simple exponential in the $\mid \ell m\rangle$ representation basis. Wigner D-function $D^{\ell}_{m,m'}(\alpha,\beta,\gamma)$ can then be written as :

$$D^{\ell}_{m,m'}(\alpha,\beta,\gamma) = e^{-im\alpha} d^{\ell}_{m,m'}(\beta) e^{-im\gamma} \tag{5.47}$$

Among many other forms, the functions $d^{\ell}_{m,m'}(\beta)$ can be expressed in terms of the Jacobi polynomials[221, chap.4.3.4]:

$$d^{\ell}_{m,m'}(\beta) = \xi_{m,m'} \left[\frac{s!(s+\mu+\nu)!}{(s+\mu)!(s+\nu)!}\right]^{\frac{1}{2}} \left(\sin\frac{\beta}{2}\right)^{\mu} \left(\cos\frac{\beta}{2}\right)^{\nu} P_s^{(\mu,\nu)}(\cos\beta) \tag{5.48}$$

where μ, ν and s are related to m, m' and s by :

$$\begin{cases} \mu &= |m-m'| \\ \nu &= |m+m'| \\ s &= \ell - \frac{\mu+\nu}{2} \\ \xi_{m,m'} &= \begin{cases} 1 & \text{if} \quad m \le m' \\ (-1)^{m-m'} & \text{if} \quad m > m' \end{cases} \end{cases} \tag{5.49}$$

The next step is to use the recurrence relations for the Jacobi polynomials to construct the finite rotations $d^{\ell}_{m,1}(\theta)$. The cases where $m' = -1$ or where the angle is $(\pi - \theta)$ will be deduce easily from this construction.

After a few computations, we get the following recurrence relation for the finite rotations:

$$\boxed{m=0} \quad \begin{cases} d^{1}_{0,1}(\theta) &=& \frac{\sin\theta}{\sqrt{2}} & (\ell=1) \\ d^{2}_{0,1}(\theta) &=& \sqrt{\frac{3}{2}}\cos\theta\sin\theta & (\ell=2) \\ d^{\ell}_{0,1}(\theta) &=& \frac{1}{\sqrt{\ell^2-1}}\left[(2\ell-1)\cos\theta\ d^{\ell-1}_{0,1}(\theta) - \sqrt{\ell(\ell-2)}\ d^{\ell-2}_{0,1}(\theta)\right] & \forall \ell \geq 3 \end{cases}$$

$$\boxed{m>0} \quad \begin{cases} d^{m}_{m,1}(\theta) &=& \sqrt{\frac{(2m)!}{(m-1)!(m+1)!}}\frac{1+\cos\theta}{2}\left(\frac{-\sin\theta}{2}\right)^{m-1} & (\ell=m) \\ d^{m+1}_{m,1}(\theta) &=& \sqrt{\frac{(2m+1)!}{m!(m+2)!}}\left((m+1)\cos\theta-1\right)\frac{1+\cos\theta}{2}\left(\frac{-\sin\theta}{2}\right)^{m-1} & (\ell=m+1) \\ d^{\ell}_{m,1}(\theta) &=& \frac{1}{\sqrt{\ell^2-1}\sqrt{\ell^2-m^2}}\Big[(2\ell-1)(\ell\cos\theta-\frac{m}{\ell-1})\ d^{\ell-1}_{m,1}(\theta) & \\ & & -\frac{\ell}{\ell-1}\sqrt{(\ell-1)^2-m^2}\sqrt{(\ell-1)^2-1}\ d^{\ell-2}_{m,1}(\theta)\Big] & \forall \ell \geq m+2 \end{cases}$$

The terms $d^{\ell}_{m,-1}(\theta)$ remain to be computed. Using (5.48), one can show that $d^{\ell}_{m,-1}(\theta) = (-1)^{\ell+m} d^{\ell}_{m,1}(\pi-\theta)$, then with the replacement $\cos\theta \to (-\cos\theta)$ in all previous recurrence relations, we obtain the intended quantities.

Now, for cases where $m < 0$, we can show from the expressions (5.49) of the dependence with respect to the coefficients m and m', that when $m > 0$ and $m' = \pm 1$, the case for $\xi_{m,m'}$ is always changed when the signs of m and m' are switched at the same time, and $d^{\ell}_{-m,-m'}(\beta) = (-1)^{m-m'} d^{\ell}_{m,m'}(\beta)$. It follows that the sum or difference of finite rotations appearing in the scattering formula change as:

$$\begin{aligned} \left[d^{\ell}_{-m,1}(\theta) + d^{\ell}_{-m,-1}(\theta)\right] &= (-1)^{m+1}\left[d^{\ell}_{m,1}(\theta) + d^{\ell}_{m,-1}(\theta)\right] \\ \left[d^{\ell}_{-m,1}(\theta) - d^{\ell}_{-m,-1}(\theta)\right] &= (-1)^{m}\left[d^{\ell}_{m,1}(\theta) - d^{\ell}_{m,-1}(\theta)\right] \ . \end{aligned} \tag{5.50}$$

5.3 Transformation to real and simpler quantities

5.3.1 Negative values of m

Here we study specifically the case of negative values for m, the index of a spherical mode that corresponds to an eigenvalue $m\hbar$ for $\mathbf{J}_z$, the z-component of the total angular momentum operator $\mathbf{J}$. From expressions (5.27) of the four blocks involved in the scattering matrix, together with the transformation rules (5.43,5.50) when the sign of m changes, we deduce that blocks C and D acquire a phase (-1) when we make the change $m \to -m$, while blocks A and B do not change. For the writing of the scattering matrix with four blocks corresponding of the polarizations in the spherical modes, given by Eq.(5.22), it follows that:

$$\mathcal{M}^{(-m)}(\imath\xi) = \begin{pmatrix} \mathcal{M}^{(m)}_{EE}(\imath\xi) & -\mathcal{M}^{(m)}_{EM}(\imath\xi) \\ -\mathcal{M}^{(m)}_{ME}(\imath\xi) & \mathcal{M}^{(m)}_{MM}(\imath\xi) \end{pmatrix} .$$

Prop. 5 *When the block-operator* $\begin{pmatrix} A & B \\ C & D \end{pmatrix}$ *is made of square-blocks of the same size, and* A *is invertible, the determinant does not change when applying the changes* $B \to \alpha B$ *and* $C \to \frac{1}{\alpha}C$, *with* $\alpha \in \mathbb{C}^*$.

(For proof see **Appendix A.4** p.214)

In our case, **Prop.5** with $\alpha = -1$ gives $\det \mathcal{D}^{(m)}(\xi) = \det \mathcal{D}^{(m)}(\xi)$. Finally, the integrand $\Phi(\xi)$ in the scattering formula can be written with positive values of m only:

$$\Phi(\xi) = \ln\det \mathcal{D}(\imath\xi) = \sum_{m\in\mathbb{Z}} \ln\det \mathcal{D}^{(m)}(\imath\xi) = 2{\sum_{m}}' \ln\det \mathcal{D}^{(m)}(\imath\xi)\ . \tag{5.51}$$

5.3.2 Real quantities for the spherical harmonics

Expressions for the finite rotations and the spherical harmonics often contain $\sin\theta$ terms, and for numerical purpose one wants to keep real quantities as long as possible. To that purpose we will replace the sine in the expression by its rotated number on the positive real axis:

$$s(\theta) = \imath\sin\theta = \frac{k}{\hat{\xi}} = \sqrt{\cos^2\theta - 1} \geq 0\ . \tag{5.52}$$

A quantity X will be noted X^s after n replacements $\sin\theta \to s(\theta)$, and some $(-i)^n$ corrective multiplicative terms will appear to maintain the correct expression.

For $Y^s_{\ell,m}$ with $m \geq 1$ and $\ell \geq m$, a corrective term $(-i)^m$ is necessary. This is consistent with the case $m = 0$ where no change is applied. The new real expressions are then given by the modified recurrence relations:

$$\boxed{m=0}\ \begin{cases} Y^s_{1,0}(\theta) = Y_{1,0}(\theta) &=& \sqrt{\frac{3}{4\pi}}\cos\theta & (\ell=1)\\ Y^s_{2,0}(\theta) = Y_{2,0}(\theta) &=& \sqrt{\frac{5}{16\pi}}(3\cos^2\theta - 1) & (\ell=2)\\ Y^s_{\ell,0}(\theta) = Y_{\ell,0}(\theta) &=& \frac{\sqrt{4\ell^2-1}}{\ell}\cos\theta\ Y^s_{\ell-1,0}(\theta) - \frac{\ell-1}{\ell}\sqrt{\frac{2\ell+1}{2\ell-3}}\ Y^s_{\ell-2,0} & \forall\ell\geq 3 \end{cases}$$

$$\boxed{m>0}\ \begin{cases} Y^s_{m,m}(\theta) &=& \frac{1}{(-i)^m}\ Y_{m,m}(\theta) & \\ &=& (-1)^m\sqrt{\frac{2m+1}{4\pi(2m)!}}(2m-1)!!\ (s(\theta))^m & (\ell=m)\\ Y^s_{m+1,m}(\theta) &=& \frac{1}{(-i)^m}\ Y_{m+1,m}(\theta) & \\ &=& \sqrt{2m+3}\cos\theta Y^s_{m,m}(\theta) & (\ell=m+1)\\ Y^s_{\ell,m}(\theta) &=& \frac{1}{(-i)^m}\ Y_{\ell,m}(\theta) & \\ &=& \sqrt{\frac{2\ell+1}{\ell^2-m^2}}\left(\sqrt{2\ell-1}\cos\theta\ Y^s_{\ell-1,m}(\theta)\right. & \\ & & \left. -\sqrt{\frac{(\ell-1)^2-m^2}{2\ell-3}}\ Y^s_{\ell-2,m}(\theta)\right) & \forall\ell\geq m+2\ . \end{cases}$$

Concerning the θ-derivative, the transformation depends on the value of m. For $m = 0$, there is one term $\sin\theta$ for $\ell = 1$, and for $\ell > 1$, as $Y_{\ell,0}$ does not have $\sin\theta$ terms, $\partial_\theta Y_{\ell,0}$ have '-1' $\sin\theta$ terms. To have a ℓ-independent corrective term, the definition of the first term can be transformed into $\partial_\theta Y_{1,0}(\theta) = +\sqrt{\frac{3}{4\pi}}s(\theta)$, so that a global corrective term $(-i)^{-1}$ is necessary.

$$\boxed{m=0}\ \begin{cases} \partial_\theta Y^s_{1,0}(\theta) &=& \frac{-1}{(-i)}\ \partial_\theta Y_{1,0}(\theta) = \sqrt{\frac{3}{4\pi}}s(\theta) & (\ell=1)\\ \partial_\theta Y^s_{\ell,0}(\theta) &=& \frac{1}{(-i)^{-1}}\ \partial_\theta Y_{\ell,0}(\theta) & \\ &=& \frac{\ell}{s(\theta)}\left(\cos\theta\ Y^s_{\ell,0}(\theta) - \sqrt{\frac{2\ell+1}{2\ell-1}}\ Y^s_{\ell-1,0}\right) & \forall\ell\geq 2\ . \end{cases}$$

For $m > 0$, the $\ell = m$ term has $1+(m-2) = m-1$ times the $\sin\theta$ term, and so does the expression for $\ell > m$. Thus a corrective term $(-i)^{m-1}$ is necessary, which is again consistent with the case $m = 0$, and the new expressions are:

$$\boxed{m>0} \quad \begin{cases} \partial_\theta Y^s_{m,m}(\theta) &= \frac{1}{(-i)^{m-1}}\,\partial_\theta Y_{m,m}(\theta) & \\ &= (-1)^m\sqrt{\frac{2m+1}{4\pi(2m)!}}(2m-1)!!\; m\,(s(\theta))^{m-1}\cos\theta & (\ell = m) \\ \partial_\theta Y^s_{\ell,m}(\theta) &= \frac{1}{(-i)^{m-1}}\,\partial_\theta Y_{\ell,m}(\theta) & \\ &= \frac{1}{s(\theta)}\left(\ell\cos\theta\; Y^s_{\ell,m}(\theta) - \sqrt{\ell^2-m^2}\sqrt{\frac{2\ell+1}{2\ell-1}}\; Y^s_{\ell-1,m}\right) & \forall \ell \geq m+1 \end{cases}$$

The **Table 3** sums up the management of the corrective terms, valid for any $m \geq 0$ and any $\ell \geq m$, that have to be added as a premultiplicative factor with the real expressions here presented.

function	$Y_{\ell,m}$	$\partial_\theta Y_{\ell,m}$
corrective term	$(-i)^m$	$(-i)^{m-1}$

Table 3: Corrective terms appearing for the spherical harmonics when $\sin\theta$ is changed to the real-valued function $s(\theta)$.

Moreover, spherical harmonics and their derivative only appear in the elements (5.27) of the scattering formula through the variable $(\pi - \theta)$. It is thus interesting to have some information on their parity with respect to $\cos\theta$. From simple recurrence it can be shown that:

$$Y^s_{\ell,m}(\pi-\theta) = (-1)^{m+\ell} Y^s_{\ell,m}(\theta)\ . \tag{5.53}$$

For the θ-derivative of the spherical harmonics, the result is deduces as:

$$\partial_\theta Y^s_{\ell,m}(\pi-\theta) = (-1)^{m+\ell+1} \partial_\theta Y^s_{\ell,m}(\theta)\ . \tag{5.54}$$

5.3.3 Real quantities for the finite rotations

The same transformation can be applied to the finite rotations. For $m = 0$, a $(-i)$ correction factor comes out, and for the $m > 0$ case, a $(-i)^{m-1}$ correction factor comes out. To get a factor that does not depend on m, we change the sign in the $m = 0$ case, so that a factor $(-i)^{-1}$ comes out.

The new expressions are :

$$\boxed{m=0}\begin{cases} d^{1,s}_{0,1}(\theta) &=& \frac{1}{(-\imath)^{-1}}\, d^{1}_{0,1}(\theta) = -\frac{s(\theta)}{\sqrt{2}} & (\ell=1)\\ d^{2,s}_{0,1}(\theta) &=& \frac{1}{(-\imath)^{-1}}\, d^{2}_{0,1}(\theta) = -\sqrt{\frac{3}{2}}\cos\theta s(\theta) & (\ell=2)\\ d^{\ell,s}_{0,1}(\theta) &=& \frac{1}{(-\imath)^{-1}}\, d^{\ell}_{0,1}(\theta) & \\ &=& \frac{1}{\sqrt{\ell^2-1}}\left[(2\ell-1)\cos\theta\; d^{\ell-1,s}_{0,1}(\theta) - \sqrt{\ell(\ell-2)}\; d^{\ell-2,s}_{0,1}(\theta)\right] & \forall \ell\geq 3 \end{cases}$$

$$\boxed{m>0}\begin{cases} d^{m,s}_{m,1}(\theta) &=& \frac{1}{(-\imath)^{m-1}}\, d^{m}_{m,1}(\theta) = \sqrt{\frac{(2m)!}{(m-1)!(m+1)!}}\frac{1+\cos\theta}{2}\left(\frac{-s(\theta)}{2}\right)^{m-1} & (\ell=m)\\ d^{m+1,s}_{m,1}(\theta) &=& \frac{1}{(-\imath)^{m-1}}\, d^{m+1}_{m,1}(\theta) & \\ &=& \sqrt{\frac{(2m+1)!}{m!(m+2)!}}\left((m+1)\cos\theta-1\right)\frac{1+\cos\theta}{2}\left(\frac{-s(\theta)}{2}\right)^{m-1} & (\ell=m+1)\\ d^{\ell,s}_{m,1}(\theta) &=& \frac{1}{(-\imath)^{m-1}}\, d^{\ell}_{m,1}(\theta) & \\ &=& \frac{1}{\sqrt{\ell^2-1}\sqrt{\ell^2-m^2}}\left[(2\ell-1)(l\cos\theta-\frac{m}{\ell-1})\; d^{\ell-1,s}_{m,1}(\theta)\right. & \\ & & \left. -\frac{\ell}{\ell-1}\sqrt{(\ell-1)^2-m^2}\sqrt{(\ell-1)^2-1}\; d^{\ell-2,s}_{m,1}(\theta)\right] & \forall \ell\geq m+2\ . \end{cases}$$

The terms $d^{\ell}_{m,-1}(\theta)$ change exactly the same way, as they are equal to $(-1)^{\ell+m}d^{\ell}_{m,1}(\pi-\theta)$. **Table 4** sums up the management of the corrective terms valid for any $m\geq 0$ and any $\ell\geq m$, that have to be added as a premultiplicative factor with the new expressions.

function	$d^{\ell}_{m,1}(\theta)$	$d^{\ell}_{m,-1}(\theta)$
corrective term	$(-i)^{m-1}$	$(-i)^{m-1}$

Table 4: Corrective terms appearing for the finite rotations when $\sin\theta$ is changed to the real-valued function $s(\theta)$.

5.4 Conclusion

Taking into account the transformations presented in the two previous sections, and replacing $\sin\theta$ by $-\imath s(\theta)$, the A, B, C, D blocks of Eqs.(5.28) now write for $m\geq 0$:

$$\begin{aligned} A^{(m)}_{\ell_1,\ell_2,p} &= m(-1)^{\ell_2}\int_1^{\infty}\frac{\mathrm{d}\cos\theta}{s(\theta)} d^{\ell_1,s}_{m}[\text{sum}]\; Y^{s}_{\ell_2 m}(\theta)\; r_p(\imath\xi,k)\; e^{-2\hat{\xi}\mathcal{L}\cos\theta}\\ B^{(m)}_{\ell_1,\ell_2,p} &= (-1)^{\ell_2+1}\int_1^{\infty}\mathrm{d}\cos\theta\; d^{\ell_1,s}_{m}[\text{dif}]\; \partial_\theta Y^{s}_{\ell_2 m}(\theta)\; r_p(\imath\xi,k)\; e^{-2\hat{\xi}\mathcal{L}\cos\theta}\\ C^{(m)}_{\ell_1,\ell_2,p} &= (-1)^{\ell_2}\int_1^{\infty}\mathrm{d}\cos\theta\; d^{\ell_1,s}_{m}[\text{sum}]\; \partial_\theta Y^{s}_{\ell_2 m}(\theta)\; r_p(\imath\xi,k)\; e^{-2\hat{\xi}\mathcal{L}\cos\theta}\\ D^{(m)}_{\ell_1,\ell_2,p} &= m(-1)^{\ell_2+1}\int_1^{\infty}\frac{\mathrm{d}\cos\theta}{s(\theta)} d^{\ell_1,s}_{m}[\text{dif}]\; Y^{s}_{\ell_2 m}(\theta)\; r_p(\imath\xi,k)\; e^{-2\hat{\xi}\mathcal{L}\cos\theta} \end{aligned} \tag{5.55}$$

where we have defined the two combinations:

$$\begin{aligned} d^{\ell,s}_{m}[\text{sum}] &= d^{\ell,s}_{m,1}(\theta) + (-1)^{\ell+m}d^{\ell,s}_{m,1}(\pi-\theta)\\ d^{\ell,s}_{m}[\text{dif}] &= d^{\ell,s}_{m,1}(\theta) - (-1)^{\ell+m}d^{\ell,s}_{m,1}(\pi-\theta)\ . \end{aligned} \tag{5.56}$$

We observe in Eqs.(5.55) that the A, B, C, D blocks only contain real quantities, which yields that the off-diagonal blocks (5.24) and (5.25) of the operator $\mathcal{M}^{(m)}$ are purely imaginary. We therefore introduce the real-valued operator $\mathcal{N}^{(m)}(\imath\xi)$, better suited for numerics:

$$\mathcal{N}^{(m)}(\xi) = \begin{pmatrix} \mathcal{M}^{(m)}_{EE}(\xi) & -\imath\mathcal{M}^{(m)}_{EM}(\xi) \\ \\ \imath\mathcal{M}^{(m)}_{ME}(\xi) & \mathcal{M}^{(m)}_{MM}(\xi) \end{pmatrix}. \tag{5.57}$$

From **Prop.5** with $\alpha = -\imath$, we get $\det \mathcal{D}^{(m)}(\imath\xi) = \det\left(I - \mathcal{M}^{(m)}(\imath\xi)\right) = \det\left(I - \mathcal{N}^{(m)}(\imath\xi)\right)$. Finally, defining the reduced frequency $\tilde{\xi} = \frac{R}{c}\xi$, where R is the sphere's radius, and the reduced length of the cavity $\tilde{\mathcal{L}} = \frac{\mathcal{L}}{R} = 1 + \frac{L}{R}$, the Casimir energy E and the Casimir free-energy $\mathcal{F}$ can be expressed as:

$$\begin{aligned} E &= \frac{\hbar c}{\pi R}\int_0^\infty \mathrm{d}\tilde{\xi} \sum_m{}' \ln\det\left[I - \mathcal{N}^{(m)}(\tilde{\xi})\right] \\ \mathcal{F} &= 2k_B T \sum_n{}' \sum_m{}' \ln\det\left[I - \mathcal{N}^{(m)}(\tilde{\xi}_n)\right] \end{aligned} \tag{5.58}$$

where the Matsubara reduced frequencies are the $\tilde{\xi}_n = n\frac{2\pi R}{\lambda_T}$ and the real-valued operator $\mathcal{N}$ writes:

$$\mathcal{N}^{(m)}(\tilde{\xi}) = \begin{pmatrix} \mathcal{N}^{(m)}_{EE}(\tilde{\xi}) & \mathcal{N}^{(m)}_{EM}(\tilde{\xi}) \\ \\ \mathcal{N}^{(m)}_{ME}(\tilde{\xi}) & \mathcal{N}^{(m)}_{MM}(\tilde{\xi}) \end{pmatrix}, \quad \text{with the four blocks:} \tag{5.59}$$

$$\begin{aligned} \left(\mathcal{N}^{(m)}_{EE}(\tilde{\xi})\right)_{\ell_1,\ell_2} &= \sqrt{\tfrac{(2\ell_1+1)\pi}{\ell_2(\ell_2+1)}}a_{\ell_1}(i\tilde{\xi})\left(A^{(m)}_{\ell_1,\ell_2,\mathrm{TE}}(\tilde{\xi}) + B^{(m)}_{\ell_1,\ell_2,\mathrm{TM}}(\tilde{\xi})\right) \\ \left(\mathcal{N}^{(m)}_{EM}(\tilde{\xi})\right)_{\ell_1,\ell_2} &= \sqrt{\tfrac{(2\ell_1+1)\pi}{\ell_2(\ell_2+1)}}a_{\ell_1}(i\tilde{\xi})\left(C^{(m)}_{\ell_1,\ell_2,\mathrm{TE}}(\tilde{\xi}) + D^{(m)}_{\ell_1,\ell_2,\mathrm{TM}}(\tilde{\xi})\right) \\ \left(\mathcal{N}^{(m)}_{ME}(\tilde{\xi})\right)_{\ell_1,\ell_2} &= \sqrt{\tfrac{(2\ell_1+1)\pi}{\ell_2(\ell_2+1)}}b_{\ell_1}(i\tilde{\xi})\left(C^{(m)}_{\ell_1,\ell_2,\mathrm{TM}}(\tilde{\xi}) + D^{(m)}_{\ell_1,\ell_2,\mathrm{TE}}(\tilde{\xi})\right) \\ \left(\mathcal{N}^{(m)}_{MM}(\tilde{\xi})\right)_{\ell_1,\ell_2} &= \sqrt{\tfrac{(2\ell_1+1)\pi}{\ell_2(\ell_2+1)}}b_{\ell_1}(i\tilde{\xi})\left(A^{(m)}_{\ell_1,\ell_2,\mathrm{TM}}(\tilde{\xi}) + B^{(m)}_{\ell_1,\ell_2,\mathrm{TE}}(\tilde{\xi})\right) . \end{aligned} \tag{5.60}$$

For perfect mirrors, for which $r_{\mathrm{TE}} = -1$ and $r_{\mathrm{TM}} = 1$, the formula can be simplified, joining the (A, B) or (C, D) terms in (5.60). To that purpose, we will use the following relation between spherical harmonics and finite rotation, and its transformed form for the real valued terms:

$$\frac{m}{\sin\theta}Y_{\ell,m}(\theta,0) + \partial_\theta Y_{\ell,m}(\theta,0) = -\sqrt{\frac{\ell(\ell+1)(2\ell+1)}{4\pi}}d^{\ell}_{m,1}(\theta) \tag{5.61}$$

$$\frac{m}{s(\theta)}Y^s_{\ell,m}(\theta,0) + \partial_\theta Y^s_{\ell,m}(\theta,0) = -\sqrt{\frac{\ell(\ell+1)(2\ell+1)}{4\pi}}d^{\ell,s}_{m,1}(\theta) . \tag{5.62}$$

Inserting this relation, we obtain with the help of (5.53-5.54):

$$\begin{aligned}
\left(\mathcal{N}^{(m)}_{EE}(\tilde{\xi})\right)_{\ell_1,\ell_2} &= \frac{(-1)^{\ell_2+1}}{2}\sqrt{(2\ell_1+1)(2\ell_2+1)}a_{\ell_1}(i\tilde{\xi})\int_1^\infty \mathrm{d}\cos\theta\ \Delta^{(+)}_{m,\ell_1,\ell_2}(\theta)\ e^{-2\tilde{\xi}\tilde{\mathcal{L}}\cos\theta}\\
\left(\mathcal{N}^{(m)}_{EM}(\tilde{\xi})\right)_{\ell_1,\ell_2} &= \frac{(-1)^{\ell_2+1}}{2}\sqrt{(2\ell_1+1)(2\ell_2+1)}a_{\ell_1}(i\tilde{\xi})\int_1^\infty \mathrm{d}\cos\theta\ \Delta^{(-)}_{m,\ell_1,\ell_2}(\theta)\ e^{-2\tilde{\xi}\tilde{\mathcal{L}}\cos\theta}\\
\left(\mathcal{N}^{(m)}_{ME}(\tilde{\xi})\right)_{\ell_1,\ell_2} &= \frac{(-1)^{\ell_2}}{2}\sqrt{(2\ell_1+1)(2\ell_2+1)}b_{\ell_1}(i\tilde{\xi})\int_1^\infty \mathrm{d}\cos\theta\ \Delta^{(-)}_{m,\ell_1,\ell_2}(\theta)\ e^{-2\tilde{\xi}\tilde{\mathcal{L}}\cos\theta}\\
\left(\mathcal{N}^{(m)}_{MM}(\tilde{\xi})\right)_{\ell_1,\ell_2} &= \frac{(-1)^{\ell_2}}{2}\sqrt{(2\ell_1+1)(2\ell_2+1)}b_{\ell_1}(i\tilde{\xi})\int_1^\infty \mathrm{d}\cos\theta\ \Delta^{(+)}_{m,\ell_1,\ell_2}(\theta)\ e^{-2\tilde{\xi}\tilde{\mathcal{L}}\cos\theta}
\end{aligned} \tag{5.63}$$

with

$$\Delta^{(\pm)}_{m,\ell_1,\ell_2}(\theta) = d^{\ell_1,s}_{m,1}(\theta)d^{\ell_2,s}_{m,1}(\theta) \pm (-1)^{\ell_1+\ell_2}d^{\ell_1,s}_{m,1}(\pi-\theta)d^{\ell_2,s}_{m,1}(\pi-\theta)\ . \tag{5.64}$$

For $(m=0)$, as $d^{\ell,s}_{0,1}(\pi-\theta) = (-1)^{\ell-1}d^{\ell,s}_{0,1}(\theta)$, it simplifies to:

$$\begin{aligned}
\Delta^{(+)}_{0,\ell_1,\ell_2}(\theta) &= 2d^{\ell_1,s}_{0,1}(\theta)d^{\ell_2,s}_{0,1}(\theta)\\
\Delta^{(-)}_{0,\ell_1,\ell_2}(\theta) &= 0\ .
\end{aligned} \tag{5.65}$$

6 Numerical issues

In section we present some of the most important numerical issues encountered when evaluating the Casimir energy from expressions of previous **Section 5.4** (78). They will be presented in order of importance, and do not reflect the chronology of programming. That will allow to present numerical tests in the first parts assuming other issues are taken care of.

6.1 From operators to matrices: the truncation to $\ell_{\max}$

The first issue one can think of when planning to numerically evaluate the Casimir effect from expressions in the previous section is that the scattering operator $\mathcal{D}(\imath\xi)$ acts on the infinite-dimensional vector space $\mathcal{E}_\omega$ of electromagnetic fields in vacuum with frequency ω. However discrete, the basis of spherical modes $\mid m,\ell,P\rangle$ is an infinite set, with $\ell \in \mathbb{N}^*$ and $m \in \mathbb{Z}$ the quantum numbers ($|m| \leq \ell$), and $P \in \{\mathrm{E},\mathrm{M}\}$ the polarization. We thus need to truncate the dimension of the operator $\mathcal{D}(\imath\xi)$ by considering its restriction to a finite-dimensional subspace of $\mathcal{E}_\omega$.

6.1.1 The impact parameter

We introduce here a qualitative argument for the truncation in the quantum number ℓ, which will be confirmed by forthcoming numerical evaluations. The localization principle [222] connects a given angular momentum ℓ to an impact parameter $b = \frac{c\ell}{\tilde{\xi}}$. Then the spherical modes with $\ell \gg \tilde{\xi}\left(=\xi\frac{R}{c}\right)$ have $b = \frac{\ell R}{\tilde{\xi}} \gg R$, and thus correspond to rays that do not hit the sphere. They will therefore have a negligible role in the Casimir effect. Moreover, only frequencies $\tilde{\xi} \lesssim \frac{R}{L}$ have a significant contribution in the integration (or discrete sum) over $\tilde{\xi}$, because translation operators bring a factor $e^{-2\tilde{\xi}\tilde{\mathcal{L}}}$ at imaginary frequencies. As a consequence, modes with $\ell \gg \frac{R}{L}$ will have an impact parameter $b = \frac{\ell R}{\tilde{\xi}} \gtrsim \ell L \gg R$ and will be negligible for the Casimir effect.

We will then truncate the dimension of $\mathcal{D}(\imath\xi)$ by setting a maximum value $\ell_{\max}$ for the orbital index ℓ, that scales as $\frac{R}{L}$ but is $\tilde{\xi}$-independant:

$$\ell \leq \ell_{\max} = \alpha\frac{R}{L}\ . \tag{6.1}$$

From $|m| \leq \ell$, the angular momentum m will accordingly be limited to a finite number of values from $-\ell_{\max}$ to $+\ell_{\max}$. As we will only consider non-negative values of m, thanks to symmetry, the built subspace of $\mathcal{E}_\omega$ will have the dimension:

$$\begin{aligned} D(\ell_{\max}) &= \left(\sum_{m=0}^{\ell_{\max}} \#\ell(m)\right) = \left(\ell_{\max} + \sum_{m=1}^{\ell_{\max}} (\ell_{\max} - m + 1)\right) \\ &= \frac{1}{2}(\ell_{\max})^2 + \frac{3}{2}\ell_{\max}\ . \end{aligned}$$

6.1.2 Numerical tests

We here show the results of some numerical tests that we run in order to check that this truncation is realistic and that the results indeed converge with $\ell_{\max}$ to a fixed result for any situation. We will then aim at observing the required $\ell_{\max}$ to obtain a given accuracy, for various values of the ratio $\frac{L}{R}$. We will finally give a prescription as a rounded value for α, depending on the accuracy one aims at, to chose a truncation $\ell_{\max} = \alpha\frac{R}{L}$.

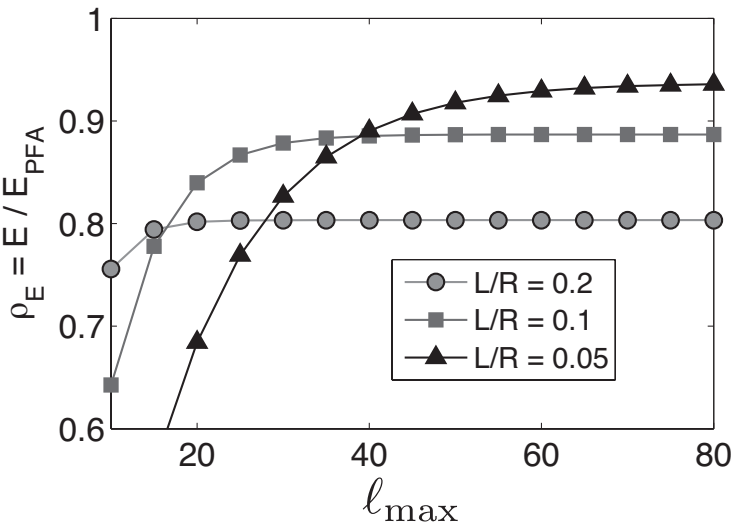

Figure 28: Casimir energy normalized by its PFA estimation $\rho_E = E/E^{\rm PFA}$ in the sphere-plane configuration, with respect to the truncation $\ell_{\rm max}$, for different values of the aspect ratio $\frac{L}{R} = 0.05, 0.1, 0.2$.

In **Fig. 28** we first observe how the convergence with $\ell_{\rm max}$ is modified when $\frac{L}{R}$ changes. The different curves present the ratio $\rho_E = E/E^{\rm PFA}$ of the computed Casimir energy at zero temperature E from (5.58), normalized by the PFA result $E^{\rm PFA}$, as functions of $\ell_{\rm max}$ used to compute E, for various values of the aspect ratio $\frac{L}{R}$. We see that for $\frac{L}{R} = 0.2$ (line with circles), the result E has roughly converged already at $\ell_{\rm max} \simeq 20$. When going to a twice smaller ratio $\frac{L}{R} = 0.1$ (line with squares), the convergence with respect to $\ell_{\rm max}$ is twice slower and happens roughly at $\ell_{\rm max} = 40$. Again, if the ratio is reduced to 0.05 (line with triangles), the convergence occurs for $\ell_{\rm max}$ around 80. The proportionality of $\ell_{\rm max}$ and $\frac{R}{L}$ is here illustrated, and it seems reasonable to choose the truncation with $\ell_{\rm max} = \alpha\frac{R}{L}, \alpha > 0$. Similar observations hold for the Casimir free-energy, force, and force gradient, but are not presented here.

We now study quantitatively the proportionality relation between $\frac{R}{L}$ and the number $\ell_{\rm max}$ necessary to obtain a given accuracy. To do so, we first observe that the convergence is exponential in $\ell_{\rm max}$, a feature that is illustrated in **Fig. 29**.

In this graph, we present as a function of $\ell_{\rm max}$ the relative difference Δ between the free-energy, computed with $\ell_{\rm max}$, and the same term, computed with a higher value $\ell_{\rm max}^{\rm ref}$. Δ is plotted with a curve for each value of the ratio $\frac{L}{R}$. When $\ell_{\rm max}$ is sufficiently smaller than $\ell_{\rm max}^{\rm ref}$, this relative difference can be considered as the relative distance to the exact result:

$$\Delta = \left| \frac{\mathcal{F}(\ell_{\rm max}) - \mathcal{F}(\ell_{\rm max}^{\rm ref})}{\mathcal{F}(\ell_{\rm max}^{\rm ref})} \right| \simeq \left| \frac{\mathcal{F}(\ell_{\rm max}) - \mathcal{F}(\infty)}{\mathcal{F}(\infty)} \right| .$$

The points in **Fig. 29** align on a straight line in this domain, which indicates that the relative error made by the truncation ($\ell < \ell_{\rm max}$) follows an exponential law:

$$\Delta = e^{a\ell_{\rm max}+b} \quad , \quad a, b \in \mathbb{R},\ a < 0 .$$

From a linear fit of the curves in the logarithmic plot, we have extracted the coefficients a and b for each value of the ratio $\frac{L}{R}$. With those values, we have then extrapolated the curves for any values of $\ell_{\rm max}$, and inverted the previous relation to get the required $\ell_{\rm max}$ for a given accuracy Δ for a given value of $\frac{L}{R}$. The results of this study are summed up in **Table 5**. From each column, representing a sought-after accuracy Δ, we average the coefficient $\alpha = \ell_{\rm max}\frac{L}{R}$ to give a 'rule of thumb' prescription.

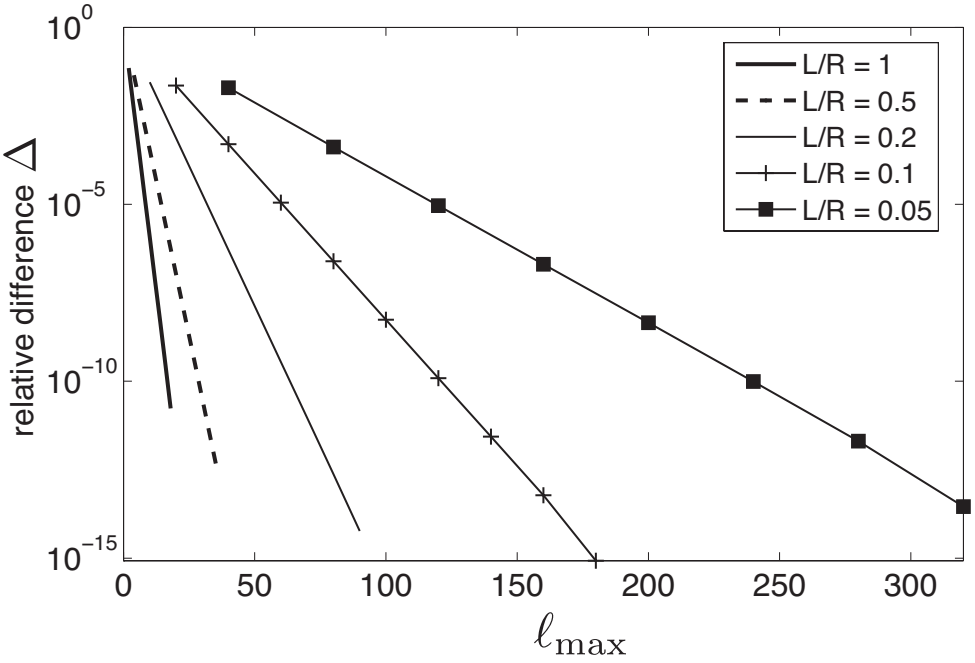

Figure 29: Convergence of the Casimir free-energy $\mathcal{F}$ with respect to $\ell_{\max}$. We plot, as a function of $\ell_{\max}$, the relative difference Δ between the $\ell_{\max}$-truncated quantities and a much more accurate reference value (computed with $\ell_{\max}^{\text{ref}} = 20$ for $\frac{L}{R} = 1$, 40 for $\frac{L}{R} = 0.5$, 100 for $\frac{L}{R} = 0.2$, 200 for $\frac{L}{R} = 0.1$, and 400 for $\frac{L}{R} = 0.05$). This numerical test has been done with a perfect sphere of radius $R = 100$ μm and a thermal wavelength λ_T =7.6 μm, corresponding to ambient temperature.

	$\Delta = 10^{-2}$	$\Delta = 10^{-3}$	$\Delta = 10^{-4}$	$\Delta = 10^{-5}$	$\Delta = 10^{-6}$	$\Delta = 10^{-7}$
$\frac{L}{R} = 1$	4	6	7	9	11	12
$\frac{L}{R} = 0.5$	6	9	12	15	18	21
$\frac{L}{R} = 0.2$	13	20	26	32	39	45
$\frac{L}{R} = 0.1$	25	37	49	61	73	85
$\frac{L}{R} = 0.05$	47	71	95	118	142	165
$\frac{L}{R} = 0.02$	115	173	230	288	346	404
$\frac{L}{R} = 0.01$	225	340	454	569	683	798
$\frac{L}{R} = 0.005$	397	584	771	958	1146	1333
coefficient α	3	4	5	6	7	8

Table 5: Necessary $\ell_{\max}$ to obtain an accuracy Δ in the truncation when computing the Casimir free-energy, at a given value of the aspect ratio $\frac{L}{R}$. The numbers are computed from linear fitting of the previous convergence curves. The last line indicates a 'rule of thumb' to roughly choose a coefficient α for $\ell_{\max} = \alpha \frac{R}{L}$.

6.1.3 Remarks on the prospect of theory-experiments comparison

This truncation is a fundamental element in the process of computation, as it transforms an exact, yet unworkable expression into an approximate, finite-dimensional one with matrices that are possible to handle with numerical codes. This prerequisite to the numerical evaluation yields that for a given choice of $\ell_{\max}$, the computation will only be accurate for not-too-small values of the ratio $\frac{L}{R}$. This feature shows that the multiple scattering method we presented is naturally well-suited for situations when the sphere is not too large compared to the surface-to-surface distance L. However, thanks to the power of numerical computations, it will be possible to apply our method also quite far in the opposite domain where L becomes smaller than R. If one is interested in investigating this opposite domain in depth, with very small values of $\frac{L}{R}$, the bigger $\ell_{\max}$ the computation can handle, the more performing the code. We have developed a numerical code that is able to handle a truncation as far as $\ell_{\max} = 520$ for any temperature, allowing to handle a minimum $\frac{L}{R}$ between 0.005 and 0.02, depending on the required numerical accuracy.

In Casimir experiments L is always much smaller than R to get a measurable signal, because of the weakness of the force. Indeed, to have a stronger interaction, the two possible solutions are to increase the area by choosing a larger sphere or to increase the interaction strength by reducing the distance. Both solutions lead to a smaller aspect ratio $\frac{L}{R}$.

In static measurements presented in [223], the spherical lens has a radius of curvature of 15.6 cm and is placed at distances from the plane that range from 0.7 to 7 μm. The corresponding ratios $\frac{L}{R}$ lie in $[4.5 \times 10^{-6}, 4.5 \times 10^{-5}]$ which is well below the numbers presented in this section. It thus seems unreasonable to try and use this method to get direct theoretical predictions to be compared to experimental results in this case.

However, in dynamic measurements performed by [224], smaller spheres are considered, with various radii from 10 to 150 μm. The distance ranges from 160 nm to 1 μm, which means that the aspect ratio is of the order of $[10^{-3}, 10^{-1}]$, in reach of our calculation.

6.2 Differentiations with respect to L and T

The scattering formula described in **Section 5.4** is valid to compute the Casimir energy, but the force $F = -\frac{\partial \mathcal{F}}{\partial L}$ and force gradient $G = -\frac{\partial F}{\partial L}$ are also of great interest, in order to compare to both the results obtained within the PFA method and the experimental results. They can be obtained through differentiation of the expression with respect to $\mathcal{L}$ or L. For thermodynamic studies, it can be also interesting to compute the entropy $S = -\frac{\partial \mathcal{F}}{\partial T}$, which can be obtained through differentiation with respect to the temperature T. In this section, we present how the differentiations can be done numerically at a final stage, or analytically at a deeper stage.

6.2.1 Numerical differentiation

With a numerical method, the quantity Q to differentiate with respect to $x \in \{L, T\}$ is computed for several values x around x_0. Those values are used to numerically approximate the first and/or second order derivatives with respect to x. We present here two of the methods that can be used with for instance with finite differences (h small):

$$\begin{array}{l} 2^{\text{nd}} \text{ order scheme :} \\ \text{(three-point stencil)} \end{array} \quad \left\{ \begin{array}{rcl} \frac{\partial Q}{\partial x} & = & \frac{-f(x-h)+f(x+h)}{2h} + \mathcal{O}(h^2) \\ \frac{\partial^2 Q}{\partial x^2} & = & \frac{f(x-h)-2f(x)+f(x+h)}{h^2} + \mathcal{O}(h^2) \end{array} \right. \tag{6.2}$$

$$\begin{array}{l} 4^{\text{th}} \text{ order scheme :} \\ \text{(five-point stencil)} \end{array} \quad \left\{ \begin{array}{rcl} \frac{\partial Q}{\partial x} & = & \frac{f(x-2h)-8f(x-h)+8f(x+h)-f(x+2h)}{12h} + \mathcal{O}(h^4) \\ \frac{\partial^2 Q}{\partial x^2} & = & \frac{-f(x-2h)+16f(x-h)-30f(x)+16f(x+h)-f(x+2h)}{12h^2} + \mathcal{O}(h^4) \end{array} \right. \tag{6.3}$$

Although simple and easy, numerical differentiation can give unstable results, especially for the second derivative, as it is very sensitive to small changes in the function to differentiate. We will thus prefer to use an analytical differentiation.

6.2.2 Analytical differentiation (method 1)

For the two analytical methods of differentiation, the idea is to write an explicit formula for F, G or S by taking analytically the derivative of the expression for $\mathcal{F}$. If we take the non-zero temperature case for example, we see immediatly that these quantities are obtained from the derivatives of $\ln\det \mathcal{D}^{(m)}$:

$$\begin{aligned} \mathcal{F} &= 2k_B T \sum_n{}' \sum_m{}' \ln\det \mathcal{D}^{(m)}(\tilde{\xi}_n) \\ F &= -2k_B T \sum_n{}' \sum_m{}' \frac{\partial \ln\det \mathcal{D}^{(m)}}{\partial \mathcal{L}}(\tilde{\xi}_n) \\ G &= 2k_B T \sum_n{}' \sum_m{}' \frac{\partial^2 \ln\det \mathcal{D}^{(m)}}{\partial \mathcal{L}^2}(\tilde{\xi}_n) \\ S &= -2k_B \sum_n{}' \sum_m{}' \ln\det \mathcal{D}^{(m)}(\tilde{\xi}_n) - 2k_B \sum_{n=1}^{\infty} \sum_m{}' \tilde{\xi}_n \frac{\partial \ln\det \mathcal{D}^{(m)}}{\partial \tilde{\xi}}(\tilde{\xi}_n) \end{aligned}$$

where for the last term in the expression of the entropy, we transformed the T-derivative to a frequency derivative:

$$\frac{\partial}{\partial T} \ln\det \mathcal{D}^{(m)}(\tilde{\xi}_n) = \frac{\partial \tilde{\xi}_n}{\partial T} \frac{\partial}{\partial \tilde{\xi}_n} \ln\det \mathcal{D}^{(m)}(\tilde{\xi}_n) = \frac{\tilde{\xi}_n}{T} \frac{\partial \ln\det \mathcal{D}^{(m)}}{\partial \tilde{\xi}}(\tilde{\xi}_n)$$

We first present a general method to compute $\frac{\partial}{\partial x}(\ln\det C)$ and $\frac{\partial^2}{\partial x^2}(\ln\det C)$, where the $(C_{i,j})$ coefficients depend on x. For the logarithm to be well-defined, we make the assumption that C is invertible.

Prop. 6 *For C an invertible matrix,*

- *its derivative with respect to the (i,j)-coefficient reads:*

$$\frac{\partial}{\partial C_{i,j}}\ln\det C = \left(C^{-1}\right)_{j,i}$$

- *The derivative of the inverse is:* $\left(C^{-1}\right)' = -C^{-1}C'C^{-1}$.
- *Finally the derivatives of* $\ln\det C$ *are:*

$$\frac{\partial}{\partial x}(\ln\det C) = Tr\left(C'C^{-1}\right) = Tr\left(C^{-1}C'\right)$$
$$\frac{\partial^2}{\partial x^2}(\ln\det C) = Tr\left(C''C^{-1} - C'C^{-1}C'C^{-1}\right)$$

(For proof, see Appendix A.5 p.214)

This analytical method is simple, but needs the computation of the inverse matrix $\mathcal{D}^{-1}$. The inversion process is not only computationally expensive, but as the matrix $\mathcal{D}$ will turn out to be very badly conditioned, it will be also very unstable.

6.2.3 Analytical differentiation (method 2)

We therefore propose an alternative method to compute $\frac{\partial}{\partial x}(\ln\det C)$ and $\frac{\partial^2}{\partial x^2}(\ln\det C)$ that does not involve any inversion of matrix. We start from the simple expressions for the derivative of a logarithm:

$$\begin{aligned}\frac{\partial}{\partial x}(\ln\det C) &= \frac{(\det C)'}{\det C}\\ \frac{\partial^2}{\partial x^2}(\ln\det C) &= \frac{(\det C)''}{\det C} - \left[\frac{(\det C)'}{\det C}\right]^2\end{aligned}$$

To perform this second analytical differentiation method, we will need to compute three terms : $\det C$, $(\det C)'$ and$(\det C)''$. Writing the matrix as a set of columns, we can use the nature of the determinant to obtain the following expressions:

$$\det C = \det\left(C_1|C_2|\cdots|C_n\right) \tag{6.4}$$

$$(\det C)' = \sum_{i=1}^{n}\det\left(C_1|\cdots|C_{i-1}|C_i'|C_{i+1}|\cdots|C_n\right) = \sum_{i=1}^{n}\det C_{,i} \tag{6.5}$$

$$\begin{aligned}(\det C)'' &= \sum_{i=1}^{n}\det\left(C_1|\cdots|C_{i-1}|C_i''|C_{i+1}|\cdots|C_n\right)\\ &\quad+\sum_{i=1}^{n}\sum_{j\neq i}\left(C_1|\cdots|C_{i-1}|C_i'|C_{i+1}|\cdots|C_{j-1}|C_j'|C_{j+1}|\cdots|C_n\right)\\ &= \sum_{i=1}^{n}\det C_{,ii} + \sum_{i=1}^{n}\sum_{j\neq i}\det C_{,ij}\end{aligned} \tag{6.6}$$

There we only need the matrices C, $C_{,i}$ and $C_{,ij}$, $\forall i,j \in [1,n]$. Using the canonical basis of matrices $(E_{i_0,j_0})_{(i,j)} = \delta_{i,i_0}\delta_{j,j_0}$, we build those matrices from C, C' and C'' :

$$\begin{aligned} C_{,i} &= C + (C' - C) \times E_{ii} \\ C_{,ii} &= C + (C'' - C) \times E_{ii} \\ C_{,ij} &= C + (C' - C) \times (E_{ii} + E_{jj}) \end{aligned}$$

Finally, back to our case, we only need the terms $\mathcal{D}^{(m)}$, $\mathcal{D}^{(m)\,\prime}$ and $\mathcal{D}^{(m)\,\prime\prime}$, which are matrices made of the derivatives for each component of the matrix $\mathcal{D}^{(m)}$. To obtain the Casimir force F and force gradient G, the only dependancy upon $\mathcal{L}$ on the matrix $\mathcal{D}^{(m)}$ appears through the term $e^{-2\tilde{\xi}\tilde{\mathcal{L}}\cos\theta}$ coming from the translations. Then differentiating turns out to be equivalent to multiplying by the term $\frac{-2\tilde{\xi}\cos(\theta)}{R}$ in each component of the matrix. For the Casimir entropy S, the situation is quite more complex, as the reduced frequency $\tilde{\xi}$ not only enters the translations with $e^{-2\tilde{\xi}\tilde{\mathcal{L}}\cos\theta}$ but also the Fresnel and Mie reflection coefficients.

The case of perfect mirrors is however easier to handle, as the Fresnel coefficients are constant, and one only needs expressions for the derivative of the Mie coefficients (5.40) with respect to their parameter $\tilde{\xi}$. They read, for perfect mirrors:

$$a'_\ell(x) = (-1)^\ell \frac{\pi}{2} \frac{(x^2 + \ell(\ell+1)) \left(I_{\ell-1/2}(x)K_{\ell+1/2}(x) + I_{\ell+1/2}(x)K_{\ell-1/2}(x)\right)}{\left(\ell K_{\ell+1/2}(x) + xK_{\ell-1/2}(x)\right)^2} \tag{6.7}$$

$$b'_\ell(x) = (-1)^{\ell+1} \frac{\pi}{2} \frac{I_{\ell-1/2}(x)K_{\ell+1/2}(x) + I_{\ell+1/2}(x)K_{\ell-1/2}(x)}{\left(K_{\ell+1/2}(x)\right)^2} \tag{6.8}$$

This second analytical method is more stable when used in the numerical evaluations of the force, force gradient or entropy. The major drawback is the numerical cost, as the expression (6.5) for the first-order derivative involves the evaluation of n determinants, and (6.6) for the second-order derivative involves the evaluation of n^2 determinants, where n is the number of columns in the matrix $\mathcal{D}^{(m)}$ and the order of complexity will then increase.

6.3 Integration/sum over $\tilde{\xi}$

The Casimir free-energy at zero and non-zero temperatures can be written with the help of the integrand function Φ:

$$E = \frac{\hbar c}{2\pi R} \int_0^\infty d\tilde{\xi}\ \Phi(\tilde{\xi}) \quad , \quad \Phi(\tilde{\xi}) = 2 {\sum_m}' \ln\det \mathcal{D}^{(m)}(\tilde{\xi})$$

$$\mathcal{F} = \frac{\hbar c}{2\pi R} {\sum_n}' \frac{2\pi R}{\lambda_T} \Phi(\tilde{\xi}_n) \quad , \quad \text{with} \quad \tilde{\xi}_n = n\frac{2\pi R}{\lambda_T}$$

Both expressions have to be adapted for the numerical computation: E involves an integration of $\Phi(\tilde{\xi})$ that needs to be carried out numerically, and $\mathcal{F}$ contains an infinite sum that needs to be truncated for a numerical evaluation. In this section we describe the choices we have made for methods and cut-offs in the numerical implementation.

6.3.1 Shape of the function to be integrated/summed

Thanks to the use of imaginary frequencies, the integrand functions $\Phi(\tilde{\xi}) = 2{\sum_m}' \ln\det \mathcal{D}^{(m)}(\tilde{\xi})$ are smooth and well-behaved. At low frequencies they converge to a finite negative value, and exponentially decrease to zero for large frequencies.

- At low frequency the behaviour differs with the model for the materials. We define the order of low-frequency convergence as the integer n such that:

$$\frac{\Phi(\tilde{\xi}) - \Phi(0)}{\Phi(0)} = \mathcal{O}\left(\tilde{\xi}^n\right)$$

For perfect mirrors and plasma model, $n = 2$, whereas with the Drude model there is a linear convergence ($n = 1$). It can be explained by the low-frequency expansions of the Fresnel coefficients (7.18-7.19) (p.112 and p.113). It follows that the integrand Φ converges at much lower frequencies when using the Drude model, than with the plasma or perfectly reflecting models, as illustrated in **Fig. 30**.

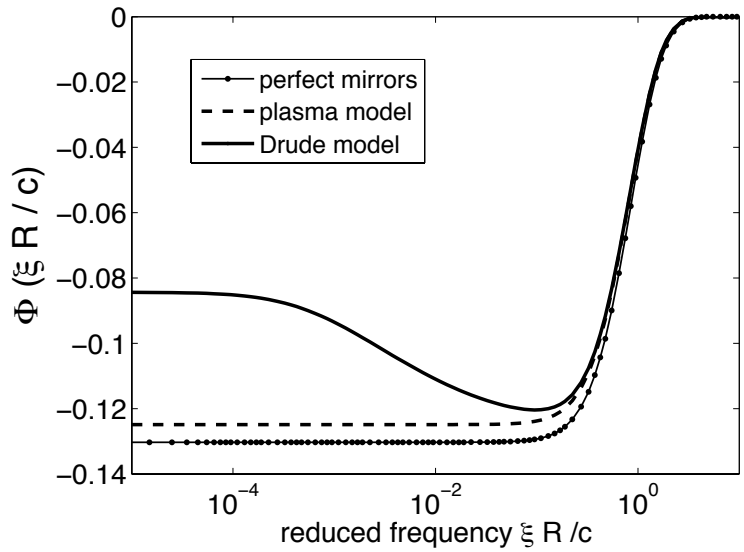

Figure 30: Integrand for the energy $\Phi(\tilde{\xi}) = 2\sum'_m \ln\det \mathcal{D}^{(m)}(\tilde{\xi})$ for $L = R = 1$ μm. The case of perfect mirrors is illustrated by a thin dotted-line, the plasma model by a dashed-line and the Drude model by a solid line.

When the reduced frequency $\tilde{\xi}$ decreases below unity, the integrand function Φ reaches quickly a minimum for perfect and plasma models. For Drude, the integrand is similar to the one from plasma model for not-too-small frequencies, as $\xi \gg \gamma$ yields that the dielectric function (2.7) (p.41) does not see the effects of dissipation. For lower frequencies $\xi \lesssim \gamma$ however, dissipation plays a role and the integrand departs from the one of plasma, to reach a different value, lower in magnitude.

- At high frequencies, because of the $e^{-2\tilde{\mathcal{L}}\tilde{\xi}\cos\theta}$ term present in each element of the matrix from the two translations, Φ decreases exponentially. More precisely, because of the high-frequency expansions of the modified Bessel functions:

$$I_\alpha(x) \sim \frac{e^x}{\sqrt{2\pi x}} \qquad\qquad K_\alpha(x) \sim \sqrt{\frac{\pi}{2x}} e^{-x} \tag{6.9}$$

one can show that the Mie coefficients $a_\ell(\tilde{\xi})$ and $b_\ell(\tilde{\xi})$ diverge like $e^{2\tilde{\xi}}$ at high frequencies. Thus the exponential decrease is better described by the function $e^{-2\tilde{\xi}(\tilde{\mathcal{L}}\cos\theta - 1)}$. It means that a cut-off $\tilde{\xi}_{\max}$ for the integration or the summation over Matsubara frequencies will be mainly determined by the value of $(\tilde{\mathcal{L}}\cos\theta - 1)$. From the exponential decrease $e^{-2\tilde{\xi}(\tilde{\mathcal{L}}\cos\theta - 1)}$,

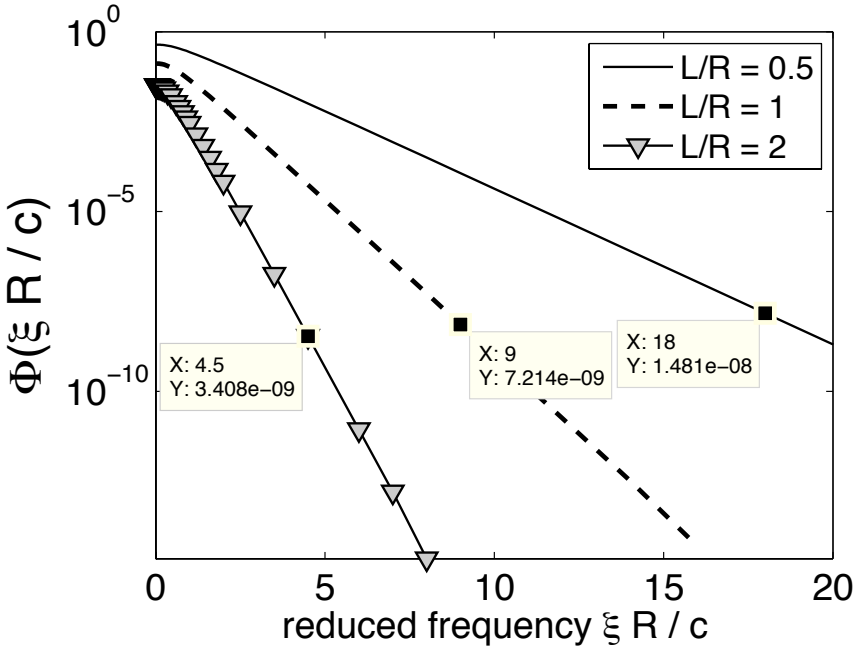

Figure 31: High-frequency decrease of the integrand for the energy $\Phi(\tilde{\xi}) = 2\sum'_m \ln\det \mathcal{D}^{(m)}(\tilde{\xi})$, with different values of $\frac{L}{R}$. The boxes indicate the value of Φ for a cut-off $\tilde{\xi}_{\max} = 9\frac{R}{L}$.

we can see that at high frequencies, only terms with $\cos\theta \simeq 1$ have an important contribution. Then the important parameter for the cut-off will be $\tilde{\mathcal{L}} - 1 = \frac{\mathcal{L}}{R} - 1 = \frac{L}{R}$.

In **Fig. 31**, we observe the high-frequency exponential decrease of $\Phi(\tilde{\xi})$ for increasing values of this parameter $\frac{L}{R}$, from right to left. When the aspect ratio $\frac{L}{R}$ doubles, the cut-off $\tilde{\xi}_{\max}$ necessary to reach a given small value is divided by 2. In the numerics, we will thus use $\tilde{\xi}_{\max} = K\frac{R}{L}$, with $K \in \mathbb{R}$ a constant parameter to be determined upon desired accuracy.

- Another factor of high-frequency decrease comes from the optical properties of the material: for example a metal is a very bad reflector for high-frequencies, where $\varepsilon \simeq 1$, which yields a very small contribution to the Casimir effect. As the dielectric functions ε for a plasma or a Drude model, with the same plasma frequency ω_P, become equal for high frequencies $\xi \gg \gamma$, we can limit this study for metals to the plasma case. We observe that $\varepsilon - 1 \ll 1$ when $\xi \gg \omega_P$, or equivalently $\tilde{\xi} \gg \frac{2\pi R}{\lambda_P}$. It means that a second cut-off can be chosen such that $\tilde{\xi}_{\max} = K'\frac{2\pi R}{\lambda_P}$. The case of dielectric materials is quite similar, with $\varepsilon - 1 \ll 1$ when $\xi \gg \omega_1$, or equivalently $\tilde{\xi} \gg \frac{2\pi R}{\lambda_1}$.

  Although the introduction of this second cut-off is not necessary with the Matsubara summation, it can be important when computing the continuous integral for the Casimir energy at zero temperature: if this cut-off were not introduced, the range of frequencies where the integrand takes noticeable values would not be correctly predicted and it could result in a poor numerical accuracy.

6.3.2 Method for integration

For the numerical evaluation of the Casimir energy at zero temperature, we need to perform a numerical integration of the continuous function $\Phi(\tilde{\xi})$ on a segment $[0, \tilde{\xi}_{\max}]$. There is a great variety of methods to numerically implement this computation, the simplest being the rectangle rule

where the segment $[0, \tilde{\xi}_{\max}]$ is broken up in N equal sub-intervals, and the function is interpolated as a constant number in each sub-interval. The integral is then the sum of each sub-integral that is carried out analytically:

$$\begin{aligned}\int_a^b f(x)dx &= \int_{a_0}^{a_N} f(x)dx = \sum_{i=0}^{N-1} \int_{a_i}^{a_{i+1}} f(x)dx \\ &\simeq \sum_{i=0}^{n-1} \int_{a_i}^{a_{i+1}} f\left(\frac{a_i + a_{i+1}}{2}\right) dx = \sum_{i=0}^{n-1} (a_{i+1} - a_i) f\left(\frac{a_i + a_{i+1}}{2}\right) \\ &\simeq \frac{b-a}{N} \sum_{i=0}^{n-1} f\left(\frac{a_i + a_{i+1}}{2}\right)\end{aligned}$$

and the result converges to the exact result when $N \to \infty$. There exist more elaborate ways to interpolate the function in each sub-interval, for example with a first order polynomial $\left(\frac{x-a_i}{a_{i+1}-a_i} f(a_{i+1}) + \frac{a_{i+1}-x}{a_{i+1}-a_i} f(a_i)\right)$, leading to the trapezoidal rule:

$$\int_a^b f(x)dx \simeq \frac{b-a}{N} \left(\frac{f(a) + f(b)}{2} + \sum_{i=1}^{n-1} f(a_i) \right)$$

or with a second order polynomial, leading to the Simpson's rule:

$$\int_a^b f(x)dx \simeq \frac{b-a}{3N} \left(\frac{f(a) + f(b)}{2} + \sum_{i=1}^{n-1} f(a_i) + 2 \sum_{i=0}^{N-1} f\left(\frac{a_i + a_{i+1}}{2}\right) \right)$$

Another possible sophistication in the integration is to have an iterative process to split again and again the sub-intervals where the integration is not accurate enough. This is done by the Gauss-Kronrod quadrature algorithm which is used by most of modern integration libraries. However, because in our case the integrand is numerically unstable for low frequencies, as will be discussed in **Section 6.6** (p.101), we want to control and restrict the values $\tilde{\xi}$ at which Φ is evaluated. Furthermore, the function is well-behaved on $[0, \tilde{\xi}_{\max}]$ and a simple rectangle rule, however not optimal, is safer. The accuracy will then only be influenced by the step $\Delta\tilde{\xi} = \frac{\tilde{\xi}_{\max}}{N}$, where N is the number of sub-intervals. Of course, the smaller the step, the better the accuracy.

6.3.3 Numerical tests

Two parameters remain to be chosen to reach the wanted accuracy: K for the cut-off $\tilde{\xi}_{\max}$, and $\Delta\tilde{\xi}$ for the division of the interval $[0, \tilde{\xi}_{\max}]$. We give in **Table 6** the relative difference between the numerically computed integral for a given constant step and a chosen cut-off, and a reference integral, computed with a very small step and a very large cut-off, assumed to be much more accurate. The first line indicates the choice of the step $\Delta\tilde{\xi}$, the first column the choice of the cut-off $\tilde{\xi}_{\max}$.

In the second line, representing a cut-off at $5\frac{R}{L}$, the relative difference quickly saturates for a decreasing step around 1e-4, meaning that $\int_0^\infty \Phi(\tilde{\xi})d\tilde{\xi}$ and $\int_0^{\tilde{\xi}_{\max}} \Phi(\tilde{\xi})d\tilde{\xi}$ also have this relative difference. To get a more accurate result, refining the step will not work, the only solution is to increase the cut-off.

In the fourth column, representing a step of $0.1\frac{R}{L}$, the relative difference also saturates when increasing $\tilde{\xi}_{\max}$, meaning that the error in the integration is dominated by the lack of interpolation points. The only solution to improve the numerical accuracy is there to reduce the step.

step $\Delta\tilde{\xi}$	$0.5\frac{R}{L}$	$0.2\frac{R}{L}$	$0.1\frac{R}{L}$	$0.05\frac{R}{L}$	$0.02\frac{R}{L}$	$0.01\frac{R}{L}$	$0.005\frac{R}{L}$
$\tilde{\xi}_{\max} = 5\frac{R}{L}$	1.7e-3	7.3e-5	8.2e-5	8.7e-5	8.8e-5	8.8e-5	8.7e-5
$\tilde{\xi}_{\max} = 10\frac{R}{L}$	1.8e-3	8.5e-5	5.8e-6	3.6e-7	5.4e-9	3.5e-9	4.1 e-9
$\tilde{\xi}_{\max} = 20\frac{R}{L}$	1.8e-3	8.5e-5	5.8e-6	3.7e-7	9.5e-9	5.9e-10	3.7 e-11

Table 6: Accuracy of the numerical integration over $\tilde{\xi}$ as the relative difference between the result computed with a rectangle rule of constant step $\Delta\tilde{\xi}$ and high-frequency cut-off $\tilde{\xi}_{\max}$, and a reference value, assumed to be much more accurate. The columns represent a choice of $\Delta\tilde{\xi}$, the rows a choice of $\tilde{\xi}_{\max}$. The green boxes indicate the deduced prescriptions of this test with respect to a $10^{-4}, 10^{-6}$, or 10^{-8} intended numerical accuracy. The integrand has been evaluated for $\frac{L}{R} = 1, \ell_{\max} = 10$ and the objects are perfect reflectors.

Finally, if we aim at an accuracy of 10^{-4} in the relative difference with the exact integral, useful for qualitative observations and tests, a good choice will be $\left(\tilde{\xi}_{\max} = 5\frac{R}{L}, \Delta\tilde{\xi} = 0.2\frac{R}{L}\right)$, which represents 25 points of evaluation for the function Φ, and the smallest evaluated frequency will be $0.1\frac{R}{L}$.

If we aim at an accuracy of 10^{-6} in the relative difference with the exact integral, a good choice will be $\left(\tilde{\xi}_{\max} = 10\frac{R}{L}, \Delta\tilde{\xi} = 0.05\frac{R}{L}\right)$, which represents 200 points of evaluation for the function Φ, and the smallest evaluated frequency will be $0.025\frac{R}{L}$. We will use this criteria in the continuation of the manuscript for the integration over $\tilde{\xi}$. The cut-off $\tilde{\xi}_{\max} = 10\frac{R}{L}$ will also be chosen when doing the Matsubara sum to get the Casimir free-energy at non-zero temperatures.

If we aim at a very high numerical accuracy, such as 10^{-8} in the relative difference with the exact integral, a good choice will be $\left(\tilde{\xi}_{\max} = 10\frac{R}{L}, \Delta\tilde{\xi} = 0.02\frac{R}{L}\right)$, which represents 500 points of evaluation for the function Φ, and the smallest evaluated frequency will be $0.01\frac{R}{L}$.

6.4 Integration over $\cos\theta$

Each element of the scattering operator $\mathcal{D}(\imath\xi)$ given by Eqs.(5.55) contains an integral over $\cos\theta$, in order to take into account all possible transverse component of the wavevector. Generally, because of the complexity of the function to be integrated, this integral will be carried out numerically. However, in the special case of perfectly reflecting mirrors, it is possible to have an analytical form of the integral. While this method is not applicable in the general case, it will be helpful for testing the numerical integration methods, as it gives for some cases the exact result.

In this section, we first present the analytical integration method valid for perfect mirrors, we then come to the numerical integration, first with an analysis of the shape of the functions of $\cos\theta$, then with the description of the chosen numerical method, and finally with numerical tests to check that the obtained results are sufficiently accurate.

6.4.1 Analytical integration for perfect mirrors

In the case of perfect mirrors, the function to integrate over $\cos\theta$ is given in Eq.(5.63) as an exponential term $e^{-2\tilde{\xi}\tilde{\mathcal{L}}\cos\theta}$ multiplied by $\Delta^{(\pm)}_{m,\ell_1,\ell_2}(\theta)$, which is a polynomial in $\cos\theta$. It is then possible to integrate analytically this function, thanks to the following property:

Prop. 7 *The function $f(x) = P_N(x)e^{-\gamma x}$, with $P_N = \sum_{i=0}^{N} a_i x^i$, has for primitive the functions $F(x) = Q_N(x)e^{-\gamma x} + c$, with $c \in \mathbb{R}$ and $Q_N = \sum_{i=0}^{N} b_i x^i$, the coefficients being defined with the*

lowering recurrence relations:

$$\begin{aligned} b_N &= -\frac{a_N}{\gamma} \\ b_i &= -\frac{a_i}{\gamma} + \frac{(i+1)b_{i+1}}{\gamma} \quad , \ \forall i \in [\![0, N-1]\!] \end{aligned} \tag{6.10}$$

Then, if $\gamma > 0$, $I = \int_1^\infty f(x)\mathrm{d}x = -Q_N(1)e^{-\gamma} = e^{-\gamma}\sum_{i=0}^N b_i$.

For numerical purpose, the polynomials will be described by a vector, the elements of which are the polynomial's coefficients:

$$P_N = \sum_{i=0}^{N} a_i x^i \ \rightarrow \ P = \begin{bmatrix} a_0 \\ a_1 \\ \vdots \\ a_N \end{bmatrix} \in \mathbb{R}^{N+1}$$

Let us give four more technical properties of this vectorial representation, that will turn out to be useful in the future computations:

Prop. 8 *For a given polynomial* P_N *of degree* N*, the polynomial* Q_N *(that allows to obtain the primitive of* $f(x) = P_N(x)e^{-\gamma x}$ *as in the previous property) has a related vector* Q *that can be obtained by solving the system :*

$$AQ = P \quad with \quad A = \begin{bmatrix} -\gamma & 1 & 0 & \cdot & 0 \\ 0 & -\gamma & 2 & \ddots & \vdots \\ \vdots & \ddots & \ddots & \ddots & 0 \\ \vdots & & \ddots & -\gamma & N \\ 0 & \cdots & \cdots & 0 & -\gamma \end{bmatrix}$$

Prop. 9 *The multiplication by* x *of the polynomial* P_N *has for vectorial equivalent*[8] *the multiplication by a matrix* K_{up}*:*

$$[x \rightarrow xP_N(x)] = K_{up} \times P_N \quad with \quad K_{up} = \begin{bmatrix} 0 & \cdots & \cdots & \cdots & 0 \\ 1 & 0 & & & \vdots \\ 0 & 1 & \ddots & & \vdots \\ \vdots & \ddots & \ddots & \ddots & \vdots \\ 0 & \cdots & 0 & 1 & 0 \end{bmatrix}$$

[8] Assuming the vector has a sufficient size, that is to say, greater than $N + 2$.

Prop. 10 *Changing x to $(-x)$ inside the polynomial P_N has for vectorial equivalent the multiplication by a matrix Π:*

$$[x \to P_N(-x)] = \Pi \times P_N \quad with \quad \Pi = \begin{bmatrix} 1 & 0 & \cdots & \cdots & 0 \\ 0 & -1 & 0 & & \vdots \\ \vdots & 0 & 1 & \ddots & \vdots \\ \vdots & & \ddots & \ddots & 0 \\ 0 & \cdots & \cdots & 0 & (-1)^N \end{bmatrix}$$

Prop. 11 *The product of two polynomials $P_{N_1} = \sum_{i=0}^{N_1} a_i x^i$ and $Q_{N_2} = \sum_{i=0}^{N_2} b_i x^i$ is the polynomial $R_N = \sum_{i=0}^{N} c_i x^i$ such that:*

$$\begin{cases} N &= N_1 + N_2 \\ \\ c_k &= \displaystyle\sum_{i=max(0,k-N_2)}^{min(N_1,k)} a_i b_{k-i} \quad , \ \forall k \in [\![0, N]\!] \end{cases}$$

To use this formalism in our computation, the polynomial P_N of the integrand function, or equivalently, its related vector, remains to be computed.

We start with the case $(m = 0)$, where the polynomial $\Delta^{(\pm)}_{0,\ell_1,\ell_2}(\theta)$ is given by (5.65). The task is then to express the finite rotation terms as polynomials. Following **Section 5.3.3**, we construct the vectors $D_0^{\ell_1} \in \mathbb{R}^{\ell_1}$ in the following way:

$$D_0^1 = -\frac{1}{\sqrt{2}} \begin{bmatrix} 1 \\ 0 \\ \vdots \\ 0 \end{bmatrix} \in \mathbb{R}^{\ell_1} \quad ; \quad D_0^2 = -\sqrt{\frac{3}{2}} \begin{bmatrix} 0 \\ 1 \\ 0 \\ \vdots \\ 0 \end{bmatrix} \in \mathbb{R}^{\ell_1}$$

$$D_0^\ell = \frac{2\ell - 1}{\sqrt{\ell^2 - 1}} K_{up} \times D_0^{\ell-1} - \frac{\sqrt{\ell(\ell-2)}}{\sqrt{\ell^2 - 1}} D_0^{\ell-2} \in \mathbb{R}^{\ell_1} \quad , \ \forall \ell \in [\![3, \ell_1]\!]$$

The sequence ends up with the vector $D_0^{\ell_1}$ related to the polynomial of degree $(\ell_1 - 1)$ such that $d^{\ell_1,s}_{0,1}(\theta) = s(\theta) D_0^{\ell_1}(\cos\theta)$. Doing the same for the second term with ℓ_2, one gets the product $P = d^{\ell_1}_{0,1}(\theta) d^{\ell_2}_{0,1}(\theta) = (\cos^2\theta - 1) \times D_0^{\ell_1} \times D_0^{\ell_2}$ which is a polynomial of degree $(\ell_1 + \ell_2)$ representing the integrand, that can be computed from **Prop. 11** and **Prop. 9**. The last step is to compute $Q = A^{-1}P$ and then sum over its coefficients. Finally, one gets the result of the analytical integration over $\cos\theta$ as:

$$\begin{aligned} \int_1^\infty d\cos\theta \ \Delta^{(+)}_{0,\ell_1,\ell_2}(\theta) \ e^{-2\tilde{\xi}\tilde{\mathcal{L}}\cos\theta} &= -2Q(1)e^{-2\tilde{\xi}\tilde{\mathcal{L}}} \\ \int_1^\infty d\cos\theta \ \Delta^{(-)}_{0,\ell_1,\ell_2}(\theta) \ e^{-2\tilde{\xi}\tilde{\mathcal{L}}\cos\theta} &= 0 \end{aligned} \tag{6.11}$$

Now, for the case ($m > 0$), the polynomial $\Delta^{(\pm)}_{m,\ell_1,\ell_2}(\theta)$ is given by (5.64). The situation is quite similar, the only difference being the presence of terms like $d^{\ell}_{m,1}(\pi-\theta)$ which are represented by $\Pi \times D^{\ell}_{m}$, as described in **Prop. 10**. Following the definitions of **Section 5.3.3**, we construct the vector $D^{\ell_1}_m$ as:

$$D^m_m = -\left(\frac{-1}{2}\right)^m \sqrt{\frac{(2m)!}{(m-1)!(m+1)!}} \begin{bmatrix} 1 \\ 1 \\ 0 \\ \vdots \\ 0 \end{bmatrix} \quad \in \mathbb{R}^{\ell_1-m+2}$$

$$D^{m+1}_m = \sqrt{\frac{2m+1}{m(m+2)}}\left((m+1)K_{up} - Id\right) \times D^m_m \quad \in \mathbb{R}^{\ell_1-m+2}$$

$$D^{\ell}_m = \frac{1}{\sqrt{(\ell^2-1)(\ell^2-m^2)}}\left[(2\ell+1)\left(\ell K_{up} - \frac{m}{\ell-1}Id\right) \times D^{\ell-1}_m \right.$$
$$\left. -\frac{\ell}{\ell-1}\sqrt{(\ell-1)^2-m^2}\sqrt{(\ell-1)^2-1}D^{\ell-2}_m\right] \ , \ \forall \ell \in [\![m+2, \ell_1]\!]$$

It ends up with the vector $D^{\ell_1}_m$ related to the polynomial such that $d^{\ell_1,s}_{m,1}(\theta) = (s(\theta))^{m-1} \times D^{\ell_1}_m(\cos\theta)$. The polynomial to integrate is now

$$P^{(\pm)} = (\cos^2\theta - 1)^{m-1} \times \left[D^{\ell_1}_m \times D^{\ell_2}_m \pm (-1)^{\ell_1+\ell_2}(\Pi \times D^{\ell_1}_m) \times (\Pi \times D^{\ell_2}_m)\right]$$

which is of degree $(\ell_1 - m + 1) + (\ell_2 - m + 1) + 2(m-1) = \ell_1 + \ell_2$. The last step is to compute $Q^{(\pm)} = A^{-1}P^{(\pm)}$ and then sum over its coefficients. Finally, one gets the result of the analytical integration over $\cos\theta$ as:

$$\int_1^{\infty} d\cos\theta \ \Delta^{(\pm)}_{m,\ell_1,\ell_2}(\theta) \ e^{-2\tilde{\xi}\tilde{\mathcal{L}}\cos\theta} = -Q^{(\pm)}(1)e^{-2\tilde{\xi}\tilde{\mathcal{L}}} \tag{6.12}$$

The use of vectors to represent the polynomials is of great interest in this case, as it simplifies the computation of the analytical integration by means of matrix-vector products. The computation of the $\tilde{\mathcal{L}}$-derivative of matrix elements can be done in the same way, with P replaced by $P' = (-2\tilde{\xi}\cos\theta) \times P$ of degree $(\ell_1 + \ell_2 + 1)$ for the first derivative, and $P'' = (4\tilde{\xi}^2\cos^2\theta) \times P$ of degree $(\ell_1 + \ell_2 + 2)$ for the second derivative.

This method is only valid for perfect mirrors, as the Fresnel coefficients are no more polynomials for the common models of dielectrics and metals. But in this case it allows to check if the numerical scheme for $\cos\theta$-integration is valid, by comparing the results obtained numerically in the perfectly-reflecting case to the analytical ones.

6.4.2 Shape of the function to be numerically integrated

In order to choose a method to implement the integrations over $\cos\theta$ in (5.55), we first study the shape of the four integrands f_A, f_B, f_C, f_D. All of those $\cos\theta$-functions are dependent on the parameters $(m, \ell_1, \ell_2, \tilde{\xi}, \tilde{\mathcal{L}})$ and of the material optical properties. We will only consider the set of $f_A(\cos\theta)$, the integrands of the elements of the block matrix A, as they are quite similar to each other from a numerical point of view:

$$f_A(\cos\theta) = \frac{d^{\ell_1,s}_m[\text{sum}] \ Y^s_{\ell_1,m}(\cos\theta)}{\sqrt{\cos^2\theta - 1}} r_p(\tilde{\xi}, \cos\theta) \ e^{-2\tilde{\mathcal{L}}\tilde{\xi}\cos\theta} \tag{6.13}$$

The exponential $e^{-2\tilde{\mathcal{L}}\tilde{\xi}\cos\theta}$ coming from the translation operators will obviously have a dominant role, as it yields a strong decrease for large values of $\cos\theta$. As a consequence the integration scheme will be very dependant on the value of $(\tilde{\xi}\tilde{\mathcal{L}})$. In **Fig. 32** we observe the shape of f_A for fixed values of (m, ℓ_1, ℓ_2) when $(\tilde{\mathcal{L}}\tilde{\xi})$ changes.

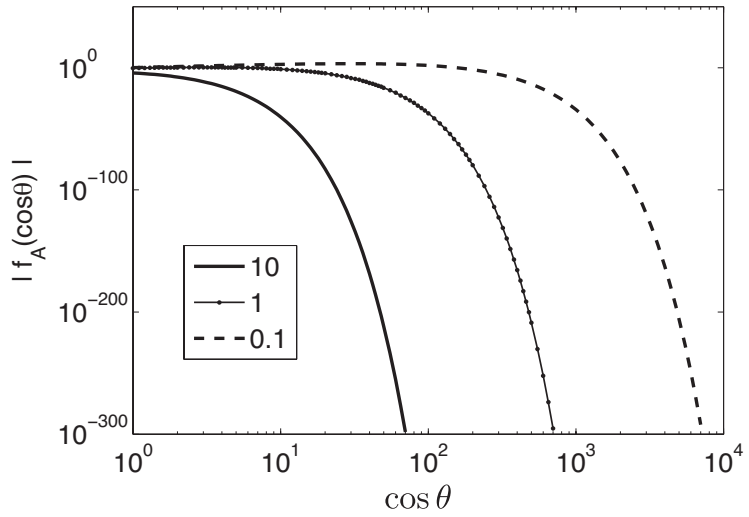

Figure 32: Absolute value of $f_A(\cos\theta)$ in logarithmic scale, for fixed $(m = 1, \ell_1 = 2, \ell_2 = 3)$ and various values of $(\tilde{\mathcal{L}}\tilde{\xi}) = 10, 1, 0.1$. The Fresnel coefficients are taken as unity $r_p = 1$.

As expected, the curves have noticeable values for small $\cos\theta$, then decrease strongly exponentially for large values of $\cos\theta$, especially when $(\tilde{\mathcal{L}}\tilde{\xi})$ increases. Evaluating the integrand f_A for too-high values could then cause numerical instability, as $f_A(\cos\theta)$ can quickly reach numbers lower than the smallest numerically representable number (typically 10^{-300} for a 64-bit double precision float number). A cut-off $c_{\max}$ for the integration domain of $\cos\theta$ must then be carefully chosen, and should be inversely proportional to $(\tilde{\mathcal{L}}\tilde{\xi})$.

The other functions of $\cos\theta$ in f_A are polynomials in $\cos\theta$ for the finite rotations and spherical harmonics, and bounded to $[-1, 1]$ for the Fresnel coefficients. The order of the polynomials will depend on the matrix's indices (ℓ_1, ℓ_2) and the block index m. In **Fig. 33** we study the dependance on the three numbers (ℓ_1, ℓ_2 and m) by showing the absolute value of the integrand function $|f_A(\cos\theta)|$ for a fixed $(\tilde{\mathcal{L}}\tilde{\xi}) = 0.1$ and various set of indices (m, ℓ_1, ℓ_2).

The first observation from **Fig. 33** is a relatively weak dependency on m for the shape of the integrand when the indices of the matrix are fixed: the three upper curves, solid red, red circles and solid purple, are evaluated with $\ell_1 = \ell_2 = 20$. Although they correspond to different values of $m \in \{1, 10, 20\}$, they have almost the same shape. Accordingly, we will not consider the variations of m in the integration method and keep the example of $m = 0$ or 1.

Second, for a fixed $m = 1$, we observe that the shape of the curve depends on the sum $(\ell_1 + \ell_2)$: the black dashed curve, for which $\ell_1 + \ell_2 = 2$ is much lower than the two blue curves, for which $\ell_1 + \ell_2 = 21$, which lie again lower than the three red curves, for which $\ell_1 + \ell_2 = 40$. The greater the sum of the matrix indices, the greater the maximum value of the integrand. However, the exponential decrease is not affected by the changes in ℓ_1 and ℓ_2, as the integrand reaches for large values of $\cos\theta$ similarly negligible values with respect to its maximum. It will be an important feature when looking for a possible cut-off for large values of $\cos\theta$, as the parameter $(\ell_1 + \ell_2)$ will be replaced by $2\ell_{\max}$.

The red and blue curves exhibit a power law in $\cos\theta$ before the maximum of f_A is reached, as the curves are straight lines in the logarithmic plot. This can be explained by the fact that the

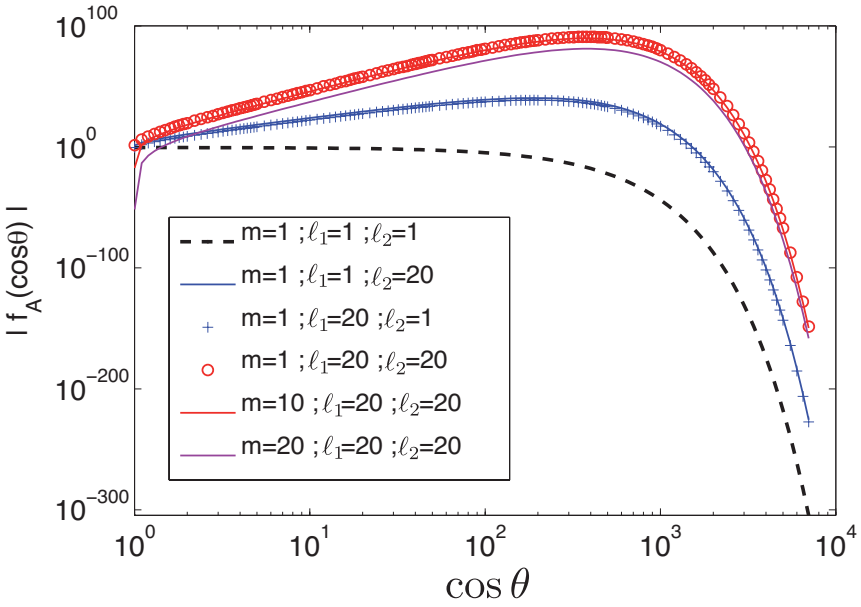

Figure 33: Absolute value of $f_A(\cos\theta)$ in logarithmic scale, for fixed $(\tilde{\mathcal{L}}\tilde{\xi}) = 0.1$ and various values of $(m = 1, \ell_1 = 2, \ell_2 = 3)$. The two red and the purple curves on the top are for $\ell_1 = \ell_2 = 20$ and m varies. The blue curves on the middle show what happens when the values of ℓ_1 and ℓ_2 are switched. The black dashed curve on bottom, together with the two former sets, show the $(\ell_1 + \ell_2)$-dependency at fixed m. The Fresnel coefficients are taken as unity $r_p = 1$.

dominant term in the finite rotations $d^{\ell,s}_m$ and in the spherical harmonics $Y^s_{\ell,m}$ is proportional to $(\cos\theta)^\ell$ when $\cos\theta$ becomes large, as will be derived in **Section 7.3** (p.113).

From all previous remarks, we deduce a simple model for the integrand function that reproduces its shape for any set of parameters:

$$f_0(\cos\theta) = (\cos\theta)^{\ell_1+\ell_2}\, e^{-2\tilde{\mathcal{L}}\tilde{\xi}\cos\theta} \tag{6.14}$$

This 'chameleon' function f_0 is first growing like $(\cos\theta)^{\ell_1+\ell_2}$ for small values of $\cos\theta$, then reaches a maximum value of $\|f_0\|_\infty = \left(\frac{\ell_1+\ell_2}{2\tilde{\xi}\tilde{\mathcal{L}}}\right)^{\ell_1+\ell_2} e^{-(\ell_1+\ell_2)}$ at $c_0 = \frac{\ell_1+\ell_2}{2\tilde{\xi}\tilde{\mathcal{L}}}$, and finally decreases exponentially. In **Fig. 34** we test the model f_0 by comparing it with actual integrand functions f_A for different values of ℓ_1 and ℓ_2. The first top graph is for $\tilde{\xi} = 1$, the two lower graphs are for $\tilde{\xi} = 0.1$ (left) and $\tilde{\xi} = 10$ (right).

On the upper graph of **Fig. 34**, we observe that f_0 seems to reproduce quite well the shape of the integrand f_A. It works even better for smaller values of $\tilde{\xi}$, as seen in the left-bottom graph. For larger frequencies however, some differences appear, especially for small values of $\cos\theta$. In all cases, the 'chameleon' function f_0 effectively predicts the position of the maximum and the exponential decrease. This is a very important feature because when we will compute the integral of f_A, the most important contribution will come from values of $\cos\theta$ close to c_0. The chameleon function f_0 has thus the utility to give us information on the range of $\cos\theta$ where the function to be integrated take noticeable values. Furthermore, it seems that $c_{\max} = Kc_0$, with $K = 10$ and c_0 computed for $\ell_1 = \ell_2 = \ell_{\max}$ could be a good choice for the upper-limit of the integration. Indeed,

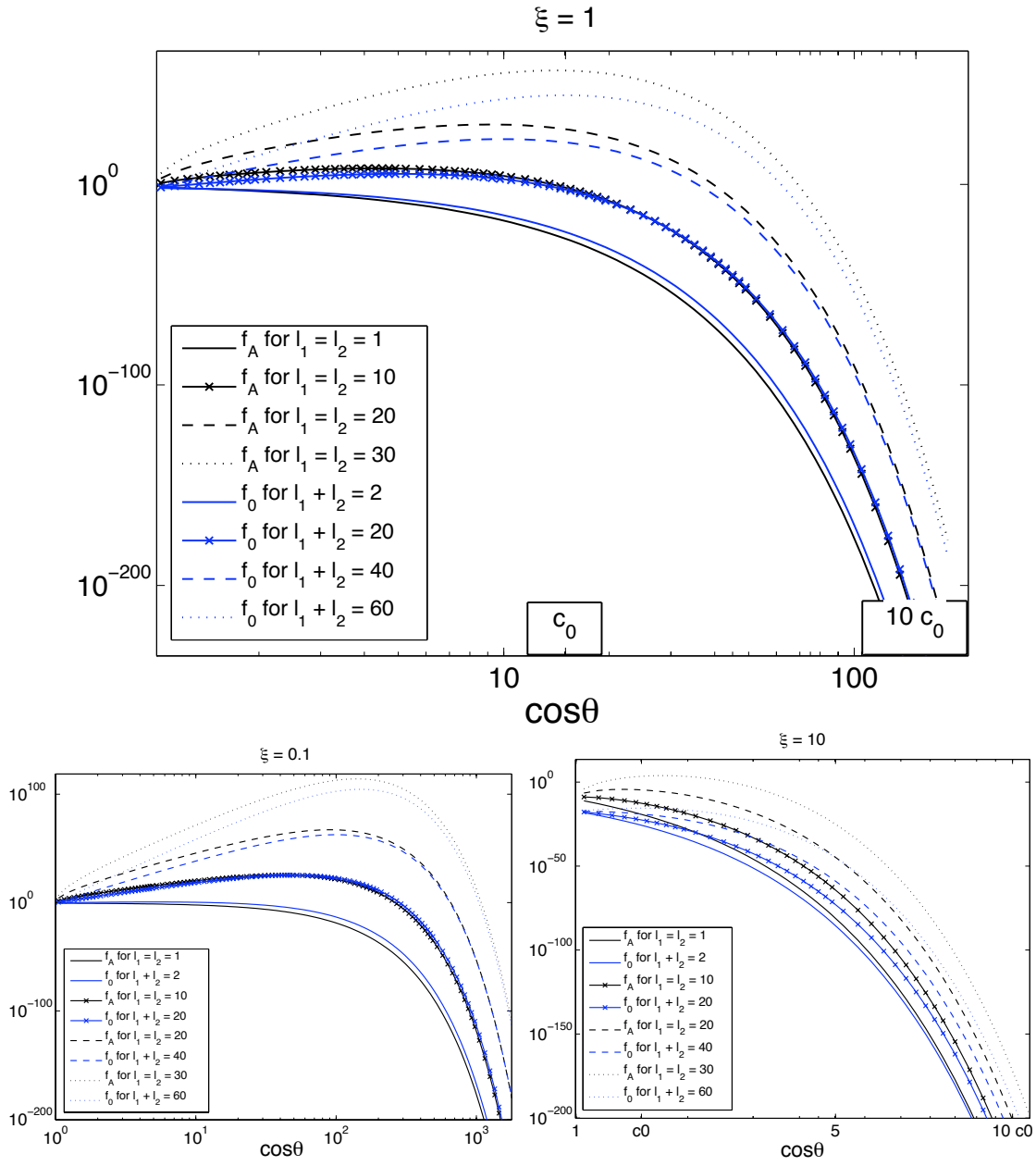

Figure 34: Absolute value of f_A (black) and f_0(blue) in logarithmic scale for $m = 1$ and various values of ℓ_1 and ℓ_2. For the upper graph $\tilde{\xi} = 1$, then for the lower graphs $\tilde{\xi} = 0.1$ and $\tilde{\xi} = 10$, respectively. The position c_0 of the expected maximum for $\ell_1 = \ell_2 = \ell_{\max}$ is indicated in the $\cos\theta$-axis. The model used for the Fresnel coefficients is the plasma model with $L = R = \lambda_P$.

the ratio between the integrand evaluated at (Kc_0) and c_0 is:

$$\frac{f_0(Kc_0)}{f_0(c_0)} = K^{2\ell_{\max}} e^{-2(K-1)\ell_{\max}}$$

which is of the order of 10^{-6} with $K = 10$, in the worst case when $\ell_{\max} = 1$, and becomes already as small as 10^{-12} when $\ell_{\max} = 2$. For large values of the indices, the ratio remains in a numerically representable range, as it is $\sim 10^{-175}$ when $\ell_{\max} = 30$.

Another advantage of f_0 is that it is possible to compute analytically its integral from **Prop. 7**, which gives:

$$\int_1^\infty (\cos\theta)^{\ell_1+\ell_2} e^{-2\tilde{\mathcal{L}}\tilde{\xi}\cos\theta} d\cos\theta = \left(\sum_{i=0}^{\ell_1+\ell_2} \frac{(\ell_1+\ell_2)!}{(\ell_1+\ell_2-i)!} \frac{1}{(2\tilde{\mathcal{L}}\tilde{\xi})^i} \right) \frac{e^{-2\tilde{\mathcal{L}}\tilde{\xi}}}{2\tilde{\mathcal{L}}\tilde{\xi}}$$

This result will be helpful in the test of numerical methods to integrate f_A, as we can firstly test them on f_0 by comparing the numerical result to the exact analytical one.

6.4.3 Method of integration

There exists a great variety of numerical methods for computing the integral of a function, the most efficient ones being usually based on a Gaussian quadrature or adaptations, such as the Gauss-Kronrod algorithm. However, as we have gathered here a lot of information about the functions f_A that we want to integrate over $\cos\theta$, we can choose a less-general method that would be better adapted to our case. Indeed we know that the important contributions to the integral will come from values of $\cos\theta$ around c_0, a strongly varying parameter, that we have learned to predict. The integration will then greatly benefit from any kind of tightening of quadrature points around this value.

We have chosen to use a change of variable such that a constant-step quadrature of $]-1,1[$ for a variable u transforms onto a quadrature of $]1,+\infty[$ for $\cos\theta$, with a tuneable condensation of points around c_0:

$$\cos\theta = 1 + (c_0 - 1)\left(\frac{1+u}{1-u}\right)^\alpha \quad \text{with } u \in]-1,1[\ , \quad \alpha > 0 \tag{6.15}$$

$$u = \frac{\left(\frac{\cos\theta - 1}{c_0 - 1}\right)^{1/\alpha} - 1}{\left(\frac{\cos\theta - 1}{c_0 - 1}\right)^{1/\alpha} + 1} \quad \text{with } \cos\theta \in]1,+\infty[\ , \quad \alpha > 0 \tag{6.16}$$

$$\text{with the Jacobian:} \quad \mathrm{d}\cos\theta = 2\alpha(c_0 - 1)\frac{(1+u)^{\alpha-1}}{(1-u)^{\alpha+1}}\mathrm{d}u$$

With this change of variable, $(u \to -1^+)$ corresponds to the $(\cos\theta \to 1^+)$-limit, while $(u \to +1^-)$ corresponds to the $(\cos\theta \to +\infty)$-limit. The cut-off $u_{\max}$ for the variable u will be computed from the cut-off $c_{\max}$ for the variable $\cos\theta$, using Eq.(6.16). The middle point $(u = 0)$ coincides with $\cos\theta = c_0$. The real quantity α is a tuneable parameter for the change of variable. To better understand its role, let us consider a regular quadrature with a fixed step h of the domain for u, so that the smallest (resp. largest) value of u is $-1 + \frac{h}{2}$ (resp. $1 - \frac{h}{2}$). With $h \ll 1$, the smallest and largest elements for $\cos\theta$ will be, using (6.15):

$$c_{\min} = 1 + (c_0 - 1)\left(\frac{h/2}{2 - h/2}\right)^\alpha \simeq 1 + (c_0 - 1)\left(\frac{h}{4}\right)^\alpha$$

$$c_{\max} = 1 + (c_0 - 1)\left(\frac{2 - h/2}{h/2}\right)^\alpha \simeq 1 + (c_0 - 1)\left(\frac{4}{h}\right)^\alpha$$

As $\frac{h}{4} \ll 1$, a large value of α will spread values of $\cos\theta$ between a $c_{\min}$ very close to 1 and a very large $c_{\max}$, while a small value of α will gather the points and make the quadrature in $\cos\theta$ denser around c_0. The limiting case of $\alpha = 0$ brings all quadrature points together on c_0.

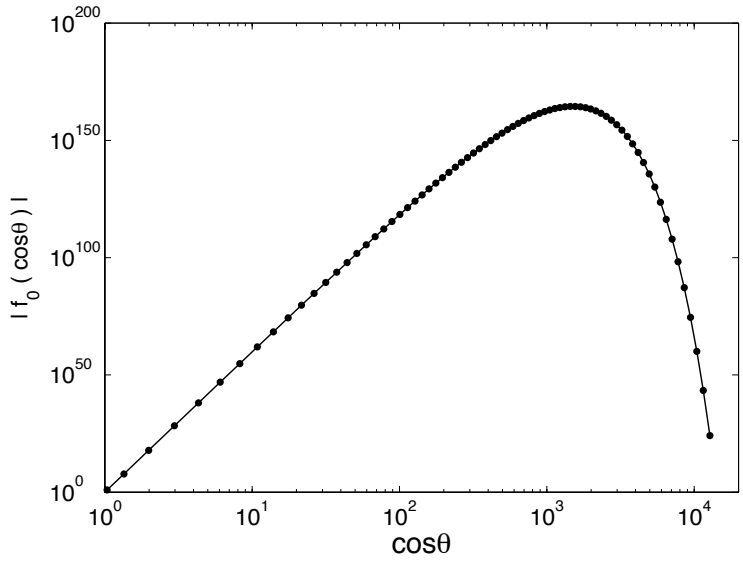

Figure 35: Quadrature points for $\cos\theta$ with the presented tuneable method. The line is the 'chameleon function' f_0, the dots are the points where the evaluation occurs for computing the integral. For illustrative purpose, we have set $h = 0.02$ and $\alpha = 2$. The other parameters are $\tilde{\xi} = 0.01, \ell_1 = \ell_2 = 30, \tilde{\mathcal{L}} = 2$.

This special treatment of values close to c_0 from this method is illustrated in **Fig. 35** where the quadrature points for $\cos\theta$ are presented with dots. The parameter α, and the step h of quadrature for the variable u, remain to be adequately chosen by numerical tests. We will also check that our prescribed factor $K = 10$ is a good choice for the cut-off $c_{\max}$.

6.4.4 Numerical tests

For the 'chameleon function', it is easy to test an integration method since we have an analytical expression for the exact result. After some preliminary trials, we came to the conclusion that $\left[h = 0.01, \alpha = 4, K = 10, c_0 = \ell_{\max}/(\tilde{\xi}\tilde{\mathcal{L}})\right]$ would make a good candidate if one aims at a numerical accuracy of 10^{-6}. To make sure that this is still a good choice for the actual functions to integrate, such as f_A, we test it by comparing the result with a five times smaller step $h' = 0.002$. With this refinement, the quadrature in $\cos\theta$ is denser and wider and the result of the numerical integration is more accurate. If there is only a negligible change our method will be numerically stable. We measure the relative difference between the integrals resulting from the candidate quadrature and the refined one for different values of the matrix indices ℓ_1 and ℓ_2, and for low, medium and high frequencies $\tilde{\xi}$. The results of the numerical tests are presented in **Table 7**.

The obtained relative changes are always below 10^{-8}, which confirms that the candidate for the set of parameters works well with the realistic functions we want to integrate in our computations. It is also a confirmation that we are allowed to take a (ℓ_1, ℓ_2)-independent c_0, which will speed up the numerics, as a simple quadrature will be used to compute all the matrix elements[9].

We also studied the influence of the factor K for the cut-off, by changing it to $K' = 5$ and

[9] It will even allow to directly integrate the matrix itself, seen as a function of $\cos\theta$.

various $(\tilde{\xi}, \ell_1, \ell_2)$	$\tilde{\xi} = 0.01$	$\tilde{\xi} = 1$	$\tilde{\xi} = 100$
$\ell_1 = 1, \ell_2 = 1$	1e-9	1 e-9	7 e-9
$\ell_1 = 10, \ell_2 = 20$	2e-13	6e-15	5e-9
$\ell_1 = 30, \ell_2 = 30$	1e-9	1 e-9	7 e-9

Table 7: Accuracy of the numerical integration of f_A over $\cos\theta$, as the relative difference between the result computed with $\left[h = 0.01, \alpha = 4, K = 10, c_0 = \ell_{\max}/(\tilde{\xi}\tilde{\mathcal{L}})\right]$, and a refined quadrature. The columns represent the tests for different values of the frequency $\tilde{\xi}$. The lines represent the tests for different values of the matrix indices ℓ_1 and ℓ_2. The integrand has been evaluated for $\frac{L}{R} = 1, \ell_{\max} = 30, m = 1$ and the Fresnel coefficients are unity.

$K' = 20$. The relative difference is always of the order of 10^{-12} or smaller, meaning that we can switch to $K = 5$ for the cut-off if needed, as it will be more stable for high values of $\ell_{\max}$. Finally, we make a last restriction ($c_0 \geq 2$) to avoid too small values at large $(\tilde{\mathcal{L}}\tilde{\xi})$.

6.5 Modified Bessel functions

The modified Bessel functions of the first and second kind I and K can be defined by recurrence for half-integer indices:

$$I_{1/2}(x) = \sqrt{\frac{2}{\pi x}}\sinh x \qquad ; \qquad I_{3/2}(x) = \sqrt{\frac{2}{\pi x}}\left(\cosh x - \frac{\sinh x}{x}\right)$$
$$I_{\ell+1/2}(x) = -\frac{2\ell-1}{x} I_{\ell-1/2}(x) + I_{\ell-3/2} \qquad (\forall \ell \geq 2) \tag{6.17}$$

$$K_{1/2}(x) = \sqrt{\frac{\pi}{2x}}\, e^{-x} \qquad ; \qquad K_{3/2}(x) = \sqrt{\frac{\pi}{2x}}\left(1 + \frac{1}{x}\right)\, e^{-x}$$
$$K_{\ell+1/2}(x) = \frac{2\ell-1}{x} K_{\ell-1/2}(x) + K_{\ell-3/2} \qquad (\forall \ell \geq 2) \tag{6.18}$$

Numerically, the construction by recurrence behaves well for the K's, but is highly unstable for the I's. This is due to the fact that the recurrence relation (6.17) contains a difference between very close numbers, then some numerical error propagate and invalidate the result, sometimes in less than 10 steps. An alternative iterative process of construction well-suited for numerics is described in [225]. It results on computing for a given $x > 0$ at step ℓ the number $K_{\ell+3/2}(x)$ from (6.18), and then use it together with $\left(I_{\ell-1/2}(x), K_{\ell+1/2}(x)\right)$ obtained at the previous step, to construct $I_{\ell+1/2}(x)$. For that final computation we will use a property of the Wronskian:

$$\begin{aligned} W &= I_\nu(x)K'_\nu(x) - K_\nu(x)I'_\nu(x) \\ &= -\left(I_\nu(x)K_{\nu+1}(x) + K_\nu(x)I_{\nu+1}(x)\right) \\ &= -\frac{1}{x} \end{aligned}$$

It enables to express $I_\nu(x)$ by a downward recurrence, by writing $I_\nu(x) = \left[x\left(K_{\nu+1}(x) + f_\nu(x)K_\nu(x)\right)\right]^{-1}$ with $f_\nu(x) = \frac{I_{\nu+1}(x)}{I_\nu(x)}$, this ratio remaining to be computed. It can be shown [226] that it is success-

fully expressed as the following continued fraction:

$$f_\nu(x) = \frac{I_{\nu+1}(x)}{I_\nu(x)} = \cfrac{1}{\frac{2(\nu+1)}{x} + \cfrac{1}{\frac{2(\nu+2)}{x} + \cdots}} \,. \tag{6.19}$$

By using the standard notation for a finite part of a continued fractions (here truncated at $N = 4$):

$$[a_1, a_2, , a_3, a_4] = a_1 + \cfrac{1}{a_2 + \cfrac{1}{a_3 + \frac{1}{a_4}}} \,,$$

we express the continued fraction (6.19) as a limit of its increasing finite parts: $f_\nu(x) = \lim_{N\to\infty} f_\nu^N(x)$, where $\left(f_\nu^N(x)\right)^{-1} = [a_1, \ldots, a_N]$, with $a_n = \frac{2(\nu+n)}{x}$. In the numerical computation, N will be increased until some given accuracy is obtained in the convergence.

If one chooses to compute directly (6.19), each increment for $f_\nu^N(x)$ would require a computation from the starting point of the finite continued fraction. We here present a better adapted formulation, derived in [227].

Prop. 12

$$[a_1, \ldots, a_N] = \frac{[a_1] \times [a_2, a_1] \times \cdots \times [a_N, \ldots, a_2, a_1]}{[a_2] \times [a_3, a_2] \times \cdots \times [a_N, \ldots, a_3, a_2]}$$

(For proof, see **Appendix A.6** p.216)

With this useful property, $f_\nu^N(x)$ is updated at each step by the simple operation:

$$\left(f_\nu^N(x)\right)^{-1} = \frac{p_1(N)}{p_2(N)} \left(f_\nu^{N-1}(x)\right)^{-1}$$

$$p_1(N) = [a_N, \ldots, a_1] = a_N + \frac{1}{p_1(N-1)}$$

$$p_2(N) = [a_N, \ldots, a_2] = a_N + \frac{1}{p_2(N-1)}$$

until sufficient convergence is reached.

6.6 Numerical stability

A critical issue in the numerical evaluation of the Casimir effect with the formerly presented method is the numerical stability. Indeed the translation operators and the Mie coefficients, when evaluated at imaginary frequencies, yield very large and very small quantities depending on the indices ℓ_1, ℓ_2. It results in a scattering operator $\mathcal{N}^{(m)}$ whose elements can differ by many orders of magnitude. Such a dispersal in the elements magnitudes will result in a badly-conditionned matrix, responsible for numerical instabilities, but also in the risk of obtaining non-computable numbers. Indeed numerical codes work with a finite range of representable numbers, whose width depends on the allocated memory for each number ("precision").

In **Fig. 36** we illustrate this statement with a practical case, with $\frac{L}{R} = 1$ and $m = 1$. The magnitude of the matrix elements are encoded with colours, on a logarithmic scale. A quantity r in the color bars corresponds to an element with an absolute value of 10^r. The four graphs are obtained with different values of the reduced frequency $\tilde{\xi}$ and cut-off $\ell_{\max}$, to observe the dependence of the magnitudes in the matrix with respect to these two parameters.

The decomposition of the matrices $\mathcal{N}^{(m)}$ in four blocks corresponding to the polarizations $P = E, M$ is visible in **Fig. 36**. For each block, while the elements around the diagonal are stable, the off-diagonal elements have very different magnitudes: when the line index ℓ_1 is large and

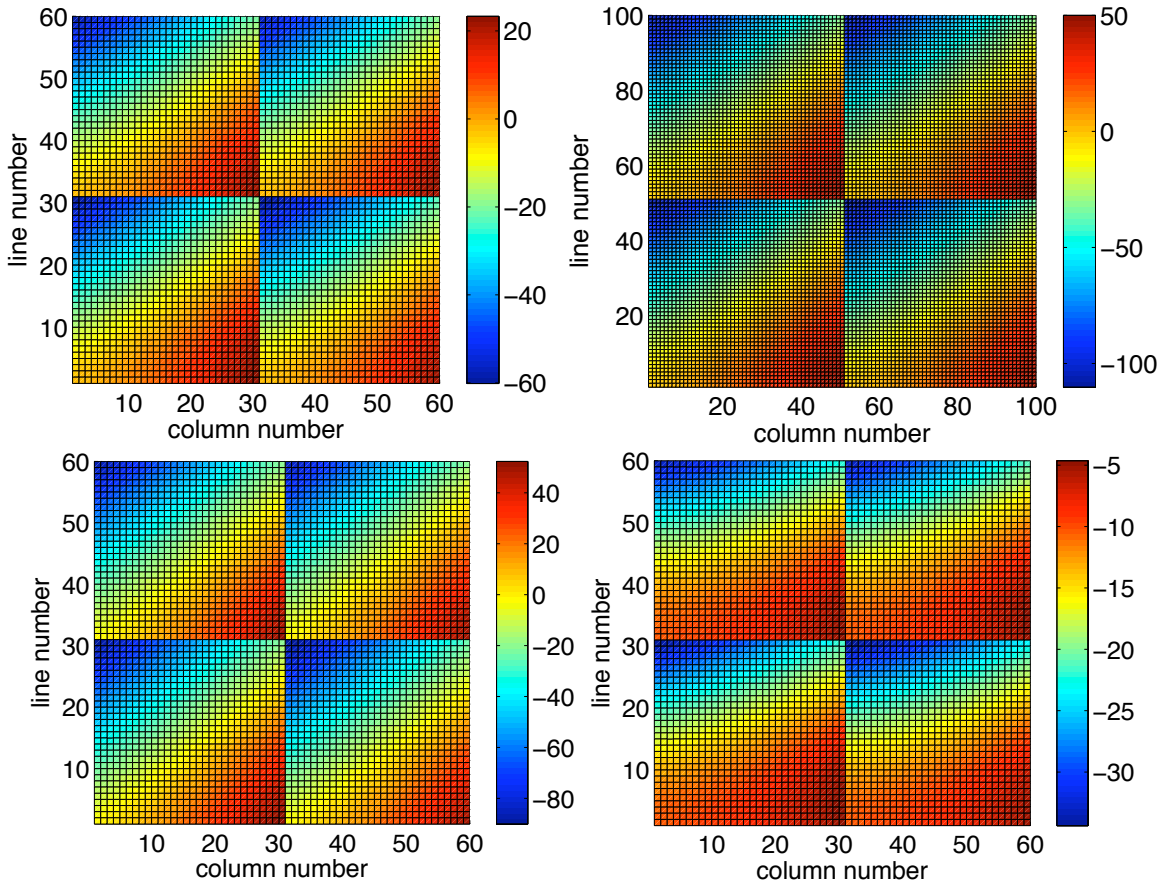

Figure 36: Magnitude of the elements of $\mathcal{N}^{(1)}$, for different cases. The upper graphs are for $\tilde{\xi} = 1$, with $\ell_{\max} = 30$ (left) and 50 (right). The lower graphs are for $\ell_{\max} = 30$, with $\tilde{\xi} = 0.1$ (left) and 10 (right). The colours are given in logarithmic scale, with the numbers r in the colour bars representing an element of magnitude 10^r. The aspect ratio is $\frac{L}{R} = 1$.

the column index ℓ_2 is small the magnitude of the matrix element can become very small, and oppositely when ℓ_2 is large and ℓ_1 small the magnitude can become very large.

The comparison of the two upper graphs in **Fig. 36** show that the dispersal of the elements magnitudes is more pronounced for larger values of ℓ, when the cut-off $\ell_{\max}$ is increased. This shows that the the stability of the numbers involved in the numerical evaluation will become an issue when smaller aspect ratio $\frac{L}{R}$, and thus larger values of $\ell_{\max}$, will be sought.

The comparison of the two lower graphs in **Fig. 36** show that a small reduced frequency makes the dispersal worse, while large values of $\tilde{\xi}$ tend to stabilise the elements. This entails that a great care must be taken in the integration process over the frequencies, in order to avoid evaluations of the matrix $\mathcal{N}$ at too-small values of $\tilde{\xi}$.

Before computing the determinant of such a badly-conditionned matrix, a simple extern regularization can be applied to each polarization block in order to reduce the dispersal of the elements magnitude. It consists of multiplying the columns and dividing the lines by the same quantity, a process which let the determinant of the matrix unchanged. We take for example a bock-matrix of size n, which corner elements are called A, B, C, D, with A and D the corners along the diagonal, and B and C the off-diagonal corners, B being an elements with a large magnitude and C with a small magnitude. Defining the small positive quantity K:

$$\begin{bmatrix} A & \cdots & B \\ \vdots & \ddots & \vdots \\ C & \cdots & D \end{bmatrix} \quad \longrightarrow \quad K = \left|\frac{A}{B}\right|^{\frac{1}{n-1}} ,$$

we multiply the column of index j by K^{j-1} and the line of index i by K^{1-i}. The resulting block matrix will have the same determinant, the same elements A and D, and its off-diagonal corner elements will verify $|B'| = |A|$ and $|C'| = \left|\frac{BC}{A}\right|$, which will be much more regular than C. In practice this process is very efficient, as can be understood from the observation in **Fig. 36** that the magnitudes are regularly spread through the block-matrices.

For the numerical evaluation of the matrix determinant at small values of the reduced frequency $\tilde{\xi}$, apart from the first Matsubara term, an intern regularization can be done with the help of the low-frequency expansions that will be analytically derived in **Section 7.6**. This process consists of guessing what the magnitude of the element will be, in terms of the reduced frequency $\tilde{\xi}$ and the indices ℓ_1, ℓ_2, and normalize the computed elements by its approximated value. In Eq.(7.30) (p.117), we see that the dominant cause for the dispersal of the elements magnitude in the low-frequency limit is the term:

$$K(\ell_1, \ell_2, \tilde{\xi}) = \frac{(2\ell_2+1)!!}{(2\ell_1+1)!!}\tilde{\xi}^{\ell_1-\ell_2}$$

which is antisymmetric in (ℓ_1, ℓ_2) for the product. The intern regularization process will then consists of computing each element of the matrix normalized by $K(\ell_1, \ell_2, \tilde{\xi})$. Once the matrix $\mathcal{N}$ is produced, an extern regularization can also be applied.

In order to reach high cut-offs $\ell_{\max}$, an alternative solution to delay the stability issue is to use a number representation which allows for wider values. For example the range of computable numbers with double precision floating-point format (64 bits) is $[2.2 \times 10^{-308}, 1.8 \times 10^{308}]$, while for quadruple precision floating-point format (128 bits) it stretches to $[3.4 \times 10^{-4932}, 1.2 \times 10^{4932}]$, which makes room for large and small values, and delays the appearance of stability issues. This improvement in the stability however have drawbacks in term of computation time and access to standard functions and methods.

In the numerical evaluations presented in this manuscript, we have used quadruple precision number, together with the two mentioned regularization processes, allowing for stable results up

to $\ell_{\max} = 520$ in the general case. The instabilities are unavoidably caused by the Wick rotation to imaginary frequencies, but the situation remains easier to handle than with real frequencies, for which the integration of an oscillating function of $\tilde{\xi}$ is numerically very challenging.

6.7 Computation of the zero-frequency term

The zero-frequency term of the integrand $\Phi(\tilde{\xi}) = \ln\det\mathcal{D}\left(\tilde{\xi}\right)$, which will be derived analytically in **Section 7.6** (p.117), is for example for the Drude model:

$$\det\left(I-\mathcal{M}^{(m)}\right) \simeq \det\left(I-\sqrt{\frac{\pi(2\ell_1+1)}{\ell_2(\ell_2+1)}}a_{\ell_1}B^{(m)}_{\ell_1,\ell_2,\mathrm{TM}}\right)$$
$$= \det\left(\delta_{\ell_1,\ell_2}-\frac{1}{\left(2\tilde{\mathcal{L}}\right)^{\ell_1+\ell_2+1}}\frac{(\ell_1+\ell_2)!}{\sqrt{(\ell_1-m)!}\sqrt{(\ell_1+m)!}\sqrt{(\ell_2-m)!}\sqrt{(\ell_2+m)!}}\right).$$

Its numerical evaluation can be problematic, as it contains factorial terms like $(\ell_1+\ell_2)!$ that can become very large, all the more that this simpler zero-frequency form for the matrix allows to employ a larger cut-off $\ell_{\max}$. As an example, 171! cannot be computed with usual double precision floating-point format (64 bits) and 1800! is also too big a number for quadruple precision floating-point format (128 bits).

To avoid the occurrence of such non-computable numbers, each side of the fraction has to be balanced out with the other side. A possibility is to compute the matrix elements line by line (from top to bottom), and then for each line (from the left to the right), each element being updated with eq. (6.20) from its left-neighbour, except the first element of the row, which is updated from the upper line with eq. (6.21).

$$\mathcal{M}^{(m)}_{\ell_1,\ell_2} = \mathcal{M}^{(m)}_{\ell_1,\ell_2-1}\times\frac{\ell_1+\ell_2}{2\tilde{\mathcal{L}}\sqrt{\ell_2^2-m^2}} \tag{6.20}$$

$$\mathcal{M}^{(m)}_{\ell_1,\ell_2} = \mathcal{M}^{(m)}_{\ell_1-1,\ell_2}\times\frac{\ell_1+\ell_2}{2\tilde{\mathcal{L}}\sqrt{\ell_1^2-m^2}} \tag{6.21}$$

For the other block matrix appearing in the case of perfect mirrors, the situation is similar, except that the update (6.21) contains an additional multiplicative term $\frac{\ell_1^2}{\ell_1^2-1}$. For the case of dielectrics, it is also quite similar.

With this balanced construction of the matrices $\mathcal{M}^{(m)}$, we observe from our numerical tests that numerical stability does not seem to be an issue anymore, and the numerical evaluation of the first Matsubara term can be performed with high values for the cut-off $\ell_{\max}$. In **Fig. 37** we present a numerical test on the convergence of the Casimir free-energy in the high-temperature limit with respect to $\ell_{\max}$. This convergence is exponentially decreasing with $\ell_{\max}$, and thus never saturates. Numerical evaluations up to $\ell_{\max} = 5000$ have been performed for the study of the high-temperature regime, but higher values are manageable, in exchange for longer computation time.

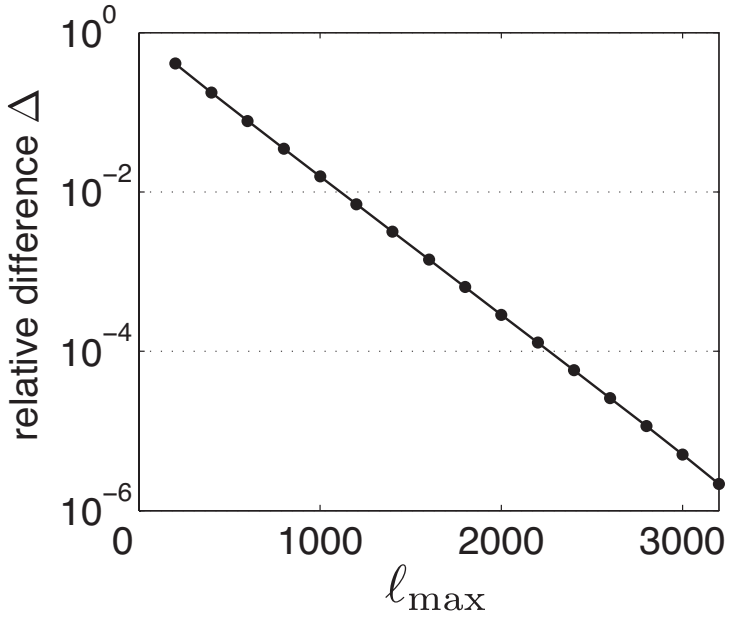

Figure 37: Convergence of the Casimir free-energy $\mathcal{F}^{\mathrm{HT}}$ in the high-temperature limit, with respect to $\ell_{\max}$. The aspect ratio is $\frac{L}{R} = 0.002$. We plot, as a function of $\ell_{\max}$, the relative difference Δ between the $\ell_{\max}$-truncated quantities and a much more accurate reference value (computed with $\ell_{\max}^{\mathrm{ref}} = 3800$).

Part III.
Analytical limits

Table of Contents

Before starting any numerical evaluation of the Casimir effect in the sphere-plane geometry, we present in this part some analytic derivations that can be done from the scattering formula presented in **Section 5.4** (p.78) for some limiting regimes. The motivation for this study is first to extract from the complex scattering expression as much physical information as possible, in particular in the qualitative comparison between the results obtained from plasma, Drude, dielectric and perfect mirrors models. The possession of such explicit analytic expansions can also be used to test the numerical evaluations.

In **Section 7** we investigate the low-frequency expansion of the scattering operator $\mathcal{D}$. In this regime we obtain very simple forms for its determinant, which will be useful to compute the first Matsubara term in the non-zero temperature evaluations of the Casimir effect. This expansion will also give an insight on the high-temperature regime for the Casimir effect, which turns out to be very dependent on the description of the materials optical properties.

The long-distance regime, where the distance L becomes much larger than the sphere radius R, is investigated in **Section 8**. The analytical expansions obtained in this regime will be particularly useful to study the temperature dependance of the Casimir effect in the sphere-plane geometry: if the curvature has a non-trivial interplay with thermal effects, those correlations should be enhanced in this regime.

This part only contains analytical expansions and their derivation. Their physical interpretation and their comparison to numerical evaluations will be discussed in **Parts IV** and **V**.

7 Low-frequency limit

In this section, we study the ($\tilde{\xi} \to 0$)-limit of the integrand function $\Phi^{(m)}(\tilde{\xi}) = \ln\det \mathcal{D}^{(m)}(\tilde{\xi})$ appearing in the scattering formula (5.58) (p.79) in the sphere-plane configuration. The expressions that we will derive in this limit will be useful first of all for the numerics, because this low-frequency limit is numerically unstable, as explained in **Section 6.6** (p.101). Moreover, having an analytical expression for the integrand at the first Matsubara frequency $\Phi(0)$ is also interesting to have information on the Casimir interaction in the limit of high-temperature ($\mathcal{L} \gg \frac{\lambda_T}{2\pi}$), as the Matsubara sum then reduces to its first term in Eq.(3.6) (p.49).

In this regime we know from the shape of the functions of $\cos\theta$ studied in **Section 6.4.2** (p.94) that main contributions to the integral over $\cos\theta$ will come from large values of $\cos\theta$, proportionally to $\tilde{\xi}^{-1}$, because of the translation $e^{-2\tilde{\xi}\tilde{\mathcal{L}}\cos\theta}$ term.

We will here begin by deriving the low-frequency limit (or large $\cos\theta$ limit) for various quantities involved in the scattering operator $\mathcal{D}^{(m)}$, then do the integration over $\cos\theta$ for each term of this operator, and finally simplify the expression of its determinant.

7.1 Mie coefficients

Let us first recall that for a non-magnetic sphere of radius R and relative permittivity $\varepsilon = n^2$, the Mie coefficients of order ℓ and parameter $\tilde{\xi} = \frac{R\xi}{c}$, introduced in **Section 5.2.2** (p.70), write:

$$a_\ell(\tilde{\xi}) = (-1)^{\ell+1}\frac{\pi}{2}\frac{n^2 s_\ell^{(a)}(\tilde{\xi}) - s_\ell^{(b)}(\tilde{\xi})}{n^2 s_\ell^{(c)}(\tilde{\xi}) - s_\ell^{(d)}(\tilde{\xi})} \qquad b_\ell(\tilde{\xi}) = (-1)^{\ell+1}\frac{\pi}{2}\frac{s_\ell^{(a)}(\tilde{\xi}) - s_\ell^{(b)}(\tilde{\xi})}{s_\ell^{(c)}(\tilde{\xi}) - s_\ell^{(d)}(\tilde{\xi})} \tag{7.1}$$

with

$$\begin{aligned}
s_\ell^{(a)}(\tilde{\xi}) &= I_{\ell+1/2}(n\tilde{\xi})\left[\ell I_{\ell+1/2}(\tilde{\xi}) - \tilde{\xi} I_{\ell-1/2}(\tilde{\xi})\right] \\
s_\ell^{(b)}(\tilde{\xi}) &= I_{\ell+1/2}(\tilde{\xi})\left[\ell I_{\ell+1/2}(n\tilde{\xi}) - n\tilde{\xi} I_{\ell-1/2}(n\tilde{\xi})\right] \\
s_\ell^{(c)}(\tilde{\xi}) &= I_{\ell+1/2}(n\tilde{\xi})\left[\ell K_{\ell+1/2}(\tilde{\xi}) + \tilde{\xi} K_{\ell-1/2}(\tilde{\xi})\right] \\
s_\ell^{(d)}(\tilde{\xi}) &= K_{\ell+1/2}(\tilde{\xi})\left[\ell I_{\ell+1/2}(n\tilde{\xi}) - n\tilde{\xi} I_{\ell-1/2}(n\tilde{\xi})\right] \ .
\end{aligned} \tag{7.2}$$

In the case of perfect mirrors, they simplify to:

$$a_\ell(\tilde{\xi}) = (-1)^{\ell+1}\frac{\pi}{2}\frac{\ell I_{\ell+1/2}(\tilde{\xi}) - \tilde{\xi} I_{\ell-1/2}(\tilde{\xi})}{\ell K_{\ell+1/2}(\tilde{\xi}) + \tilde{\xi} K_{\ell-1/2}(\tilde{\xi})} \qquad b_\ell(\tilde{\xi}) = (-1)^{\ell+1}\frac{\pi}{2}\frac{I_{\ell+1/2}(\tilde{\xi})}{K_{\ell+1/2}(\tilde{\xi})} \ . \tag{7.3}$$

We are interested in the low-frequency limit, thus we will use the following expansion of the modified Bessel functions for small values of the parameter ($x \ll 1$):

$$I_{\ell+1/2}(x) \simeq \sqrt{\frac{2}{\pi}}\frac{x^{\ell+1/2}}{(2\ell+1)!!} + \sqrt{\frac{1}{2\pi}}\frac{x^{\ell+5/2}}{(2\ell+3)!!} + \cdots \tag{7.4}$$

$$K_{\ell+1/2}(x) \simeq \sqrt{\frac{\pi}{2}}\frac{(2\ell-1)!!}{x^{\ell+1/2}} + \cdots \tag{7.5}$$

We consider various materials for the sphere, as their dielectric functions $\varepsilon(\tilde{\xi})$ will lead to different low-frequency behaviour of the Mie coefficients.

7.1.1 Perfect mirrors

Inserting the first order expansions (7.4-7.5) in (7.3), we get the following low-frequency asymptotic expressions for the Mie coefficients:

$$a_\ell \simeq \frac{\ell+1}{\ell}\frac{(-1)^\ell \tilde{\xi}^{(2\ell+1)}}{(2\ell+1)!!(2\ell-1)!!} \qquad b_\ell \simeq \frac{(-1)^{(\ell+1)} \tilde{\xi}^{(2\ell+1)}}{(2\ell+1)!!(2\ell-1)!!}\ . \tag{7.6}$$

The Mie coefficients become very small at the limit of low-frequencies, as illustrated by the term $\tilde{\xi}^{(2\ell+1)}$. Physically, this low-frequency extinction of the Mie coefficients can be understood with the impact parameter $b = \frac{R\ell}{\tilde{\xi}}$ introduced in **Section 6.1.1** (p.81): when $\tilde{\xi}$ goes to 0, b becomes much larger than the sphere radius, and correspond to rays that do not hit the sphere.

We observe furthermore that this decrease is even more pronounced when the order ℓ is increased. For perfect mirrors, the two coefficients a_ℓ and b_ℓ have the same power law in $\tilde{\xi}$ in this limit, but not the same coefficient, as $a_\ell \simeq -\frac{\ell+1}{\ell} b_\ell$.

7.1.2 Dielectrics

Dielectrics have a relative permittivity function $\varepsilon(\tilde{\xi})$ with a finite $(\tilde{\xi} \to 0)$-limit $\varepsilon(0)$. In this case, when using the low-parameter asymptotic expressions (7.4-7.5) in (7.2), we obtain:

$$\begin{aligned}
s_\ell^{(a)}(\tilde{\xi}) &\simeq -\frac{2}{\pi}\frac{\ell+1}{(2\ell+1)!!(2\ell+1)!!} n_0^{\ell+1/2} \tilde{\xi}^{2\ell+1} \\
s_\ell^{(b)}(\tilde{\xi}) &\simeq -\frac{2}{\pi}\frac{\ell+1}{(2\ell+1)!!(2\ell+1)!!} n_0^{\ell+1/2} \tilde{\xi}^{2\ell+1} \\
s_\ell^{(c)}(\tilde{\xi}) &\simeq \frac{\ell}{2\ell+1} n_0^{\ell+1/2} \\
s_\ell^{(d)}(\tilde{\xi}) &\simeq -\frac{\ell+1}{2\ell+1} n_0^{\ell+1/2}
\end{aligned} \tag{7.7}$$

with $n_0 = \sqrt{\varepsilon(0)} \in \mathbb{R}$. Those expansions are sufficient to compute $a_\ell(\tilde{\xi})$, but for $b_\ell(\tilde{\xi})$ we need to go one order further and use the second term in (7.4) as $s_\ell^{(a)}(\tilde{\xi})$ and $s_\ell^{(b)}(\tilde{\xi})$ have the same dominant term. Then the difference in the numerator for $b_\ell(\tilde{\xi})$ is:

$$s_\ell^{(a)}(\tilde{\xi}) - s_\ell^{(b)}(\tilde{\xi}) \simeq \frac{2}{\pi}\frac{(n^2-1)n^{\ell+1/2}\tilde{\xi}^{2\ell+3}}{(2\ell+1)!!(2\ell+3)!!}$$

and the low-frequency asymptotic expressions for the Mie coefficients finally read:

$$\begin{aligned}
a_\ell(\tilde{\xi}) &\simeq (-1)^\ell\ \frac{\ell+1}{\ell}\frac{\varepsilon(0)-1}{\varepsilon(0)+\frac{\ell+1}{\ell}}\frac{\tilde{\xi}^{(2\ell+1)}}{(2\ell+1)!!(2\ell-1)!!} \\
b_\ell(\tilde{\xi}) &\simeq (-1)^{(\ell+1)}\ (\varepsilon(0)-1)\frac{\tilde{\xi}^{(2\ell+3)}}{(2\ell+3)!!(2\ell+1)!!}\ .
\end{aligned} \tag{7.8}$$

Unlike perfect mirrors, we observe that for dielectrics the two coefficients a_ℓ and b_ℓ do not have the same power law decrease at low-frequency, yielding $b_\ell = \mathcal{O}\left(\tilde{\xi}^2\right) \times a_\ell$ in this limit for any value of the index ℓ. It follows that we will in this case only consider the first Mie coefficient a_ℓ when taking the low-frequency expansion of the expressions.

7.1.3 Drude model for dissipative metals

Introducing $\alpha = 2\pi\frac{R}{\lambda_P}$ and $\delta = \frac{\lambda_P}{\lambda_\gamma}$, the relative permittivity $\varepsilon(\tilde{\xi})$ for the Drude model can be written as:

$$\varepsilon(\tilde{\xi}) = 1 + \frac{1}{\frac{\tilde{\xi}}{\alpha}\left(\frac{\tilde{\xi}}{\alpha} + \delta\right)} \ . \tag{7.9}$$

When the reduced frequency $\tilde{\xi}$ goes to zero, the dielectric function (7.9) diverges to $+\infty$ like $\frac{\alpha}{\delta\tilde{\xi}}$. This means that the refractive index $n \sim \sqrt{\frac{\alpha}{\delta\tilde{\xi}}}$ goes to $+\infty$ like $\tilde{\xi}^{-1/2}$ and that $n\tilde{\xi} \sim \sqrt{\frac{\alpha\tilde{\xi}}{\delta}}$ goes to 0 like $\tilde{\xi}^{1/2}$. The low-frequency limit in (7.2) then evaluates to:

$$\begin{aligned}
s_\ell^{(a)}(\tilde{\xi}) &\simeq -\frac{2}{\pi}\frac{\ell+1}{(2\ell+1)!!(2\ell+1)!!}\left(\sqrt{\frac{\alpha}{\delta}}\right)^{\ell+1/2}\tilde{\xi}^{3\ell/2+3/4} \\
s_\ell^{(b)}(\tilde{\xi}) &\simeq -\frac{2}{\pi}\frac{\ell+1}{(2\ell+1)!!(2\ell+1)!!}\left(\sqrt{\frac{\alpha}{\delta}}\right)^{\ell+1/2}\tilde{\xi}^{3\ell/2+3/4} \\
s_\ell^{(c)}(\tilde{\xi}) &\simeq \frac{\ell}{2\ell+1}\left(\sqrt{\frac{\alpha}{\delta}}\right)^{\ell+1/2}\tilde{\xi}^{-\ell/2-1/4} \\
s_\ell^{(d)}(\tilde{\xi}) &\simeq -\frac{\ell+1}{2\ell+1}\left(\sqrt{\frac{\alpha}{\delta}}\right)^{\ell+1/2}\tilde{\xi}^{-\ell/2-1/4} \ .
\end{aligned} \tag{7.10}$$

Like in the previous case of dielectrics, those expansions are sufficient to compute $a_\ell(\tilde{\xi})$, but for $b_\ell(\tilde{\xi})$ we need to go one order further and use the second term in (7.4), as $s_\ell^{(a)}(\tilde{\xi})$ and $s_\ell^{(b)}(\tilde{\xi})$ have the same dominant term. Then the difference in the numerator for $b_\ell(\tilde{\xi})$ read:

$$s_\ell^{(a)}(\tilde{\xi}) - s_\ell^{(b)}(\tilde{\xi}) \simeq \frac{2}{\pi}\left(\sqrt{\frac{\alpha}{\delta}}\right)^{\ell+5/2}\frac{\tilde{\xi}^{3\ell/2+7/4}}{(2\ell+1)!!(2\ell+3)!!}$$

and the low-frequency asymptotic expressions for the Mie coefficients finally are:

$$\begin{aligned}
a_\ell &\simeq (-1)^\ell\ \frac{\ell+1}{\ell}\frac{\tilde{\xi}^{(2\ell+1)}}{(2\ell+1)!!(2\ell-1)!!} \\
b_\ell &\simeq (-1)^{(\ell+1)}\ \frac{\alpha}{\delta}\frac{\tilde{\xi}^{(2\ell+2)}}{(2\ell+3)!!(2\ell+1)!!} \ .
\end{aligned} \tag{7.11}$$

Again, the two coefficients do not have the same power law in $\tilde{\xi}$ for their low-frequency decrease, with this time $b_\ell = \mathcal{O}\left(\tilde{\xi}\right) \times a_\ell$. The first coefficient a_ℓ is the same as the one obtained with perfect mirrors. We remark that the analytical limit for the second coefficient b_ℓ contains the term $\frac{\alpha}{\delta} = \frac{2\pi R\lambda_\gamma}{\lambda_P^2}$, but not for the first term a_ℓ. We will discuss more this result in the next paragraph when comparing it to the case of plasma model.

7.1.4 Plasma model for loss-less metals

Introducing $\alpha = 2\pi\frac{R}{\lambda_P}$, the relative permittivity $\varepsilon(\tilde{\xi})$ for the plasma model can be written as:

$$\varepsilon(\tilde{\xi}) = 1 + \frac{\alpha^2}{\tilde{\xi}^2} \ . \tag{7.12}$$

When the reduced frequency $\tilde{\xi}$ goes to zero, the dielectric function (7.12) diverges to $+\infty$ like $\frac{\alpha^2}{\tilde{\xi}^2}$, meaning that $n \sim \frac{\alpha}{\tilde{\xi}}$ goes to $+\infty$ like $\tilde{\xi}^{-1}$, and more importantly, that $n\tilde{\xi} \sim \alpha$ remains finite. Thus the $(\tilde{\xi} \to 0)$-limit in (7.2) is here:

$$\begin{aligned}
s_\ell^{(a)}(\tilde{\xi}) &\simeq -\sqrt{\frac{2}{\pi}}\frac{\left[(\ell+1)I_{\ell+1/2}(\alpha)\right]}{(2\ell+1)!!}\tilde{\xi}^{\ell+1/2} \\
s_\ell^{(b)}(\tilde{\xi}) &\simeq \sqrt{\frac{2}{\pi}}\frac{\left[\ell I_{\ell+1/2}(\alpha) - \alpha I_{\ell-1/2}(\alpha)\right]}{(2\ell+1)!!}\tilde{\xi}^{\ell+1/2} \\
s_\ell^{(c)}(\tilde{\xi}) &\simeq \sqrt{\frac{\pi}{2}}\left[\ell I_{\ell+1/2}(\alpha)\right](2\ell-1)!!\;\tilde{\xi}^{-\ell-1/2} \\
s_\ell^{(d)}(\tilde{\xi}) &\simeq \sqrt{\frac{\pi}{2}}\left[\ell I_{\ell+1/2}(\alpha) - \alpha I_{\ell-1/2}(\alpha)\right](2\ell-1)!!\;\tilde{\xi}^{-\ell-1/2}\,.
\end{aligned} \tag{7.13}$$

Those first-order expansions are sufficient to compute the low-frequency asymptotic expression for the Mie coefficients:

$$\begin{aligned}
a_\ell &\simeq (-1)^\ell\,\frac{\ell+1}{\ell}\frac{\tilde{\xi}^{(2\ell+1)}}{(2\ell+1)!!(2\ell-1)!!} \\
b_\ell &\simeq (-1)^{(\ell+1)}\,\frac{\tilde{\xi}^{(2\ell+1)}}{(2\ell+1)!!(2\ell-1)!!}\left(1 - \frac{2\ell+1}{\alpha}\frac{I_{\ell+1/2}(\alpha)}{I_{\ell-1/2}(\alpha)}\right)\,.
\end{aligned} \tag{7.14}$$

Like in the case of perfect mirrors, the two Mie coefficients a_ℓ and b_ℓ have the same power-law decay $\tilde{\xi}^{(2\ell+1)}$ at low frequencies. The first one is again the same as with perfect mirrors or Drude model, but the second is an intermediate case between the two former situations: when the parameter α is large ($R \gg \lambda_P$), $\left(1 - \frac{2\ell+1}{\alpha}\frac{I_{\ell+1/2}(\alpha)}{I_{\ell-1/2}(\alpha)}\right) \to 1$ and the perfect reflector case is recovered. When α is very small ($R \ll \lambda_P$), $\left(1 - \frac{2\ell+1}{\alpha}\frac{I_{\ell+1/2}(\alpha)}{I_{\ell-1/2}(\alpha)}\right) \to 0$ and $b_\ell = o\left(\tilde{\xi}^{2\ell+1}\right)$, as in the Drude model[10].

The plasma model then leads to a situation where both electric and magnetic multipoles contributions are important, like for a perfectly reflecting sphere. The Drude model leads to a qualitatively different situation at the limit of low-frequencies, as magnetic multipoles contributions are negligible with respect to the electric ones with the same order ℓ.

We remark that taking the limit of vanishing dissipation ($\delta \to 0$) in the expression (7.11) of the b_ℓ coefficients is not appropriate to recover the loss-less plasma case. It follows that the limits $(\delta \to 0)$ and $(\tilde{\xi} \to 0)$ do not commute, and one must be very careful when working with those two limits at the same time.

7.2 Fresnel coefficients

The Fresnel coefficients, described in **Section 5.2.1** (p.70), are functions of $\cos\theta$, and the reduced frequency $\tilde{\xi}$ through the relative permittivity $\varepsilon(\tilde{\xi})$. They can be written at imaginary frequencies as:

$$r_{\mathrm{TE}} = \frac{1 - \sqrt{1 + \frac{(\varepsilon-1)}{\cos^2\theta}}}{1 + \sqrt{1 + \frac{(\varepsilon-1)}{\cos^2\theta}}} \qquad r_{\mathrm{TM}} = \frac{1 + (\varepsilon-1) - \sqrt{1 + \frac{(\varepsilon-1)}{\cos^2\theta}}}{1 + (\varepsilon-1) + \sqrt{1 + \frac{(\varepsilon-1)}{\cos^2\theta}}}\,. \tag{7.15}$$

[10] A low-α expansion of the factor $\left(1 - \frac{2\ell+1}{\alpha}\frac{I_{\ell+1/2}(\alpha)}{I_{\ell-1/2}(\alpha)}\right)$ gives $\frac{\alpha^2}{(2\ell+1)(2\ell+3)} + o\left(\alpha^2\right)$ and leads to the Drude expression for b_ℓ in (7.11) with $\alpha^2\tilde{\xi}^{2\ell+1}$ replacing $\frac{\alpha}{\delta}\tilde{\xi}^{2\ell+2}$. We recall that this case is only mentioned as a remark, as the plasma model does not offer a proper description of spheres with $R \ll \lambda_P$, for which confinement has to be taken into account.

We recall that with this convention of signs, $r_{\mathrm{TE}} \in [-1, 0]$ and $r_{\mathrm{TM}} \in [0, 1]$. When studying the low-frequency expansion of the Fresnel coefficients, we will take into account the fact that $\cos\theta$ becomes very large (like $\tilde{\xi}^{-1}$). For metals, the dielectric function ε also diverges at the low-frequency, and there will be a competition between the two terms.

7.2.1 Perfect mirrors

The relative permittivity for the perfect mirrors model is intrinsically infinite. Then the Fresnel coefficients are in this case obtained as the $(\varepsilon \to +\infty)$-limit of expressions (7.15), and turn out to be frequency-independant:

$$r_{\mathrm{TE}} = -1 \qquad\qquad r_{\mathrm{TM}} = 1 \ . \tag{7.16}$$

In this case, the electric and magnetic polarizations have the same contribution, except for the sign, and the Fresnel coefficients have a non-vanishing limit for low frequencies.

7.2.2 Dielectrics

Dielectrics have a dielectric function $\varepsilon(\tilde{\xi})$ with a finite limit at low frequencies $\varepsilon(0) \geq 1$. It follows that the $\cos\theta$ is the only diverging quantity, and $\frac{\varepsilon-1}{\cos^2\theta} = \mathcal{O}\left(\tilde{\xi}^2\right)$. The low-frequency limit for the Fresnel coefficients then read:

$$r_{\mathrm{TE}} = \mathcal{O}\left(\tilde{\xi}^2\right) \qquad\qquad r_{\mathrm{TM}} = \frac{\varepsilon(0)-1}{\varepsilon(0)+1} \tag{7.17}$$

with the refractive index at zero frequency $n_0 = \sqrt{\varepsilon(0)}$. We observe in this case that the contribution of the electric polarization is negligible compared to the magnetic one. Moreover, the amplitude for the latter is, as expected, determined by the value n_0: the higher n_0, the greater the reflection.

7.2.3 Drude model

Introducing $\alpha = 2\pi\frac{R}{\lambda_P}$ and $\delta = \frac{\lambda_P}{\lambda_\gamma}$, the relative permittivity for the Drude model writes $\varepsilon - 1 = \frac{\alpha^2}{\tilde{\xi}^2+\delta\alpha\tilde{\xi}} = \mathcal{O}(\tilde{\xi}^{-1})$ at low frequencies. As $\cos\theta = \mathcal{O}(\tilde{\xi}^{-1})$, the ratio $\frac{\varepsilon-1}{\cos^2\theta} \sim \frac{\alpha}{\delta\tilde{\xi}\cos^2\theta} = \mathcal{O}\left(\tilde{\xi}\right)$, appearing in both coefficients, diverges at the limit $(\tilde{\xi} \to 0)$. It yields the following asymptotic forms for the low-frequency Fresnel coefficients:

$$r_{\mathrm{TE}} = \mathcal{O}\left(\tilde{\xi}\right) \qquad\qquad r_{\mathrm{TM}} = 1 + \mathcal{O}\left(\tilde{\xi}\right) \ . \tag{7.18}$$

We observe in this case the extinction of the reflection for transverse electric modes at the limit of zero frequency, a feature that is not observed with perfect mirrors. This extinction is responsible for the ratio 2 between the Casimir free-energies obtained from perfect and Drude models, appearing in the plane-plane geometry for large distances, as illustrated in **Fig. 23** (p.51). The reflection coefficient for transverse magnetic modes r_{TM} converges to the value 1, as in the perfectly reflecting case.

7.2.4 Plasma model

Introducing $\alpha = 2\pi\frac{R}{\lambda_P}$, the relative permittivity for the plasma model writes $\varepsilon - 1 = \frac{\alpha^2}{\tilde{\xi}^2}$. Then at low frequencies, $\frac{\varepsilon-1}{\cos^2\theta} = \left(\frac{\alpha}{\tilde{\xi}\cos\theta}\right)^2 = \mathcal{O}(1)$ remains finite. The asymptotic form of the low-frequency

Fresnel coefficients still depends on the value of α in this case:

$$r_{\mathrm{TE}} = \frac{1-\sqrt{1+\left(\frac{\alpha}{\tilde{\xi}\cos\theta}\right)^2}}{1+\sqrt{1+\left(\frac{\alpha}{\tilde{\xi}\cos\theta}\right)^2}} \qquad r_{\mathrm{TM}} = 1+\mathcal{O}\left(\tilde{\xi}^2\right) \ . \tag{7.19}$$

As $\tilde{\xi}\cos\theta$ scales as $\frac{R}{\mathcal{L}}$, the important parameter in the r_{TE} coefficient is $\frac{\alpha}{\tilde{\xi}\cos\theta} \propto \frac{2\pi\mathcal{L}}{\lambda_P}$. When $\mathcal{L} \gg \lambda_P$, $r_{\mathrm{TE}} \to -1$, and one recovers the perfect reflector result. When $\mathcal{L} \ll \lambda_P$, $r_{\mathrm{TE}} \to 0$, and the Drude model result is recovered. The plasma model is again at low frequency an intermediate case between the perfectly reflecting and Drude models, as with the Mie coefficients. It is again impossible to obtain the asymptotic expressions (7.19) of the Fresnel coefficients for plasma model from the one of Drude model (7.18) by simply taking the limit $\delta \to 0$.

Except for dielectrics, the coefficient for transverse magnetic modes is always 1 at zero frequency, but the one for transverse electric modes depends on the model. In this sense, the r_{TM} coefficients is similar to the Mie coefficient a_ℓ, while r_{TE} is the planar equivalent of b_ℓ for a sphere.

7.3 Spherical harmonics and finite rotations

For large values of $\cos\theta$, we have $s(\theta) = \sqrt{\cos^2\theta - 1} \simeq \cos\theta$. For the spherical harmonics, we can derive from **Section 5.3.2** (p.76), and specially from the first terms in the recurrence relations, the $(\cos\theta \to +\infty)$-expansion of the transformed spherical harmonics $Y^s_{\ell,m}$ and their θ-derivatives $\partial_\theta Y^s_{\ell,m}$:

$$Y^s_{\ell,m} \simeq \frac{(-1)^m\sqrt{(2\ell-1)!!}\sqrt{(2\ell+1)!!}}{2\sqrt{\pi}\sqrt{(\ell-m)!}\sqrt{(\ell+m)!}}(\cos\theta)^\ell \tag{7.20}$$

$$\partial_\theta Y^s_{\ell,m} \simeq \frac{(-1)^m\ell\sqrt{(2\ell-1)!!}\sqrt{(2\ell+1)!!}}{2\sqrt{\pi}\sqrt{(\ell-m)!}\sqrt{(\ell+m)!}}(\cos\theta)^\ell \ . \tag{7.21}$$

This result can be proven by direct recurrence from the definition of **Section 5.3.2** (p.76).

For finite rotations, following **Section 5.3.3** (p.77), we get the following asymptotic expansions at the $(\cos\theta \to +\infty)$-limit:

$$d^{\ell,s}_{m,1} \simeq (-1)^{m+1}\sqrt{\frac{\ell}{\ell+1}}\frac{(2\ell-1)!!}{\sqrt{(\ell-m)!}\sqrt{(\ell+m)!}}(\cos\theta)^\ell \ . \tag{7.22}$$

Again, this leading order term can be derived by simple recurrence from the definition of **Section 5.3.3** (p.77). This is however not sufficient for our purpose here: indeed, expressions for the scattering matrix do not contain a simple finite rotation, but rather a combination of $d^{\ell,s}_{m,1}(\theta)$ and $d^{\ell,s}_{m,1}(\pi-\theta)$.

As the factor $(\cos\theta)^\ell$ in (7.22) is in reality $s(\theta)(\cos\theta)^{\ell-1}$ for $m=0$, and $(s(\theta))^{m-1}(\cos\theta)^{\ell-m+1}$ for $m \geq 1$, the dominant term of $d^{\ell,s}_{m,1}(\pi-\theta)$ will be $(-1)^{\ell-m+1}$ times the one for $d^{\ell,s}_{m,1}(\theta)$. For $d^{\ell,s}_m[\mathrm{dif}] = d^{\ell,s}_{m,1}(\theta) - (-1)^{\ell+m}d^{\ell,s}_{m,1}(\pi-\theta)$, the two dominant terms add up. But for $d^{\ell,s}_m[\mathrm{sum}] = d^{\ell,s}_{m,1}(\theta) + (-1)^{\ell+m}d^{\ell,s}_{m,1}(\pi-\theta)$, they cancel out.

Instead of going to the next order, we have chosen to derive a direct construction rule for the leading oder of $d^{\ell,s}_m[\mathrm{sum}]$. First, for $m=0$, by simple recurrence with the definition of $d^{\ell,s}_{0,1}(\theta)$, we can show that it is an even function with respect to $\cos\theta$ for odd ℓ, and an odd function for even ℓ. Thus $d^{\ell,s}_0[\mathrm{sum}]$ is simply zero for all ℓ:

$$d^{\ell,s}_0[\mathrm{sum}] = d^{\ell,s}_{0,1}(\theta) + (-1)^{\ell+0}(-1)^{\ell+1}d^{\ell,s}_{0,1}(\theta) = 0 \quad \forall \ell \geq 1. \tag{7.23}$$

Then, for $m \geq 1$, when inserting the definition of $d_{0,1}^{\ell,s}(\theta)$ in $d_m^{\ell,s}[\text{sum}]$, we get:

$$\begin{aligned}
d_m^{m,s}[\text{sum}] =& \sqrt{\frac{(2m)!}{(m-1)!(m+1)!}} \left(\frac{-s(\theta)}{2}\right)^{m-1} \\
d_m^{m+1,s}[\text{sum}] =& \sqrt{\frac{(2m+1)!}{m!(m+2)!}} \left(\frac{-s(\theta)}{2}\right)^{m-1} m\cos\theta \\
d_m^{\ell,s}[\text{sum}] =& \frac{1}{\sqrt{\ell^2-1}\sqrt{\ell^2-m^2}} \left[\ell(2\ell-1)\cos\theta d_m^{\ell-1,s}[\text{sum}] - \frac{m(2\ell-1)}{\ell-1} d_m^{\ell-1,s}[\text{dif}]\right] \\
&+ \frac{\sqrt{(\ell-1)^2-1}\sqrt{(\ell-1)^2-m^2}}{\sqrt{\ell^2-1}\sqrt{\ell^2-m^2}} \left[\frac{-\ell}{\ell-1} d_m^{\ell-2,s}[\text{sum}]\right]
\end{aligned} \tag{7.24}$$

And from that coupled recurrence relations we can extract the asymptotic expansions for the combinations of the finite rotations, which are summed up in the following property:

Prop. 13 *$d_m^{\ell,s}[sum]$ and $d_m^{\ell,s}[dif]$ have the following asymptotic expansions:*

$$\begin{aligned}
&d_m^{\ell,s}[sum] \simeq K(\ell,m)\frac{m}{\ell}\left(s(\theta)\right)^{m-1}(\cos\theta)^{\ell-m} \simeq \frac{m}{\ell}K(\ell,m)(\cos\theta)^{\ell-1} \\
&d_m^{\ell,s}[dif] \simeq K(\ell,m)\left(s(\theta)\right)^{m-1}(\cos\theta)^{\ell-m+1} \simeq K(\ell,m)(\cos\theta)^{\ell} \\
&\textit{with} \quad K(\ell,m) = (-1)^{m+1}\sqrt{\frac{\ell}{\ell+1}}\frac{2(2\ell-1)!!}{\sqrt{(\ell-m)!}\sqrt{(\ell+m)!}}
\end{aligned}$$

(For proof, see **Appendix A.7** p.216)

The former remarks are important, as we observe that $d_m^{\ell,s}[\text{sum}]$ looses an order in $\cos\theta$ compared to $d_m^{\ell,s}[\text{dif}]$, and it will enable to discard some terms when comparing the contributions of all parts of the scattering matrix.

7.4 Integration over $\cos\theta$

The next step in order to compute the leading terms of the elements of the scattering operator is the integration over $\cos\theta$ for the four blocks elements A, B, C, D given in Eq.(5.55) (p.78). From the results (7.20,7.21) and **Prop.13** in the previous section, we can predict that the power in $\cos\theta$ in the integrands as the following:

$$\begin{aligned}
A_{\ell_1,\ell_2,p}^{(m)} &\simeq K_A(\ell_1,\ell_2,m)\int_1^\infty d\cos\theta\ (\cos\theta)^{\ell_1+\ell_2-2}\ r_p(\theta)\ e^{-2\tilde{\xi}\tilde{\mathcal{L}}\cos\theta} \\
B_{\ell_1,\ell_2,p}^{(m)} &\simeq K_B(\ell_1,\ell_2,m)\int_1^\infty d\cos\theta\ (\cos\theta)^{\ell_1+\ell_2}\ r_p(\theta)\ e^{-2\tilde{\xi}\tilde{\mathcal{L}}\cos\theta} \\
C_{\ell_1,\ell_2,p}^{(m)} &\simeq K_C(\ell_1,\ell_2,m)\int_1^\infty d\cos\theta\ (\cos\theta)^{\ell_1+\ell_2-1}\ r_p(\theta)\ e^{-2\tilde{\xi}\tilde{\mathcal{L}}\cos\theta} \\
D_{\ell_1,\ell_2,p}^{(m)} &\simeq K_D(\ell_1,\ell_2,m)\int_1^\infty d\cos\theta\ (\cos\theta)^{\ell_1+\ell_2-1}\ r_p(\theta)\ e^{-2\tilde{\xi}\tilde{\mathcal{L}}\cos\theta}
\end{aligned} \tag{7.25}$$

where we have merged the $\cos\theta$-independent part of the integrand outside the integration with the introduction of the $K(\ell_1,\ell_2,m)$ terms. The first observation is that the blocks $B^{(m)}$ are going to play a dominant role in the future expansion, as they exhibit a higher exponent in $\cos\theta$.

In the following we restrict ourselves to the case where the low-frequency limit of the Fresnel coefficient does not depend on the lateral vector component[11]. We are left with the following

[11]This is always the case, except for plasma model with TE-polarization

integration, reformulated with the help of the change of variable $\left[t = 2\tilde{\xi}\tilde{\mathcal{L}}\cos\theta\right]$:

$$\begin{aligned}\int_1^\infty d\cos\theta\ (\cos\theta)^N e^{-2\tilde{\xi}\tilde{\mathcal{L}}\cos\theta} &= \int_{2\tilde{\xi}\tilde{\mathcal{L}}}^\infty \frac{dt}{2\tilde{\xi}\tilde{\mathcal{L}}}\left(\frac{t}{2\tilde{\xi}\tilde{\mathcal{L}}}\right)^N e^{-t} \\ &\simeq \frac{1}{\left(2\tilde{\xi}\tilde{\mathcal{L}}\right)^{N+1}}\int_0^\infty dt\ t^N e^{-t} \\ &\simeq \frac{N!}{\left(2\tilde{\xi}\tilde{\mathcal{L}}\right)^{N+1}}\ .\end{aligned}$$

The leading terms of the elements in the scattering operator then become:

$$\begin{aligned}A^{(m)}_{\ell_1,\ell_2,p} &\simeq \frac{K_A(\ell_1,\ell_2,m)(\ell_1+\ell_2-2)!}{\left(2\tilde{\xi}\tilde{\mathcal{L}}\right)^{\ell_1+\ell_2-1}}\ r_p \\ B^{(m)}_{\ell_1,\ell_2,p} &\simeq \frac{K_B(\ell_1,\ell_2,m)(\ell_1+\ell_2)!}{\left(2\tilde{\xi}\tilde{\mathcal{L}}\right)^{\ell_1+\ell_2+1}}\ r_p \\ C^{(m)}_{\ell_1,\ell_2,p} &\simeq \frac{K_C(\ell_1,\ell_2,m)(\ell_1+\ell_2-1)!}{\left(2\tilde{\xi}\tilde{\mathcal{L}}\right)^{\ell_1+\ell_2}}\ r_p \\ D^{(m)}_{\ell_1,\ell_2,p} &\simeq \frac{K_D(\ell_1,\ell_2,m)(\ell_1+\ell_2-1)!}{\left(2\tilde{\xi}\tilde{\mathcal{L}}\right)^{\ell_1+\ell_2}}\ r_p\end{aligned} \tag{7.26}$$

where the dominant role of the blocks $B^{(m)}$ at low-frequency becomes all the more significant.

7.5 Determinant of the scattering matrix

Using the Fresnel and Mie coefficients asymptotic expressions found in the previous sections and the expressions (7.26) of the integrated blocks, the dominant power laws in $\tilde{\xi}$ for the elements of the operator $\mathcal{N}^{(m)}$ at low frequencies are presented in **Table 8**, depending on the model used for the optical response of the materials. After dividing all lines ℓ_1 by $\tilde{\xi}^{\ell_1}$ and multiplying all columns ℓ_2 by $\tilde{\xi}^{\ell_2}$, which leaves the determinant of $\mathcal{D}^{(m)} = I - \mathcal{N}^{(m)}$ unchanged, the dominant powers of $\tilde{\xi}$ at low frequencies for the scattering operator do not depend anymore on the indices ℓ_1 and ℓ_2, but only on the block. The order of the dominant terms in the blocks of the transformed operator are presented in **Table 9**.

For perfect mirrors and plasma model, we see that the determinant of the scattering operator only involves the diagonal blocks:

$$\det\left(\mathcal{D}^{(m)}\right) \simeq \det\left(I - \sqrt{\frac{\pi(2\ell_1+1)}{\ell_2(\ell_2+1)}}a_{\ell_1}B^{(m)}_{\ell_1,\ell_2,\mathrm{TM}}\right)\det\left(I - \sqrt{\frac{\pi(2\ell_1+1)}{\ell_2(\ell_2+1)}}b_{\ell_1}B^{(m)}_{\ell_1,\ell_2,\mathrm{TE}}\right) \tag{7.27}$$

while for the Drude model and dielectrics it only involves the first block:

$$\det\left(\mathcal{D}^{(m)}\right) \simeq \det\left(I - \sqrt{\frac{\pi(2\ell_1+1)}{\ell_2(\ell_2+1)}}a_{\ell_1}B^{(m)}_{\ell_1,\ell_2,\mathrm{TM}}\right)\ . \tag{7.28}$$

	perfect	plasma	Drude	dielectric
$\mathcal{N}^{(m)}(E,E)_{\ell_1,\ell_2}$ $\sim a_{\ell_1}\left(A^{(m)}_{\ell_1,\ell_2,\mathrm{TE}}+B^{(m)}_{\ell_1,\ell_2,\mathrm{TM}}\right)$	$\ell_1-\ell_2$	$\ell_1-\ell_2$	$\ell_1-\ell_2$	$\ell_1-\ell_2$
$\mathcal{N}^{(m)}(E,M)_{\ell_1,\ell_2}$ $\sim a_{\ell_1}\left(C^{(m)}_{\ell_1,\ell_2,\mathrm{TE}}+D^{(m)}_{\ell_1,\ell_2,\mathrm{TM}}\right)$	$\ell_1-\ell_2+1$	$\ell_1-\ell_2+1$	$\ell_1-\ell_2+1$	$\ell_1-\ell_2+1$
$\mathcal{N}^{(m)}(M,E)_{\ell_1,\ell_2}$ $\sim b_{\ell_1}\left(C^{(m)}_{\ell_1,\ell_2,\mathrm{TM}}+D^{(m)}_{\ell_1,\ell_2,\mathrm{TE}}\right)$	$\ell_1-\ell_2+1$	$\ell_1-\ell_2+1$	$\ell_1-\ell_2+2$	$\ell_1-\ell_2+3$
$\mathcal{N}^{(m)}(M,M)_{\ell_1,\ell_2}$ $\sim b_{\ell_1}\left(A^{(m)}_{\ell_1,\ell_2,\mathrm{TM}}+B^{(m)}_{\ell_1,\ell_2,\mathrm{TE}}\right)$	$\ell_1-\ell_2$	$\ell_1-\ell_2$	$\ell_1-\ell_2+2$	$\ell_1-\ell_2+4$

Table 8: Dominant power exponent in $\tilde{\xi}$ for the elements of the operator $\mathcal{N}^{(m)}$ when $\tilde{\xi}$ goes to zero.

	perfect	plasma	Drude	dielectric
$\mathcal{D}^{(m)}(E,E)=I-\mathcal{N}^{(m)}(E,E)$	$\mathcal{O}(1)$	$\mathcal{O}(1)$	$\mathcal{O}(1)$	$\mathcal{O}(1)$
$\mathcal{D}^{(m)}(E,M)=-\mathcal{N}^{(m)}(E,M)$	$\mathcal{O}(\tilde{\xi})$	$\mathcal{O}(\tilde{\xi})$	$\mathcal{O}(\tilde{\xi})$	$\mathcal{O}(\tilde{\xi})$
$\mathcal{D}^{(m)}(M,E)=-\mathcal{N}^{(m)}(M,E)$	$\mathcal{O}(\tilde{\xi})$	$\mathcal{O}(\tilde{\xi})$	$\mathcal{O}(\tilde{\xi}^2)$	$\mathcal{O}(\tilde{\xi}^3)$
$\mathcal{D}^{(m)}(M,M)=I-\mathcal{N}^{(m)}(M,M)$	$\mathcal{O}(1)$	$\mathcal{O}(1)$	$1+\mathcal{O}(\tilde{\xi}^2)$	$1+\mathcal{O}(\tilde{\xi}^4)$

Table 9: Dominant power exponent in $\tilde{\xi}$ for the elements of the operator $\mathcal{D}^{(m)}$ when $\tilde{\xi}$ goes to zero, after a balancing transformation.

7.6 Conclusion: the first Matsubara term and the high-temperature limit

We conclude on this low-frequency limit derivation with explicit expressions for the first Matsubara term $\Phi(\tilde{\xi}_0) = 2\sum_m{}' \ln\det\mathcal{D}^{(m)}(0)$. This term appears in the scattering formula as a contribution to the Casimir free-energy at non-zero temperature, and is directly connected to the high-temperature limit through:

$$\mathcal{F}^{\mathrm{HT}} = \frac{\kappa_B T}{2}\Phi(0) = k_B T \sum_m{}' \ln\det\mathcal{D}^{(m)}(0)\ .$$

Those explicit expressions will be of great interest, not only for the numerical evaluations of Casimir effect at non-zero and high temperatures, but also for analytical derivations, such as the long-distance regime studied in the next section. Moreover, the comparison between the different models of reflection give a physical insight of what happens in terms of scattering at very low frequencies in this geometry.

From Eqs.(7.27,7.28), we see that we only need to consider the two terms:

$$\sqrt{\frac{\pi(2\ell_1+1)}{\ell_2(\ell_2+1)}}a_{\ell_1}B^{(m)}_{\ell_1,\ell_2,\mathrm{TM}} \simeq \sqrt{\frac{\pi(2\ell_1+1)}{\ell_2(\ell_2+1)}}\frac{K_B(\ell_1,\ell_2,m)(\ell_1+\ell_2)!}{\left(2\tilde{\xi}\tilde{\mathcal{L}}\right)^{\ell_1+\ell_2+1}}\ a_{\ell_1}r_{\mathrm{TM}}$$

$$\sqrt{\frac{\pi(2\ell_1+1)}{\ell_2(\ell_2+1)}}b_{\ell_1}B^{(m)}_{\ell_1,\ell_2,\mathrm{TE}} \simeq \sqrt{\frac{\pi(2\ell_1+1)}{\ell_2(\ell_2+1)}}\frac{K_B(\ell_1,\ell_2,m)(\ell_1+\ell_2)!}{\left(2\tilde{\xi}\tilde{\mathcal{L}}\right)^{\ell_1+\ell_2+1}}\ b_{\ell_1}r_{\mathrm{TE}}$$

where we can give an explicit expression for the coefficient $K_B(\ell_1,\ell_2,m)$ by:

$$\sqrt{\frac{\pi(2\ell_1+1)}{\ell_2(\ell_2+1)}}K_B(\ell_1,\ell_2,m) =$$
$$(-1)^{\ell_2}\sqrt{\frac{\ell_1(2\ell_1+1)}{\ell_2(2\ell_2+1)}}\frac{\ell_2}{\sqrt{\ell_1+1}\sqrt{\ell_2+1}}\frac{(2\ell_2+1)!!(2\ell_1-1)!!}{\sqrt{(\ell_1-m)!}\sqrt{(\ell_1+m)!}\sqrt{(\ell_2-m)!}\sqrt{(\ell_2+m)!}}\ . \quad (7.29)$$

The first term of Eq.(7.27) can then be simplified into the following determinant:

$$\det\left(I - \sqrt{\frac{\pi(2\ell_1+1)}{\ell_2(\ell_2+1)}}a_{\ell_1}B^{(m)}_{\ell_1,\ell_2,\mathrm{TM}}\right)$$
$$= \det\left(\delta_{\ell_1,\ell_2} - \frac{(-\tilde{\xi})^{\ell_1-\ell_2}}{\left(2\tilde{\mathcal{L}}\right)^{\ell_1+\ell_2+1}}\sqrt{\frac{\ell_2(\ell_1+1)(2\ell_1+1)}{\ell_1(\ell_2+1)(2\ell_2+1)}}\frac{(2\ell_2+1)!!}{(2\ell_1+1)!!}\right.$$
$$\left.\times\frac{(\ell_1+\ell_2)!}{\sqrt{(\ell_1-m)!}\sqrt{(\ell_1+m)!}\sqrt{(\ell_2-m)!}\sqrt{(\ell_2+m)!}}\right)$$

$$= \det\left(\delta_{\ell_1,\ell_2} - \frac{1}{\left(2\tilde{\mathcal{L}}\right)^{\ell_1+\ell_2+1}}\frac{(\ell_1+\ell_2)!}{\sqrt{(\ell_1-m)!}\sqrt{(\ell_1+m)!}\sqrt{(\ell_2-m)!}\sqrt{(\ell_2+m)!}}\right)$$
$$= \det\left(\mathbb{D}^{(m)}_{a,\mathrm{TM}}(\tilde{\mathcal{L}})\right)\ , \quad (7.30)$$

where the lines ℓ_1 have been divided by $\frac{(-\tilde{\xi})^{\ell_1}}{(2\ell_1+1)!!}\sqrt{\frac{(\ell_1+1)(2\ell_1+1)}{\ell_1}}$ and the columns ℓ_2 have been multiplied by $\frac{(-\tilde{\xi})^{\ell_2}}{(2\ell_2+1)!!}\sqrt{\frac{(\ell_2+1)(2\ell_2+1)}{\ell_2}}$, leaving the determinant unchanged. The operator $\mathbb{D}^{(m)}_{a,\mathrm{TM}}(\tilde{\mathcal{L}})$ is infinite-dimensional, but can be truncated to a maximum value $\ell_{\max}$ for the indices ℓ_1 and ℓ_2. If one chooses the minimum number $\ell_{\max}=1$, as in the long-distance limit ($\tilde{\mathcal{L}}\gg 1$) studied in the next section, the determinants of the obtained 1-dimensional matrices for the only possible values $m\in\{0,1\}$ simplify to:

$$\det_{\ell_{\max}=1}\left(\mathbb{D}^{(0)}_{a,\mathrm{TM}}(\tilde{\mathcal{L}})\right)\simeq 1-\frac{1}{4\tilde{\mathcal{L}}^3}\qquad\qquad \det_{\ell_{\max}=1}\left(\mathbb{D}^{(1)}_{a,\mathrm{TM}}(\tilde{\mathcal{L}})\right)\simeq 1-\frac{1}{8\tilde{\mathcal{L}}^3}\,. \tag{7.31}$$

The second term can be simplified in a similar way:

$$\begin{aligned}
&\det\left(I-\sqrt{\frac{\pi(2\ell_1+1)}{\ell_2(\ell_2+1)}}b_{\ell_1}B^{(m)}_{\ell_1,\ell_2,\mathrm{TE}}\right)\\
&\qquad=\det\left(\delta_{\ell_1,\ell_2}-\frac{(-\tilde{\xi})^{\ell_1-\ell_2}}{\left(2\tilde{\mathcal{L}}\right)^{\ell_1+\ell_2+1}}\sqrt{\frac{\ell_2(\ell_1+1)(2\ell_1+1)}{\ell_1(\ell_2+1)(2\ell_2+1)}}\frac{(2\ell_2+1)!!}{(2\ell_1+1)!!}\right.\\
&\qquad\qquad\left.\times\frac{\ell_1}{\ell_1+1}\frac{(\ell_1+\ell_2)!}{\sqrt{(\ell_1-m)!}\sqrt{(\ell_1+m)!}\sqrt{(\ell_2-m)!}\sqrt{(\ell_2+m)!}}\right)\\
&=\det\left(\delta_{\ell_1,\ell_2}-\frac{1}{\left(2\tilde{\mathcal{L}}\right)^{\ell_1+\ell_2+1}}\frac{\ell_1}{\ell_1+1}\frac{(\ell_1+\ell_2)!}{\sqrt{(\ell_1-m)!}\sqrt{(\ell_1+m)!}\sqrt{(\ell_2-m)!}\sqrt{(\ell_2+m)!}}\right)\\
&=\det\left(\mathbb{D}^{(m)}_{b,\mathrm{TE}}(\tilde{\mathcal{L}})\right)
\end{aligned}\tag{7.32}$$

which is very similar to expression (7.30), except for a factor $\frac{\ell_1}{\ell_1+1}$. Again, with a truncation to $\ell_{\max}=1$, the determinants of the obtained 1-dimensional matrices for the only possible value for m simplify to:

$$\det_{\ell_{\max}=1}\left(\mathbb{D}^{(0)}_{a,\mathrm{TM}}(\tilde{\mathcal{L}})\right)\simeq 1-\frac{1}{8\tilde{\mathcal{L}}^3}\qquad\qquad \det_{\ell_{\max}=1}\left(\mathbb{D}^{(1)}_{a,\mathrm{TM}}(\tilde{\mathcal{L}})\right)\simeq 1-\frac{1}{16\tilde{\mathcal{L}}^3} \tag{7.33}$$

where the factor 2 with respect to Eq.(7.31) appear, because of the $\frac{\ell_1}{\ell_1+1}$ term.

7.6.1 Perfect mirrors

From Eq.(7.27), the determinants of the scattering operators $\mathcal{D}^{(m)}$ for perfect mirrors at the limit of low frequencies are given by:

$$\det\left(\mathcal{D}^{(m)}\right)\simeq\det\left(I-\sqrt{\frac{\pi(2\ell_1+1)}{\ell_2(\ell_2+1)}}a_{\ell_1}B^{(m)}_{\ell_1,\ell_2,\mathrm{TM}}\right)\det\left(I-\sqrt{\frac{\pi(2\ell_1+1)}{\ell_2(\ell_2+1)}}b_{\ell_1}B^{(m)}_{\ell_1,\ell_2,\mathrm{TE}}\right)$$

which is just the product of the two derived expressions (7.30) and (7.32). Then the first Matsubara term and the high-temperature limit (HT) of the Casimir free-energy write as a sum of the two

contributions:

$$\Phi^{\rm perf}(0) = 2{\sum_m}' \ln\det \mathcal{D}^{(m)} \simeq 2{\sum_m}' \left[\ln\det\left(\mathbb{D}^{(m)}_{a,\rm TM}(\tilde{\mathcal{L}})\right) + \ln\det\left(\mathbb{D}^{(m)}_{b,\rm TE}(\tilde{\mathcal{L}})\right)\right]$$
$$\mathcal{F}^{\rm perf}_{\rm HT} = \frac{k_B T}{2}\Phi(0) \simeq k_B T {\sum_m}' \left[\ln\det\left(\mathbb{D}^{(m)}_{a,\rm TM}(\tilde{\mathcal{L}})\right) + \ln\det\left(\mathbb{D}^{(m)}_{b,\rm TE}(\tilde{\mathcal{L}})\right)\right] . \tag{7.34}$$

If we additionally take the long-distance limit (LD) in the former expression, assuming $\tilde{\mathcal{L}} \gg 1$, we can truncate the operators to the maximum value $\ell_{\rm max}$ for the indices ℓ_1 and ℓ_2. Using truncated expressions (7.31) and (7.33), we obtain the long-distance limit of the first Matsubara term $\Phi^{\rm perf}_{\rm LD}(0)$, and the high-temperature, long-distance limit of the Casimir free-energy $\mathcal{F}^{\rm perf}_{\rm HT,LD}$ in the sphere-plane configuration:

$$\begin{aligned}\Phi^{\rm perf}_{\rm LD}(0) &= 2\left[\frac{1}{2}\ln \det_{\ell_{\rm max}=1}\left(\mathbb{D}^{(0)}_{a,\rm TM}(\tilde{\mathcal{L}})\right) + \ln \det_{\ell_{\rm max}=1}\left(\mathbb{D}^{(1)}_{a,\rm TM}(\tilde{\mathcal{L}})\right)\right.\\ &\quad \left. + \frac{1}{2}\ln \det_{\ell_{\rm max}=1}\left(\mathbb{D}^{(0)}_{b,\rm TE}(\tilde{\mathcal{L}})\right) + \ln \det_{\ell_{\rm max}=1}\left(\mathbb{D}^{(1)}_{b,\rm TE}(\tilde{\mathcal{L}})\right)\right]\\ &= -\frac{3R^3}{4\mathcal{L}^3}\\ \mathcal{F}^{\rm perf}_{\rm HT,LD} &= -\frac{3k_B T R^3}{8\mathcal{L}^3} .\end{aligned} \tag{7.35}$$

7.6.2 Drude model

For Drude model, because of the extinction of the coefficients $r_{\rm TE}$ and b_ℓ at low frequencies, the diagonal blocks $\mathcal{N}^{(m)}(M,M)$ give a negligible contribution, as seen on the lower row of **Tables 8** and **9**. The determinants of the scattering operators $\mathcal{D}^{(m)}$ then only involve one term:

$$\det\left(\mathcal{D}^{(m)}\right) \simeq \det\left(I - \sqrt{\frac{\pi(2\ell_1+1)}{\ell_2(\ell_2+1)}}a_{\ell_1} B^{(m)}_{\ell_1,\ell_2,\rm TM}\right)$$

which is the first term (7.30) in the perfect mirrors case. It follows that the first Matsubara term and the high temperature limit of the Casimir free-energy for Drude model write as:

$$\Phi^{\rm Drud}(0) = 2{\sum_m}' \ln\det \mathcal{D}^{(m)} \simeq 2{\sum_m}' \ln\det\left(\mathbb{D}^{(m)}_{a,\rm TM}(\tilde{\mathcal{L}})\right)$$
$$\mathcal{F}^{\rm Drud}_{\rm HT} = \frac{k_B T}{2}\Phi(0) \simeq k_B T {\sum_m}' \ln\det\left(\mathbb{D}^{(m)}_{a,\rm TM}(\tilde{\mathcal{L}})\right) . \tag{7.36}$$

Interestingly enough, the obtained low-frequency expansion (7.36) is independent of the material properties, such as its plasma wavelength and dissipation rate, that describe the optical response of the objects. It only contains the geometric parameter $\tilde{\mathcal{L}} = 1 + \frac{L}{R}$ and the multipolar indices (ℓ_1, ℓ_2, m).

If we additionally take the long-distance limit (LD) in the former expression, assuming $\tilde{\mathcal{L}} \gg 1$, we can truncate the operators to the maximum value $\ell_{\rm max}$ for the indices ℓ_1 and ℓ_2. Using the truncated expression (7.31), we obtain the long-distance limit of the first Matsubara term $\Phi^{\rm Drud}_{\rm LD}(0)$, and the high-temperature, long-distance limit of the Casimir free-energy $\mathcal{F}^{\rm Drud}_{\rm HT,LD}$ in the sphere-plane

configuration:

$$\begin{aligned}\Phi_{\rm LD}^{\rm Drud}(0) &= 2\left[\frac{1}{2}\ln \det_{\ell_{\max}=1}\left(\mathbb{D}^{(0)}_{a,\rm TM}(\tilde{\mathcal{L}})\right) + \ln \det_{\ell_{\max}=1}\left(\mathbb{D}^{(1)}_{a,\rm TM}(\tilde{\mathcal{L}})\right)\right] \\ &= -\frac{R^3}{2\mathcal{L}^3} \\ \mathcal{F}_{\rm HT,LD}^{\rm Drud} &= -\frac{k_B T R^3}{4\mathcal{L}^3} \end{aligned} \tag{7.37}$$

which is $\frac{2}{3}$ times the perfect mirrors result (7.35). While in the plane-plane the reduction factor of the high-temperature limit with respect to the perfect case is a constant factor 2, in the considered situation of a sphere and a plane it does not stand anymore. For large distance, the factor is $\frac{3}{2}$, and for intermediate distance $\tilde{\mathcal{L}} \not\gg 1$, the situation is more complex.

7.6.3 Plasma model

In the case of the loss-less plasma model for metals, the determinants of the scattering operators $\mathcal{D}^{(m)}$ at the limit of low frequencies are given by:

$$\det\left(\mathcal{D}^{(m)}\right) \simeq \det\left(I - \sqrt{\frac{\pi(2\ell_1+1)}{\ell_2(\ell_2+1)}}a_{\ell_1}B^{(m)}_{\ell_1,\ell_2,\rm TM}\right)\det\left(I - \sqrt{\frac{\pi(2\ell_1+1)}{\ell_2(\ell_2+1)}}b_{\ell_1}B^{(m)}_{\ell_1,\ell_2,\rm TE}\right) .$$

Because the coefficients a_ℓ and $r_{\rm TM}$ have the same low-frequency expansion as for the perfect mirrors and Drude model, the first term read $\det\left(\mathbb{D}^{(m)}_{a,\rm TM}(\tilde{\mathcal{L}})\right)$, like in those cited cases. However, for the second term still contains an integration, because of the Fresnel coefficients, and an additional factor from the expression (7.14) of the b_ℓ coefficient:

$$\begin{aligned}&\det\left(I - \sqrt{\frac{\pi(2\ell_1+1)}{\ell_2(\ell_2+1)}}b_{\ell_1}B^{(m)}_{\ell_1,\ell_2,\rm TE}\right) = \\ &\quad\det\left[\delta_{\ell_1,\ell_2} - \frac{1}{\left(2\tilde{\mathcal{L}}\right)^{\ell_1+\ell_2+1}}\frac{\ell_1}{\ell_1+1}\frac{1}{\sqrt{(\ell_1-m)!}\sqrt{(\ell_1+m)!}\sqrt{(\ell_2-m)!}\sqrt{(\ell_2+m)!}}\right. \\ &\qquad\left.\times\left(1-\frac{2\ell_1+1}{\alpha}\frac{I_{\ell_1+1/2}(\alpha)}{I_{\ell_1-1/2}(\alpha)}\right)\left(\int_0^\infty dt\; t^{\ell_1+\ell_2}\frac{\sqrt{1+(2\alpha\tilde{\mathcal{L}}/t)^2}-1}{\sqrt{1+(2\alpha\tilde{\mathcal{L}}/t)^2}+1}e^{-t}\right)\right] ,\end{aligned} \tag{7.38}$$

using the change of variable $\left[t = 2\tilde{\mathcal{L}}\tilde{\xi}\cos\theta\right]$ and $\alpha = \frac{2\pi R}{\lambda_P}$, which does not seem to be manageable analytically.

When $(R \gg \lambda_P)$, as $\tilde{\mathcal{L}} > 1$ and $t \not\gg 1$ because of the exponential, the integral reduces to $(\ell_1+\ell_2)!$, and $\left(1-\frac{2\ell_1+1}{\alpha}\frac{I_{\ell_1+1/2}(\alpha)}{I_{\ell_1-1/2}(\alpha)}\right) \to 1$, as discussed after Eq.(7.14). It yields that for the first Matsubara term of the plasma model in the $(R \gg \lambda_P)$-limit, we fully recover the perfect reflectors expressions (7.34).

On the contrary, when $(R \ll \lambda_P)$, the factor $\left(1-\frac{2\ell_1+1}{\alpha}\frac{I_{\ell_1+1/2}(\alpha)}{I_{\ell_1-1/2}(\alpha)}\right)$ vanishes, the contribution of the second term (7.38) thus becomes negligible, and the Drude expressions (7.36) are recovered.

Some explicit results can be obtained in the large-distance limit (LD) when $\tilde{\mathcal{L}} \gg 1$, as the integral in Eq.(7.38) simplifies into $(\ell_1+\ell_2)!$. Then, truncating to a maximum value $\ell_{\max} = 1$ for

the indices ℓ_1 and ℓ_2, the expression (7.38) becomes, for $m \in \{0, 1\}$:

$$\det_{\ell_{\max}=1}\left(I - \sqrt{\frac{\pi(2\ell_1+1)}{\ell_2(\ell_2+1)}} b_{\ell_1} B^{(0)}_{\ell_1,\ell_2,\mathrm{TE}}\right) = 1 - \left(1 - \frac{3I_{3/2}(\alpha)}{\alpha I_{1/2}(\alpha)}\right)\frac{1}{8\tilde{\mathcal{L}}^3}$$
$$\det_{\ell_{\max}=1}\left(I - \sqrt{\frac{\pi(2\ell_1+1)}{\ell_2(\ell_2+1)}} b_{\ell_1} B^{(1)}_{\ell_1,\ell_2,\mathrm{TE}}\right) = 1 - \left(1 - \frac{3I_{3/2}(\alpha)}{\alpha I_{1/2}(\alpha)}\right)\frac{1}{16\tilde{\mathcal{L}}^3}$$

which, together with the results for the first term (7.31), gives the long-distance limit of the first Matsubara term $\Phi^{\mathrm{plas}}_{\mathrm{LD}}(0)$, and the corresponding long-distance (LD) and high-temperature (HT) limit for the Casimir free-energy $\mathcal{F}^{\mathrm{plas}}_{\mathrm{HT,LD}}$ in the sphere-plane configuration:

$$\begin{aligned}
\Phi^{\mathrm{plas}}_{\mathrm{LD}} &= 2\left[\frac{1}{2}\ln \det_{\ell_{\max}=1}\left(\mathbb{D}^{(0)}_{a,\mathrm{TM}}(\tilde{\mathcal{L}})\right) + \ln \det_{\ell_{\max}=1}\left(\mathbb{D}^{(1)}_{a,\mathrm{TM}}(\tilde{\mathcal{L}})\right)\right. \\
&\quad \left. + \frac{1}{2}\ln\left(1 - \left(1 - \frac{3I_{3/2}(\alpha)}{\alpha I_{1/2}(\alpha)}\right)\frac{1}{8\tilde{\mathcal{L}}^3}\right) + \ln\left(1 - \left(1 - \frac{3I_{3/2}(\alpha)}{\alpha I_{1/2}(\alpha)}\right)\frac{1}{16\tilde{\mathcal{L}}^3}\right)\right] \\
&= 2\left[-\frac{1}{4}\frac{R^3}{\mathcal{L}^3} - \left(1 - \frac{3I_{3/2}(\alpha)}{\alpha I_{1/2}(\alpha)}\right)\frac{1}{8}\frac{R^3}{\mathcal{L}^3}\right] \\
&= -\frac{3R^3}{4\mathcal{L}^3}\left(1 - \frac{\coth\alpha}{\alpha} + \frac{1}{\alpha^2}\right) \\
\mathcal{F}^{\mathrm{plas}}_{\mathrm{HT,LD}} &= -\frac{3k_B T R^3}{8\mathcal{L}^3}\left(1 - \frac{\coth\alpha}{\alpha} + \frac{1}{\alpha^2}\right)
\end{aligned} \tag{7.39}$$

where we used explicit expressions (8.4) (p.126) for the modified Bessel functions $I_{3/2}$ and $I_{1/2}$. We remark that this result depends on the parameter $\alpha = 2\pi\frac{R}{\lambda_P}$, and thus on the material optical properties.

7.6.4 Dielectrics

The determinants of the scattering operators $\mathcal{D}^{(m)}$ for dielectrics, like the ones for Drude model, only involve one term with a_ℓ and r_{TM} at the low-frequency limit, because the other coefficients become relatively small. The expression of this term is however different, because of the forms (7.8) and (7.17), obtained for the Mie coefficient a_ℓ and the Fresnel coefficient r_{TM}, respectively:

$$\begin{aligned}
\det\left(\mathcal{D}^{(m)}\right) &\simeq \det\left(I - \sqrt{\frac{\pi(2\ell_1+1)}{\ell_2(\ell_2+1)}} a_{\ell_1} B^{(m)}_{\ell_1,\ell_2,\mathrm{TM}}\right) \\
&= \det\left(\delta_{\ell_1,\ell_2} - \frac{1}{\left(2\tilde{\mathcal{L}}\right)^{\ell_1+\ell_2+1}} \frac{(\varepsilon(0)-1)^2}{(\varepsilon(0)+1)\left(\varepsilon(0)+\frac{\ell_1+1}{\ell_1}\right)}\right. \\
&\qquad \left. \times \frac{(\ell_1+\ell_2)!}{\sqrt{(\ell_1-m)!}\sqrt{(\ell_1+m)!}\sqrt{(\ell_2-m)!}\sqrt{(\ell_2+m)!}}\right) \\
&= \det\left(\mathbb{D}^{(m)}_{\mathrm{diel}}(\tilde{\mathcal{L}}, \varepsilon(0))\right) \ .
\end{aligned} \tag{7.40}$$

It follows that the first Matsubara term and the high temperature limit of the Casimir free-energy for Drude model write as:

$$\Phi(0) = 2{\sum_{m}}' \ln\det \mathcal{D}^{(m)} \simeq 2{\sum_{m}}' \ln\det\left(\mathbb{D}^{(m)}_{\rm diel}(\tilde{\mathcal{L}},\varepsilon(0))\right)$$
$$\mathcal{F}^{\rm diel}_{\rm HT} = \frac{k_B T}{2}\Phi(0) \simeq k_B T {\sum_{m}}' \ln\det\left(\mathbb{D}^{(m)}_{\rm diel}(\tilde{\mathcal{L}},\varepsilon(0))\right) \ . \tag{7.41}$$

Surprisingly, when we take the high-reflectivity limit ($\varepsilon(0)\to\infty$) with a dielectric material, the Drude result is recovered, as Eq.(7.40) then recovers the expression in (7.30), but not the perfect mirrors one. It means that low-frequency and high-reflectivity limits do not commute for dielectrics.

If we additionally take the long-distance limit (LD) in the former expression, assuming $\tilde{\mathcal{L}} \gg 1$, we can truncate the operators to the maximum value $\ell_{\rm max}$ for the indices ℓ_1 and ℓ_2. Using a truncated expression of (7.40), we obtain the long-distance limit of the first Matsubara term $\Phi^{\rm diel}_{\rm LD}(0)$, and the corresponding long-distance (LD) and high-temperature (HT) limit for the Casimir free-energy $\mathcal{F}^{\rm diel}_{\rm HT,LD}$ in the sphere-plane configuration:

$$\begin{aligned}\Phi^{\rm diel}_{\rm LD}(0) &= 2\left[\frac{1}{2}\ln \det_{\ell_{\rm max}=1}\left(\mathbb{D}^{(0)}_{\rm diel}(\tilde{\mathcal{L}})\right) + \ln \det_{\ell_{\rm max}=1}\left(\mathbb{D}^{(1)}_{\rm diel}(\tilde{\mathcal{L}})\right)\right] \\ &= -\frac{R^3}{2\mathcal{L}^3}\frac{(\varepsilon(0)-1)^2}{(\varepsilon(0)+1)(\varepsilon(0)+2)} \\ \mathcal{F}^{\rm diel}_{\rm HT,LD} &= -\frac{k_B T R^3}{4\mathcal{L}^3}\frac{(\varepsilon(0)-1)^2}{(\varepsilon(0)+1)(\varepsilon(0)+2)}\end{aligned} \tag{7.42}$$

which is the same as for Drude mirrors, except for the $\varepsilon(0)$-dependent last factor.

7.6.5 Remarks

The former results have been obtained in the situation where the sphere and the plane were made of the same material. It is also possible to obtain similar result for an hybrid situation, say with a dielectric sphere and a Drude-modelled plane for example. The results are not presented here because of the numerous possible combinations.

We checked the previously derived formulas for the ($\tilde{\xi}\to 0$)-limit of the integrand function $\Phi(\tilde{\xi})$ through comparison with numerical evaluations for decreasing values of the reduced frequency $\tilde{\xi}$. In **Fig. 38** is plotted the relative difference for the determinant as a function of the reduced frequency $\tilde{\xi}$. Clearly the numerical results for decreasing frequency converge into the analytical result, until the unavoidable round-off error (here around 10^{-16} for floats with double representation).

We then checked the fact that for Drude materials, the low-frequency limit of the integrand does not depend on the material properties by studying the low-frequency convergence in numerical evaluations to the analytic formula (7.36), for different set of parameters (λ_P,δ). In **Fig. 39**, we illustrate this test by taking $\frac{\lambda_1}{R}=\delta=1$. As expected, for the two sets of parameters describing the material's optical properties, the corresponding integrands functions both converge to the analytical limit.

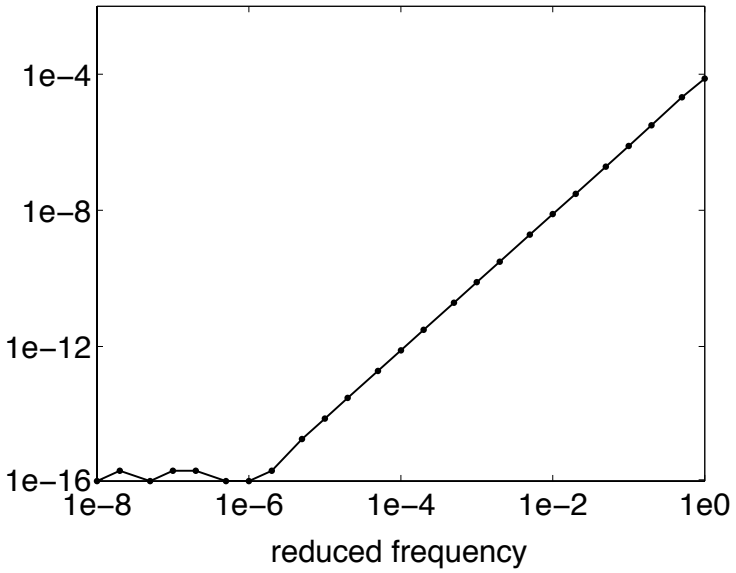

Figure 38: Relative difference between the numerical evaluations and the ($\tilde{\xi} = 0$)-analytical limit (7.34), as a function of the reduced frequency $\tilde{\xi}$, in the case of perfectly reflecting mirrors. Here the aspect ratio is $\frac{L}{R} = 1$, and the truncation is done at $\ell_{\max} = 20$.

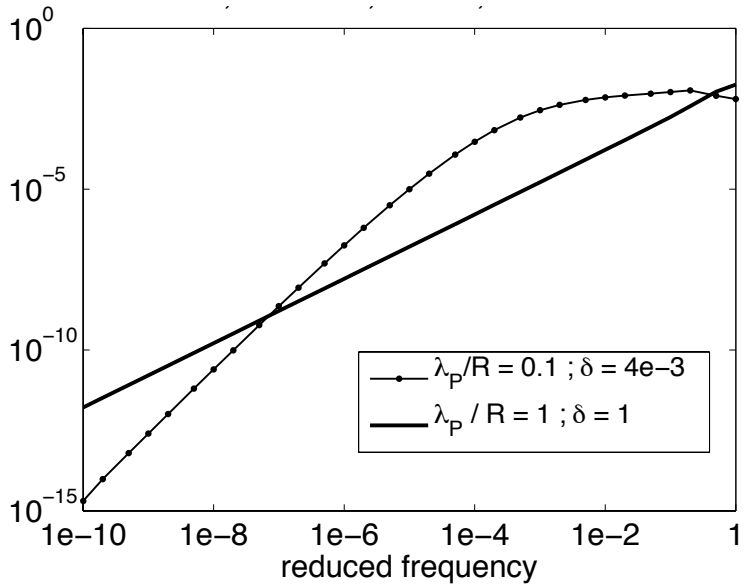

Figure 39: Relative difference between the numerical evaluations and the ($\tilde{\xi} = 0$)-analytical limit (7.36), as a function of the reduced frequency $\tilde{\xi}$, in the case of mirrors described by the Drude model. Here the aspect ratio is $\frac{L}{R} = 1$, and the truncation is done at $\ell_{\max} = 20$. The first set of parameter for the material are the usual ones for a micrometer gold sphere ($\frac{\lambda_P}{R} = 0.1, \delta = 4e - 3$), the second set is taken arbitrarily to unity.

8 Long-distance limit

In this section we study the Casimir effect in the plane-sphere geometry when the distance between the sphere and the plane is very large, compared to the radius of the sphere. This region of high values for the aspect ratio ($\frac{L}{R} \gg 1$) can be understood as the small-sphere limit, or as the large-distance limit. We have chosen to refer to the latter appellation, and in this section we will write it indistinctly ($\mathcal{L} \gg R$) or ($L \gg R$).

As discussed in **Section 6.1.1** (p.81), a spherical mode with index $\ell \gg \tilde{\xi}$ has an impact parameter $b = \frac{\ell R}{\tilde{\xi}} \ll R$, and corresponds to a ray that does not hit the sphere. It enabled us to establish a proportionality between the truncation in the index $\ell_{\max}$ we had to choose to get sufficiently accurate results, with the inverse aspect ratio: the lower the aspect ratio $\frac{L}{R}$, the slower the convergence of the truncated result to $\ell_{\max}$, as illustrated in **Fig. 28** (p.82). Similarly, in the long-distance limit $\frac{L}{R} \gg 1$, the convergence is very fast, and one only needs to consider modes with $\ell = 1$ to get the complete result. In this section, we will thus truncate all the operators to $\ell_{\max} = 1$, which enables to obtain simple analytical formulas.

A first interest of analytical formulas in the long-distance regime will be to check the results obtained from general numerical evaluation. The Proximity Force Approximation being a way to check the results for small values of $\frac{L}{R}$, we will thereby be able to check both opposite regimes for the aspect ratio. Besides, this formulas will be helpful to better understand the physical effects that could appear because of the finite size of the sphere: with a very small sphere, those effects should be enhanced and more universal. That will turn out to be especially the case with the introduction of a non-zero temperature and of dissipation in the materials.

The section on the long-distance limit is organised as follows: in **Section 8.1** we introduce the dipolar-simple scattering approximation, which is valid in the ($\mathcal{L} \gg R$)-limit, and apply it to the scattering formula. The simple case of perfect mirrors is first studied in **Section 8.2** for all temperatures, then the expressions are adapted in **Section 8.3** for loss-less metals described by the plasma model and in **Section 8.4** for dissipative metals described by the Drude model. The case of dielectrics is lastly treated in **Section 8.5**.

8.1 The dipolar-simple scattering approximation

In general, because of the presence of the term $e^{-2\tilde{\mathcal{L}}\tilde{\xi}\cos\theta} < e^{-2\tilde{\mathcal{L}}\tilde{\xi}}$ in each element of the scattering matrix (5.60) (p.79), coming from the translations operators, all reduced frequencies such that $\tilde{\mathcal{L}}\tilde{\xi} \gg 1$ will give a negligible contribution. The main contribution to the Casimir energy then comes from reduced frequencies $\tilde{\xi} \not\gg \frac{R}{\mathcal{L}}$, which will be noted $\tilde{\xi} \lesssim \frac{R}{\mathcal{L}}$ from now on.

In the particular case of the here studied long-distance limit, $\frac{R}{\mathcal{L}} \ll 1$ yields only frequencies such that $\tilde{\xi} \ll 1$ play an important role in the Casimir effect. We will thus make the hypothesis $\tilde{\xi} \ll 1$ in this section. Nevertheless, the situation is slightly different from the low frequency expansion studied in **Section 7**: indeed, the term ($\tilde{\mathcal{L}}\tilde{\xi}$) was zero when the strict ($\tilde{\xi} \to 0$)-limit was considered, whereas we have ($\tilde{\mathcal{L}}\tilde{\xi}$) $\lesssim 1$ here. Another difference is that generally $\cos\theta \gg 1$ does not hold anymore here, except when the first Matsubara term is considered. In this case one must first take the strict ($\tilde{\xi} \to 0$)-limit from **Section 7.6** (p.117), then extract a long-distance expansion.

In **Section 7.1** (p.108), we have seen that the Mie coefficients of order ℓ scale as $\tilde{\xi}^{2\ell+1}$ or even higher orders for small values of the reduced frequency. It follows that the elements of matrices $\mathcal{N}$ are very small, and the dominant elements are for $\ell_1 = \ell_2 = 1$, which corroborates the hypothesis $\ell_{\max} = 1$. Using the development for the determinant around the identity matrix:

$$\det(\mathcal{I} + aX) = 1 + \mathrm{Tr}(X)a + O\left(a^2\right) \tag{8.1}$$

where a is a real scalar with $a \ll 1$, we can write for a block of the scattering operator that $\det \mathcal{D}^{(m)} \simeq 1 - \mathrm{Tr}\mathcal{M}^{(m)} = 1 - \mathrm{Tr}\mathcal{N}^{(m)}$. Then $\mathrm{Tr}\mathcal{N}^{(m)}$ is dominated by the ($\ell_1 = \ell_2 = 1$)-terms,

which only arise for $m = 0, \pm 1$. The integrand ϕ for the scattering formula then takes a simpler form:

$$\begin{aligned}\Phi(\tilde{\xi}) &= 2{\sum_m}' \ln\det \mathcal{D}^{(m)}\left(\tilde{\xi}\right) \simeq 2{\sum_m}' \ln\left(1 - \mathrm{Tr}\left[\mathcal{M}^{(m)}\left(\tilde{\xi}\right)\right]\right) \simeq -2{\sum_m}' \mathrm{Tr}\left[\mathcal{M}^{(m)}\left(\tilde{\xi}\right)\right] \\ &\simeq -\left(\mathcal{N}^{(0)}_{EE}(\tilde{\xi})\right)_{(1,1)} - \left(\mathcal{N}^{(0)}_{MM}(\tilde{\xi})\right)_{(1,1)} - 2\left(\mathcal{N}^{(1)}_{EE}(\tilde{\xi})\right)_{(1,1)} - 2\left(\mathcal{N}^{(1)}_{MM}(\tilde{\xi})\right)_{(1,1)} . \end{aligned} \tag{8.2}$$

This approximation can be understood as a double simplification in the scattering process: first we discarded multiple scattering when we simplified $\ln\det(\mathcal{I} - \mathcal{N}) = \mathrm{Tr}\ln(\mathcal{I} - \mathcal{N})$ to $\mathrm{Tr}(-\mathcal{N})$, as it is equivalent to the simplification $\ln(\mathcal{I} - \mathcal{N}) = -\sum_{k\geq 1}\mathcal{N}^k/k = -\mathcal{N}$ by keeping only the first term. Second we reduced the scattering on the sphere to a dipole approximation by only keeping terms with $\ell = 1$. Those two simplifications are physically reasonable in the $(\mathcal{L} \gg R)$-regime, as a smaller sphere yields a less-stable pseudo-cavity for the propagating fields, and its reflective properties are close to the ones of a dipole. From the expression (5.60) (p.79) of the operator $\mathcal{N}$, the four terms of Eq.(8.2) read:

$$\begin{aligned}\left(\mathcal{N}^{(0)}_{EE}(\tilde{\xi})\right)_{1,1} &= \sqrt{\frac{3\pi}{2}} a_1(\tilde{\xi}) B^{(0)}_{1,1,\mathrm{TM}}(\tilde{\xi}) \\ \left(\mathcal{N}^{(0)}_{MM}(\tilde{\xi})\right)_{1,1} &= \sqrt{\frac{3\pi}{2}} b_1(\tilde{\xi}) B^{(0)}_{1,1,\mathrm{TE}}(\tilde{\xi}) \\ \left(\mathcal{N}^{(1)}_{EE}(\tilde{\xi})\right)_{1,1} &= \sqrt{\frac{3\pi}{2}} a_1(\tilde{\xi}) \left[A^{(1)}_{1,1,\mathrm{TE}}(\tilde{\xi}) + B^{(1)}_{1,1,\mathrm{TM}}(\tilde{\xi})\right] \\ \left(\mathcal{N}^{(1)}_{MM}(\tilde{\xi})\right)_{1,1} &= \sqrt{\frac{3\pi}{2}} b_1(\tilde{\xi}) \left[A^{(1)}_{1,1,\mathrm{TM}}(\tilde{\xi}) + B^{(1)}_{1,1,\mathrm{TE}}(\tilde{\xi})\right] . \end{aligned}$$

Those expressions only contain three A and B blocks, defined in Eqs.(5.55) (p.78). We recall their expression for those involved:

$$\begin{aligned} B^{(0)}_{1,1,p}(\tilde{\xi}) &= \int_1^\infty d\cos\theta \; d_0^{1,s}[\mathrm{dif}] \; \partial_\theta Y^s_{1,0}(\theta) \; r_p(\tilde{\xi},\theta) \; e^{-2\tilde{\xi}\tilde{\mathcal{L}}\cos\theta} \\ A^{(1)}_{1,1,p}(\tilde{\xi}) &= -\int_1^\infty \frac{d\cos\theta}{s(\theta)} \; d_1^{1,s}[\mathrm{sum}] \; Y^s_{1,1}(\theta) \; r_p(\tilde{\xi},\theta) \; e^{-2\tilde{\xi}\tilde{\mathcal{L}}\cos\theta} \\ B^{(1)}_{1,1,p}(\tilde{\xi}) &= \int_1^\infty d\cos\theta \; d_1^{1,s}[\mathrm{dif}] \; \partial_\theta Y^s_{1,1}(\theta) \; r_p(\tilde{\xi},\theta) \; e^{-2\tilde{\xi}\tilde{\mathcal{L}}\cos\theta} . \end{aligned}$$

The finite rotation and spherical harmonics terms for $\ell = 1$ read:

$$\begin{aligned} d_0^{1,s}[\mathrm{dif}] &= -\sqrt{2}s(\theta) & \partial_\theta Y^s_{1,0}(\theta) &= \sqrt{\frac{3}{4\pi}}s(\theta) \\ d_1^{1,s}[\mathrm{sum}] &= 1 & Y^s_{1,1}(\theta) &= -\sqrt{\frac{3}{8\pi}}s(\theta) \\ d_1^{1,s}[\mathrm{dif}] &= \cos\theta & \partial_\theta Y^s_{1,1}(\theta) &= -\sqrt{\frac{3}{8\pi}}\cos\theta . \end{aligned}$$

and by incorporating those expressions in the A and B blocks, we obtain from Eq.(8.2) the integrand Φ_{LD} for the Casimir energy E and free-energy $\mathcal{F}$:

$$\begin{aligned}\Phi_{\mathrm{LD}}(\tilde{\xi}) = \frac{3}{2}\int_1^\infty \mathrm{d}\cos\theta e^{-2\tilde{\xi}\tilde{\mathcal{L}}\cos\theta} \\ \times \left[a_1(\tilde{\xi})\left(r_{\mathrm{TM}}(2\cos^2\theta - 1) - r_{\mathrm{TE}}\right) + b_1(\tilde{\xi})\left(r_{\mathrm{TE}}(2\cos^2\theta - 1) - r_{\mathrm{TM}}\right)\right] . \end{aligned} \tag{8.3}$$

For the latter, we can obtain the explicit expression for $\ell = 1$ without use of special functions, thanks to the functions:

$$I_{1/2}(x) = \sqrt{\frac{2}{\pi x}}\sinh x \qquad K_{1/2}(x) = \sqrt{\frac{\pi}{2x}}e^{-x}$$
$$I_{3/2}(x) = \sqrt{\frac{2}{\pi x}}\left(\cosh x - \frac{\sinh x}{x}\right) \qquad K_{3/2}(x) = \sqrt{\frac{\pi}{2x}}\left(1+\frac{1}{x}\right)e^{-x}\,. \tag{8.4}$$

Incorporating these functions in their expression (5.38) (p.72), we obtain the explicit forms:

$$a_1(\tilde\xi) = \frac{\sinh(n\tilde\xi)\cosh(\tilde\xi)\left(\tilde\xi + n^2(\tilde\xi^3-\tilde\xi)\right) + \sinh(\tilde\xi)\cosh(n\tilde\xi)\left(n\tilde\xi - n^3(\tilde\xi+\tilde\xi^3)\right)}{\cosh(n\tilde\xi)\left(n^3(\tilde\xi+\tilde\xi^2+\tilde\xi^3) - n(\tilde\xi+\tilde\xi^2)\right)}\cdots$$
$$\cdots\frac{+\sinh(n\tilde\xi)\sinh(\tilde\xi)\left(n^2-1\right) + \cosh(n\tilde\xi)\cosh(\tilde\xi)\left(\tilde\xi^2(n^2-n)\right)}{+\sinh(n\tilde\xi)\left(1+\tilde\xi+n^2(-1-\tilde\xi+\tilde\xi^3)\right)}e^{\tilde\xi}$$

$$b_1(\tilde\xi) = \frac{n^2\tilde\xi\sinh(n\tilde\xi)\cosh(\tilde\xi) - n\tilde\xi\sinh(\tilde\xi)\cosh(n\tilde\xi) - (n^2-1)\sinh(n\tilde\xi)\sinh(\tilde\xi)}{n\tilde\xi\cosh(n\tilde\xi)+\sinh(n\tilde\xi)\left(n^2(1+\tilde\xi)-1\right)}e^{\tilde\xi} \tag{8.5}$$

and for perfect mirrors, they simplify to:

$$a_1(\tilde\xi) = \frac{\tilde\xi\cosh(\tilde\xi) - \sinh(\tilde\xi) - \tilde\xi^2\sinh(\tilde\xi)}{1+\tilde\xi+\tilde\xi^2}e^{\tilde\xi} \qquad b_1(\tilde\xi) = \frac{\tilde\xi\cosh(\tilde\xi)-\sinh(\tilde\xi)}{1+\tilde\xi}e^{\tilde\xi}\,. \tag{8.6}$$

The general formula (8.3) is valid for any materials, as soon as the sphere is far from the plane, and can be used to obtain the Casimir energy and free-energy. For specific materials, it is possible to go further in the analytical derivation, by specifying the Fresnel and Mie coefficients. This dependance on the material properties is visible in Eq.(8.5), where for taking the low-$\tilde\xi$ expansion one needs to specify the dependance of the refractive index n with respect to $\tilde\xi$.

We begin with the simple case of perfect mirrors, in order to obtain from (8.3) explicit and simple expressions for the Casimir energy E and free-energy $\mathcal{F}$ in the long-distance limit. Then the cases of metals with plasma or Drude models, and of dielectrics, will be discussed from the results with perfect mirrors.

8.2 Perfect mirrors

For perfectly reflecting mirrors, the Fresnel coefficients are simply $r_{\rm TE} = -1, r_{\rm TM} = 1$, as discussed in **Section 5.2.1** (p.70), and the Mie coefficients are given by (8.6). We can now use the fact that $\tilde\xi \ll 1$ to obtain the expansions:

$$a_1(\tilde\xi) = -\frac{2}{3}\tilde\xi^3 + \frac{1}{5}\tilde\xi^5 - \frac{4}{9}\tilde\xi^6 + \frac{1}{7}\tilde\xi^7 + \mathcal{O}\left(\tilde\xi^8\right)$$
$$b_1(\tilde\xi) = \frac{1}{3}\tilde\xi^3 + \frac{1}{5}\tilde\xi^5 - \frac{1}{9}\tilde\xi^6 + \frac{1}{7}\tilde\xi^7 + \mathcal{O}\left(\tilde\xi^8\right) \tag{8.7}$$

where we give a few orders for illustrative purpose, but only keep the dominant term in $\tilde\xi^3$. Incorporating those in Eq.(8.3) for a small but non-zero reduced frequency $\tilde\xi$, we get the integrand:

$$\Phi_{\rm LD}^{\rm perf}(\tilde\xi) = -3\tilde\xi^3\int_1^\infty {\rm d}\cos\theta\ \cos^2\theta\ e^{-2\tilde\xi\tilde{\mathcal{L}}\cos\theta}$$
$$= -\frac{3}{4}\frac{1}{\tilde{\mathcal{L}}^3}\left(1+2\tilde\xi\tilde{\mathcal{L}}+2\left(\tilde\xi\tilde{\mathcal{L}}\right)^2\right)e^{-2\tilde\xi\tilde{\mathcal{L}}} \tag{8.8}$$

The first Matsubara term $\tilde{\xi}_0 = 0$ is obtained by first taking the $(\tilde{\xi} \to 0)$-limit of the general integrand Φ, then using the long-distance limit, as described in Eqs.(7.35) (p.119) and we recall its expression in the case of perfect mirrors:

$$\Phi^{\text{perf}}_{\text{LD}}(0) = -\frac{3R^3}{4\mathcal{L}^3} \,. \tag{8.9}$$

We remark that this corresponds to the $(\tilde{\xi} \to 0)$-limit of (8.8). This result was not obvious and is equivalent to say that the two limits $\tilde{\xi} \to 0$ and $\frac{\mathcal{L}}{R} \to \infty$ do commute. In the following, we will then use the expression (8.8) for the intergand over the whole range of frequencies $\tilde{\xi} \leq 0$, including the zero frequency.

- In the case of low temperatures ($L \ll \lambda_T$), the Matsubara sum converges to the continuous integral of the $(T = 0)$-case. We can then use the integral $(a > 0)$:

$$\int_0^\infty dx \left(1 + 2ax + 2a^2x^2\right) e^{-2ax} = \frac{3}{2a}$$

  with $a = \tilde{\mathcal{L}} = \frac{\mathcal{L}}{R}$, to finally obtain the long-distance expansion of the Casimir energy:

$$E^{\text{perf}}_{\text{LD}} = \frac{\hbar c}{2\pi R} \int_0^\infty d\tilde{\xi} \Phi^{\text{perf}}_{\text{LD}}(\tilde{\xi}) = -\frac{9\hbar c R^3}{16\pi \mathcal{L}^4} \quad ; \quad (R \ll L \ll \lambda_T) \tag{8.10}$$

  which is in agreement with [228, eq.(12)].

- In the high-temperature limit ($L \gg \lambda_T$), where only the first Matsubara frequency $\tilde{\xi}_0$ is kept in the Matsubara sum, we already derived the result (7.35) (p.119) in the previous section, which we rewrite as:

$$\mathcal{F}^{\text{perf}}_{\text{LD,HT}} = -\frac{3k_BTR^3}{8\mathcal{L}^3} = -\frac{3\hbar c R^3}{8\lambda_T \mathcal{L}^3} \quad ; \quad (R, \lambda_T \ll L) \tag{8.11}$$

  This last result is more realistic in the long-distance regime, as for a fixed temperature, we always get to the $(\mathcal{L} \gg \lambda_T)$-regime when increasing the distance. It is not always possible, in contrast, to have in practice an intermediate regime of distances $(R \ll L \ll \lambda_T)$ when R and λ_T differ by only a few orders of magnitude.

  We remark that the high-temperature free-energy (8.11) is linear with T and does not contain anymore $\hbar$. This feature is always fulfilled in the high-temperature regime, regardless of the aspect ratio $\frac{L}{R}$, thanks to the reduction of the Matsubara sum for the scattering formula to $\frac{k_BT}{2}\Phi(0)$. Physically, this is due to the fact that in the high-temperature regime thermal fluctuations dominate the quantum ones, the Casimir is then a purely classical effect, and as thermal fluctuations are proportional to the temperature, so is the Casimir effect.

  An other observation is that we lose an order in $\mathcal{L}$ in the decaying of the free-energy: while the $(T = 0)$-expression in (8.10) had a $\mathcal{L}^{-4}$-decay at large separation, the high-temperature limit has a $\mathcal{L}^{-3}$-decay. The introduction of the thermal length λ_T enables the expression to keep the dimension of an energy.

- For the non-zero temperature case, using the Matsubara summation (3.4) (p.48) for the long-distance expansion of the integrand (8.8), we obtain the following series:

$$\mathcal{F}^{\text{perf}}_{\text{LD}} = -\frac{3k_BTR^3}{4\mathcal{L}^3} {\sum_n}' \left(1 + 2(\tilde{\xi}_n\tilde{\mathcal{L}}) + 2(\tilde{\xi}_n\tilde{\mathcal{L}})^2\right) e^{-2\tilde{\xi}_n\tilde{\mathcal{L}}}$$

with $\tilde{\xi}_n\tilde{\mathcal{L}} = n\frac{2\pi\mathcal{L}}{\lambda_T} = n\nu$. The parameter ν measures the influence of temperature on the Casimir effect: for very low values ($\nu \ll 1$) the discrete sum converges to the integral and the Casimir free-energy to the ($T = 0$)-energy, while for large values ($\nu \gg 1$) we enter the high-temperature regime studied above.

Prop. 14

$$\begin{aligned}\phi(\nu) &= {\sum_n}' \left(1 + 2\nu n + 2\nu^2 n^2\right) e^{-2\nu n} \\ &= \frac{1 + e^{-2\nu}(-1 + 4\nu + 4\nu^2) + e^{-4\nu}(-1 - 4\nu + 4\nu^2) + e^{-6\nu}}{2(1 - e^{-2\nu})^3} \qquad (8.12) \\ &= \frac{\nu \sinh\nu + \cosh\nu\left(\nu^2 + \sinh^2\nu\right)}{2\sinh^3\nu} \qquad (8.13)\end{aligned}$$

(For proof, see **Appendix A.8** p.217)

Then the long-distance expansion of the Casimir free-energy $\mathcal{F}_{\rm LD}^{\rm perf}$ for perfect mirrors, valid for any temperature T, reads:

$$\mathcal{F}_{\rm LD}^{\rm perf} = -\frac{3\hbar c R^3}{4\lambda_T \mathcal{L}^3}\phi\left(\frac{2\pi\mathcal{L}}{\lambda_T}\right) \quad ; \quad (\mathcal{L} \gg R) \qquad (8.14)$$

where $\nu = \frac{2\pi\mathcal{L}}{\lambda_T}$, and $\phi(\nu)$ can be expressed by (8.12) or (8.13). We remark that this result is very general, because it contains the low-temperature result (8.10) and the high-temperature result (8.11), as limiting cases:

$$\phi(\nu) \sim \frac{3}{2\nu} \text{ when } \nu \ll 1 \qquad\qquad \phi(\nu) \sim \frac{1}{2} \text{ when } \nu \gg 1$$

At low temperatures, with a low-$\tilde{\xi}$ expansion of the function ϕ, we can go further in the low-temperature expansion of the free-energy:

$$\begin{aligned}\phi(\nu) &= \frac{3}{2}\nu^{-1} - \frac{1}{90}\nu^3 + \frac{2}{315}\nu^5 - \frac{1}{630}\nu^7 + \mathcal{O}\left(\nu^9\right) \\ \mathcal{F}_{\rm LD}^{\rm perf} &= -\frac{9\hbar c R^3}{16\pi\mathcal{L}^4}\left(\frac{2}{3}\nu\phi(\nu)\right) \\ &= -\frac{9\hbar c R^3}{16\pi\mathcal{L}^4}\left[1 - \frac{1}{135}\left(\frac{2\pi\mathcal{L}}{\lambda_T}\right)^4 + \frac{4}{945}\left(\frac{2\pi\mathcal{L}}{\lambda_T}\right)^6 - \frac{1}{945}\left(\frac{2\pi\mathcal{L}}{\lambda_T}\right)^8 + \mathcal{O}\left(\left(\frac{\mathcal{L}}{\lambda_T}\right)^{10}\right)\right]\end{aligned} \qquad (8.15)$$

where the leading order expansion gives back (8.10). The following order terms allow to write the difference between the free-energy and the ($T = 0$)-energy for low temperatures:

$$\mathcal{F}_{\rm LD}^{\rm perf} - E_{\rm LD}^{\rm perf} = \frac{\hbar c\pi^3 R^3}{45\lambda_T^4}\left[1 - \frac{144\pi^2\mathcal{L}^2}{21\lambda_T^2} + \frac{144\pi^4\mathcal{L}^4}{21\lambda_T^4} + \mathcal{O}\left(\left(\frac{\mathcal{L}}{\lambda_T}\right)^6\right)\right] . \qquad (8.16)$$

The first term in this expansion is in agreement with [229, eq.(83)].

By taking the derivative of all former expressions for the Casimir free-energy with respect to the distance $\mathcal{L}$ or temperature T, it is possible to obtain similar results for the Casimir force F, force gradient G, and entropy $\mathcal{S}$, summed up in **Table 10**. Let us observe that the first correction in

	T	$T=0$	high temperature
$\mathcal{F}$	$-\frac{3\hbar c R^3}{4\lambda_T \mathcal{L}^3}\phi(\nu)$	$-\frac{9\hbar c R^3}{16\pi \mathcal{L}^4}$	$-\frac{3\hbar c R^3}{8\lambda_T \mathcal{L}^3}$
F	$-\frac{3\hbar c R^3}{4\lambda_T \mathcal{L}^4}\left(3\phi(\nu)-\nu\phi'(\nu)\right)$	$-\frac{9\hbar c R^3}{4\pi \mathcal{L}^5}$	$-\frac{9\hbar c R^3}{8\lambda_T \mathcal{L}^4}$
G	$-\frac{3\hbar c R^3}{4\lambda_T \mathcal{L}^5}\left(12\phi(\nu)-6\nu\phi'(\nu)+\nu^2\phi''(\nu)\right)$	$-\frac{45\hbar c R^3}{4\pi \mathcal{L}^6}$	$-\frac{9\hbar c R^3}{2\lambda_T \mathcal{L}^5}$
$\mathcal{S}$	$\frac{3k_B R^3}{4\mathcal{L}^3}\left(\phi(\nu)+\nu\phi'(\nu)\right)$	0	$\frac{3k_B R^3}{8\mathcal{L}^3}$

Table 10: Summary of long-distance expansions for the Casimir quantities with perfect mirrors.

(8.15) is $\mathcal{L}$-independent, and will not appear in F, nor in G. The derivatives of ϕ have the explicit expressions:

$$\phi'(\nu) = -\frac{4\nu^2\left(e^{-2\nu}+4e^{-4\nu}+e^{-6\nu}\right)}{(1-e^{-2\nu})^4} \tag{8.17}$$

$$\phi''(\nu) = -\frac{8\nu\left(e^{-2\nu}(-1+\nu)+e^{-4\nu}(-3+11\nu)+e^{-6\nu}(3+11\nu)+e^{-8\nu}(1+\nu)\right)}{(1-e^{-2\nu})^5} \tag{8.18}$$

with the asymptotic expansions:

$$\phi'(\nu)\sim -\frac{3}{2\nu^2} \quad \text{when } \nu\ll 1 \qquad\qquad \phi'(\nu)\sim -4\nu e^{-2\nu} \quad \text{when } \nu\gg 1$$

$$\phi''(\nu)\sim \frac{3}{\nu^3} \quad \text{when } \nu\ll 1 \qquad\qquad \phi''(\nu)\sim -8\nu^2 e^{-2\nu} \quad \text{when } \nu\gg 1$$

For future analysis, we define the thermal factor $\vartheta_X = \frac{X(T)}{X(0)}$ to measure the effect of temperature on the Casimir interaction. Their long-distance limit for $X=\mathcal{F},F,G$ is then, from **Table 10**:

$$\begin{aligned}
\vartheta_{\mathcal{F}} &= \frac{2}{3}\nu\phi(\nu)\\
\vartheta_F &= \frac{\nu}{2}\phi(\nu)-\frac{\nu^2}{6}\phi'(\nu)\\
\vartheta_G &= \frac{2\nu}{5}\phi(\nu)-\frac{\nu^2}{5}\phi'(\nu)+\frac{\nu^3}{30}\phi''(\nu)\ .
\end{aligned} \tag{8.19}$$

We can also define a thermal factor for the entropy, but with respect to the high-temperature case which is non-zero:

$$\vartheta_{\mathcal{S}} = \frac{\mathcal{S}(T)}{\mathcal{S}(T\to\infty)} = 2\left(\phi(\nu)+\nu\phi'(\nu)\right) \tag{8.20}$$

Those four thermal factors are presented in **Fig. 40**, as functions of the thermal parameter $\nu = 2\pi\frac{\mathcal{L}}{\lambda_T}$. We observe that all curves have a non-monotonic behaviour: they decrease to a minimum before being increasing again for large values of ν. The positions and values of the minima are given in **Table 11**. The ϑ_G-curve has a specificity: it first slightly increases for very small values of ν, to reach a maximum before going down to its minimum value.

By analysing the low-ν expansions of ϕ and its derivatives, we can obtain the low-temperature expansions for the thermal factors:

$$\vartheta_{\mathcal{F}} = 1-\frac{1}{135}\nu^4+\frac{4}{945}\nu^6-\frac{1}{945}\nu^8+\mathcal{O}\left(\nu^{10}\right) \qquad \vartheta_F = 1-\frac{2}{945}\nu^6+\frac{1}{945}\nu^8+\mathcal{O}\left(\nu^{10}\right)$$

$$\vartheta_G = 1+\frac{2}{4725}\nu^6-\frac{1}{1975}\nu^8+\mathcal{O}\left(\nu^{10}\right) \qquad \vartheta_{\mathcal{S}} = -\frac{4}{45}\nu^3+\frac{8}{105}\nu^5-\frac{8}{315}\nu^7+\mathcal{O}\left(\nu^9\right) \tag{8.21}$$

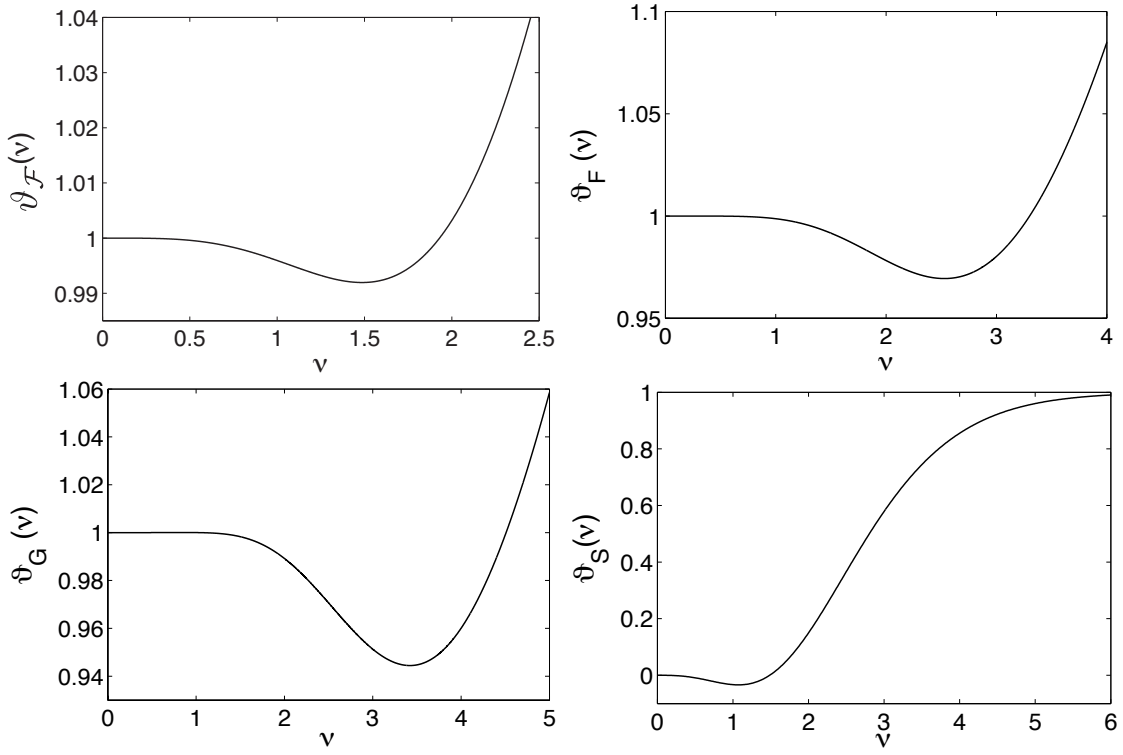

Figure 40: Thermal factors $\vartheta_{\mathcal{F}}, \vartheta_F, \vartheta_G$, and $\vartheta_{\mathcal{S}}$ as functions of $\nu = \frac{2\pi\mathcal{L}}{\lambda_T}$.

	$\vartheta_{\mathcal{F}}$	ϑ_F	ϑ_G	$\vartheta_{\mathcal{S}}$
$\nu_{\min}$	1.49	2.53	3.42	1.07
$\vartheta(\nu_{\min})$	0.9919	0.9694	0.9445	-0.0339

Table 11: Minimum position and value for the thermal factors $\vartheta_{\mathcal{F}}, \vartheta_F, \vartheta_G$, and $\vartheta_{\mathcal{S}}$.

and so can we for the high-temperature expansions:

$$\vartheta_{\mathcal{F}} \simeq \frac{\nu}{3} \qquad \vartheta_F \simeq \frac{\nu}{4} \qquad \vartheta_G \simeq \frac{\nu}{5} \qquad \vartheta_{\mathcal{S}} \simeq 1 \tag{8.22}$$

8.3 Metallic scatterers modelled with the plasma model

We now consider the case of metallic mirrors, modelled by a loss-less plasma model. This description is fully contained in the dielectric function, introduced in **Section 2.2** (p.39):

$$\varepsilon^{\text{plas}}(\tilde{\xi}) = 1 + \frac{\alpha^2}{\tilde{\xi}^2} \quad \text{with} \quad \alpha = 2\pi\frac{R}{\lambda_P}$$

and here we aim at expressing the integrand in (8.3) more simply, and derive the corresponding Casimir free-energy. We have observed in **Section 7** that the parameters $n = \sqrt{\varepsilon}$ and $n\tilde{\xi}$ played a significant role when taking asymptotic expressions for low frequencies, and could lead to different expansions for the Fresnel and Mie coefficients.

Here we will only consider situations where $R \not\ll \lambda_P$ (or equivalently $R \gtrsim \lambda_P$), as the plasma (and Drude) model are bad description of the movement of electrons for $R \ll \lambda_P$, a situation where they should rather be confined in the sphere, as discussed in the end of **Section 2.2** (p.39). This restriction also writes $\alpha \not\ll 1$, and together with the long distance limit $\mathcal{L} \gg R$, it yields ($\mathcal{L} \gg \lambda_P$).

We first consider non-zero frequencies, the first Matsubara term will be derived from **Section 7.6** (p.117) separately, as in the previous case of perfect mirrors. From the fact that the main contribution to the energy for the integrand comes from frequencies scaling as $\tilde{\xi} \lesssim \frac{R}{L}$, we have $\alpha = \frac{2\pi R}{\lambda_P} = \frac{2\pi\mathcal{L}}{\lambda_P}\frac{R}{\mathcal{L}} \gg \frac{R}{\mathcal{L}}$ thus $\alpha \gg \tilde{\xi}$. It entails that the dielectric function ε takes very large values, and that the second important parameter ($n\tilde{\xi}$) is finite:

$$\varepsilon^{\text{plas}} - 1 = \frac{\alpha^2}{\tilde{\xi}^2} \gg 1 \qquad\qquad n\tilde{\xi} = \sqrt{\varepsilon^{\text{plas}}}\tilde{\xi} \simeq \alpha\ .$$

As $\cos\theta \not\gg 1$ (see discussion at the beginning of **Section 8** p.124) , $\frac{\varepsilon^{\text{plas}}-1}{\cos^2\theta} \gg 1$ and the Fresnel coefficients are the same as in the perfect reflectors case: $r_{\text{TE}} = -1$ and $r_{\text{TM}} = 1$. The Mie coefficients are described by (8.5) (p.126), and in order to get properly their expansion for small $\tilde{\xi}$, we replace the terms $n\tilde{\xi}$ by α that remain finite, and replace n by $\frac{\alpha}{\tilde{\xi}}$. When doing so, we obtain the following expansion:

$$\begin{aligned}
a_1(\tilde{\xi}) &= -\frac{2}{3}\tilde{\xi}^3 + \frac{\alpha(\alpha^2-5)\cosh(\alpha) + (5+4\alpha^2)\sinh(\alpha)}{5\alpha^2(\alpha\cosh(\alpha) - \sinh(\alpha))}\tilde{\xi}^5 - \frac{4}{9}\tilde{\xi}^6 + \mathcal{O}\left(\tilde{\xi}^7\right) \\
b_1(\tilde{\xi}) &= \left(\frac{1}{3} + \frac{1}{\alpha^2} - \frac{\coth\alpha}{\alpha}\right)\tilde{\xi}^3 + \frac{\alpha(5+2\alpha^2) - 5(2\alpha^2-3)\coth(\alpha) + 15\alpha\coth(\alpha)^2}{10\alpha^3}\tilde{\xi}^5 \\
&\quad - \left(\frac{1}{3} + \frac{1}{\alpha^2} - \frac{\coth\alpha}{\alpha}\right)^2\tilde{\xi}^6 + \mathcal{O}\left(\tilde{\xi}^7\right)
\end{aligned} \tag{8.23}$$

Incorporating the leading order, proportional to $\tilde{\xi}^3$, together with the former Fresnel coefficients, in Eq.(8.3), we get the long-distance expansion of the integrand $\Phi_{\text{LD}}^{\text{plas}}(\tilde{\xi})$ for non-zero frequencies:

$$\begin{aligned}
\Phi_{\text{LD}}^{\text{plas}}(\tilde{\xi}) &= -3\tilde{\xi}^3\left(1 + \frac{1}{\alpha^2} - \frac{\coth\alpha}{\alpha}\right)\int_1^\infty \mathrm{d}\cos\theta\ \cos^2\theta\ e^{-2\tilde{\xi}\tilde{\mathcal{L}}\cos\theta} \\
&= -\frac{3}{4}\frac{1}{\tilde{\mathcal{L}}^3}\left(1 + \frac{1}{\alpha^2} - \frac{\coth\alpha}{\alpha}\right)\left(1 + 2\tilde{\xi}\tilde{\mathcal{L}} + 2\left(\tilde{\xi}\tilde{\mathcal{L}}\right)^2\right)e^{-2\tilde{\xi}\tilde{\mathcal{L}}}
\end{aligned} \tag{8.24}$$

which is the same as (8.8) multiplied by the function $f(\alpha) = 1 + \frac{1}{\alpha^2} - \frac{\coth\alpha}{\alpha}$.

The first Matsubara term ($\tilde{\xi} = 0$) has been derived in Eq.(7.39), and read:

$$\Phi_{\rm LD}^{\rm plas}(0) = -\frac{3}{4}\frac{R^3}{\mathcal{L}^3} f(\alpha) \tag{8.25}$$

which is again the same as the perfect mirrors result (8.9), multiplied by the factor $f(\alpha)$. Moreover, it can also be obtained by taking the continuous ($\tilde{\xi} \to 0$)-limit in the non-zero frequency expression (8.24), which validity can be extended for any $\tilde{\xi} \geq 0$.

It follows that all results previously derived for the perfect mirrors can be adapted to the plasma case with a multiplication by $f(\alpha) = 1 + \frac{1}{\alpha^2} - \frac{\coth\alpha}{\alpha}$. This factor that compares the radius R of the sphere with the plasma length λ_P is presented in **Fig. 41** as a function of α. The function

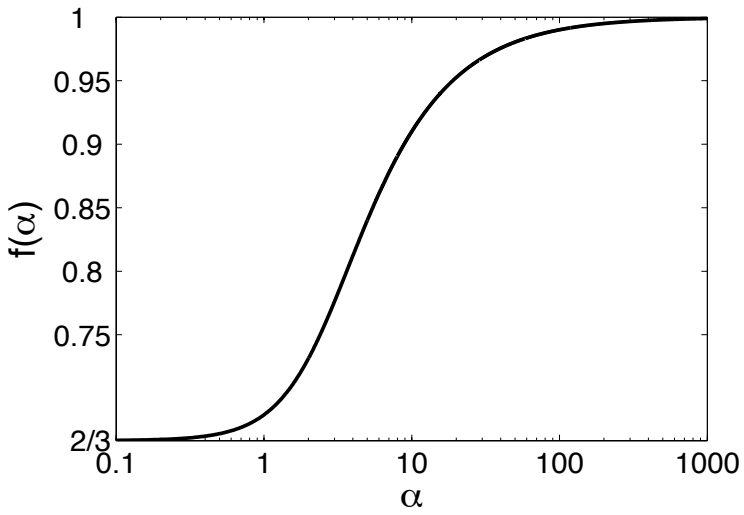

Figure 41: Function $f(\alpha) = \frac{\mathcal{F}_{\rm LD}^{\rm plas}}{\mathcal{F}_{\rm LD}^{\rm perf}} = 1 + \frac{1}{\alpha^2} - \frac{\coth\alpha}{\alpha}$ as a function of $\alpha = 2\pi\frac{R}{\lambda_P}$, valid for any temperatures at the large-distance limit ($\mathcal{L} \gg R$).

f appears to be a monotonically increasing function, from $\frac{2}{3}$ to 1. For a large highly-reflecting sphere ($\lambda_P \ll R$), $\alpha \gg 1$ and we find $f(\alpha) \simeq 1$, meaning that the perfect mirrors case is strictly recovered. In the plane-plane case, this recovery happens when ($\lambda_P \ll \mathcal{L}$) only. The additional condition ($\lambda_P \ll R$) in the sphere-plane configuration is therefore a new result. Here we observe a very important feature of the plane-sphere geometry that comes from the finite size of the sphere: the perfectly reflecting limit for the Casimir effect is obtained when λ_P is small not only compared to $\mathcal{L}$, to get perfect reflection on the plane, but also compared to R, to obtain perfect reflection on the sphere. The ratio $f(\alpha)$ comes from the form of the magnetic Mie coefficient b_1 and will reveal very fundamental for this geometry.

For a small poorly-reflecting sphere[12] ($R \ll \lambda_P$), $\alpha \ll 1$ and the function f decreases to a minimum value $\frac{2}{3}$ for $\alpha \to 0$.

8.4 Metallic scatterers modelled with the Drude model

We now consider the Drude model that includes dissipation in the description of the materials. The dielectric function $\varepsilon^{\rm Drud}(\tilde{\xi})$, introduced in **Section 2.3** (p.41), is such that

$$\varepsilon^{\rm Drud} - 1 = \frac{1}{(\tilde{\xi}/\alpha)^2 + \delta\tilde{\xi}/\alpha} \quad , \quad \text{with} \quad \alpha = \frac{2\pi R}{\lambda_P} \quad \text{and} \quad \delta = \frac{\lambda_P}{\lambda_\gamma} \ .$$

[12]Let us repeat that this case is however out of scope for metallic spheres, as the confinement of electrons inside the sphere is not modelled correctly by the permittivity function.

Again, we will restrict ourselves to the situation where $R \ll \lambda_P$ for the optical properties of the metal to be well described by a Drude model, yielding together with $(\mathcal{L} \gg R)$ that $(\mathcal{L} \gg \lambda_P)$.

We first consider the special case $\left(\mathcal{L} \gg R, \frac{\lambda_P^2}{\lambda_\gamma}, \frac{R^2\lambda_\gamma}{\lambda_P^2}\right)$ by making two additional long-distance assumptions:

$$\text{(HYP1)}: \quad \mathcal{L} \gg \frac{\lambda_P^2}{\lambda_\gamma} \qquad\qquad \text{(HYP2)}: \quad \mathcal{L} \gg \frac{R^2\lambda_\gamma}{\lambda_P^2} \tag{8.26}$$

and from (HYP2), together with $R \ll \lambda_P$, we get $(\mathcal{L} \gg \lambda_\gamma)$. It is reasonable to do such assumptions, as we are interested in the long-distance regime, and we can take $\mathcal{L}$ as large as we want. The first assumption (HYP1) $\mathcal{L} \gg (\delta\lambda_P)$ is easily checked for usual metals, as $\delta = \frac{\lambda_P}{\lambda_\gamma}$ is generally small (see **Table 1** p.42). But the second (HYP2) $\mathcal{L} \gg \left(R\frac{R}{\lambda_P}\frac{1}{\delta}\right)$ is more restrictive, as $\frac{R}{\lambda_P} \gtrsim 1$ and $\frac{1}{\delta}$ is large.

We first only consider non-zero frequencies, the first Matsubara term $\tilde{\xi}_0 = 0$ will be derived from **Section 7.6** (p.117) later on. The denominator in $\varepsilon - 1$ contains the terms $\frac{\tilde{\xi}}{\alpha} = \frac{\lambda_P\tilde{\xi}}{2\pi R} \lesssim \frac{\lambda_P}{2\pi\mathcal{L}} \ll 1$, and $\frac{\delta\tilde{\xi}}{\alpha} = \frac{\lambda_P^2}{2\pi R\lambda_\gamma}\tilde{\xi} \lesssim \frac{\lambda_P^2}{2\pi\lambda_\gamma\mathcal{L}} \ll 1$ from (HYP1). Finally $\varepsilon - 1 \gg 1$, and the Fresnel coefficients are again $r_{\text{TE}} = -1$ and $r_{\text{TM}} = 1$, like in the case of perfect mirrors.

We now study the parameter:

$$n\tilde{\xi} = \sqrt{\varepsilon^{\text{Drud}}}\,\tilde{\xi} \simeq \sqrt{\varepsilon^{\text{Drud}} - 1}\,\tilde{\xi} = \frac{\tilde{\xi}}{\sqrt{\left(\frac{\tilde{\xi}}{\alpha}\right)^2 + \delta\frac{\tilde{\xi}}{\alpha}}} = \frac{\alpha}{\sqrt{1 + \frac{\alpha\delta}{\tilde{\xi}}}} \simeq \sqrt{\frac{\alpha\tilde{\xi}}{\delta}}$$

where the last expression comes from the fact that using $(\mathcal{L} \gg \lambda_\gamma)$, we have in the denominator $\frac{\alpha\delta}{\tilde{\xi}} = \frac{2\pi R}{\lambda_\gamma}\frac{1}{\tilde{\xi}} \gtrsim \frac{2\pi\mathcal{L}}{\lambda_\gamma} \gg 1$. Then, using (HYP2), we can write $\frac{\alpha\tilde{\xi}}{\delta} = \frac{2\pi R\lambda_\gamma}{\lambda_p^2}\tilde{\xi} \lesssim \frac{2\pi R^2\lambda_\gamma}{\lambda_P^2\mathcal{L}} \ll 1$, and finally $n\tilde{\xi} \ll 1$. From the Mie coefficients in Eq.(8.5) (p.126), we take an expansion for small $\tilde{\xi}$, by replacing $\left(n\tilde{\xi} \to \sqrt{\frac{\alpha\tilde{\xi}}{\delta}}\right)$ and $\left(n \to \sqrt{\frac{\alpha}{\delta\tilde{\xi}}}\right)$. Doing so, we get the following expansions:

$$\begin{aligned} a_1(\tilde{\xi}) &= -\frac{2}{3}\tilde{\xi}^3 + 2\frac{\delta}{\alpha}\tilde{\xi}^4 + \left(\frac{2}{5} - 4\left(\frac{\delta}{\alpha}\right)^2\right)\tilde{\xi}^5 + \mathcal{O}\left(\tilde{\xi}^6\right) \\ b_1(\tilde{\xi}) &= \frac{1}{45}\frac{\alpha}{\delta}\tilde{\xi}^4 + \left(-\frac{2}{945}\left(\frac{\alpha}{\delta}\right)^2 - \frac{1}{45}\right)\tilde{\xi}^5 + \left(\frac{1}{4725}\left(\frac{\alpha}{\delta}\right)^3 + \frac{1}{135}\frac{\alpha}{\delta}\right)\tilde{\xi}^6 + \mathcal{O}\left(\tilde{\xi}^7\right) \end{aligned} \tag{8.27}$$

where we clearly see that we need $\frac{\delta\tilde{\xi}}{\alpha} \ll 1$ thanks to (HYP1) for a_1, and $\frac{\alpha\tilde{\xi}}{\delta} \ll 1$ thanks to (HYP2) for b_1 to consider these expressions as expansions.

In the following we will only keep the dominant term for the a_1-coefficient, and consider the dominant term of the b_1-coefficient to be negligible because $\frac{\alpha\tilde{\xi}}{\delta} \ll 1$. Incorporating the dominant term of the a_1-coefficient with the Fresnel coefficients in Eq.(8.3) (p.125), we get the long-distance expansion of the integrand $\Phi_{\text{LD}}^{\text{Drud}}(\tilde{\xi})$ for non-zero frequencies::

$$\begin{aligned} \Phi_{\text{LD}}^{\text{Drud}}(\tilde{\xi}) &= -2\tilde{\xi}^3\int_1^\infty \mathrm{d}\cos\theta\ \cos^2\theta\ e^{-2\tilde{\xi}\tilde{\mathcal{L}}\cos\theta} \\ &= -\frac{1}{2}\frac{1}{\tilde{\mathcal{L}}^3}\left(1 + 2\tilde{\xi}\tilde{\mathcal{L}} + 2\left(\tilde{\xi}\tilde{\mathcal{L}}\right)^2\right)e^{-2\tilde{\xi}\tilde{\mathcal{L}}} \end{aligned} \tag{8.28}$$

which is the same as the perfect mirrors result (8.8) (p.126), multiplied by the factor $\frac{2}{3}$. The first-Matsubara term has been obtained in Eq.(7.37) (p.120) and read:

$$\Phi_{\text{LD}}^{\text{Drud}}(0) = -\frac{R^3}{2\mathcal{L}^3} \tag{8.29}$$

which is again the same as the perfect mirrors result (8.9) (p.127), multiplied by the factor $\frac{2}{3}$. This result can also be obtained as the $(\tilde{\xi} \to 0)$-limit of the integrand (8.28), which is thus valid for any frequency $\tilde{\xi} \geq 0$.

From Eq.(8.28) it follows that all results previously derived for the perfect mirrors can be adapted to the Drude case through a multiplication by $\frac{2}{3}$. We observe that this result does not depend[13] on the ratio $\frac{R}{\lambda_P}$, unlike the plasma case. The long-distance behaviour is here more universal with the inclusion of dissipation, than for the lossless model.

If we now consider a more general situation where we remove the former assumptions (HYP1) and (HYP2), the situation becomes more complicated, as we cannot say anymore (in the general case) that $(\varepsilon^{\text{Drud}} - 1)$ is a big number. It is then not possible to derive a simple expression for the integrand $\Phi(\tilde{\xi})$ as in the previous case, a simple example being the expansion of the Fresnel coefficients. It is however still possible to use the zero-frequency limit (8.29), because it does not contain any dependance neither on λ_P nor on λ_γ, to get the high-temperature limit $(L \gg \lambda_T)$ for the free-energy, as derived in Eq.(7.37) (p.120):

$$\mathcal{F}^{\text{Drud}}_{\text{LD,HT}} = -\frac{\hbar c R^3}{4\lambda_T \mathcal{L}^3} \quad ; \quad (\mathcal{L} \gg \lambda_T, R) \ . \tag{8.30}$$

8.5 Dielectric scatterers

We now consider the Casimir effect between two dielectric materials, whose dielectric function $\varepsilon^{\text{diel}}(\imath\xi)$ remains finite at any frequency $\tilde{\xi} \geq 0$ and converges to a finite value $\varepsilon(0)$ in the $(\tilde{\xi} \to 0)$-limit. The dielectric function is thus never a big number, and $\varepsilon^{\text{diel}} - 1 \not\gg 1$. While it is possible to expand the Mie coefficients with a finite value for n, it is not for the Fresnel coefficients. It is then not possible to get simple expressions for the long-distance regime, except for the first Matsubara term, which has been derived in Eq.(7.42) (p.122) and leads to the high-temperature free-energy:

$$\mathcal{F}^{\text{diel}}_{\text{HT,LD}} = -\frac{\hbar c R^3}{4\lambda_T \mathcal{L}^3} \frac{(\varepsilon(0) - 1)^2}{(\varepsilon(0) + 1)(\varepsilon(0) + 2)} \ . \tag{8.31}$$

[13] Apart from the initial assumption that $R \ll \lambda_P$.

Part IV.
Results at zero temperature

Table of Contents

The quantum fluctuations of the vacuum, responsible for the Casimir effect, can be separated in two parts: the zero-point energy fluctuations, and the thermal ones. The zero temperature case is then an idealization of the situation, that allows to study the purely quantum part of the Casimir effect, by considering only the contribution of quantum fluctuations.

Although not realistic for objects separated by a distance $L \gtrsim 1\mu$m, for which the thermal contribution to the Casimir free-energy is important, this removal is less determinant for the case where the objects are only separated by a few hundreds of nanometers or less. This is especially true for materials modeled by perfectly reflecting mirrors or non-dissipative metals. For dissipative metals on the other hand, an ambiant temperature of $300K$ can already have an influence on the Casimir effect for $L \gtrsim 100$ nm, as seen in **Fig. 23** (p.51).

This zero-temperature case is a first step in the complete treatment, and will allow a simpler and clearer study of the influence of geometry and finite conductivity in the material on the Casimir effect. We will thus observe carefully how the exact treatment of the geometry compares to approximations, for various materials. This section is organised as follows: we first recall in **Section 9** some of the previous works done to measure the deviation of the results obtained through the Proximity Force Approximation (PFA) from the exact quantities. We then study quickly in **Section 10** the simple case where the sphere and the plane are perfectly reflecting all frequencies. The case of metallic reflectors is then treated in **Section 11**, with a special care given on the correlations between the effects of finite conductivity and geometry. Finally, in **Section 12**,

we compare the exact results with approximations methods based on the Casimir-Polder potential, with the example of a metallic plate and a dielectric sphere.

9 Beyond-PFA computations in the literature

The Proximity Force Approximation (PFA), introduced in **Section 4** (p.55), has been used for years to obtain theoretical predictions for the Casimir force in the sphere-plane configuration, mostly in its simplest form $F_{\mathrm{PFA}}(L,R) = 2\pi R E_{\mathrm{PP}}(L)/A$, where R is the radius of the sphere, L the distance between the surfaces of the two objects, and E_{PP}/A the Casimir energy per unit area for two planes separated by a distance L. The approximation has been shown to be exact [149] in the no-curvature limit $\left(\frac{L}{R} \to 0\right)$, for perfect reflectors at zero temperature.

However, the two configurations differ in some fundamental properties: first the sphere is an object with a finite size, and creates with the plane a finite cavity. This is different from the plane-plane configuration, for which one must consider quantities per unit area, as the two objects are infinite in the x and y-directions. This finite size can also create resonance effects inside the sphere for some value of the frequency if the reflection is imperfect. Second the surface of the sphere is curved, which induces a dispersion in the scattering of light and affects resonance effects for surface waves. Finally when replacing a plane by a sphere we lose the translational invariances, and the two polarizations of the electromagnetic modes become coupled to each other in the scattering process. We may thus expect some coupling effects that are present neither with the plane-plane configuration, nor with the cylinder-plane configuration.

Moreover, the Proximity Force Approximation has for major drawback that it is difficult to estimate the difference between the approximated result and the exact one for small values of $\frac{L}{R}$. Unlike methods such as perturbation approximations or finite elements methods, one cannot say from the principles of the method if the error made by the approximation is linear $\left(\mathcal{O}\left(\frac{L}{R}\right)\right)$, quadratic or else; and even less what the coefficient of such an order would be.

We introduce in **Section 9.1** the linear correction coefficient β, and present some of the works done in the past to try and estimate β in the sphere-plane configuration with beyond-PFA techniques, first by considering separately the two electromagnetic polarizations, which we will call a scalar approach in **Section 9.2**, then with an electromagnetic treatment in **Section 9.3**. We conclude in **Section 9.4** by mentioning an experimental work devoted to estimate this coefficient β.

9.1 Ways to measure the accuracy of PFA

For the last ten years, great effort has been put to try to master the error made by the Proximity Force Approximation with the help of 'beyond-PFA' methods. Their goal is to estimate how results obtained from PFA differ from exact ones when the curvature parameter $\frac{L}{R}$ increases from 0, and their conclusions can be expressed in two ways: the first is a prescription of a maximum value $\left(\frac{L}{R}\right)_{\max}$ if one aims at a precision of 1% or 0.1%, the second possibility, more universal, is to write the Casimir energy E normalized by the PFA result E_{PFA} as a first order Taylor expansion in $\frac{L}{R}$ for small values of this parameter, as presented in **Section 4.3.2** (p.58):

$$\rho_E = \frac{E}{E_{\mathrm{PFA}}} = 1 + \beta_E \frac{L}{R} + \mathcal{O}\left(\left(\frac{L}{R}\right)^2\right) \tag{9.1}$$

where β_E is the first order coefficient of the beyond-PFA correction for the Casimir energy. In the linear regime, where one assumes the former first order expansion correct, those two indicators are related by: $\Delta_E = |\beta_E| \left(\frac{L}{R}\right)_{\max}$, where $\Delta_E = |\rho_E - 1|$ is the accuracy (or relative difference) limit one fixes.

Similar tools to measure the accuracy of PFA can be developed for the force F (resp. for the force gradient G), and the Taylor expansion of ρ_F (resp. ρ_G) has a first order coefficient β_F (resp. β_G). The coefficients β are related through the energy and its derivatives in the plane-plane case,

as derived in **Section 4.3.2** (p.58), and for perfect mirrors at zero temperature their relations take the simpler form:

$$\beta_F = \beta_E \left(1 - \frac{D_{\rm PP}}{L E_{\rm PP}}\right) = \frac{1}{2}\beta_E \quad \text{for perfect mirrors at } T = 0 \tag{9.2}$$

$$\beta_G = \beta_F \left(1 - \frac{E_{\rm PP}}{L F_{\rm PP}}\right) = \frac{2}{3}\beta_F \quad \text{for perfect mirrors at } T = 0\ . \tag{9.3}$$

9.2 Scalar results for perfect mirrors

In the geometry of an infinite cylinder of radius R_0, parallel to an infinite plane and at a surface-surface distance L, the electromagnetic field can be decomposed in two uncoupled scalar fields, obeying Dirichlet or Neumann boundary conditions on the objects' surfaces, thanks to the translational invariance. An analytic expansion for the energy per unit length when the cylinder is close to the plane is derived in [230] using a path integral approach and gives:

$$\frac{E^{\rm cyl}}{u.l.} = -\frac{\hbar c \pi^2 \sqrt{R_0}}{960\sqrt{2}L^{5/2}}\left[1 + \left(\frac{7}{36} - \frac{20}{3\pi^2}\right)\frac{L}{R_0} + \mathcal{O}\left(\left(\frac{L}{R_0}\right)^2\right)\right] \tag{9.4}$$

where the term outside the brackets is the PFA result, and $\beta_E^{\rm cyl} = \left(\frac{7}{36} - \frac{20}{3\pi^2}\right) \simeq -0.481$.

Several studies have been aiming at getting the same kind of result in the sphere-plane geometry, and were thus in the beginning only devoted to the study of a scalar field. A first quantitative beyond-PFA analysis that studied the effect of curvature is contained in the results of the analytical study [149], where a semiclassical expression for the Casimir energy between two very close spheres ($L \ll R_1, R_2$) is derived. The sphere-plane case is obtained when taking one of the radii infinite, which transforms [149, Eq.(3.20)] into the following expression:

$$E_{[149]} = -\frac{\hbar c}{8\pi L}\sum_{n=1}^{\infty}\frac{1}{n^2\sinh^2(n\alpha)} \quad \text{with} \quad \alpha = \sqrt{1+\frac{L}{R}} - \sqrt{\frac{L}{R}}\ . \tag{9.5}$$

Keeping only the first order term in the expansion of the denominator $n^2\sinh^2(n\alpha)$ for small values of $\frac{L}{R}$, one gets $n^4\frac{L}{R}$, which, after summation over n, gives the PFA result $E_{\rm PFA} = -\frac{\hbar c \pi^3 R}{720 L^2}$. A next-to-leading order expansion of the denominator gives $n^4\frac{L}{R}\left(1 + (n^2-1)\frac{L}{3R}\right)$, and yields a beyond-PFA parameter[14]:

$$\frac{E_{[149]}}{E_{\rm PFA}} \simeq \frac{\frac{R}{L}\zeta(4) - \frac{1}{3}\zeta(2) + \frac{1}{3}\zeta(4)}{\frac{R}{L}\zeta(4)} = 1 + \left(\frac{1}{3} - \frac{5}{\pi^2}\right)\frac{L}{R} \tag{9.6}$$

where $\zeta(s) = \sum_{n=1}^{\infty} n^{-s}$ is the Riemann zeta function, and $\beta_E^{[149]} = \left(\frac{1}{3} - \frac{5}{\pi^2}\right) \simeq -0.173$.

A first numerical approach is [156], where worldline numerics are used with fluctuating scalar fields obeying Dirichlet boundary conditions, in order to observe the effect of curvature, and to assess the range of validity of the PFA results. The conclusion is that for $\frac{L}{R} \gtrsim 0.2$, "curvature effects are not properly taken into account", and a prescription for a maximal curvature parameter $\left(\frac{L}{R}\right)_{\rm max} = 0.02$ is given, if one aims at an accuracy at the percent level. The authors also pose the problem of the incorrect power laws in L and R in the PFA result: the two possible forms, $\frac{R}{L^2}$ for a 'plane-based' PFA and $\frac{R^2}{L^3}$ for a 'sphere-based' PFA, both differ from the form $\frac{R^3}{L^4}$ predicted at large separations [232]. Those two formulations for the Proximity Force Approximation are presented in **Appendix B.1**(p.219).

[14] This derivation is not in the cited article, but appears in [231], and the result is given in order to compare the first-order correction beyond PFA with other techniques.

A more detailed analysis of the beyond-PFA effects on the sphere-plane geometry with Dirichlet boundary conditions is done with the same technique in [157, 158]. The 1%-accuracy prescription on $\left(\frac{L}{R}\right)_{\max}$ becomes 0.00755 and the 0.1%-accuracy prescription on $\left(\frac{L}{R}\right)_{\max}$ is 7.3 10^{-4}. The authors fit their numerical data in the short-distance regime to get a beyond-PFA parameter that is centered around the curve:

$$\frac{E_{[157]}}{E_{\text{PFA}}} = 1 + 0.35\frac{L}{R} - 1.92\left(\frac{L}{R}\right)^2 . \tag{9.7}$$

The first order correction coefficient is obtained through forcing the fit to be linear, and the authors obtain the value

$$\beta_E^{[157]} = 0.33 \pm 0.06 . \tag{9.8}$$

It is somewhat surprising that this result is positive, as we expect PFA to overestimate the Casimir effect from a physical point of view. This mainly comes from the fact that only Dirichlet boundary conditions are considered, as we will see in the rest of this section. The authors already emphasized that "Casimir energies for the Dirichlet scalar should generally not be taken as an estimate for those for the electromagnetic (EM) field", the latter being useful for the comparison with experimental results.

An approach to the Casimir effect based on classical ray optics is presented in [151, 160, 161], where the sphere-plane configuration with Dirichlet boundary conditions is considered. Paths with up to four reflections are included, and results of the precedent numerical studies [156, 157, 158] are recovered [151] up to $\frac{L}{R} \lesssim 0.1$ at the percent level. After some refinements in the method, it turned out that the agreement was better in [160] for the long-distance regime, as they differ from results of [157, 158] by no more than 30% at $\frac{L}{R} = 5$. The authors estimate the accuracy of the usual PFA by the beyond-PFA parameter for the Casimir energy and force:

$$\frac{E_{[160]}}{E_{\text{PFA}}} = 1 + 0.05\frac{L}{R} + \mathcal{O}\left(\left(\frac{L}{R}\right)^2\right) \tag{9.9}$$

$$\frac{F_{[161]}}{F_{\text{PFA}}} = 1 - 0.1\frac{L}{R} + \mathcal{O}\left(\left(\frac{L}{R}\right)^2\right) \tag{9.10}$$

with a very small and positive first order correction coefficient for the energy $\beta_E^{[160]} = 0.05$, and quite surprisingly given Eq.(9.2), a negative first order correction for the force $\beta_F^{[161]} = -0.1$.

An analytic computation of the scalar Casimir energy [162], based on a semiclassical approximation, studies the two-sphere system. The sphere-plane case is contained in the results, and give the beyond-PFA ratio:

$$\frac{E_{[162]}}{E_{\text{PFA}}} = 1 + \left(\frac{1}{3} - \frac{5}{\pi^2}\right)\frac{L}{R} + \mathcal{O}\left(\left(\frac{L}{R}\right)^2\right) \tag{9.11}$$

where the negative first order correction coefficient obtained in (9.6) is recovered: $\beta_E^{[162]} = \left(\frac{1}{3} - \frac{5}{\pi^2}\right) \simeq -0.173$.

The result (9.11) is also found in [163] using a path integral approach, where the calculations for Dirichlet and for Neumann boundary conditions are performed separately. It follows that the

beyond-PFA first order correction is a sum of two terms:

$$\frac{E^{\text{Dirichlet}}_{[163]}}{E_{\text{PFA}}} = \frac{1}{2}\left[1 + \frac{1}{3}\frac{L}{R} + \mathcal{O}\left(\left(\frac{L}{R}\right)^2\right)\right] \qquad \beta_E^{[163],\text{Dirichlet}} \simeq 0.333 \tag{9.12}$$

$$\frac{E^{\text{Neumann}}_{[163]}}{E_{\text{PFA}}} = \frac{1}{2}\left[1 + \left(\frac{1}{3} - \frac{10}{\pi^2}\right)\frac{L}{R} + \mathcal{O}\left(\left(\frac{L}{R}\right)^2\right)\right] \qquad \beta_E^{[163],\text{Neumann}} \simeq -0.680 \tag{9.13}$$

$$\frac{E^{\text{sca}}_{[163]}}{E_{\text{PFA}}} = 1 + \left(\frac{1}{3} - \frac{5}{\pi^2}\right)\frac{L}{R} + \mathcal{O}\left(\left(\frac{L}{R}\right)^2\right) \qquad \beta_E^{[163]} \simeq -0.173\ . \tag{9.14}$$

The first part (9.12) explains the positive value of the coefficient (9.8) obtained from worldline numerics in [157, 158] with Dirichlet boundary conditions.

An alternative numerical approach is proposed in [167], based on a multipole expansion of fluctuating charges, where the interaction only depends on the scattering matrix of two compact objects[15]. From the multipolar nature of the method, numerical results are only accurate for values of $\frac{L}{R}$ above a minimum, which value depends on the number of included multipole orders $\ell_{\max}$. For the region $\frac{L}{R} \to 0$, the ratio $\frac{E}{E_{\text{PFA}}}$ is extrapolated to the value 1 by a second order polynomial fit. The latter contains the beyond-PFA informations. Among the various studied configurations the Dirichlet and Neumann boundary conditions give the following beyond-PFA parameters:

$$\frac{E^{\text{Dirichlet}}_{[167]}}{E_{\text{PFA}}} = 1 + 0.33\frac{L}{R} + \mathcal{O}\left(\left(\frac{L}{R}\right)^2\right) \tag{9.15}$$

$$\frac{E^{\text{Neumann}}_{[167]}}{E_{\text{PFA}}} = 1 - 2.43\frac{L}{R} + \mathcal{O}\left(\left(\frac{L}{R}\right)^2\right)\ . \tag{9.16}$$

While the Dirichlet case (9.15) corresponds well to both the results (9.8) and (9.12), the Neumann case do not match the analytic result (9.13).

Thanks to the works presented in this section, the scalar case is well known and explained with the help of very different techniques. However, unlike the plane-cylinder case, the geometry does not include any translational invariance, and thus uncoupling the two electromagnetic modes of different polarizations possibly induces different results. In order to assess the accuracy of PFA for experimental data analysis, a vectorial electromagnetic treatment is then necessary.

9.3 Electromagnetic results for perfect mirrors

A first numerical treatment of the sphere-plane geometry with electromagnetic field fluctuations (EM) is carried out in [167] with a multipole expansion. Numerical evaluations performed in [176] with a truncation to $\ell_{\max} = 29$ in the multipolar modes are accurate for $\frac{L}{R} \gtrsim 0.07$ and are extrapolated for smaller values with a quadratic fit for smaller values, making the connection to the PFA result at $\frac{L}{R} \to 0$. The slope of the fit at the origin then gives the parameter $\beta_E^{[167]} = -1.42$, which is very different from results obtained with scalar fluctuating fields.

Quite shortly after that the numerical study [233], also using a multipolar approach but with a different derivation, obtained similar results, with $\beta_E^{[233]} \simeq -1.4$. These two numerical works have shown the necessity of a full vectorial treatment of the vacuum fluctuations.

An analytical study [164] generalized the work of [163] to vectorial fields with the same technique, and obtained additional logarithmic terms in the beyond-PFA factor before the second order

[15] This paper also treats the electromagnetic case, we here only refer to the computations for a scalar field.

correction:

$$\rho_E = 1 + \left(\alpha + \beta \ln \frac{L}{R} + \gamma \left(\ln \frac{L}{R}\right)^2\right) \frac{L}{R} + \mathcal{O}\left(\left(\frac{L}{R}\right)^2\right) \tag{9.17}$$

with $\alpha = -5.2$, $\beta = -0.0044$ and $\gamma = 8.5\ 10^{-6}$. Actually, the parameter α is the dominant one in (9.17) for usual configurations, as $\alpha \not\gg -\beta \ln x$ when $x \lesssim 10^{-500}$ and $\alpha \not\gg -\gamma(\ln x)^2$ when $x \lesssim 10^{-340}$. We will thus use $\beta_E = -5.2$ to compare with other studies. This result is very different from the numerical ones [167, 233], and [176] proposes that this discrepancy could come from the range of validity for the analytic computation that might be restricted to much smaller values of $\frac{L}{R}$ than usual. We also remark that this analytic derivation would yield a range of parameter for very small distances $\frac{L}{R} \leq 4.03\ 10^{-246}$ where PFA overestimates the Casimir energy ($\rho_E > 1$).

9.4 Experimental prescription on β and conclusion

While theoretical works were focussed on measuring the error of PFA results, experimental data show no contradiction with them. A group of experimentalists designed a set of measurement[224] dedicated to determine an exclusion domain for β. They measured the Casimir force gradient with a gold plane and a gold sphere for different radii, and extract from the data a prescription on β_G. The result of their study is that

$$\beta_G^{[224]} < 0.4 \tag{9.18}$$

which is in contradiction with all theoretical results for perfect mirrors with vectorial fields, as [167] and [233] predict $\beta_G \simeq 0.47$, and [164] predicts $\beta_G \simeq 1.73$ in the range of parameters used in experiments.

From the analysis of some of the beyond-PFA studies devoted to the estimation of the first order correction coefficient β, we first conclude that it is necessary to consider the two electromagnetic polarizations together, as their coupling in the sphere-plane configuration has an effect on the Casimir effect such that scalar computations differ from electromagnetic ones. The seeming disagreement between the experimental prescription (9.18) and the numerical results obtained with perfectly reflecting conductors encourages one to investigate a more realistic description of the material, as finite conductivity plays a role in the considered distances. This motivates an analysis of the beyond-PFA effects from a multipole expansion, with a full electromagnetic treatment, for metallic reflectors. In the rest of the section, we will first develop the study with perfect reflectors to introduce the different parameters, and then come to the case of metallic reflectors.

10 Results for perfect mirrors

In this section we first consider the case where the plane and the sphere are modelled by perfect mirrors, at zero temperature. The description of the scattering is then purely geometrical, and only depends on the aspect ratio $\frac{L}{R}$, where L is the distance of closest separation between the two bodies and R is the radius of the sphere. We also define the center-to-plate distance $\mathcal{L} = L + R$ which is the distance between the reference points of each object.

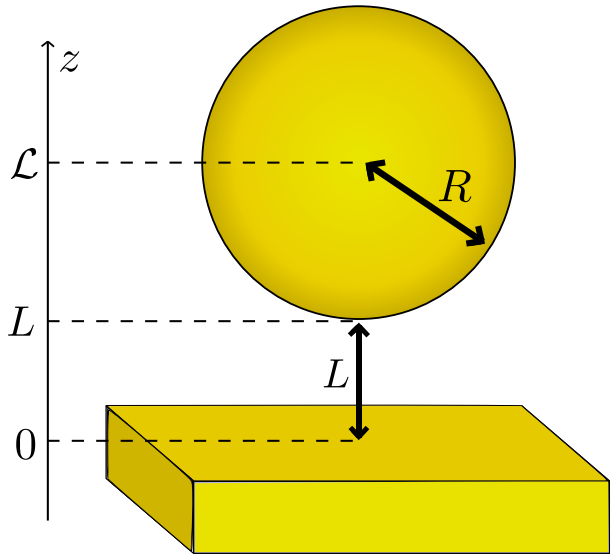

Figure 42: Schema of the sphere-plane configuration. The plane is infinite in the x and y-directions, and lies in the $(z \leq 0)$-region. The sphere has a radius R and its center is located at $(0, 0, \mathcal{L})$, with $\mathcal{L} = L + R$.

Here we present and analyse the results of numerical evaluations for the Casimir effect in this configuration, using the scattering formula described in **Section 5.4**(p.78):

$$E = \frac{\hbar c}{2\pi R} \int_0^\infty \mathrm{d}\tilde{\xi} \ln\det \mathcal{D}(\tilde{\xi}) \ . \tag{10.1}$$

To perform those numerical evaluations, we used the numerical methods developed in **Section 6**(p.81) with a sufficient number of modes $\ell_{\max}$ in order to get an accuracy of the order of 10^{-4}.

In this section we first check the numerical results with the two analytical expressions valid in the opposing limits of short and large distances, then we study the dependance of the energy with respect to the geometrical parameters L and R, and finally we estimate the beyond-PFA corrections at short distances.

10.1 Behaviour of numerical results at short and large separation

In **Section 8.2** (p.126), we have derived a long-distance expression for the Casimir force at zero temperature, valid when $L \gg R$. Moreover, the regime of validity of PFA is the short-distance regime ($L \ll R$), we can thus compare the numerical results we obtain for the two opposite extreme

range of the aspect ratio $\frac{L}{R}$:

$$(L \gg R) \;:\; E = -\frac{9\hbar c R^3}{16\pi \mathcal{L}^4} \tag{10.2}$$

$$(L \ll R) \;:\; E = -\frac{\hbar c \pi^3 R}{720 L^2} \;. \tag{10.3}$$

This comparison is shown in **Fig. 43**, where in the left graph, we observe that the numerical results converge well to the two limiting cases, and in the right graph that the ratio of the exact result to one of the approximation goes to unity when the corresponding limit is approached. The scattering approach thus allow to numerically evaluate the Casimir effect between a sphere and a plane for intermediate geometries, where the aspect ratio $\frac{L}{R}$ is neither small nor large.

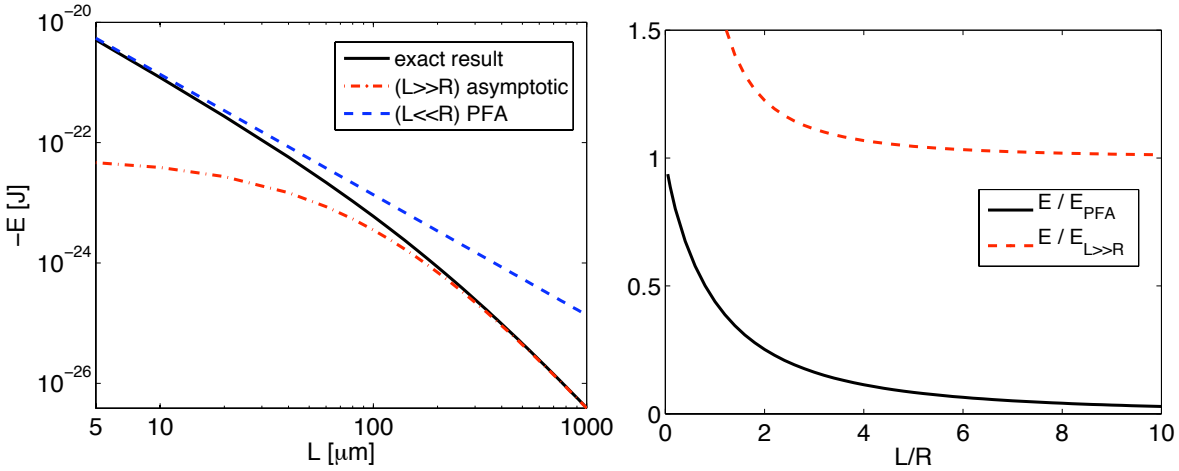

Figure 43: (left) Absolute value of the Casimir energy at $T = 0$ for perfect mirrors, with respect to distance L in micrometers (logarithmic scale). The plain black line is the exact result, computed for $\ell_{\max} = 100$, the blue dotted-dashed curves is the large-separation asymptotic result expressed in Eq.(10.2), and the red dashed curve is the PFA result expressed in Eq.(10.3). The sphere radius is $R = 100\mu$m. (right) Ratio of the exact energy to its approximations, with respect to the ratio $\frac{L}{R}$ (linear scale). The plain black line is for a short-distance approximation with PFA, the red dashed curve is for a large-distance approximation.

10.2 Power laws

We observe that the two opposite regimes (10.2,10.3) for the aspect ratio exhibit a different power law in L and R. In this subsection we study how this change occurs in the intermediate regime. We define ν and μ to be the logarithmic derivatives for the energy:

$$\nu(L,R) = -\frac{\partial \ln |E|}{\partial \ln L} \qquad \mu(L,R) = \frac{\partial \ln |E|}{\partial \ln R} \tag{10.4}$$

where the minus sign in the definition of ν is introduced in order to have positive quantities. If the energy obeys a simple power law in L and R, those numbers are constant. For example the large-distance expression (10.3) gives $(\nu = 4; \mu = 3)$ and the PFA formula (10.2) at short separations gives $(\nu = 2; \mu = 1)$. For a more general dependance on L and R, the parameters $\nu(L,R)$ and $\mu(L,R)$ thus express a 'local power-law' in $\frac{1}{L}$ and R for the energy E.

In **Fig. 44**, we present how ν changes from 2 to 4, while μ changes from 1 to 3 when the aspect ratio $\frac{L}{R}$ varies from zero to infinity. As the problem only involves two lengthscales, L and R, the parameters ν and μ only depend on their ratio $\frac{L}{R}$. Therefore, the obtained curve is the same for any value of R, which has been numerically checked.

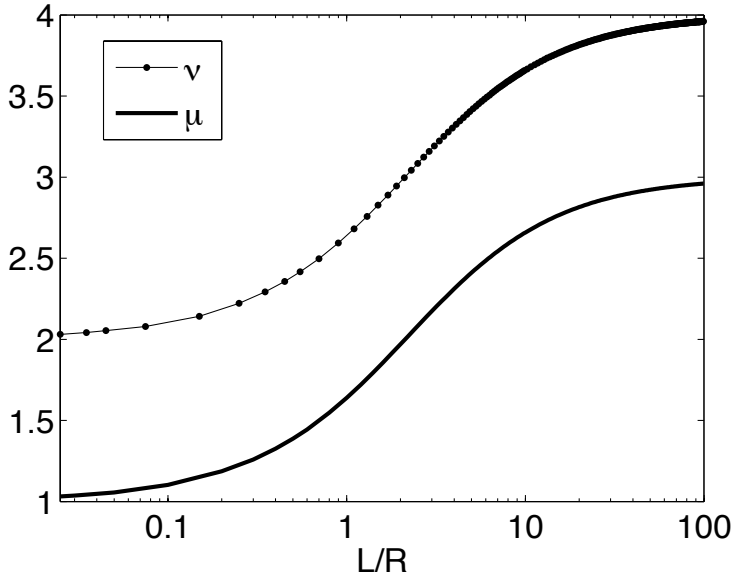

Figure 44: Parameters $\nu(L,R)$ (dotted thin line) and $\mu(L,R)$ (wide line), as defined in (10.4), with respect to the aspect ratio $\frac{L}{R}$ (logarithmic scale). Each dot represent a numerical evaluation. The radius has been chosen as $R = 100\mu$m, but any value of R would give the same curves.

We observe that the two curves for ν and μ in **Fig. 44** have the same shape, with a vertical decay of 1. This can be explained from the fact that the scattering process is purely geometric and can be described by the aspect ratio $\frac{L}{R}$ only. From the scattering formula (10.1), we can write the Casimir energy as $E = \frac{\phi(L/R)}{R} < 0$, then the logarithmic derivatives are:

$$\begin{aligned}
\nu &= -\frac{\partial \ln(-E)}{\partial \ln L} = -\frac{L}{(-E)}\frac{\partial(-E)}{\partial L} = -\frac{LR}{\phi(L/R)}\frac{\phi'(L/R)}{R^2} = -\frac{L}{R}\frac{\phi'}{\phi} \\
\mu &= \frac{\partial \ln(-E)}{\partial \ln R} = \frac{R}{(-E)}\frac{\partial(-E)}{\partial R} = \frac{R^2}{\phi(L/R)}\frac{\partial}{\partial R}\left(\frac{\phi(L/R)}{R}\right) \\
&= \frac{R^2}{\phi(L/R)}\left(-\frac{\phi(L/R)}{R^2} - \frac{L\phi'(L/R)}{R^3}\right) = -\frac{L}{R}\frac{\phi'}{\phi} - 1
\end{aligned}$$

and the relation $\nu = \mu + 1$ between the two curves in **Fig. 44** is checked.

It is possible to construct a simple function that reproduces the same changes in the power-laws for L and R in the extreme regimes of their ratio $\frac{L}{R}$:

$$f(L,R) = a\frac{R}{L^2\left(1 + b\frac{L}{R}\right)^2} \quad , \quad a, b \in \mathbb{R} \ .$$

If we additionally require that the same coefficients as in Eqs.(10.2,10.3) are to be obtained by f

in the two limiting regimes of $\frac{L}{R}$, it fixes the values of a and b and the function becomes:

$$f(L,R) = -\frac{\hbar c \pi^3}{720} \frac{R}{L^2 \left(1 + \frac{\pi^2}{9\sqrt{5}} \frac{L}{R}\right)^2} \ . \tag{10.5}$$

10.3 Beyond-PFA corrections

We now study how our numerical results compare to the PFA quantities in the limit of short distances. To that purpose we will use the beyond-PFA ratio ρ_E, introduced in Eq.(9.1) (p.137), which takes the ratio of the numerical evaluation for the Casimir energy E and the corresponding PFA quantity $E_{\rm PFA}$. As $E_{\rm PFA}$ scales as $\frac{R}{L^2}$, and E can be written as $\frac{1}{R}\phi(L/R)$, their ratio only depends on L and R through the aspect ratio $\frac{L}{R}$. It means that in the case of perfect mirrors, ρ_E is a universal function of $\frac{L}{R}$ and does not depend on the particular value of each one, because it is scale invariant.

In **Fig. 45** we show the beyond-PFA ratio ρ_E for small but reachable values of $\frac{L}{R}$. The obtained results superimpose on those of [233], as the method is the same, but while $\ell_{\rm max}$ was 27 in this study, here we are able to take into account as much as $\ell_{\rm max} = 520$ modes, allowing us to compute up to a precision of 10^{-4} numerical results for $\frac{L}{R} \geq 0.01$. For the energy E, as well as for the force

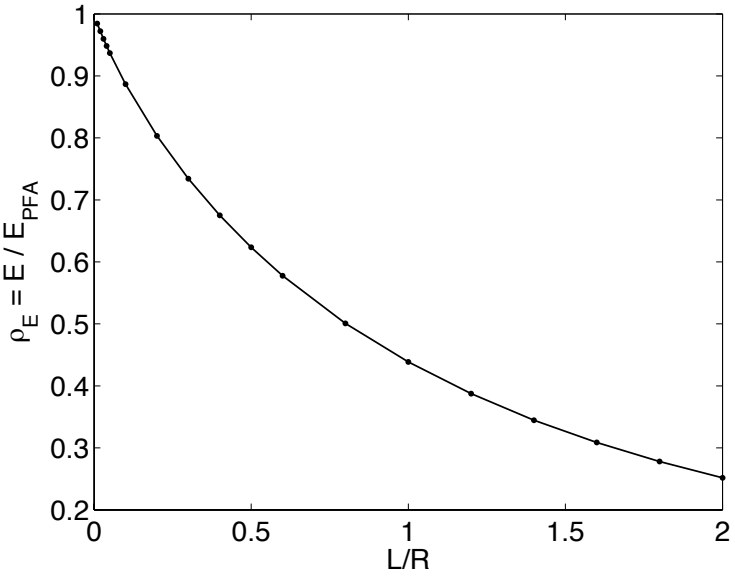

Figure 45: Ratio of the exact Casimir energy over the PFA result $\rho_E = \frac{E}{E_{\rm PFA}}$ with respect to the size ratio $\frac{L}{R}$ (linear scale). The dots represent numerical evaluations. The first dot is placed at $\frac{L}{R} = 0.01$.

F and force gradient G, we always observe $\rho < 1$, which means that PFA always overestimates the Casimir interaction. The ratio seems to go nicely to 1 at the proximity limit $\frac{L}{R} \to 0$. The obtained value of ρ_E for small values of the aspect ratio $\frac{L}{R}$ are presented in **Table 12**.

To extract informations on the accuracy of PFA from those numerical results, we extrapolate the beyond-PFA function ρ_E with a quadratic fit of the numerical data that fulfill the condition $\rho_E(L=0) = 1$. **Fig. 46** illustrates this procedure: we fit with a second-order polynomial the data points in the range $\frac{L}{R} \in [0.01, 0.05]$, pointed out with blue circles, together with an additional point $\left(\frac{L}{R} = 0; \rho_E = 1\right)$. The obtained best quadratic fit, represented by a thick curve, is then used to extrapolate the function ρ_E to the proximity limit $\frac{L}{R} \to 0$.

$\frac{L}{R}$	0.01	0.02	0.05	0.1	0.2	0.5	1
$\rho_E\left(\frac{L}{R}\right)$	0.9845	0.9719	0.9371	0.8865	0.8033	0.6234	0.4387

Table 12: Values of the beyond-PFA correction factor $\rho_E = \frac{E}{E_{\mathrm{PFA}}}$.

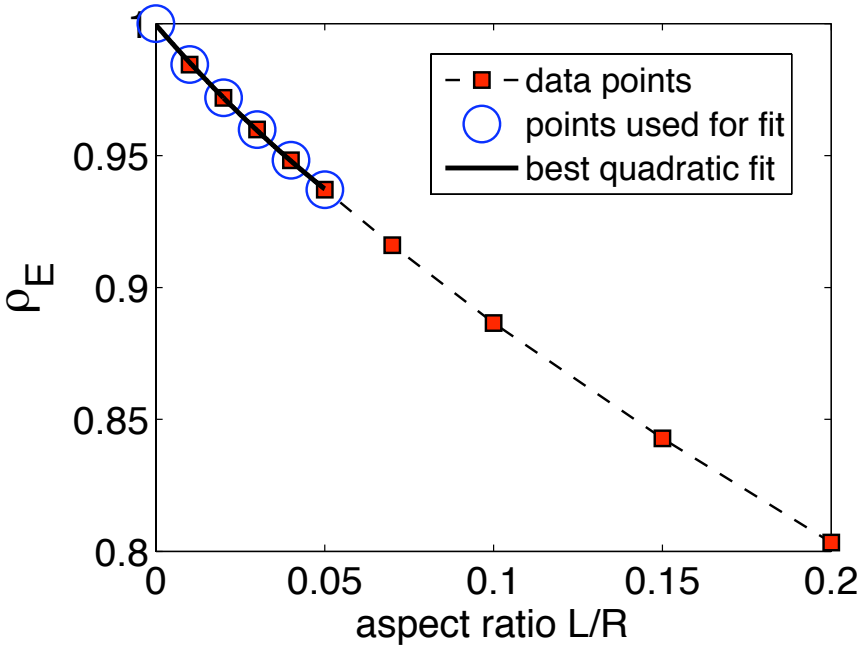

Figure 46: Beyond-PFA ratio $\rho_E = \frac{E}{E_{\mathrm{PFA}}}$ for the Casimir energy, with respect to the aspect ratio $\frac{L}{R}$ (linear scale). From the set of data points (red squares), we select the ones with a small value of $\frac{L}{R}$ and add the point $\left(\frac{L}{R} = 0; \rho_E = 1\right)$ (blue circles) for fit. The best quadratic fit is $y = 1 - 1.47x + 4.6x^2$. This result is independent of the sphere radius R.

With this method we obtain a beyond-PFA first order coefficient $\beta_E = -1.47$, which is compatible with other similar studies [167, 233]. When compared to analytical results obtained for both scalar or vector fields, the obtained number is very different, as seen on **Fig. 47**.

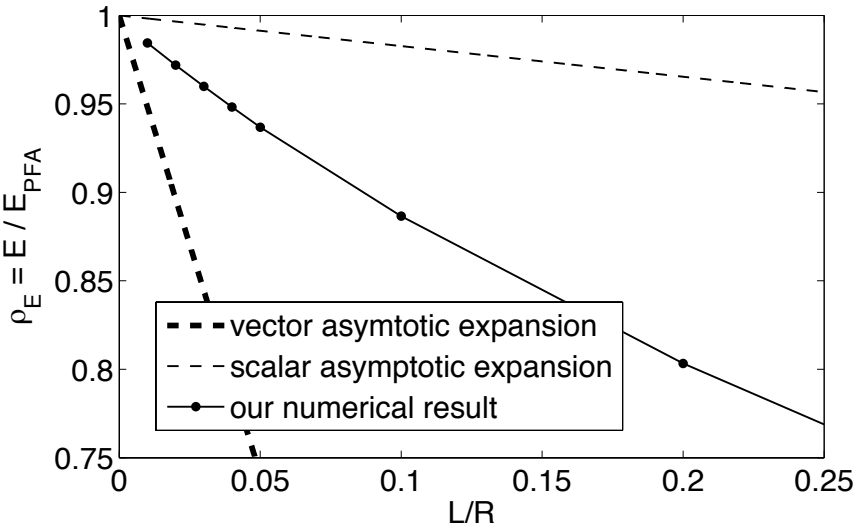

Figure 47: Comparison of several beyond-PFA factors $\rho_E = \frac{E}{E_{\mathrm{PFA}}}$ with respect to the size ratio $\frac{L}{R}$ (linear scale). The line with dots is our numerical result, each dot corresponding to a numerical evaluation. The first dot is placed at $\frac{L}{R} = 0.01$. The thin dashed-line presents the result of analytic scalar derivations, such as [163]. The thick dashed-line the result of electromagnetic analytical derivation [164].

The linear factor $\beta_E^{[163]} = -0.173$, commonly obtained for a scalar decomposition of the electromagnetic field, is presented with a thin dashed-line, and is more than 8 times smaller than our β_E. The linear factor $\beta_E^{[164]} = -5.2$, effective part of the analytical computation for electromagnetic field, corresponds to the thick dashed-line, and is more than 3 times larger than our β_E.

We recall that the experimental work [224] prescripts that $|\beta_G|$ should be lower than 0.4, as discussed in **Section 9.4**. Our result $\beta_E \simeq -1.47$, for the energy yields the following first order beyond-PFA correction coefficients for the Casimir force and force gradient:

$$\beta_E \simeq -1.47 \quad ; \quad \beta_F = \frac{1}{2}\beta_E \simeq -0.74 \quad ; \quad \beta_G = \frac{1}{3}\beta_E \simeq -0.49 \tag{10.6}$$

thanks to the relations (4.18) (p.59) between the β coefficients for perfect mirrors at zero temperature. In conclusion our result, like the ones from the studies [167, 233], seems to be in disagreement with the experimental prescription. As experimental works have been performed with metallic reflectors, the situation in each side is not the same, and this could be the reason for this seeming disagreement. It motivated to carry out a similar study with a more realistic description of the material optical properties. This study is presented in the next section.

11 Results for metallic mirrors

We will now study the same situation as in the previous section, but we will introduce a more accurate description of the optical response for metallic materials. Indeed, an ideal mirror reflects perfectly incoming electromagnetic waves at all frequencies, a feature that is modeled by taking the dielectric function of the material to be infinite for all frequencies. Metals are however poor reflectors for the high-frequency part of the incoming wave, and become fully transparent in the high-frequency limit. This behavior can be modelled by a dielectric function which obeys the plasma model, introduced in **Section 2.2** (p.39) and recalled below. As metals have a finite DC conductivity, dissipation inside the materials should be accounted for and the dielectric function can be improved by using the Drude model, introduced in **Section 2.3** (p.41) and recalled below:

$$\varepsilon^{\text{plas}}(i\xi) = 1 + \frac{\omega_P^2}{\xi^2} \qquad \varepsilon^{\text{Drud}}(i\xi) = 1 + \frac{\omega_P^2}{\xi\,(\xi+\gamma)}\ . \tag{11.1}$$

From the study of the plane-plane configuration, we would expect the introduction of high-frequency transparency to have only an influence on frequencies $\xi \gtrsim \omega_P$, or equivalently on distances $L \lesssim \lambda_P$, as $\xi \lesssim \frac{c}{L}$ (see for example the correction factor η_E^P in **Fig. 20** p.44). As we will see in the remainders of this section, this is not true anymore for the sphere-plane configuration, as the long-distance limit for the energy also depends on the ratio $\frac{R}{\lambda_P}$. This coupling between the effects of geometry and finite conductivity will be studied in a detailed manner. Concerning the accuracy of PFA results, we will show that this more realistic description of the materials solves the seeming discrepancy between the theoretical and experimental values of the linear correction factor β.

In this section, we first study the effect of finite conductivity and dissipation with the finite conductivity factor η^P, and its dependance on the sphere radius R. We then describe the dependance of the Casimir effect with the two parameters L and R in this situation and the correlations between the effects of finite conductivity and geometry. Finally, we tackle in the end of this section the question of the beyond-PFA correction at short distances.

11.1 Observation of the effect of imperfect reflection

To study how the inclusion of a more realistic optical response for the materials affect the Casimir effect, we define the finite conductivity correction factor η^P:

$$\eta_E^P = \frac{E^{\text{plas}}}{E^{\text{perf}}} \tag{11.2}$$

where E^{perf} denotes the Casimir energy with perfect mirrors and E^{plas} the energy with mirrors described by a plasma model, which can be replaced by E^{Drud} if the mirrors are described by a Drude model. An analogous factor can be defined for the change in the Casimir force (η_F^P), or the Casimir force gradient (η_G^P).

This finite conductivity correction factor is illustrated for the plane-plane geometry in **Fig. 20** (p.44), where one can see that for both models, plasma and Drude, η_E^P is a monotonically growing function with the distance L, tending to unity at the limit of large distances. Let us recall that the explanation of this behavior was that at large distances, only low frequencies $\xi \lesssim \frac{c}{L}$ contribute to the Casimir effect, at which the metallic mirrors perfectly reflect the field (dielectric function $\varepsilon(i\xi)$ going to infinity when $\xi \to 0$). For smaller distances, higher frequencies $\xi \gtrsim \omega_P$ also play a role, and for those, the dielectric function is finite, revealing the imperfect reflection on metals.

From the analytical study at the limit of large distances ($L \gg R$) conducted in **Section 8** (p.124), this correction factor should no longer tend to unity when $L \to \infty$ in the sphere-plane geometry: indeed we found in **Section 8.3** (p.131), for the plasma model with the additional

hypothesis ($R \ll \lambda_P$), that this ratio should rather tend to a value in $\left[\frac{2}{3}, 1\right]$, determined by the value of $\alpha = \frac{2\pi R}{\lambda_P}$ through the function f:

$$f(\alpha) = 1 + \frac{1}{\alpha^2} - \frac{\coth \alpha}{\alpha} ,$$

a function that is illustrated in **Fig. 41** (p.132). For very small values of α, the function f tends to $\frac{2}{3}$, while for very large values of α, it goes to unity. For the Drude model, we found in **Section 8.4** (p.132) that the finite conductivity correction factor η_E^P should always go to $\frac{2}{3}$ at the limit of large distances, for any value of the radius R.

To study this qualitative change of dependance in the optical properties of the materials, we plot in **Fig. 48** the finite conductivity correction factor η_E^P for the Casimir energy with respect to the distance L, for various values of the sphere radius ($R = 0.1, 1, 10$ μm). The plasma model for lossless metals is used in the left graph, the Drude model, which includes dissipation in the material, is used in the right graph. The chosen values of the parameters for those models correspond to gold ($\lambda_P = 136$ nm; $\delta = \frac{\lambda_P}{\lambda_\gamma} = 0.004$).

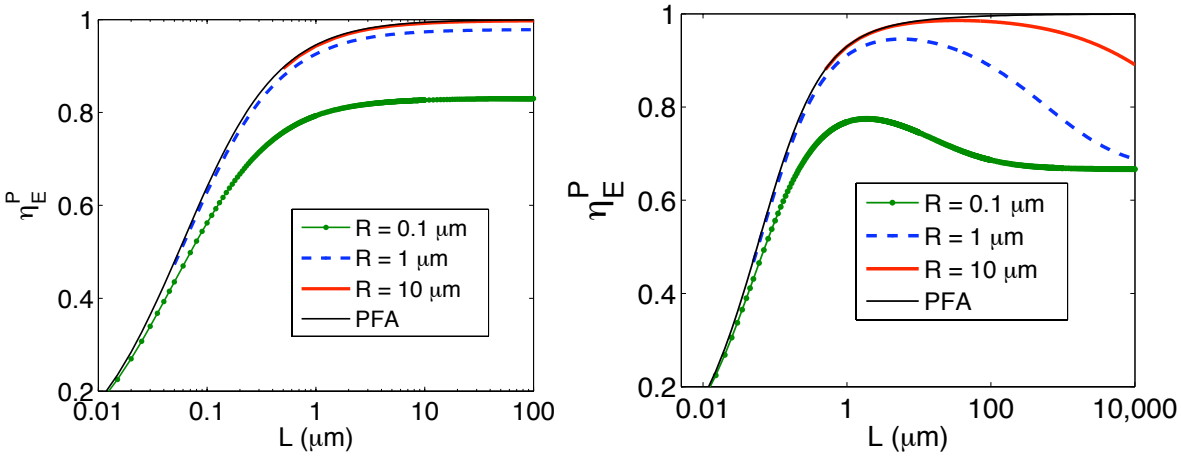

Figure 48: Finite conductivity correction factors for the Casimir energy $\eta_E^P = \frac{E^{\rm plas}}{E^{\rm perf}}$ (left) and $\frac{E^{\rm Drud}}{E^{\rm perf}}$ (right), with respect to the distance L, for the plasma model (left) and the Drude model (right). Green dotted lines represent the case of a small sphere, the dashed blue curves an intermediate sphere, and the red solid curve a large sphere. The PFA results are plotted with a thin black line. The plasma wavelength is $\lambda_P = 136$ nm, and the dissipation ratio $\delta = \frac{\lambda_P}{\lambda_\gamma}$ is 0.004. (left) The long-distance limit of the correction factor for the three radii with plasma model are 0.83, 0.98 and 0.998, respectively. (right) The long-distance limit of the correction factors for the three radii with Drude model is $\frac{2}{3}$ within the numerical error.

When the plasma model is used to described the optical properties of the objects, we observe in the left graph of **Fig. 48** that the finite conductivity correction factor η_E^P increases with the distance L, to reach at $L \sim 10$ μm a limit, which is around 0.83 for the small sphere case (0.1 μm radius), 0.98 for the medium sphere case (1 μm radius), and 0.998 for the large sphere case (10 μm radius). Those values are in perfect agreement with the corresponding values of the function f. We deduce from this study that the case of perfectly reflecting mirrors is recovered from the plasma model in the sphere-plane geometry when λ_P is small compared to both L and R.

When the Drude model is used to described the optical properties of the objects, we observe in the right graph of **Fig. 48** that the finite conductivity correction factor η_E^P first increases with the

distance L, to reach a maximum smaller than 1, then decreases and tends to the value $\frac{2}{3}$. The bigger the radius, the larger is the distance needed to converge to this value.

The observations for the two models are very different from what happens in the plane-plane configuration: for plasma model the long-distance limit for η_E^P is below 1, except for very large spheres ($R \gtrsim 10$ μm), and for Drude it is always $\frac{2}{3}$. We here observe the appearance of a coupling between the effects of geometry and finite conductivity, which could not have been predicted from PFA comptutations.

Those observations are entirely consistent with the analytical large-distance limit derived in **Section 8.4** (p.132). First they corroborate the unexpected result that the value of this correction at the large-distance limit is independent of the materials parameters, as long as the dissipation is non-zero. Second, we observe in the right graph of **Fig. 48** that when the radius is increased by a factor 10, the large-distance limit is delayed by a factor of the order of 100. This is consistent with the condition (HYP2) $\left(\mathcal{L} \gg \frac{R^2\lambda_\gamma}{\lambda_P^2}\right)$, formulated in the large distance expansion in **Section 8.4** (p.132). The other condition (HYP1) $\left(\mathcal{L} \gg \frac{\lambda_P^2}{\lambda_\gamma}\right)$ is always fulfilled in the computed range of distances, as $\delta = \frac{\lambda_P}{\lambda_\gamma}$ is small. We deduce from this study that the case of perfectly reflecting mirrors can never be recovered from the Drude model in the sphere-plane geometry at the limit of large distances, as soon as the dissipation is non-zero. In other words, for dissipative media, the limits $(\lambda_P \to 0)$ and $(L \to +\infty)$ do not commute.

11.2 Power laws

Like in the former section where perfect mirrors were considered, we can study the change in the power laws thanks to the logarithmic slopes ν and μ, defined in (10.4). The former is the local power law in the inverse distance $\frac{1}{L}$, while the latter is the local power law in the sphere radius R.

In the plane-plane geometry, high-frequency transparency of the metals leads to a change of the dependance with respect to the distance L in the short-distance regime: while for a large distance ($L \gg \lambda_P$), the imperfect reflection does not play a role, at short distances ($L \ll \lambda_P$) the finite conductivity correction factor η_E^P is proportional to $\frac{L}{\lambda_P}$, and the logarithmic slope ν is thus decreased by one. For the Casimir-Polder energy between a plate and an atom, the same behavior appears, changing the $\frac{1}{L^4}$-law into a $\frac{1}{L^3}$-law at short distances, also called the van der Waals regime.

We expect a similar decrease in the power-law of $\frac{1}{L}$ for the Casimir energy in the sphere-plane geometry, which we present for the plasma model in the left graph of **Fig. 49**, with respect to the aspect ratio $\frac{L}{R}$ for different values of the sphere radii $R = 0.1, 1, 10$ μm.

The perfectly reflecting case is recalled by a solid black curve, and shifts from $\nu = 4$ at high values of the aspect ratio ($L \gg R$) to $\nu = 2$ for small values ($L \ll R$). When taking into account the imperfect reflection, the shift is as expected increased by one for small distances and the logarithmic slope ν tends to the value 1 at very short distances ($L \ll \lambda_P, R$). This result is in agreement with the PFA result obtained from a derivation in the plane-plane geometry (see discussion on Eq.(2.14) p.44), in the plasmon limit (PL) when ($L \ll \lambda_P$):

$$E_{\rm PFA}^{\rm PL} = -\frac{\hbar c \pi^3 \alpha R}{240 \lambda_P L} \quad \text{with} \quad \alpha \simeq 1.1933 \ .$$

The curves for the plasma model depart from the one for perfect reflectors at $L \lesssim 1$ μm, as it occurs at $\frac{L}{R} \lesssim 10$ for the green dotted-line ($R = 0.1$ μm), at $\frac{L}{R} \lesssim 1$ for the blue dashed-line ($R = 1$ μm), and at $\frac{L}{R} \lesssim 0.1$ for the red solid line ($R = 10$ μm). This is consistent with the curve for the finite conductivity correction factor η_E^P presented in **Fig. 48**, which also deviates from its long-distance limit around $L \lesssim 1$ μm.

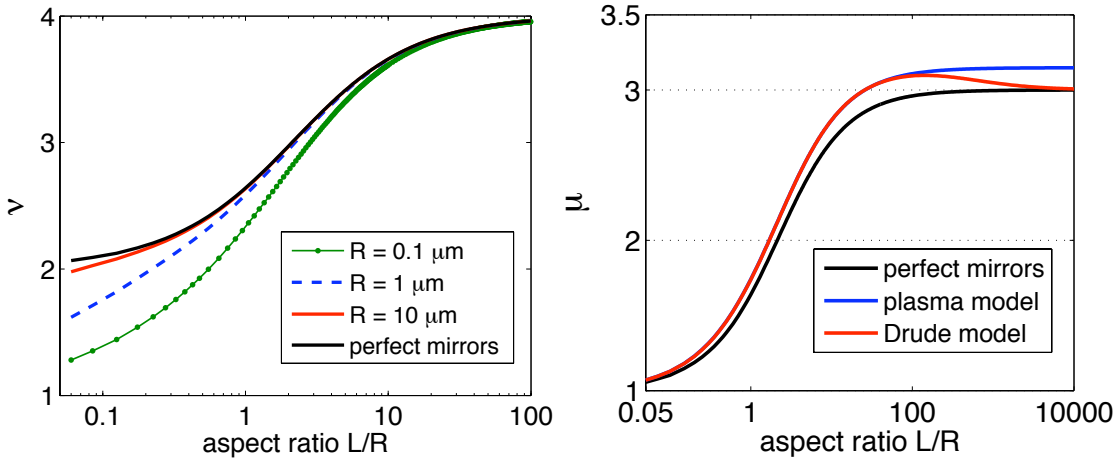

Figure 49: Logarithmic slopes $\nu = -\frac{\partial \ln |E|}{\partial \ln L}$ and $\mu = \frac{\partial \ln |E|}{\partial \ln R}$ with respect to the aspect ratio $\frac{L}{R}$. The black solid curves are obtained for perfect mirrors and are independent of the sphere radius R. (left) The mirrors are described by a plasma model, the green dotted line represents the case of a small sphere, the dashed blue curves an intermediate sphere, and the red solid curve a large sphere. (right) The sphere radius is $R = 0.1$ μm, the blue curve represents the plasma model and the red curve the Drude model. The plasma wavelength is $\lambda_P = 136$ nm, the dissipation ratio is $\delta = \frac{\lambda_P}{\lambda_\gamma} = 0.004$.

The dependance of the Casimir energy on the radius R is presented in the right graph of **Fig. 49**, again with respect to the aspect ratio $\frac{L}{R}$ but for a sphere size of $R = 0.1$ μm with different models for the mirrors. The perfectly reflecting case, independent of R, is recalled with a solid black curve, and goes from a volumetric dependance at large separations ($\mu = 3$ at $L \gg R$) to a linear dependance at short separations ($\mu = 1$ at $L \ll R$).

The plasma case, illustrated with a blue curve, also increases monotonously with the distance, but converges to a value $\mu^\infty > 3$ at large distances. This over-volumetric dependance can be understood with the previous study of the finite conductivity correction factor η_E^P presented in **Fig. 48**: when R increases, the long-distance limit of η_E^P increases (up to 1), and thus $|E^{\rm plas}|$ with plasma mirrors increases more than $|E^{\rm perf}|$ with perfect reflectors. It yields a higher power-law with respect to R, and finally explains the obtained value $\mu^\infty \simeq 3.148$ at the limit of large distances for $R = 0.1$ μm. This feature progressively disappears when the sphere radius is increased to a few microns, as the long distance limit of the finite conductivity correction factor η_E^P saturates at 1 in the limit ($R \gg \lambda_P$). We find $\mu^\infty = 3.021$ for $R = 1$ μm, and $\mu^\infty = 3.002$ for $R = 10$ μm.

For dissipative metals, described with a Drude model, the same over-dependance of μ in R is observed, up to $\mathcal{L} \sim \frac{R^2 \lambda_\gamma}{\lambda_P^2}$, which for gold means $\frac{L}{R} \sim 1000R$, with R in μm. In the limit of large distance, μ then decreases again to the perfect reflectors value $\mu^\infty = 3$, as illustrated with the red curve in the right graph of **Fig. 49**, which departs from the blue curve representing plasma model for $\frac{L}{R} \gtrsim 100$. This is again explained by the study of the finite conductivity correction factor η_E^P presented in **Fig. 48**: for Drude metals, the R-independent long-distance limit of η_E^P is $\frac{3}{2}$, thus $|E^{\rm Drud}|$ and $|E^{\rm perf}|$ have the same dependance on R at large distances. This decrease back to $\mu^\infty = 3$ happens for a larger distance when the radius increases, for the same reason as for the delay in the convergence of η_E^P, connected to (HYP2) and discussed in the previous section.

11.3 Correlations between the effects of finite conductivity and geometry

We call two influences A and B 'uncorrelated' (or 'uncoupled') when the correction factor η^{AB}, that take into account both A and B at the same time, is equal to the product of η_A and η_B, the correction factors that only take into account A or B. With this convention, we define the correlation number δ^{AB}, which is zero when the influences of A and B are uncorrelated:

$$\delta^{AB} = \frac{\eta^{AB}}{\eta^A \eta^B} - 1 \ . \tag{11.3}$$

If $\delta^{AB} \neq 0$, it means that it is not allowed to consider separately the influences of the two effects A and B. This generalises the tool introduced in [207, Eq.(4-24)], used in Eq.(3.13) (p.53) to study the correlations between the effect of temperature and finite conductivity in the plane-plane configuration.

Here we consider the sphere-plane geometry with metallic materials at zero temperature, there is then two different effects that modify the Casimir force from the perfect mirrors with PFA result $F_{\rm PFA} = -\frac{\hbar c \pi^3 R}{360 L^3}$: the geometry (G) and the finite conductivity (P). The correction factor for the latter is just the finite conductivity one η^P defined in **Section 11.1**, but within the PFA. The correction factor for the geometry is the factor ρ defined in Eq.(9.1) (p.137) for perfect mirrors. Finally, we sum up the different correction factors for the Casimir force involved in the study of the G-P correlations:

$$\eta_F^G = \frac{F^{\rm perf}}{F_{\rm PFA}^{\rm perf}} \quad ; \quad \eta_F^P = \frac{F_{\rm PFA}^{\rm plas}}{F_{\rm PFA}^{\rm perf}} \quad ; \quad \eta_F^{GP} = \frac{F^{\rm plas}}{F_{\rm PFA}^{\rm perf}} \tag{11.4}$$

$$\delta_F^{GP} = \frac{F^{\rm plas} F_{\rm PFA}^{\rm perf}}{F^{\rm perf} F_{\rm PFA}^{\rm plas}} - 1 = \frac{\eta^P}{\eta_{\rm PFA}^P} - 1 = \frac{\rho^{\rm plas}}{\rho^{\rm perf}} - 1 \ . \tag{11.5}$$

From **Fig. 48** (p.149), we see that generally $\eta^P \neq \eta_{\rm PFA}^P$, especially with small spheres, for which the finite conductivity correction factor is not going to unity at the limit of large distances. This is a clear sign of correlation between the effect of curvature and imperfect reflection. In **Fig. 50** we present the three force corrections factors introduced in (11.4) for a nanosphere of radius $R = 100$ nm, with respect to the distance L.

The geometry correction factor η_F^G (upper solid green curve) is important for large distances ($L \gtrsim R$) and is always smaller than one, meaning that PFA results overestimate the Casimir force. It goes to unity for short distances. On the contrary, the finite conductivity correction factor η_F^P (upper solid red curve) is important for short distances ($L \lesssim \lambda_P$) and goes to unity for large distances. The product of the two simple corrections $\eta_F^P \eta_F^G$ (lower dashed purple curve) is then a combination of those two corrective curves.

The total correction factor η_F^{GP} (lower solid purple curve) departs from this product in the intermediate regime and takes on lower values in general. It shows that the two corrections are correlated and that the correlation number δ_F^{GP} is generally negative. More surprisingly, it is also non-zero in the large-distance regime, where the finite-conductivity should not have any more effect. This observation is consistent with the large-distance limit lower than unity obtained for the finite conductivity correction factor η^P with a small sphere radius in **Fig. 48** (p.149), as $\delta^{GP} = \frac{\eta^P}{\eta_{\rm PFA}^P} - 1$.

For larger spheres, the domains ($L \gtrsim R$) and ($L \lesssim \lambda_P$) where the two corrections have a large effect do not have a large overlap anymore, and we expect less correlations in this case. In the large distance limit for the plasma model, it is indeed the case, as $\eta^P \simeq \eta_{\rm PFA}^P$ when ($L \gg R, \lambda_P$). For the Drude model however, the correlations remain non-zero at large separations, even with large spheres, as η^P always converges to the value $\frac{2}{3}$. This feature is illustrated by **Fig. 51**, where the correlation number δ^{GP} is plotted for various size of the sphere radius R. As the finite conductivity

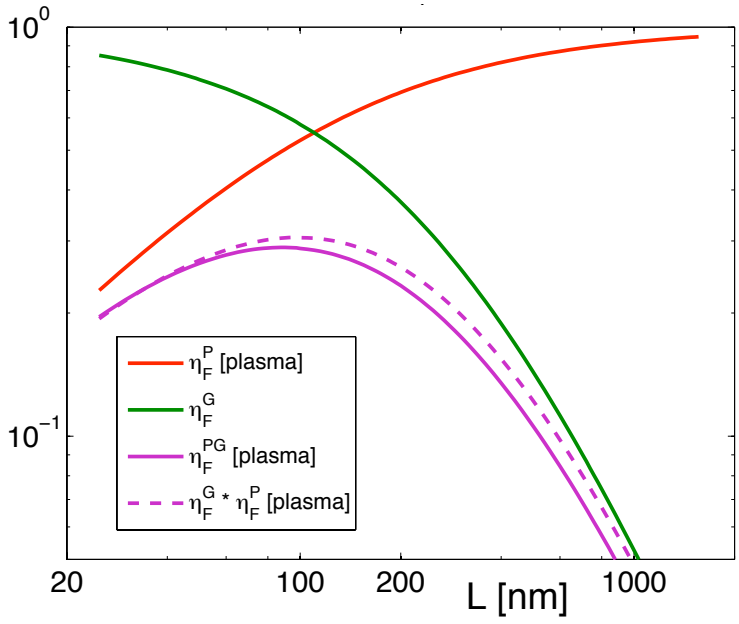

Figure 50: Force correction factors, with respect to the distance, for the imperfect reflection (η_F^P, upper solid red curve), for the geometry (η_F^G, upper solid green curve), and for both (η_F^{PG}, lower solid purple curve). The product of the two single corrections is presented in a dashed purple curve for comparison. The sphere radius is $R = 0.1$ μm, the plasma wavelength is $\lambda_P = 136$ nm.

correction factor for PFA goes to unity at large separation, the correlation number always tends here to:

$$\lim_{L\to\infty} \delta^{GP} = \lim_{L\to\infty} \left(\frac{\eta^P(L)}{\eta^P_{\rm PFA}(L)} - 1 \right) = \frac{2/3}{1} - 1 = -\frac{1}{3} \,. \tag{11.6}$$

11.4 Influence of conductivity on the beyond-PFA corrections

Until now we merely focussed on the intermediate and large values of the aspect ratio $\frac{L}{R}$, but on this section we rather focus on the short-separation regime to study the beyond-PFA corrections in the presence of metallic mirrors. For perfect mirrors, we have estimated in Eq.(10.6) the first-order coefficient of the beyond-PFA correction to be $\beta_E \simeq -1.47$ for the energy, which yields an equivalent coefficient $\beta_G \simeq -0.49$. The latter number is in a seeming contradiction with the experimental prescription $|\beta_G| < 0.4$ discussed in **Section 9.4** (p.141). We here explain how the contradiction is solved by the introduction of finite conductivity in the description of the materials. This specific point has been the subject of a published article [234].

Eq.(11.5) of the correlation number shows that the beyond-PFA is not the same for perfect reflectors ($\rho^{\rm perf}$) and mirrors described by a metallic model ($\rho^{\rm Drud}$) when the effects of geometry and finite conductivity are coupled. Writing that $\rho^{\rm Drud} = \frac{\eta^P}{\eta^P_{\rm PFA}} \rho^{\rm perf}$, one can see how the change in this geometry correction is directly connected with the previous section on the finite conductivity correction. In most of the studied cases, we observed that for the Casimir energy $\frac{\eta^P}{\eta^P_{\rm PFA}} \leq 1$, or in other words a negative correlation number $\delta_E^{GP} \leq 0$. We thus expect to have a lower beyond-PFA correction $\rho_E^{\rm Drud} \leq \rho_E^{\rm perf}$ than with perfect mirrors for the Casimir energy.

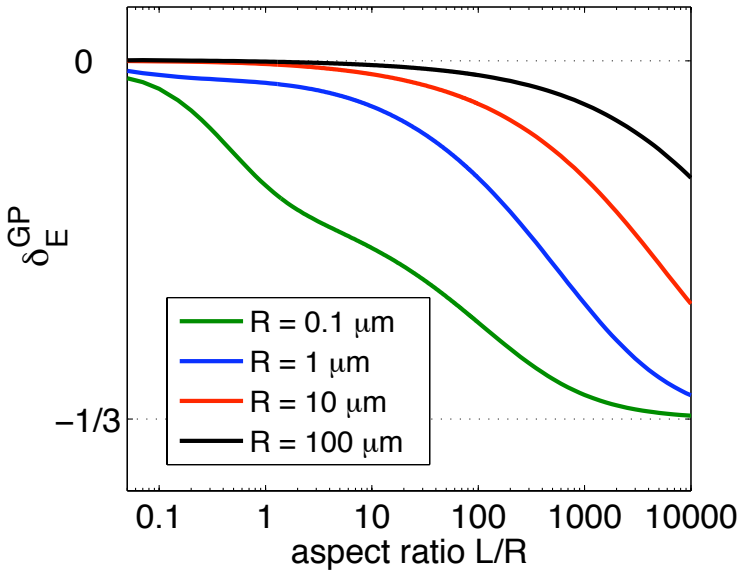

Figure 51: Correlation number for the Casimir energy δ_E^{GP} between the effects of geometry and finite conductivity for the Drude model. Green curve represents the case of a small sphere, blue curve an intermediate sphere, and the red and black curves larger spheres. All curves converge to the value $-\frac{1}{3}$ at the limit of large distances. The parameters for the Drude model are those of gold ($\lambda_P = 136$ nm; $\delta = 0.004$).

In **Fig. 52** we confirm this conjecture by plotting the beyond-PFA correction factor $\rho_E^{\rm Drud}$ for the Casimir energy, using the Drude model to describe the reflection on each object. The same factor for perfect mirrors $\rho_E^{\rm perf}$ is recalled with a dashed-line. For small spheres, we observe indeed that $\rho_E^{\rm Drud} \leq \rho_E^{\rm perf}$, while for larger spheres the function for perfect mirrors is recovered in the range of distances considered. However, because of the long-distance limit $-\frac{1}{3}$ of the correlation number derived in Eq.(11.6), we know that for larger distances we should obtain at some point a separation, as $\frac{\rho_E^{\rm Drud}}{\rho_E^{\rm perf}} \longrightarrow \frac{2}{3}$.

The fact that $\rho_E^{\rm Drud} \leq \rho_E^{\rm perf}$ means that the description of the imperfect reflection on the objects with the Drude model makes the error of PFA worse than in the case of perfect mirrors, and lead to a first order corrective coefficient $\beta_E^{\rm Drud} \leq \beta_E^{\rm perf} \simeq -1.47$ larger in magnitude. The coefficient $\beta_G^{\rm perf} \simeq -0.49$ for the force gradient with perfect mirrors is too large in magnitude to enter the experimental prescription $|\beta_G| < 0.4$, and the former remark seems to make the excess in magnitude even worse. This is actually the opposite, and this comes from the relations between the β coefficients for the Casimir energy E, force F and force gradient G, derived in **Section 4.3.2** (p.58), and which can be written as:

$$
\begin{aligned}
\beta_G = \frac{(\nu_E - 1)(\nu_F - 1)}{\nu_E \nu_F} \times \beta_E \quad &= \quad f_\beta(L)\beta_E \\
\gamma_G = \frac{(\nu_E - 2)(\nu_F - 2)}{\nu_E \nu_F} \times \gamma_E \quad &= \quad f_\gamma(L)\gamma_E \\
\text{where} \quad \nu_E(L) = -\frac{\partial \ln |E_{\rm PFA}|}{\partial \ln L} &= \frac{LF_{\rm PFA}}{E_{\rm PFA}} = \frac{LE_{\rm PP}(L)}{D_{\rm PP}(L)} \\
\text{and} \quad \nu_F(L) = -\frac{\partial \ln |F_{\rm PFA}|}{\partial \ln L} &= \frac{LG_{\rm PFA}}{F_{\rm PFA}} = \frac{LF_{\rm PP}(L)}{E_{\rm PP}(L)} \ .
\end{aligned}
\tag{11.7}
$$

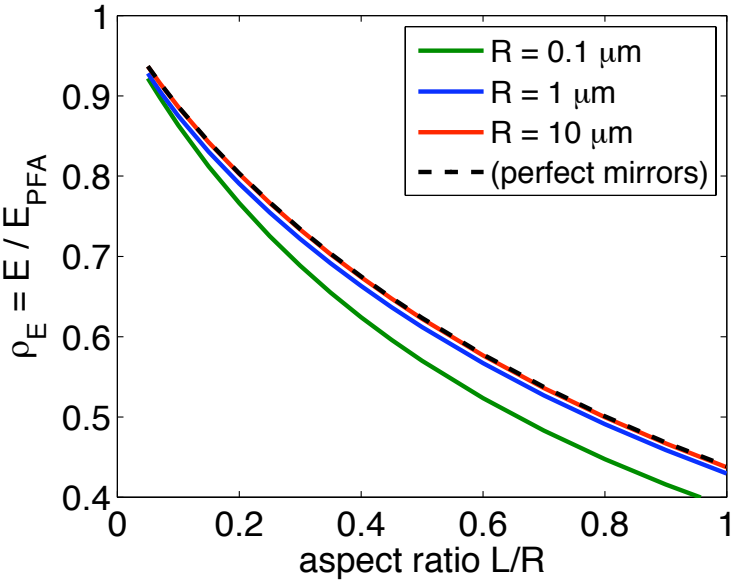

Figure 52: Beyond-PFA correction factor for the Casimir energy $\rho_E = \frac{E}{E_{\rm PFA}}$ between a metallic sphere and a metallic plane, modelled with the Drude model. Green curve represents the case of a small sphere, blue curve an intermediate sphere, and the red and black curves larger spheres. The R-independent factor $\rho_E^{\rm perf}$ for perfect mirrors is drawn with a dashed-curve. The parameters for the Drude model are those of gold ($\lambda_P = 136$ nm; $\delta = 0.004$).

From the study in the plane-plane configuration with metallic mirrors discussed in **Section 2.5** (p.42), we know that $\nu_E \in]1,2[$ and $\nu_F \in]2,3[$, where the minimum values are obtained when $L \ll \lambda_P$ and the maximum values when $L \gg \lambda_P$. For perfect mirrors at zero temperature, we always have $\nu_E = 2$ and $\nu_F = 3$. The two functions f_β and f_γ are plotted in **Fig 53** as functions of the distance L.

The first function f_β, represented by a black dashed-line, takes values in $\left]0, \frac{1}{3}\right[$, and is always smaller than $f_\beta(L \gg \lambda_P)$. It yields that the coefficient $\beta_G^{\rm Drud} = f_\beta(L) \times \beta_E^{\rm Drud}$ for mirrors described by the Drude model can be significantly diminished with respect to the one for perfect mirrors. It thus makes room for the possibility of a β_G within the experimental bound.

The second function f_γ is always negative, meaning that the coefficients γ_E and γ_G do not have the same sign when considering the Drude model. From the convexity of ρ_E, visible on **Fig. 52**, we assume that the second order coefficient γ_E for the beyond-PFA correction $\rho_E^{\rm Drud}$ of the Casimir energy is positive. It yields that $\gamma_G < 0$ and the correction ρ_GDrud for the force gradient should be a concave function for small values of the aspect ratio $\frac{L}{R}$.

We present in **Fig. 54** the results of numerical evaluations of the Casimir force gradient G for small values of the aspect ratio, and their extrapolation to even smaller values with the help of a polynomial fit. The chosen model is the loss-less plasma one, but the dissipative Drude model gives similar results for the considered sphere radius and distance range.

For intermediate aspect ratios ($L \sim R$), we observe in the right part of the curve that $\rho^{\rm plas} < \rho^{\rm perf}$, which means that the error made by PFA is increased when accounting for imperfect reflection in the optical response of the mirrors. But for smaller distances, the two curves cross each other, and the beyond-PFA correction for plasma $\rho^{\rm plas}$ is greater than the one for perfect reflectors $\rho^{\rm perf}$. This yields that for small aspect ratios, the correlation number δ_G^{TG} for the force gradient is positive, and that the error of PFA is decreased when accounting for imperfect reflection in the mirrors

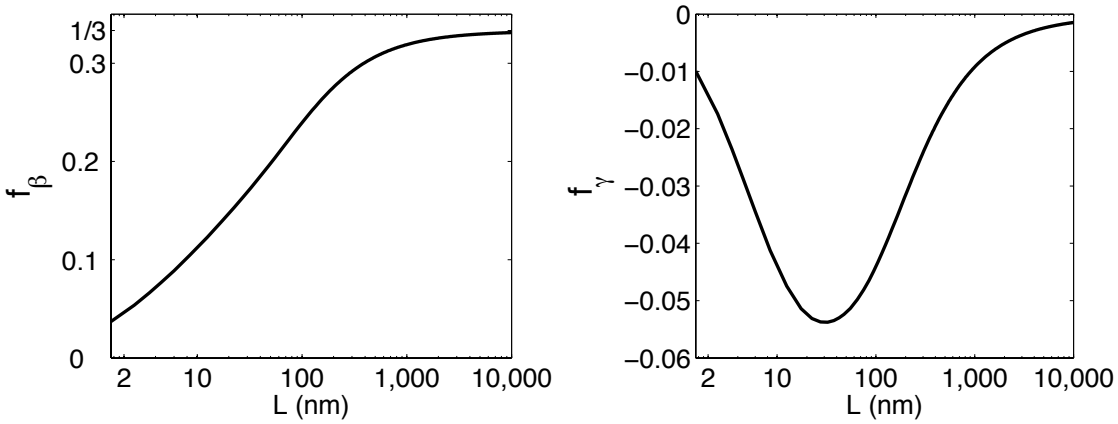

Figure 53: Functions f_β (left) and f_γ (right) as functions of the distance L. The former increases from 0 to $\frac{1}{3}$, the latter is 0 at the two extremities, and undergoes a minimum -0.0538 at $L \simeq 32.5$ nm. The parameters for the Drude model are $\lambda_P = 136$ nm and $\delta = 0.004$.

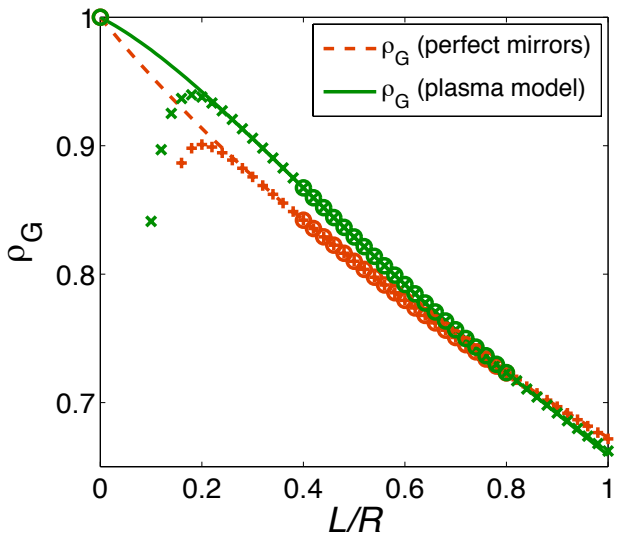

Figure 54: Beyond-PFA correction factor for the Casimir force gradient $\rho_G = \frac{G}{G_{\rm PFA}}$ and its extrapolation to smaller values of the aspect ratio $\frac{L}{R}$. Red elements correspond to perfect reflectors, while green to mirrors described by the plasma model. Crosses are the numerically obtained data for the force gradient G, normalized by the PFA result $G_{\rm PFA}$. The drop-ff on the left side is due to the numerical $\ell_{\rm max}$ cut-off. Circles are the trustable data points used to compute the extrapolation fit. The red dashed-line and solid green curve are the extrapolation fit, for perfect and plasma models, respectively. The sphere radius is $R = 0.1$ μm, the plasma wavelength is $\lambda_P = 136$ nm.

optical response.

As the curve is approaching to unity at the limit of infinite radius ($\frac{L}{R} \to 0$), this cross-over yields a bending of the curve $\rho^{\text{plas}}\left(\frac{L}{R}\right)$ for small aspect ratios, which becomes as expected a concave function in this region. This last feature has an influence on the linear correction β_G extracted from the initial slope of the fitting polynomial. For perfect reflectors in Eq.(10.6) (p.147), this slope was $\beta_G^{\text{perf}} \simeq -0.49$. It clearly becomes much smaller in magnitude for mirrors described by the plasma model. For the nanospheres ($R = 100$ nm) here considered, we find $\beta_G \simeq -0.2$. This implies that the result of this extrapolation on the beyond-PFA correction is no more in contradiction with the experimental bound ($|\beta_G| < 0.4$) stated in [224] and discussed in **Section 9.4** (p.141).

12 Results for dielectric nanospheres

In this section we will apply our findings to the particular situation of the long-range interaction between a dielectric nanosphere and a metallic surface. This study is motivated by the intriguing phenomenon of small heating of ultra-cold neutrons (UCNs) in traps [80, 81, 82]. This thermal shift could be explained by the interaction between UCNs and nanospheres levitated in the quantum states created by their interaction with surfaces [235]. In order to characterize this phenomenon and compute the properties of the quantum states, one needs a detailed and careful treatment of the interaction potential. We will see along this discussion that for this configuration the commonly used Casimir-Polder formula (12.1), even improved by integration techniques, is not sufficient to this purpose. The results presented in this section have been the object of a published article [235].

The Casimir-Polder interaction [236] describes the change of energy experienced by an atom close to a reflecting surface. The origin of the effect is quite similar to the Casimir energy of two plates, except that the cavity, formed by the atom and the plane, is open. While for very small distances the dominant force is an electrostatic attraction between the atomic dipole and its image [40], for larger distances the effect of retardation becomes important and has to be included.

For an atom with a polarizability $\alpha(i\xi)$, in front of a plane whose Fresnel reflection coefficients are $r_{\mathrm{TE}}, r_{\mathrm{TM}}$, the Casimir-Polder interaction energy at zero-temperature can be written as [237, 40, 238, 239, 240]:

$$E_{\mathrm{CP}} = \hbar \int_0^\infty \frac{d\xi}{2\pi} \frac{\alpha(i\xi)}{4\pi\epsilon_0} \int_0^\infty \frac{kdk}{\kappa} \left[\frac{\xi^2}{c^2} |r_{\mathrm{TE}}| + \left(\kappa^2 + k^2\right) |r_{\mathrm{TM}}| \right] e^{-2\kappa L} \tag{12.1}$$

The Casimir-Polder formula is founded on a point-like description of the atom, as its size is neglected and never appears in the description. The idea is appealing and in principle reasonable for 'small' objects, but the meaning of this restriction remains to be defined.

The scattering formula does not assume an object as point-like but instead takes into account the full optical response of an object to compute the interaction with a surface. We will see that in the situation of a nanosphere in front of a plane, the scattering formula turns out to be equivalent to the Casimir-Polder formula when the radius R of the nanosphere is small compared to all other length scales. Our method behaves specifically well when the object is small compared to the distance, a limiting case similar to the point-like approximation, because only a few multipoles must be taken into account, but is however not restricted to this situation. We will thus be able to test the limits of applicability of the Casimir-Polder formula to small objects.

This section is organised as follows: we first show in **Section 12.1** that the Casimir-Polder expression is recovered from the scattering formula in the limit of a punctual sphere, and study the long and short distance regimes of the Casimir-Polder formula. Then we study in **Section 12.2** the complete multipolar expression E that we obtain from the scattering formalism. Finally we compare in **Section 12.3** the results from the scattering formalism and from Casimir-Polder formula, and its improvement through an averaging over the sphere's volume.

12.1 The Casimir-Polder formula for a dielectric nanosphere

In this section, we consider the scattering formula for the Casimir energy at the limit of a punctual sphere ($R \ll L$), which is equivalent to the long-distance limit studied in **Section 8** (p.124). We show that the Casimir-Polder expressions are recovered for very small spheres, as expected.

For that derivation, we will make the additional hypothesis that the material for the sphere is not a perfect reflector, and that its permittivity $\varepsilon_S(i\xi)$ remains finite at all frequencies. In doing so, we will remove the unphysical possibility of a non-vanishing magnetic response for the point-like sphere, which will become clearer during the derivation. We also keep the same description of the dielectric function $\varepsilon_S(i\xi)$ for small values of R, which would not have been possible for metallic

nanospheres, because of the confinement effect for conduction electrons [210, 211]. The material for the planar surface is not yet specified, and its optical properties are contained in the specular Fresnel coefficients $r_{\mathrm{TE}}, r_{\mathrm{TM}}$.

12.1.1 The scattering formula at the limit of a punctual sphere

We start from the scattering formula in the sphere-plane configuration, explicitly given in **Section 5.4** (p.78):

$$E = \frac{\hbar c}{2\pi}\int_0^\infty \mathrm{d}\hat{\xi}\,\ln\det\mathcal{D}(\hat{\xi})$$

with $\hat{\xi} = \frac{\xi}{c} = \frac{\tilde{\xi}}{R}$. In **Section 8.1** (p.124), we explained that in the long distance limit ($L \gg R$), this formula could be simplified by a dipolar-simple scattering approximation. It resulted in a simpler expression for the integrand function:

$$\begin{aligned}\Phi_{\mathrm{LD}}(\hat{\xi}) = \frac{3}{2}\int_1^\infty \mathrm{d}\cos\theta e^{-2\hat{\xi}\mathcal{L}\cos\theta} \\ \times\left[a_1(R\hat{\xi})\left(r_{\mathrm{TM}}(2\cos^2\theta-1)-r_{\mathrm{TE}}\right)+b_1(R\hat{\xi})\left(r_{\mathrm{TE}}(2\cos^2\theta-1)-r_{\mathrm{TM}}\right)\right]\end{aligned} \tag{12.2}$$

where $a_1(R\hat{\xi})$ and $b_1(R\hat{\xi})$ are the Mie coefficients for the reflection on the sphere with $\ell = 1$, and r_{TE} and r_{TM} the Fresnel coefficients for the reflection on the plane. With a finite $\varepsilon_S(i\xi)$, the Mie coefficients have the following expansion for small values of the parameter $(R\hat{\xi})$:

$$\begin{aligned}a_1(R\hat{\xi}) &= -\frac{2}{3}\frac{\varepsilon_S-1}{\varepsilon_S+2}\left(R\hat{\xi}\right)^3+\frac{2}{5}\frac{(\varepsilon_S-2)(\varepsilon_S-1)}{(\varepsilon_S+2)^2}\left(R\hat{\xi}\right)^5 \\ &\quad -\frac{4}{9}\left(\frac{\varepsilon_S-1}{\varepsilon_S+2}\right)^2\left(R\hat{\xi}\right)^6+\mathcal{O}\left(\left(R\hat{\xi}\right)^7\right) \\ b_1(R\hat{\xi}) &= \frac{\varepsilon_S-1}{45}\left(R\hat{\xi}\right)^5-\frac{(\varepsilon_S-1)(2\varepsilon_S-5)}{945}\left(R\hat{\xi}\right)^7 \\ &\quad +\frac{\varepsilon_S^2(\varepsilon_S-1)}{4725}\left(R\hat{\xi}\right)^9+\mathcal{O}\left(\left(R\hat{\xi}\right)^{10}\right)\end{aligned} \tag{12.3}$$

where the dependence of ε_S on the imaginary frequency $\imath\xi$ is implicit.

Because of the term $e^{-2\hat{\xi}\mathcal{L}\cos\theta}$ in Eq.(12.2) in the integrand, $\hat{\xi} \lesssim \frac{1}{\mathcal{L}}$ and $R\hat{\xi} = \tilde{\xi} \lesssim \frac{R}{L} \ll 1$ (as discussed previously in the beginning of **Section 8.1**, p.124). Then the coefficient b_1 will give a negligible contribution compared to the coefficient a_1. This would not be the case with a perfectly reflecting sphere, whose low-frequency Mie coefficients (7.6) (p.109) are $a_1 \simeq -\frac{2}{3}\left(R\hat{\xi}\right)^3$ for the electric and $b_1 \simeq \frac{1}{3}\left(R\hat{\xi}\right)^3$ for the magnetic dipole. The additional hypothesis we made about the finite conductivity is then equivalent to keeping only the electric dipole, and discarding the magnetic one.

The integrand function (12.2) then simplifies to:

$$\begin{aligned}\Phi_{\mathrm{LD}}(\hat{\xi}) &= \frac{3}{2}\int_0^\infty \mathrm{d}\cos\theta e^{-2\hat{\xi}\mathcal{L}\cos\theta}a_1(R\hat{\xi})\left[r_{\mathrm{TM}}(2\cos^2\theta-1)-r_{\mathrm{TE}}\right] \\ &= -\frac{\varepsilon_S-1}{\varepsilon_S+2}R^3\int_{\hat{\xi}}^\infty \mathrm{d}\kappa\; e^{-2\kappa\mathcal{L}}\left[r_{\mathrm{TM}}(2\kappa^2-\hat{\xi}^2)-\hat{\xi}^2 r_{\mathrm{TE}}\right] \\ &= -\frac{\varepsilon_S-1}{\varepsilon_S+2}R^3\int_0^\infty \frac{k\mathrm{d}k}{\kappa}\; e^{-2\kappa\mathcal{L}}\left[r_{\mathrm{TM}}(k^2+\kappa^2)-\hat{\xi}^2 r_{\mathrm{TE}}\right]\end{aligned}$$

Using $\mathcal{L} = L + R \simeq L$, to replace $\mathcal{L}$ by L in the translation operators $e^{-2\kappa\mathcal{L}}$, we finally obtain an energy $E_{\rm CP}$, whose expression is similar to the Casimir-Polder formula (12.1), with an electric polarizability[16] $\alpha_S(i\xi)$ for the sphere obeying a Clausius-Mosotti relation:

$$E_{\rm CP} = -\hbar \int_0^\infty \frac{d\xi}{2\pi} \frac{\alpha_S}{4\pi\epsilon_0} \int_0^\infty \frac{k\mathrm{d}k}{\kappa} \left(\hat{\xi}^2 |r_{\rm TE}| + \left(k^2 + \kappa^2\right) |r_{\rm TM}| \right) e^{-2\kappa L} \qquad (12.4)$$

$$\text{with} \quad \frac{\alpha_S}{4\pi\epsilon_0} = \frac{\varepsilon_S(i\xi) - 1}{\varepsilon_S(i\xi) + 2} R^3 \ .$$

Here we have used the fact that $r_{\rm TE}\,(i\xi) < 0$ and $r_{\rm TM}\,(i\xi) > 0$ with our convention for the sign of the Fresnel coefficients. We repeat at this point that the energy $E_{\rm CP}$ in the formula (12.4) has been obtained from the scattering formula for E after two simplifications corresponding to the perturbative approximation and electric dipolar approximation. We will see in the next sections that it contains in particular the limits of non-retarded van der Waals and retarded Casimir-Polder expressions [239, 240], as does the Casimir-Polder interaction between atoms [236]. The energy $E_{\rm CP}$ always scales as R^3, that is also the volume of the sphere. This result means that the nanosphere behaves as a big atom with a polarizability α_S proportional to its volume at the limit $R \ll L$. As we will see in the next sections, this simple behavior does not remain true for arbitrary values of the radius R, outside the range of validity of the electric dipolar-simple scattering approximation. This is already visible from the ratio of the two energies E and $E_{\rm CP}$ presented in **Fig. 55**. While at the limit of large distances ($L \gg R$), $E_{\rm CP}$ efficiently predicts the correct quantity for the energy, E and $E_{\rm CP}$ depart from each other when the distance decreases, as soon as $L \lesssim 100R$.

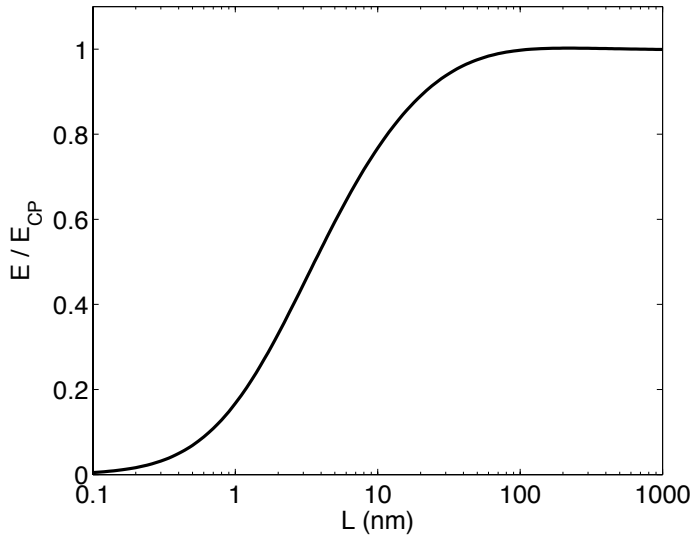

Figure 55: Ratios of the exact energy E to its Casimir-Polder-like expression $E_{\rm CP}$ obtained from electric dipolar-simple scattering approximation. The sphere radius is $R = 1$ nm.

We now study how the formula for the Casimir-Polder energy (12.4) behaves in the limiting cases of small and large distances. At short separations we expect to recover the non retarded Van der Walls expression, while at large separations the retarded Casimir-Polder one should be obtained. First we need to characterize the sense of 'short' and 'large' distances, with lengthscales characterizing the optical response of the materials. Then the expression (12.4) for the energy will be derived in each limiting case. We emphasis that the expression (12.4) has been derived from

[16] In SI units.

the scattering with the assumption ($R \ll L$), which is then implicit in every additional limiting case studied.

12.1.2 Description of the materials properties

We first specify the materials for the two objects for illustrative purpose, and choose the case of interest for UCN studies [235], namely a diamond nanosphere above a copper plane. We model the optical response of copper by a plasma model:

$$\varepsilon_P(i\xi) = 1 + \frac{\omega_P^2}{\xi^2} \tag{12.5}$$

where ω_P^2 is the squared plasma frequency, proportional to the density of conduction electrons in the metal. For explicit calculations, we will use the relation $\omega_P = 2\pi c/\lambda_P$ with the plasma wavelength $\lambda_P = 136$nm. We do not choose a Drude model for practical purpose in the derivations. It would be possible to include dissipation in the metal through a damping rate γ, however this parameter would be small compared to ω_P for a good metal such as copper, and its influence would also be small at the not too large distances considered in the present study (see [140] for more details and references).

The dielectric function of diamond is described by a Sellmeier model:

$$\varepsilon_S(i\xi) = 1 + \sum_i \frac{B_i \omega_i^2}{\omega_i^2 + \xi^2} \tag{12.6}$$

for which a sufficient description is obtained with a single component. We use $B_1 = 4.91$ and $\omega_1 = 2\pi c/\lambda_1$ with the wavelength $\lambda_1 = 106$nm. The damping is disregarded here since it does not play any significant role.

For copper, $\varepsilon_P(i\xi)$ is very large for ξ much smaller than ω_P, which means that the metal tends to become a very good reflector. For diamond, $\varepsilon_S(i\xi)$ tends to its static value $\varepsilon_S(0) = 1 + B_1$ for ξ much smaller than ω_1. For larger frequencies in contrast, the dielectric properties become poorer for diamond as well as copper. As ω_P and ω_1 have similar values, we thus expect a transition to take place between van der Waals and Casimir-Polder regimes [236] when the distance between two objects is of the order of λ_P or λ_1. The two presented models (12.5-12.6) could easily be improved by taking into account dissipation and interband transitions for copper, and multiple components and damping in the Sellmeier model for diamond, but are here simplified for illustrative purpose.

12.1.3 Long distance regime ($L \gg \lambda_1, \lambda_P$)

The long-distance regime will be determined by the contribution of low frequencies to the Casimir effect, and the optical properties of the two objects specified in the previous will take a simpler form. For the dielectric nanosphere modeled by a Sellmeier equation (12.6), the condition $L \gg \lambda_1$ allows to write that $\xi \lesssim \frac{c}{L} \ll \frac{2\pi c}{\lambda_1} = \omega_1$ and finally the dielectric constant simplifies to its static value $\varepsilon_S(\xi) \simeq \varepsilon_S(0) = 1 + B_1$. For the metallic plane, the condition $L \gg \lambda_P$ allows to write that $\frac{\xi}{\omega_P} \lesssim \frac{\lambda_P}{2\pi L} \ll 1$, and the Fresnel coefficients go to unity: $r_{\mathrm{TE}} = -1$, $r_{\mathrm{TM}} = 1$. For practical purpose we introduce the dimensionless parameters:

$$\bar{\kappa} = \kappa L \quad ; \quad \bar{\xi} = \frac{\xi L}{c} \quad ; \quad \bar{k} = kL$$
$$\overline{\alpha_0} = \frac{\varepsilon_S(0) - 1}{\varepsilon_S(0) + 2} = \frac{\alpha_S(0)}{4\pi\epsilon_0 R^3} = \frac{B_1}{B_1 + 3} \ .$$

With those low-frequency simplifications on the optical properties, the Casimir energy $E_{\rm CP}$ can be computed analytically:

$$\begin{aligned}
E_{\rm CP} &\simeq -\frac{\hbar c}{2\pi L^4}\int_0^\infty \mathrm{d}\bar{\xi}\ \overline{\alpha_0}R^3\int_0^\infty \frac{\bar{k}\mathrm{d}\bar{k}}{\bar{\kappa}}\left(\bar{\xi}^2+\bar{k}^2+\bar{\kappa}^2\right)e^{-2\bar{\kappa}} \\
&= -\frac{\hbar c\overline{\alpha_0}R^3}{2\pi L^4}\int_0^\infty \mathrm{d}\bar{\xi}\ \int_{\bar{\xi}}^\infty \mathrm{d}\bar{\kappa}\ 2\bar{\kappa}^2 e^{-2\bar{\kappa}} \\
&= -\frac{\hbar c\overline{\alpha_0}R^3}{\pi L^4}\int_0^\infty \mathrm{d}\bar{\xi}\ I_2(\bar{\xi}) \\
&= -\frac{\hbar c\overline{\alpha_0}R^3}{4\pi L^4}\int_0^\infty \mathrm{d}\bar{\xi}\ e^{-2\bar{\xi}}\left(1+2\bar{\xi}+2\bar{\xi}^2\right) \\
&= -\frac{3\hbar c\overline{\alpha_0}R^3}{8\pi L^4} \qquad (R,\lambda_1,\lambda_P \ll L) \\
E_4 &= -\frac{c_4}{L^4}\left(\frac{4}{3}\pi R^3\right) \quad \text{with } c_4 = \frac{9\hbar c\overline{\alpha_0}}{32\pi^2}
\end{aligned} \tag{12.7}$$

and an energy with a L^{-4} power law is obtained, similarly to a retarded Casimir-Polder expression. This long-distance limit of $E_{\rm CP}$ will be noted E_4 from now on.

12.1.4 Short distance regime ($L \ll \lambda_P$)

In the short-distance regime, we reverse the condition to $L \ll \lambda_P$, and we do not need any assumption on λ_1. This limit is usually referred to as the plasmon limit in many situations, and yields simplifications in the Fresnel coefficients. Let us first observe that $\bar{\kappa} \sim 1$ with the following re-orderings of the Casimir-Polder formula (12.4) for a dielectric nanosphere:

$$\begin{aligned}
E_{\rm CP} &= -\frac{\hbar cR^3}{2\pi L^4}\int_0^\infty \mathrm{d}\bar{\xi}\ \left(\frac{\varepsilon_S(\bar{\xi})-1}{\varepsilon_S(\bar{\xi})+2}\right)\int_{\bar{\xi}}^\infty \mathrm{d}\bar{\kappa}\ \left(\bar{\xi}^2|r_{\rm TE}|+(\bar{k}^2+\bar{\kappa}^2)|r_{\rm TM}|\right)e^{-2\bar{\kappa}} \\
&= -\frac{\hbar cR^3}{2\pi L^4}\int_0^\infty \mathrm{d}\bar{\kappa}\ e^{-2\bar{\kappa}}\int_0^{\bar{\kappa}} \mathrm{d}\bar{\xi}\left(\frac{\varepsilon_S(\bar{\xi})-1}{\varepsilon_S(\bar{\xi})+2}\right)\left(\bar{\xi}^2|r_{\rm TE}|+(\bar{k}^2+\bar{\kappa}^2)|r_{\rm TM}|\right) \\
&= -\frac{\hbar cR^3}{2\pi L^4}\int_0^\infty \mathrm{d}\bar{\kappa}\ \phi(\bar{\kappa})\ .
\end{aligned}$$

For $\bar{\kappa} \gg 1$, $\phi(\bar{\kappa})$ is small because of the term $e^{-2\bar{\kappa}}$. For $\bar{\kappa} \ll 1$, $\phi(\bar{\kappa})$ is small because the integration domain for $\bar{\xi}$ becomes very small. Therefore, the former integral only contains noticeable contribution from values $\bar{\kappa} \sim 1$.

Let us now study the Fresnel coefficients in the plasmon limit ($L \ll \lambda_P$). We first define the parameter x from the permittivity $\varepsilon_P(\imath\xi)$ for the plane (12.5):

$$x = \frac{\bar{\xi}}{\bar{\kappa}}\sqrt{\varepsilon_P - 1} = \frac{2\pi L}{\bar{\kappa}\lambda_P}$$

where $\frac{\lambda_P}{2\pi L} \gg 1$ in the plasmon limit, leading to $x \ll 1$. The Fresnel coefficients can be easily studied by using their expression depending on the parameter x:

$$r_{\rm TE} = \frac{1-\sqrt{1+x^2}}{1+\sqrt{1+x^2}} \qquad\qquad r_{\rm TM} = \frac{1+\left(\frac{\bar{\kappa}}{\bar{\xi}}\right)^2 x^2-\sqrt{1+x^2}}{1+\left(\frac{\bar{\kappa}}{\bar{\xi}}\right)^2 x^2+\sqrt{1+x^2}}\ .$$

In the present case, with $x \ll 1$, we conclude that the first coefficient is negligible: $r_{\mathrm{TE}} = -\frac{x^2}{4} + \mathcal{O}\left(x^4\right)$ and that the only contribution in the integral over $\bar{\kappa}$ are for $\bar{\kappa} \gg \bar{\xi}$, which allow r_{TM} to have noticeable values. In this case the second reflection coefficient takes a Lorentzian form:

$$r_{\mathrm{TM}} = \frac{\left(\frac{\bar{\kappa}}{\bar{\xi}}\right)^2 x^2 + \mathcal{O}\left(x\right)}{2 + \left(\frac{\bar{\kappa}}{\bar{\xi}}\right)^2 x^2 + \mathcal{O}\left(x^2\right)} \simeq \frac{1}{1 + \left(\frac{\bar{\xi}}{K_P}\right)^2} \quad \text{with} \quad K_P = \frac{2\pi L}{\sqrt{2}\lambda_P} \ .$$

Then the reduced polarizability $\alpha_S(\bar{\xi})$ for the sphere can also be written in a Lorentzian form:

$$\frac{\varepsilon_S(\bar{\xi}) - 1}{\varepsilon_S(\bar{\xi}) + 2} = \frac{\overline{\alpha_0}}{1 + (1 - \overline{\alpha_0})\left(\frac{\xi}{\omega_1}\right)^2} = \frac{\overline{\alpha_0}}{1 + \left(\frac{\bar{\xi}}{K_S}\right)^2} \qquad \text{with } K_S = \frac{2\pi L}{\lambda_1\sqrt{1 - \overline{\alpha_0}}}$$

and the computation of the Casimir energy can then be carried out as an integration of a product of two Lorentzian forms:

$$\begin{aligned}
E_{\mathrm{CP}} &\simeq -\frac{\hbar c R^3}{2\pi L^4} \int_0^\infty \mathrm{d}\bar{\xi} \ \left(\frac{\varepsilon_S(\bar{\xi}) - 1}{\varepsilon_S(\bar{\xi}) + 2}\right) \int_{\bar{\xi}}^\infty \mathrm{d}\bar{\kappa} \ (\bar{k}^2 + \bar{\kappa}^2) r_{\mathrm{TM}}(\bar{\xi}, \bar{\kappa}) e^{-2\bar{\kappa}} \\
&= -\frac{\hbar c R^3}{\pi L^4} \int_0^\infty \frac{\mathrm{d}\bar{\xi}}{1 + \left(\frac{\bar{\xi}}{K_P}\right)^2} \left(\frac{\varepsilon_S(\bar{\xi}) - 1}{\varepsilon_S(\bar{\xi}) + 2}\right) \int_0^\infty \mathrm{d}\bar{k} \ \bar{k}^2 e^{-2\bar{k}} \\
&= -\frac{\hbar c R^3}{4\pi L^4} \int_0^\infty \frac{\mathrm{d}\bar{\xi}}{1 + \left(\frac{\bar{\xi}}{K_P}\right)^2} \frac{\overline{\alpha_0}}{1 + \left(\frac{\bar{\xi}}{K_S}\right)^2} \\
&= -\frac{\hbar c R^3 \overline{\alpha_0}}{8L^4} \frac{K_P K_S}{K_P + K_S} \\
&= -\frac{\hbar c \pi \overline{\alpha_0} R^3}{4\left(\sqrt{2}\lambda_P + \lambda_1\sqrt{1 - \overline{\alpha_0}}\right) L^3} \qquad (R \ll L \ll \lambda_P) \qquad (12.8) \\
E_3 &= -\frac{c_3}{L^3}\left(\frac{4}{3}\pi R^3\right) \quad \text{with } c_3 = \frac{3\hbar c \overline{\alpha_0}}{16\left(\sqrt{2}\lambda_P + \lambda_1\sqrt{1 - \overline{\alpha_0}}\right)} \ .
\end{aligned}$$

An energy with a L^{-3} power law is obtained, similar to a non-retarded van der Waals expression. It shows that the power-law in L changes from L^{-4} to L^{-3} just because of the imperfect reflection on the plane, leading to the plasmon limit for short distances $L \ll \lambda_P$.

This last result is a first clue that using a point-like picture for the nanosphere, underlying the Casimir-Polder formula, can lead to difficulties. For instance, if one wants to solve the Schrödinger equation for the wave function of a small object close to the surface, the problem becomes singular at the origin when the potential behaves like L^{-n}, with $n \geq 2$ [241]. The short-distance limit E_3 thus shows that the Casimir-Polder formula cannot lead to a well-posed mathematical problem, and that it is necessary to consider another approach, which would take into account the finite size of the nanosphere. In the next section, we show how using the complete multipolar expression from the scattering formalism allows to solve this kind of problem.

12.2 The complete multipolar expression E

We now consider the complete multipolar and multiscattering expression for the Casimir energy E when we remove the small sphere hypothesis ($R \ll L$). This term is given by the complete

scattering formula. We first consider the large and short separation limits, then we analyse the dependance on the parameters L and R to observe the differences with the dipolar-simple scattering Casimir-Polder quantity $E_{\rm CP}$.

For the large distance limit of the expression E, the condition $(L \gg \lambda_P, \lambda_1, R)$ is recovered, and the retarded Casimir-Polder result E_4 of Eq.(12.7) is obtained. This is illustrated by the convergence to unity of the ratio $\frac{E}{E_{\rm CP}}$ in **Fig. 55** (p.160), and is connected to the fact that the limits of small sphere and large distance are compatible.

12.2.1 The short distance limit

The short distance limit however writes $(L \ll \lambda_P, \lambda_1, R)$, and the relation between L and R is inverted with respect to E_3 presented in Eq.(12.8), which may change the resulting expansion of the energy. In this limit, the proximity force approximation is valid and allows to derive an asymptotic expression for the energy $E^{\rm plas}_{\rm PFA} = 2\pi R D^{\rm plas}_{\rm PP}$ from the primo-potential $D^{\rm plas}_{\rm PP}$ in the plane-plane configuration, introduced in **Section 4.2** (p.56).

The plasmon limit $L \ll \lambda_P$ has been studied in the case of two plates of the same material modelled by the plasma model in [121, 133] for the Casimir force F, whose results are discussed in **Section 2.5** (p.42) and lead to a finite conductivity correction factor $\eta_F^P \simeq \alpha \frac{L}{\lambda_P}$, with a constant $\alpha \simeq 1.1933$. In the limit of short distances, the power of $\frac{1}{L}$ in the Casimir force thus loses one order. Below we present the corresponding result for the plane-plane energy $E^{\rm plas}_{\rm PP}$ and primo-potential $D^{\rm plas}_{\rm PP}$, obtained through consecutive integrations of $F^{\rm plas}_{\rm PP}$, and the finally resulting PFA energy in the sphere-plane case:

$$
\begin{aligned}
F^{\rm plas}_{\rm PP} &= \eta_F^P F^{\rm perf}_{\rm PP} \simeq -\frac{\hbar c \pi^2 \alpha A}{240 \lambda_P L^3} && \eta_F^P \simeq \alpha \frac{L}{\lambda_P} \\
E^{\rm plas}_{\rm PP} &\simeq -\frac{\hbar c \pi^2 \alpha A}{480 \lambda_P L^2} && \eta_E^P \simeq \frac{3\alpha}{2} \frac{L}{\lambda_P} \\
D^{\rm plas}_{\rm PP} &\simeq -\frac{\hbar c \pi^2 \alpha A}{480 \lambda_P L} && \eta_D^P \simeq 3\alpha \frac{L}{\lambda_P} \\
E^{\rm plas}_{\rm PFA} &= 2\pi R \frac{D^{\rm plas}_{\rm PP}}{A} \simeq -\frac{\hbar c \pi^3 \alpha R}{240 \lambda_P L} && (12.9) \\
\text{with} \quad \alpha &= \frac{30}{\sqrt{2}\pi^2} \sum_{n=1}^{\infty} \frac{1}{n^3} \frac{(4n-3)!!}{(4n-2)!!} \simeq 1.1933 \ .
\end{aligned}
$$

A similar conductivity reduction factor η_F^P has been derived [218] for the case of a plasma plate in front of a Sellmeier plate, and yields:

$$
\begin{aligned}
\eta_F^P &= \frac{15}{2\pi^{7/2}} \sum_{n=1}^{\infty} \frac{\left(\frac{B_1}{B_1+2}\right)^n}{n^3} \sum_{k=0}^{n-1} \frac{\Gamma(n+k)\Gamma(n-k-1/2)}{\Gamma(n)\Gamma(n-k)\Gamma(k+1)} \left(\frac{(-1)^n \Omega_p^{2k+1} \Omega_1^{*2n} + (-1)^k \Omega_p^{2n} \Omega_1^{*2k+1}}{(\Omega_P^2 - \Omega_1^{*2})^{n+k}} \right) \\
&= \alpha^* \frac{L}{\lambda^*} \qquad (12.10)
\end{aligned}
$$

with $\Omega_P = \frac{2\pi L}{\lambda_P}$, $\Omega_1^* = \sqrt{B_1+2}\frac{2\pi L}{\lambda_1}$, and $\frac{\lambda^*}{\alpha^*} = 108.51$ nm for the present values of the parameters. From the power law for Ω_P and Ω_1^* in (12.10), we see that the conductivity reduction factor takes the usual form $\alpha^* \frac{L}{\lambda^*}$, where λ^* is a combination of λ_P, λ_1 and B_1, and α^* is a complicated, yet numerically computable, number that depends only on B_1. Finally, thanks to a procedure similar to the one presented in (12.9), we get $E_{\rm PFA}$, which is the short distance limit of the complete multipolar Casimir energy E:

$$
E_{\rm PFA} = -\frac{\hbar c \pi^3 \alpha^* R}{240 \lambda^* L} \qquad (L \ll \lambda_P, \lambda_1, R) \ . \qquad (12.11)
$$

This result is very different from E_3 obtained in Eq.(12.8) for the short-distance limit of the Casimir-Polder limit, the clearer sign being the observation that $E_3 \propto \frac{R^3}{L^3}$, and $E_{\rm PFA} \propto \frac{R}{L}$. This change comes from the integration of all multipoles in the description of the scattering, and can be illustrated from the oversimplified following derivation, inspired by the low-frequency expansion of the Mie coefficients $a_\ell \sim \tilde{\xi}^{2\ell+1} \propto \left(\frac{R}{L}\right)^{2\ell+1}$:

$$\sum_{\ell=1}^{\infty} \left(\frac{R}{L}\right)^{2\ell+1} = \underbrace{\frac{R^3}{L^3}}_{\text{dipolar}} + \underbrace{\frac{R^5}{L^5}}_{\text{quadrupolar}} + \cdots = \frac{R^3}{L^3}\frac{1}{1+\left(\frac{R}{L}\right)^2} = \frac{R^3}{L(L^2+R^2)}$$

which becomes $\frac{R^3}{L^3}$ when $L \gg R$, as in E_3, and $\frac{R}{L}$ when $L \ll R$, as in $E_{\rm PFA}$.

The ill-behaved Schrödinger problem caused by the L^{-3} dependance in E_3 for the commonly used Casimir-Polder formula is then solved for the present case of a nanosphere by taking into account its finite size through a full multipolar and multiscattering treatment of the cavity. The exact solution E for a finite value of R predicts a smoother power law L^{-1} in the vicinity of the surface and thus leads to a regular solution for the Shrödinger equation [235]. This plays a crucial role in the determination of the quantum states obtained by solving the Schrödinger equation for the wave function of the nanosphere in this potential, in the study of the interaction between UCNs and nanospheres, but could also for possible other applications [242].

12.2.2 Power laws in L and R for the Casimir energy

To study the dependence for the Casimir energy on the surface-surface distance L and on the radius of the sphere R, we will use as previously the logarithmic slopes (log-log derivatives) of the absolute value of the energy $|E| = -E$:

$$\nu = -\frac{\partial \ln|E|}{\partial \ln L} = \frac{LF}{E} \qquad\qquad \mu = \frac{\partial \ln|E|}{\partial \ln R}$$

where $F = -\frac{\partial E}{\partial L}$ is the Casimir force derived from an energy E.

The parameter μ is always 3 for the perturbative electric dipolar approximation $E_{\rm CP}$ in (12.4), as it is equivalent to a Casimir-Polder formula with a Clausius-Mosotti relation for the polarizability of the sphere. On the contrary, ν should shift from 4 at long distance to 3 at short distance for $E_{\rm CP}$, as expected from the asymptotic forms of the retarded Casimir-Polder energy E_4 and the non-retarded van der Waals energy E_3 obtained in Eqs. (12.7) and (12.8), respectively.

The complete expression of the Casimir energy E between the plane and the nanosphere, coming from the scattering formula, takes into account the size of the nanosphere with the inclusion of higher multipoles in its optical response, and higher order reflections inside the cavity. While the large distance behavior should be the same as $E_{\rm CP}$, the short distance behavior is now given by the PFA result (12.11), and differs significantly from the computation with a point-like sphere (12.8), as it has the power law parameters ($\nu = 1; \mu = 1$), compared to ($\nu = 3; \mu = 3$) for E_3 under the same conditions.

We see on the left graph of **Fig. 56** that ν tends to the expected value 4 at large distances. At small distances in contrast, the van der Waals value $\nu = 3$ obtained in (12.8) is never a good approximation, which can be understood by inspecting the conditions ($R \ll L \ll \lambda_P$) for E_3 to be valid. For any finite value of the radius R, we have indeed to cross the conditions $L \sim R$ when the distance is decreased far below λ_P and (12.8) can no longer be valid after this crossing.

The right graph of **Fig. 56** shows that μ approaches the value 3 at the limit of large distances, but departs from it everywhere else, anew indicating that (12.8) is not a good approximation.

The difference in the observations of the local power laws ν and μ, outside the range of validity of the long distance regime, seems to be caused by the lack of acknowledgement of the nanosphere's

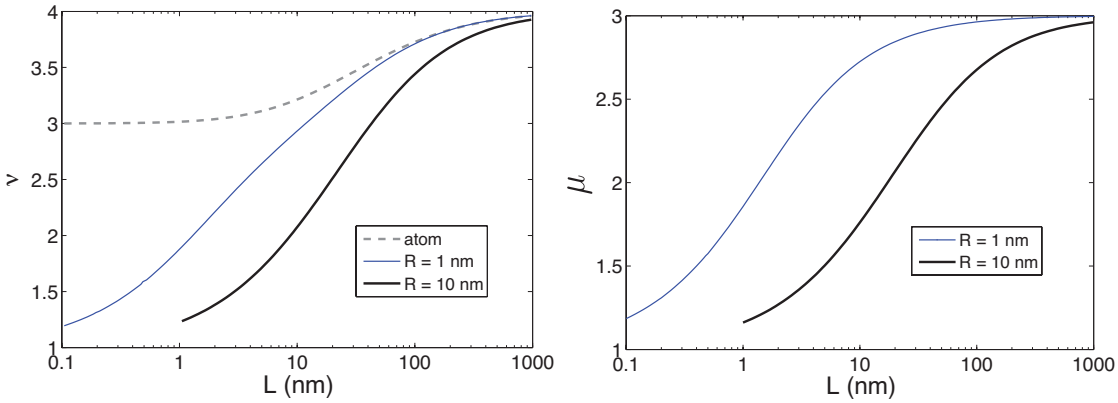

Figure 56: (left)Logarithmic slope ν as a function of the distance L. The solid curves represent the complete formula for E with different values for the radius R. The dashed curve represents the atomic limit, that is a nanosphere with $R \to 0$. (right) Logarithmic slope μ for variation with the radius R, as a function of the distance L. The solid curves represent the nanosphere case with different values for the radius R. The atom surface interaction corresponds in comparison to a constant $\mu = 3$.

size. In the next section, we present an attempt to include the size R in the geometry within a Casimir-Polder approach.

12.3 Averaging Casimir-Polder over the sphere's volume

12.3.1 Applying Hamaker method to the Casimir-Polder expressions

We now give an improved version of the formula for a point-like sphere (12.4) which explains some of the features of the exact energy E. As E_{CP} has been demonstrated above in the limit of a punctual sphere $R \to 0$, we may improve it for a finite size of the sphere through an averaging summation over the volume of the sphere, called Hamaker method. This procedure is described in **Appendix B.2.5** (p.227), and for the general Casimir-Polder formula (12.4) and it yields:

$$\begin{aligned} \overline{E_{\mathrm{CP}}} &= \int_{\mathrm{sphere}} \mathcal{E}_{\mathrm{CP}}(\mathbf{x}) \mathrm{d}V \quad , \text{with} \quad \mathcal{E}_{\mathrm{CP}} = \frac{E_{\mathrm{CP}}}{\frac{4}{3}\pi R^3} \\ &= \pi \int_L^{L+2R} \mathcal{E}_{\mathrm{CP}}(z) \left(-z^2 + 2z(L+R) - L(L+2R)\right) \mathrm{d}z \ . \end{aligned} \tag{12.12}$$

The latter integration has to be numerically computed in the general case. The derivation for the simpler formula obtained at the short and large distance limits (12.7) and (12.8) can be done analytically (see **Appendix B.2.5** (p.227) for details):

$$\begin{aligned} \overline{E_3} &= -\pi c_3 \left(\frac{2R\,(L+R)}{L\,(L+2R)} - \ln \frac{L+2R}{L} \right) \\ \overline{E_4} &= -\frac{4\pi c_4 R^3}{3L^2\,(L+2R)^2} \ . \end{aligned} \tag{12.13}$$

The long and short distance expansions of this formulas give:

$$[L \gg R] \begin{cases} \overline{E_4} \simeq -\dfrac{4c_4\pi}{3}\dfrac{R^3}{L^4} \\ \\ \overline{E_3} \simeq -\dfrac{4c_3\pi}{3}\dfrac{R^3}{L^3} \end{cases} \qquad [L \ll R] \begin{cases} \overline{E_4} \simeq -\dfrac{c_4\pi}{3}\dfrac{R}{L^2} \\ \\ \overline{E_3} \simeq -c_3\pi\dfrac{R}{L} \end{cases}$$

and the same power laws as the complete expression E are recovered for $\overline{E_4}$ at large distance, and for $\overline{E_3}$ at short distances. This is a first clue that the averaged general Casimir-Polder energy $\overline{E_{\rm CP}}$ should be better than $E_{\rm CP}$ to describe the finite size of the nanosphere in the short separation regime.

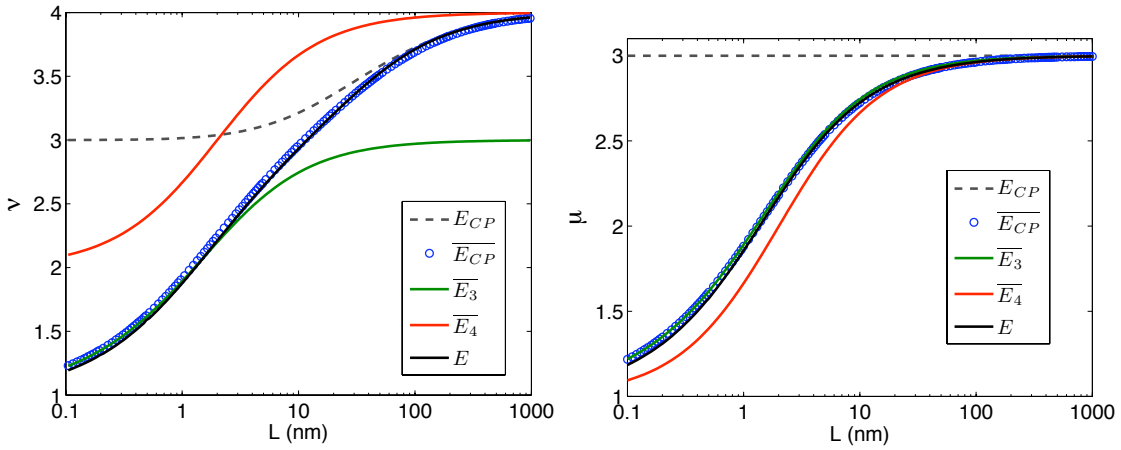

Figure 57: (left) Logarithmic slope ν as a function of the distance L. The dashed curve represents the Casimir-Polder energy $E_{\rm CP}$, and the blue circles its averaged quantity $\overline{E_{\rm CP}}$. The solid red (resp. green) line is for the averaged retarded Casimir-Polder (resp. non-retarded van der Waals) quantity $\overline{E_4}$ (resp. $\overline{E_3}$). The solid black line is the exact energy E. (right) Logarithmic slope μ as a function of the distance L (same conventions as in left figure). The sphere radius is $R = 1$ nm.

In **Fig. 57** we illustrate our findings by plotting the logarithmic slopes (ν, μ), that represent the local power laws in $1/L$ and R, for E and $\overline{E_{\rm CP}}$. We observe that the two latter quantities are very similar over a great range of distances. The parameters (ν, μ) are also given for $E_{\rm CP}$, $\overline{E_3}$ and $\overline{E_4}$ for illustrative purpose.

12.3.2 Comparison of the various obtained quantities $E_{\rm CP}, \overline{E_{\rm CP}}, \overline{E_3}, \overline{E_4}$ and E

In order to assess the quality of the estimations (12.12) and (12.13), we now plot on **Fig.58** the ratios $E/\overline{E_4}$, $E/\overline{E_3}$ and $E/\overline{E_{\rm CP}}$. The ratio $E/E_{\rm CP}$, already studied in **Fig. 55** (p.160) is reminded.

As expected, we find that $\overline{E_4}$ tends to reproduce the result E of the full numerical computation at large distances. We also see that $\overline{E_3}$ obeys the same power law than E at small distances (ratio tending to a constant value), but fails to predict the correct magnitude (the limit of the ratio is not 1). If one writes the short distance limits respective to $E_{\rm CP}$ and E as $\overline{E_3} = -c_3\pi\frac{R}{L}$ and $E_{\rm PFA} = -c_3'\pi\frac{R}{L}$, a close inspection of the coefficients shows that:

$$\frac{c_3}{c_3'} = \frac{45\overline{\alpha_0}\lambda^*}{\pi^2\left(\sqrt{2}\lambda_P + \lambda_1\sqrt{1-\overline{\alpha_0}}\right)\alpha^*} \simeq 0.84 \quad \text{for the present values of the parameters.}$$

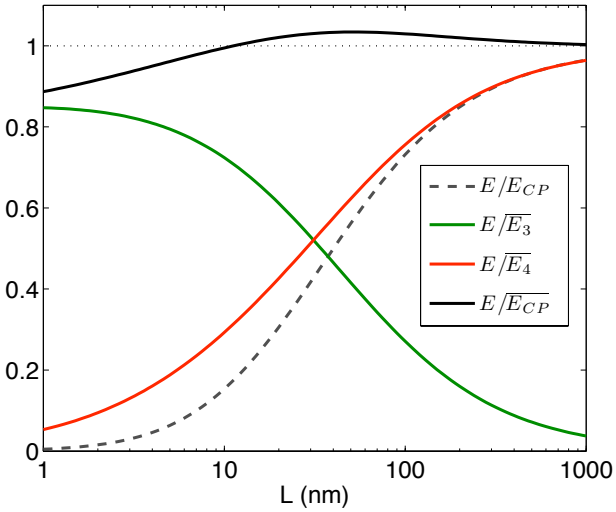

Figure 58: Ratios of the exact energy E to the various approximations from Casimir-Polder formula. The black dashed curve uses the original small sphere regime $E_{\rm CP}$, the solid black curve its averaged quantity $\overline{E_{\rm CP}}$, and the solid green (resp. red) curve is the averaged short (resp. large) distance regime $\overline{E_3}$ (resp. $\overline{E_4}$). The sphere radius is R =10 nm.

This difference is due to the fact that $\overline{E_3}$ in (12.13) has been obtained through an integration over the sphere of the van der Waals energies, whereas $E_{\rm PFA}$ in (12.11) has been calculated by taking into account the multiple interferences occurring in the Fabry-Perot cavity [216]. This explains the behavior seen on the short distance region of **Fig.58**.

Finally, the averaged Casimir-Polder expression $\overline{E_{\rm CP}}$ in (12.12), while it contains the right power laws in L and R in the limiting cases of short and large distances, remains incapable of predicting the sphere-plane Casimir energy when $L \lesssim 100R$, mainly for the reason invoked above. In this regime, neither the Casimir-Polder formula, nor an averaged version, are good approximations to compute the Casimir effect, and a complete multipolar and multiscattering approach is necessary.

Part V.
Results at non-zero temperature

Table of Contents

We now include the effect of the temperature in the Casimir effect, by replacing the integral in the scattering formula to a discrete sum over the Matsubara frequencies, obtaining the Matsubara formula derived in **Section 5.4** (p.78):

$$\mathcal{F} = 2k_BT \sum_n{}' \sum_m{}' \ln\det\left[\mathcal{I} - \mathcal{N}^{(m)}(\tilde{\xi}_n)\right] \qquad \tilde{\xi}_n = n\frac{2\pi R}{\lambda_T} ,$$

where $\lambda_T = \frac{\hbar c}{k_B T}$ is the thermal length ($\lambda_T = 7.6$ μm for ambient temperature $T = 300$ K). Doing so, we add the classical thermal fluctuations of the electromagnetic field to the purely quantum ones, and obtain the Casimir free-energy $\mathcal{F} = E - T\mathcal{S}$, where E is the Casimir energy at zero temperature, T is the temperature of the two objects and of the vacuum, and $\mathcal{S}$ is the Casimir entropy.

In order to study the different thermal regimes, we introduce the parameter $\alpha_T = 2\pi\frac{L}{\lambda_T}$. The low and high temperature regimes, respectively, are derived in Eqs.(3.5,3.6) (p.48) and lead to the two opposite regimes:

$$(L \ll \lambda_T) \qquad \mathcal{F} = k_BT \sum_n{}' \ln\det\mathcal{D}(\tilde{\xi}_n) \simeq \frac{\hbar c}{2\pi R}\int_0^\infty \mathrm{d}\tilde{\xi}\ \ln\det\mathcal{D}(\tilde{\xi}) = E$$

$$(L \gg \lambda_T) \qquad \mathcal{F} = k_BT \sum_n{}' \ln\det\mathcal{D}(\tilde{\xi}_n) \simeq \frac{k_BT}{2}\ln\det\mathcal{D}(0) = \mathcal{F}_{\mathrm{HT}} .$$

The inclusion of temperature in the scattering approach will enable us to study the dependence of the Casimir effect on the temperature in the sphere-plane configuration. For the closed cavity of two parallel planes, studied in **Section 3.2** (p.49), the Casimir free-energy increases monotonically in magnitude with the temperature for perfectly reflecting mirrors. For metallic mirrors, a qualitative difference appears whether dissipation is included or not: while the result obtained when using the lossless plasma model is quite similar to those of the perfect mirrors model, the Casimir free-energy with mirrors described by the Drude model depends non-monotonically on the temperature, which yields negative values for the Casimir entropy. This is illustrated by the thermal correction factors plotted in **Fig. 23** (p.51). In the high-temperature regime, this difference takes the form of a factor 2 betweeen the two results [137], which generated a series of studies about the thermal effect on the Casimir force [141, 142, 143, 144, 145].

For the sphere-plane configuration, we expect to observe differences with the former situation, due to the change of geometry. Indeed, geothermal effects [159, 172, 173] have been observed for the Casimir effect between perpendicular or inclined plates, as interplays between the effects of geometry and temperature. Moreover, the sphere-plane configuration is an open geometry, and should therefore be more sensitive to the spectral reweighting in the Casimir effect caused by the inclusion of temperature [174]. This promising investigation has led very recently to studies [243, 173, 175, 229, 228] dedicated to this configuration.

In **Section 13**, we will first consider the materials to be perfect reflectors, in order to focus on the influence of the temperature on the Casimir effect between a sphere and a plane. Indeed this new situation involves an increasing number of lengthscales, and as we will see in **Section 14**, the imperfect reflection and the dissipation on the materials have some interplay with the thermal effects, and make the analysis even more complicated. We conclude with a study of the high-temperature regimes in **Section 15** for different materials, using the analytical expansions obtained in **Section 7.6** (p.117).

13 Perfect mirrors at ambient temperature

In this section, we only consider the mirrors to be perfect reflectors at all frequencies, in order to focus on the influence of thermal effects on the Casimir interaction between a sphere and a plane. When this dependence is studied within PFA methods, the thermal effects are incorporated in the model through the Casimir interaction calculated between two planes. Thus the influence of the temperature T is decoupled from the geometric nature of the sphere, which makes the PFA method not suitable to describe the geometry-temperature interplays [174].

We will first observe in **Section 13.1** how the temperature affects the Casimir free-energy $\mathcal{F}$ for various values of the distance L and the radius R. This dependance on the different lengthscales will be studied more quantitatively through the local power laws in **Section 13.2**. The non-trivial interplay between geometry and thermal effects is investigated and characterized in **Section 13.3**, as well as its consequences on the Casimir entropy in **Section 13.4**. Finally, the question of the accuracy of results obtained from PFA at short distances will be addressed in **Section 13.5**.

13.1 Observation of the thermal effects

To study the influence of the temperature, we define the thermal increase factor $\vartheta_{\mathcal{F}}$ for the Casimir free-energy obtained from the scattering formula:

$$\vartheta_{\mathcal{F}} = \frac{\mathcal{F}(T)}{\mathcal{F}(0)} \qquad\qquad \vartheta_{\mathcal{F}}^{\mathrm{PFA}} = \frac{\mathcal{F}_{\mathrm{PFA}}(T)}{\mathcal{F}_{\mathrm{PFA}}(0)} = \frac{D_{\mathrm{PP}}(T)}{D_{\mathrm{PP}}(0)} \tag{13.1}$$

which measures the increase of free energy when the thermal fluctuations (also called "thermal photons") are added to the quantum vacuum fluctuations. The same factor for quantities computed with PFA is denoted $\vartheta_{\mathcal{F}}^{\mathrm{PFA}}$. It simplifies to the thermal increase factor for the primo-potential D_{PP} in the plane-plane case. In particular, $\vartheta_{\mathcal{F}}^{\mathrm{PFA}}$ does not depend on the sphere radius R within PFA computations.

The numerical results for the thermal increase factor $\vartheta_{\mathcal{F}}$ are presented in **Fig. 59**, as a function of the temperature, for different values of the sphere's radius $R = 0.1, 1$ and 10 μm. For the sake of comparison, the R-independent factor $\vartheta_{\mathcal{F}}^{\mathrm{PFA}}$ obtained from PFA results is presented by a thin solid black curve. The upper graph is for a distance $L = 1\mu$m, at which the thermal effects are beginning to be noticeable for an ambient temperature $T = 300\ K$ in the plane-plane configuration. The two lower graphs are plotted for distances of 500 nm (left) and 2 μm (right), respectively. The vertical axis in the graphs has been zoomed to better observe the shape of the curves.

Obviously the factor ϑ computed in the sphere-plane configuration differs largely from the one computed within PFA and strongly depends on the radius of the sphere R. In the plane-plane configuration, the thermal factor ϑ_{PFA}, presented by a thin solid black curve in **Fig. 59**, is a monotonically growing function from 1 at low temperatures to a high-temperature diverging quantity, proportional to T (see **Section 3.2** (p.49) for more details on the plane-plane configuration with temperature). It follows that ϑ_{PFA} is always larger than one and the relative increase exceeds the percent already at $T = 50$ K for $L = 1$ μm. In the sphere-plane configuration, small spheres seem to be far less sensitive to the temperature than large ones, and undergo a delay in the thermal increase from low to high temperatures. This is especially visible in the short-range case (lower left graph on **Fig. 59**), where the ratio ϑ for a 0.1 μm radius sphere remains equal to 1 at much larger temperature than for larger sphere radii. This R-dependance is missed by the PFA computations, as it decouples the effects curvature from those of temperature.

Physically, the temperature dependance of the Casimir energy can be understood by recalling the thermal wavelength $\lambda_T = \frac{\hbar c}{k_B T}$ associated with thermal fluctuations, equal to 7.6 μm at ambient temperature. For two planes, as well as for any cavity, temperature does not have an influence when the mirrors separation is too small, because even the fundamental mode $\frac{\lambda_T}{2}$ does not fit

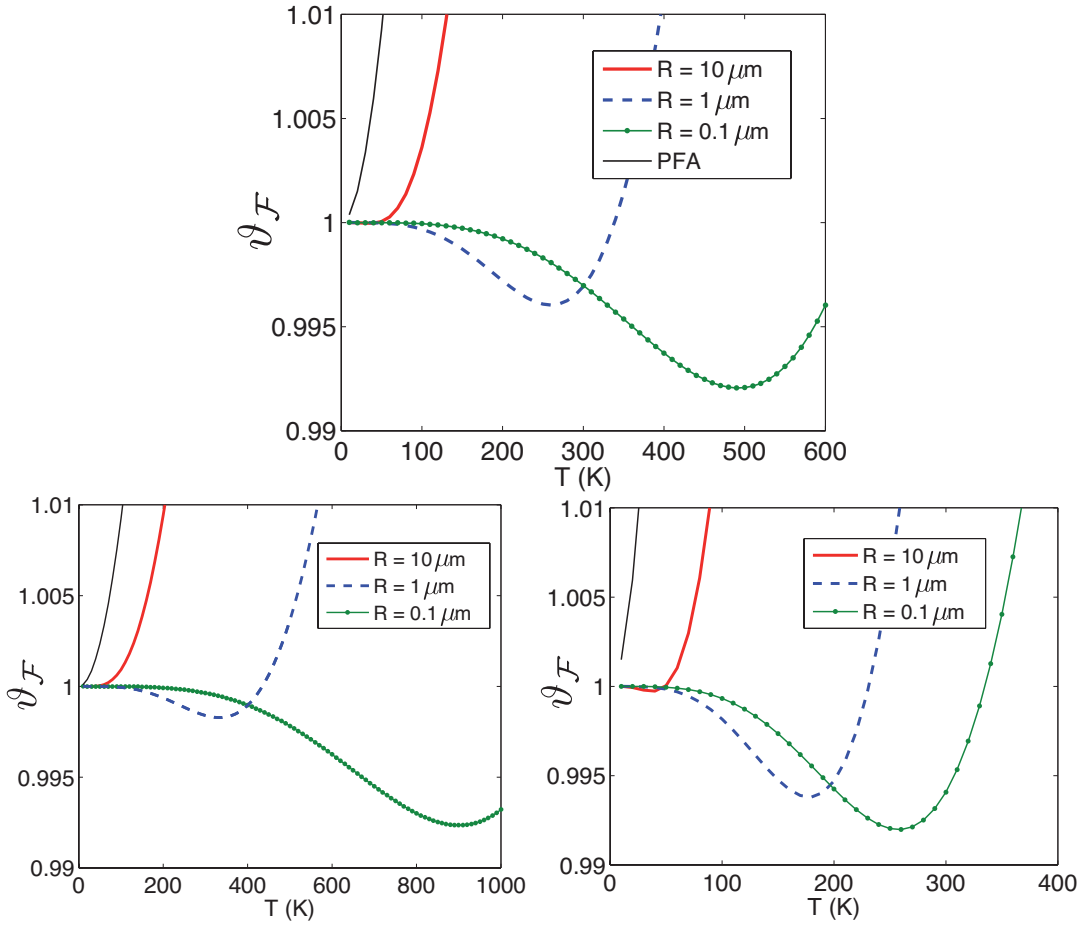

Figure 59: Thermal increase factor $\vartheta_{\mathcal{F}}$ for the Casimir free-energy with respect to the temperature, by increments of 10 K. The leftmost (coldest) point is for $T = 10$ K. Red solid curves represent the case of a large sphere, the dashed blue curves an intermediate sphere, and the green dotted lines a small sphere. The R-independent PFA factor $\vartheta_{\mathcal{F}}^{\rm PFA}$ is presented by a thin solid black curve for the sake of comparison. The distance is $L = 1$ μm in the upper graph, $L = 0.5$ μm in the lower left graph, and $L = 2$ μm in the lower right graph.

inside the cavity. This low-temperature regime is then associated with the condition ($L \ll \lambda_T$) and is illustrated by the fact that ϑ goes to 1 when the temperature goes to 0, as the thermal wavelength λ_T is inversely proportional to the temperature T.

For a sphere in front of a plane, the finite size of the sphere gives a second possible cause for thermal-insentivity: from the localisation principle, rays with a wavelength much bigger than the sphere radius are less sensitive to the presence of the sphere. As the thermal fluctuations are related to modes with typical wavelength of the order of λ_T, small sphere will not see them, and a second low-temperature regime appears with the condition ($R \ll \lambda_T$). Then the smaller the sphere, the higher temperature necessary to begin to see the thermal effects, as clearly observed from the lower left graph of **Fig. 59**: at a distance $L = 0.5$ μm, the factor ϑ remains longer on a value close to 1 for small spheres when the temperature is increased.

A much more surprising observation is that the thermal factor ϑ can in some cases become lower than 1, meaning a decrease in the Casimir free-energy when the temperature is increased from $T = 0$ K to a given $T > 0$. In other terms, under certain conditions the thermal photons may have a repulsive contribution to the Casimir effect. In the three graphs of **Fig. 59** this is always observed for small spheres ($R = 0.1$ μm), for which the thermal factor ϑ is first decreasing at low temperatures, before reaching a minimum at around $\alpha_T = \frac{2\pi L}{\lambda_T} \simeq 1.3$, and finally increases for high temperatures. For bigger spheres, this seems to happen only when the distance L is large enough, as the red curve in lower right graph of **Fig. 59** decreases to a minimum before reaching the increase of the high-temperature regime.

This decrease in the free-energy with temperature was highly unexpected, as it does neither occur in the plane-plane configuration with perfect mirrors, nor in the PFA computations for the sphere-plane configuration. However one finds the same phenomenon when using considering dissipative metals such as gold modelled by a Drude model for the dielectric function. It will be studied more thoroughly in **Section 13.3**, as a signature of a non-trivial interplay between the effects of temperature and geometry in the Casimir effect.

13.2 Power laws

In the ideal case of perfectly reflecting mirrors at non-zero temperature T, only three length scales are involved in the problem: the distance L between the surfaces of the two objects, the sphere radius R, and the thermal wavelength $\lambda_T = \frac{\hbar c}{k_B T}$. It follows that the Casimir effect only depends on the two ratios $\left(\frac{L}{R}, \frac{L}{\lambda_T}\right)$, and therefore we can distinguish between four different asymptotic regimes. For each one we have an simple analytical expression of the Casimir free-energy, either from the proximity force approximation (PFA) when $L \ll R$, or from the long-distance limit (LD) computed in **Section 8.2** when $L \gg R$. These expressions are summed up in **Table 13**.

	$\frac{L}{R} \ll 1$	$\frac{L}{R} \gg 1$
$\frac{L}{\lambda_T} \ll 1$	$\mathcal{F}_{\rm PFA}^{T=0} = -\frac{\hbar c \pi^3 R}{720 L^2}$	$\mathcal{F}_{\rm LD}^{T=0} = -\frac{9\hbar c R^3}{16\pi \mathcal{L}^4}$
$\frac{L}{\lambda_T} \gg 1$	$\mathcal{F}_{\rm PFA}^{T\to\infty} = -\frac{\zeta(3)\hbar c R}{4\lambda_T L}$	$\mathcal{F}_{\rm LD}^{T\to\infty} = -\frac{3\hbar c R^3}{8\lambda_T \mathcal{L}^3}$

Table 13: Four asymptotic regimes for the Casimir free-energy between two perfectly reflecting mirrors at temperature T.

From those explicit expressions, we observe that the Casimir free-energy undergoes a rich variety of changes in the power law with respect to the distance L and the radius R. To describe them,

we define, as previously, two parameters (ν, μ) describing the local power-law in $\frac{1}{L}$ and R:

$$\nu = -\frac{\partial \ln |\mathcal{F}|}{\partial \ln L} = \frac{LF}{\mathcal{F}} \qquad\qquad \mu = \frac{\partial \ln |\mathcal{F}|}{\partial R}$$

where $F = -\frac{\partial \mathcal{F}}{\partial L}$ is the Casimir force. When the distance L increases from zero ($L \ll R, \lambda_T$) to infinity ($L \gg R, \lambda_T$) for fixed R and λ_T, the parameter ν changes from a 2 to 3, and the proportionality with respect to the sphere radius ($\mathcal{F} \propto R$) becomes a proportionality with respect to the sphere volume ($\mathcal{F} \propto R^3$). Moreover, the shift of the local power-law ν for $\frac{1}{L}$ from 2 to 3 can undergo an intermediate regime that can be up to 4 if the regime ($R \ll L \ll \lambda_T$) exists (upper right box), or down to 1 if the regime ($\lambda_T \ll L \ll R$) exists (lower left box).

In **Fig. 60**, we present how ν, the local power law in $\frac{1}{L}$, changes from 2 to 3 with respect to the aspect ratio $\frac{L}{R}$. The different curves represent various values of the sphere radius, at ambient temperature. The low-temperature $\nu_{\rm LT}$ and high-temperature $\nu_{\rm HT}$ cases are given in blue solid line and black dashed-curve, respectively.

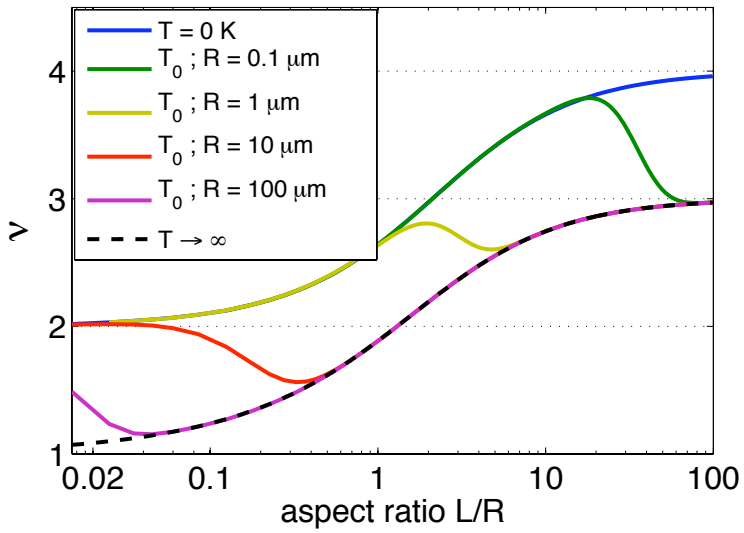

Figure 60: Logarithmic slope ν as a function of the aspect ratio $\frac{L}{R}$. The blue solid line (resp. black dashed-line) represents the low-temperature (resp. high-temperature) regime, while green, yellow, red and purple curves are for ambient temperature with increasing radii of the sphere (0.1 μm, 1 μm, 10 μm and 100 μm). Ambient temperature is $T_0 = 300$ K.

We observe that the curves for ambient temperature T_0 shift from the low-temperature curve $\nu_{\rm LT}$ to the high-temperature curve $\nu_{\rm HT}$ when the distance increases. For a large sphere, as illustrated by the purple curve for $R = 100$ μm, the parameter ν quickly recovers $\nu_{\rm HT}$, and goes from 2 to 3 with an intermediate minimum tending to 1. For small spheres, the low-temperature curve $\nu_{\rm LT}$ is followed for larger distance, and ν can have an intermediate maximum up to 4, as illustrated by the green curve for $R = 100$ nm. This was expected, as for a given aspect ratio $\frac{L}{R}$ and temperature T, the low and high temperature regimes, characterized by low and high ratios $\frac{L}{\lambda_T}$, thus by small and large distances L, are equivalent to large and small radii R, respectively.

We now present the local power law in the sphere radius R in **Fig. 61**. Again, different curves are for various radii of the sphere, at ambient temperature, while blue solid line and black dashed-curve are for zero and infinite temperatures, respectively. The two thermal limiting cases have a logarithmic slope μ for the variable R that goes from 1 to 3 when the distance increase, but the two do not superimpose. A possible interpretation is that the way the aspect ratio $\frac{L}{R}$, and thus the geometry, influence the dimensionality of the free-energy $\mathcal{F}$ with respect to the radius

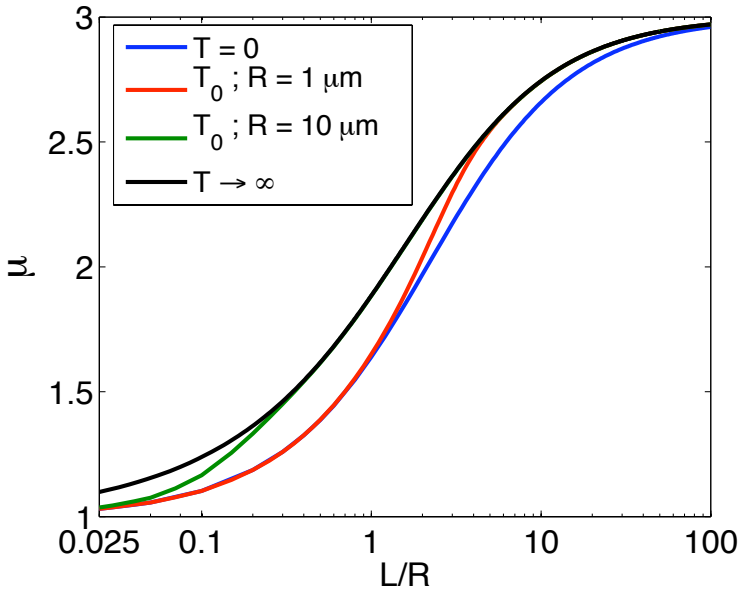

Figure 61: Logarithmic slope μ as a function of the aspect ratio $\frac{L}{R}$. Blue (resp. black) curve represents the low-temperature (resp. high-temperature) regime, red and green curves are for ambient temperature with radii of the sphere of 1 μm and 10 μm. Ambient temperature is $T_0 = 300$ K.

of the sphere R is not the same, depending on the temperature. The free-energy goes from the low-T regime at short separation to the high-T regime at large separation, for the same reason as explained in the study of ν.

We finally remark that the high-temperature regime for the free-energy, given in **Section 7.6** as the zero-frequency limit of the integrand $\Phi(0)$, only depends on $\tilde{\mathcal{L}}$, thus on the aspect ratio $\frac{L}{R}$. It yields that $\nu = \mu$ in this regime, meaning that the black solid curves on **Figs. 60-61** are exactly the same.

13.3 Correlations between curvature and thermal effects

In **Section 13.1**, we observed that the thermal increase factor depends on the sphere radius R, which is a clear sign of a correlation between the effects of curvature and temperature. We now study more specifically this interplay, and its unexpected role on the thermal correction factor ϑ. The consequence on other parameters, such as the entropy $\mathcal{S}$ or the accuracy of PFA, will be discussed separately in **Sections 13.4-13.5**.

We keep the same definition of the correlation number as in **Section 11.3** (p.152), and in this case the correlation number for the effects of temperature (T) and geometry (G) reads:

$$\delta_{\mathcal{F}}^{TG} = \frac{\eta_{\mathcal{F}}^{TG}}{\eta_{\mathcal{F}}^{T}\eta_{\mathcal{F}}^{G}} - 1 = \frac{\frac{\mathcal{F}(T)}{\mathcal{F}_{\rm PFA}(0)}}{\frac{\mathcal{F}_{\rm PFA}(T)}{\mathcal{F}_{\rm PFA}(0)}\frac{\mathcal{F}(0)}{\mathcal{F}_{\rm PFA}(0)}} - 1 = \frac{\mathcal{F}(T)\mathcal{F}_{\rm PFA}(0)}{\mathcal{F}(0)\mathcal{F}_{\rm PFA}(T)} - 1 \tag{13.2}$$

where the geometry correction factor $\eta_{\mathcal{F}}^{G} = \rho_{\mathcal{F}} = \frac{\mathcal{F}}{\mathcal{F}_{\rm PFA}}$ is taken at $(T = 0)$, and the thermal correction factor $\eta_{\mathcal{F}}^{T} = \vartheta_{\mathcal{F}}^{\rm PFA} = \frac{\mathcal{F}_{\rm PFA}(T)}{\mathcal{F}_{\rm PFA}(0)}$ is the one from a PFA computation.

Until now, we only considered correlations of effects with opposite domain of applicability:

- In the plane-plane case, studied in **Section 3.2.3**, the imperfect reflection on the materials had an impact only for small distances ($L \lesssim \lambda_P$), whereas temperature had noticeable

influence only for large distances ($L \gtrsim \lambda_T$). It followed that the correlations were only observed in a limited intermediate regime $\lambda_T \lesssim L \lesssim \lambda_P$.

- In the sphere-plane case at zero temperature, studied in **Section 11**, we observed correlations between the effects of geometry and metallic response of materials. The effect of curvature were only important at large distance ($L \gtrsim R$), while the imperfect reflection again only had an influence for short distance ($L \lesssim \lambda_P$). Nevertheless, influence of the correlation was observable even for large distance.

In the present case, temperature and geometry have an effect for the same regime of long distance, ($L \gtrsim \lambda_T$) for the former, and ($L \gtrsim R$) for the latter. One can thus expect a much more significant and profound correlation.

In **Fig. 62** we present the three terms involved in the definition (13.2) of the correlation number δ_F^{TG}, for the Casimir force. If the effect of temperature and geometry were uncorrelated, the total correction factor for the force η_F^{TG} would be equal to the product of the two simple correction factors η_F^T and η_F^G. We will see that this is generally not the case, apart from short-distance limit.

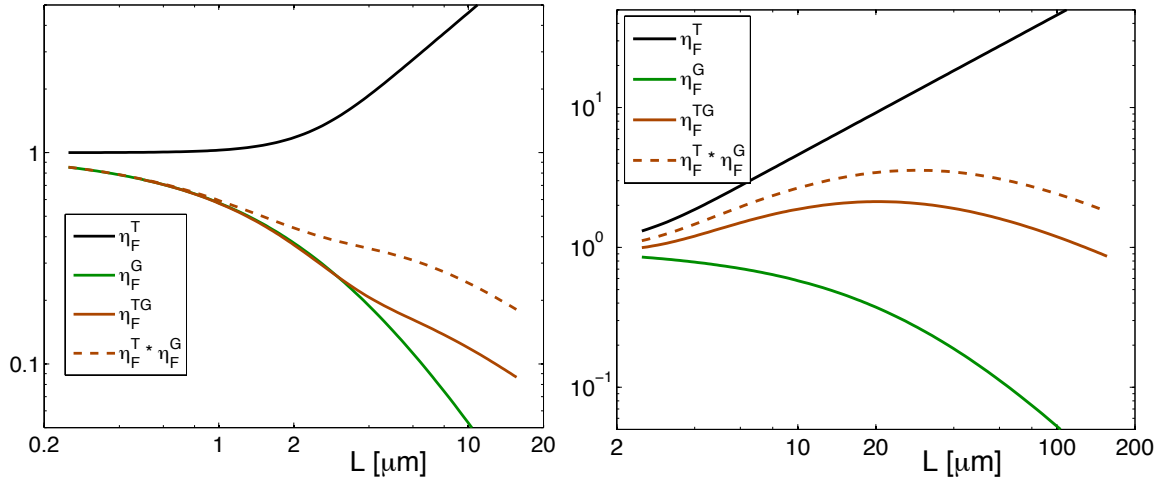

Figure 62: Force correction factor, with respect to the distance, for the temperature (η_F^T, upper solid black curve), for the geometry (η_F^G, lower solid green curve), and for both (η_F^{TG}, solid brown curve). The product of the two single corrections is presented in a dashed brown curve for comparison. The left graph is for a sphere radius $R = 1$ μm, the right graph is for a sphere radius $R = 10$ μm. The temperature is constant at $300K$, yielding a thermal wavelength $\lambda_T = 7.6$ μm.

As expected, the thermal correction factor $\eta_F^T = \vartheta_{\mathcal{F}}^{\mathrm{PFA}}$, presented by the solid black curve in **Fig. 62**, is going to 1 for small distances, where the thermal photons do not contribute to the force, and increases linearly with L for large distances, where classical thermal fluctuations have a predominant part in the Casimir effect over the purely quantum ones. The curvature correction factor η_F^G is, as presented in **Section 10.3** (p.145), lower than 1 for large distances, and goes to unity when the sphere approaches the plane.

When the two effects are taken into account, we observe that the result is not the same, depending on whether they are incorporated simultaneously or that the corrections are just multiplied together. This is illustrated in both graphs of **Fig. 62**, where the solid and dashed brown curves do not superimpose, apart from the short-distance limit. This is a clear sign of a non-trivial interplay between the effects of curvature and of temperature in the Casimir effect for the sphere-plane configuration. The complete correction (solid brown curve) is always smaller than the product of the two single corrections (dashed brown curve), which yields that $\delta^{TG} \leq 0$ is always fulfilled, the

equality being approached in the limit of short-distances.

Eq.(13.2) can also be expressed in two different points of view, one being a ratio of thermal increase factors, the other being a ratio of correction factors of PFA:

$$\delta^{TG} + 1 = \frac{\vartheta}{\vartheta_{\rm PFA}} = \frac{\rho(T)}{\rho(0)} \leq 1 \tag{13.3}$$

We first study the correlations in terms of the thermal increase factor ϑ, the second viewpoint will be used to measure the accuracy of PFA results in **Section 13.5**. From the previous remark that $\delta^{TG} \leq 0$ is always fulfilled, we deduce that we should observe $\vartheta \leq \vartheta_{\rm PFA}$. In other words, we expect the PFA result to always overestimate the thermal correction factor for the Casimir free-energy.

This is indeed the case, as illustrated in **Fig. 63**, were the factor for the Casimir free-energy $\vartheta_{\mathcal{F}}$ is presented with respect to the distance L, for various sizes of the sphere, at fixed ambient temperature ($T = 300K$). We plot the PFA thermal increase factor $\vartheta_{\mathcal{F}}^{\rm PFA}$, independent of the sphere radius, with a dashed curve. The long-distance expansion for $\vartheta_{\mathcal{F}}$, given by Eq.(8.19) (129), in which $\mathcal{L}$ has been replaced by L to get a R-independent quantity, is represented by a dotted line. Finally the exact quantities are presented by solid curves, each colour being associated to a given value of the sphere radius R, within the range [0.1 μm, 50 μm].

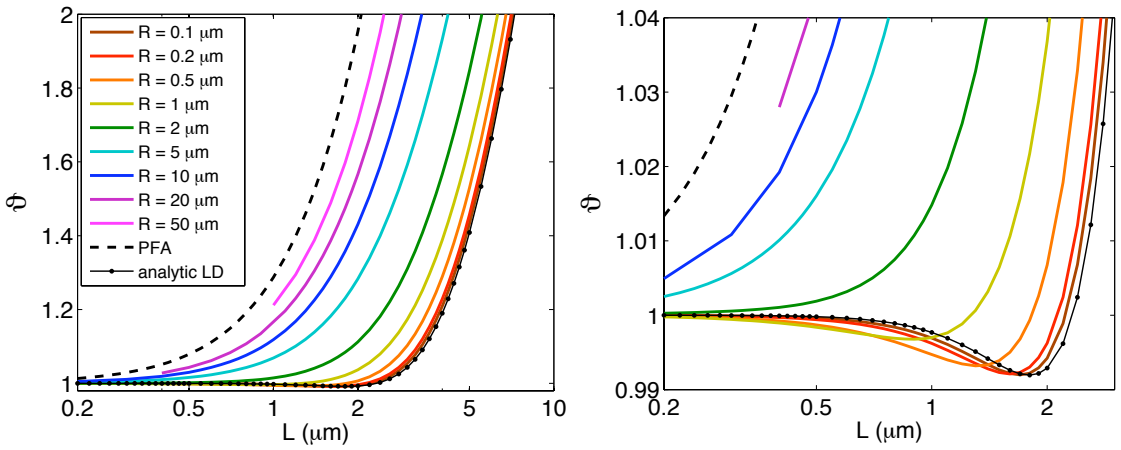

Figure 63: Thermal increase factor for the Casimir free-energy $\vartheta_{\mathcal{F}}$ with respect to the distance L in μm. The temperature is fixed to $T = 300K$ and is associated to a thermal wavelength $\lambda_T = 7.6$ μm. The solid curves represent the exact quantities, computed from the scattering formula with $\ell_{\rm max} = 250$ for leftmost points at $\frac{L}{R} = 0.02$. The upper dashed curve is the PFA thermal correction $\vartheta_{\mathcal{F}}^{\rm PFA}$, and the lower dotted-line is the analytic formula derived in the long-distance regime in **Section 8.2**. The only difference between the two graphs is the scale, the left one being focussed on large distance, and the right one being a zoom to smaller distances.

Curves for large values of R come closer to the PFA result, which can be seen as a $(R \to \infty)$-limit case for given L and λ_T. Inversely, curves for small values of R tend to recover the long-distance regime, which can be seen as a $(R \to 0)$-limit case for given L and λ_T.

In the left graph of **Fig. 63**, we focus on large distances to observe the increase of the Casimir free-energy due to the contribution of the classical thermal fluctuations. We notice that $\vartheta_{\rm PFA}$ increases faster and for shorter distances than the exact quantities, which corroborates the observations made in **Fig. 59** (p.172): the smaller the sphere, the higher the temperature at which the increase gets in. This progression undergoes a saturation effect, limited by the curve obtained at the limit

of large distances ($L \gg R$). For even larger distances, as R is fixed for each solid curve, this limit will be reached and every solid curve will collapse to the long-distance dotted-line.

In the right graph of **Fig. 63**, we focus on small distances to observe the unexpected local decrease of free energy that appears when accounting for the contribution of classical thermal fluctuations. At ambient temperature, this phenomena is found for $R \lesssim 1$ μm and is more pronounced, in terms of magnitude and distance range, when the sphere radius is smaller. This progression again saturates to the limiting curve of the long-distance case $\vartheta_{\mathcal{F}}^{\mathrm{LD}}$. The local decrease is of less than one percent, and is centered at a distance between 1 and 2 μm.

This behavior is more pronounced when switching to the study of the force instead of the free-energy, as the minimum value of the thermal increase factor ϑ_F, presented in the long-distance regime in **Table 11** (p.130), is expected to be lower than for the free-energy. We plot on the left graph of **Fig. 64** this factor $\vartheta_F^{\mathrm{LD}}$ for the force with respect to the surface-surface distance L. We observe a local decrease for $R \lesssim 2$ μm in the case of the Casimir force, with up to 3% of magnitude, on a wider range in L than the free-energy, centered at a distance between 2 and 3 μm.

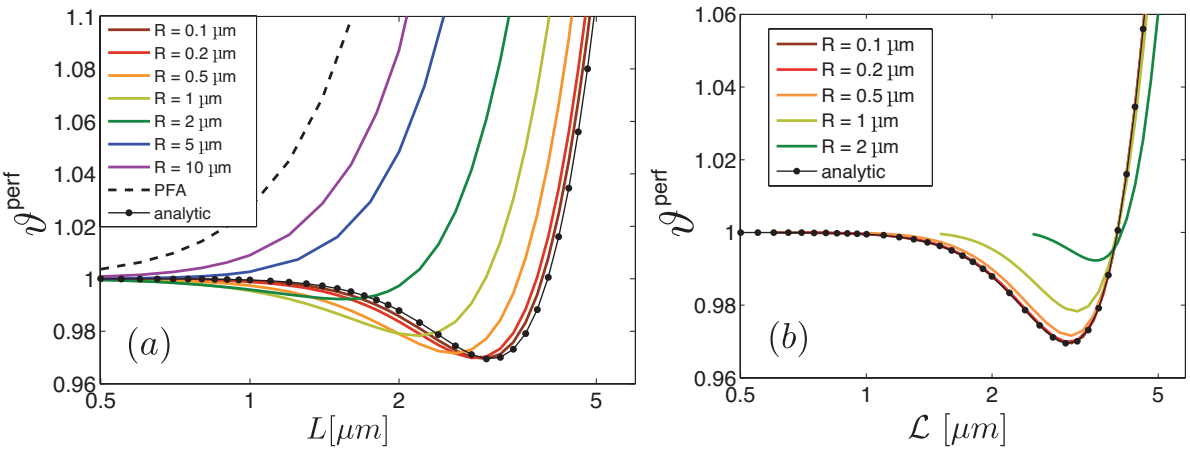

Figure 64: Thermal increase factor for the Casimir force ϑ_F with respect to the surface-surface distance L (left graph) and the plate-to-center distance $\mathcal{L} = L + R$ (right graph). The temperature is fixed to $T = 300K$ and is associated to a thermal wavelength $\lambda_T = 7.6$ μm. The solid curves represent the exact quantities, computed within the scattering formalism with $\ell_{\max} = 85$ for the leftmost points at $\frac{L}{R} = 0.05$. The upper dashed curve is the PFA thermal correction $\vartheta_F^{\mathrm{PFA}}$, and the lower dotted-line is the analytic formula derived in the long-distance regime in **Section 8.2** (p.126).

Curves for small values of the sphere radii seem to be similar to the long-distance curve, but shifted by a distance R to the left. This would mean that for small radii, L is not the right parameter for the description of the distance, and that the center-to-plate distance $\mathcal{L} = L + R$ should be rather chosen. This is confirmed by the right graph of **Fig. 64**, where the thermal increase factor for the force ϑ_F is presented with respect to the parameter $\mathcal{L}$: for sphere radii smaller than 1 μm, the curve for the exact result superimpose the long-distance regime.

This non-monotonic behavior of the thermal increase factor was highly unexpected, and represents a non-trivial consequence of the correlation between the effects of geometry and temperature in the Casimir effect. If one separates the total Casimir force at ambient temperature in two parts, one being the contribution of (quantum) vacuum fluctuations, the other of (classical) thermal fluctuations, $\vartheta < 1$ means that the second term does not have the same sign as the first one. In other words, the contribution of thermal photons to the Casimir force is repulsive.

13.4 Casimir entropy

The non-monotonic behavior of the free-energy with respect to the temperature, presented in the last section, is a feature that does not arise for simpler geometries such as the plane-plane cavity. To study more specifically this non-trivial dependence on the temperature, we focus in this section on the Casimir entropy $\mathcal{S}$ derived from the free-energy $\mathcal{F}$. As the classical high-temperature regime yields a Casimir free energy proportional to the temperature T (see Eq.(3.6) p.49), the entropy for a given system goes to a constant value when T goes to infinity, and we can define a normalized entropy with this constant value, in the same way as in **Section 8.2** (p.126):

$$\mathcal{S} = -\frac{\partial \mathcal{F}}{\partial T} \qquad\qquad \vartheta_{\mathcal{S}} = \frac{\mathcal{S}(T)}{\mathcal{S}(T \to \infty)} \tag{13.4}$$

In **Fig. 65**, we present this normalized Casimir entropy $\vartheta_{\mathcal{S}}$ with respect to the temperature T, for different values of the sphere radius, at fixed surface-to-surface distance $L = 1$ μm. The long-distance analytical expansion derived by Eq.(8.19) (129) is also presented, and can be understood as the limit $R \to 0$ for a fixed L.

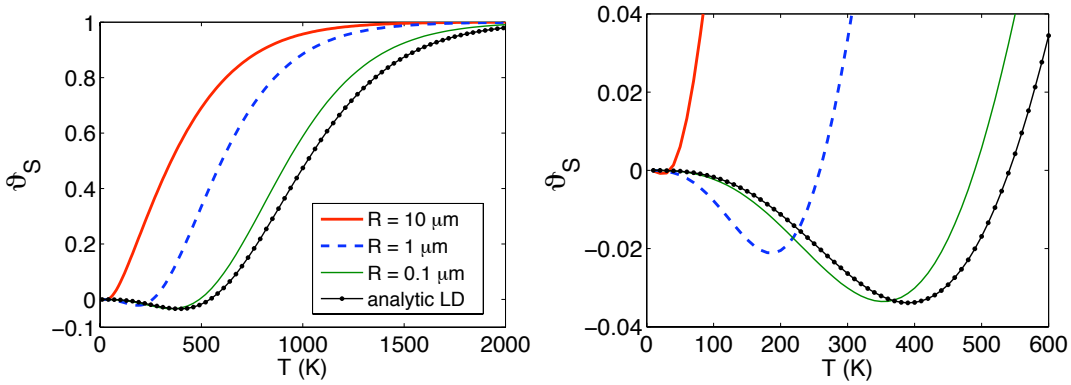

Figure 65: Casimir entropy normalized by its high-temperature limit $\vartheta_{\mathcal{S}} = \frac{\mathcal{S}(T)}{\mathcal{S}(\infty)}$ with respect to the temperature. The red solid curves represent the case of a large (10 μm radius) sphere, the dashed blue curves an intermediate (1 μm radius) sphere, and the green dotted lines a small (0.1 μm radius) sphere. The black dotted-lines represent the analytic formula derived in the long-distance limit. The surface-to-surface distance L is 1 μm. The only difference between the two graphs is the scale, the left one being focussed on high temperatures, and the right one being a zoom on lower temperatures.

The left graph focuses on the high temperature regime, which is reached the sooner the larger the sphere. This statement is in agreement with a previous discussion on the fact that spheres will make the thermal effect appear for higher temperatures, especially when they are small.

The right graph presents the non-monotonic nature of the entropy for small values of the temperature. It shows that, for any size of the sphere, when the temperature increases from zero, the entropy first decreases to a minimum before increasing to reach its constant value at high temperatures, as it does for the long-distance regime. This minimum is more pronounced in depth and width when the radius of the sphere is smaller, with a saturation effect when the curve reaches the long-distance limit, equivalent to a $(R \to 0)$-limit when L is fixed.

We now study the Casimir entropy as a function of the distance L for a fixed ambient temperature $(T = 300K)$. **Fig. 66** shows the Casimir entropy $\mathcal{S}$, divided by R^3 in order to compare the curves with different radii. In the left graph the entropy is plotted with respect to the surface-to-surface distance L, in the right graph with respect to the center-to-surface distance $\mathcal{L}$.

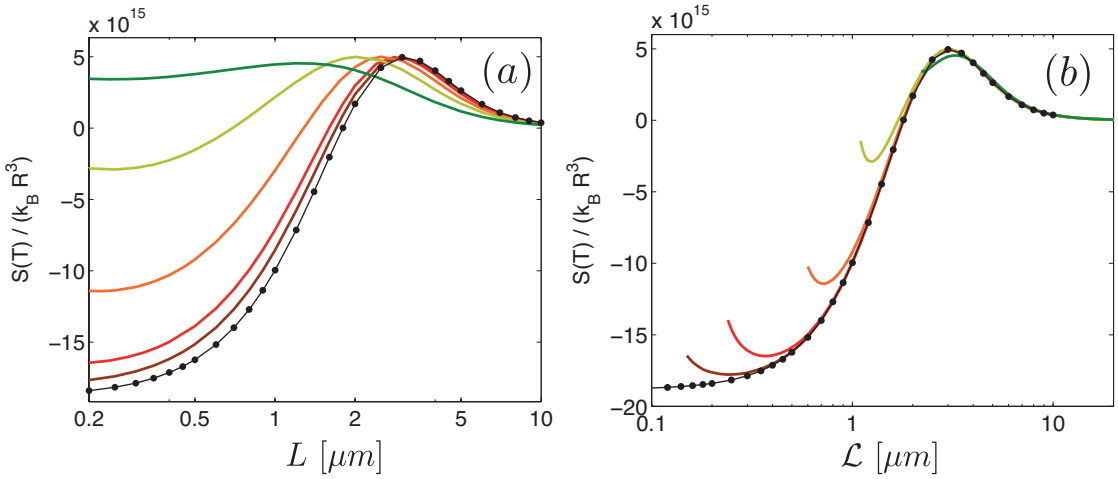

Figure 66: Normalized Casimir entropy $\frac{\mathcal{S}}{k_B R^3}$ with respect to the surface-to-surface distance L (left graph) or the center-to-surface distance $\mathcal{L}$ (right graph). The colors are the same as for **Fig. 64**. The temperature is $T = 300K$.

The left graph of **Fig. 66** presents the same feature as previously, that is to say the possibility of a negative entropy for some range of values of the parameters. But at ambient temperature, this negative entropy only appears for small enough spheres ($R \lesssim 1\mu$m), even at small separations, which is different from the situation of a fixed distance presented in **Fig. 65**, where negative entropies always occur for any radius of the sphere at low enough temperature.

The right graph of **Fig. 66** shows the Casimir entropy at ambient temperature with respect to the center-to-plate distance $\mathcal{L} = L + R$. It illustrates the fact that the analytical expansion of the Casimir entropy derived in the long-distance limit is recovered for aspect ratios $\frac{L}{R} \gtrsim 4$.

The study of the Casimir entropy in the sphere-plane configuration for perfect mirrors shows that this interaction entropy can take negative values in some cases. While in the plane-plane configuration the appearance of negative values for the entropy was related to the dissipation in the materials, it is here clearly related to the geometry, as this feature is particularly visible when using small spheres, for which curvature is more pronounced. This result is not in contradiction with basic thermodynamic principles [140, 244] as the Casimir energy is an interaction energy and can thus be understood as a difference of energies.

13.5 Comparison with PFA at short distance

From Eq. (13.3) (p.177), one sees that the previously discussed negative correlation number $\delta_{\mathcal{F}}^{TG} \leq 0$ implies that $\rho_{\mathcal{F}}(T) < \rho_{\mathcal{F}}(T = 0)$. Hence the overestimation made by PFA on results for the magnitude of Casimir effect is even more pronounced when the temperature is non-zero. In this section we study the effect of temperature on the accuracy of the PFA results with the help of the parameter $\rho_{\mathcal{F}} = \frac{\mathcal{F}}{\mathcal{F}_{\rm PFA}}$.

In the large distance limit studied in **Section 8.2** (p.126), the importance of the influence of temperature for the Casimir effect was found to be mainly dependent on the dimensionless quantity $\frac{2\pi\mathcal{L}}{\lambda_T}$. For small distances ($L \ll R$) however, we find that the important parameter for the thermal effect is $\alpha_T = \frac{2\pi L}{\lambda_T}$.

We illustrate this statement in **Fig. 67**, where we draw the ratio $\rho_{\mathcal{F}}$ of the exact Casimir free-energy $\mathcal{F}$ divided by the free-energy calculated within PFA, $\mathcal{F}_{\rm PFA}$, with respect to the aspect ratio $\frac{L}{R}$. The different curves show how $\rho_{\mathcal{F}}$ gradually shifts from the low-temperature to the high-temperature regime when the thermal index α_T increases.

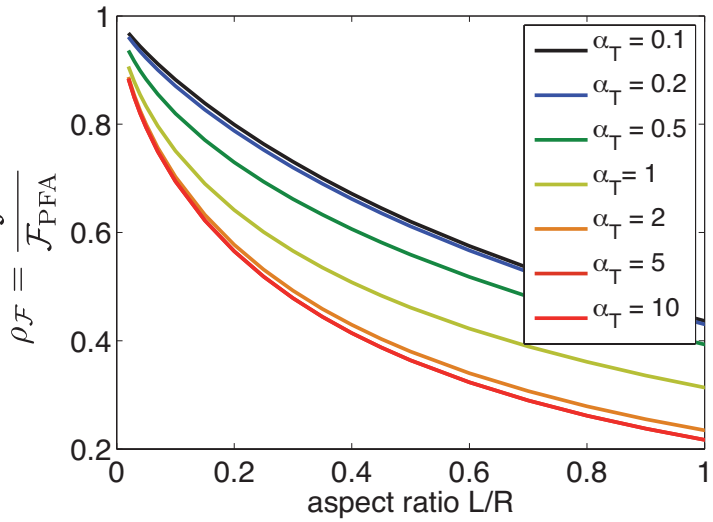

Figure 67: Correction factor for the effects of curvature $\rho = \frac{\mathcal{F}}{\mathcal{F}_{\rm PFA}}$ with respect to the aspect ratio $\frac{L}{R}$. Each curve represents a constant value of $\alpha_T = \frac{2\pi L}{\lambda_T}$, from the lower value 0.1 at the top to the higher value 10 at the bottom. Curves for $\alpha_T = 5, 10$ are superimposed. The leftmost point is for $\frac{L}{R} = 0.02$, computed with $\ell_{\rm max} = 250$.

As expected all curves go to unity when $\frac{L}{R} \to 0$, meaning that the PFA result is correct at the limit of a very large sphere, even when the temperature is non-zero. We also observe that for $\alpha_T \gtrsim 2$ the curves for $\rho(L/R)$ collapse into a high-temperature regime, which is equivalent to distances $L \gtrsim 2.5$ μm at ambient temperature $T = 300$ K. Similarly, a low-temperature regime is obtained for $\alpha_T \lesssim 0.2$, which is equivalent to the distance range $L \lesssim 0.25$ μm at ambient temperature. In between, the curves shift from the latter to the former in an intermediate thermal regime for $\alpha_T \in [0.2, 2]$, centered around $L \sim 1$ μm.

The fact that $\rho_{\mathcal{F}}(T)$ takes on lower values than $\rho_{\mathcal{F}}(0)$ means that the error made by PFA is increased by the inclusion of thermal effects in the model. The proximity force approximation not only overestimates the magnitude of the Casimir energy or force, but it also overestimates the thermal contribution to it. This additional error of PFA is again due to the correlations between the effects of geometry and temperature. As a consequence, the linear first-order beyond-PFA correction term $\beta_{\mathcal{F}}$ will be greater in magnitude as soon as the temperature plays a role.

To give an example of the change, we present in **Fig. 68** a polynomial fitting of the data points to smaller values of the aspect ratio $\frac{L}{R}$, for a small and a large value of α_T. For the low-temperature regime with $\alpha_T = 0.1$, the first order correction coefficient $\beta_{\mathcal{F}} \simeq -1.5$ is close to the value obtained at zero temperature, whereas for the high-temperature regime for $\alpha_T = 10$, a quadratic fit gives $\beta_{\mathcal{F}} \simeq -6.5$, which is four times bigger.

The situation is even more complicated for the more realistic situation where the radius R and the temperature T are fixed, and only the distance L can vary. Indeed, curves for a given value of R, as presented in **Fig. 69** for the Casimir force, go from a high-temperature regime at large values of the aspect ratio $\frac{L}{R}$ to a low-temperature regime at small values of $\frac{L}{R}$, because the distance L has to decrease when R is fixed, and so does the parameter α_T at fixed temperature. The change of regime is centered around $L \sim 1 - 2\mu$m, which corresponds to a different value of $\frac{L}{R}$, depending on the sphere radius.

This behavior shows that because of the interplay between the thermal effects and the curvature, a beyond-PFA function $\rho(L/R)$ is not sufficient to measure the accuracy of PFA, as this would depend greatly on the relative value of R and T when they are fixed. The beyond-PFA function is

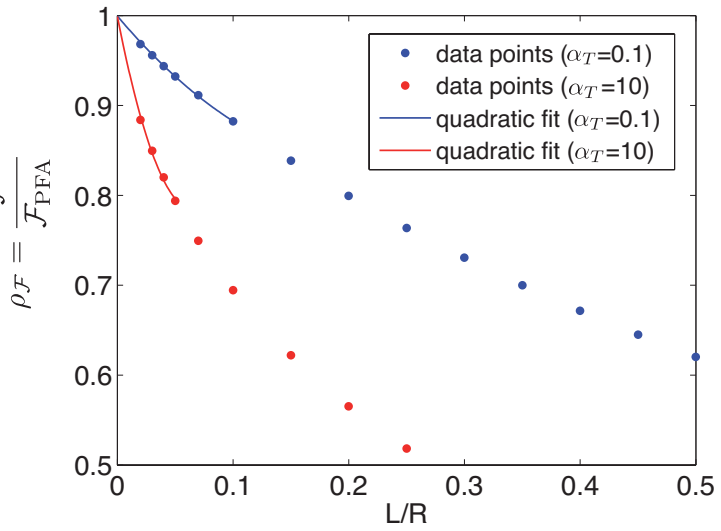

Figure 68: Extrapolation to short distances of the correction factor $\rho = \frac{\mathcal{F}}{\mathcal{F}_{\mathrm{PFA}}}$ thanks to a best quadratic fit (with an additional point $\rho(0) = 1$). The upper blue curve represents the low-temperature regime ($\alpha_T = 0.1$), the lower red curve represents the high-temperature regime ($\alpha_T = 10$). The polynomial fit is $y = 1 - 1.52x + 3.53x^2$ in the low-temperature regime, and $y = 1 - 6.53x + 49.6x^2$ for the high-temperature regime. The leftmost point is for $\frac{L}{R} = 0.02$, computed with $\ell_{\max} = 250$.

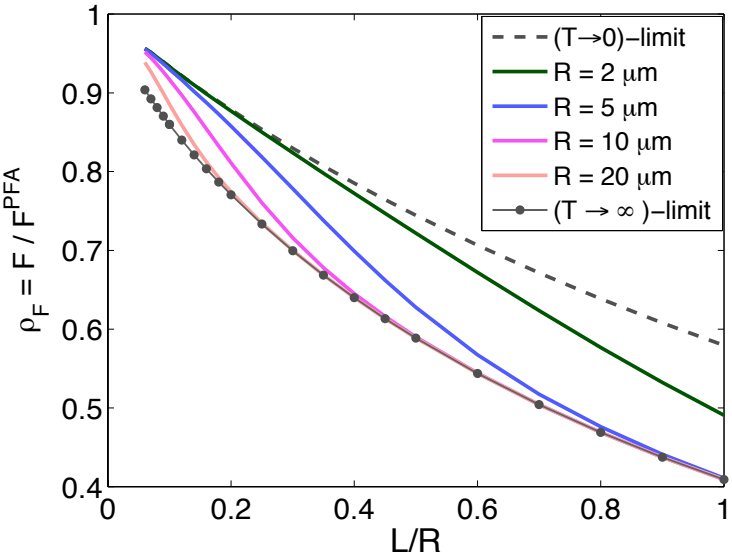

Figure 69: Correction factor for the effects of curvature $\rho_F = \frac{F}{F_{\mathrm{PFA}}}$ with respect to the aspect ratio $\frac{L}{R}$. Each curve represents a sphere radius R. The temperature is fixed at $300K$. The leftmost point is for $\frac{L}{R} = 0.05$, computed with $\ell_{\max} = 85$.

rather dependent of two ratios of lengthscales, and thus we should write $\rho\left(\frac{L}{R}, \frac{L}{\lambda_T}\right)$ for the present purpose. **Fig. 67** encourages to choose a fixed temperature and distance, and to vary only the radius of the sphere. Unfortunately this procedure is not realistic for an experiment. However, it can give good hints on the magnitude of the first order correction β, depending on the thermal regime.

14 Metallic mirrors at ambient temperature

In this section, as in the previous one, we study the Casimir interaction between a sphere and a plane at ambient temperature, but now we introduce additionally a more accurate description of the optical response for real materials, accounting for imperfect reflection. To do so, we use again dielectric functions for the materials that is the lossless plasma model, or the dissipative Drude model, the expressions of which are recalled in Eq.(11.1) (p.148).

Let us recall some observations from **Section 11** (p.148) for the zero-temperature case. Although every material is a poor reflector at high frequencies, which correspond to short separations, the effect of imperfect reflection can also have an influence for long distances, as it is coupled to the effect of curvature. An example of such an influence is the finite conductivity correction factor η_E^P, studied in **Section 11.1** (p.148), which does not go to unity at the limit of large distances when considering a small sphere ($R \not\gg \lambda_P$). We expect to see a similar behavior in the thermal case, especially as an increasing temperature yields an increasing importance of the zero-frequency contribution, studied analytically in **Section 7** (p.108), which is very dependent on optical properties of the material.

We first study in **Section 14.1** how the inclusion of the thermal fluctuations affects the Casimir effect between a metallic sphere and a metallic plane, via the thermal increase factor ϑ and the Casimir entropy, and compare these results with those obtained for perfect reflectors in the previous section. We then change the point of view and consider in **Section 14.2** the effects of the introduction of a metallic response of materials for the Casimir effect at zero and ambient temperatures. The various couplings between the effects of temperature, curvature, imperfect reflection and dissipation are studied in details in in **Section 14.3**, and finally a most-realistic beyond-PFA correction is analyzed in **Section 14.4**. In **Section 14.5** we try and characterize the different regimes in terms of power laws for the most realistic configuration of dissipative metals at ambient temperature.

14.1 Influence of temperature for metallic materials

In the case of perfect reflectors studied in **Section 13** (p.171), we found correlations between the thermal and curvature effects, leading to an overestimation of the thermal increase factor made by PFA. The results obtained from the scattering formula even showed that the magnitude of the Casimir free-energy at ambient temperature could be lower than the one for zero temperature, especially when considering relatively small spheres. This was illustrated in **Fig. 63** (p.177), where the thermal increase factor $\vartheta_{\mathcal{F}}$ is lower than 1 for spheres of radius $R \lesssim 1$ μm. We have related this feature to the appearance of negative values for the entropy for some range of the temperature T and distance L.

With a dissipative metal, whose optical properties can be described by a Drude model, negative entropies can already arise in the plane-plane geometry [140]. Thus there exists a range of distances where $\vartheta_{\mathcal{F}} < 1$ for quantities calculated within PFA in the sphere-plane geometry. In **Fig. 70**, the thermal increase factor within PFA ϑ_{PFA} is presented by a dashed curve, the different exactly calculated increase factors for various sizes of the sphere by solid lines.

Naturally, the thermal increase factor ϑ_{PFA} obtained within PFA is radius-independent. It first decreases with increasing L at short separations, reaches a minimum of 0.74 at $L \simeq 2$ μm, and increases again when entering a high-temperature regime linear in T. The thermal increase factor obtained from the scattering formalism ϑ has the same global shape, but depends on the sphere radius R. For a large radius of 5 μm (blue curve) the ratio is close to the one obtained from PFA, which is expected since for a fixed value of L, the aspect ratio $\frac{L}{R}$ is then small. For smaller spheres, the minimum moves to larger distances and decreases in depth.

The first general observation that the thermal increase factor ϑ_F depends on the radius R

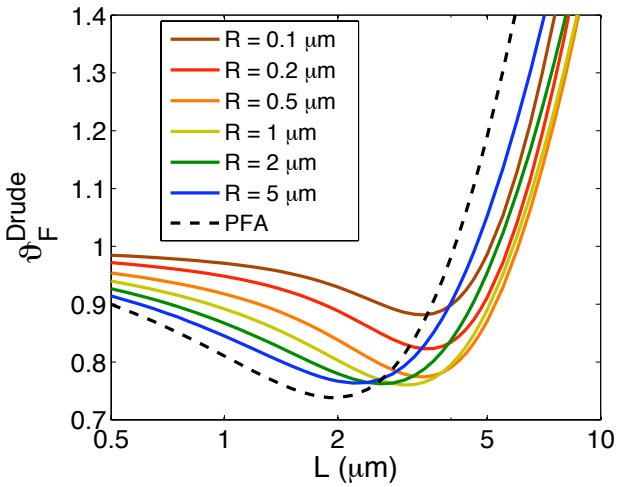

Figure 70: Thermal increase factor ϑ_F for the Casimir force ϑ_F with respect to the distance L in μm. The temperature is fixed to $T = 300K$ and is associated to a thermal wavelength $\lambda_T = 7.6$ μm. The solid curves represent the exact quantities, computed within the scattering formalism with a sufficient number $\ell_{\max}$ of modes to get result far more accurate than the curves' width. The lower dashed curve is the PFA thermal correction $\vartheta_{\rm PFA}$.

of the sphere means that, like for perfect conductors, there is a correlation between the effects of curvature and temperature when metals are considered. However, in contrast to the perfect reflectors calculations, for which PFA always overestimates the thermal correction factor, this correlation has here an opposite effect for small distances, as the PFA underestimates the thermal factor. Thus the contribution of the thermal photons to the Casimir force is indeed repulsive for small distances, but less than what was to be expected from PFA predictions. For larger distances, PFA overestimates the thermal correction factor, but the overestimation remains smaller than for perfect mirrors.

In **Fig. 71**, we compare more specifically the obtained thermal increase factors for the Casimir free-energy $\vartheta_{\mathcal{F}}^{\rm Drud}$ for metals described by a Drude model (red), with the ones for perfect reflectors $\vartheta_{\mathcal{F}}^{\rm perf}$ (black), for a limited set of sphere radii ($R = 0.1, 1, 10$ μm), and with the R-independent PFA computations.

Clearly the thermal correction is greater for perfect mirrors than for metallic ones, for each sphere radius and independently of whether calculated within PFA or exactly via scattering theory. Together with the previous statement that PFA overestimates the thermal factor for perfect reflectors, underestimates it for Drude mirrors at short distances, and overestimates it less than for perfect mirrors at large distances, we deduce that the relative difference $\left|\frac{\vartheta_{\mathcal{F}}^{\rm perf}}{\vartheta_{\mathcal{F}}^{\rm Drud}} - 1\right|$ between the thermal increase factors obtained for perfect and Drude mirrors is smaller when calculated with exact quantities than within PFA computations. This result is corroborated by **Fig. 71**, where the difference between dashed lines corresponding to PFA calculations is always larger than the difference between solid lines corresponding to the results obtained with the scattering approach.

14.2 Influence of imperfect reflection at ambient temperature

The effect of imperfect reflection on the Casimir effect between a sphere and a plane has been discussed at zero temperature in **Section 11.1** (p.148), where we observed a non-trivial dependance on the radius of the sphere. Unlike in the plane-plane geometry, the finite conductivity correction

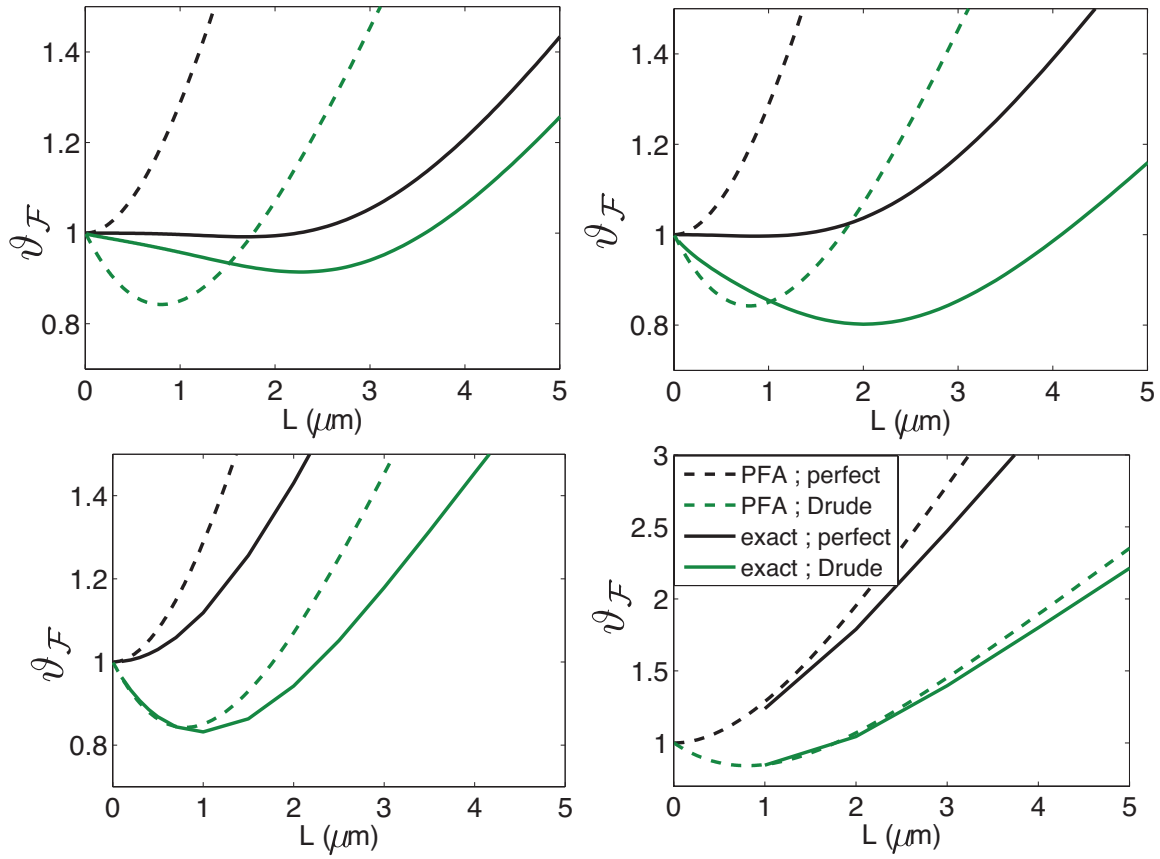

Figure 71: Thermal increase factor $\vartheta_{\mathcal{F}}$ for the Casimir free-energy $\mathcal{F}$ with respect to the distance L in μm. The radii of the sphere are 0.1 μm (upper left graph), 1 μm (upper right graph), 10 μm (lower left graph), and 100 μm (lower right graph). The temperature is fixed to $T = 300$ K and is associated to a thermal wavelength $\lambda_T = 7.6$ μm. The black curves are for perfect reflectors, the green for mirrors described by the Drude model. The dashed-curves have been obtained within PFA, the solid lines represents exact calculations, performed with $\ell_{\max} = 500$ for the leftmost points at $\frac{L}{R} = 0.01$.

factor $\eta_E^P = \frac{E^{\rm Drud}}{E^{\rm perf}}$, which measures the decrease in the Casimir energy due to the introduction of imperfect reflection, is not going to unity at the limit of large distances, but rather to $\frac{2}{3}$ for mirrors described by a Drude model.

At ambient temperature the finite conductivity correction factor η^P is going to $\frac{1}{2}$ at large distances in the plane-plane geometry, as the TE polarization vanishes for dissipative metals in this limit. In the sphere-plane geometry however, the situation is more complicated since different polarizations are coupled to each other, and not equivalent. We thus expect, as for the zero-temperature case, that η^P behaves differently than predicted by PFA.

In **Fig. 72** we present the finite conductivity correction factor for the Casimir free-energy $\eta_{\mathcal{F}}^P$ for various sizes of the sphere ($R = 0.1, 1, 10$ or 100 μm) with respect to the distance L. The PFA results, coming from the study of the plane-plane geometry are presented by dashed lines, while solid curves correspond to exact results in the sphere-plane geometry. The results for $T = 0K$ are recalled in blue, the new quantities for ambient temperature ($T = 300K$) are plotted in red.

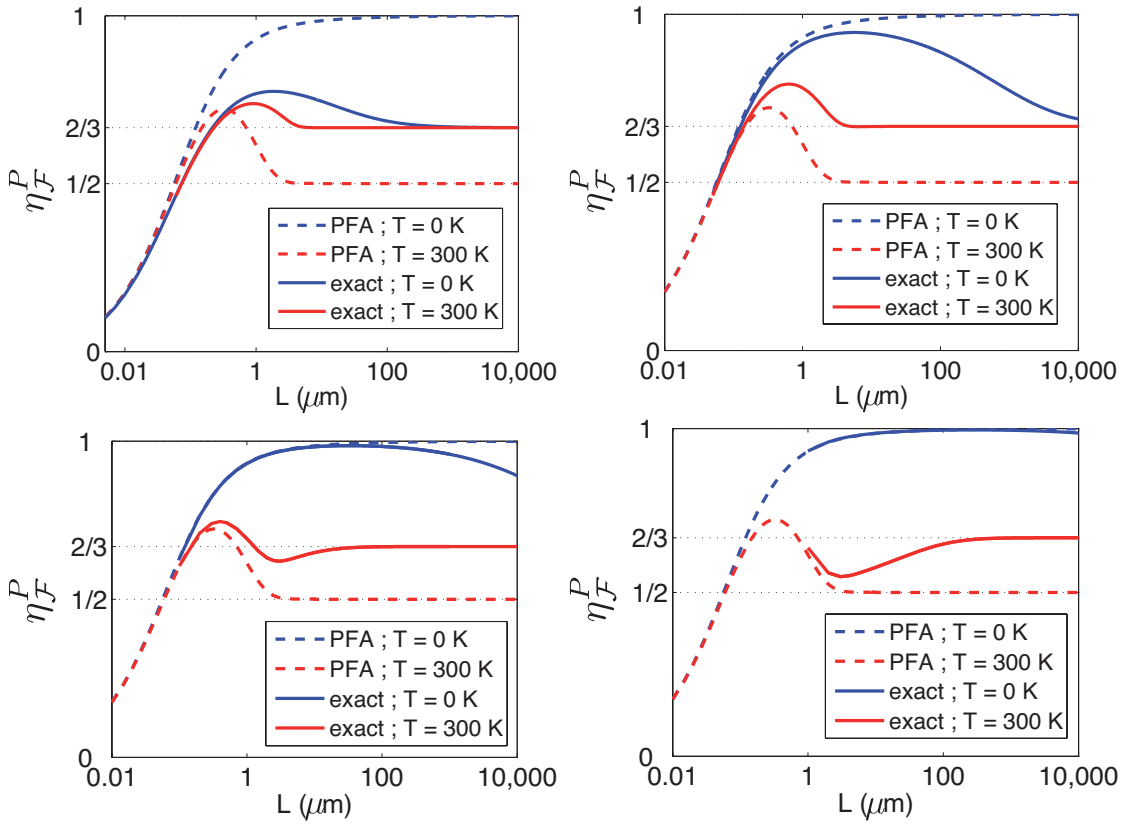

Figure 72: Finite conductivity correction for the Casimir free-energy $\eta_{\mathcal{F}}^P = \frac{\mathcal{F}^{\rm Drud}}{\mathcal{F}^{\rm perf}}$ as a function of the distance L, for the Drude model. The sphere radii is 0.1 μm (upper left graph), 1 μm (upper right graph), 10 μm (lower left graph), and 100 μm (lower right graph). Blue curves represent zero temperature, red curves ambient temperature ($T = 300$ K). Solid lines are used for exact quantities, computed from the scattering formula with $\ell_{\rm max} = 500$ for the leftmost points at $\frac{L}{R} = 0.01$, dashed curves are for PFA quantities. The plasma wavelength is $\lambda_P = 136$ nm, the dissipation ratio $\delta = \frac{\lambda_P}{\lambda_\gamma}$ is 0.004.

For the four sphere radii, we observe that the finite conductivity correction factor $\eta_{\mathcal{F}}^P$ changes with temperature, and like in PFA computations, that it is always lowered by the introduction of the temperature. In other terms, we always have $\frac{\eta_{\mathcal{F}}^P(T)}{\eta_{\mathcal{F}}^P(T=0)} \leq 1$, which is consistent with the

statement of the previous section that $\frac{\vartheta_{\mathcal{F}}^{\rm Drud}}{\vartheta_{\mathcal{F}}^{\rm perf}} \leq 1$, as:

$$\frac{\eta_{\mathcal{F}}^{P}(T)}{\eta_{\mathcal{F}}^{P}(T=0)} = \frac{\mathcal{F}^{\rm Drud}(T)\mathcal{F}^{\rm perf}(0)}{\mathcal{F}^{\rm perf}(T)\mathcal{F}^{\rm Drud}(0)} = \frac{\vartheta_{\mathcal{F}}^{\rm Drud}}{\vartheta_{\mathcal{F}}^{\rm perf}} \ .$$

This gives informations on the sign of the correlation number $\delta_{\mathcal{F}}^{TP} \leq 0$ for the effects of temperature and finite conductivity, and will be studied in more detail in **Section 14.3**.

When calculated within scattering theory the finite conductivity correction $\eta_{\mathcal{F}}^{P}$ at zero temperature turns out to be smaller than when calculated within PFA, while it is larger than its PFA counterpart at ambient temperature, except for $R = 0.1$ μm and distances $L \lesssim 1$ μm. As a consequence, the difference between the finite conductivity factors at zero and ambient temperatures is smaller than expected from PFA predictions.

At large distances the predictions of the scattering theory become qualitatively different from PFA predictions. As explained in **Section 3.2.3** (p.51), in the long-distance limit for the plane-plane geometry, the finite conductivity correction factor is 1 at zero temperature and $\frac{1}{2}$ at ambient temperature, which means that the dissipation at large distances plays a qualitatively different role for vacuum and for thermal fluctuations. This ratio of $\frac{1}{2}$ between the two limits has recently given rise to a controversy [137, 245, 246, 247, 248, 249, 250, 251, 252, 141] on the validity of the theory and the description of dissipation. Here, we show that in the sphere-plane geometry, both finite conductivity correction factors $\eta_{\mathcal{F}}^{P}(T)$ and $\eta_{\mathcal{F}}^{P}(0)$ tend to the same large-distance limit of $\frac{2}{3}$ when calculated within the scattering formalism.

14.3 Study of various interplays

The most realistic configuration studied in this manuscript, a sphere and a plane made of dissipative metals at ambient temperature, involves no less than five independent lengthscales: the distance L, the sphere radius R, the thermal wavelength λ_T, the plasma wavelength λ_P related to high-frequency transparency, and λ_γ related to dissipation in the material. A great variety of behaviors emerge in this rich landscape when these lengthscales are changed.

In order to see the dependance on the different parameters, we separate the influence of different effects, such as the temperature (T), the finite conductivity (P), the geometry (G) and the dissipation in the materials. In this section we study the interplays between those effects, first by couples of the three former, then separately for the dissipation.

14.3.1 Interplays between the effects of temperature and finite conductivity (TP)

For the effects of temperature and finite conductivity, the correlation number $\delta_{\mathcal{F}}^{TP}$ for the Casimir free-energy can be written as:

$$\delta_{\mathcal{F}}^{TP} = \frac{\eta_{\mathcal{F}}^{TP}}{\eta_{\mathcal{F}}^{T}\eta_{\mathcal{F}}^{P}} - 1 = \frac{\mathcal{F}^{\rm Drud}(T)\mathcal{F}^{\rm perf}(0)}{\mathcal{F}^{\rm perf}(T)\mathcal{F}^{\rm Drud}(0)} - 1 = \frac{\vartheta_{\mathcal{F}}^{\rm Drud}}{\vartheta_{\mathcal{F}}^{\rm perf}} - 1 \tag{14.1}$$

$$= \frac{\eta_{\mathcal{F}}^{P}(T)}{\eta_{\mathcal{F}}^{P}(T=0)} - 1 \ . \tag{14.2}$$

The study of this correlation number in PFA computations can be performed by considering the plane-plane geometry, as in [207] and the results of which are recalled in **Section 3.2.3** (p.51). Whereas at zero temperature the finite conductivity has only an effect for short distances, the combination with thermal effects does make an important change at large distances, as seen in the dashed-curves in **Fig. 72** in the previous section. Indeed, the thermal increase factor $\vartheta_{\rm PFA}$ is twice smaller for Drude mirrors than for perfect mirrors at the limit of large distances, yielding a

limiting value $-\frac{1}{2}$ for $\delta_{\mathcal{F}}^{TP}$ in this limit, as illustrated by **Fig. 25** (p.53). For short distances, the temperature does not play a role anymore, and the correlation number should vanish. In between, it is possible to infer from the curves in **Fig. 24** (p.52) that $\delta_{\mathcal{F}}^{TP}$ is always negative for Drude model, whereas it is always positive for plasma model (Fig.4.4 in [207]).

For the sphere-plane geometry, the difference between the thermal increase factors ϑ calculated with the Drude model and the one for perfect mirrors, observed in **Fig. 71** (p.186) can provide a first guess on the correlation number, thanks to the relation (14.1). The very existence of a nonzero difference is a clear sign of the appearance of correlations between the effects of temperature and finite conductivity in the sphere-plane geometry. Moreover this correlation number $\delta_{\mathcal{F}}^{TP}$ should always be negative, as in the observed range of parameters the curves for perfect reflectors in **Fig. 71** (p.186) lie above those for Drude mirrors.

From the alternative expression (14.2) of the correlation number, the comparison of the finite conductivity correction factors η^P at zero and ambient temperature give an equivalent insight on $\delta_{\mathcal{F}}^{TP}$. From **Fig. 72** (p.187), we also come to the conclusion that the correlation number should be negative, as we observe $\eta^P(T) \leq \eta^P(0)$ for any case.

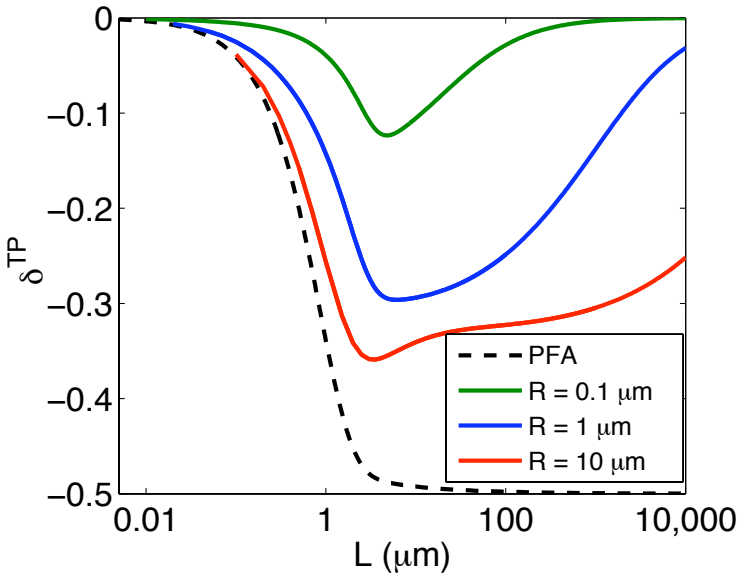

Figure 73: Correlation number $\delta_{\mathcal{F}}^{TP}$ quantifying the correlations between imperfect reflection (with Drude model) and temperature, as defined in Eqs.(14.1-14.2), with respect to the distance L. The dashed-line represents the PFA computation, the solid lines are results of the exact calculations with different colors for different radii, computed from the scattering formula with $\ell_{\max} = 500$ for the leftmost points at $\frac{L}{R} = 0.01$. The plasma wavelength is $\lambda_P = 136$ nm, the dissipation ratio $\delta = \frac{\lambda_P}{\lambda_\gamma}$ is 0.004.

In **Fig. 73**, we show the numerical evaluations of the correlation number $\delta_{\mathcal{F}}^{TP}$ as a function of the distance L. The PFA computation for the free-energy $\mathcal{F}_{\rm PFA}$ are presented by a dashed-line and is independent on the sphere radius R, since it is related to the primo-potential $D_{\rm PP}$ in the plane-plane geometry. The correlation number is negative as expected, going to 0 at short distances, and to $-\frac{1}{2}$ at large distances.

Within the scattering formalism, $\delta_{\mathcal{F}}^{TP}$ is also negative, but shows a rich dependance on the sphere radius with a rather complex non-monotonicity. At the limit of large distances there are no more correlations between the effects of temperature and finite conductivity, as $\delta_{\mathcal{F}}^{TP}$ tends to vanish.

This long-distance disappearance of the correlations is confirmed by expression (14.2) and the

observation that both $\eta_{\mathcal{F}}^{P}(T)$ and $\eta_{\mathcal{F}}^{P}(0)$ tend to the value $\frac{2}{3}$ at the limit of large distances in the sphere-plane geometry, as seen on **Fig. 72** (p.187).

14.3.2 Interplays between the effects of temperature and geometry (TG)

Both thermal and geometrical effects have a growing influence in the large-distance regime. Thus their combination should not yield any change for short separations, whereas at larger distance it is reasonable to expect a strong coupling between them. The correlation number for the Casimir free-energy between the effects of temperature (T) and geometry (G) writes:

$$\delta_{\mathcal{F}}^{TG} = \frac{\eta_{\mathcal{F}}^{TG}}{\eta_{\mathcal{F}}^{T}\eta_{\mathcal{F}}^{G}} - 1 = \frac{\mathcal{F}(T)\mathcal{F}_{\rm PFA}(0)}{\mathcal{F}(0)\mathcal{F}_{\rm PFA}(T)} - 1 = \frac{\vartheta_{\mathcal{F}}}{\vartheta_{\mathcal{F}}^{\rm PFA}} - 1 \tag{14.3}$$

$$= \frac{\rho_{\mathcal{F}}(T)}{\rho_{\mathcal{F}}(T=0)} - 1 \tag{14.4}$$

and can be defined within any model for the mirrors material properties.

Perfectly reflecting mirrors have been studied in **Section 13.3** (p.175) and a negative correlation number has been found, yielding non-trivial interplay between the effects of curvature and temperature. Indeed in **Fig. 62** (p.176) we observed that we always have $\eta_{\mathcal{F}}^{TG} \leq \eta_{\mathcal{F}}^{T}\eta_{\mathcal{F}}^{G}$ for perfect mirrors, where the equality is recovered at the limit of short separations.

In the study of the influence of temperature for Drude metals conducted in **Section 14.1** (p.184), we found that for short distances the thermal correction factor was larger than expected from PFA ($\vartheta \geq \vartheta^{\rm PFA}$), whereas for large distances the opposite occurs. These two different regimes, associated with the expression (14.3) for δ^{TG}, mean that the correlation number for Drude metals should change sign from positive to negative when the distance L increases.

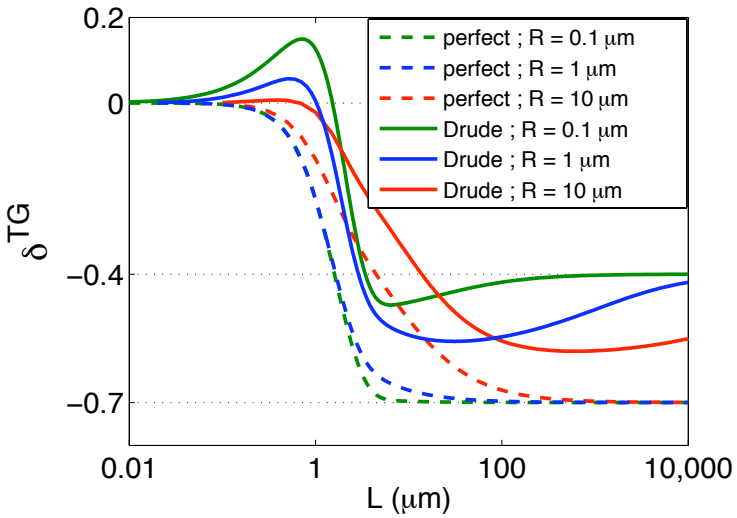

Figure 74: Correlation number $\delta_{\mathcal{F}}^{TG}$ between the effects of temperature (T) and geometry (G), as defined in Eqs.(14.3-14.4), with respect to the distance L. Dashed-lines are for perfect mirrors, solid curves for Drude mirrors. The sphere radii R are 0.1 μm (green), 1 μm (blue), and 10 μm (red). The quantities from scattering formula are calculated with $\ell_{\rm max} = 500$ for the leftmost points at $\frac{L}{R} = 0.01$. The plasma wavelength is $\lambda_P = 136$ nm, the dissipation ratio $\delta = \frac{\lambda_P}{\lambda_\gamma}$ is 0.004, and the temperature is $T = 300$ K.

We present in **Fig. 74** the numerical results for the correlation number $\delta_{\mathcal{F}}^{TG}$ with perfect mirrors (dashed lines) and metallic mirrors described by the Drude model (solid curves), for different sizes

of the sphere, as a function of the distance L. As expected, $\delta_{\mathcal{F}}^{TG}$ is always negative for perfect mirrors, and decreases from 0 to a R-independent large-distance limit. For Drude mirrors we observe the expected change in sign, as $\delta_{\mathcal{F}}^{TG}$ is positive at short distances and negative for large distances. The correlation number first raises to a maximum that is larger for small spheres, then decreases to a minimum, with a change of sign that occurs around $L \sim 1$ μm, before increasing again to a R-independent large-distance limit.

The large-distance limit of the correlation number can be computed analytically from the thermal correction factors ϑ and ϑ^{PFA}. Within the PFA computation, we start from the high-temperature thermal correction for the Casimir free-energy in the plane-plane geometry, given by Eq.3.11 (p.51) for perfect mirrors, which is twice the result for mirrors modelled by the Drude model. They translate into the equivalent thermal correction factors for the free-energy within PFA:

$$\vartheta_{\mathrm{PFA}}^{\mathrm{perf}}\left(L\to\infty\right) = \frac{180\zeta(3)L}{\pi^3\lambda_T} \qquad\qquad \vartheta_{\mathrm{PFA}}^{\mathrm{Drud}}\left(L\to\infty\right) = \frac{90\zeta(3)L}{\pi^3\lambda_T}\ . \tag{14.5}$$

The exact thermal correction factors can be extracted from the analytical large-distance results obtained in **Section 8** (p.124). In particular, we found that for large distances the zero-temperature and high-temperature limits for the Casimir free-energy with Drude mirrors both correspond to $\frac{2}{3}$ times the respective limit with perfect mirrors. Using Eq.(8.22) (p.131), it follows that:

$$\vartheta^{\mathrm{perf}}\left(L\to\infty\right) = \vartheta^{\mathrm{Drud}}\left(L\to\infty\right) = \frac{2\pi L}{3\lambda_T}\ . \tag{14.6}$$

Finally, by taking the ratio of (14.6) with (14.5), we obtain the correlation numbers for the free-energy $\delta_{\mathcal{F}}^{TG}$ for perfect and Drude mirrors at the limit of large separations:

$$\text{[perfect mirrors]}\quad \delta_{\mathcal{F}}^{TG}\left(L\to\infty\right) = \frac{\pi^4}{270\zeta(3)} - 1 \simeq -0.69987 \tag{14.7}$$

$$\text{[Drude mirrors]}\quad \delta_{\mathcal{F}}^{TG}\left(L\to\infty\right) = \frac{\pi^4}{135\zeta(3)} - 1 \simeq -0.3997 \tag{14.8}$$

which are in agreement with the convergences observed in **Fig. 74**.

From the alternative expression (14.4) for the correlation number with beyond-PFA correction factors, we deduce that the change in the sign of $\delta_{\mathcal{F}}^{TG}$ for mirrors described by the Drude model can be associated with a crossing of the two functions $\rho_{\mathcal{F}}^{\mathrm{Drud}}(T)$ and $\rho_{\mathcal{F}}^{\mathrm{Drud}}(0)$: for large distances, we should have $\rho_{\mathcal{F}}^{\mathrm{Drud}}(T) < \rho_{\mathcal{F}}^{\mathrm{Drud}}(0)$, as with perfect mirrors, but for smaller distances $L \lesssim 1$ μm we expect the opposite relation, especially for small spheres. This will be studied thoroughly in **Section 14.4**.

14.3.3 Interplays between the effects of geometry and finite conductivity (GP)

The correlation between the effects of curvature and finite conductivity has already been studied for the zero temperature case in **Section 11.3** (p.152). Here we extend the former study to the case of ambient temperature, and recall the expressions for the correlation number between those two effects:

$$\delta_{\mathcal{F}}^{GP} = \frac{\eta_{\mathcal{F}}^{GP}}{\eta_{\mathcal{F}}^{G}\eta_{\mathcal{F}}^{P}} - 1 = \frac{\mathcal{F}^{\mathrm{Drud}}\mathcal{F}_{\mathrm{PFA}}^{\mathrm{perf}}}{\mathcal{F}_{\mathrm{PFA}}^{\mathrm{Drud}}\mathcal{F}^{\mathrm{perf}}} - 1 = \frac{\rho_{\mathcal{F}}^{\mathrm{Drud}}}{\rho_{\mathcal{F}}^{\mathrm{perf}}} - 1 \tag{14.9}$$

$$= \frac{\eta_{\mathcal{F}}^{P}}{\eta_{\mathcal{F},\mathrm{PFA}}^{P}} - 1\ . \tag{14.10}$$

In the case of zero temperature, we observed in **Fig. 72** (p.187) that the finite conductivity correction factor obeys $\eta_{\mathcal{F}}^{P} \leq \eta_{\mathcal{F},\mathrm{PFA}}^{P}$ (dashed blue lines above solid blue curves). Expression (14.10)

yields $\delta_{\mathcal{F}}^{GP} \leq 0$ at zero temperature for the Casimir energy. For the force, **Fig. 50** (p.153) shows that generally $\eta_F^{GP} \leq \eta_F^P \eta_F^G$, which means that the correlation number δ_F^{GP} is negative for the Casimir force as well. For short distances however, small positive values can appear for small spheres.

For the Casimir force gradient G, we will re-inspect **Fig. 54** (p.156). The fact that the two beyond-PFA correction curves ρ for perfect and plasma mirrors cross each other is equivalent to a change of sign for δ_G^{GP}, thanks to the relation (14.9). For small distances, the correlation number for the Casimir force gradient should be positive, then it should be negative. In any case, the observation that for large distance the correlation number does not vanish is non-trivial, as finite conductivity effects should be mainly located at short distances.

For non-zero temperatures, we already observed in **Fig. 72** (p.187) that the finite conductivity correction factors generally obey $\eta_{\mathcal{F}}^P \geq \eta_{\mathcal{F},\mathrm{PFA}}^P$ (dashed red lines below solid red curves), except at short separations for the smallest sphere considered. From expression (14.10) follows then that at non-zero temperature, the correlation number $\delta_{\mathcal{F}}^{GP}$ for the Casimir free-energy is positive. The negative values at very short distances may be considered as an exception, as for such distances ($L \ll \lambda_T$) thermal fluctuations do not enter the Casimir cavity anymore, and the zero-temperature case is recovered.

After these preliminary remarks we now present in **Fig. 75** the results of the full numerical evaluations for the correlation number $\delta_{\mathcal{F}}^{GP}$ at both $T = 0\ K$ (dashed curves) and ambient temperature $T = 300\ K$ (solid lines), with respect to the distance L. Green, blue and red curves represent respectively results for spheres with a radius of 0.1 μm, 1 μm, and 10 μm.

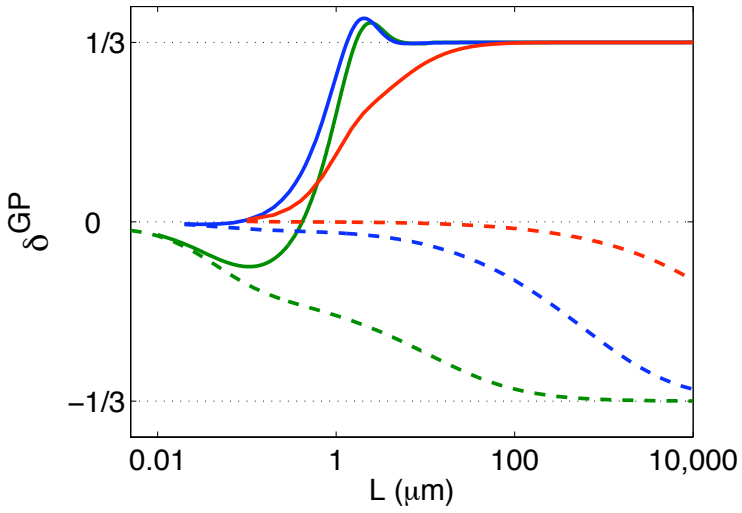

Figure 75: Correlation number $\delta_{\mathcal{F}}^{GP}$ between the effects of geometry (G) and finite conductivity (P), as defined in Eqs. (14.9-14.10), with respect to the distance L. Dashed-lines are for zero temperature, solid curves for ambient temperature ($T = 300$K). The sphere radii R are 0.1 μm (green), 1 μm (blue), and 10 μm (red). The quantities from scattering formula are calculated with $\ell_{\max} = 500$ for the leftmost points at $\frac{L}{R} = 0.01$. The plasma wavelength is $\lambda_P = 136$ nm, the dissipation ratio $\delta = \frac{\lambda_P}{\lambda_\gamma}$ is 0.004.

For zero temperature we observe, as expected, negative values for the correlation number $\delta_{\mathcal{F}}^{GP}$ which is a monotonically decreasing function of L, going from zero at short distances to $\frac{1}{3}$ at the limit of large separations. For large spheres ($R \gtrsim 1$ μm) the decrease below 0 only happens for sufficiently large distances and has a simple form. For nanospheres, the decrease starts at shorter distances, and the shape is more complex, with several inflections. This is due to the fact

that for nanospheres $R \sim \lambda_P$, meaning that the ranges of distance where the curvature and finite conductivity effects play a role intersect, giving rise to a higher correlation.

For ambient temperature the situation is more complex. At the limit of large separations the curves for any radius tend to a finite positive value $\frac{1}{3}$. Hence the correlation number is positive for large enough separations. At shorter distance, the correlation number goes to zero, but can take negative values by undergoing a minimum. This phenomena is particularly visible for nanospheres (green solid curve).

At the limit of large distances, we can use analytical solutions to confirm the numerical results. From **Section 3.2.3** (p.51) we remark that the finite conductivity correction factor η^P_{PFA} for PFA computations with Drude model, derived from the plane-plane configuration, goes to unity at zero temperature, and to the ratio $\frac{1}{2}$ at non-zero temperature. From **Section 8.4** (p.132), we know that at the limit of large distances, the same ratio for the exact quantities in the sphere-plane geometry is going to $\frac{2}{3}$, for zero or non-zero temperatures. These limits are summed up in **Fig. 72** (p.187), and from the expression (14.10), we get the following large-distance limits for the correlation number:

$$[T = 0\mathrm{K}] \qquad \delta^{GP}_{\mathcal{F}}\left(L \to \infty\right) = \frac{2/3}{1} - 1 = -\frac{1}{3} \tag{14.11}$$

$$[T = 300\mathrm{K}] \qquad \delta^{GP}_{\mathcal{F}}\left(L \to \infty\right) = \frac{2/3}{1/2} - 1 = \frac{1}{3} \tag{14.12}$$

which are in agreement with the numerical results.

From expression (14.9), it is possible to infer the relative behavior of the beyond-PFA correction factors $\rho_{\mathcal{F}}$ for perfect and Drude mirrors, with respect to the distance. When the temperature is zero or only plays a negligible role, the correlation number for the Casimir free-energy is negative and the beyond-PFA correction factor $\rho^{\mathrm{Drud}}_{\mathcal{F}}$ will be smaller than $\rho^{\mathrm{perf}}_{\mathcal{F}}$. However, with increasing distance L, when thermal fluctuations become important, the curve for $\rho^{\mathrm{Drud}}_{\mathcal{F}}$ will cross the one for $\rho^{\mathrm{Drud}}_{\mathcal{F}}$ and go above it.

Those statements are valid only for the Casimir free-energy, and could be different for the Casimir force or force gradient, as illustrated in the beginning of this section for the PFA quantities.

14.3.4 Effect of dissipation

In **Fig. 76**, we isolate the effects of the dissipation on the Casimir force by plotting the ratio between the thermal Casimir force values F^{plas} calculated with the plasma model and F^{Drud} obained with the Drude model, with respect to the distance L, and for various sphere radii. The PFA computation is given by dashed-line for reference and as usually, does not depend on the radius R.

The ratio $\frac{F^{\mathrm{plas}}}{F^{\mathrm{Drud}}}$, which measures the gain in the Casimir force when the dissipation is switched off, is always smaller than what was expected from PFA computations. It increases with L when R is fixed, but decreases with R at a given distance. The fact that this ratio depends on R is a clear signature of the interplay between geometry, temperature and dissipation. Our analysis shows that the Casimir force values obtained with and without dissipation are closer to each other than expected from PFA. This is particularly true at large distance, as the studied ratio $\frac{F^{\mathrm{plas}}}{F^{\mathrm{Drud}}}$ goes to the value 2 for PFA, as in the plane-plane configuration, but goes to $f\left(\frac{\lambda_P}{R}\right) \in \left[1, \frac{3}{2}\right]$ for the exact result in the sphere-plane geometry.

14.4 Beyond-PFA corrections

The Proximity Force Approximation, introduced in **Section 4.1** (p.55), relies on the assumption that the sphere is large compared to the closest distance between the two surfaces, and therefore

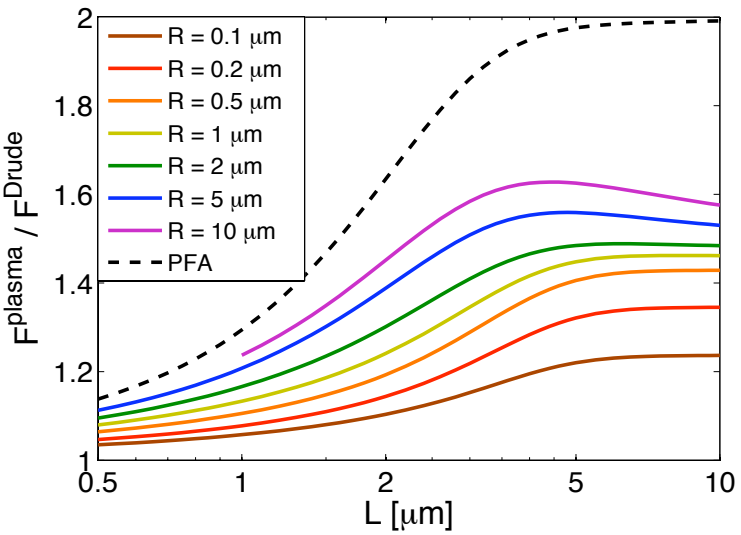

Figure 76: Ratio between thermal Casimir force values calculated with the plasma and the Drude models, with respect to the distance L for different sphere radii. The solid curves from bottom to top correspond to increasing values of sphere radii. The PFA prediction corresponds to the dashed curve. The plasma wavelength is $\lambda_P = 136$ nm, the dissipation ratio $\delta = \frac{\lambda_P}{\lambda_\gamma}$ is 0.004.

should be applicable and give accurate results in the limit of small aspect ratios $\frac{L}{R} \ll 1$. Until now it has been the only method used to obtained theoretical predictions to be compared with the experimental results. As the error made by this approximation is not mastered, it is of great interest to try and assess the accuracy of such an approximation. First beyond-PFA studies ([167, 233] and earlier works mentioned in **Section 9** (p.137)) have been devoted to evaluate the correction factor $\rho_E = \frac{E}{E_{\rm PFA}}$, and its linear coefficient for small values of $\frac{L}{R}$ in the case of perfect mirrors at zero temperature. As seen in **Sections 11.4** (p.153) for metals at zero temperature, and in **13.5** (p.180) for perfect mirrors at non-zero temperature, the beyond-PFA correction factor is greatly affected by the effects of temperature or by the introduction of finite conductivity in the description of the optical response of the materials. In the former sections we have described numerous and various correlations arising between the effects of curvature, temperature, and finite conductivity, with different behaviors in separate distance regimes. Hence the factor $\rho_{\mathcal{F}}$ will be even more affected by the complex interplay between all those influences, and should be written as $\rho_{\mathcal{F}}\left(\frac{L}{R}, \frac{L}{\lambda_T}, \frac{L}{\lambda_P}, \frac{L}{\lambda_\gamma}\right)$.

In this section we try to characterize the evolution of the beyond-PFA correction factor for the Casimir free-energy $\rho_{\mathcal{F}} = \frac{\mathcal{F}}{\mathcal{F}_{\rm PFA}}$ with Drude metals at ambient temperature when the radius of the sphere R and the distance L evolve. We first focus on the effect of finite conductivity at ambient temperature, with the perfect mirrors case studied in **Section 13.5** (p.180) as a reference. We will then change the point of view and focalize on the thermal effects for Drude metals, with the zero-temperature case discussed in **Section 11.4** (p.153) as reference.

14.4.1 Influence of finite conductivity on the beyond-PFA corrections at ambient temperature

In **Section 14.3.3** (p.191), we predicted two different regimes for the comparison of $\rho_{\mathcal{F}}^{\rm Drud}$ and $\rho_{\mathcal{F}}^{\rm perf}$ at ambient temperature: when L is small, so that the thermal effects are not predominant,

we recover a zero-temperature situation where $\rho_{\mathcal{F}}^{\mathrm{Drud}} \leq \rho_{\mathcal{F}}^{\mathrm{perf}}$. When the distance increases, the thermal fluctuations play an increasing role, and a second regime appears, where the relation gets reversed to $\rho_{\mathcal{F}}^{\mathrm{Drud}} \geq \rho_{\mathcal{F}}^{\mathrm{perf}}$.

Those predictions are corroborated by the exact numerical evaluations, which are presented in **Fig. 77**, for the beyond-PFA correction factor for the free-energy $\rho_{\mathcal{F}}$ at ambient temperature ($T = 300\mathrm{K}$) with respect to the distance L, for four different sizes of the sphere ($R = 0.1, 1, 10, 100\ \mu\mathrm{m}$). The results with perfect reflectors (black dashed-line) and dissipative metals, described by a Drude model (green solid line), are compared.

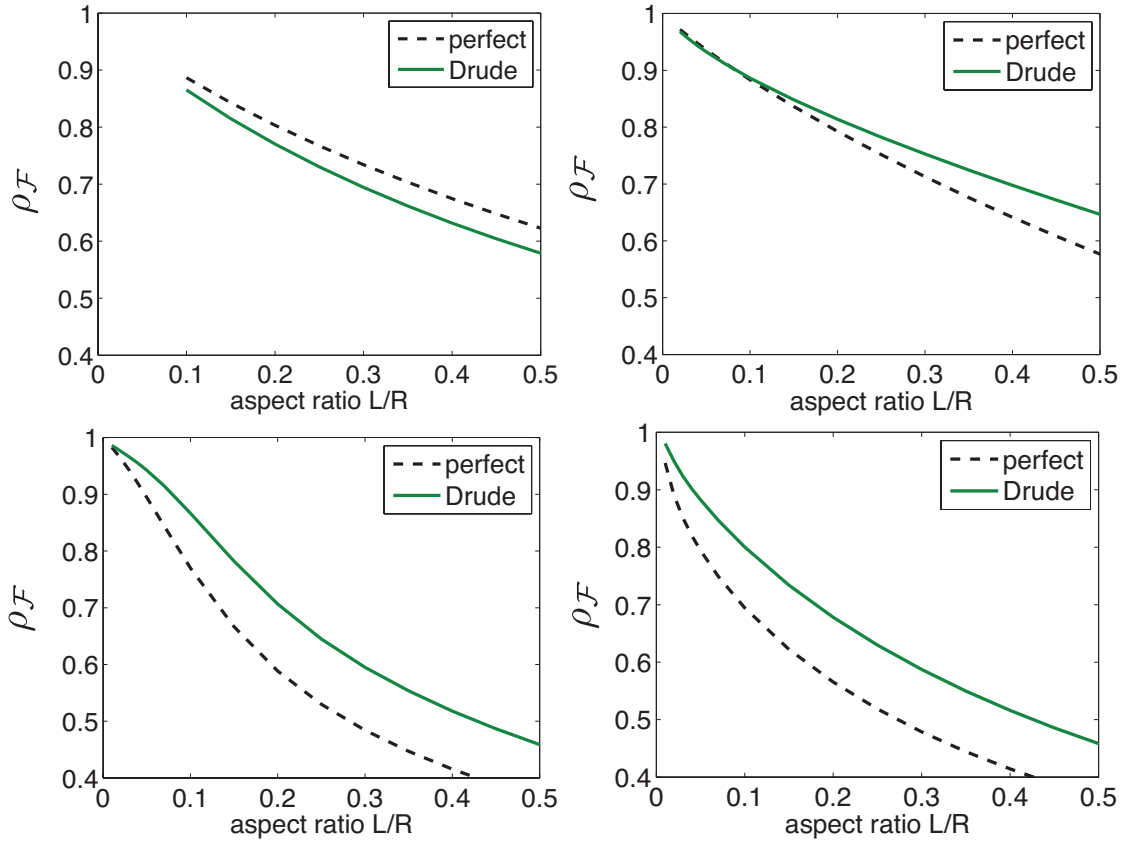

Figure 77: Beyond-PFA correction factor for the Casimir free-energy $\rho_{\mathcal{F}} = \frac{\mathcal{F}}{\mathcal{F}^{\mathrm{PFA}}}$ with respect to the aspect ratio $\frac{L}{R}$, at ambient temperature ($T = 300$ K). The sphere radii are 0.1 μm (upper left graph), 1 μm (upper right graph), 10 μm (lower left graph), and 100 μm (lower right graph). Black dashed-lines represent perfect mirrors, green solid curves are the results of computations with the Drude model. The plasma wavelength is $\lambda_P = 136$ nm, the dissipation ratio $\delta = \frac{\lambda_P}{\lambda_\gamma}$ is 0.004.

The upper left graph ($R = 0.1\ \mu$m) contains the smallest distances considered, from $L = 10$ nm to 50 nm. In this case the separation is so short that temperature does not play a role, and $\rho_{\mathcal{F}}^{\mathrm{Drud}}$ lies below $\rho_{\mathcal{F}}^{\mathrm{perf}}$, as expected. For a micrometer radius sphere (upper right graph), the distance varies from 20 nm to 500 nm. Temperature begins to play a role in the Casimir effect for Drude materials, and a crossing between the two curves occurs. For larger distances ($L \geq 0.5\ \mu$m) in the two lower graphs ($R = 1, 10\mu$m), we obtain the predicted thermal regime with $\rho_{\mathcal{F}}^{\mathrm{Drud}} \geq \rho_{\mathcal{F}}^{\mathrm{perf}}$.

14.4.2 Influence of temperature on the beyond-PFA corrections for Drude mirrors

In the case of perfect mirrors illustrated in **Fig. 67** (p.181), we observed that the relation $\rho_{\mathcal{F}}^{\rm perf}(T) \leq \rho_{\mathcal{F}}^{\rm perf}(T=0)$ is always fulfilled. It is related to the fact that PFA always overestimates the magnitude of the Casimir energy at zero temperature, and always overestimates the contribution of thermal photons to the Casimir free-energy between perfect mirrors. When the temperature increases, the curves for $\rho_{\mathcal{F}}^{\rm perf}(T)$ as a function of the aspect ratio $\frac{L}{R}$ decrease, until they reach a saturated high-temperature regime.

In **Section 14.3.2** (p.190), we predicted two different regimes for the comparison of $\rho_{\mathcal{F}}^{\rm Drud}(T)$ and $\rho_{\mathcal{F}}^{\rm Drud}(T=0)$ for Drude metals: when the separation is small ($L \lesssim 1$ μm), we should obtain $\rho_{\mathcal{F}}^{\rm Drud}(T) \geq \rho_{\mathcal{F}}^{\rm Drud}(T=0)$. When the distance increases, the finite conductivity has less influence as this distance range is dominated by the low frequency behaviour, and a second regime appears, where the relation gets reversed to the perfect reflecting result: $\rho_{\mathcal{F}}^{\rm Drud}(T) \leq \rho_{\mathcal{F}}^{\rm Drud}(T=0)$.

Again, these predictions are confirmed by the numerical evaluations presented in **Fig. 78** for the beyond-PFA correction factor for the free-energy $\rho_{\mathcal{F}}$, using Drude model to describe the optical properties of the materials, with respect to the distance L, for four different sizes of the sphere ($R = 0.1, 1, 10, 100$ μm). The results at zero temperature (blue curve), at ambient temperature (red curve) and at the limit of infinite temperature (purple dotted-line), are compared. The last curve comes from the analytical expansion at the low-frequency limit, obtained in **Section 7.6** (p.117), and is R-independent.

Like in the previous section, we analyze **Fig. 78** with an increasing distance, beginning from the upper left graph where $R = 0.1$ μm and finishing with the lower right graph for $R = 100$ μm. At very short distances (upper left graph), the temperature only has a very small influence, thus the curve for the beyond-PFA factor at ambient temperature is close to the one for zero temperature. However, the former lies already slightly above the latter. For distances between 20 and 500 nm (upper right graph), the relation $\rho_{\mathcal{F}}^{\rm Drud}(T) \geq \rho_{\mathcal{F}}^{\rm Drud}(T=0)$ predicted for the short-distance regime is also clearly fulfilled (red curve above blue one). When the distance reaches the micrometer (lower left graph), the two curves cross each other, and the second regime ($\rho_{\mathcal{F}}^{\rm Drud}(T) \leq \rho_{\mathcal{F}}^{\rm Drud}(T=0)$) is entered. For larger distances (lower right graph, $L \geq 2$ μm), the thermal fluctuations play a dominant role and the high-temperature limit (purple dotted-line) is progressively reached.

In any studied range of parameters for the distance L and the radius R, we always observe with Drude model that the beyond-PFA factor for the free-energy is greater or equal to the one for very high-temperatures. Moreover, for sufficiently long distances $L \gtrsim 2$ μm at ambient temperature, the two curves superimpose. As a consequence, this high-temperature limit, easier to compute, can give a good hint of the beyond-PFA correction factor for sufficiently large separations, and can give a maximum of the error made by PFA at shorter distances. This high-temperature limit will be studied in more details in **Section 15** both for perfect and Drude mirrors.

14.5 Power laws

For completeness, we give in **Fig. 79** the logarithmic slopes ν that describe the dependance of the Casimir free-energy on the parameters L for the complete treatment with Drude model for the mirrors, at ambient temperature. The curves are quite similar to the one for perfect mirrors obtained in **Fig 60** (p.174) at large distances, but the parameter ν goes to 1 at short separations, as expected because of the finite conductivity. This curves illustrate the statement that the Casimir free-energy depends on the radius of the sphere in a non-trivial way.

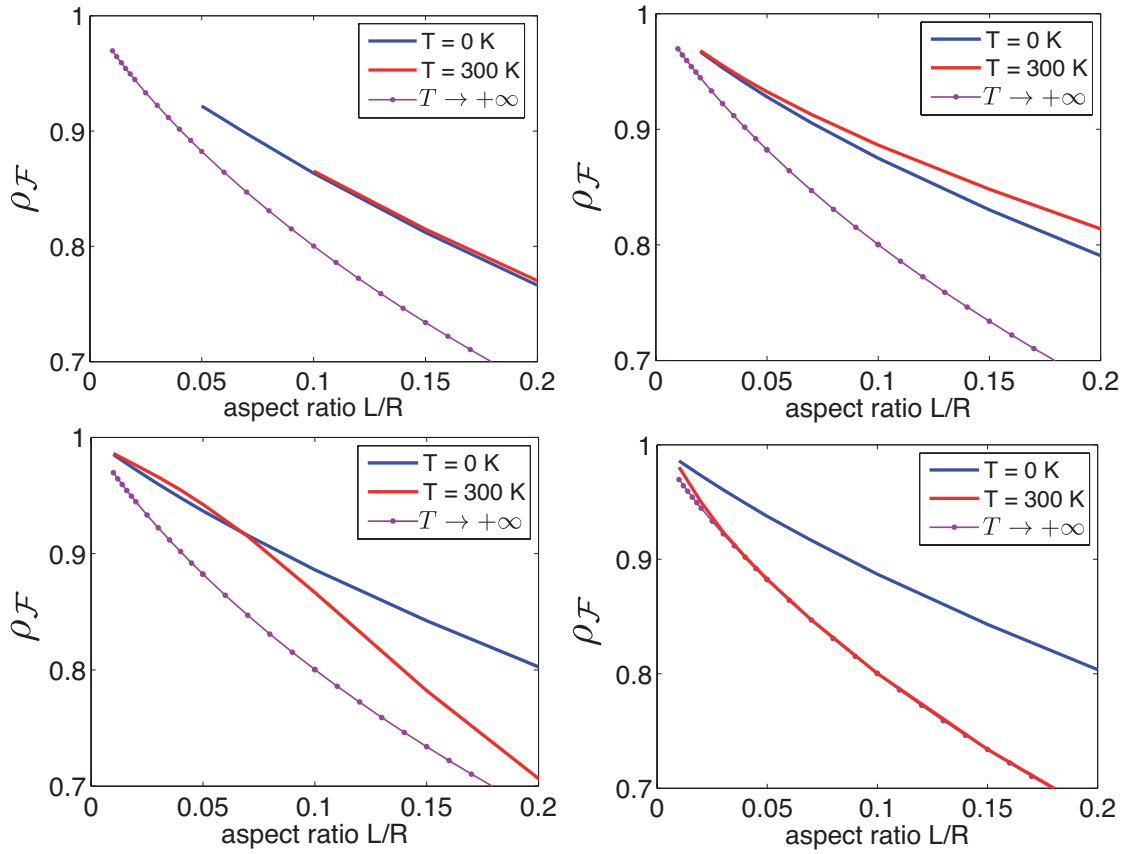

Figure 78: Beyond-PFA correction factor for the Casimir free-energy with mirrors described by the Drude model $\rho_{\mathcal{F}}^{\mathrm{Drud}} = \frac{\mathcal{F}^{\mathrm{Drud}}}{\mathcal{F}_{\mathrm{PFA}}^{\mathrm{Drud}}}$ with respect to the aspect ratio $\frac{L}{R}$. The sphere radii are 0.1 μm (upper left graph), 1 μm (upper right graph), 10 μm (lower left graph), and 100 μm (lower right graph). Blue curves represent zero temperature, red curves ambient temperature ($T = 300$ K) and purple dotted-lines are the high-temperature limit. The plasma wavelength is $\lambda_P = 136$nm, the dissipation ratio $\delta = \frac{\lambda_P}{\lambda_\gamma}$ is 0.004.

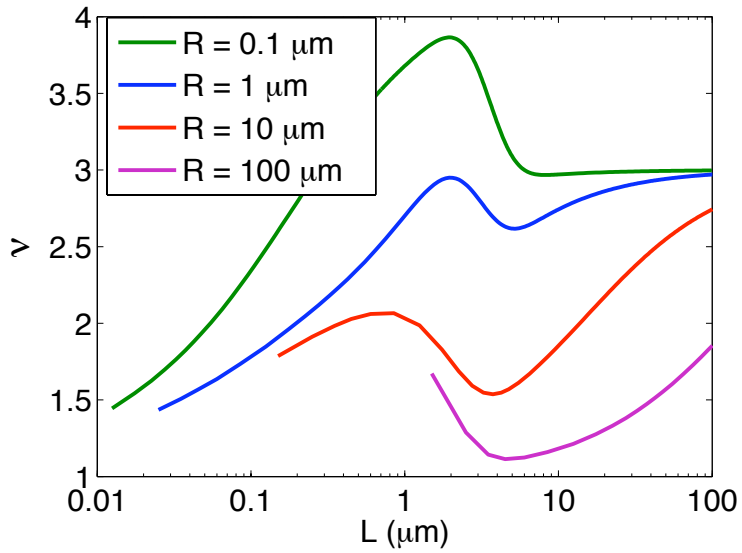

Figure 79: Logarithmic slope ν as a function of the distance L. The green curve represents the case of a small sphere, the blue curves an intermediate sphere, and red and purple curves the case of larger spheres. Ambient temperature is $T = 300K$. The plasma wavelength is $\lambda_P = 136$ nm, the dissipation ratio $\delta = \frac{\lambda_P}{\lambda_\gamma}$ is 0.004.

15 High-temperature regime

In this section we investigate the high-temperature limit ($L \gg \lambda_T$) of the Casimir free-energy $\mathcal{F}^{\rm HT}$ in the sphere-plane geometry. As discussed in Eq.(3.6) (p.49), in this limit the scattering formula reduces to a function of the scattering operator at zero frequency:

$$\mathcal{F}^{\rm HT} = \frac{k_B T}{2} \ln\det \mathcal{D}(0) \ .$$

Explicit expressions for the high-temperature have been analytically derived in **Section 7** (p.108), for perfect mirrors, metallic mirrors described by the Drude model, and dielectrics. Those expressions are functions of the aspect ratio $\frac{L}{R}$, and neither depend on the sphere radius R, nor on the parameters for the description of the reflection, except for the zero-frequency permittivity $\varepsilon(0)$ in the case of dielectric mirrors.

Moreover, these high-temperature expansions are easily computable, as they only involve the computation of a determinant whose elements are made of factorials, and their evaluation can be stabilised by a method given in **Section 6.7** (p.104). It follows that the numerical evaluation in this limit is manageable with the inclusion of more spherical modes than for the general free-energy $\mathcal{F}$, allowing for smaller aspect ratios $\frac{L}{R}$. In the present section we present numerical results for a cut-off $\ell_{\rm max}$ up to 5000, allowing to compute the high-temperature limit of the Casimir free-energy for aspect ratios $\frac{L}{R} \geq 0.001$, but higher values seem to be computable as well.

The first motivation for this study is theoretical, as zero-frequency limit is fundamentally connected to the geometry, because low-frequency modes are spread over the whole system. In this limit we should then see features specific to the sphere-plane geometry. Second, we have observed in **Section 14.4.2** (p.196) that the error made by PFA in the high-temperature limit acts as an upper bound for the usual Casimir free-energy between mirrors modelled by the Drude model for any temperature. As the numerical calculations can be pushed much farther than in the usual case, we can gain information on the magnitude of beyond-PFA corrections for very small values of the aspect ratio $\frac{L}{R}$.

We first consider the idealistic case of perfect mirrors in **Section 15.1** before moving on to more realistic description of the material, with dissipative metals described by the Drude model in **Section 15.2**. We conclude with the comparison of perfectly reflecting mirrors and metals with Drude model in **Section 15.3**.

15.1 Perfect mirrors

For two perfectly reflecting planes the high-temperature limit of the Casimir free-energy is given by Eq.(3.11) (p.51) and corresponds to the following expression for the high-temperature limit of the Casimir free-energy in the sphere-plane configuration within PFA:

$$\mathcal{F}^{\rm perf}_{\rm PFA}(T \to \infty) = -\frac{\zeta(3) k_B T R}{4L} \tag{15.1}$$

We now compare this result with the high-temperature limit from the scattering formalism $\mathcal{F}^{\rm perf} = \frac{k_B T}{2} \Phi^{\rm perf}(0)$ given by Eq.(7.34) (p.119). Although not explicit, this analytical limit only involves the computation of a determinant from a relatively simple matrix, and the numerics can be brought further than for the usual case.

In the left graph of **Fig. 80** we present the results of numerical evaluations for the high-temperature limit of the Casimir free-energy, normalized by the PFA result (15.1), to get the parameter $\rho^{\rm perf}_{\mathcal{F}}$. The smallest aspect ratio $\frac{L}{R} = 0.001$ is computed with $\ell_{\rm max} = 5000$.

The function $\rho^{\rm perf}_{\mathcal{F}}(L/R)$ built from numerical evaluations at high temperature is always smaller than 1, like the cases of zero or finite temperature. It goes to unity at very small separations, as

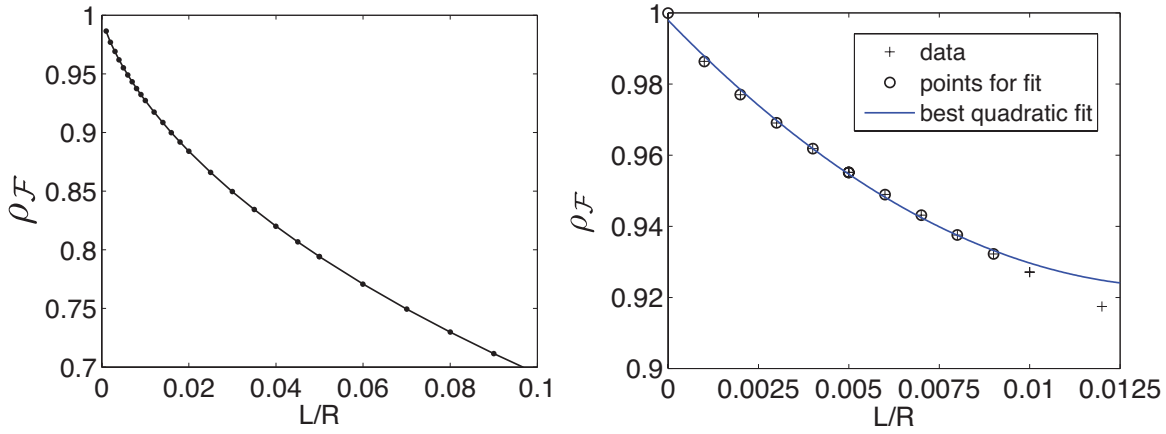

Figure 80: (left) High temperature limit for the Casimir free-energy with perfect mirrors, given by Eq.(7.34) (p.119), divided by the PFA result (15.1). The leftmost point is for an aspect ratio of $\frac{L}{R} = 0.001$, computed with $\ell_{\max} = 5000$. (right) Attempt to fit the data for $\rho_{\mathcal{F}}^{\text{perf}}$ with a quadratic fit. The best quadratic fit is the polynomial $y = 367x^2 - 10.5x + 0.998$.

expected, then decreases when the aspect ratio $\frac{L}{R}$ increases. When trying to fit those data in order to extrapolate the function to smaller values of the aspect ratio, one meets some difficulties, as second, third or fourth order polynomials fail at representing correctly the shape of the curve in the range of computed data. This is illustrated in the right graph of **Fig. 80**, where an attempt is made to fit the data for $\frac{L}{R} \in [0.001, 0.009]$ with a quadratic fit. The data points then oscillate vertically around the best fitting quadratic polynomial $y = 367x^2 - 10.5x + 0.998$, meaning that the nature of the curve is somewhat different from a polynomial.

We therefore propose a particular form of fitting functions, containing logarithmic terms, inspired by works done analytically for the sphere-plane geometry at zero temperature with an electromagnetic field [164], or with scalar fields in the cylinder-plane geometry [253]. To do so, we choose forms like in [164] by multiplying the linear correction term with a polynomial of logarithms. Hence we look for fitting functions of the form:

$$f(x) = 1 + x\left(a + b\ln x + c\,(\ln x)^2 + \dots\right) + o\,(x) \quad . \tag{15.2}$$

From this form, it is possible to construct a function $g(\ln x)$ better adapted for the fitting process, as it is a polynomial function:

$$g(y) = \frac{f(x) - 1}{x} = a + by + cy^2 + \cdots \quad \text{with} \quad y = \ln x \ .$$

The quantity $\frac{\rho(L/R)-1}{L/R}$, extracted from the numerically computed values of ρ, is presented in **Fig. 81** with respect to $\ln \frac{L}{R}$ for the case of perfect mirrors at high-temperatures, and looks much like a parabola.

This quantity turns out to be very well fitted with a second order polynomial whose coefficients (a, b, c) depend on the data points one chooses to fit. If one fits the data for $\frac{L}{R} \in [0.001, 0.1]$, the best quadratic fit is $g_1(y) = -0.932 + 0.471y - 0.197y^2$. For a more restricted range of $\frac{L}{R} \in [0.001, 0.01]$, the best quadratic fit is $g_2(y) = -1.22 + 0.362y - 0.207y^2$. For instance with the former choice g_1, the final fitting function $f_1(x)$ that represents the best extrapolation to smaller values of the aspect ratio $\frac{L}{R}$ will be:

$$f_1\left(\frac{L}{R}\right) = 1 + \frac{L}{R}\left[-0.932 + 0.471\ln\left(\frac{L}{R}\right) - 0.197\left(\ln\left(\frac{L}{R}\right)\right)^2\right] \tag{15.3}$$

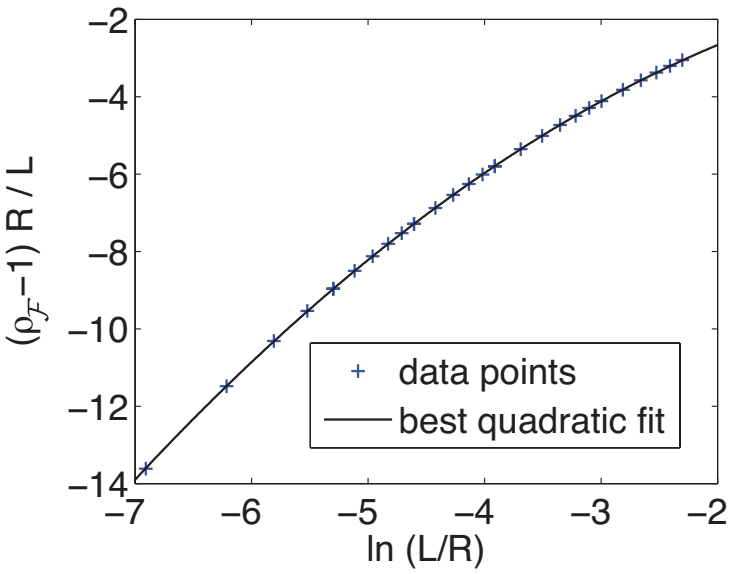

Figure 81: Function $g(L/R) = \frac{\rho_{\mathcal{F}}^{\rm perf}(L/R)-1}{L/R}$ with respect to $\ln(L/R)$, with $\rho_{\mathcal{F}}^{\rm perf} = \frac{\mathcal{F}^{\rm perf}}{\mathcal{F}_{\rm PFA}^{\rm perf}}$ numerically computed in the high-temperature limit for perfect mirrors. The best quadratic fit is $g(y) = -0.932 + 0.471y - 0.197y^2$. The leftmost point corresponds to $\frac{L}{R} = 0.001$, computed with $\ell_{\rm max} = 5000$, the rightmost point to $\frac{L}{R} = 0.1$.

The important coefficient for the extrapolation to smaller values of the aspect ratio is the third one, called c in **Eq. (15.2)**, as it is contained in the leading term $x\,(\ln x)^2$ of $f(x)$ when $x \to 0$. Fortunately this coefficient does not depend much on the choice of the data points for the fit ($c_1 \simeq c_2$) and is close to the value -0.2. We remark that the coefficient c is strictly negative, entailing that for high-temperature limit the curve is going down vertically at the origin, unlike the result of the zero-temperature derivation made in [164], where the curve was first going up because of a leading term in $x\,(\ln x)^2$ with a positive coefficient $c = 8.5 \times 10^{-6}$. This also explains why the polynomial fit in **Fig. 80** was systematically hitting a value smaller than unity at the limit $\frac{L}{R} \to 0$.

In **Fig. 82** we show that a nice fit is now obtained for the function $f_1(x) = 1 + xg_1(y)$ over a wide range of values for the aspect ratio $\frac{L}{R}$. The agreement is much better than with polynomial fitting functions. The change of the form of the curve has a great influence on the accuracy of PFA results at very small separation, as presented in **Table 14**. Formally, the first order correction factor $\beta_{\mathcal{F}} = \rho^{'}(0)$ is infinite. For computed data, for $\frac{L}{R} \in [0.001, 0.1]$, it remains of the order of magnitude of what was obtained with a polynomial fit without logarithms. For even smaller values of the aspect ratio, the slope diverges to $-\infty$.

$\frac{L}{R}$	10^{-1}	10^{-2}	10^{-3}	10^{-4}	10^{-5}	10^{-6}
$\rho\left(\frac{L}{R}\right)$	0.69	0.93	0.986	0.998	0.9997	0.99996
$\rho^{'}\left(\frac{L}{R}\right)$	-1.68	-5	-10.4	-17.9	-27.5	-39.2

Table 14: Value of the fit for the beyond-PFA correction factor ρ and its slope, in the high-temperature limit for perfect mirrors, with respect to the aspect ratio $\frac{L}{R}$.

In conclusion, the beyond-PFA study of the Casimir effect for perfect mirrors at the limit of high temperatures shows a situation where a Taylor expansion of the function $\rho\left(\frac{L}{R}\right)$ at small

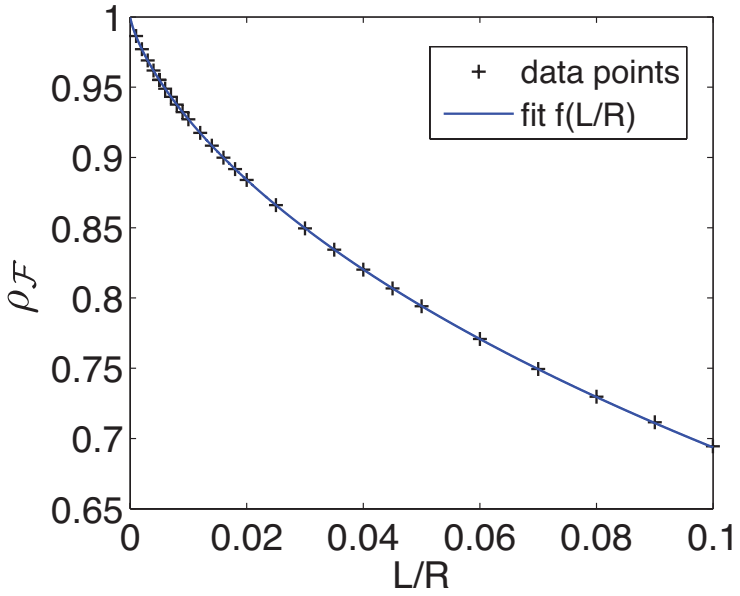

Figure 82: Comparison for the function $\rho_{\mathcal{F}}^{\text{perf}}$ in the high-temperature limit between the numerically computed data points (black crosses) and the constructed fitting function (solid blue curve) $f_1\left(\frac{L}{R}\right) = 1 + \frac{L}{R}\left(-0.932 + 0.471\ln\left(\frac{L}{R}\right) - 0.197\left(\ln\left(\frac{L}{R}\right)\right)^2\right)$.

values of $\frac{L}{R}$ seems not to be valid anymore. This observation is in agreement with the analytical study [164], carried out at zero temperature. However, we emphasize that the perfect reflector model is not realistic for the optical response of real materials, especially when one considers the short-distance regime. In the next section, we follow the same path using a realistic model of reflection for dissipative metals.

15.2 Drude model for metallic mirrors

For a dissipative metal using the Drude model for the dielectric function, the high-temperature regime in the plane-plane geometry is divided by 2 with respect to the perfectly reflecting case. This means that the PFA result is in this case half of (15.1) and reads:

$$\mathcal{F}_{\text{PFA}}^{\text{Drud}}(T \to \infty) = -\frac{\zeta(3) k_B T R}{8L} \tag{15.4}$$

Let us now compare this PFA result with the corresponding high-temperature limit from the scattering formalism $\mathcal{F}^{\text{Drud}} = \frac{k_B T}{2}\Phi^{\text{Drud}}(0)$ given by Eq.(7.36) (p.119), as in the previous section for perfectly reflecting mirrors. In the left graph of **Fig. 84** we present the results of numerical evaluations for the high-temperature limit of the Casimir free-energy, normalized by the PFA result (15.4), to get the parameter $\rho_{\mathcal{F}}^{\text{Drud}}$. The smallest aspect ratio $\frac{L}{R} = 0.001$ is computed with $\ell_{\max} = 5000$.

In the case of reflectors described by the Drude model, the curve $\rho_{\mathcal{F}}^{\text{Drud}}\left(\frac{L}{R}\right)$ in the high-temperature limit is again decreasing when the aspect ratio increases, with values reaching 1 when the distance goes to 0. The shape of the curve is however somewhat different, as it is more straight and less incurved that the one presented for perfect mirrors in the left graph of **Fig. 80**.

Unlike the perfectly reflecting case studied in the previous section, polynomial functions fit well the data, and it does not seem necessary to assume more complex forms to fit them better. Furthermore, the introduction of a function containing logarithms such as presented in (15.2) is

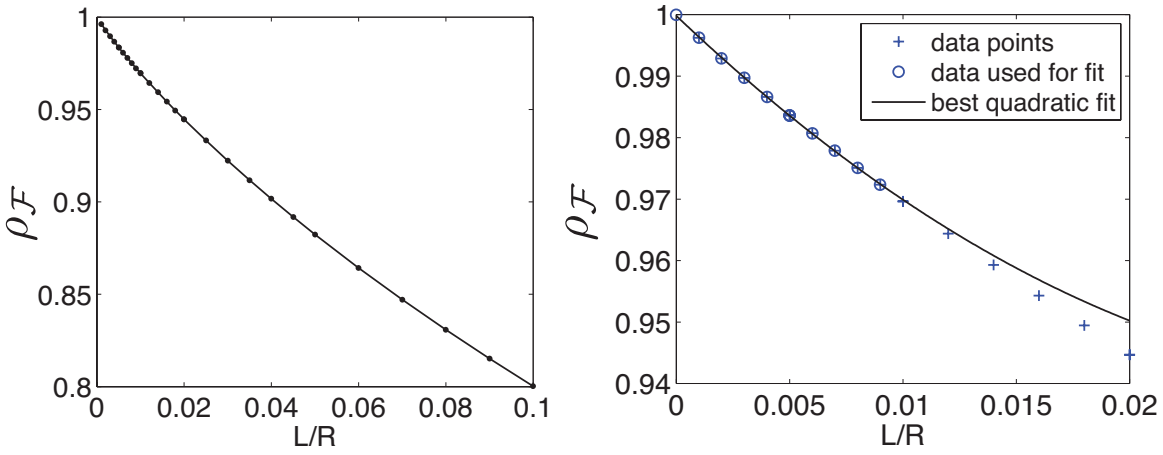

Figure 83: (left) High temperature limit for the Casimir free-energy with mirrors described by the Drude model, given by Eq.(7.36), divided by the PFA result (15.4). The leftmost point is for an aspect ratio of $\frac{L}{R} = 0.001$, computed with $\ell_{\max} = 5000$. (right) Attempt to fit the data for $\rho_{\mathcal{F}}^{\mathrm{Drud}}$ with a quadratic fit. The best quadratic fit is the polynomial $y = 51.2x^2 - 3.5x + 1$.

even less efficient, as the function $g(L/R)$ derived from the data points does not look like a simple polynomial.

In conclusion, this study shows that the accuracy of PFA with Drude-modeled mirrors in the high-temperature limit can be assessed with the help of the beyond-PFA first order correction term $\beta_{\mathcal{F}}^{\mathrm{HT,Drud}} \simeq -3.5$. This result is also useful for the general case of a finite temperature T, as the high-temperature regime give a upper limit on the magnitude of the error made by PFA calculations, and we here deduce that:

$$\left|\beta_{\mathcal{F}}^{\mathrm{Drud}}\left(\frac{L}{\lambda_T}, \frac{L}{\lambda_P}, \frac{L}{\lambda_\gamma}\right)\right| \leq \left|\beta_{\mathcal{F}}^{\mathrm{HT,Drud}}\right| \simeq 3.5 \ .$$

Consequences of these results for the comparison with theory of Casimir measurements will be discussed in the conclusion.

15.3 Ratio of perfect mirrors result over Drude metals result

It the plane-plane geometry, it has been shown that the high-temperature limit of the Casimir free-energy, or equivalently the zero frequency contribution to the finite temperature free-energy, is twice bigger for a perfect mirror than for a dissipative metal, such as described by the Drude model. The same variation of 2 of the high-temperature limit of the Casimir free-energy between perfect and Drude mirrors should be found in the sphere-plane geometry when computed within PFA, and it must thus be verified also by the exact result at the short-distance limit ($L \ll R$).

In the large distance regime ($L \gg R$) however, this high-temperature ratio has been shown to be $\frac{3}{2}$ in **Section 8.4** (p.132). It is then worth studying how this ratio varies from one value to the other when the aspect ratio $\frac{L}{R}$ changes. This shift of the ratio from 2 to $\frac{3}{2}$ is presented in **Fig. 84**.

The left graph shows the ratio of the zero-frequency limits for the integrand $\Phi\left(\tilde{\xi}\right)$ of perfectly reflecting and Drude-modeled mirrors, for a range of aspect ratios $\frac{L}{R}$ that runs from 0.001 to 100 with a logarithmic scale. As expected, the ratio 2 is approached in the short-distance limit, and the long-distance limit goes to $\frac{3}{2}$. The shift is progressive and monotonic, centered at $L \sim 0.1R$. While the value $\frac{3}{2}$ is already approached (1.501) for $L \gtrsim 10R$, the leftmost computed point at

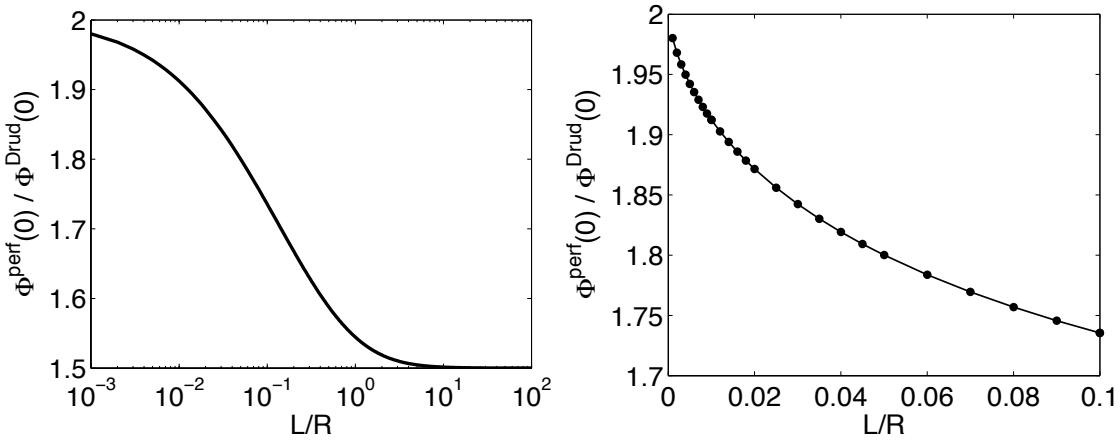

Figure 84: Ratio of the first Matsubara term $\Phi(0)$ for perfect mirrors and dissipative metals described by a Drude model, with respect to the aspect ratio $\frac{L}{R}$. The left graph uses a logarithmic scale for the abscissa, showing the complete shift of the ratio from 2 to $\frac{3}{2}$, while the right graph uses a linear scale to focus on short-distance regime.

$L = 0.001R$ lies still outside (1.98) the value expected from the plane-plane case. It means that the intermediate region exists even for a sphere very close to the plane.

The right graph focusses on the short-separation domain, with a linear scale on the aspect ratio $\frac{L}{R}$. We observe that the ratio of the high-temperature limits is far from its short-distance limit, even for $\frac{L}{R} < 0.1$. However, the curve is reaching 2 when the aspect ratio decreases in a regular manner, quite suitable to build an extrapolation function for smaller values of $\frac{L}{R}$.

Like in the discussion of the beyond-PFA correction for perfect mirrors in the high-temperature limit in **Section 15.1** (p.199), it does not seem efficient to attempt to fit the obtained data for small values of $\frac{L}{R}$ with a polynomial function. Again, we can use functions containing logarithmic terms as in Eq.(15.2 (p.200). If one fits the data for $\frac{L}{R} \in [0.001, 0.1]$, the best quadratic fit is $g_1(x) = -1.46 - 0.539 \ln x - 0.462(\ln x)^2$. For a more restricted range of $\frac{L}{R} \in [0.001, 0.01]$, the best quadratic fit is $g_2(x) = -1.51 - 0.566 \ln x - 0.465(\ln x)^2$. For this last choice, the final fitting function that represents the best extrapolation to smaller values of the aspect ratio $\frac{L}{R}$ is:

$$f\left(\frac{L}{R}\right) = 2 - \frac{L}{R}\left[1.51 + 0.566 \ln\left(\frac{L}{R}\right) + 0.465\left(\ln\left(\frac{L}{R}\right)\right)^2\right] . \tag{15.5}$$

The important coefficient for the extrapolation to smaller values of the aspect ratio is the third one, called c in Eq.(15.2, as it is contained in the leading term $x\,(\ln x)^2$ of $f(x)$ when $x \to 0$. This coefficient does not depend much on the choice of the data points for the fit ($c_1 \simeq c_2$) and is close to the value -0.46.

The presence of logarithms in the fitting function for the ratio between the high temperature limits for perfect mirrors and metals modelled by the Drude model comes directly from the shape of the curve $\rho_{\mathcal{F}}^{\mathrm{perf}}$, which already contained logarithmic terms. The infinite slope at the short distance limit, yields that the ratio 2, between an ideal description for reflection and a realistic one for metals at high-temperature, must be used with great care. As discussed above, an aspect ratio of $\frac{L}{R} = 0.001$ changes already this ratio by one percent.

The shift from 2 to $\frac{3}{2}$ of ratio between the two opposite limits in the aspect ratio $\frac{L}{R}$ can be described from the point of view of the term $\frac{\ell_1}{\ell_1+1}$, which is present in the expression (7.32) (p.118) for the operator $\mathbb{D}^{(m)}_{b,\mathrm{TE}}(\tilde{\mathcal{L}})$, and not in the expression (7.30) (p.117) for the operator $\mathbb{D}^{(m)}_{a,\mathrm{TM}}(\tilde{\mathcal{L}})$. Let us recall that the zero-frequency limit of the integrand $\Phi(\tilde{\xi})$ involves the determinant of two

matrices in the perfectly reflecting case, and only one in the case of the Drude model:

$$\mathcal{F}_{\rm HT}^{\rm perf} = k_B T \sum_m{}' \left[\ln\det \mathbb{D}^{(m)}_{a,{\rm TM}}(\tilde{\mathcal{L}}) + \ln\det \mathbb{D}^{(m)}_{b,{\rm TE}}(\tilde{\mathcal{L}}) \right] \tag{15.6}$$

$$\mathcal{F}_{\rm HT}^{\rm Drud} = k_B T \sum_m{}' \ln\det \mathbb{D}^{(m)}_{a,{\rm TM}}(\tilde{\mathcal{L}}) \ . \tag{15.7}$$

For the long-distance limit ($L \gg R$), one only keeps the ($\ell = 1$)-terms, the other being negligeable. In this case, the factor is $\frac{\ell_1}{\ell_1+1} = \frac{1}{2}$. As the terms in the operators $\mathbb{D}^{(m)}_{a,{\rm TM}}$ and $\mathbb{D}^{(m)}_{b,{\rm TE}}$ are small, one has: $\ln\det \mathbb{D}^{(m)}_{b,{\rm TE}} = \frac{1}{2} \ln\det \mathbb{D}^{(m)}_{a,{\rm TM}}$ and thus $\mathcal{F}_{\rm HT}^{\rm perf}$ is $\frac{3}{2}$ times bigger than $\mathcal{F}_{\rm HT}^{\rm Drud}$.

In contrast, when $\frac{L}{R}$ decreases, modes with more and more values of ℓ contribute to the Casimir energy. The contribution of modes ℓ with $\ell \not\gg 1$ becomes negligible when $\frac{L}{R}$ goes to 0, and for large values $\ell_1 \gg 1$, the factor $\frac{\ell_1}{\ell_1+1}$ goes to unity. Then the operators $\mathbb{D}^{(m)}_{a,{\rm TM}}$ and $\mathbb{D}^{(m)}_{b,{\rm TE}}$ tend to be the same, and $\mathcal{F}_{\rm HT}^{\rm perf}$ is asymptotically twice larger than $\mathcal{F}_{\rm HT}^{\rm Drud}$.

Conclusion and outlook

As discussed in the introduction, the recent improvements of the accuracy in the Casimir force measurements open up the possibility of a precise comparison with theoretical predictions. These recent experiments use the configuration of a sphere in front of a plane to elude the difficulty of maintaining two plates parallel during the measurements. The theoretical predictions used for this comparison are usually evaluated with the help of the Proximity-Force Approximation (PFA), and have led to controversies on the model of reflection for metals, and on the thermal effects. A reliable study of this sphere-plane geometry was thus a first necessity to dismiss a possible unsuitability of PFA method in this case, and to assess the accuracy of this approximation in the experimental range of the parameters.

The interest of the investigation of the sphere-plane geometry is also theoretical, for the reason that we will now explain. The Casimir effect has a fundamental spectral character, that is highlighted by the scattering formula:

$$E = \frac{\hbar}{2\pi} \int_0^\infty \mathrm{d}\xi \ln\det \mathcal{D}(\imath\xi)$$

where $\mathcal{D}$ is an operator containing all information on the geometry and on the materials optical properties. As a consequence, the Casimir effect has been shown to depend in a non-trivial way on the geometry, as evoked in the introduction. One of the most fascinating and promising field of manifestation for this rich dependence on the geometry are the nanostructured materials, such as gratings [184, 185, 186, 187]. In this prospect, the sphere-plane configuration offers a simple situation where the effects of finite size, curvature, non-specular scattering and coupling of the electromagnetic polarizations can be investigated.

In this manuscript we explored the Casimir interaction between a sphere and an infinite plane, with the inclusion of temperature and of realistic optical model for the materials. The evaluation of the Casimir interactions, necessary for this study, could be achieved with the general scattering approach, which connects the Casimir effect to the scattering operators of the objets.

In this particular configuration, the bases of planar and spherical electromagnetic modes are well-adapted to express the scattering process. The use of those two sets of modes requires transformation operations between them, which can be expressed from simple quantities, easy to compute numerically. Although the multipolar nature of the scattering method is better adapted to intermediate and large values of the aspect ratio $\frac{L}{R}$, the numerical code can be pushed to include a large number of spherical modes, which allows for computations of the Casimir free-energy in configurations with $\frac{L}{R}$ as small[17] as 0.01.

While the PFA quantities give the dominant term to the Casimir interaction at the short-distance limit ($L \ll R$), it is possible to derive analytically the dominant term in the long-distance limit ($L \gg R$) from the scattering formula. The numerical evaluation with several multipoles is necessary to describe accurately the intermediate region ($L \sim R$), and the two limiting cases are recovered. The long-distance analytical expressions exhibit a clear dependance on the model of reflection for the materials, which shows that the perfect mirrors results are not in general recovered from results with metals in the long-distance limit, a feature that was not generated by the specular plane-plane cavity.

At zero temperature, we observed correlations between the effect of geometry and finite conductivity. This interplay implies that the first order coefficient β of the beyond-PFA correction factor

[17] To have a more pictoral idea of this number in our scale, this aspect ratio is equivalently obtained with a football sitting 1 mm away from a table.

ρ is considerably modified when using metallic models of reflection for the objects, with respect to the perfectly reflecting model. As a consequence, the seeming contradiction between former theoretical evaluations of this parameter β and the experimental prescription is no more present when accounting for finite conductivity in the material. Another consequence of this interplay is the long-distance limit of the finite conductivity correction factor η^P for metals, which does not go to 1 like in the plane-plane configuration, but rather to the value $\frac{2}{3}$ for mirrors modelled by the dissipative Drude model, and to a value between $\frac{2}{3}$ and 1 for mirrors described with the lossless plasma model.

For perfectly reflecting sphere and plane at non-zero temperatures, the Casimir free-energy has a rich dependence on the temperature, due to a non-trivial interplay between the effects of geometry and temperature. It results in a delayed increase of the free-energy when the temperature increases with respect to the plane-plane configuration. For small spheres it even leads to a decrease of the free-energy for small temperatures, which yields a repulsive contribution of the thermal photons to the Casimir force, a decrease of the total Casimir attractive force, and negative values for the Casimir entropy. Those findings are corroborated by the analytical expressions derived in the long-distance regime, and are not related to the dissipation in the materials, but rather to geometry itself.

The study of the complete picture, at ambient temperature with the sphere and the plane described as imperfect reflectors, presents a rich landscape of parameters and has been systematically investigated. The temperature dependance of the Casimir effect is modified by the different models for the materials, and similarly, the effects of finite conductivity on the Casimir interaction are different when the temperature is included in the model. We investigated in detail this rich interplay between the effects of finite conductivity, geometry and temperature. The inclusion of dissipation in the material is also a source of correlations, which gives as in the zero-temperature case a result qualitatively different from the parallel-plate geometry in the long-distance regime. As a consequence, the quantities derived with the lossless plasma and full Drude models are closer to each other than in the parallel-plate geometry, with the long-distance ratio of 2 reduced to at most $\frac{3}{2}$.

The high-temperature regime is obtained, through the Matsubara formula, with the low-frequency limit of the scattering formula. The analytically obtained leading order has a simpler expression, which allows for numerical evaluations with a much higher number of modes included. We presented results for aspect ratios $\frac{L}{R}$ as low as 0.001, computed with $\ell_{\max} = 5000$, which enable to see that the beyond-PFA factor for perfect mirrors is in this case better fitted with the inclusion of logarithms in the fit than with simple polynomials, unlike for mirrors modelled by the Drude model. The high-temperature finite conductivity reduction factor for Drude model shifts from 2 at small separations, like in the PFA quantities, to $\frac{3}{2}$ for large distances.

Concerning the comparison between the experimental data and the theoretical predictions, the present study confirmed the validity of the Proximity-Force Approximation (PFA) when used in the limiting case of very small values of the aspect ratio $\frac{L}{R}$. The accuracy of this approximation for a finite value of the aspect ratio remains however a delicate question: as the effects of geometry have an interplay with those of temperature and finite conductivity, this accuracy is very dependant on the relative values of the physical parameters.

The high-temperature regime nevertheless enables us to get an upper bound for the error made by PFA on the Casimir free-energy with mirrors modelled by the Drude model, as illustrated by **Fig. 78** (p.197). The study of this high-temperature regime, carried out in **Section 15.2** (p.202) to very small values of the aspect ratio $\frac{L}{R}$, resulted in an estimated coefficient $\left|\beta_{\mathcal{F}}^{\mathrm{HT,Drud}}\right| \simeq 3.5$ for the first order correction beyond-PFA. This value thus represents an upper bound for the general coefficient $\beta_{\mathcal{F}}^{\mathrm{Drud}}$.

The transformation from the coefficient $\beta_{\mathcal{F}}$ for the free-energy to the one for the force gradient β_G is again dependant on the relative values of the physical parameters, as shown in the zero-temperature case in **Section 11.4** (p.153). In this case, it is possible to give an upper-bound on the coefficient β_G^{Drud}, as the parameters ν_E and ν_F introduced in Eq.(4.16) (p.59) are smaller than 2 and 3, respectively. It follows that the ratio of the two β coefficients is bounded $f_\beta(L) = \frac{\beta_G}{\beta_{\mathcal{F}}} \leq \frac{1}{3}$, and we can give the large upper bound $\left|\beta_G^{\mathrm{HT,Drud}}\right| \lesssim 1.2$.

In the future, an improvement in the comparison between theory and experiments is possible in two directions. The first possibility is a better understanding and a recognition in the theoretical model of other realistic conditions that enters the discussion of the measurements. In this prospect the effects of roughness on the surface [254, 178, 179, 255, 256, 257] and of electrostatic potential patches [258, 259, 260, 261, 262, 110, 263] seem crucial for current experiments and remain to be investigated in details. The other possibility would be to carry out a study similar to the one presented in this manuscript, with a complete treatment of the geometry for the very small values of the aspect ratio met in the experiments.

On the theoretical side, the present study has shown that a complete electromagnetic treatment of the Casimir effect, together with simultaneous considerations of exact geometry, temperature and realistic conditions for the materials, is necessary to obtain a trustful insight into the Casimir interaction on the sphere-plane geometry. This is due to the fact that the effects of geometry, temperature and finite conductivity interact in a non-trivial way, even leading to qualitative differences in many cases. The sphere-plane configuration is thus a good example where fundamental changes of the dependance of the Casimir interaction on physical conditions occur because of the geometry.

Appendix

Table of Contents

A Proofs of lemmas, properties and theorems

A.1 Lemma 1 (p.48)

$$\forall \alpha > 0, \forall \phi \in \mathcal{S}(\mathbb{R}), \forall x \in \mathbb{R}, \quad \sum_{n\in\mathbb{Z}} \phi(x + n\alpha) = \frac{\sqrt{2\pi}}{\alpha} \sum_{m\in\mathbb{Z}} \hat{\phi}\left(2\pi\frac{m}{\alpha}\right) e^{\imath 2\pi \frac{mx}{\alpha}}$$

Proof :

For a $\phi \in \mathcal{S}(\mathbb{R})$, let $\Sigma_N(x) = \sum_{n=-N}^{N} \phi(x - n\alpha)$. As $\phi(x)(1 + x^2)$ is $\mathcal{C}^\infty$ and goes to 0 when $x \to \infty$, it is bounded. Thus $\exists C > 0$ such that $\forall x \in \mathbb{R}, |\phi(x)| \leq \frac{C}{1+x^2}$. It follows that $|\Sigma_N(x)| \leq C \sum_{n=-N}^{N} \frac{1}{1+(x-n\alpha)^2}$ is normally convergent over any compact set, such as $[-\alpha, \alpha]$, to the function $\Sigma(x) = \sum_{n\in\mathbb{Z}} \phi(x - n\alpha)$. As the Σ_N are continuous and normally convergent, Σ is continuous over $[-\alpha, \alpha]$.

Moreover, by its definition, Σ is an α-periodic function, it is thus continuous over $\mathbb{R}$. As $\phi' \in \mathcal{S}(\mathbb{R})$, the same procedure applies to $\Sigma'_N(x) = \sum_{n=-N}^{N} \phi'(x - n\alpha)$ and Σ is then continuously differentiable. From Dirichlet's theorem, the Fourier series of Σ then converges uniformly to $\Sigma(x)$ at any point x.

The discrete Fourier-decomposition of Σ is:

$$\Sigma(x) = \sum_{m\in\mathbb{Z}} c_m(\Sigma) e^{\imath 2\pi \frac{mx}{\alpha}} \quad \text{with} \quad c_m(\Sigma) = \frac{1}{\alpha} \int_0^\alpha \Sigma(x) e^{-\imath 2\pi \frac{mx}{\alpha}} \mathrm{d}x$$
$$= \frac{1}{\alpha} \sum_{n\in\mathbb{Z}} \int_0^\alpha \phi(x - n\alpha) e^{-\imath 2\pi \frac{mx}{\alpha}} \mathrm{d}x$$

where the infinite sum and the integral can be exchanged thanks to normal convergence of the functions Σ_N over the compact interval $[0, \alpha]$. Then the derivation of Fourier coefficients gives, after the change of variable $[y = x - n\alpha]$:

$$c_m(\Sigma) = \frac{1}{\alpha} \sum_{n\in\mathbb{Z}} \int_{-n\alpha}^{(-n+1)\alpha} \phi(y) e^{-\imath 2\pi \frac{my}{\alpha}} e^{\imath 2\pi mn} \mathrm{d}y$$
$$= \frac{\sqrt{2\pi}}{\alpha} \hat{\phi}\left(2\pi\frac{m}{\alpha}\right)$$

Finally, we can rewrite Σ as:

$$\Sigma(x) = \frac{\sqrt{2\pi}}{\alpha} \sum_{m\in\mathbb{Z}} \hat{\phi}\left(2\pi\frac{m}{\alpha}\right) e^{\imath 2\pi \frac{mx}{\alpha}} \ .$$

□

A.2 Lemma 2 (p.48)

The Dirac comb $T = \sqrt{2\pi} \sum_{n\in\mathbb{Z}} \delta(x - n\alpha)$ is in $\mathcal{S}'(\mathbb{R})$ and its inverse Fourier transform is $\mathrm{TF}^{-1}(T) = \frac{2\pi}{\alpha} \sum_{n\in\mathbb{Z}} \delta\left(x - n\frac{2\pi}{\alpha}\right)$.

Proof :

Let us first show that T is a tempered distribution:

$$\begin{aligned}\forall \phi \in \mathcal{S}(\mathbb{R}),\ |<T,\phi>| &= \sqrt{2\pi}\left|\sum_{n\in\mathbb{Z}}\phi(n\alpha)\right| \\ &\leq \sqrt{2\pi}\sum_{n\in\mathbb{Z}}|\phi(n\alpha)|\left(1+(n\alpha)^2\right)\frac{1}{1+(n\alpha)^2} \\ &\leq C\sup_{x\in\mathbb{R}}\left[|\phi(x)|\left(1+x^2\right)\right] \qquad \text{with } C=\sqrt{2\pi}\sum_{n\in\mathbb{Z}}\frac{1}{1+(n\alpha)^2}\ .\end{aligned}$$

We now compute its inverse Fourier transform:

$$\begin{aligned}<T,\phi> &= \sqrt{2\pi}\sum_{n\in\mathbb{Z}}\phi(n\alpha) \\ &= \sqrt{2\pi}\Sigma(0) \\ &= \frac{2\pi}{\alpha}\sum_{m\in\mathbb{Z}}\hat{\phi}\left(2\pi\frac{m}{\alpha}\right) \quad \text{from } \textbf{lemma 1} \text{ (p.48)} \\ &= \left\langle \frac{2\pi}{\alpha}\sum_{m\in\mathbb{Z}}\delta\left(x-2\pi\frac{m}{\alpha}\right),\hat{\phi}\right\rangle\end{aligned}$$

which is the inverse Fourier-transform.

□

A.3 Property 4 (p.48)

- $S_N \longrightarrow \mathrm{TF}^{-1}(T)$.

- The computation of the quantity Q reduces to : $Q = \frac{\hbar}{\alpha}{\sum_n}' \Phi\left(n\frac{2\pi}{\alpha}\right)$, where the primed sum represents a sum over $\mathbb{N}$ with a coefficient $\frac{1}{2}$ for the zeroth term.

Proof :
Let us first compute the Fourier transform of $S_N = \sum_{n=-N}^{N}\cos(n\alpha x)$:

$$\begin{aligned}<\hat{S_N},\phi> &= <S_N,\hat{\phi}> \\ &= \int_{\mathbb{R}}\mathrm{d}k\left(\sum_{n=-N}^{N}\cos(n\alpha k)\right)\hat{\phi}(k) = \int_{\mathbb{R}}\mathrm{d}k\left(\sum_{n=-N}^{N}e^{in\alpha k}\right)\hat{\phi}(k) \\ &= \sum_{n=-N}^{N}\int_{\mathbb{R}}\mathrm{d}k\ e^{in\alpha k}\hat{\phi}(k) = \sqrt{2\pi}\sum_{n=-N}^{N}\phi(n\alpha) \\ &= <T_N,\phi> \quad \text{with } T_N(x)=\sqrt{2\pi}\sum_{n=-N}^{N}\delta\left(x-n\alpha\right)\ .\end{aligned}$$

Then, on the opposite direction :

$$\begin{aligned} < \hat{T_N}, \phi > &= < T_N, \hat{\phi} > \\ &= \sqrt{2\pi} \sum_{n=-N}^{N} \hat{\phi}(n\alpha) = \sum_{n=-N}^{N} \int_{\mathbb{R}} \mathrm{d}x \; e^{-in\alpha x} \phi(x) \\ &= \int_{\mathbb{R}} \mathrm{d}x \left(\sum_{n=-N}^{N} e^{-in\alpha x} \right) \phi(x) = \int_{\mathbb{R}} \mathrm{d}x \left(\sum_{n=-N}^{N} \cos(n\alpha x) \right) \phi(x) \\ &= < S_N, \phi > \end{aligned}$$

such that S_N and T_N are the Fourier transformation of each other : $\hat{S_N} = T_N$ and $\hat{T_N} = S_N$. As T_N represents a finite Dirac comb with N peaks, the series (T_N) converges to the infinite Dirac comb T: for a given $\phi \in \mathcal{S}(\mathbb{R})$, as ϕ is "rapidly decreasing", the series $\sum_{n=-N}^{N} \phi(n\alpha)$ converges to $\sum_{n\in\mathbb{Z}} \phi(n\alpha)$. Thus $T_N \longrightarrow T$ in $\mathcal{S}'(\mathbb{R})$, and by continuity of the Fourier transform, $S_N = \mathrm{TF}^{-1}(T_N) \longrightarrow \mathrm{TF}^{-1}(T)$ derived in **Lemma 2** (p.48). Finally,

$$\begin{aligned} Q_N &= \frac{\hbar}{4\pi} < S_N, \phi > \; \longrightarrow \; Q = \frac{\hbar}{4\pi} < \mathrm{TF}^{-1}(T), \phi > = \frac{\hbar}{2\alpha} \sum_{n\in\mathbb{Z}} \Phi\left(n\frac{2\pi}{\alpha}\right) \\ Q &= \frac{\hbar}{\alpha} \sum_{n}{}' \Phi\left(n\frac{2\pi}{\alpha}\right) \; . \end{aligned}$$

□

A.4 Property 5 (p.75)

When the block-operator $\begin{pmatrix} A & B \\ C & D \end{pmatrix}$ is made of square-blocks of the same size, and A is invertible, the determinant does not change when applying the changes $B \to \alpha B$ and $C \to \frac{1}{\alpha} C$, with $\alpha \in \mathbb{C}^*$.

Proof :

$$\begin{vmatrix} A & B \\ C & D \end{vmatrix} = \begin{vmatrix} A & B \\ C & D \end{vmatrix} \times \begin{vmatrix} I & -A^{-1}B \\ 0 & I \end{vmatrix} = \left| \begin{pmatrix} A & B \\ C & D \end{pmatrix} \times \begin{pmatrix} I & -A^{-1}B \\ 0 & I \end{pmatrix} \right|$$

$$= \begin{vmatrix} A & 0 \\ C & D - CA^{-1}B \end{vmatrix} = |A| \times \left| D - CA^{-1}B \right|$$

$$\begin{vmatrix} A & \alpha B \\ \alpha^{-1}C & D \end{vmatrix} = |A| \times \left| D - (\alpha^{-1}C)A^{-1}(\alpha B) \right| = |A| \times \left| D - CA^{-1}B \right|$$

□

A.5 Property 6 (p.86)

For C an invertible matrix,

- its derivative with respect to the (i,j)-coefficient reads:
$$\frac{\partial}{\partial C_{i,j}} \ln\det C = \left(C^{-1}\right)_{j,i}$$
- The derivative of the inverse is: $\left(C^{-1}\right)' = -C^{-1}C'C^{-1}$.
- Finally the derivatives of $\ln\det C$ are:
$$\frac{\partial}{\partial x}\left(\ln\det C\right) = Tr\left(C'C^{-1}\right) = Tr\left(C^{-1}C'\right)$$
$$\frac{\partial^2}{\partial x^2}\left(\ln\det C\right) = Tr\left(C''C^{-1} - C'C^{-1}C'C^{-1}\right)$$

Proof :

- by developing the determinant along the ith row, one gets: $\det C = \sum_{j=1}^{n} C_{i,j}\left(\mathrm{com}(C)\right)_{i,j}$, where none of the comatrices $\left(\mathrm{com}(C)\right)_{i,j}, (1 \le j \le n)$ contain the elements $C_{i,j}, (1 \le j \le n)$. Then $\frac{\partial \det C}{\partial C_{i,j}} = \left(\mathrm{com}(C)\right)_{i,j}$, and finally one gets:
$$\begin{aligned}\frac{\partial}{\partial C_{i,j}} \ln\det C &= \frac{1}{\det C}\frac{\partial \det C}{\partial C_{i,j}} \\ &= \frac{1}{\det C}\left(\mathrm{com}(C)\right)_{i,j} \\ &= \left(C^{-1}\right)_{j,i}\end{aligned}$$
- by taking the derivative of the identity $\mathrm{Id} = C^{-1}C$, one gets:
$$\begin{aligned}0 &= \sum_k \left(C^{-1}\right)'_{i,k} C_{k,j} + \sum_k \left(C^{-1}\right)_{i,k}\left(C'\right)_{k,j} \\ &= \left[\left(C^{-1}\right)' C\right]_{i,j} + \left[C^{-1}C'\right]_{i,j} \\ 0 &= \left(C^{-1}\right)' C + C^{-1}C' \\ &= \left(C^{-1}\right)' + C^{-1}C'C^{-1}\end{aligned}$$
- from the two former properties, one has:
$$\begin{aligned}\frac{\partial}{\partial x}\left(\ln\det C\right) &= \sum_{i,j}\frac{\partial C_{i,j}}{\partial x}\frac{\partial}{\partial C_{i,j}}\ln\det C \\ &= \sum_{i,j}\left(C'\right)_{i,j}\left(C^{-1}\right)_{j,i} \\ &= Tr\left(C'C^{-1}\right) = Tr\left(C^{-1}C'\right)\end{aligned}$$
$$\begin{aligned}\frac{\partial^2}{\partial x^2}\left(\ln\det C\right) &= \frac{\partial}{\partial x} Tr\left(C'C^{-1}\right) \\ &= Tr\left[\left(C'C^{-1}\right)'\right] \\ &= Tr\left[C''C^{-1} + C'\left(C^{-1}\right)'\right] \\ &= Tr\left[C''C^{-1} - C'C^{-1}C'C^{-1}\right]\end{aligned}$$

□

A.6 Property 12 (p.101)

$$[a_1,\dots,a_N]=\frac{[a_1]\times[a_2,a_1]\times\cdots\times[a_N,\dots,a_2,a_1]}{[a_2]\times[a_3,a_2]\times\cdots\times[a_N,\dots,a_3,a_2]}$$

Proof :

To prove this property, we begin with a lemma, which gives the numerator and denominator of a finite continued fraction independently.

Lemma 3 *$f(n)=[a_1,a_2,\dots,a_n]=\frac{h_n}{k_n}$, where the terms h_n and k_n can be constructed by recurrence:*

$$h_0=1\ \ ;\ \ h_{-1}=0 \qquad\qquad k_0=0\ \ ;\ \ h_{-1}=1 \tag{A.1}$$

$$(n\geq 1)\ \ h_n=a_nh_{n-1}+h_{n-2} \qquad (n\geq 1)\ \ k_n=a_nk_{n-1}+k_{n-2} \tag{A.2}$$

Proof :

For $n=1,2$, the statement $f(n)=\frac{h_n}{k_n}$ is easily checked. Then, for $n\geq 3$, we have:

$$\begin{aligned}f(n)=[a_1,\dots,a_{n-1},a_n]&=\left[a_1,\dots,\left(a_{n-1}+\frac{1}{a_n}\right)\right]\\&=\frac{\left(a_{n-1}+\frac{1}{a_n}\right)h_{n-2}+h_{n-3}}{\left(a_{n-1}+\frac{1}{a_n}\right)k_{n-2}+k_{n-3}}\quad\text{by recurrence hypothesis}\\&=\frac{\frac{h_{n-2}}{a_n}+h_{n-1}}{\frac{k_{n-2}}{a_n}+k_{n-1}}=\frac{a_nh_{n-1}+h_{n-2}}{a_nk_{n-1}+k_{n-2}}=\frac{h_n}{k_n}\ .\end{aligned}$$

□

Let us now define, for any $n\geq 1$, $f(n)=[a_1,\dots,a_n]$, $p_1(n)=[a_n,\dots,a_2,a_1]$ and $p_2(n)=[a_n,\dots,a_3,a_2]$ (for convention, we define $p_2(1)=1$). Thanks to the previous **Lemma 3**, it only remains to show by recurrence that:

$$h_n=p_1(1)\times p_1(2)\times\cdots p_1(n) \qquad\qquad k_n=p_2(1)\times p_2(2)\times\cdots p_1(n) \tag{A.3}$$

For $(n=1,2)$, the property (A.3) is easily checked. Then for $n\geq 3$:

$$\begin{aligned}h_n&=a_n\left(p_1(1)\times p_1(2)\times\cdots p_1(n-1)\right)+\left(p_1(1)\times p_1(2)\times\cdots p_1(n-2)\right)\\&=\left(p_1(1)\times p_1(2)\times\cdots p_1(n-2)\right)\times\left(a_np_1(n-1)+1\right)\\&=\left(p_1(1)\times p_1(2)\times\cdots p_1(n-1)\right)\times\left(a_n+\frac{1}{p_1(n-1)}\right)\\&=p_1(1)\times p_1(2)\times\cdots p_1(n-1)\times p_1(n)\end{aligned}$$

and the same proof holds for k_n with the terms p_2.

□

A.7 Property 13 (p.114)

$d_m^{\ell,s}[\text{sum}]$ and $d_m^{\ell,s}[\text{dif}]$ have the following asymptotic expansions:

$$\begin{aligned}d_m^{\ell,s}[\text{sum}]&\simeq K(\ell,m)\frac{m}{\ell}\left(s(\theta)\right)^{m-1}(\cos\theta)^{\ell-m}\simeq\frac{m}{\ell}K(\ell,m)(\cos\theta)^{\ell-1}\\d_m^{\ell,s}[\text{dif}]&\simeq K(\ell,m)\left(s(\theta)\right)^{m-1}(\cos\theta)^{\ell-m+1}\simeq K(\ell,m)(\cos\theta)^{\ell}\\\text{with}\quad K(\ell,m)&=(-1)^{m+1}\sqrt{\frac{\ell}{\ell+1}}\frac{2(2\ell-1)!!}{\sqrt{(\ell-m)!}\sqrt{(\ell+m)!}}\end{aligned}$$

Proof :
For $d_m^{\ell,s}$[dif] it is direct, from Eq.(7.22) (p.113). For $d_m^{\ell,s}$[dif], it is checked for $m=0$, thanks to Eq.(7.23). We prove the former expressions by recurrence for $m \geq 1$, with the help of Eq.(7.24) (p.114):

$\boxed{\ell = m}$ $K(m,m) = (-1)^{m+1}\sqrt{\dfrac{m}{m+1}}\dfrac{2(2m-1)!!}{\sqrt{(2m)!}} = \sqrt{\dfrac{(2m)!}{(m+1)!(m-1)!}}\left(\dfrac{-1}{2}\right)^{m-1}$

which is the coefficient of $(s(\theta))^{m-1}$ of $d_m^{m,s}$[sum] in Eq.(7.24) (p.114).

$\boxed{\ell = m+1}$ $\dfrac{mK(m+1,m)}{m+1} = \dfrac{m(-1)^{m+1}}{m+1}\sqrt{\dfrac{m+1}{m+2}}\dfrac{2(2m+1)!!}{\sqrt{(2m+1)!}} = \sqrt{\dfrac{(2m+1)!}{(m+2)!m!}}m\left(\dfrac{-1}{2}\right)^{m-1}$

which is the coefficient of $(s(\theta))^{m-1}\cos\theta$ of $d_m^{m+1,s}$[sum] in Eq.(7.24) (p.114).

$\boxed{\ell \geq m+2}$ $d_m^{\ell,s}[\text{sum}] \simeq \dfrac{(\cos\theta)^{\ell-1}m(2\ell-1)}{\sqrt{\ell^2-1}\sqrt{\ell^2-m^2}}K(\ell-1,m) + o\left((\cos\theta)^{\ell-1}\right)$

from last part of Eq.(7.24) (p.114), using the recurrence hypothesis on steps $(\ell-1)$ and $(\ell-2)$.

Then $\dfrac{m(2\ell-1)}{\sqrt{\ell^2-1}\sqrt{\ell^2-m^2}}K(\ell-1,m) = \dfrac{m}{\ell}K(\ell,m)$

□

A.8 Property 14 (p.128)

$$\phi(\nu) = \sum_n{}' \left(1+2\nu n+2\nu^2n^2\right)e^{-2\nu n} = \frac{\nu\sinh\nu+\cosh\nu\left(\nu^2+\sinh^2\nu\right)}{2\sinh^3\nu}$$

Proof :
We first study the un-primed sum, to consider the three terms separately:

$$\begin{aligned}
S(\nu) &= \sum_{n\in\mathbb{N}}\left(1+2\nu n+2\nu^2n^2\right)e^{-2\nu n} = S_1(\nu)+S_2(\nu)+S_3(\nu)\\
S_1(\nu) &= \sum_{n\in\mathbb{N}} e^{-2\nu n} = \frac{1}{1-e^{-2\nu}}\\
S_2(\nu) &= \sum_{n\in\mathbb{N}} 2\nu n e^{-2\nu n} = -\nu\frac{\partial}{\partial\nu}\left(\sum_{n\in\mathbb{N}} e^{-2\nu n}\right) = \frac{2\nu e^{-2\nu}}{(1-e^{-2\nu})^2}\\
S_3(\nu) &= \sum_{n\in\mathbb{N}} 2\nu^2n^2e^{-2\nu n} = -\frac{\nu^2}{2}\frac{\partial}{\partial\nu}\left(\frac{1}{\nu}\sum_{n\in\mathbb{N}} 2\nu n e^{-2\nu n}\right)\\
&= \frac{\nu e^{-2\nu}}{(1-e^{-2\nu})^2} - \frac{\nu}{2}\frac{\partial}{\partial\nu}\left(\frac{2\nu e^{-2\nu}}{(1-e^{-2\nu})^2}\right)\\
&= \frac{2\nu^2e^{-2\nu}}{(1-e^{-2\nu})^2} + \frac{4\nu^2e^{-4\nu}}{(1-e^{-2\nu})^3}\ .
\end{aligned}$$

We then gather the three results:

$$\begin{aligned} S(\nu) &= \frac{1}{1-e^{-2\nu}} + \frac{(2\nu+2\nu^2)e^{-2\nu}}{(1-e^{-2\nu})^2} + \frac{4\nu^2 e^{-4\nu}}{(1-e^{-2\nu})^3} \\ &= \frac{1+e^{-2\nu}(-2+2\nu+2\nu^2)+e^{-4\nu}(1-2\nu+2\nu^2)}{(1-e^{-2\nu})^3} \,, \end{aligned}$$

to finally come back to the primed sum $\phi(\nu)$:

$$\begin{aligned} \phi(\nu) &= \sum_n{}' \left(1+2\nu n+2\nu^2 n^2\right) e^{-2\nu n} = S - \frac{1}{2} \\ &= \frac{1+e^{-2\nu}(-1+4\nu+4\nu^2)+e^{-4\nu}(-1-4\nu+4\nu^2)+e^{-6\nu}}{2(1-e^{-2\nu})^3} \\ &= \frac{\nu\sinh\nu+\cosh\nu\left(\nu^2+\sinh^2\nu\right)}{2\sinh^3\nu} \end{aligned}$$

□

B Approximations methods for the sphere-plane geometry

In this section we present a few existing methods to approximate the Casimir effect between a sphere and a plane. Proximity Force Approximation (PFA) method, which splits the surface of the sphere to sum the contribution of each small part, is first considered in its diverse formulations in **Section B.1**. Then the Hamaker method, which splits the sphere volume into very small spheres before summing the contribution of each one, is derived in **Section B.2.5**. Finally, a Pair-Wise Summation (PWS) process is performed in **Section B.2** for both the sphere and the plane.

B.1 PFA methods

The Proximity-Force Approximation is introduced in **Section 4.1**, and consists in splitting the sphere's surface into infinitesimal parts $\mathrm{d}^2\sigma$, computing independently their Casimir interaction $\delta^2 E$ with the facing plane, and then integrating all these contributions. If the first and last steps are unequivocal, the way to treat the casimir interaction for an infinitesimal surface in front of the plane is however ambiguous.

The usual PFA formulation, also called "leading order PFA", leads to the expression $F_{\mathrm{PFA}} = 2\pi R \times E_{\mathrm{PP}}/A$, where R is the sphere radius and E_{PP}/A the energy per unit area in the plane-plane geometry. This expression is obtained by considering a planar infinitesimal surface $\mathrm{d}^2\sigma$ facing the plane, and its corresponding small surface on the plane directly below. This results in a so-called 'plane-based' formulation, and is illustrated in the left of **Fig. 85**.

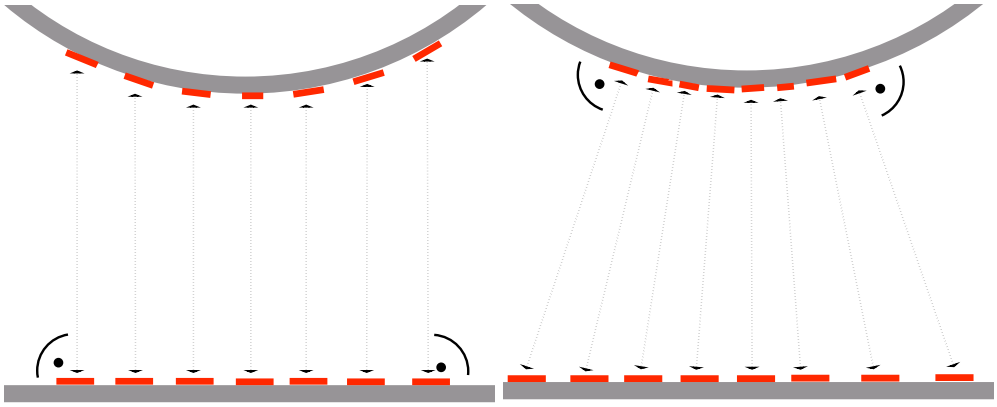

Figure 85: Choice of the pair of corresponding infinitesimal surfaces on the two objects, with a plane-based PFA (left) and sphere-based PFA (right). Courtesy of Holger Gies.

We could also have kept the infinitesimal surface on the sphere fixed, and have chosen a corresponding surface on the plane facing it on the sides. This would have resulted in a so-called 'sphere-based' formulation, and is illustrated in the right of **Fig. 85**. Plane-based and sphere-based PFAs have been used in the past years to compare with results obtained by different techniques [156, 151, 160, 162, 175].

A third possibility would be to consider the interaction of an infinitesimal part of the sphere's surface $\mathrm{d}^2\sigma$ with the whole infinite plane, without any change in the orientation of the surface, as this configuration has been studied in [264]. This possibility will however not be discussed here.

We here derive the Casimir energy separately for the plane-based and sphere-based formulations, and then compare the obtained beyond-PFA corrections in the simple case of perfect reflectors at zero temperature.

B.1.1 Plane-based PFA

We consider a sphere of radius R at a distance L above a plane located at $(z = 0)$. Let us first split the sphere in upper and lower halves. We will only consider the interaction of the plane with the lower half $(z \leq \mathcal{L})$, where $\mathcal{L} = L + R$ is the distance between the plane's surface and the sphere's center. The half-sphere is decomposed into infinitesimal surfaces $\mathrm{d}^2\sigma = R^2 \sin\theta \mathrm{d}\theta \mathrm{d}\varphi$.

For plane-based formulations of PFA, we will now consider this surface to be parallel to the plane. This can be achieved in two ways, schematically represented in **Fig. 86**: in method 1 (left graph) we simply consider it to be parallel, without any change in the area, as in a rotation $(\mathrm{d}^2\sigma^{(1)} = \mathrm{d}^2\sigma)$. In method 2 (right graph) we project it to be parallel, yielding a multiplication by a projection factor $\cos\theta$ for the area $(\mathrm{d}^2\sigma^{(2)} = \cos\theta \mathrm{d}^2\sigma)$. In both cases the local distance for the infinitesimal surface is $z = L + R(1 - \cos\theta)$.

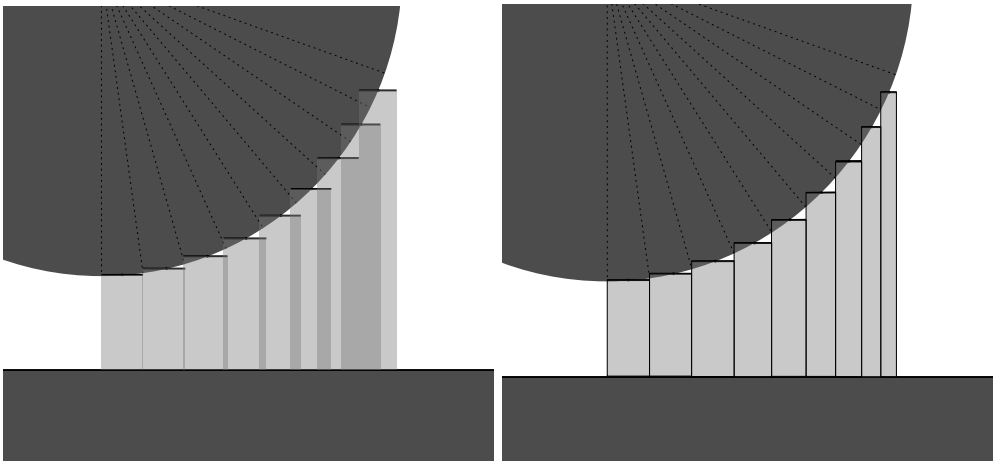

Figure 86: Two different methods to choose the corresponding surface of an infinitesimal surface on the sphere, to be parallel to the plane. The sphere is decomposed into infinitesimal surfaces $\mathrm{d}^2\sigma$. In the first case, each part has an equal radial width of $Rd\theta$, whereas in the second, the part at latitude θ has a width of $R\cos\theta d\theta$, that vanishes when $\theta = \frac{\pi}{2}$.

With **Fig. 86**, we clearly illustrate the motivation for the second formulation: the lack of projection factor in the expression of the infinitesimal surface for method 1 artificially increases the surface of interaction on the sphere, as different infinitesimal cavities overlap, and should lead to an overestimation of the Casimir interaction.

When integrating over the sphere the small contribution of each infinitesimal surface, using the

presented formulation, we get for the first method:

$$\begin{aligned}
E^{(1)}_{\mathrm{PFA}} &= \iint_{\Sigma} \frac{E_{\mathrm{PP}}(z)}{A} \mathrm{d}^2\sigma^{(1)} \\
&= \int_0^{2\pi} \mathrm{d}\varphi \int_0^{\pi/2} \mathrm{d}\theta R^2 \sin\theta \frac{E_{\mathrm{PP}}(z)}{A} \\
&= 2\pi R^2 \int_0^{\pi/2} \sin\theta \mathrm{d}\theta \frac{E_{\mathrm{PP}}(z)}{A} \quad \text{with } z = L + R(1-\cos\theta) \\
&= 2\pi R \int_L^{L+R} \frac{E_{\mathrm{PP}}(z)}{A} \mathrm{d}z \quad \text{as } \mathrm{d}z = R\sin\theta \mathrm{d}\theta \\
&= 2\pi R \left(\frac{D_{\mathrm{PP}}(L)}{A} - \frac{D_{\mathrm{PP}}(L+R)}{A} \right) \\
&= E_{\mathrm{PFA}} \left(1 - \frac{D_{\mathrm{PP}}(L+R)}{D_{\mathrm{PP}}(L)} \right) . \qquad \text{(B.1)}
\end{aligned}$$

E_{PFA} is the usual PFA formula, and neglects the second term. For the second method, the derivation is a bit more complex:

$$\begin{aligned}
E^{(2)}_{\mathrm{PFA}} &= \iint_{\Sigma} \frac{E_{\mathrm{PP}}(z)}{A} \mathrm{d}^2\sigma^{(2)} \\
&= 2\pi R^2 \int_0^{\pi/2} \sin\theta\cos\theta \mathrm{d}\theta \frac{E_{\mathrm{PP}}(z)}{A} \\
&= 2\pi \int_L^{L+R} (L+R-z) \frac{E_{\mathrm{PP}}(z)}{A} \mathrm{d}z \quad \text{as } \cos\theta = 1 - \frac{z-L}{R}
\end{aligned}$$

and the calculation can be brought one step further, with the introduction of a primitive function $C_{\mathrm{PP}}(z)$, such that $-\frac{\partial C_{\mathrm{PP}}}{\partial L} = D_{\mathrm{PP}}$. We get after integration by part for the second term:

$$\begin{aligned}
E^{(2)}_{\mathrm{PFA}} &= 2\pi(L+R) \left(\frac{D_{\mathrm{PP}}(L)}{A} - \frac{D_{\mathrm{PP}}(L+R)}{A} \right) + 2\pi \left[z \frac{D_{\mathrm{PP}}(z)}{A} \right]_L^{L+R} + 2\pi \left[\frac{C_{\mathrm{PP}}(z)}{A} \right]_L^{L+R} \\
&= 2\pi R \frac{D_{\mathrm{PP}}(L)}{A} - 2\pi \left(\frac{C_{\mathrm{PP}}(L)}{A} - \frac{C_{\mathrm{PP}}(L+R)}{A} \right) . \qquad \text{(B.2)}
\end{aligned}$$

For the simple case of perfect mirrors at zero temperature the Casimir function $D_{\mathrm{PP}}(L)/A$ has the explicit expression (4.7), and then the two PFA formulations become:

$$\begin{aligned}
E^{(1)}_{\mathrm{PFA}} &= -\frac{\hbar c \pi^3 R}{720 L^2} \left(1 - \frac{L^2}{(L+R)^2} \right) \\
&= E_{\mathrm{PFA}} \left(\frac{1 + 2L/R}{1 + 2L/R + L^2/R^2} \right) \qquad \text{(B.3)} \\
E^{(2)}_{\mathrm{PFA}} &= -\frac{\hbar c \pi^3 R}{720 L^2} + \frac{\hbar c \pi^3}{720 L} \left(1 - \frac{L}{L+R} \right) \\
&= E_{\mathrm{PFA}} \left(\frac{1}{1 + L/R} \right) . \qquad \text{(B.4)}
\end{aligned}$$

The latter corresponds to the expressions found in [160, Eq.(2.16)] and [162, Eq.(A3)]. For very short separations ($L \ll R$), when using Taylor expansions of the factors appearing in Eqs.(B.3,B.4)

we obtain:

$$\frac{E^{(1)}_{\mathrm{PFA}}}{E_{\mathrm{PFA}}} = 1 - \left(\frac{L}{R}\right)^2 + o\left(\left(\frac{L}{R}\right)^2\right) \tag{B.5}$$

$$\frac{E^{(2)}_{\mathrm{PFA}}}{E_{\mathrm{PFA}}} = 1 - \frac{L}{R} + \left(\frac{L}{R}\right)^2 + o\left(\left(\frac{L}{R}\right)^2\right) \tag{B.6}$$

and we observe that if the first formulation is similar to the usual PFA at first order, it is no more the case for the second formulation.

This last result can be reformulated with the help of the coefficients for the successive orders of the beyond-PFA correction $(\beta_E, \gamma_E, ...)$ defined for the usual PFA formula as the coefficients of a hypothetical Taylor expansion of the ratio ρ_E between the exact result and the PFA-approximated quantity:

$$\rho_E = \frac{E}{E_{\mathrm{PFA}}} = 1 + \beta_E \frac{L}{R} + \gamma_E \left(\frac{L}{R}\right)^2 + o\left(\left(\frac{L}{R}\right)^2\right) .$$

For the two methods here introduced, we can deduce from the expressions derived in Eqs.(B.5,B.6) the change induced in those beyond-PFA coefficients:

$$\begin{aligned}\rho^{(1)}_E &= \frac{E}{E^{(1)}_{\mathrm{PFA}}} = \frac{E}{E_{\mathrm{PFA}}}\frac{E_{\mathrm{PFA}}}{E^{(1)}_{\mathrm{PFA}}} \\ &= 1 + \beta_E \frac{L}{R} + (\gamma_E + 1)\left(\frac{L}{R}\right)^2 + o\left(\left(\frac{L}{R}\right)^2\right) \end{aligned} \tag{B.7}$$

$$\rho^{(2)}_E = 1 + (\beta_E + 1)\frac{L}{R} + (\gamma_E + \beta_E)\left(\frac{L}{R}\right)^2 + o\left(\left(\frac{L}{R}\right)^2\right) . \tag{B.8}$$

For the first expression (B.7), only the second order coefficient change ($\gamma^{(1)}_E = \gamma_E + 1$), the distinction with the usual and simpler formula is then not important if one is only interested in the first order coefficient β_E in the beyond-PFA correction. For the second formulation (B.8) however, this coefficient of beyond-PFA linear correction changes significantly, as $\beta^{(2)}_E = \beta_E + 1$.

We found in **Section 10.3** (p.145) that in the situation of perfect reflectors at zero temperature β_E can be estimated to lie around the value -1.4. The second formulation of the plane-based PFA then yields a better approximation of the exact result, as $\beta^{(2)}_E \simeq -0.4$. This comes from the fact that the avoided overlaps in the considered infinitesimal cavities, as illustrated by **Fig. 86**, reduce the overestimation of the Casimir effect for PFA methods.

B.1.2 Sphere-based PFA

We now consider a second possibility for the choice of corresponding surfaces in the computation of PFA, illustrated by the right graph in **Fig. 85**. When integrating over the sphere the small contribution of each infinitesimal surface, using the presented formulation, we get for the first

method:

$$\begin{aligned} E_{\text{PFA}}^{\text{s-b}} &= \iint_{\Sigma} \frac{E_{\text{PP}}(z)}{A} \mathrm{d}^2\sigma \\ &= \int_0^{2\pi} \mathrm{d}\varphi \int_0^{\pi/2} \mathrm{d}\theta R^2 \sin\theta \frac{E_{\text{PP}}(z)}{A} \\ &= 2\pi R^2 \int_0^{\pi/2} \sin\theta \mathrm{d}\theta \frac{E_{\text{PP}}(z)}{A} \quad \text{with } z = \frac{L + R(1-\cos\theta)}{\cos\theta} \\ &= 2\pi R^2 (L+R) \int_L^{\infty} \frac{\mathrm{d}z}{(z+R)^2} \frac{E_{\text{PP}}(z)}{A} \quad \text{as } \mathrm{d}z = \frac{(L+R)\sin\theta \mathrm{d}\theta}{\cos^2\theta} \,. \end{aligned} \tag{B.9}$$

In the simple case of perfectly reflecting mirrors at zero temperature, using the Casimir energy per unit area in the plane-plane configuration $\frac{E_{\text{PP}}(z)}{A} = -\frac{\hbar c \pi^2}{720 z^3}$, the integration is computable and leads to the following expression for the Casimir energy within sphere-based PFA:

$$\begin{aligned} E_{\text{PFA}}^{\text{s-b}} &= -\frac{\hbar c \pi^3 R^2 (L+R)}{360} \int_L^{\infty} \frac{\mathrm{d}z}{z^3 (z+R)^2} \\ &= -\frac{\hbar c \pi^3 R^2 (L+R)}{360} \int_L^{\infty} \mathrm{d}z \left(\frac{3}{R^4 z} - \frac{2}{R^3 z^2} + \frac{1}{R^2 z^3} - \frac{3}{R^4 (z+R)} - \frac{1}{R^3 (z+R)^2} \right) \\ &= -\frac{\hbar c \pi^3 R}{720 L^2} \left[6\frac{L^2}{R^2} \left(1 + \frac{L}{R}\right) \ln\left(1 + \frac{R}{L}\right) + 1 - 3\frac{L}{R} - 6\frac{L^2}{R^2} \right] \end{aligned} \tag{B.10}$$

which corresponds to the expressions found in [160, Eq.(2.17)] and [162, Eq.(A2)].

In the short distance limit ($L \ll R$), a first order expansion of (B.10) gives $E_{\text{PFA}}^{\text{sphere-based}} = E_{\text{PFA}} \left(1 - 3\frac{L}{R} + o\left(\frac{L}{R}\right)\right)$, and with a derivation similar to the one in Eq.(B.7), we obtain the coefficient $\beta_E^{\text{s-b}} = \beta_E + 3 \simeq +1.6$ for the first order beyond-PFA correction. The sign is reversed with respect to the same quantity for the plane-based PFA, which means that in this case PFA underestimates the Casimir effect. Moreover, remarking that $\left|\beta_E^{\text{s-b}}\right| \sim |\beta_E|$, we deduce that the error of PFA can be substantially decreased by taking the average of the usual expression $E_{\text{PFA}} = 2\pi R \frac{D_{\text{PP}}(L)}{A}$ and the sphere-based expression (B.10).

These findings are confirmed by the numerical evaluations of the beyond-PFA correction factor ρ_E presented in **Fig. 87**, where $\rho_E < 1$ for the usual plane-based PFA, and $\rho_E > 1$ for the sphere-based PFA. The averaging is done both with arithmetic and harmonic means of the plane-based and sphere-based PFA quantities:

$$\rho_E^{\text{arithm}} = \frac{2E}{E_{\text{PFA}}^{\text{plane-based}} + E_{\text{PFA}}^{\text{sphere-based}}} \qquad \rho_E^{\text{harm}} = \frac{\rho_E^{\text{plane-based}} + \rho_E^{\text{sphere-based}}}{2} \,.$$

Both remain relatively close to the exact result when the distance between the plane and the sphere increases, and the harmonic mean seems to be favored. For an aspect ratio $\frac{L}{R} = 0.1$, the obtained correction factor is 0.986 for the arithmetic mean and 0.9986 for the harmonic one. We here come to the same observation as in [156, Fig.8], which found an "accidental" but interesting agreement of the harmonic mean with numerical results beyond the domain of validity of PFA.

B.2 PWS methods

The Pairwise Summation Method (PWS) consists in considering the interaction of two objects as the sum of the interactions between all pairs of atoms, formed by taking one atom in each object. This method is commonly used in electrostatics, but its application to Casimir interaction is questionable. Here we derive the Casimir energy between a plane and a sphere within PWS

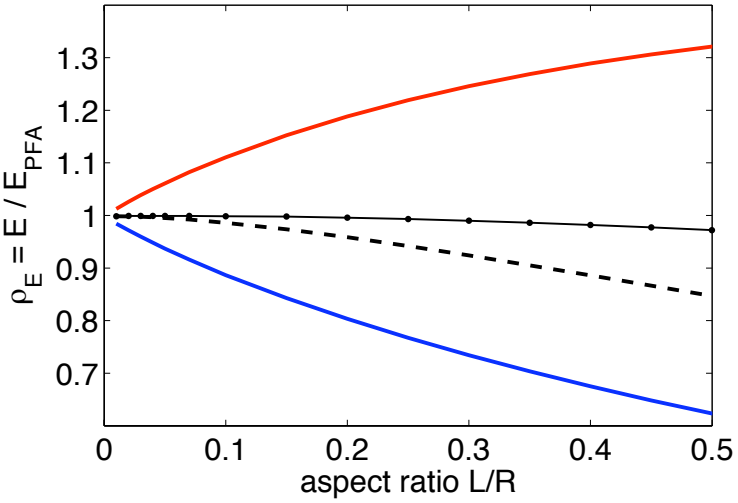

Figure 87: Beyond-PFA correction factor $\rho_E = \frac{E}{E_{\rm PFA}}$ for perfect mirrors at zero temperature, with respect to the aspect ratio $\frac{L}{R}$. The blue curve correspond to the usual PFA expression $E_{\rm PFA} = 2\pi R \frac{D_{\rm PP}(L)}{A}$, the red curve to a sphere-based PFA expression (B.10). The arithmetic mean of the plane-based and sphere-based PFAs is presented by the dashed-curve, while the dotted-line represents the harmonic mean.

calculations. The two objects are described by an atomic density n and a polarizability α for the atoms.

We start from the Casimir-Polder formula giving the interaction energy between two atoms A and B, with polarizabilities $\alpha(\omega)$, at distance R:

$$U_{aa}(R) = -\frac{\hbar c}{\pi}\int_0^\infty du\; u^4 \frac{\alpha_A(icu)\alpha_B(icu)}{(4\pi\epsilon_0)^2}\frac{e^{-2uR}}{R^2}\left(1+\frac{2}{uR}+\frac{5}{(uR)^2}+\frac{6}{(uR)^3}+\frac{3}{(uR)^4}\right) \quad \text{(B.11)}$$

where the integral is written over imaginary frequencies $\omega = icu$. We will then integrate over one slab to get the slab-atom configuration. A second integration will finally be performed with either a slab or a sphere for the second object. The latter case yield the sphere-plane Casimir energy within PWS method.

B.2.1 The slab-atom configuration

In this section, the object A is a slab of thickness e_A and atomic density n_A at a distance h along the z-axis from the atom B.

We compute the PWS interaction between the slab and the atom by summing the Casimir-Polder interactions (eq. B.11) between each atom A of the slab and the atom B:

$$U_{as}^{PWS}(h, e_A) = \int_h^{h+e_A} dz \int_0^\infty dr\; 2\pi r n_A U_{aa}(R) \quad \text{(B.12)}$$

with $r = \sqrt{x^2+y^2} = \sqrt{z^2-R^2}$. The integration over u is inverted with those of r and z. The integration over r is transformed into an integration over R:

$$U_{as}^{PWS}(h, e_A) = -2\hbar c n_A \int_0^\infty du\; u^4 \frac{\alpha_A(icu)\alpha_B(icu)}{(4\pi\epsilon_0)^2}\int_h^{h+e_A} dz\; I(z)\;, \quad \text{(B.13)}$$

with

$$\begin{aligned} I(z) &= \int_z^\infty \frac{dR}{R} e^{-2uR} \left(1 + \frac{2}{uR} + \frac{5}{(uR)^2} + \frac{6}{(uR)^3} + \frac{3}{(uR)^4}\right) \\ &= \int_{2uz}^\infty dt\ e^{-t} \left(\frac{1}{t} + \frac{4}{t^2} + \frac{20}{t^3} + \frac{48}{t^4} + \frac{48}{t^5}\right) \qquad \text{(B.14)} \\ &= -\int_{2uz}^\infty dt\ d(t) = e(2uz) - e(\infty), \qquad \text{(B.15)} \end{aligned}$$

where $e(t)$ denotes the primitive of function $d(t)$. The explicit expressions of the successive primitive functions will be given in the end of the section in Eqs.(B.19). As $e(\infty) = 0$, the energy (B.13) becomes:

$$U_{as}^{PWS}(h, e_A) = -\hbar c n_A \int_0^\infty du\ u^3 \frac{\alpha_A(icu)\alpha_B(icu)}{(4\pi\epsilon_0)^2} \int_{2uh}^{2u(h+e_A)} dt\ e(t)\ . \qquad \text{(B.16)}$$

Defining $f(t)$ the primitive of function $e(t)$, we obtain:

$$U_{as}^{PWS}(h, e_A) = -\hbar c n_A \int_0^\infty du\ u^3 \frac{\alpha_A(icu)\alpha_B(icu)}{(4\pi\epsilon_0)^2} \left[f\left(2u(h+e_A)\right) - f\left(2uh\right)\right]\ . \qquad \text{(B.17)}$$

B.2.2 The slab-slab configuration

In this section, objects A and B are slabs, of densities n_A and n_B, and of thicknesses e_A and e_B. h is the separation between the two objects.

We compute the interaction between the two slabs by summing the slab-atom result (B.17) for each atom of the slab B. As the result is infinite, because both objects are infinite, we compute the energy per unit area:

$$\begin{aligned} U_{ss}^{PWS}(h, e_A, e_B) &= \int_h^{h+e_B} dz\ n_B U_{as}^{PWS}(z, e_A) \\ &= -\hbar c n_A n_B \int_0^\infty du\ u^3 \frac{\alpha_A(icu)\alpha_B(icu)}{(4\pi\epsilon_0)^2} \int_h^{h+e_B} dz\ \left[f\left(2u(z+e_A)\right) - f\left(2uz\right)\right] \\ &= -\frac{\hbar c}{2} n_A n_B \int_0^\infty du\ u^2 \frac{\alpha_A(icu)\alpha_B(icu)}{(4\pi\epsilon_0)^2} \int_{2uh}^{2u(h+e_B)} dt\ \left[f\left(2ue_A + t\right)\right) - f\left(t\right)]\ . \end{aligned}$$

Defining $g(t)$ the primitive of function $f(t)$, we obtain:

$$\begin{aligned} U_{ss}^{PWS}(h, e_A, e_B) = -\frac{\hbar c}{2} n_A n_B \int_0^\infty du\ u^2 \frac{\alpha_A(icu)\alpha_B(icu)}{(4\pi\epsilon_0)^2} \\ \times \left[g\left(2u(h+e_A+e_B)\right) - g\left(2u(h+e_A)\right) - g\left(2u(h+e_B)\right) + g\left(2uh\right)\right]\ . \qquad \text{(B.18)} \end{aligned}$$

B.2.3 The slab-sphere configuration

In this section, object A is again a slab of thickness e_A and density n_A, while object B is now a sphere of radius R and density n_B. L is the surface-surface distance of the two objects, while $\mathcal{L}$ will be the center-to-plate distance ($\mathcal{L} = L + R$).

We compute the interaction between the two objects by summing the slab-atom result (B.17) for each atom of the sphere B which lies at a distance $(\mathcal{L} + r)$ from the slab, with $r \in [-R, R]$:

$$
\begin{aligned}
U_{PS}^{PWS} &= \int_{-R}^{R} dr \ \left(\pi(R^2-r^2)n_B\right) U_{as}^{PWS}(\mathcal{L}+r,e_A) \\
&= -\hbar c\pi n_A n_B \int_0^\infty du\ u^3 \frac{\alpha_A(icu)\alpha_B(icu)}{(4\pi\epsilon_0)^2} \int_{-R}^{R} dr\ \left(R^2-r^2\right) \\
&\quad \times \left[f\left(2u(\mathcal{L}+r+e_A)\right) - f\left(2u(\mathcal{L}+r)\right)\right] \\
&= -\frac{\hbar c\pi}{8} n_A n_B \int_0^\infty du\ \frac{\alpha_A(icu)\alpha_B(icu)}{(4\pi\epsilon_0)^2} \int_{-2uR}^{2uR} dt\ \left(4u^2R^2-t^2\right) \\
&\quad \times \left[f\left(2u(\mathcal{L}+e_A)+t\right) - f\left(2u\mathcal{L}+t\right)\right] \ .
\end{aligned}
$$

Then, splitting the term $(4u^2R^2 - t^2)$ in two parts, we need to derive:

$$
\begin{aligned}
A_1(u) &= 4u^2R^2 \int_{-2uR}^{2uR} dt\ \left(f\left(2u(\mathcal{L}+e_A)+t\right) - f\left(2u\mathcal{L}+t\right)\right) \\
&= 4u^2R^2 \left[g\left(2u(\mathcal{L}+e_A)+t\right) - g\left(2u\mathcal{L}+t\right)\right]_{-2uR}^{2uR} \\
&= 4u^2R^2 \left[g(2u(\mathcal{L}+e_A+R)) - g(2u(\mathcal{L}+e_A-R)) - g(2u(\mathcal{L}+R)) + g(2u(\mathcal{L}-R))\right]
\end{aligned}
$$

and

$$
\begin{aligned}
A_2(u) &= -\int_{-2uR}^{2uR} dt\ t^2 \left(f\left(2u(\mathcal{L}+e_A)+t\right) - f\left(2u\mathcal{L}+t\right)\right) \\
&= -\left[t^2\left(g\left(2u(\mathcal{L}+e_A)+t\right) - g\left(2u\mathcal{L}+t\right)\right)\right]_{-2uR}^{2uR} \\
&\quad +2\int_{-2uR}^{2uR} dt\ t\left(g\left(2u(\mathcal{L}+e_A)+t\right) - g\left(2u\mathcal{L}+t\right)\right) \\
&= -A_1(u) + 2\left[t\left(h\left(2u(\mathcal{L}+e_A)+t\right) - h\left(2u\mathcal{L}+t\right)\right)\right]_{-2uR}^{2uR} \\
&\quad -2\int_{-2uR}^{2uR} dt\ \left(h\left(2u(\mathcal{L}+e_A)+t\right) - h\left(2u\mathcal{L}+t\right)\right) \\
&= -A_1(u) \\
&\quad +4uR\left[h\left(2u(\mathcal{L}+e_A+R)\right) + h\left(2u(\mathcal{L}+e_A-R)\right) - h\left(2u(\mathcal{L}+R)\right) - h\left(2u(\mathcal{L}-R)\right)\right] \\
&\quad -2\left[i\left(2u(\mathcal{L}+e_A+R)\right) - i\left(2u(\mathcal{L}+e_A-R)\right) - i\left(2u(\mathcal{L}+R)\right) + i\left(2u(\mathcal{L}-R)\right)\right]
\end{aligned}
$$

with $h(t)$ the primitive of $g(t)$, and $i(t)$ the primitive of $h(t)$. Finally, the energy reads:

$$
\begin{aligned}
U_{PS}^{PWS} &= -\frac{\hbar c\pi}{4} n_A n_B \int_0^\infty du\ \frac{\alpha_A(icu)\alpha_B(icu)}{(4\pi\epsilon_0)^2} \times \\
&\quad \left(2uR\left[h\left(2u(\mathcal{L}+e_A+R)\right) + h\left(2u(\mathcal{L}+e_A-R)\right) - h\left(2u(\mathcal{L}+R)\right) - h\left(2u(\mathcal{L}-R)\right)\right]\right. \\
&\quad \left. -\left[i\left(2u(\mathcal{L}+e_A+R)\right) - i\left(2u(\mathcal{L}+e_A-R)\right) - i\left(2u(\mathcal{L}+R)\right) + i\left(2u(\mathcal{L}-R)\right)\right]\right) \ .
\end{aligned}
$$

B.2.4 Expressions for the successive primitive functions

The successive primitive functions involved in this section are:

$$\begin{aligned}
d(t) &= -e^{-t}\left(\frac{1}{t}+\frac{4}{t^2}+\frac{20}{t^3}+\frac{48}{t^4}+\frac{48}{t^5}\right)\\
e(t) &= \Gamma(0,t)+4e^{-t}\left(\frac{1}{t^2}+\frac{3}{t^3}+\frac{3}{t^4}\right)\\
f(t) &= t\Gamma(0,t)-e^{-t}\left(1+\frac{4}{t^2}+\frac{4}{t^3}\right)\\
g(t) &= \left(\frac{t^2}{2}-2\right)\Gamma(0,t)+e^{-t}\left(-\frac{t}{2}+\frac{1}{2}+\frac{2}{t}+\frac{2}{t^2}\right)\\
h(t) &= \left(\frac{t^3}{6}-2t\right)\Gamma(0,t)+e^{-t}\left(-\frac{t^2}{6}+\frac{t}{6}+\frac{5}{3}-\frac{2}{t}\right)\\
i(t) &= \left(\frac{t^4}{24}-t^2+2\right)\Gamma(0,t)+e^{-t}\left(-\frac{t^3}{24}+\frac{t^2}{24}+\frac{11t}{12}-\frac{3}{4}\right)
\end{aligned} \tag{B.19}$$

B.2.5 Hamaker method

The principle of the Hamaker method [265] is to decompose the sphere into a continuous set of small particles, which have the same optical response as very small spheres, with an infinitesimal radius δR. The volumetric energy between the plane and an infinitesimally small sphere is then integrated over the sphere of radius R.

We start from an integral expression of the Casimir-Polder energy for a point scatterer located at a distance L above a plane mirror:

$$E_{\mathrm{CP}} = -\hbar c\int_0^\infty \frac{\mathrm{d}\hat{\xi}}{2\pi}\,\frac{\alpha(\hat{\xi})}{4\pi\epsilon_0}\int_0^\infty \frac{k}{\kappa}\mathrm{d}k\,\left(\left(\kappa^2+k^2\right)|r_{\mathrm{TM}}|+\hat{\xi}^2\,|r_{\mathrm{TE}}|\right)e^{-2\kappa L}$$

where $\alpha\left(\hat{\xi}\right)$ is the polarizability of the point scatterer in SI units, spherical symmetry assumed, and $\left|r\left(\hat{\xi},k\right)\right|$ the absolute values of the reflection amplitudes. In the following we will use a polarizability described by the simple Clausius-Mosotti relation $\alpha = 4\pi\epsilon_0\frac{\varepsilon-1}{\varepsilon+2}(\delta R)^3$, with $\varepsilon(i\xi)$ being the frequency-dependant permittivity of the sphere's material. It allows to make this expression equivalent to the result of the point-like sphere limit ($\delta R \ll L$) from the scattering formula, described in **Section 12.1** (p.158).

Thanks to the volumetric nature of the polarizability within the Clausius-Mosotti relation, the Casimir energy can be expressed per unit volume of the point-like sphere:

$$\mathcal{E}_{\mathrm{CP}} = \frac{E_1}{\frac{4}{3}\pi(\delta R)^3} = \frac{3\hbar c}{8\pi^2}\int_0^\infty \mathrm{d}\hat{\xi}\,\frac{\varepsilon(i\xi)-1}{\varepsilon(i\xi)+2}\int_0^\infty \frac{k}{\kappa}\mathrm{d}k\,\left(\left(\kappa^2+k^2\right)|r_{\mathrm{TM}}|+\hat{\xi}^2\,|r_{\mathrm{TE}}|\right)e^{-2\kappa L}\ . \tag{B.20}$$

In **Sections 12.1.3** (p.161) and **12.1.4** (p.162) we observed that in some regimes, this Casimir energy could be written as the volume of the sphere times a power law in L. This allows us now to write the volumetric energy (B.20) in the simpler form:

$$\mathcal{E}_n = \frac{E_n}{\frac{4}{3}\pi(\delta R)^3} = -\frac{c_n}{L^n}\quad, n\in\{3,4\}\ .$$

The energy for the 'big' sphere of radius R is then obtained by an integration over its volume of (B.20). For the general case, one obtains the averaged energy:

$$\begin{aligned}\overline{E_{\rm CP}} &= \int_{\rm sphere} \mathcal{E}_1(\mathbf{x}) \mathrm{d}V \\ &= \pi \int_L^{L+2R} \mathrm{d}z\ \mathcal{E}_1(z) \left(-z^2 + 2z(L+R) - L(L+2R)\right)\ .\end{aligned}$$

The derivation can be done analytically for the simpler forms $\mathcal{E}_n$ and reads:

$$\begin{aligned}\overline{E_n} &= \int_{sphere} \frac{\mathcal{E}_n}{\frac{4}{3}\pi R^3} dV \\ &= -c_n \int_{sphere} \frac{dV}{L^n} \\ &= -c_n \pi \left[-L(L+2R)J_n + 2(L+R)J_{n-1} - J_{n-2}\right]\end{aligned}$$

with the integrals $J_n = \int_L^{L+2R} \frac{dx}{x^n}$ for $1 \leq n \leq 4$:

$$\begin{aligned}J_1 &= \int_L^{L+2R} \frac{dx}{x} = \ln\left(\frac{L+2R}{L}\right) \\ J_2 &= \int_L^{L+2R} \frac{dx}{x^2} = \frac{2R}{L(L+2R)} \\ J_3 &= \int_L^{L+2R} \frac{dx}{x^3} = \frac{2R(L+R)}{L^2(L+2R)^2} \\ J_4 &= \int_L^{L+2R} \frac{dx}{x^4} = \frac{2R(3L^2+6LR+4R^2)}{3L^3(L+2R)^3}\ .\end{aligned}$$

Finally the large and short distance Casimir energies, averaged on the volume of the sphere, read

$$\begin{aligned}\overline{E_4} &= -\frac{4c_4\pi R^3}{3L^2(L+2R)^2} \\ \overline{E_3} &= -c_3\pi \left[\frac{2R(L+R)}{L(L+2R)} - \ln\left(\frac{L+2R}{L}\right)\right]\ .\end{aligned}$$

Casimir Interaction between Plane and Spherical Metallic Surfaces

Antoine Canaguier-Durand,[1] Paulo A. Maia Neto,[2] Ines Cavero-Pelaez,[1] Astrid Lambrecht,[1] and Serge Reynaud[1]
[1]*Laboratoire Kastler Brossel, CNRS, ENS, Université Pierre et Marie Curie case 74, Campus Jussieu, F-75252 Paris Cedex 05, France*
[2]*Instituto de Física, UFRJ, CP 68528, Rio de Janeiro, RJ, 21941-972, Brazil*
(Received 17 January 2009; published 11 June 2009)

We give an exact series expansion of the Casimir force between plane and spherical metallic surfaces in the nontrivial situation where the sphere radius R, the plane-sphere distance L and the plasma wavelength λ_P have arbitrary relative values. We then present numerical evaluation of this expansion for not too small values of L/R. For metallic nanospheres where R, L and λ_P have comparable values, we interpret our results in terms of a correlation between the effects of geometry beyond the proximity force approximation and of finite reflectivity due to material properties. We also discuss the interest of our results for the current Casimir experiments which are performed with spheres of large radius $R \gg L$.

DOI: 10.1103/PhysRevLett.102.230404 PACS numbers: 03.70.+k, 12.20.Ds, 42.50.−p, 85.85.+j

The Casimir force is a striking macroscopic effect of quantum vacuum fluctuations which has been seen in a number of dedicated experiments in the last decade (see for example [1,2] and references therein). One aim of the Casimir force experiments is to investigate the presence of hypothetical weak forces predicted by unification models through a careful comparison of the measurements with quantum electrodynamics predictions. This aim can only be reached if theoretical computations are able to take into account a realistic and reliable modeling of the experimental conditions. Among the effects to be taken into account are the material properties and the surface geometry. Note that these effects are also able to produce phenomena of interest in nanosystems [3,4].

A number of Casimir measurements have been performed with gold-covered plane and spherical surfaces separated by distances L of the order of the plasma wavelength ($\lambda_P \simeq 136$ nm for gold), making material properties important in their analysis [5]. As those measurements use spheres with a radius $R \gg L$, they are commonly analyzed through the proximity force approximation (PFA) [6], which amounts to a trivial integration over the sphere-plate distances. An exception is the Purdue experiment dedicated to the investigation of the accuracy of PFA in the sphere-plate geometry [7], the result of which will be given as a precise statement below.

In the present Letter, we give for the first time an exact series expansion of the Casimir force between a plane and a sphere in an electromagnetic vacuum, taking into account the material properties via the plasma model (see Fig. 1). We present numerical evaluation of this expansion which are limited to not too small values of L/R, because of the multipolar nature of the series. We show below that these new results lead to a striking correlation between the effects of geometry and imperfect reflection when evaluated for nanospheres, with R, L, and λ_P having comparable values. In the end of this Letter, we also discuss the interest of these results for the Casimir experiments performed with large spheres $R \gg L$ [7].

Our starting point is a general scattering formula for the Casimir energy [8]. Using suitable plane-wave and multipole bases, we deduce the Casimir energy $\mathcal{E}_{\rm PS}$ between a plane and a spherical metallic surface in an electromagnetic vacuum. The multipole series expansion is written in terms of Fresnel reflection amplitudes for the plate and Mie coefficients for the sphere, and it is valid for arbitrary relative values of the sphere radius R, the sphere-plate distance L and the plasma wavelength λ_P. For the sake of comparison with experiments, we assume $\lambda_P \simeq 136$ nm for both, the sphere and the plate. We occasionally also consider the limit $\lambda_P \to 0$, where the formula reduces to the case of perfect reflectors in an electromagnetic vacuum, for which results were obtained recently [9–11].

In the following, we discuss the force $\mathcal{F}_{\rm PS} \equiv -\partial\mathcal{E}_{\rm PS}/\partial L$ as well as the force gradient $\mathcal{G}_{\rm PS} \equiv -\partial\mathcal{F}_{\rm PS}/\partial L$ which was measured in the experiment [7]. We write the results deduced from the scattering formula as products of PFA estimates by beyond-PFA correction factors ρ_F and ρ_G:

$$\mathcal{F}_{\rm PS} \equiv \rho_F \mathcal{F}_{\rm PS}^{\rm PFA}, \qquad \mathcal{F}_{\rm PS}^{\rm PFA} \equiv \eta_E \frac{\hbar c \pi^3 R}{360 L^3}$$
$$\mathcal{G}_{\rm PS} \equiv \rho_G \mathcal{G}_{\rm PS}^{\rm PFA}, \qquad \mathcal{G}_{\rm PS}^{\rm PFA} \equiv \eta_F \frac{\hbar c \pi^3 R}{120 L^4}. \tag{1}$$

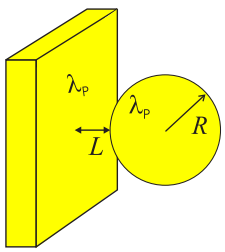

FIG. 1 (color online). The geometry of a sphere of radius R and a flat plate at a distance L (center-to-plate distance $\mathcal{L} \equiv L + R$); both mirrors are covered with a metal characterized by a plasma wavelength λ_P.

The PFA estimates $\mathcal{F}_{\rm PS}^{\rm PFA}$ and $\mathcal{G}_{\rm PS}^{\rm PFA}$ are proportional, respectively, to the energy and force calculated between two planes. They are written as products of ideal Casimir expressions and factors η_E and η_F accounting for the effect of imperfect reflection [5].

The beyond-PFA correction factors ρ_F and ρ_G appearing in (1) are the important quantities for what follows. For experiments performed with large spheres of radius $R \gg L$, the deviation from PFA is small ($\rho_F \simeq 1$). Even in this limit, it remains important to specify the accuracy of PFA in order to master the quality of theory-experiment comparison [10]. This can be done by introducing a Taylor expansion of the correction factors at small values of L/R

$$\rho_{F,G} \equiv 1 + \beta_{F,G}\frac{L}{R} + O\left(\frac{L^2}{R^2}\right). \tag{2}$$

The only experimental result available on this topic [7] may be stated as a bound on the β_G factor, namely $|\beta_G| < 0.4$. On the theoretical side, analytical as well as numerical calculations of this slope have been obtained for scalar field models [12–16]. For the situation met in experiments, with a plane and a sphere in an electromagnetic vacuum, an estimation technique has recently been proposed where the slope is deduced from a polynomial fit of the numerical values obtained at intermediate values of L/R [9,10]. The slope obtained in this manner is much larger ($\sim$8 times larger) than expected from scalar field models [10]. As a consequence, the value of β_G falls out of the bound of [7], in contrast with the scalar prediction which lies within the bound. More precise statements on this point will be given below.

On the other hand all these results correspond to perfect reflection, whereas the experiment [7] was performed with gold-covered surfaces. The apparent contradiction noticed in the preceding paragraph may thus be cured if the value of β_G differs for metallic and perfect mirrors, that is also if the effects of geometry and finite reflectivity are correlated. We show in the sequel of this Letter that this is indeed the case.

We start from the formula for the Casimir energy $\mathcal{E}_{\rm PS}$ between two scatterers in vacuum [8]

$$\begin{aligned}\mathcal{E}_{\rm PS} &= \hbar\int_0^\infty \frac{d\xi}{2\pi}\,\mathrm{logdet}(1-\mathcal{M})\\ \mathcal{M} &\equiv \mathcal{R}_S e^{-\mathcal{K}\mathcal{L}}\mathcal{R}_P e^{-\mathcal{K}\mathcal{L}}.\end{aligned} \tag{3}$$

In the geometry depicted on Fig. 1 with a sphere of radius R, a plate, and a sphere-plate separation L along the z axis (center-to-plate distance $\mathcal{L} \equiv L + R$), $\mathcal{R}_S$ and $\mathcal{R}_P$ represent the reflection operators for the spherical and the plane scatterers, respectively. They are evaluated with reference points placed at the sphere center and at its projection on the plane, respectively. The operator $e^{-\mathcal{K}\mathcal{L}}$ describes the one-way propagation between these two reference points. ξ is the imaginary field frequency integrated over the upper imaginary axis.

In order to evaluate explicitly this expression, we use two mode decompositions. The first one is a plane-wave basis $|\mathbf{k}, \phi, p\rangle_\xi$ with $\mathbf{k}$ the transverse wave vector parallel to the xy plane, p = TE, TM the polarization, and $\phi = \pm 1$ for rightward or leftward propagation directions. It is well adapted to the description of free propagation and reflection on the plane: the propagation operator $e^{-\mathcal{K}\mathcal{L}}$ is diagonal with matrix elements $e^{-K\mathcal{L}}$ such that $K = \sqrt{\xi^2/c^2 + k^2}$ ($k \equiv |\mathbf{k}|$) while reflection on the plane preserves all plane-wave quantum numbers but ϕ. The nonzero elements of $\mathcal{R}_P$ are the standard Fresnel reflection amplitudes r_p. Given values of $\mathbf{k}(k, \varphi)$ and $\phi = \pm 1$ define a direction in reciprocal space corresponding to the azimuthal angle φ and a complex angle $\theta^\pm$ such that $\sin\theta^\pm = -i\frac{ck}{\xi}$ and $\cos\theta^\pm = \pm\frac{cK}{\xi}$.

The second basis, which is adapted to the spherical symmetry of $\mathcal{R}_S$, is a multipole basis $|\ell m P\rangle_\xi$, with $\ell(\ell+1)$ and m the angular momentum eigenvalues ($\ell = 1, 2, \ldots$, $m = -\ell, \ldots, \ell$) and $P = E$, M for the electric and magnetic multipoles. By rotational symmetry around the z axis, $\mathcal{M}$ commutes with J_z. Hence it is block diagonal, with each block $\mathcal{M}^{(m)}$ corresponding to a common value of m and yielding a contribution $\mathcal{E}_{\rm PS}^{(m)}$ to the Casimir energy $\mathcal{E}_{\rm PS}$ (opposite values $\pm m$ provide identical contributions). The contribution $\mathcal{E}_{\rm PS}^{(m)}$ is written as in (3) with $\mathcal{M}$ replaced by the block matrix

$$\mathcal{M}^{(m)} = \begin{pmatrix} M^{(m)}(E,E) & M^{(m)}(E,M) \\ M^{(m)}(M,E) & M^{(m)}(M,M)\end{pmatrix}. \tag{4}$$

Each block in this matrix is the sum of TE and TM contributions $M^{(m)}(P_1, P_2) = \sum_p M_p^{(m)}(P_1, P_2)$. The diagonal blocks are written as

$$\begin{aligned}
M_{\rm TE}^{(m)}(E,E)_{\ell_1,\ell_2} &= \sqrt{\frac{\pi(2\ell_1+1)}{\ell_2(\ell_2+1)}}A^{(m)}_{\ell_1,\ell_2,\rm TE}a_{\ell_1}(i\xi)\\
M_{\rm TM}^{(m)}(E,E)_{\ell_1,\ell_2} &= \sqrt{\frac{\pi(2\ell_1+1)}{\ell_2(\ell_2+1)}}B^{(m)}_{\ell_1,\ell_2,\rm TM}a_{\ell_1}(i\xi)\\
M_{\rm TM}^{(m)}(M,M)_{\ell_1,\ell_2} &= \sqrt{\frac{\pi(2\ell_1+1)}{\ell_2(\ell_2+1)}}A^{(m)}_{\ell_1,\ell_2,\rm TM}b_{\ell_1}(i\xi)\\
M_{\rm TE}^{(m)}(M,M)_{\ell_1,\ell_2} &= \sqrt{\frac{\pi(2\ell_1+1)}{\ell_2(\ell_2+1)}}B^{(m)}_{\ell_1,\ell_2,\rm TE}b_{\ell_1}(i\xi),
\end{aligned} \tag{5}$$

$a_\ell(i\xi)$ and $b_\ell(i\xi)$ are the Mie coefficients [17] for electric and magnetic multipoles. A and B are matrices which do not depend on the radius nor on the refractive index of the sphere and are written in terms of the spherical harmonics $Y_{\ell,m}(\theta, \varphi = 0)$ and the finite rotation matrix elements $d^\ell_{m,m'}(\theta) = \langle \ell, m|e^{-i\theta J_y}|\ell, m'\rangle$ [18]

$$
\begin{aligned}
A^{(m)}_{\ell_1,\ell_2,p} &= -im\int_0^\infty \frac{dk}{K}(d^{\ell_1}_{m,1}(\theta^+) + d^{\ell_1}_{m,-1}(\theta^+)) \\
&\quad \times Y_{\ell_2 m}(\theta^-) r_p(k) e^{-2K\mathcal{L}} \\
B^{(m)}_{\ell_1,\ell_2,p} &= -\frac{c}{\xi}\int_0^\infty \frac{kdk}{K}(d^{\ell_1}_{m,1}(\theta^+) - d^{\ell_1}_{m,-1}(\theta^+)) \\
&\quad \times \partial_\theta Y_{\ell_2 m}(\theta^-) r_p(k) e^{-2K\mathcal{L}}.
\end{aligned} \tag{6}
$$

Similar expressions are found for the nondiagonal blocks, with the matrices A and B replaced, respectively, by

$$
\begin{aligned}
C^{(m)}_{\ell_1,\ell_2,p} &= \frac{c}{\xi}\int_0^\infty \frac{kdk}{K}(d^{\ell_1}_{m,1}(\theta^+) + d^{\ell_1}_{m,-1}(\theta^+)) \\
&\quad \times \partial_\theta Y_{\ell_2 m}(\theta^-) r_p(k) e^{-2K\mathcal{L}} \\
D^{(m)}_{\ell_1,\ell_2,p} &= im\int_0^\infty \frac{dk}{K}(d^{\ell_1}_{m,1}(\theta^+) - d^{\ell_1}_{m,-1}(\theta^+)) \\
&\quad \times Y_{\ell_2 m}(\theta^-) r_p(k) e^{-2K\mathcal{L}}.
\end{aligned} \tag{7}
$$

In order to go further, we assume the materials to have a dielectric response described by the plasma model $\epsilon(i\xi) = 1 + \omega_P^2/\xi^2$, with ω_P the plasma frequency and $\lambda_P = 2\pi c/\omega_P$ the plasma wavelength. Although the formalism easily allows for different values of λ_P for both surfaces, we take a common value as in the recent experiment [7]. We calculate the Casimir energy $\mathcal{E}_{\rm PS}$ and deduce the force $\mathcal{F}_{\rm PS}$ and gradient $\mathcal{G}_{\rm PS}$, both quantities being functions of the 3 length scales R, L, and λ_P. The case of perfect reflection [10] can be recovered as the limit $\lambda_P \ll R, L$ (see [19] for the opposite non-retarded limit). A large distance limit may also be taken as $\lambda_P, R \ll L$. Its result reduces to the Rayleigh expression [20] in the case ($R \ll \lambda_P$) or to 3/2 of it [9,10] in the case ($\lambda_P \ll R$).

As already discussed, the PFA expression is also contained in our general result, and it is recovered asymptotically for $R \gg L$. In the following, we discuss the results of numerical computations of the ratios $\rho_{F,G}$ defined in (1) which measure the deviation from PFA. For dimensionality reasons $\rho_{F,G}$ are functions of two dimensionless parameters built upon L, R, and λ_P ($\eta_{E,F}$ are functions of L/λ_P only [5]) and they approach unity at the PFA limit $L/R \ll 1$. Their numerical computation is done after truncating the vector space at some maximum value $\ell_{\rm max}$ of the orbital number ℓ. As a consequence of the "localization principle" [21], the results are accurate only for R/L smaller than some value which increases with $\ell_{\rm max}$. At the moment, our numerical calculations are limited to $\ell_{\rm max} = 24$, allowing us to obtain accurate results down to $L/R \simeq 0.2$ but not in close vicinity of the PFA limit.

This method gives new and interesting results, in particular, for nanospheres having a radius R with the same order of magnitude as the plasma wavelength λ_P. In this case, we can perform accurate calculations for L having a comparable magnitude, and thus explore the rich functional dependence of $\rho_{F,G}$ versus two dimensionless parameters built up on L, R, and λ_P. Figure 2 shows the results obtained for ρ_F and ρ_G with metallic and perfect mirrors. Clearly the deviation from the PFA calculated for metallic mirrors differs markedly from that already known for perfect mirrors. For small values of L/R the violation of PFA for the Casimir force and gradient turns out to be less pronounced for metallic mirrors than for perfect mirrors, while for large values of L/R it is more pronounced.

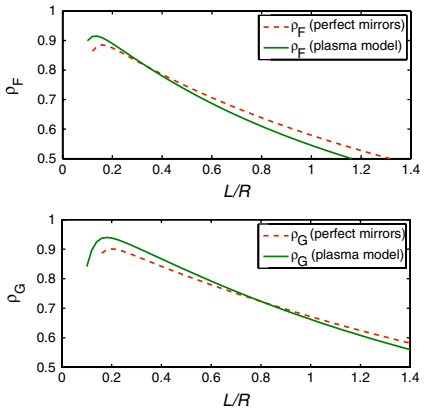

FIG. 2 (color online). Top graph: variation of ρ_F as a function of L/R, for a nanosphere of radius $R = 100$ nm; the solid green line corresponds to gold-covered plates ($\lambda_P = 136$ nm) and the dashed red line to perfect reflectors. Bottom graph: variation of ρ_G as a function of L/R, with the same conventions as in the top graph. The decreases at low values of L/R represent a numerical inaccuracy due to the limited value of $\ell_{\rm max} = 24$.

However, at values $L/R \simeq 0.2$ we find a clear correlation between geometry and finite reflectivity effects, therefore making measurements with nanospheres at small plate-sphere separations particularly interesting. This nontrivial interplay becomes evident when a polynomial fit of the numerical values of $\rho_{F,G}$ is used for inferring the behavior at small values of L/R [9,10]. In Fig. 3 we plot the quartic polynomial fits of the function ρ_G for the two cases of gold-covered and perfect mirrors. The curves were obtained by finding the best fit of the numerically computed

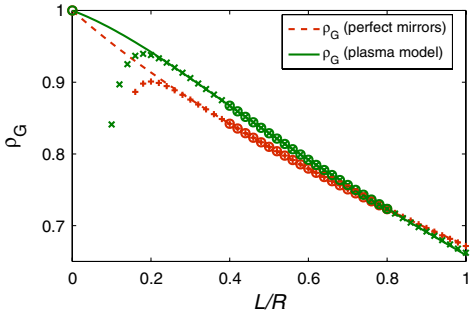

FIG. 3 (color online). Quartic polynomial fit of the function $\rho_G(L/R)$, for a nanosphere of radius $R = 100$ nm; the solid green line corresponds to gold-covered plates and the dashed red line to perfect reflectors. The crosses represent numerically evaluated points and the circles indicate those points which are used for the fit.

values of ρ_G (crosses on Fig. 3) in the window $0.4 < L/R < 0.8$ (circled crosses on Fig. 3) in the set of quartic polynomials (Taylor expansion defined as in (2) and truncated at fourth order). The left-hand bound of the window is fixed by the requirement of using only points accurately calculated with $\ell_{\max} = 24$ while the right-hand bound is determined by the truncation at fourth order of the Taylor expansion. The best fits correspond to the following polynomials for gold-covered (GM) and perfect (PM) mirrors, respectively, ($x \equiv L/R$)

$$\begin{aligned} \text{GM}&: 1 - 0.207x - 0.530x^2 + 0.645x^3 - 0.249x^4 \\ \text{PM}&: 1 - 0.483x + 0.297x^2 - 0.221x^3 + 0.080x^4. \end{aligned} \tag{8}$$

The two fits are clearly different and this, in particular, is the case for the values obtained for the slope at $L/R = 0$. The slope ($\beta_G \sim -0.21$) obtained for gold mirrors differs by more than a factor 2 from the one ($\beta_G \sim -0.48$) obtained for perfect mirrors. This is related to the bending of the curve for gold mirrors at small L/R, which describes the effect of imperfect reflection in the beyond-PFA factor ρ_G and has to be contrasted with the unbent curve for perfect mirrors. For the same reason, we observe that the slope obtained for gold mirrors is less stable under the variation of the conditions of the best-fit procedure than that for perfect mirrors. To appreciate the meaning of the bending let us recall that the slope obtained for perfect mirrors in an electromagnetic vacuum is ~ 8 times larger than expected from scalar computations [15,16] and one cannot but notice that it lies outside the bound $|\beta_G| < 0.4$ of [7]. In contrast, the slope obtained for metallic mirrors lies within the bound. Let us emphasize that there is no contradiction between the results presented here (obtained for nanospheres with $R = 100$ nm) and the experiments (performed with spheres having $R >$ a few tenths of μm).

For spheres with large radii ($L/R > 0.2$) the beyond-PFA factors $\rho_{F,G}$ have the same values for gold-covered and perfect mirrors, because the value of L is much larger than λ_P. If we extracted a slope from these results, we would obtain a value close to that of perfect mirrors, thus lying outside the bound of [7]. However, the arguments discussed before show that one should refrain from doing so. Indeed, a bending of the curve has to be expected in this case too, for values of L becoming comparable to λ_P and thus much smaller than R. In contrast, this bending has no reason to appear for perfect mirrors since there is no length scale like λ_P in this case. If the bending is similar for large and small spheres, it may turn out that the slope for gold-covered mirrors meets the bound [7] while that for perfect mirrors does not.

To sum up our results, we have written a new and exact expansion for the Casimir force between plane and spherical metallic surfaces in an electromagnetic vacuum. The results go beyond the proximity force approximation, and show a clear correlation between the plane-sphere geometry and the material properties of the metallic surfaces. They constitute a new step in the direction of accurate comparisons between Casimir experiments and QED theoretical predictions. More work is needed to obtain exact results for the Casimir force between a metallic sphere and plate in the so far experimentally explored parameter region of $L/R \simeq 0.01$, using, for example, different approaches based on semiclassical methods. Our results also indicate a complementary way to observe deviations from PFA and the interplay between geometrical and reflectivity effects in new experiments performed with nanospheres.

The authors thank M. T. Jaekel, C. Genet, D. A. R. Dalvit, D. Delande, B. Gremaud, and V. Nesvizhevsky for stimulating discussions. P. A. M. N. thanks CNPq, CAPES, Institutos do Milênio de Informação Quântica e Nanociências and ENS for financial support. I. C. P. and A. L. acknowledge financial support from the French Carnot Institute LETI.

[1] R. Onofrio, New J. Phys. **8**, 237 (2006).
[2] R. Decca, D. Lopez, and E. Fischbach *et al.*, Phys. Rev. D **75**, 077101 (2007).
[3] H. B. Chan, Y. Bao, and J. Zou *et al.*, Phys. Rev. Lett. **101**, 030401 (2008).
[4] A. Lambrecht and V. N. Marachevsky, Phys. Rev. Lett. **101**, 160403 (2008).
[5] A. Lambrecht and S. Reynaud, Eur. Phys. J. D **8**, 309 (2000).
[6] B. V. Deriagin, I. I. Abrikosova, and E. M. Lifshitz, Quart. Rev. **10**, 295 (1968).
[7] D. E. Krause, R. S. Decca, D. Lopez, and E. Fischbach, Phys. Rev. Lett. **98**, 050403 (2007).
[8] A. Lambrecht, P. A. Maia Neto, and S. Reynaud, New J. Phys. **8**, 243 (2006).
[9] T. Emig and R. L. Jaffe, J. Phys. A **41**, 164001 (2008); T. Emig, J. Stat. Mech. (2008) P04007.
[10] P. A. Maia Neto, A. Lambrecht, and S. Reynaud, Phys. Rev. A **78**, 012115 (2008).
[11] O. Kenneth and I. Klich, Phys. Rev. B **78**, 014103 (2008).
[12] M. Schaden and L. Spruch, Phys. Rev. Lett. **84**, 459 (2000).
[13] H. Gies and K. Klingmüller, Phys. Rev. Lett. **96**, 220401 (2006).
[14] A. Scardicchio and R. L. Jaffe, Nucl. Phys. B **743**, 249 (2006).
[15] A. Wirzba, J. Phys. A **41**, 164003 (2008).
[16] M. Bordag and V. Nikolaev, J. Phys. A **41**, 164002 (2008).
[17] C. F. Bohren and D. R. Huffman, *Absorption and Scattering of Light by Small Particles* (Wiley, New York, 1983), Chap. 4.
[18] A. R. Edmonds, *Angular Momentum in Quantum Mechanics* (Princeton University Press, Princeton, 1957).
[19] C. Noguez, C. E. Román-Velázquez, R. Esquivel-Sirvent, and C. Villarreal, Europhys. Lett. **67**, 191 (2004).
[20] S. Y. Buhmann, D.-G. Welsch, and T. Kampf, Phys. Rev. A **72**, 032112 (2005).
[21] H. M. Nussenzveig, *Diffraction Effects in Semiclassical Scattering* (Cambridge University Press, Cambridge, England, 1992).

Thermal Casimir Effect in the Plane-Sphere Geometry

Antoine Canaguier-Durand,[1] Paulo A. Maia Neto,[2] Astrid Lambrecht,[1] and Serge Reynaud[1]
[1]*Laboratoire Kastler Brossel, CNRS, ENS, Université Pierre et Marie Curie case 74, Campus Jussieu, F-75252 Paris Cedex 05, France*
[2]*Instituto de Física, UFRJ, CP 68528, Rio de Janeiro, RJ, 21941-972, Brazil*
(Received 4 November 2009; published 29 January 2010)

The thermal Casimir force between two metallic plates is known to depend on the description of material properties. For large separations the dissipative Drude model leads to a force a factor of 2 smaller than the lossless plasma model. Here we show that the plane-sphere geometry, in which current experiments are performed, decreases this ratio to a factor of $3/2$, as revealed by exact numerical and large-distance analytical calculations. For perfect reflectors, we find a repulsive contribution of thermal photons to the force and negative entropy values at intermediate distances.

DOI: 10.1103/PhysRevLett.104.040403 PACS numbers: 03.70.+k, 05.70.−a, 12.20.Ds, 78.20.Ci

Interest in the Casimir force, arising due to the confinement of the vacuum fluctuations of electromagnetic fields between two reflecting bodies, has been continuously growing during the last decade and the motivation for measuring it precisely has led to a number of original experiments using various modern technologies [1–7]. The Casimir force depends on a number of factors, including the bodies' material properties [8,9], their surface state [10–12] and shape. Current experiments are performed using a spherical and a plane surface. The force in this plane-sphere geometry is usually calculated within the proximity force approximation (PFA) [13] which averages the force calculated in the plane-plane geometry over the local intersurface distances. Only recently have studies been devoted to Casimir force evaluations going beyond the domain of validity of PFA [14–19].

The influence of temperature on the Casimir effect has given rise to intense discussions over the last decade [20,21], in particular, because the force exhibits an unexpectedly strong correlation with the detailed description of optical properties of the metallic surfaces used in the experiments. The dielectric function of metals is often modeled by the plasma model where the plasma frequency ω_P, depending on the density of conduction electrons, acts as a cutoff frequency above which the reflectivity goes to zero. In the Drude model which also accounts for the relaxation of conduction electrons, the dielectric function at imaginary frequencies $\omega = i\xi$ is given by $\varepsilon(i\xi) = 1 + \frac{\omega_P^2}{\xi(\xi+\gamma)}$, with the relaxation frequency γ related to the reduced dc conductivity $\sigma_0 = \frac{\omega_P^2}{\gamma}$ (see [22]). The plasma model permittivity is obtained from the Drude model one in the limit $\gamma \to 0$, while the perfect reflector's infinite permittivity is recovered with the further limit $\omega_P \to \infty$.

While the dissipative Drude model seems a more appropriate description of metallic mirrors, it turns out that recent force measurements are in better agreement with the predictions of the lossless plasma model [1]. In addition, the Casimir force between two plates at large separations turns out to be a factor of 2 smaller when calculated with the Drude model compared to the one obtained with the plasma or the perfect reflector model. This significant difference is attributed to the vanishing contribution of TE modes at zero frequency for dissipative mirrors entailing that for the Casimir force, contrary to the dielectric function, there is no continuity from the Drude to the plasma model at the limit of a vanishing relaxation [22]. In contrast to the other two models, the Drude model also leads to negative Casimir entropy values between two plates [23].

In the present Letter, we treat plane and spherical metallic surfaces coupled to electromagnetic vacuum and thermal fields with material properties described by either the perfect reflector, plasma, or Drude models, and show that the above mentioned features are considerably altered in this situation. First, the factor of 2 between the long distance forces in Drude and plasma models is reduced to a factor of $3/2$ decreasing even more below this value when small spheres are considered. Second, negative entropies are found also for the perfect reflector model, in which case they can only be related to the plane-sphere geometry and not to dissipation. Finally, PFA underestimates the Casimir force within the Drude model for short distances, while it overestimates it at all distances for the perfect reflector and plasma model.

We consider a large parameter space generated by the five length scales involved in the problem: the surface separation L, the sphere radius R, the thermal wavelength $\lambda_T = \hbar c/k_B T$ at temperature T, the plasma wavelength $\lambda_P = 2\pi c/\omega_P$, and the wavelength associated with relaxation frequency $\lambda_\gamma = 2\pi c/\gamma$. The general scattering formula [24] for the Casimir free energy $\mathcal{F}$ between a plane and a sphere is given by

$$\mathcal{F} = k_B T {\sum_n}' \log\det(1 - \mathcal{M}(\xi_n)), \qquad \xi_n = \frac{2\pi n k_B T}{\hbar}$$
$$\mathcal{M}(\xi_n) \equiv \mathcal{R}_S(\xi_n) e^{-\mathcal{K}(\xi_n)\mathcal{L}} \mathcal{R}_P(\xi_n) e^{-\mathcal{K}(\xi_n)\mathcal{L}}. \qquad (1)$$

According to (1), the operator $\mathcal{M}$ contains the reflection operators $\mathcal{R}_S$ and $\mathcal{R}_P$ of the sphere and the plane, respectively, the latter being evaluated with reference points

placed at the sphere center and at its projection on the plane, as well as the translation operators $e^{-\mathcal{K}(\xi_n)\mathcal{L}}$ describing one-way propagation between the reference points on a distance $\mathcal{L} = L + R$; the primed sum is a sum over the Matsubara frequencies ξ_n ($n \geq 0$) with the $n = 0$ term counted for a half.

The upper expression is conveniently written through a decomposition on suitable plane-wave and multipole bases. The resulting elements of the matrix $\mathcal{R}_P$ are proportional to the Fresnel reflection coefficients r_p with $p =$ TE and TM for the two electromagnetic polarizations, while those of $\mathcal{R}_S$ are proportional to the Mie coefficients a_ℓ, b_ℓ [25] for electric and magnetic multipoles at order $\ell = 1, 2, \ldots$, respectively. Because of rotational symmetry around the z axis, each eigenvalue of the angular momentum m gives a separate contribution to the Casimir free energy $\mathcal{F}^{(m)}$, obtained through the same formula as (1), with $\mathcal{M}$ reduced to the block matrix $\mathcal{M}^{(m)}$ collecting the couplings for a fixed value of m. The numerical computations presented below are done after truncating the vector space at some maximum value $\ell_{\max}$ of the orbital number ℓ. The results are thus accurate only for R/L smaller than some value which increases with $\ell_{\max}$, typically $R/L < 10$ for our $\ell_{\max} = 34$, remaining a factor of 10 below current experimental values $R/L > 10^2$.

The results of the numerical computations are shown on Fig. 1 for perfect reflectors. We have calculated the Casimir force F^{perf} between the plane and the sphere at ambient temperature and then plotted the ratio ϑ^{perf} of this force to its value at zero temperature:

$$F^{\text{perf}}(L,T) \equiv -\frac{\partial \mathcal{F}^{\text{perf}}}{\partial L}, \qquad \vartheta^{\text{perf}} \equiv \frac{F^{\text{perf}}(L,T)}{F^{\text{perf}}(L,0)}. \quad (2)$$

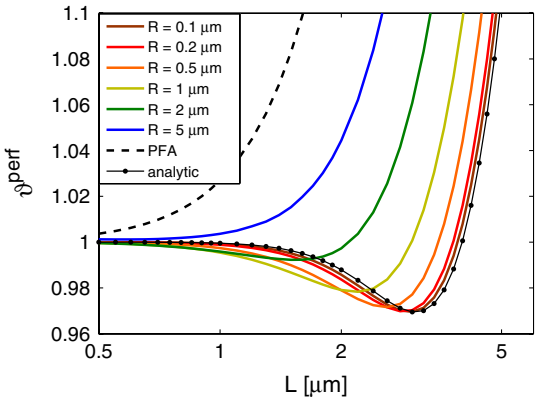

FIG. 1 (color online). Thermal Casimir force at $T = 300$ K computed between perfectly reflecting sphere and plane, divided by the zero temperature force. Solid lines from bottom to top correspond to increasing values of sphere radii. The upper dashed curve represents the PFA expression while the lower dotted curve is the analytical asymptotic expression in the $L \gg R$ limit.

The various solid curves are drawn for different radii R of the sphere as a function of the distance L, with increasing values of R from bottom to top; the upper dashed curve on Fig. 1 represents the quantity $\vartheta^{\text{perf}}_{\text{PFA}}$ as it would be obtained from (2) by using PFA ; the lower dotted curve is an analytical asymptotic expression discussed below.

Figure 2 shows the variation of the ratio ϑ^{Drud}, defined as in (2) for the Drude model with $\lambda_P = 136$ nm, $\lambda_\gamma/\lambda_P = 250$, and $\lambda_T = 7.6$ μm. The dashed curve on Fig. 2 represents $\vartheta^{\text{Drud}}_{\text{PFA}}$ as obtained for the Drude model by using PFA. We do not plot the variation of ϑ^{plas}, defined as in (2) for the plasma model, since it is as expected quite close to the one shown on Fig. 1 for perfect mirrors.

In most cases, the ratio ϑ, starting from unity at small distances, decreases below unity when the distance increases, then reaches a minimum before increasing at very large distances. While such behavior was already observed for dissipative Drude mirrors in the plane-plane geometry [21,23] (the dashed PFA curve on Fig. 2 is also below unity for $L \lesssim 4$ μm), or in the atom-surface configuration out of equilibrium [26], our computations show quite unexpectedly that in the sphere-plane geometry such a behavior takes place even for the perfect reflector and plasma models at thermodynamical equilibrium. Hence, for all three models the contribution of the thermal photons to the Casimir force can be repulsive, which suggests that the entropy could be negative for some values of the parameters (see below).

A second important feature comes out in a striking manner from the comparison of Figs. 1 and 2: the PFA always overestimates the effect of temperature on the force between mirrors described by a perfect reflector or plasma model; in contrast, it underestimates the temperature effect for the Drude model at small distances, while it overestimates it at large distances. The overestimation is, however, smaller than for perfect mirrors. As a consequence, for small separations the Drude and plasma models lead to

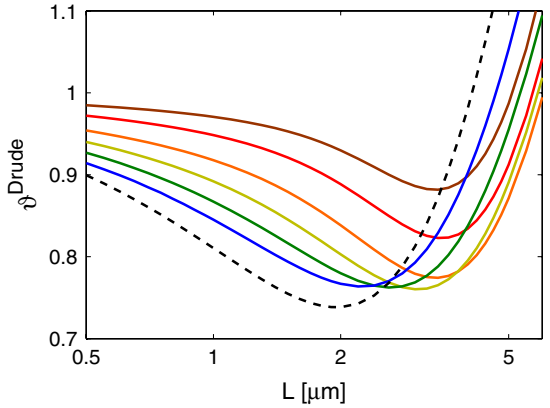

FIG. 2 (color online). Same plot as in Fig. 1 for the Casimir force at $T = 300$ K computed with the Drude model, divided by its value at zero temperature. The dashed curve correspond to the PFA expression.

Casimir force values much closer than predicted by PFA. These results clearly demonstrate the strong correlation between the effects of plane-sphere geometry, temperature and dissipation.

In the following we will corroborate the previous numerical results by presenting analytical calculations of the thermal Casimir energy in the limit of large distances ($L \gg R$). Since the number of modes $\ell_{\max}$ needed to get an accurate result decreases when L/R increases, we may take $\ell_{\max} = 1$ in this limit. Another consequence of this limit is that the reduced frequency $\tilde{\xi} \equiv \xi R/c$ is very small, since the characteristic frequencies, which give the main contribution to the Casimir force, scale as $\xi \sim c/L$.

For perfect reflectors, where $\lambda_P = 0$, the dielectric function ε is infinite at all frequencies and we obtain the following low-frequency expansions for the Mie coefficients a_1 and b_1 describing the scattering on the sphere:

$$a_1^{\text{perf}} = -\frac{2\tilde{\xi}^3}{3}, \qquad b_1^{\text{perf}} = \frac{\tilde{\xi}^3}{3}. \tag{3}$$

The other steps in the calculation of the Casimir force may then be done analytically and the sum over all Matsubara frequencies may be given in a closed form. One obtains in this manner the following approximation of the Casimir free energy:

$$\mathcal{F}^{\text{perf}} = -\frac{3\hbar c R^3}{4\lambda_T L^3}\phi(\nu), \qquad \nu \equiv \frac{2\pi L}{\lambda_T},$$
$$\phi(\nu) \equiv \frac{\nu\sinh\nu + \cosh\nu(\nu^2 + \sinh^2\nu)}{2\sinh^3\nu}, \qquad L \gg R. \tag{4}$$

The fact that the upper expression is a relevant approximation is shown on Fig. 1: the lower dotted curve, representing the value of the ratio ϑ^{perf} deduced as in (2) through a derivation of expression (4), is close to curves computed for small radii $R \ll L$. Using (4), it is straightforward to derive an analytical expression of the entropy $S \equiv -\partial\mathcal{F}/\partial T$:

$$S^{\text{perf}} = \frac{3k_B R^3}{4L^3}(\phi(\nu) + \nu\phi'(\nu)), \qquad L \gg R, \tag{5}$$

which gives negative values for $\nu \lesssim 1.5$, that is $L \lesssim 1.8$ μm at $T = 300$ K.

In addition, we can derive from (4) low- and high-temperature expressions for the free energy:

$$\mathcal{F}^{\text{perf}} \simeq -\frac{9\hbar c R^3}{16\pi L^4}\left(1 - \frac{\nu^4}{135} + \frac{4\nu^6}{945}\right), \qquad \lambda_T \gg L \gg R,$$
$$\mathcal{F}^{\text{perf}} \simeq -\frac{3\hbar c R^3}{8\lambda_T L^3}, \qquad L \gg \lambda_T, R. \tag{6}$$

Equation (6) is the large-distance high-temperature limit which can be generalized to metallic scatterers described by either the plasma or the Drude model. Starting with the lossless plasma model ($\gamma = 0$) we obtain for $L \gg \lambda_P$ Fresnel coefficients with unit modulus $r_{\text{TE}} \approx -1$, $r_{\text{TM}} \approx 1$, while the low-frequency expansion of the Mie coefficients [27], and the resulting free energy, are read, introducing the parameter $\alpha \equiv \frac{2\pi R}{\lambda_P}$:

$$a_1^{\text{plas}} \simeq -\frac{2\tilde{\xi}^3}{3}, \qquad b_1^{\text{plas}} \simeq \left(\frac{1}{3} + \frac{1}{\alpha^2} - \frac{\coth\alpha}{\alpha}\right)\tilde{\xi}^3,$$
$$\mathcal{F}^{\text{plas}} \simeq -\frac{3\hbar c R^3}{8\lambda_T L^3}\left(1 + \frac{1}{\alpha^2} - \frac{\coth\alpha}{\alpha}\right), \qquad L \gg \lambda_T, R. \tag{7}$$

The result for perfect reflection is reproduced by (7) when both $L, R \gg \lambda_P$.

For the dissipative Drude model ($\gamma \neq 0$), the low-frequency limit of the two Fresnel coefficients have the well-known form $r_{\text{TE}} \to 0$, $r_{\text{TM}} \approx 1$. The low-frequency expansion of the Mie coefficients and the ensuing free energy are read

$$a_1^{\text{Drud}} \simeq -\frac{2\tilde{\xi}^3}{3} + \frac{c\tilde{\xi}^4}{\sigma_0 R}, \qquad b_1^{\text{Drud}} \simeq \frac{\sigma_0 R\tilde{\xi}^4}{45c},$$
$$\mathcal{F}^{\text{Drud}} \simeq -\frac{\hbar c R^3}{4\lambda_T L^3}, \qquad L \gg \lambda_T, R. \tag{8}$$

The long distance free energy for the Drude model amounts to $\frac{2}{3}$ of the value for perfect mirrors whereas this ratio is $\frac{1}{2}$ in the plane-plane geometry. The latter result is explained by the fact that the TE reflection coefficient vanishes at zero frequency so that only the TM modes contribute [20,21]. The change of the ratio $\frac{1}{2}$ to $\frac{2}{3}$ in the plane-sphere geometry has to be attributed to the redistribution of the TE and TM contributions into electric and magnetic spherical eigenmodes.

Formally the results for the Drude model (8) can be obtained from the plasma model results (7) by taking the limit $R \ll \lambda_P$. In this limit, however, we should take into account the effect of quantum confinement in the small sphere, which is out of the scope of the present Letter. Two further features in (8) must be emphasized. First, the coefficient b_1 is vanishingly small in the Drude model but not in the plasma model; the latter can thus not be obtained by turning the relaxation frequency γ to zero (or σ_0 to ∞). In addition, the free energy for the Drude model is independent of the values of λ_P and γ, whereas the one for the plasma model depends on λ_P.

On Fig. 3, we illustrate the comparison of the two models by plotting the ratio of the thermal Casimir forces F^{plas} calculated with the plasma model and F^{Drud} obtained with the Drude model. Again, the plots correspond to $\lambda_P = 136$ nm and $\lambda_\gamma/\lambda_P = 250$. The results of our calculations are shown by the solid curves with the sphere radius increasing from bottom to top as in Fig. 1. The ratio $F^{\text{plas}}/F^{\text{Drud}}$ varies in the plane-sphere geometry as a function of the sphere radius, which clearly demonstrates the strong interplay between the effects of temperature, dissipation and geometry. For large spheres ($R \gg \lambda_P$), the ratio converges at long distances to the value $3/2$ which has

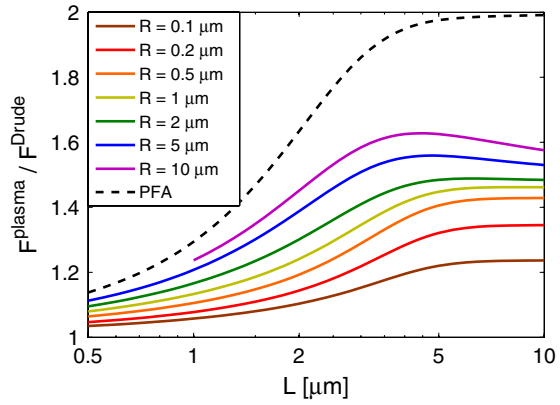

FIG. 3 (color online). Ratio of thermal Casimir force at $T = 300$ K calculated with the plasma model and the Drude model, as a function of surface separation L for different radii of the sphere. The solid curves from bottom to top correspond to increasing values of sphere radii. The dashed curve is the PFA prediction.

been obtained analytically in the preceding paragraphs, whereas it remains smaller for small spheres (down to 1.2 for $R \sim 100$ nm). The dashed curve gives the variation of the same ratio as calculated within the PFA which leads to a factor of 2 in the limits of large distances or high temperatures. We emphasize that the factor of 2 deduced within PFA is never approached at the large-distance limit within the calculations performed in the plane-sphere geometry.

To summarize we have computed exact results for the Casimir free energy and force at nonzero temperature in the plane-sphere geometry. We have given plain evidence for a strong correlation between the effects of geometry, temperature, and dissipation based on the perfect reflector, plasma, and Drude model to describe material properties. The correlation becomes clearly visible in the relative approaching of the Casimir force values computed with the Drude and plasma model, the appearance of negative entropies evidently not related to the presence of dissipation and the fact that PFA underestimates the Casimir force for the Drude model at short distances while it overestimates it for the plasma model. If the latter feature were conserved for the experimental parameter region R/L ($>10^2$), the actual values of the Casimir force calculated within plasma and Drude model could turn out to be closer than what PFA suggests, eventually diminishing the discrepancy between experimental results and predictions of the thermal Casimir force using the Drude model. Settling this question is an open and highly topical program in Casimir physics.

The authors thank G.-L. Ingold for many fruitful discussions, CAPES-COFECUB and the French Contract No. ANR-06-Nano-062 for financial support, and the ESF Research Networking Programme CASIMIR [28] for providing excellent opportunities for discussions on the Casimir effect and related topics. P. A. M. N. thanks CNPq and Faperj for financial support.

[1] R. S. Decca, D. López, E. Fischbach, G. L. Klimchitskaya, D. E. Krause, and V. M. Mostepanenko, Phys. Rev. D **75**, 077101 (2007) and references therein for prior experiments.
[2] H. B. Chan, Y. Bao, J. Zou, R. A. Cirelli, F. Klemens, W. M. Mansfield, and C. S. Pai, Phys. Rev. Lett. **101**, 030401 (2008).
[3] P. J. van Zwol, G. Palasantzas, and J. Th. M. De Hosson, Phys. Rev. B **77**, 075412 (2008).
[4] J. N. Munday, F. Capasso, and V. A. Parsegian, Nature (London) **457**, 170 (2009).
[5] G. Jourdan, A. Lambrecht, F. Comin, and J. Chevrier, Europhys. Lett. **85**, 31001 (2009).
[6] M. Masuda and M. Sasaki, Phys. Rev. Lett. **102**, 171101 (2009).
[7] S. de Man, K. Heeck, R. J. Wijngaarden, and D. Iannuzzi, Phys. Rev. Lett. **103**, 040402 (2009).
[8] E. M. Lifshitz, Sov. Phys. JETP **2**, 73 (1956).
[9] A. Lambrecht and S. Reynaud, Eur. Phys. J. D **8**, 309 (2000).
[10] G. L. Klimchitskaya, U. Mohideen, and V. M. Mostepanenko, Phys. Rev. A **61**, 062107 (2000).
[11] P. A. Maia Neto, A. Lambrecht, and S. Reynaud, Phys. Rev. A **72**, 012115 (2005).
[12] A. Lambrecht and V. N. Marachevsky, Phys. Rev. Lett. **101**, 160403 (2008).
[13] B. V. Deriagin, I. I. Abrikosova, and E. M. Lifshitz, Q. Rev. Chem. Soc. **10**, 295 (1956).
[14] D. E. Krause, R. S. Decca, D. Lopez, and E. Fischbach, Phys. Rev. Lett. **98**, 050403 (2007).
[15] P. A. Maia Neto, A. Lambrecht, and S. Reynaud, Phys. Rev. A **78**, 012115 (2008).
[16] K. Klingmuller and H. Gies, J. Phys. A **41**, 164042 (2008).
[17] O. Kenneth and I. Klich, Phys. Rev. B **78**, 014103 (2008).
[18] T. Emig, J. Stat. Mech. (2008) P04007.
[19] A. Canaguier-Durand, P. A. Maia Neto, I. Cavero-Pelaez, A. Lambrecht, and S. Reynaud, Phys. Rev. Lett. **102**, 230404 (2009).
[20] M. Boström and B. E. Sernelius, Phys. Rev. Lett. **84**, 4757 (2000).
[21] I. Brevik, S. A. Ellingsen, and K. A. Milton, New J. Phys. **8**, 236 (2006), and references therein.
[22] G.-L. Ingold, A. Lambrecht, and S. Reynaud, Phys. Rev. E **80**, 041113 (2009).
[23] V. B. Bezerra, G. L. Klimchitskaya, and V. M. Mostepanenko, Phys. Rev. A **65**, 052113 (2002).
[24] A. Lambrecht, P. A. Maia Neto, and S. Reynaud, New J. Phys. **8**, 243 (2006).
[25] C. F. Bohren and D. R. Huffman, *Absorption and Scattering of Light by Small Particles* (Wiley, New York, 1983).
[26] M. Antezza, L. P. Pitaevskii, and S. Stringari, Phys. Rev. Lett. **95**, 113202 (2005).
[27] D. B. Tanner, Phys. Rev. B **30**, 1042 (1984).
[28] http://www.casimir-network.com

PHYSICAL REVIEW A **82**, 012511 (2010)

Thermal Casimir effect for Drude metals in the plane-sphere geometry

Antoine Canaguier-Durand,[1] Paulo A. Maia Neto,[2] Astrid Lambrecht,[1] and Serge Reynaud[1]
[1]*Laboratoire Kastler Brossel, Centre National de la Recherche Scientifique, Ecole Normale Supérieure, Université Pierre et Marie Curie case 74, Campus Jussieu, F-75252 Paris Cedex 05, France*
[2]*Instituto de Física, Universidade Federal do Rio de Janeiro, Caixa Postale 68528, Rio de Janeiro, Rio de Janeiro 21941-909, Brazil*
(Received 20 May 2010; published 29 July 2010)

We compute the Casimir interaction between a plane and a sphere, the configuration employed in the most precise experiments. The scattering formula is developed by taking a suitably chosen plane-wave and multipole basis and is valid for arbitrary values of the sphere radius, interplate distance, temperature, and arbitrary dielectric functions for both sphere and plate. Our analytical and numerical results for metallic surfaces show a nontrivial interplay between the effects of curvature, temperature, finite conductivity, and dissipation.

DOI: 10.1103/PhysRevA.82.012511 PACS number(s): 31.30.jh, 03.70.+k, 05.70.−a, 78.20.Ci

I. INTRODUCTION

Measuring the Casimir force [1,2] has been the aim of an increasing number of experiments in the past few years [3–17]. The comparison of these measurements with predictions from quantum electrodynamics theory have been applied to put constraints on hypothetical new forces predicted by unification models [18,19]. Accurate theoretical computations, which account for a modeling of experimental conditions, are sorely needed for all comparisons to be reliable [20,21].

The Casimir force is indeed very sensitive to experimental conditions. The effect of finite conductivity [22] plays an essential role in the accurate determination of the force, while the contribution of thermal fluctuations gives rise to a remarkable interplay with the latter effect [23–28]. In the calculations performed for the geometry of two parallel plates, the Casimir force computed within the dissipative Drude model turns out to be a factor of 2 smaller than the result obtained within the lossless plasma model. As a consequence, the plasma theory of the Casimir effect cannot be obtained from the Drude one by taking the corresponding relaxation constant to zero. The current experimental results [11] do not explore the region where the calculations for lossy and lossless models give large differences, but their precision is sufficient to favor the plasma over the Drude theory, in spite of the dissipative nature of the metallic plates used in the experiments.

Now, the most precise experiments are performed with a spherical metallic surface in front of a plane surface. The force is usually derived from the force evaluated in the parallel-plate geometry with subsequent averaging over the local separation distances. This proximity force approximation (PFA) [29] is expected to provide an accurate description in the limit of large sphere radii (see Refs. [30,31] for derivations with perfect mirrors at zero temperature). Even if spheres used in the experiments are much larger than the typical distance between them, it remains necessary to master the beyond-PFA geometry correction [32] even for large spheres in order to match the experimental accuracy level.

There is no reason why the thermal finite conductivity and beyond-PFA corrections could be expected to be independent. Therefore, an accurate description of the experimental conditions has to take these effects into account simultaneously within a single theoretical model. In this paper, we develop the beyond-PFA scattering approach [20] for the plane-sphere geometry at finite temperature, with material properties described by either the perfect reflector, the plasma, or the Drude models. We show that the interplay between temperature and material properties is drastically affected when the parallel-plate configuration is replaced by the plane-sphere geometry. The results obtained from the Drude and plasma models are generally closer to each other than in the parallel-plate geometry. In particular, the factor of 2 between the two models reached at the limit of long distances between parallel plates is reduced to 3/2 for a plate and a sphere, and even less if small spheres are considered. Finally, we find that PFA underestimates the thermal contribution to the Casimir force for the Drude model at short distances, whereas it overestimates it at all distances for the perfect reflector and plasma models.

We start from the scattering theory of Casimir interaction [20], which allows one to consider nontrivial geometries at finite temperatures together with a realistic description of the material properties. The Casimir free energy is written in terms of general reflection operators, which describe nonspecular diffraction by the material surfaces. The resulting formula provides a compact way of taking the multiple scatterings between the interacting bodies into account [33]. In the particular case of parallel-plane surfaces, the reflection operators are diagonal in the plane-wave basis, so that the Casimir free energy is given in terms of specular reflection coefficients [34]. In the plane-sphere geometry, scattering on the sphere is easily made explicit in the multipole spherical-wave basis [35] (see also Ref. [36] for a treatment of nonretarded interactions). It is also essential to combine the multipole basis with the plane-wave basis [37] well adapted to the treatment of nonideal reflection by metals. By judiciously employing the two bases at appropriate steps of the derivation, the scattering formalism, thus, allows to analyze the interplay between geometry and finite conductivity at zero [38] and nonzero temperatures [39].

Let us note that, in recent years, several papers have been devoted to the study of the Casimir effect in nonplanar geometries. In addition to the already cited papers, let us refer to the following applications of the scattering approach [40–47] or of alternative methods [48–55]. The first application of the scattering approach to nontrivial geometries and nonideal reflectors can be found in Refs. [56–58]. An historical

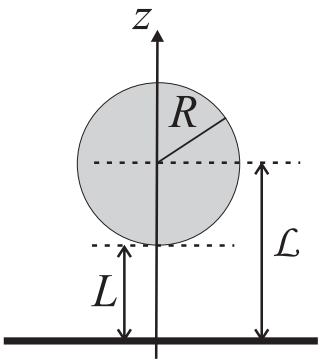

FIG. 1. Sphere of radius R and a flat plate at a distance L, with center-to-plate distance $\mathcal{L} \equiv L + R$.

overview of the various forms of the multiple-scattering method can be found in Ref. [59]. In this paper, we analyze, in a detailed manner, the full interplay between finite conductivity, finite temperature, and plane-sphere geometry, which was only briefly discussed in Ref. [39].

This paper is organized as follows: Our main goals and basic notations are presented in Sec. II. In Sec. III, we develop the scattering approach for the plane-sphere geometry and derive the formal results used in Secs. IV (perfect reflectors) and V (plasma and Drude models). Concluding remarks are presented in Sec. VI.

II. DEFINITIONS AND GENERAL OUTLOOK

We consider the Casimir interaction between a metallic sphere of radius R and a metallic plate at a distance of closest approach L at an arbitrary temperature T, as shown in Fig. 1. The center-to-plate distance is

$$\mathcal{L} = L + R.$$

Experimental results for the Casimir force in the plane-sphere geometry are usually compared with PFA-based theoretical models [29]. The spherical surface is assumed to be nearly flat over a scale of the order of L, and then the total Casimir energy is obtained by adding the contributions corresponding to different local interplate distances over the sphere surface. Although the Casimir energy is not additive, PFA is usually expected to provide an accurate description when $R \gg L$. The resulting Casimir force $F^{\rm PFA}$ is

$$F^{\rm PFA} = 2\pi R \frac{\mathcal{F}_{\rm PP}}{A}. \tag{1}$$

$\mathcal{F}_{\rm PP}$ is the Casimir free energy for two parallel plates of area A. Thus, PFA neglects diffraction due to the sphere curvature and provides a direct connection to the parallel-plate geometry. The resulting force is proportional to the Casimir free energy per unit area calculated for this much simpler geometry.

In this paper, we develop an exact theoretical model that takes diffraction fully into account. We first compute the Casimir free energy $\mathcal{F}(L,T)$ for the plane-sphere geometry from the scattering formula [20] (Sec. III) and then derive the force F and the entropy S from

$$F = -\frac{\partial \mathcal{F}}{\partial L}, \quad S = -\frac{\partial \mathcal{F}}{\partial T}. \tag{2}$$

The latter is at the core of the ongoing debate about a possible violation of the third law of thermodynamics in the dissipative Drude model [25,27]. Negative Casimir entropy values found for parallel plates have been explained in terms of the coupling to a heat bath associated with dissipation [28]. However, here, we find negative entropies even for the perfect reflector model, which shows that geometry itself plays a nontrivial thermodynamical role, provided that beyond-PFA diffraction effects are taken into account.

To quantify the deviation from PFA, we define the quantity:

$$\rho_F = \frac{F}{F^{\rm PFA}}. \tag{3}$$

The ratio,

$$\vartheta = \frac{F(L,T)}{F(L,0)} \tag{4}$$

represents the temperature correction at a given separation distance and for a given model. In Secs. IV and V, we calculate ρ_F and ϑ for the perfect reflector, plasma, and Drude models for metallic surfaces.

The Drude dielectric function,

$$\epsilon(i\xi) = 1 + \frac{\omega_P^2}{\xi(\xi+\gamma)}, \tag{5}$$

at imaginary frequencies $\omega = i\xi$, contains two frequency scales: the plasma frequency ω_P and the relaxation frequency γ. The plasma dielectric function is obtained from Eq. (5) in the lossless limit $\gamma \to 0$. Note, however, that there is no continuity in the Casimir force from the Drude to the plasma model in this limit [28]. By taking the further limit $\omega_P \to \infty$ from the plasma model, we recover the perfect reflector limit (to be discussed in Sec. IV), which corresponds to an infinite dielectric function at all frequencies.

In Sec. V, we provide a detailed comparison between plasma and Drude models for the Casimir effect. Since the dc conductivity $\sigma_0 = \omega_P^2/\gamma$ diverges in the limit $\gamma \to 0$, the Drude model is expected, in principle, to provide a more realistic description of normal (i.e., nonsuperconducting) metals. However, experimental data are surprisingly in better agreement with the plasma model when PFA is employed to analyze the plane-sphere geometry [11]. Here, we show that the results from the two models are actually closer than predicted by PFA-based theories, which might help to solve this paradox. We consider a rich parameter space containing five different length scales: In addition to the geometrical scales L and R, our problem contains the thermal wavelength (k_B is the Boltzmann constant),

$$\lambda_T = \frac{\hbar c}{k_B T},$$

the plasma wavelength $\lambda_P = 2\pi c/\omega_P$, and the wavelength that corresponds to the relaxation frequency $\lambda_\gamma = 2\pi c/\gamma$. Different orderings of these length scales can, in principle, be considered, which lead to various regimes associated with nontrivial interplays between temperature, geometry, finite conductivity, and dissipation. Most experiments are performed with gold at room temperature, hence, the numerical results presented in Secs. III, IV and V correspond to $\lambda_T = 7.6\ \mu$m, $\lambda_P = 136$ nm (plasma and Drude), and $\lambda_\gamma/\lambda_P = 250$ (Drude).

III. SCATTERING APPROACH IN THE PLANE-SPHERE GEOMETRY

In this section, we apply the scattering approach to the plane-sphere geometry (see Fig. 1) at finite temperature. The Casimir free energy is written as a sum over the Matsubara frequencies ξ_n ($n \geqslant 0$) [20]:

$$\mathcal{F} = k_B T \sum_n{}' \ln\det[1-\mathcal{M}(\xi_n)], \quad \xi_n = \frac{2\pi n k_B T}{\hbar}, \\ \mathcal{M}(\xi) \equiv \mathcal{R}_S(\xi) e^{-\mathcal{K}(\xi)\mathcal{L}} \mathcal{R}_P(\xi) e^{-\mathcal{K}(\xi)\mathcal{L}}, \tag{6}$$

where the primed sum means that the $n=0$ term is counted for a half. The reflection operators of the sphere $\mathcal{R}_S(\xi)$ and the plate $\mathcal{R}_P(\xi)$ are evaluated with reference points at the sphere center and at its projection on the plane, respectively. The operator $e^{-\mathcal{K}(\xi)\mathcal{L}}$ accounts for one-way propagation along the z axis between these points, separated by the length $\mathcal{L}$. Thus, the operator $\mathcal{M}(\xi)$ represents one round-trip propagation inside the open cavity formed by the two surfaces.

The plane-wave basis $|\mathbf{k},\pm,p\rangle_\xi$ [$\mathbf{k}$ = wave-vector component parallel to the xy plane, p = TE,TM for polarization and +(−) for upward (downward) propagation direction] is well adapted to the description of the propagation operator $e^{-\mathcal{K}(\xi)\mathcal{L}}$, which is diagonal in this basis with matrix elements $e^{-\kappa\mathcal{L}}$, where $\kappa = \sqrt{\xi^2/c^2 + k^2}$ represents the wave-vector z component associated with the imaginary frequency ξ. Reflection on the plane also preserves all plane-wave quantum numbers but the propagation direction, and the nonzero elements of $\mathcal{R}_P(\xi)$ are given by the standard Fresnel specular reflection amplitudes $r_p(\mathbf{k},\xi)$ for a homogenous medium.

On the other hand, the multipole basis $|\ell m P\rangle_\xi$, with $\ell(\ell+1)$ and m, which denote the usual angular momentum eigenvalues (with $\ell = 1,2,\ldots,m=-\ell,\ldots,\ell$) and $P = E,M$, which represent electric and magnetic multipoles, is well adapted to the spherical symmetry of $\mathcal{R}_S(\xi)$. By rotational symmetry around the z axis, $\mathcal{M}(\xi)$ commutes with the angular momentum operator J_z. Hence, $\mathcal{M}(\xi)$ is block diagonal, and each block $\mathcal{M}^{(m)}(\xi)$ (which corresponds to a given subspace m) yields an independent contribution to the Casimir energy. We find its matrix elements in the multipole basis after introducing the spectral resolution of the identity operator in the plane-wave basis:

$$\mathcal{M}^{(m)}(\xi)_{1,2} = \int \frac{d^2\mathbf{k}}{(2\pi)^2} \sum_{p=\mathrm{TE,TM}} \langle \ell_1 m P_1|\mathcal{R}_S(\xi)|\mathbf{k},+,p\rangle \\ \times r_p(\mathbf{k},\xi) e^{-2\kappa\mathcal{L}} \langle \mathbf{k},-,p|\ell_2 m P_2\rangle. \tag{7}$$

This expression has a simple interpretation when read from right to left: A multipole wave $|\ell_2 m P_2\rangle$ is first decomposed into plane waves (coefficients $\langle \mathbf{k},-,p|\ell_2 m P_2\rangle$), which propagate toward the plane (factor $e^{-\kappa\mathcal{L}}$). After reflection by the plane [specular amplitude $r_p(\mathbf{k},\xi)$], the plane-wave components propagate back to the sphere (second factor $e^{-\kappa\mathcal{L}}$) and are finally scattered into a new multipole wave $|\ell_1 m P_1\rangle$.

The matrix elements of $\mathcal{R}_S$ in Eq. (7) represent the multipole components of the field scattered by the sphere for a given incident plane wave. In Mie scattering calculations, one usually assumes that the incident plane wave propagates along the z direction [60]. Here, this is no longer possible, since we have to consider field modes that propagate simultaneously along all possible directions. It is then useful to reformulate [61] the Mie scattering expressions in terms of the matrix elements of finite rotation [62],

$$d^\ell_{m,m'}(\theta) = \langle \ell m|e^{-i\theta J_y}|\ell m'\rangle,$$

with $m' = \pm 1$ accounting for the photon spin.

The resulting expressions for $\langle \ell_1 m P_1|\mathcal{R}_S(\xi)|\mathbf{k},+,p\rangle$ (see the Appendix), are proportional to the Mie coefficients $a_\ell(i\xi)$ and $b_\ell(i\xi)$ [60], which represent the scattering amplitudes for electric and magnetic multipole waves. At the imaginary frequency axis, they are written in terms of the modified Bessel functions [63] evaluated at the size parameter,

$$\tilde{\xi} = \frac{\xi R}{c},$$

as follows:

$$a_\ell(i\tilde{\xi}) = \frac{\pi}{2} \frac{n^2 s_\ell^{(a)} - s_\ell^{(b)}}{n^2 s_\ell^{(c)} - s_\ell^{(d)}}, \tag{8}$$

$$b_\ell(i\tilde{\xi}) = \frac{\pi}{2} \frac{s_\ell^{(a)} - s_\ell^{(b)}}{s_\ell^{(c)} - s_\ell^{(d)}}, \tag{9}$$

$$s_\ell^{(a)} = I_{\ell+1/2}(n\tilde{\xi})[I_{\ell+1/2}(\tilde{\xi}) - \tilde{\xi} I_{\ell-1/2}(\tilde{\xi})], \\ s_\ell^{(b)} = I_{\ell+1/2}(\tilde{\xi})[I_{\ell+1/2}(n\tilde{\xi}) - n\tilde{\xi} I_{\ell-1/2}(n\tilde{\xi})], \\ s_\ell^{(c)} = I_{\ell+1/2}(n\tilde{\xi})[K_{\ell+1/2}(\tilde{\xi}) + \tilde{\xi} K_{\ell-1/2}(\tilde{\xi})], \\ s_\ell^{(d)} = K_{\ell+1/2}(\tilde{\xi})[I_{\ell+1/2}(n\tilde{\xi}) - n\tilde{\xi} I_{\ell-1/2}(n\tilde{\xi})],$$

with $n = \sqrt{\epsilon}$ representing the sphere refractive index.

In the Appendix, we also derive the change-of-basis matrix elements $\langle \mathbf{k},-,p|\ell_2 m P_2\rangle$. They yield, when replaced into Eq. (7), explicit expressions for the matrix elements of the round-trip operator $\mathcal{M}^{(m)}(\xi)$, which we organize as a block matrix:

$$\mathcal{M}^{(m)}(\xi) = \begin{bmatrix} \mathcal{M}^{(m)}(E,E) & \mathcal{M}^{(m)}(E,M) \\ \mathcal{M}^{(m)}(M,E) & \mathcal{M}^{(m)}(M,M) \end{bmatrix}. \tag{10}$$

Each block is the sum of TE and TM contributions: $\mathcal{M}^{(m)}(P_1,P_2) = \sum_p \mathcal{M}^{(m)}_p(P_1,P_2)$. For the diagonal blocks, we find

$$\mathcal{M}^{(m)}_{\mathrm{TE}}(E,E)_{\ell_1,\ell_2} = \sqrt{\frac{(2\ell_1+1)\pi}{\ell_2(\ell_2+1)}} A^{(m)}_{\ell_1,\ell_2,\mathrm{TE}} a_{\ell_1}(i\xi), \tag{11}$$

$$\mathcal{M}^{(m)}_{\mathrm{TM}}(E,E)_{\ell_1,\ell_2} = \sqrt{\frac{(2\ell_1+1)\pi}{\ell_2(\ell_2+1)}} B^{(m)}_{\ell_1,\ell_2,\mathrm{TM}} a_{\ell_1}(i\xi), \tag{12}$$

$$\mathcal{M}^{(m)}_{\mathrm{TM}}(M,M)_{\ell_1,\ell_2} = \sqrt{\frac{(2\ell_1+1)\pi}{\ell_2(\ell_2+1)}} A^{(m)}_{\ell_1,\ell_2,\mathrm{TM}} b_{\ell_1}(i\xi), \tag{13}$$

$$\mathcal{M}^{(m)}_{\mathrm{TE}}(M,M)_{\ell_1,\ell_2} = \sqrt{\frac{(2\ell_1+1)\pi}{\ell_2(\ell_2+1)}} B^{(m)}_{\ell_1,\ell_2,\mathrm{TE}} b_{\ell_1}(i\xi). \tag{14}$$

The matrices $A^{(m)}$ and $B^{(m)}$ neither depend on the radius R nor on the refractive index of the sphere (spherical harmonics

$Y_{\ell m}(\theta,\varphi)$ [62] calculated at the azimuthal angle $\varphi = 0$):

$$A^{(m)}_{\ell_1,\ell_2,p} = -im\int_0^\infty \frac{dk}{\kappa}\left[d^{\ell_1}_{m,1}(\theta^{(+)}) + d^{\ell_1}_{m,-1}(\theta^{(+)})\right] \times Y_{\ell_2 m}(\theta^-)\, r_p(k)\, \exp(-2\kappa\mathcal{L}), \tag{15}$$

$$B^{(m)}_{\ell_1,\ell_2,p} = -\frac{c}{\xi}\int_0^\infty dk\,\frac{k}{\kappa}\left[d^{\ell_1}_{m,1}(\theta^{(+)}) - d^{\ell_1}_{m,-1}(\theta^{(+)})\right] \times \partial_\theta Y_{\ell_2 m}(\theta^-)\, r_p(k)\, \exp(-2\kappa\mathcal{L}), \tag{16}$$

$$\sin\theta^\pm = -i\frac{ck}{\xi}, \quad \cos\theta^\pm = \pm\frac{c\kappa}{\xi}, \quad \kappa \equiv \sqrt{\xi^2/c^2 + k^2}. \tag{17}$$

Similar expressions are found for the nondiagonal blocks:

$$\mathcal{M}^{(m)}_{\mathrm{TE}}(E,M)_{\ell_1,\ell_2} = i\sqrt{\frac{(2\ell_1+1)\pi}{\ell_2(\ell_2+1)}}\,C^{(m)}_{\ell_1,\ell_2,\mathrm{TE}}\,a_{\ell_1}(i\xi),$$

$$\mathcal{M}^{(m)}_{\mathrm{TM}}(E,M)_{\ell_1,\ell_2} = i\sqrt{\frac{(2\ell_1+1)\pi}{\ell_2(\ell_2+1)}}\,D^{(m)}_{\ell_1,\ell_2,\mathrm{TM}}\,a_{\ell_1}(i\xi),$$

$$\mathcal{M}^{(m)}_{\mathrm{TM}}(M,E)_{\ell_1,\ell_2} = -i\sqrt{\frac{(2\ell_1+1)\pi}{\ell_2(\ell_2+1)}}\,C^{(m)}_{\ell_1,\ell_2,\mathrm{TM}}\,b_{\ell_1}(i\xi),$$

$$\mathcal{M}^{(m)}_{\mathrm{TE}}(M,E)_{\ell_1,\ell_2} = -i\sqrt{\frac{(2\ell_1+1)\pi}{\ell_2(\ell_2+1)}}\,D^{(m)}_{\ell_1,\ell_2,\mathrm{TE}}\,b_{\ell_1}(i\xi).$$

$C^{(m)}$ and $D^{(m)}$ are also written in terms of spherical harmonics and rotation matrices:

$$C^{(m)}_{\ell_1,\ell_2,p} = \frac{c}{\xi}\int_0^\infty dk\,\frac{k}{\kappa}\left[d^{\ell_1}_{m,1}(\theta^{(+)}) + d^{\ell_1}_{m,-1}(\theta^{(+)})\right] \times \partial_\theta Y_{\ell_2 m}(\theta^-)\, r_p(k)\, \exp(-2\kappa\mathcal{L}), \tag{18}$$

$$D^{(m)}_{\ell_1,\ell_2,p} = im\int_0^\infty \frac{dk}{\kappa}\left[d^{\ell_1}_{m,1}(\theta^{(+)}) - d^{\ell_1}_{m,-1}(\theta^{(+)})\right] \times Y_{\ell_2 m}(\theta^-)\, r_p(k)\, \exp(-2\kappa\mathcal{L}). \tag{19}$$

By inspection of Eqs. (15) and (16), it is easy to show that the diagonal blocks are invariant when we replace $m \to -m$, whereas the nondiagonal blocks given by Eqs. (18) and (19) change sign. Thus, the matrix $\mathcal{M}^{(0)}$ is block diagonal and $\det[1 - \mathcal{M}^{(m)}(\xi_n)]$ does not depend on the sign of m, by allowing us to write the Casimir free energy as a double primed sum (with only nonnegative values of m):

$$\mathcal{F} = 2k_BT\sum_n{}'\sum_m{}'\ln\det[1 - \mathcal{M}^{(m)}(\xi_n)]. \tag{20}$$

The zero-temperature limit can also be obtained from Eq. (20) by changing the sum over Matsubara frequencies by an integral over ξ:

$$k_BT\sum_n{}' \to \hbar\int_0^\infty \frac{d\xi}{2\pi} \quad (T \to 0). \tag{21}$$

A. Numerical considerations

When evaluating the free energy from Eq. (20), one needs to truncate the vector space at some maximum value $\ell_{\max}$ of angular momentum. From the localization principle [64], the value of $\ell_{\max}$ required for a given accuracy level is expected to scale with the size parameter $\tilde{\xi}$, which captures the dependence of $\mathcal{M}^{(m)}$ on the sphere radius according to Eqs. (8) and (9). Characteristic frequencies give the main contribution to the Casimir energy scale as $\xi \sim c/L$. As a consequence, the required $\ell_{\max}$ should scale as R/L for intermediate and short separation distances. This is verified by the numerical evaluations discussed in the following. They are limited to $\ell_{\max} = 85$ at the moment ($\ell_{\max} = 45$ for Drude model), by allowing us to calculate for $R/L < 20$ ($R/L < 10$ for Drude model), not far from the experimental range [32] $R/L \gtrsim 10^2$, which would require a larger $\ell_{\max}$.

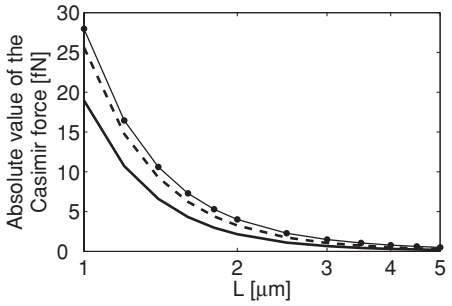

FIG. 2. Casimir force as a function of distance L at $T = 300$ K for a sphere radius $R = 10$ μm, computed for perfect reflectors (dashed) or gold surfaces described by the Drude model (solid). The dotted line represents the PFA result for perfect reflectors.

Apart from this restriction, we are able to calculate the exact Casimir free energy and force for parameters closely mimicking the experimental conditions. As a first example, in Fig. 2, we plot the Casimir force as a function of L for a sphere of radius $R = 10$ μm at room temperature. The dashed and solid lines correspond to the perfect reflector model (to be discussed in detail in Sec. IV) and to the Drude model (Sec. V), respectively. We also show the PFA result for perfect reflectors (dotted line). The interplay between the effects of temperature, geometry, finite conductivity, and dissipation is better understood when considering the ratios defined in Sec. II, which are analyzed in detail in Secs. IV and V. At the limit of large separation distances, simple analytical results can be derived, as discussed later.

B. Large-distance limit

When $R \ll \mathcal{L}$, the characteristic size parameters scale as $\tilde{\xi} \sim R/\mathcal{L} \ll 1$ and the Mie coefficients $a_\ell(i\xi) \sim \tilde{\xi}^{2\ell+1}$, with the magnetic coefficients $b_\ell(i\xi)$ of the same order or smaller than $a_\ell(i\xi)$ depending on the material properties of the sphere. The resulting matrix elements $\mathcal{M}^{(m)}(P,P')_{\ell_1,\ell_2}$ are very small, and the dominant contribution comes from $\ell = 1$ ($m = 0,1$), which corresponds to the dipole contributions:

$$\ln\det(1 - \mathcal{M}^{(m)}) \approx -\sum_{P=E,M}\mathcal{M}^{(m)}(P,P)_{1,1}. \tag{22}$$

The explicit expressions for the electric dipole matrix elements are obtained from Eqs. (11), (12), (15)

and (16):

$$\mathcal{M}^{(0)}(E,E)_{1,1} = -\frac{3a_1(i\xi)}{2(\xi/c)^3}\int_0^\infty dk\frac{k^3}{\kappa}r_{\rm TM}e^{-2\kappa\mathcal{L}}, \tag{23}$$

$$\mathcal{M}^{(1)}(E,E)_{1,1} = \frac{3a_1(i\xi)}{4(\xi/c)^3}\int_0^\infty dk\left(\frac{k\xi^2}{c^2\kappa}r_{\rm TE} - k\kappa\, r_{\rm TM}\right)e^{-2\kappa\mathcal{L}}. \tag{24}$$

The magnetic dipole elements are obtained from Eqs. (23) and (24) by replacing $a_1(i\xi) \to b_1(i\xi)$ and by interchanging $r_{\rm TM} \leftrightarrow r_{\rm TE}$. When the refractive index is finite, its contribution is negligible, and then the dominant contribution is the electric dipole one (Rayleigh scattering). To proceed further, we need to specify the material properties for the sphere and the plane and the corresponding Mie and Fresnel coefficients that appear in Eqs. (23) and (24). In Secs. IV and V, we consider perfect reflectors, plasma, and Drude metals.

IV. PERFECT REFLECTORS

Within the perfect reflector model for metals, the dielectric permittivity is taken to be infinite at all frequencies. This simple albeit unphysical model for metals provides an accurate description at large separations in the ideal zero-temperature case. At finite temperatures, however, it is still unclear if the perfect reflector model reproduces the correct long-distance regime for real metals. In fact, for parallel plates, it predicts a force twice as large as the value obtained within the dissipative Drude model for metals in the long-distance limit, while we would, in principle, expect the two results to agree in this limit.

It is, thus, extremely important to compare the results obtained from the different models for the plane-sphere geometry. In this section, we start with the perfect reflector model, with Fresnel reflection coefficients $r_{\rm TE}^{\rm perf} = -r_{\rm TM}^{\rm perf} = -1$. The Mie coefficients are obtained by taking $n \gg 1$ and $n\tilde{\xi} \gg 1$ in Eqs. (8) and (9):

$$a_\ell^{\rm perf}(i\xi) = \frac{\pi}{2}(-)^{\ell+1}\frac{\ell I_{\ell+1/2}(\tilde{\xi}) - \tilde{\xi} I_{\ell-1/2}(\tilde{\xi})}{\ell K_{\ell+1/2}(\tilde{\xi}) + \tilde{\xi} K_{\ell-1/2}(\tilde{\xi})}, \tag{25}$$

$$b_\ell^{\rm perf}(i\xi) = \frac{\pi}{2}(-)^{\ell+1}\frac{I_{\ell+1/2}(\tilde{\xi})}{K_{\ell+1/2}(\tilde{\xi})}. \tag{26}$$

The Fresnel and Mie coefficients written previously can also be obtained from the plasma model expressions (discussed in Sec. V) by taking the limit $\lambda_P \to 0$.

A. Large-distance limit for perfect reflectors

For $\tilde{\xi} \ll 1$, we may take the power expansion of Eqs. (25) and (26):

$$a_1^{\rm perf}(i\tilde{\xi}) = -\tfrac{2}{3}\tilde{\xi}^3 + O(\tilde{\xi})^5, \quad b_1^{\rm perf}(i\tilde{\xi}) = \tfrac{1}{3}\tilde{\xi}^3 + O(\tilde{\xi})^5. \tag{27}$$

Note that b_1, which represents the magnetic dipole contribution, is of the same order of the electric dipole coefficient a_1 for $\tilde{\xi} \ll 1$. This property holds whenever $n\tilde{\xi} \gg 1$, which is also the case for the plasma model at low frequencies when $\lambda_P \ll R$. On the other hand, for any finite-dielectric constant, the magnetic dipole is always of the order of the electric quadrupole and, thus, much smaller than the electric dipole contribution in the low-frequency limit. We find this so-called Rayleigh scattering regime when discussing the long-distance limit within the Drude model in Sec. V.

We insert Eq. (27) and the values for the Fresnel coefficients into Eqs. (20)–(24) and write the resulting expression for the free energy in terms of the thermal wavelength λ_T:

$$\mathcal{F}^{\rm perf} = -\frac{3R^3}{4\mathcal{L}^3}\frac{\hbar c}{\lambda_T}{\sum_n}'(1 + 2\nu n + 2\nu^2 n^2)e^{-2\nu n}, \tag{28}$$

$$\nu = \frac{2\pi\mathcal{L}}{\lambda_T}. \tag{29}$$

The evaluation of the sum over Matsubara frequencies in Eq. (28) is straightforward:

$$\mathcal{F}^{\rm perf} = -\frac{3\hbar c R^3}{4\lambda_T\mathcal{L}^3}\phi(\nu), \quad \mathcal{L} \gg R,$$
$$\phi(\nu) \equiv \frac{\nu\,\sinh\,\nu + \cosh\,\nu(\nu^2 + \sinh^2\,\nu)}{2\,\sinh^3\,\nu}. \tag{30}$$

The low-temperature approximation is derived by expanding $\phi(\nu)$ in powers of ν:

$$\mathcal{F}^{\rm perf} \approx -\frac{9\hbar c R^3}{16\pi\mathcal{L}^4}\left(1 - \frac{\nu^4}{135} + \frac{4\nu^6}{945}\right), \quad \lambda_T \gg \mathcal{L} \gg R. \tag{31}$$

Note that the zero-temperature limit contained in the preceding expression can also be obtained by replacing the sum over n in Eq. (28) by an integral over ξ as in Eq. (21).

The first finite-temperature correction in Eq. (31) does not depend on $\mathcal{L}$ so that the temperature correction to the Casimir force comes from the next-to-leading-order term, proportional to $(k_BT)^6$. It is a repulsive contribution from thermal photons that makes the net force slightly less attractive. We discuss this point further in the context of the numerical evaluations presented as follows. We can compute the high-temperature limit by taking $\nu \to \infty$ in Eq. (30) or by considering the $n = 0$ Matsubara frequency contribution in Eq. (28):

$$\mathcal{F}^{\rm perf} \approx -\frac{3\hbar c R^3}{8\lambda_T\mathcal{L}^3}, \quad \mathcal{L} \gg \lambda_T, R. \tag{32}$$

It is also interesting to compute the Casimir entropy from Eq. (30):

$$S^{\rm perf} = \frac{3k_BR^3}{4\mathcal{L}^3}[\phi(\nu) + \nu\phi'(\nu)], \quad \mathcal{L} \gg R. \tag{33}$$

Remarkably, this expression yields $S^{\rm perf} < 0$ for $\nu \lesssim 1.5$, that is $L \lesssim 1.8\ \mu$m at $T = 300$ K. In the parallel-plate geometry, negative entropies have been found for the dissipative Drude model only [65]. Here, we also find negative entropies for perfect reflectors over a wide separation distance range, as discussed in the following.

B. Numerical results

In Fig. 3(a), we plot the ratio $\vartheta^{\rm perf}$ [see Eq. (4)], by quantifying the thermal correction to the Casimir force, for different sphere radii as a function of the separation distance L. We also show the results obtained by using the PFA

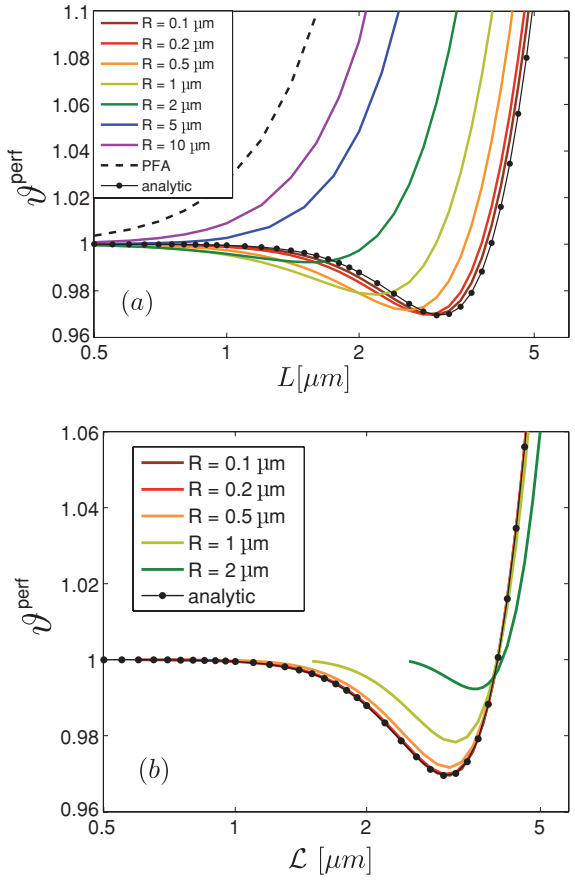

FIG. 3. (Color online) Thermal Casimir force at $T = 300$ K computed between perfectly reflecting sphere and plane, divided by the zero-temperature force, as function of (a) surface distance L and (b) distance-to-center $\mathcal{L}$. Solid lines from bottom to top correspond to increasing values of sphere radii. The upper dashed curve represents the PFA result, while the lower dotted line corresponds to the analytical large-distance expression.

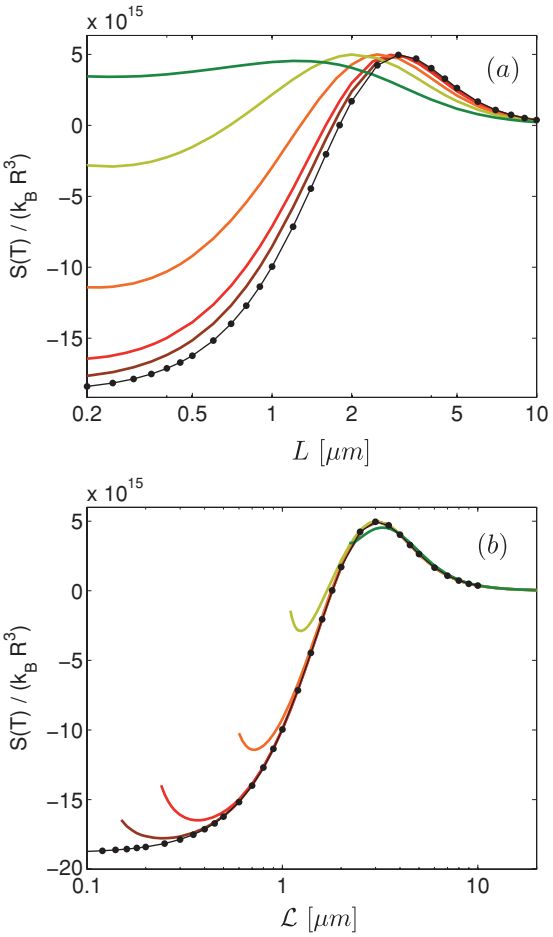

FIG. 4. (Color online) Casimir entropy at $T = 300$ K computed for perfectly reflecting sphere and plane, as a function of (a) surface separation distance L and (b) center-to-plate distance $\mathcal{L}$. The conventions are the same as in Fig. 3.

formula Eq. (1) (dashed line) and by deriving the analytical long-distance expression Eq. (30) with respect to L after replacing $\mathcal{L} \approx L$ (dotted line). As expected, the agreement with the analytical formula is better than if we keep the variable $\mathcal{L}$ in Eq. (30), as shown in Fig. 3(b), where we plot $\vartheta^{\rm perf}$ as a function of $\mathcal{L}$.

At very short distances $L \ll \lambda_T$, we recover, as expected, the zero-temperature result ($\vartheta = 1$). As the distance increases, we find, in most cases, that ϑ decreases below one, reaches a radius-dependent minimum, and then increases again at long distances. As long as R is not too large, the thermal photons provide a repulsive contribution (thus, decreasing the magnitude of the overall attractive force) over a distance range that becomes wider as R decreases. This range corresponds to $L \lesssim \lambda_T/\pi$ when $R \ll L$, as obtained from Eq. (30).

The reduction of the Casimir force is consistent with the negative Casimir entropies found from Eq. (33) in the limit $R \ll L$. We plot S as a function of L [Fig. 4(a)] or $\mathcal{L}$ [Fig. 4(b)] for different sphere radii. Figure 4(b) shows that Eq. (33) provides an accurate description for $\mathcal{L}/R > 4$. Negative entropies are found for R as large as 1 μm.

An additional relevant property can be inferred from Fig. 3: The PFA always overestimates the thermal correction for perfect reflectors, where the overestimation is smaller for larger radii (at a given separation distance L) as expected.

In Fig. 5, we plot the beyond-PFA correction ρ at room temperature as a function of L/R, for different values of R. At zero temperature, the different curves shown in this figure would collapse into a single one [35,37]. For a given ratio L/R, the thermal reduction effect already apparent in Fig. 3 is larger for larger radii. The fact that ρ_F depends on R for a given L/R is again a clear signature of the interplay between thermal and geometry effects, which can damage the precision of PFA. In Sec. V, we discuss how this interplay is modified when finite conductivity and dissipation are included in the model.

V. PLASMA AND DRUDE METALS

The plasma model provides the simplest way to take the finite conductivity of metals into account. The Drude model is a more accurate description of nonsuperconducting metals, since it also includes the relaxation of conduction electrons and the associated finite dc conductivity. In this section, we

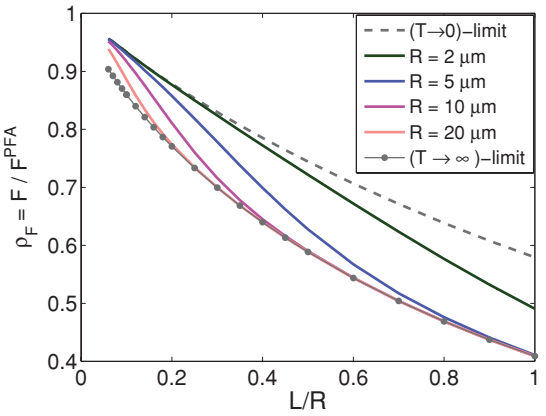

FIG. 5. (Color online) Beyond-PFA correction factor computed for perfectly reflecting sphere and plane at ambient temperature (solid lines) and for asymptotic cases (dashed and dotted lines), as a function of surface separation L.

take the dielectric constant ϵ given by Eq. (5) (with $\gamma = 0$ in the plasma model) and derive analytical and numerical results for the Casimir free energy and force.

A. Large distance high-temperature limit

When $\mathcal{L} \gg R$, we take the low-frequency expansion of the Mie coefficients and find, for the plasma model [66],

$$a_1^{\rm plas} \simeq -\frac{2\tilde{\xi}^3}{3}, \quad b_1^{\rm plas} \simeq \left(\frac{1}{3} + \frac{1}{\alpha^2} - \frac{\coth\alpha}{\alpha}\right)\tilde{\xi}^3, \tag{34}$$

$$\alpha = \frac{2\pi R}{\lambda_P}. \tag{35}$$

Here, we also assume that $\mathcal{L} \gg \lambda_T$ (high-temperature limit), so that we take only the first Matsubara frequency $\xi_0 = 0$ when computing the Casimir free energy from Eq. (20). With the additional hypothesis that $\mathcal{L} \gg \lambda_P$, the Fresnel coefficients are given by $r_{\rm TE} \approx -r_{\rm TM} \approx -1$, and then we find, from plugging Eq. (34) into Eqs. (22)–(24):

$$\mathcal{F}^{\rm plas} \approx -\frac{3\hbar c R^3}{8\lambda_T \mathcal{L}^3}\left(1 + \frac{1}{\alpha^2} - \frac{\coth\alpha}{\alpha}\right), \quad \mathcal{L} \gg \lambda_T, \lambda_P, R. \tag{36}$$

This result reproduces, as a particular case, the perfectly reflecting limit given by Eq. (32) when $\lambda_P \ll R$.

For the Drude model, the TE Fresnel reflection coefficient has the well-known low-frequency limit $r_{\rm TE} \to 0$, whereas the TM coefficient behaves as in the plasma model: $r_{\rm TM} \approx 1$. The low-frequency expansion of the Mie coefficients are also quite different from the plasma case. For the electric dipole coefficient, we find

$$a_1^{\rm Drud} \approx -\frac{2\tilde{\xi}^3}{3} + \frac{c\tilde{\xi}^4}{\sigma_0 R}. \tag{37}$$

As discussed in Sec. IV, the magnetic dipole b_1 is always much smaller than the electric dipole a_1 for any finite value of ϵ in the limit $\tilde{\xi} \to 0$. For any nonzero value of the relaxation frequency γ in Eq. (5), the zero-frequency limit of ϵ is finite. In contrast with the perfect-reflector and plasma cases, the magnetic dipole contribution is then negligible,

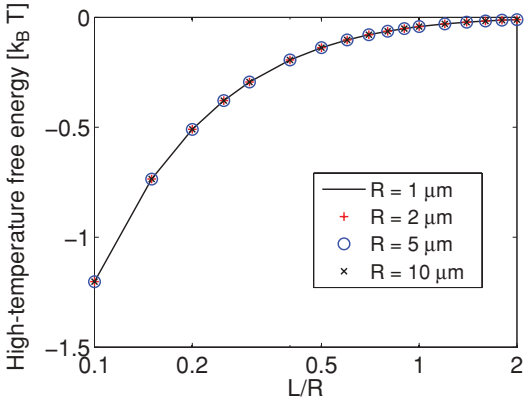

FIG. 6. (Color online) High-temperature Casimir free energy as a function of L/R calculated with the Drude model. The results neither depend separately on L and R nor depend on the material parameters λ_P and λ_γ.

$$b_1^{\rm Drud} \approx \frac{\sigma_0 R\tilde{\xi}^4}{45c} \ll a_1^{\rm Drud} \tag{38}$$

for any finite value of the Drude dc conductivity $\sigma_0 = \omega_P^2/\gamma$. The Drude sphere at low frequencies, thus, behaves as an inducible electric dipole for any finite value of σ_0, by corresponding to the Rayleigh scattering limit.

The resulting high-temperature large-distance limit for the free energy reads

$$\mathcal{F}^{\rm Drud} \approx -\frac{\hbar c R^3}{4\lambda_T \mathcal{L}^3}, \quad \mathcal{L} \gg \lambda_T, R. \tag{39}$$

Remarkably, this result does not depend on the length scales λ_P and λ_γ, which characterize the material response, whereas the corresponding plasma result Eq. (36) clearly depends on λ_P. One can show that this is always the case in the high-temperature limit $\lambda_T \ll \mathcal{L}$, with $\mathcal{F}^{\rm Drud}$ converging to the universal function of L/R shown in Fig. 6, which is determined by the contribution of higher multipoles $\ell \leqslant \ell_{\rm max} \sim R/L$.

The expression Eq. (39) corresponds to $\frac{2}{3}$ of the value for perfect reflectors Eq. (32), to be compared with the ratio $\frac{1}{2}$ found in the parallel-plane geometry [23], which results from the fact that the Fresnel coefficient $r_{\rm TE}$ vanishes at the zero-frequency limit. Here, the TE and TM contributions are redistributed into electric and magnetic multipole spherical modes, thus, to explain the change from $\frac{1}{2}$ to $\frac{2}{3}$. In fact, for perfect reflectors, the magnetic dipole contribution proportional to b_1 is one-third of the total free energy Eq. (32), as can be surmised from Eq. (27), which shows that $|b_1| = |a_1|/2$. Since this contribution is negligible in the Drude model, the free energy is reduced by the factor $\frac{2}{3}$.

B. Numerical results

An important consequence of the discussion presented previously is that results from Drude and perfect reflector as well as plasma models are closer in the plane-sphere geometry than in the parallel-plane geometry. We have computed the Casimir force numerically for arbitrary (not too small) values of the surface distance L. For the plasma model, the thermal

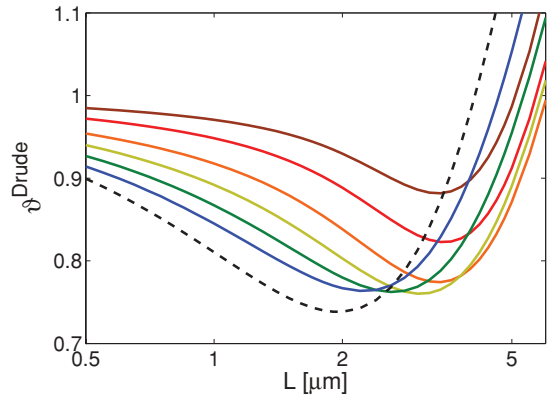

FIG. 7. (Color online) Thermal Casimir force correction computed with the Drude model. The conventions are the same as in Fig. 3.

correction $\vartheta^{\mathrm{plas}}$ (not shown) is found to be close to the values for perfect reflectors shown in Fig. 3. On the other hand, the variation of $\vartheta^{\mathrm{Drud}}$ calculated within the Drude model is remarkably different, as shown in Fig. 7.

In contrast with the perfect reflectors and plasma model calculations, for which PFA always overestimates the thermal correction, PFA underestimates the thermal correction at short distances for the Drude model, while it overestimates it at long distances. The overestimation is, however, clearly smaller than for perfect reflectors. Since PFA results for plasma metals are above the values calculated for Drude metals, the exact beyond-PFA Casimir force values at short distances for Drude and plasma models turn out to be much closer than predicted by the PFA-based theoretical models used in the analysis of experimental data.

In order to highlight this striking feature, in Fig. 8, we plot the ratio between the thermal Casimir force values F^{plas} calculated with the plasma model and F^{Drud} obtained with the Drude model, as a function of the distance L, and for different values of the sphere radius R, which increase from bottom to top. The fact that $F^{\mathrm{plas}}/F^{\mathrm{Drud}}$ depends on R is a clear signature of the interplay between geometry, temperature,

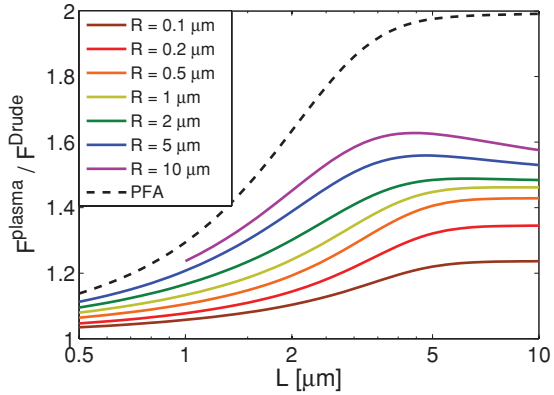

FIG. 8. (Color online) Ratio between thermal Casimir force values calculated with the plasma and the Drude models, as a function of surface separation L for different sphere radii. The solid curves from bottom to top correspond to increasing values of sphere radii. The PFA prediction corresponds to the dashed curve.

and dissipation. We also show the ratio computed within PFA (dashed line), which approaches 2 at large distances, since the PFA result is proportional to the energy for parallel planes. On the other hand, the exact ratio approaches 3/2 for large radii $R \gg \lambda_P$ and, more generally, a value between 1 and 3/2 obtained from Eqs. (36) and (39):

$$\frac{F^{\mathrm{plas}}}{F^{\mathrm{Drud}}} \approx \frac{3}{2}\left(1+\frac{1}{\alpha^2}-\frac{\coth\alpha}{\alpha}\right), \quad L \gg \lambda_T, \lambda_P, R.$$

The factor 2 predicted by PFA in the large-distance limit is never approached by our exact results.

VI. CONCLUSION

In this paper, we have used the scattering approach to compute the Casimir free energy and force in the plane-sphere geometry, by taking into account both the nonzero-temperature and the metallic nature of reflectors.

For the simpler case of perfect metals at intermediate distances, we observe, from numerical computations, a strong correlation between thermal and geometry effects, and negative entropy values for small spheres, which are clearly not related to dissipation but rather to geometry itself. For small spheres, thermal photons provide a repulsive contribution, thus, diminishing the total attractive Casimir force. Those results are endorsed by analytical derivations in the long-distance regime.

For the case of Drude metals, evidence of correlations between temperature and dissipation, qualitatively different from those in the parallel-plate geometry, is given. As a consequence, the results for the lossless plasma and full Drude models are closer to each other than in the parallel-plate geometry, with the long-distance ratio of 2 reduced to, at most, 3/2. If these results also hold in the experimental range $R/L > 10^2$, it might diminish the discrepancy between experimental results and predictions of the thermal Casimir force by using the Drude model.

ACKNOWLEDGMENTS

The authors thank I. Cavero-Pelaez and G.-L. Ingold for discussions, CAPES-COFECUB and the French Contract No. ANR-06-Nano-062 for financial support, and the ESF Research Networking Programme CASIMIR (www.casimir-network.com) for providing excellent opportunities for discussions on the Casimir effect and related topics. P.A.M.N. thanks H.M. Nussenzveig for discussions and CNPq and Faperj for financial support.

APPENDIX: MATRIX ELEMENTS OF THE ROUND-TRIP OPERATOR $\mathcal{M}^{(m)}$

In this appendix, we derive explicit expressions for the matrix elements $\mathcal{M}^{(m)}(\xi)_{1,2}$ given by Eq. (7). The different coefficients that appear in this equation are first calculated for real frequencies ω. Given values of ω and $\mathbf{k}(k,\varphi)$ define two directions in the three-dimensional reciprocal space corresponding to the azimuth angle φ and the inclination angle θ given by:

$$\sin\theta^{\pm} = \frac{ck}{\omega}, \quad \cos\theta^{\pm} = \pm\frac{ck_z}{\omega}, \quad k_z \equiv \sqrt{\omega^2/c^2 - k^2}. \tag{A1}$$

We first consider the matrix elements that implement the change from the multipole to the plane-wave basis. The free-space magnetic multipole fields have the Fourier representation [67] [$\mathbf{K} = K\hat{\mathbf{K}}(\theta,\varphi)$ with $\hat{\mathbf{K}}(\theta,\varphi)$ representing a three-dimensional unit vector]

$$\mathbf{I}^{(M)}_{\omega\ell m}(\mathbf{K}) = (2\pi)^2 \frac{\delta(K-\omega/c)}{\omega/c} \frac{\mathbf{L}_{\hat{\mathbf{K}}} Y_{\ell m}(\hat{\mathbf{K}})}{\sqrt{\ell(\ell+1)}}, \tag{A2}$$

$$\mathbf{L}_{\hat{\mathbf{K}}} \equiv i \left[\frac{\hat{\boldsymbol{\theta}}}{\sin\theta} \partial_\varphi - \hat{\boldsymbol{\varphi}}_k \partial_\theta \right]. \tag{A3}$$

The electric multipole fields are, in turn, given by $\mathbf{I}^{(E)}_{K_0\ell m}(\mathbf{K}) = -\hat{\mathbf{K}} \times \mathbf{I}^{(M)}_{\omega\ell m}(\mathbf{K})$.

In order to specify the plane-wave basis, we take the usual TE and TM polarizations adapted to treat the reflection by the plane at $z = 0$:

$$\hat{\boldsymbol{\epsilon}}_{\mathrm{TE}} = \hat{\mathbf{z}} \times \hat{\mathbf{k}} = \hat{\boldsymbol{\varphi}}, \tag{A4}$$

$$\hat{\boldsymbol{\epsilon}}_{\mathrm{TM}} = \hat{\boldsymbol{\epsilon}}_{\mathrm{TE}} \times \hat{\mathbf{K}} = \hat{\boldsymbol{\theta}}. \tag{A5}$$

The matrix element $\langle \mathbf{k},-,p|\ell,m,P\rangle$ is then obtained from the scalar product $\hat{\boldsymbol{\epsilon}}_p \cdot \mathbf{I}^{(P)}_{\omega\ell m}(\mathbf{K}^{(-)})$ with $\mathbf{K}^{(-)} = (\omega/c)\hat{\mathbf{K}}(\theta^-,\varphi)$ after multiplication by the square root of the Jacobian $dk_z/d(\omega/c) = \omega/(ck_z)$:

$$\langle \mathbf{k},-,\mathrm{TE}|\ell m E\rangle = \frac{2\pi m\sqrt{\omega/c}}{k\sqrt{k_z}} \frac{Y_{\ell m}(\theta^-,\varphi)}{\sqrt{\ell(\ell+1)}}, \tag{A6}$$

$$\langle \mathbf{k},-,\mathrm{TE}|\ell m M\rangle = -\frac{2\pi i}{\sqrt{k_z\omega/c}} \frac{\partial_\theta Y_{\ell m}(\theta^-,\varphi)}{\sqrt{\ell(\ell+1)}}, \tag{A7}$$

$$\langle \mathbf{k},-,\mathrm{TM}|\ell m E\rangle = \langle \mathbf{k},-,\mathrm{TE}|\ell m M\rangle, \tag{A8}$$

$$\langle \mathbf{k},-,\mathrm{TM}|\ell m M\rangle = -\langle \mathbf{k},-,\mathrm{TE}|\ell m E\rangle. \tag{A9}$$

We now derive the Mie scattering matrix elements $\langle \ell m P|\mathcal{R}_S(\xi)|\mathbf{k},+,p\rangle$. We write the electric field in terms of the Debye potentials (scalar fields that satisfy the Helmholtz equation) $\Pi^{(E)}(\mathbf{r})$ and $\Pi^{(M)}(\mathbf{r})$ for the electric and magnetic multipole components. In order to have the Debye potentials for a TE-polarized plane wave that propagates along an arbitrary direction $\hat{\mathbf{K}}(\theta,\varphi)$ (amplitude E_0), we take a rotation with Euler angles $\alpha = \varphi, \beta = \theta, \gamma = 0$. In terms of the coordinates x',y',z' that correspond to the rotated axis, the Debye potentials have the usual form [60] that corresponds to a plane wave that propagates along the z' axis linearly polarized along the y' axis. To write in terms of the original coordinates, we use the matrix elements of finite rotations and find ($j_\ell(Kr)$ are the spherical Bessel functions [63]):

$$\Pi^{E}_{\mathbf{K},\mathrm{TE}}(r,\Theta,\Phi) = \frac{E_0}{2K} \sum_{\ell,m}^{\infty} i^\ell \sqrt{\frac{4\pi(2\ell+1)}{\ell(\ell+1)}}\, j_\ell(Kr) \times e^{-im\varphi}\left[d^\ell_{m,1}(\theta) + d^\ell_{m,-1}(\theta)\right] Y_{\ell m}(\Theta,\Phi), \tag{A10}$$

$$\Pi^{M}_{\mathbf{K},\mathrm{TE}}(r,\Theta,\Phi) = \frac{E_0}{2iK} \sum_{\ell,m}^{\infty} i^\ell \sqrt{\frac{4\pi(2\ell+1)}{\ell(\ell+1)}}\, j_\ell(Kr) \times e^{-im\varphi}\left[d^\ell_{m,1}(\theta) - d^\ell_{m,-1}(\theta)\right] Y_{\ell m}(\Theta,\Phi). \tag{A11}$$

We use the same method to derive the Debye potentials for TM incident polarization: Either we take the polarization along the x' direction (instead of the y' direction as done in the derivation for TE polarization), or we take the third Euler angle to be $\gamma = -\pi/2$ so that the rotated Oy' axis coincides with $\hat{\boldsymbol{\epsilon}}_{\mathrm{TM}}$ instead of $\hat{\boldsymbol{\epsilon}}_{\mathrm{TE}}$. This allows the introduction of an additional phase $e^{\mp i\gamma} = \pm i$. Hence, the potentials $\Pi^{E,M}_{\mathbf{K},\mathrm{TM}}(r,\Theta,\Phi)$ are obtained from Eqs. (A10) and (A11) by replacing $d^\ell_{m,\pm1}(\theta) \to (\pm i) d^\ell_{m,\pm1}(\theta)$.

Since the scattered field propagates outward from the sphere, the corresponding potentials are written in terms of the spherical Hankel functions $h^{(1)}_\ell(Kr)$ [63]. The Debye potentials for the scattered field are then obtained by considering the boundary conditions at the surface of the sphere. In the resulting expression, each partial-wave term is multiplied by the corresponding Mie coefficient a_ℓ (electric multipoles) or b_ℓ (magnetic multipoles) [61]. As expected from spherical symmetry, the Mie coefficients neither depend on m nor on the direction of incidence. They are written in terms of the Riccati-Bessel functions $\psi_\ell(\beta) = \beta j_\ell(\beta)$, $\zeta_\ell(\beta) = \beta h^{(1)}_\ell(\beta)$ evaluated at the size parameter $\beta = \omega R/c$ and at $n\beta$ [60]:

$$a_\ell(\omega) = \frac{n\psi_\ell(n\beta)\psi'_\ell(\beta) - \psi_\ell(\beta)\psi'_\ell(n\beta)}{n\psi_\ell(n\beta)\zeta'_\ell(\beta) - \zeta_\ell(\beta)\psi'_\ell(n\beta),} \tag{A12}$$

$$b_\ell(\omega) = \frac{\psi_\ell(n\beta)\psi'_\ell(\beta) - n\psi_\ell(\beta)\psi'_\ell(n\beta)}{\psi_\ell(n\beta)\zeta'_\ell(\beta) - n\zeta_\ell(\beta)\psi'_\ell(n\beta)}. \tag{A13}$$

From the Debye potentials for the scattered field, we find the explicit multipole expansion for the scattered electric field (in position representation) $\langle \mathbf{r}|\mathcal{R}_S|\mathbf{K},p\rangle$, with $p = \mathrm{TE},\mathrm{TM}$ representing the incident polarization, which can also be cast into the formal decomposition,

$$\langle \mathbf{r}|\mathcal{R}_S|\mathbf{K},p\rangle = \sum_{\ell m P} \int_0^\infty \frac{d\omega}{2\pi c} \langle \mathbf{r}|\omega\ell m P\rangle\langle \omega\ell m P|\mathcal{R}_S|\mathbf{K},p\rangle, \tag{A14}$$

where the vector fields $\langle \mathbf{r}|\omega\ell m P\rangle$ are the inverse Fourier transforms of $\mathbf{I}_{\omega\ell m P}(\mathbf{K})$ [see Eq. (A2)]. Since the scattering does not change the frequency, the matrix elements of $\mathcal{R}_S$ have the general form ($\mathbf{K} = \mathbf{k} + k_z\hat{\mathbf{z}}$, $k_z > 0$),

$$\langle \omega\ell m P|\mathcal{R}_S|\mathbf{K},p\rangle = 2\pi\delta(K-\omega/c)\sqrt{\frac{ck_z}{\omega}}\langle \ell m P|\mathcal{R}_S|\mathbf{k},+,p\rangle, \tag{A15}$$

with the square root of the Jacobian $dk_z/d(\omega/c)$ once more providing the connection to our plane-wave basis $|\mathbf{k},\pm,p\rangle_\omega$ associated with a given frequency ω.

By comparing the explicit expressions for $\langle \mathbf{r}|\mathcal{R}_S|\mathbf{K},p\rangle$ with the formal decomposition Eq. (A14) and by taking Eq. (A15) into account, we find

$$\langle \ell m E|\mathcal{R}_S|\mathbf{k},+,\mathrm{TE}\rangle = \sqrt{\frac{\pi(2\ell+1)}{k_z\omega/c}} a_\ell(\omega) \times e^{-im\varphi}\left[d^\ell_{m,1}(\theta^+) + d^\ell_{m,-1}(\theta^+)\right], \tag{A16}$$

$$\langle \ell m M|\mathcal{R}_S|\mathbf{k},+,\mathrm{TE}\rangle = i\sqrt{\frac{\pi(2\ell+1)}{k_z\omega/c}} b_\ell(\omega) \times e^{-im\varphi}\left[d^\ell_{m,1}(\theta^+) - d^\ell_{m,-1}(\theta^+)\right]. \tag{A17}$$

For TM polarization, the matrix elements are obtained from Eqs. (A16) and (A17) by substituting $d^{\ell}_{m,\pm1}(\theta) \to (\pm i) d^{\ell}_{m,\pm1}(\theta)$.

The Casimir free energy may be written as an integral over the positive frequency semiaxis (which includes the evanescent sector $0 \leqslant \omega < ck$). By using analyticity properties of the reflection operators for plane and sphere over the upper complex frequency plane, we transform the integral over real positive frequencies into an integral over complex frequencies $\omega = i\xi + \eta$, with ξ running from $+\infty$ to 0 and $\eta \to 0^+$ by keeping the Matsubara poles $i\xi_n$ outside the closed contour of integration employed in connection with Cauchy theorem [20]. The resulting expression is given by Eq. (6), with the matrix elements $\mathcal{M}^{(m)}(\xi)_{1,2}$ obtained by taking $\omega \to i\xi$ and $k_z \to i\kappa$ in Eqs. (A6)–(A9) and (A16)–(A17) and by plugging the results into Eq. (7). The final explicit expressions are given in Sec. III.

[1] H. B. G. Casimir, Proc. K. Ned. Akad. Wet. **51**, 793 (1948).
[2] S. K. Lamoreaux, Am. J. Phys. **67**, 850 (1999).
[3] S. K. L. Lamoreaux, Phys. Rev. Lett. **78**, 5 (1997).
[4] U. Mohideen and A. Roy, Phys. Rev. Lett. **81**, 4549 (1998).
[5] B. W. Harris, F. Chen, and U. Mohideen, Phys. Rev. A **62**, 052109 (2000).
[6] T. Ederth, Phys. Rev. A **62**, 062104 (2000).
[7] H. B. Chan, V. A. Aksyuk, R. N. Kleiman, D. J. Bishop, and F. Capasso, Science **291**, 1941 (2001); Phys. Rev. Lett. **87**, 211801 (2001).
[8] G. Bressi, G. Carugno, R. Onofrio, and G. Ruoso, Phys. Rev. Lett. **88**, 041804 (2002).
[9] R. S. Decca, D. López, E. Fischbach, and D. E. Krause, Phys. Rev. Lett. **91**, 050402 (2003).
[10] F. Chen, G. L. Klimchitskaya, U. Mohideen, and V. M. Mostepanenko, Phys. Rev. A **69**, 022117 (2004).
[11] R. S. Decca, D. López, E. Fischbach, G. L. Klimchitskaya, and V. M. Mostepanenko, Phys. Rev. D **75**, 077101 (2007).
[12] J. N. Munday and F. Capasso, Phys. Rev. A **75**, 060102 (2007).
[13] P. J. van Zwol, G. Palasantzas, and J. T. M. De Hosson, Phys. Rev. B **77**, 075412 (2008).
[14] J. N. Munday, F. Capasso, and V. A. Parsegian, Nature (London) **457**, 170 (2009).
[15] G. Jourdan, A. Lambrecht, F. Comin, and J. Chevrier, Europhys. Lett. **85**, 31001 (2009).
[16] M. Masuda and M. Sasaki, Phys. Rev. Lett. **102**, 171101 (2009).
[17] S. de Man, K. Heeck, R. J. Wijngaarden, and D. Iannuzzi, Phys. Rev. Lett. **103**, 040402 (2009).
[18] R. Onofrio, New J. Phys. **8**, 237 (2006).
[19] G. L. Klimchitskaya, U. Mohideen, and V. M. Mostepanenko, Rev. Mod. Phys. **81**, 1827 (2009).
[20] A. Lambrecht, P. A. Maia Neto, and S. Reynaud, New J. Phys. **8**, 243 (2006).
[21] S. Reynaud, A. Canaguier-Durand, R. Messina, A. Lambrecht, and P. A. Maia Neto, in *Quantum Field Theory Under the Influence of External Conditions*, edited by K. A. Milton and M. Bordag (World Scientific, Singapore, 2010), pp. 55–67.
[22] A. Lambrecht and S. Reynaud, Eur. Phys. J. D **8**, 309 (2000).
[23] M. Boström and B. E. Sernelius, Phys. Rev. Lett. **84**, 4757 (2000).
[24] I. Brevik, S. A. Ellingsen, and K. Milton, New J. Phys. **8**, 236 (2006).
[25] G. L. Klimchitskaya and V. M. Mostepanenko, Contemp. Phys. **47**, 131 (2006).
[26] I. Brevik, S. E. Ellingsen, J. S. Høye, and K. A. Milton, J. Phys. A **41**, 164017 (2008).
[27] K. A. Milton, J. Phys. Conf. Ser. **161**, 012001 (2008).
[28] G.-L. Ingold, A. Lambrecht, and S. Reynaud, Phys. Rev. E **80**, 041113 (2009).
[29] B. V. Deriagin, I. I. Abrikosova, and E. M. Lifshitz, Quart. Rev. **10**, 295 (1968).
[30] M. Schaden and L. Spruch, Phys. Rev. A **58**, 935 (1998); Phys. Rev. Lett. **84**, 459 (2000).
[31] R. L. Jaffe and A. Scardicchio, Phys. Rev. Lett. **92**, 070402 (2004).
[32] D. E. Krause, R. S. Decca, D. López, and E. Fischbach, Phys. Rev. Lett. **98**, 050403 (2007).
[33] R. Balian and B. Duplantier, Ann. Phys. (NY) **104**, 300 (1977); **112**, 165 (1978).
[34] M. T. Jaekel and S. Reynaud, J. Phys. (Paris) **1**, 1395 (1991).
[35] T. Emig, J. Stat. Mech. (**2008**) P04007.
[36] C. Noguez, C. E. Roman-Velazquez, R. Esquivel-Sirvent, and C. Villareal, Europhys. Lett. **67**, 191 (2004).
[37] P. A. Maia Neto, A. Lambrecht, and S. Reynaud, Phys. Rev. A **78**, 012115 (2008).
[38] A. Canaguier-Durand, P. A. Maia Neto, I. Cavero-Pelaez, A. Lambrecht, and S. Reynaud, Phys. Rev. Lett. **102**, 230404 (2009).
[39] A. Canaguier-Durand, P. A. Maia Neto, A. Lambrecht, and S. Reynaud, Phys. Rev. Lett. **104**, 040403 (2010).
[40] A. Bulgac, P. Magierski, and A. Wirzba, Phys. Rev. D **73**, 025007 (2006).
[41] M. Bordag, Phys. Rev. D **73**, 125018 (2006).
[42] O. Kenneth and I. Klich, Phys. Rev. Lett. **97**, 160401 (2006); Phys. Rev. B **78**, 014103 (2008).
[43] T. Emig, N. Graham, R. L. Jaffe, and M. Kardar, Phys. Rev. Lett. **99**, 170403 (2007).
[44] K. A. Milton and J. Wagner, Phys. Rev. D **77**, 045005 (2008); J. Phys. A **41**, 155402 (2008).
[45] M. Bordag and V. Nikolaev (2009) e-print arXiv:0911.0146.
[46] M. Bordag and I. Pirozhenko, Phys. Rev. D **81**, 085023 (2010).
[47] S. J. Rahi, T. Emig, N. Graham, R. L. Jaffe, and M. Kardar, Phys. Rev. D **80**, 085021 (2009).
[48] H. Gies, K. Langfeld, and L. Moyaerts, J. High Energy Phys. 06 (2003) 018.
[49] H. Gies and K. Klingmüller, Phys. Rev. Lett. **96**, 220401 (2006).
[50] O. Schröder, A. Scardicchio, and R. L. Jaffe, Phys. Rev. A **72**, 012105 (2005).
[51] T. Emig, R. L. Jaffe, M. Kardar, and A. Scardicchio, Phys. Rev. Lett. **96**, 080403 (2006).
[52] D. A. R. Dalvit, F. C. Lombardo, F. D. Mazzitelli, and R. Onofrio, Phys. Rev. A **74**, 020101 (2006).
[53] F. D. Mazzitelli, D. A. R. Dalvit, and F. C. Lombardo, New J. Phys. **8**, 240 (2006).
[54] A. Rodriguez, M. Ibanescu, D. Iannuzzi, F. Capasso, J. D. Joannopoulos, and S. G. Johnson, Phys. Rev. Lett. **99**, 080401 (2007).

[55] A. Weber and H. Gies, e-print arXiv:1003.0430; e-print arXiv:1003.3420.

[56] P. A. Maia Neto, A. Lambrecht, and S. Reynaud, Europhys. Lett. **69**, 924 (2005); Phys. Rev. A **72**, 012115 (2005).

[57] R. B. Rodrigues, P. A. Maia Neto, A. Lambrecht, and S. Reynaud, Phys. Rev. Lett. **96**, 100402 (2006); Phys. Rev. A **75**, 062108 (2007).

[58] R. B. Rodrigues, P. A. Maia Neto, A. Lambrecht, and S. Reynaud, Europhys. Lett. **76**, 822 (2006).

[59] K. Milton and J. Wagner, J. Phys. A **41**, 155402 (2008).

[60] C. F. Bohren and D. R. Huffman, *Absorption and Scattering of Light by Small Particles* (Wiley, New York, 1983), Chap. 4.

[61] A. Mazolli, P. A. Maia Neto, and H. M. Nussenzveig, Proc. R. Soc. London, Ser. A **459**, 3021 (2003).

[62] D. A. Varshalovich, A. M. Moskalev, and V. K. Khersonskii, *Quantum Theory of Angular Momentum* (World Scientific, Singapore, 1988).

[63] M. Abramowitz and I. Stegun, *Handbook of Mathematical Functions* (Dover, New York, 1972).

[64] H. M. Nussenzveig, *Diffraction Effects in Semiclassical Scattering* (Cambridge University Press, Cambridge, UK, 1992).

[65] V. B. Bezerra, G. L. Klimchitskaya, and V. M. Mostepanenko, Phys. Rev. A **65**, 052113 (2002).

[66] D. B. Tanner, Phys. Rev. B **30**, 1042 (1984).

[67] C. Cohen-Tannoudji, J. Dupont-Roc, and G. Grynberg, *Photons et Atomes, Introduction à l'Électrodynamique Quantique* (CNRS, Paris, 1987), Chap. I. Note that our convention for the Fourier transform differs by a factor $(2\pi)^{3/2}$.

Erratum: Thermal Casimir effect for Drude metals in the plane-sphere geometry [Phys. Rev. A 82, 012511 (2010)]

Antoine Canaguier-Durand, Paulo A. Maia Neto, Astrid Lambrecht, and Serge Reynaud

(Received 8 March 2011; published 16 March 2011)

DOI: 10.1103/PhysRevA.83.039905 PACS number(s): 31.30.jh, 03.70.+k, 05.70.−a, 78.20.Ci, 99.10.Cd

There were misprints in Eqs. (8) and (9) of our article, which may make the derivations difficult to follow. These typographical errors however do not affect any other formula in the rest of the paper. All results of the paper are unchanged.

The corrected equations are

$$a_\ell(i\tilde{\xi}) = \frac{\pi}{2}(-)^{\ell+1}\frac{n^2 s_\ell^{(a)} - s_\ell^{(b)}}{n^2 s_\ell^{(c)} - s_\ell^{(d)}}, \tag{8}$$

$$\begin{aligned} b_\ell(i\tilde{\xi}) &= \frac{\pi}{2}(-)^{\ell+1}\frac{s_\ell^{(a)} - s_\ell^{(b)}}{s_\ell^{(c)} - s_\ell^{(d)}}, \\ s_\ell^{(a)} &= I_{\ell+1/2}(n\tilde{\xi})\left(\ell I_{\ell+1/2}(\tilde{\xi}) - \tilde{\xi} I_{\ell-1/2}(\tilde{\xi})\right), \\ s_\ell^{(b)} &= I_{\ell+1/2}(\tilde{\xi})\left(\ell I_{\ell+1/2}(n\tilde{\xi}) - n\tilde{\xi} I_{\ell-1/2}(n\tilde{\xi})\right), \\ s_\ell^{(c)} &= I_{\ell+1/2}(n\tilde{\xi})\left(\ell K_{\ell+1/2}(\tilde{\xi}) + \tilde{\xi} K_{\ell-1/2}(\tilde{\xi})\right), \\ s_\ell^{(d)} &= K_{\ell+1/2}(\tilde{\xi})\left(\ell I_{\ell+1/2}(n\tilde{\xi}) - n\tilde{\xi} I_{\ell-1/2}(n\tilde{\xi})\right). \end{aligned} \tag{9}$$

PHYSICAL REVIEW A **83**, 032508 (2011)

Casimir interaction between a dielectric nanosphere and a metallic plane

Antoine Canaguier-Durand,[1] Antoine Gérardin,[1] Romain Guérout,[1] Paulo A. Maia Neto,[2] Valery V. Nesvizhevsky,[3] Alexei Yu. Voronin,[4] Astrid Lambrecht,[1] and Serge Reynaud[1]

[1]*Laboratoire Kastler Brossel, CNRS, ENS, UPMC, Case 74, F-75252 Paris, France*

[2]*Instituto de Física, UFRJ, C.P. 68528, 21941-909 Rio de Janeiro-RJ, Brazil*

[3]*Institut Laue-Langevin, 6 rue Jules Horowitz, B.P. 156, F-38042 Grenoble, France*

[4]*P.N. Lebedev Physical Institute, 53 Leninsky Prospect, 117924 Moscow, Russia*

(Received 27 January 2011; published 24 March 2011)

We study the Casimir interaction between a dielectric nanosphere and a metallic plane, using the multiple scattering theory. Exact results are obtained with the dielectric described by a Sellmeier model and the metal by a Drude model. Asymptotic forms are discussed for small spheres and large or small distances. The well-known Casimir-Polder formula is recovered at the limit of vanishingly small spheres, while an expression that behaves better at small distances is found for any finite value of the radius. The exact results are of particular interest for the study of quantum states of nanospheres in the vicinity of surfaces.

DOI: 10.1103/PhysRevA.83.032508 PACS number(s): 31.30.jh, 03.70.+k, 34.35.+a

I. INTRODUCTION

The Casimir effect, due to the scattering of quantum fluctuations of the electromagnetic vacuum [1], is the dominant interaction between neutral bodies at distances that are large compared to atomic scales [2,3] (see [4] and references therein). For this reason, it has a strong impact in various important domains such as atomic and molecular physics, condensed matter and surface physics, chemical and biological physics, and micro- and nanotechnology [5].

In this paper, we consider the case of dielectric nanospheres in the vicinity of a metallic surface. This study is part of a discussion of the intriguing phenomenon of small heating of ultracold neutrons (UCNs) in traps [6–8], which could be explained by the interaction between UCNs and nanospheres levitated in the quantum states created by the interaction of nanospheres with surfaces [9]. In order to characterize this phenomenon and compute the properties of the quantum states, one needs to have a detailed and careful treatment of the interaction potential. In particular, as shown below, the commonly used Casimir-Polder formula [10] is not sufficient for this purpose.

We first recall how the scattering formula [11] can be applied to the study of a sphere of radius R at a distance L of closest approach to the plane. We then give numerical evaluations and graphical plots of the interaction energy. The Casimir-Polder formula is recovered when the radius of the nanosphere is smaller than all other length scales. The short- and long-distance limits are then found to show subtle interplays with the limit of small radius.

Important consequences of these results are obtained for the behavior of the interaction at small distances. While the Casimir-Polder energy scales as L^{-3} at small values of L, the full expression is found to behave better for any finite value of R, which leads to a regular solution for the quantum states.

II. SCATTERING FORMALISM

In this paper, we do not consider the effect of thermal fluctuations on the interaction. (They are expected to be small at the not-so-large separations considered here.) We thus start from the scattering formula for the Casimir energy at zero temperature [11]:

$$E = \hbar \int_0^\infty \frac{\mathrm{d}\xi}{2\pi} \ln\det \mathcal{D}\,, \quad \mathcal{D} = (I - \mathcal{M})\,, \\ \mathcal{M} = \mathcal{R}_S e^{-\mathcal{K}\mathcal{L}} \mathcal{R}_P e^{-\mathcal{K}\mathcal{L}}\,, \quad \mathcal{L} = L + R. \tag{1}$$

The Casimir energy is written in terms of reflection operators $\mathcal{R}_S$ and $\mathcal{R}_P$, which describe the diffraction by the sphere and the plate. These operators are evaluated with reference points at the sphere center and at its projection on the plane, respectively. The operator $e^{-\mathcal{K}\mathcal{L}}$ accounts for one-way propagation along the distance $\mathcal{L} = L + R$ separating these two points. The operator $\mathcal{M}$ thus represents one round-trip propagation inside the cavity formed by the two surfaces. All quantities are written at imaginary frequencies $\omega = i\xi$ after a Wick rotation.

The scattering formula (1) provides a compact way of taking the multiple scatterings between the interacting bodies into account. It can be considered as a generalization of the Dzyaloshinskii-Lifshitz-Pitaevskii formula [12] to arbitrary scattering properties of the two bodies. It can be applied in various geometries and has in particular been recently used for calculating the Casimir interaction between a metallic sphere and a metallic plane [13–16] (see also [17,18]). In the following, we use the same techniques and notations as in [15,16] and apply them to the case of a dielectric nanosphere above a metallic plane.

The reflection on the plane is conveniently written by using a plane-wave basis $|\mathbf{k}, \pm, p\rangle$ where $\mathbf{k}$ is the wave-vector component parallel to the plane xy of the metallic surface, $p = \mathrm{TE}, \mathrm{TM}$ is the polarization, and $+/-$ denotes the upward/downward propagation direction. This basis is well adapted to the description of the propagation operator $e^{-\mathcal{K}\mathcal{L}}$, since $\mathcal{K}$ is thus diagonal with elements $\kappa = \sqrt{\xi^2/c^2 + k^2}$ representing the (Wick-rotated) wave-vector z component for the imaginary frequency ξ. The reflection operator $\mathcal{R}_P$ preserves all plane-wave quantum numbers but the propagation direction, and its elements are given by the standard Fresnel specular reflection amplitudes for a homogenous medium.

Then the reflection on the sphere is more easily written by using the multipole basis $|\ell m P\rangle$, where $\ell(\ell+1)$ and

m denote the angular momentum eigenvalues (with $\ell = 1,2,\ldots$; $m = -\ell,\ldots,\ell$) and $P = \mathrm{E,M}$, representing electric and magnetic multipoles. The reflection operator $\mathcal{R}_S$ has its elements given by the standard Mie scattering amplitudes. Thanks to rotational symmetry, the operator $\mathcal{M}$ commutes with the angular momentum operator J_z. Hence, $\mathcal{M}$ is block diagonal, and each block $\mathcal{M}^{(m)}$ (corresponding to a given subspace m) yields an independent contribution to the Casimir energy:

$$E = \frac{\hbar}{\pi}\int_0^\infty d\xi \sum_m{}' \ln\det(I - \mathcal{M}^{(m)}),$$
$$\mathcal{M}^{(m)} = \begin{pmatrix} \mathcal{M}^{(m)}_{\mathrm{EE}} & \mathcal{M}^{(m)}_{\mathrm{EM}} \\ \mathcal{M}^{(m)}_{\mathrm{ME}} & \mathcal{M}^{(m)}_{\mathrm{MM}} \end{pmatrix}, \tag{2}$$

The primed sum is a sum over positive integers with the term $m = 0$ counted for its half. We have organized $\mathcal{M}^{(m)}$ in terms of block matrices built up on electric and magnetic contributions. The corresponding matrix elements are given and discussed in [16].

We now apply these formulas to the case of a dielectric nanosphere above a metallic plane. In particular, the plots shown below are calculated for the case of interest for UCN studies [9], namely a diamond nanosphere above a copper plane. We model copper dielectric response with a Drude model:

$$\varepsilon(i\xi) = 1 + \frac{\omega_P^2}{\xi(\xi+\gamma)}. \tag{3}$$

This is written at imaginary frequencies $\omega = i\xi$, where ω_P^2 is the squared plasma frequency proportional to the density of conduction electrons in the metal, and γ is the damping rate which measures the relaxation of these electrons. For explicit calculations and plots, we use the relations $\omega_P = 2\pi c/\lambda_P$ with the plasma wavelength $\lambda_P = 136$ nm and $\gamma = 0.0033\omega_P$. Because γ is small when compared to ω_P for a good metal such as copper, its influence is small at the not-too-large distances considered in the present study (see [19] for more details and references). The diamond dielectric response is described by a Sellmeier model:

$$\varepsilon(i\xi) = 1 + \sum_i \frac{B_i\omega_i^2}{\omega_i^2 + \xi^2}. \tag{4}$$

For diamond, a good enough description is obtained with a single component in this formula with $B_1 = 4.91$ and $\omega_1 = 2\pi c/\lambda_1$ with the wavelength $\lambda_1 = 106$ nm. The damping is disregarded here because it does not play any significant role.

The two permittivities are shown in Fig. 1, where the dashed curve is for diamond, and the solid (red) curve is for copper. For copper, $\varepsilon(i\xi)$ is very large for ξ much smaller than ω_P, which means that the metal tends to become a very good reflector. For diamond, $\varepsilon(i\xi)$ tends to its static value $\varepsilon(0) = 1 + B_1$ for ξ much smaller than ω_1. For larger frequencies, in contrast, the dielectric properties become poorer for diamond as well as copper. Because ω_P and ω_1 have similar values, we thus expect a transition to take place between van der Waals and Casimir-Polder regimes [10] when the distance between two objects is of the order of λ_P or λ_1. The simple models (3) and (4) are sufficient for the purpose of the present work.

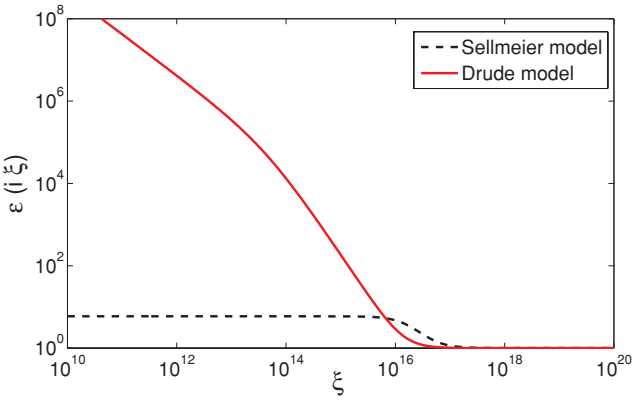

FIG. 1. (Color online) Relative permittivity $\varepsilon(i\xi)$ for copper [Drude model, solid (red) line] and diamond (Sellmeier model, dashed line).

They could easily be improved to take into account interband transitions for copper, multiple components, and damping in the Sellmeier model for diamond.

III. NUMERICAL EVALUATIONS

For evaluating the determinant in Eqs. (1) and (2), one needs to truncate the vector space at some maximum value $\ell_{\max}$ of angular momentum [13–16]. A qualitative understanding of the associated effects may be obtained from the localization principle [20]: the value of $\ell_{\max}$ required for a given accuracy level is expected to scale with the size parameter $\hat{\xi}R$ (where $\hat{\xi} = \xi/c$), which captures the dependence of scattering amplitudes on the sphere radius. Meanwhile, the frequencies giving the main contribution to the Casimir energy scale as $\hat{\xi} \sim 1/L$. As a consequence, the required $\ell_{\max}$ scales as R/L for intermediate and short separation distances. In this paper, we are interested in nanospheres $R \leqslant 20$ nm so that calculating with $\ell_{\max} = 100$ is sufficient for good accuracy for the results discussed below.

The numerical results are shown in Fig. 2 for different values of R (2, 5, 10, and 20 nm). We plot the absolute value $|E|$ of the Casimir energy ($E \leqslant 0$), with respect to the distance L, from 1 to 500 nm. We see that two regimes appear, which are reminiscent of a nonretarded van der Waals regime at short distances [21], and a retarded Casimir-Polder regime at large distances [10], with different dependences upon the distance L (see the slopes of the curves) and the radius R (see the vertical spacing between the curves). Our results do not coincide with these well-known limits because they take into account higher-order multipole contributions to the scattering upon the sphere [22]. Of course, the Casimir-Polder expression is recovered for small values of the radius, as shown in Sec. IV.

IV. LIMIT OF SMALL NANOSPHERES

In this section, we consider the limit of a punctual sphere when the radius R is smaller than any other length scale. (In loose terms, we take the limit $R \to 0$.) We show that the Casimir-Polder expressions are recovered, as expected. As the derivations presented here are applied to dielectric

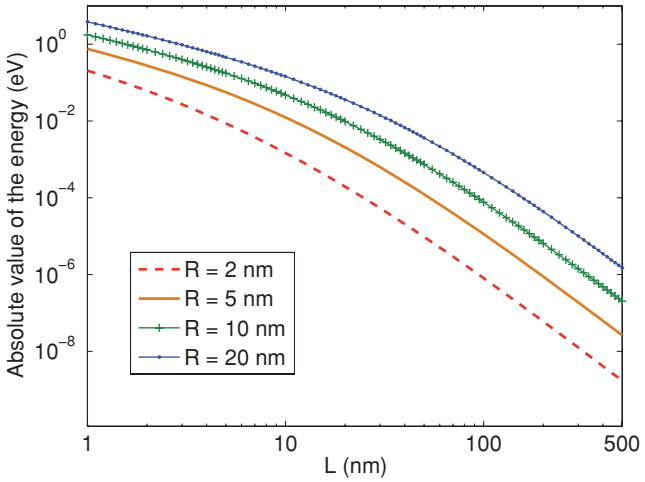

FIG. 2. (Color online) Absolute value $|E|$ of the Casimir energy E (measured in eV) with respect to the distance L for nanospheres of radii $R = 2$, 5, 10, and 20 nm. Logarithmic scales are used on both axes.

nanospheres, we use the fact that the permittivity for the nanosphere remains finite at all frequencies. We also keep the same description of the dielectric response for the small values of the radius considered here. Note that for metallic nanospheres, in contrast, it would be necessary to take into account the confinement effect for conduction electrons [23,24].

We start from the formulas (1) and (2) giving the Casimir energy for a sphere of radius R at a distance L of closest approach to a plane. Reflection on the plane is described by Fresnel amplitudes $r_{\rm TE}$ and $r_{\rm TM}$ while scattering on the sphere is described by Mie amplitudes a_ℓ and b_ℓ (defined as in [25]). The following expressions, valid at low values of the parameter $R\hat{\xi}$, are sufficient for calculating the energy at the limit $R \to 0$:

$$a_\ell \simeq (-1)^\ell \frac{\ell+1}{\ell\varepsilon+\ell+1} \frac{(\varepsilon-1)(R\hat{\xi})^{2\ell+1}}{(2\ell+1)!!(2\ell-1)!!},$$
$$b_\ell \simeq (-1)^{(\ell+1)} \frac{(\varepsilon-1)(R\hat{\xi})^{2\ell+3}}{(2\ell+3)!!(2\ell+1)!!}. \tag{5}$$

Because the dimensionless number $R\hat{\xi}$ is much smaller than unity (for $L\hat{\xi} \sim 1$; see the discussion in the previous section) and ε remains finite at all frequencies, it follows that all these amplitudes are small and, simultaneously, that the amplitude a_1 dominates all other Mie amplitudes.

The calculation of the energy is therefore much simpler than in the general case. As a first simplification, one may indeed replace the nonlinear expression (2) by a linearized one (perturbative approximation),

$$E = -\frac{\hbar}{\pi}\int_0^\infty d\xi \sum_m{}' \mathrm{tr}\mathcal{M}^{(m)}. \tag{6}$$

Then, one may keep only the contributions to this sum that are proportional to the amplitude a_1 (electric dipolar approximation),

$$E_1 \simeq -\frac{\hbar}{\pi}\int_0^\infty d\xi \left(\frac{1}{2}\mathcal{M}^{(0)}_{EE} + \mathcal{M}^{(1)}_{EE}\right),$$

$$\mathcal{M}^{(0)}_{EE} = -\frac{3}{2}\frac{a_1}{\hat{\xi}^3}\int_0^\infty \frac{k^3\,dk}{\kappa} r_{\rm TM} e^{-2\kappa L}, \tag{7}$$
$$\mathcal{M}^{(1)}_{EE} = \frac{3}{4}\frac{a_1}{\hat{\xi}^3}\int_0^\infty \frac{k\,dk}{\kappa}(\hat{\xi}^2 r_{\rm TE} - \kappa^2 r_{\rm TM}) e^{-2\kappa L}.$$

We also rewrite a_1 in terms of a dynamical electric polarizability $\alpha(\xi)$ defined for the small nanosphere (where αR^3 is a reduced polarizability having the dimension of a volume; the SI polarizability is $\varepsilon_0 \alpha R^3$):

$$a_1 = -\frac{2}{3}\alpha R^3 \hat{\xi}^3, \quad \alpha = \frac{\varepsilon-1}{\varepsilon+2}. \tag{8}$$

Collecting the results, we finally recover the full Casimir-Polder formula [10] as written in [26,27],

$$E_1 \simeq -\frac{\hbar c R^3}{2\pi}\int_0^\infty d\hat{\xi}\alpha(\hat{\xi}) \times \int_0^\infty \frac{k\,dk}{\kappa}(\hat{\xi}^2|r_{\rm TE}| + (k^2+\kappa^2)|r_{\rm TM}|)e^{-2\kappa L}. \tag{9}$$

We have used the fact that $r_{\rm TE}(i\xi) < 0$ and $r_{\rm TM}(i\xi) > 0$.

We repeat at this point that formula (9) has been obtained after two simplifications corresponding to the perturbative approximation and electric dipolar approximation. As the Casimir-Polder interaction between atoms [10], it contains in particular the limits of nonretarded van der Waals and retarded Casimir-Polder expressions [26,27]. In both cases, the energy scales as R^3, which is also the volume of the sphere. This result means that the nanosphere behaves at the limit $R \to 0$ as a big atom with an electric polarizability αR^3. As we see in Sec. V, this simple behavior does not remain true for arbitrary values of the radius R.

V. ASYMPTOTIC BEHAVIOR AT SHORT AND LONG DISTANCES

In this section, we discuss the asymptotic behaviors of the Casimir energy E at short and long distances. As a first step toward this aim, we write a Casimir-Polder formula $E_{\rm CP}$ deduced from E_1 in the limit $L \gg \lambda_P, \lambda_1$, where copper may be considered perfectly reflecting and diamond as having a constant electric polarizability:

$$E_{\rm CP} = -\frac{4\pi c_4 R^3}{3L^4}, \quad c_4 = \frac{9\hbar c\alpha_0}{32\pi^2}, \quad \alpha_0 = \frac{\varepsilon(0)-1}{\varepsilon(0)+2}. \tag{10}$$

We proceed similarly with the van der Waals prediction $E_{\rm vdW}$ deduced from E_1 for $L \ll \lambda_P, \lambda_1$:

$$E_{\rm vdW} = -\frac{4\pi c_3 R^3}{3L^3}, \quad c_3 = \frac{3\hbar c\alpha_0}{16(\sqrt{2}\lambda_P + \sqrt{1-\alpha_0}\lambda_1)}. \tag{11}$$

The values $E_{\rm CP}$ and $E_{\rm vdW}$ are equal at a crossing length

$$L_* = \frac{c_4}{c_3} = \frac{3(\sqrt{2}\lambda_P + \sqrt{1-\alpha_0}\lambda_1)}{2\pi^2}, \tag{12}$$

which is approximately 39 nm with the values corresponding to copper and diamond.

As expected from already-presented qualitative arguments, the exact Casimir expression E [given by Eq. (1)] is well

approximated by $E_{\rm CP}$ when R is the smallest length scale and L the largest one:

$$E \simeq E_{\rm CP}\,, \quad R \ll L_* \ll L. \tag{13}$$

Meanwhile, the exact Casimir expression E is well approximated by $E_{vd\rm W}$ when R is the smallest length scale and L is smaller than L_*:

$$E \simeq E_{vd\rm W}\,, \quad R \ll L \ll L_*. \tag{14}$$

Of course, there exist a variety of behaviors when the two latter conditions are not met.

In order to explore this variety, we plot in Fig. 3 the logarithmic slope (log-log-derivative) of the energy $|E|$ versus distance L,

$$\nu = -\frac{\partial \ln|E|}{\partial \ln L} = \frac{LF(L)}{E(L)}, \quad F(L) = -\frac{\partial E}{\partial L}. \tag{15}$$

The parameter ν would be a constant if the energy $|E|$ obeyed a power-law dependence $1/L^\nu$ (for example, $\nu = 4$ for $E_{\rm CP}$ or $\nu = 3$ for $E_{vd\rm W}$). In the general case, ν depends on L and can thus be understood as describing a "local" power law in the vicinity of L.

We see in Fig. 3 that ν tends to the expected value of 4 at large distances. At small distances, in contrast, the van der Waals value $\nu = 3$ is never a good approximation, which can be understood by inspecting the conditions for (14) to be true. For any finite value of the radius R, we have indeed to cross the conditions $L \sim R$ when the distance is decreased, and Eq. (14) can no longer be valid after this crossing.

Another facet of the same problem becomes apparent when we look at the dependence of E versus R. We plot in Fig. 4 a logarithmic slope μ calculated as in (15),

$$\mu = \frac{\partial \ln|E|}{\partial \ln R}. \tag{16}$$

The parameter μ would be a constant if $|E|$ obeyed a simple power-law dependence R^μ. In particular, the volumetric value $\mu = 3$ is obtained for both $E_{\rm CP}$ and $E_{vd\rm W}$. We see in Fig. 4 that μ approaches this value at the limit of large distances but departs from it everywhere else, indicating anew that $E_{vd\rm W}$ is not a good approximation.

We now give an improved version of the van der Waals formula (11) which explains some of the features of the exact energy E. As $E_{vd\rm W}$ has been demonstrated above in the limit of a punctual sphere $R \to 0$, we may improve it for a finite size of the sphere through a pairwise summation over the volume. We thus obtain the Hamaker expression [28]

$$\begin{aligned} \overline{E_{vd\rm W}} &\simeq -\pi c_3 \left(\frac{2R\,(L+R)}{L\,(L+2R)} - \ln \frac{L+2R}{L} \right), \\ \overline{E_{\rm CP}} &\simeq -\frac{4\pi c_4 R^3}{3L^2\,(L+2R)^2}. \end{aligned} \tag{17}$$

For completeness, we did proceed similarly with the Casimir-Polder formula $E_{\rm CP}$.

These results allow one to understand the behaviors apparent in Figs. 3 and 4. Let us again consider that we start from small nanospheres $R \ll L_*$ at large distances $L \gg L_*$. Using the expression $E_{\rm CP}$, one obtains $\nu = 4$ and $\mu = 3$. When the distance L is decreased, we cross two transitions $L \sim L_*$ and $L \sim R$ and end up with the formula $\overline{E_{vd\rm W}}$, for which we get $\nu = 1$ and $\mu = 1$. This line of reasoning reproduces the global variations seen in Figs. 3 and 4.

In order to assess the quality of the estimations (17), we now plot in Fig. 5 the ratios $E/\overline{E_{\rm CP}}$ and $E/\overline{E_{vd\rm W}}$. As expected, we find that $\overline{E_{\rm CP}}$ tends to reproduce the result E of the full numerical computation at large distances. We also see that $\overline{E_{vd\rm W}}$ obeys the same power law as E at small distances (ratio tending to a constant value) but fails to predict the correct magnitude (the limit of the ratio is not 1). This feature can be understood through a close inspection of the case where L is the smallest of all length scales.

When $L \ll R$, we can use the proximity force approximation and express the plane-sphere result in terms of the plane-plane one [29]. We are thus left with the evaluation of the Casimir effect between copper and diamond plane plates.

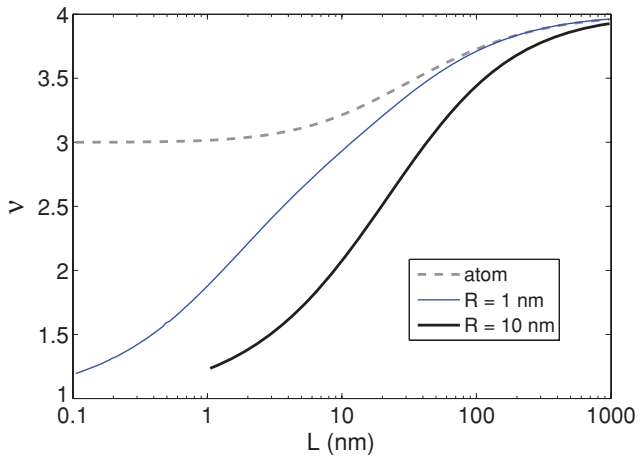

FIG. 3. (Color online) Logarithmic slope ν as a function of the distance L. Solid curves represent the nanosphere case with different values for the radius R, and the dashed curve represents the atomic limit, that is, a nanosphere with $R \to 0$.

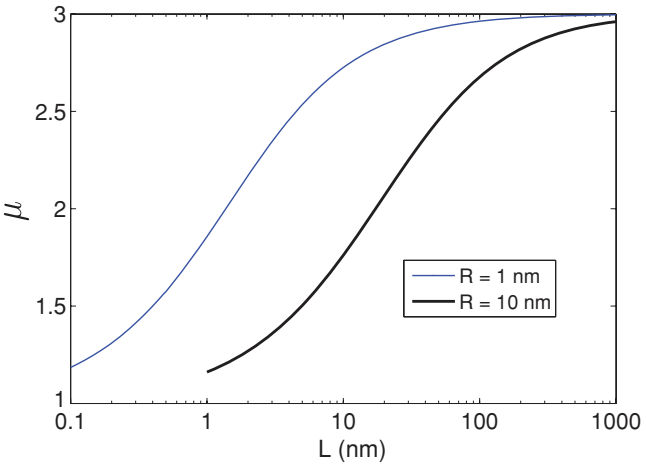

FIG. 4. (Color online) Logarithmic slope μ for variation with the radius R, as a function of the distance L. Solid curves represent the nanosphere case with different values for the radius R; in comparison, the atom case is a constant $\mu = 3$.

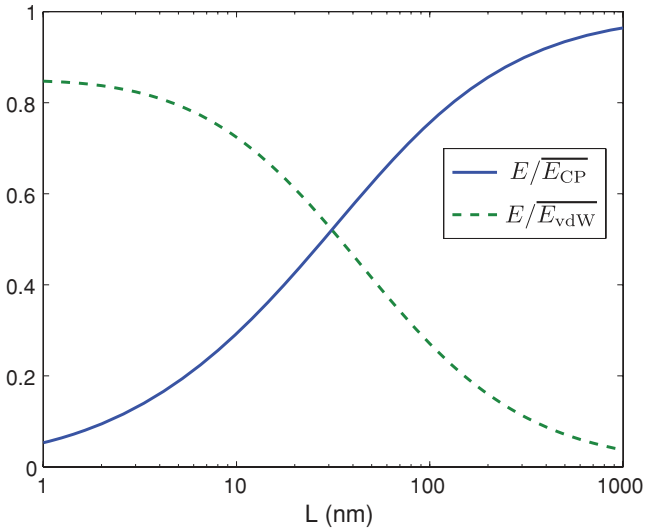

FIG. 5. (Color online) Ratios of the exact energy E to the expressions $\overline{E_{\rm CP}}$ [solid (blue) curve] and $\overline{E_{\rm vdW}}$ [dashed (green) curve]. The two curves are calculated for $R = 10$ nm.

Because $L \ll L_*$, it is then possible to use the method designed in [30] to find

$$E_{\rm PFA} \simeq -\pi c_3' \frac{R}{L}, \quad L \ll R, L_*. \tag{18}$$

This expression shows the same functional dependencies as the Hamaker expression $\overline{E_{\rm vdW}} \sim -\pi c_3 R/L$ while giving a different proportionality constant. This difference is due to the fact that (17) has been obtained through a pairwise integration of van der Waals forces, whereas (18) has been calculated by taking into account the multiple interferences occurring in the Fabry-Perot cavity [30]. The numerical values thus obtained ($c_3' = 0.84\, c_3$ with the numbers corresponding to diamond and copper) explain the behavior seen in Fig. 5.

VI. CONCLUSIONS

In this paper, we have presented an exact calculation of the Casimir interaction between a dielectric nanosphere and a metallic plane, using the multiple scattering formalism as developed recently for the plane-sphere geometry [13–16]. In order to qualitatively discuss the results obtained in this manner, we have also investigated the limits of a punctual sphere as well as the asymptotic behaviors at short and long distances.

This study has important applications for discussing the intriguing phenomenon of heating of ultracold neutrons in traps [6–8]. This heating could be explained by the interaction between UCNs and nanospheres levitated in the quantum states created by their interaction with surfaces [9]. In order to quantitatively characterize this phenomenon, detailed knowledge of the interaction potential is required. In particular, the small-distance behavior of the Casimir energy plays a crucial role in the determination of the quantum states obtained by solving the Schrödinger equation for the wave function of the nanosphere in this potential.

The commonly used Casimir-Polder formula, which also corresponds to the limit of our calculations for a vanishingly small radius R, leads to significant difficulties since it predicts a power law $|E| \propto R^3/L^3$ in the vicinity of the surface and thus leads to an ill-behaved Schrödinger problem. The exact solution presented in this paper for a finite value of the radius R predicts a smoother power law $|E| \propto R/L$ in the vicinity of the surface and thus leads to a regular solution for the Schrödinger equation [9].

The plate roughness has been disregarded here and it is treated in a phenomenological manner in [9]. It would be interesting to analyze its effect by using techniques already developed for treating the scattering on rough surfaces [31–33].

It would also be worth investigating the same problem for the interaction between an atom and a plane. In analogy with the discussion of the present paper, taking into account the higher-order multipoles and multiple interferences could lead to an expression of the energy more regular than with the commonly used electric dipole approximation.

ACKNOWLEDGMENTS

The authors thank M.-C. Angonin, I. Cavero-Pelaez, G.-L. Ingold, R. Messina, H. M. Nussenzveig, S. Pelisson, and P. Wolf for discussions, and the ESF Research Networking Programme CASIMIR (www.casimir-network.com) for providing excellent opportunities for discussions on the Casimir effect and related topics. PAMN thanks CNPq and FAPERJ for financial support.

[1] H. B. G. Casimir, Proc. K. Ned. Akad. Wet. **51**, 793 (1948).
[2] P. W. Milonni, *The Quantum Vacuum* (Academic, New York, 1994).
[3] S. K. Lamoreaux, Am. J. Phys. **67**, 850 (1999).
[4] A. Lambrecht, A. Canaguier-Durand, R. Guérout, S. Reynaud, in *Casimir Physics*, *Lecture Notes in Physics*, edited by D. Dalvit, P. Milonni, D. Roberts, and F. da Rosa (Springer, New York, 2011), e-print arXiv:1006.2959.
[5] V. A. Parsegian, *Van der Waals Forces: A Handbook for Biologists, Chemists, Engineers, and Physicists* (Cambridge University, Cambridge, UK, 2006).
[6] V. V. Nesvizhevsky, Phys. At. Nucl. **65**, 400 (2002).
[7] E. V. Lychagin *et al.*, Phys. At. Nucl. **65**, 1995 (2002).
[8] D. G. Kartashov *et al.*, Int. J. Nanosci. **6**, 501 (2007).
[9] V. V. Nesvizhevsky, A. Yu. Voronin, A. Lambrecht, S. Reynaud *et al.* (unpublished).
[10] H. B. G. Casimir and D. Polder, Phys. Rev. **73**, 360 (1948).
[11] A. Lambrecht, P. A. Maia Neto, and S. Reynaud, New J. Phys. **8**, 243 (2006).
[12] I. E. Dzyaloshinskii, E. M. Lifshitz, and L. P. Pitaevskii, Sov. Phys. Usp. **4**, 153 (1961).

[13] P. A. Maia Neto, A. Lambrecht, and S. Reynaud, Phys. Rev. A **78**, 012115 (2008).
[14] A. Canaguier-Durand, P. A. Maia Neto, I. Cavero-Pelaez, A. Lambrecht, and S. Reynaud, Phys. Rev. Lett. **102**, 230404 (2009).
[15] A. Canaguier-Durand, P. A. Maia Neto, A. Lambrecht and S. Reynaud, Phys. Rev. Lett. **104**, 040403 (2010).
[16] A. Canaguier-Durand, P. A. Maia Neto, A. Lambrecht, and S. Reynaud, Phys. Rev. A **82**, 012511 (2010).
[17] T. Emig, J. Stat. Mech. (2008) P04007.
[18] T. Emig, Int. J. Mod. Phys. A **25**, 2177 (2010).
[19] G. L. Ingold, A. Lambrecht, and S. Reynaud, Phys. Rev. E **80**, 041113 (2009).
[20] H. M. Nussenzveig, *Diffraction Effects in Semiclassical Scattering* (Cambridge University, Cambridge, UK, 1992).
[21] P. Johansson and P. Apell, Phys. Rev. B **56**, 4159 (1997).
[22] C. Noguez, C. E. Roman-Velazquez, R. Esquivel-Sirvent, and C. Villarreal, Europhys. Lett. **67**, 191 (2004).
[23] G. Celep *et al.*, Phys Rev. B **70**, 165409 (2004).
[24] E. Cottancin, G. Celep, J. Lermé, M. Pellarin, J. R. Huntzinger, J. L. Vialle, and M. Broyer, Theor. Chem. Acta **116**, 514 (2006).
[25] C. F. Bohren and D. R. Huffman, *Absorption and Scattering of Light by Small Particles* (Wiley, New York, 1983), Chap. 4.
[26] D. A. R. Dalvit, P. A. Maia Neto, A. Lambrecht, and S. Reynaud, Phys. Rev. Lett. **100**, 040405 (2008).
[27] R. Messina, D. A. R. Dalvit, P. A. Maia Neto, A. Lambrecht, and S. Reynaud, Phys. Rev. A **80**, 022119 (2009).
[28] H. C. Hamaker, Physica **4**, 1058 (1937).
[29] B. V. Derjaguin and I. I. Abrikosova, Sov. Phys. JETP **3**, 819 (1957).
[30] C. Genet, A. Lambrecht, and S. Reynaud, Ann. Fond. L. de Broglie **29**, 311 (2004).
[31] P. A. Maia Neto, A. Lambrecht, and S. Reynaud, Europhys. Lett. **69**, 924 (2005).
[32] P. A. Maia Neto, A. Lambrecht, and S. Reynaud, Phys. Rev. A **72**, 012115 (2005).
[33] A. M. Contreras-Reyes, R. Guérout, P. A. Maia Neto, D. A. R. Dalvit, A. Lambrecht, and S. Reynaud, Phys. Rev. A **82**, 052517 (2010).

References

[1] D. Sedley, "Two conceptions of vacuum," Phronesis **27**, 175–193 (1982). (document)

[2] B. Jarrosson, *Invitation à la philosophie des sciences* (Éditions du Seuil, 1992). (document)

[3] B. Russell, *History of western philosophy*, Routledge classics (Routledge, 2004). (document)

[4] M. Jaekel, A. Lambrecht, and S. Reynaud, "Relativity of Motion in Vacuum," Arxiv preprint quant-ph/9801071 (1998). (document)

[5] Parménide, *Sur la nature ou sur l'étant. La langue de l'être ?*, édité, traduit et commenté par B. Cassin (Éditions du Seuil, Paris, 1998). (document)

[6] M. Henn, *Parmenides of Elea: a verse translation with interpretative essays and commentary to the text*, 88 (Praeger Publishers, 2003). (document)

[7] E. Grant, *Much ado about nothing: theories of space and vacuum from the Middle Ages to the scientific revolution*, The Cambridge history of science series (Cambridge University Press, 1981). (document)

[8] M. Sharratt, *Galileo: decisive innovator*, vol. 6 (Cambridge Univ Pr, 1996). (document)

[9] R. Descartes, *Les principes de la philosophie* (1644). (document)

[10] E. Torricelli, *Opera geometrica* (typis A. Masse & L. de Landis, 1644). (document)

[11] B. Pascal, "Expériences nouvelles touchant le vide," Ibidem. Pascal B. Les ecrits des cures de Paris//Ibidem. Pascal B. Les provinciales//Ibidem (1647). (document)

[12] B. Pascal, "Préface pour le traité du vide," von Jacques Chevalier. Paris: Pléiade (1954). (document)

[13] T. Young, "The Bakerian lecture: Experiments and calculations relative to physical optics," Philosophical transactions of the Royal Society of London **94**, 1–16 (1804). (document)

[14] R. Hooke and W. Library, *Micrographia* (Cramer, 1961). (document)

[15] C. Huygens, "Treatise on light, 1690," (1962). (document)

[16] L. Euler, "Nova theoria lucis et colorum (1746)," Leonhardi Euleri Opera Omnia pp. 1–45 (1962). (document)

[17] L. Zuppiroli, M. Bussac, and C. Grimm, *Traité de la lumière* (PPUR, 2009). (document)

[18] A. Michelson, "The relative motion of the Earth and the Luminiferous ether," American Journal of Science **22**, 120–129 (1881). (document)

[19] A. Michelson and E. Morley, "On the relative motion of the Earth and the luminiferous ether," American Journal of Science **34**, 333–345 (1887). (document)

[20] A. Einstein, "Zur elektrodynamik bewegter körper," Annalen der Physik **322**, 891–921 (1905). (document)

[21] J. Clerk-Maxwell, "On Physical Lines of Force," Philosophical Magazine **21**, 168 (1861). (document)

[22] W. Heisenberg, "Über den anschaulichen Inhalt der quantentheoretischen Kinematik und Mechanik," Zeitschrift für Physik A Hadrons and Nuclei **43**, 172–198 (1927). (document), 2

[23] W. Heisenberg and C. Eckart, *The physical principles of the quantum theory* (Dover Pubns, 1930). 2

[24] J. Lévy-Leblond and F. Balibar, "When did the Indeterminacy Principle become the Uncertainty Principle?" American Journal of Physics pp. 278–279 (1998). 2

[25] É. Klein, *Petit voyage dans le monde des quanta* (Flammarion, 2004). 2

[26] M. Born, W. Heisenberg, and P. Jordan, "Zur Quantenmechanik. II." Zeitschrift für Physik A Hadrons and Nuclei **35**, 557–615 (1926). (document)

[27] P. Dirac, "The quantum theory of the emission and absorption of radiation," Proceedings of the Royal Society of London. Series A **114**, 243–265 (1927). (document)

[28] P. Dirac, "The quantum theory of dispersion," Proceedings of the Royal Society of London. Series A **114**, 710 (1927). (document)

[29] J. van der Waals, *Over de continuiteit van den gaz-en vloeistoftoestand. Academisch proefschrift ter verkrijging van den graad van doctor in de wis-en natuurkunde aan de Hoogeschool te Leiden. op zaterdag den 14 den juni 1873* (AW Sijthoff, 1873). (document)

[30] R. Eisenschitz and F. London, "Über das Verhältnis der van der Waalsschen Kräfte zu den homöopolaren Bindungskräften," Zeitschrift für Physik A Hadrons and Nuclei **60**, 491–527 (1930). (document)

[31] F. London, "Properties and applications of molecular forces," Zeit. Physik. Chem. B **11**, 222 (1930). (document)

[32] F. London, "Theory and systematics of molecular forces," Z. Phys **63**, 245 (1930). (document)

[33] F. London, "The general theory of molecular forces," Trans. Faraday Soc. **33**, 8b–26 (1937). (document)

[34] E. Verwey, J. Overbeek, and K. van Nes, *Theory of the stability of lyophobic colloids: the interaction of sol particles having an electric double layer* (Elsevier Pub. Co., 1948). (document)

[35] H. Casimir and D. Polder, "Influence of retardation on the London–van der Waals forces," Nature **158**, 787–788 (1946). (document)

[36] H. Casimir, "Some remarks on the history of the so-called Casimir effect," The Casimir Effect 50 Years Later pp. 3–9 (1999). (document)

[37] H. Casimir, "Sur les forces van der Waals-London," J. Chim. phys **46**, 407 (1949). (document)

[38] H. Casimir, "On the attraction between two perfectly conducting plates," in "Proc. K. Ned. Akad. Wet," , vol. 51 (1948), vol. 51, p. 793. (document), I, 1.4

[39] H. Casimir, "Normal modes of the electromagnetic (EM) field between (ideal metal) plates," in "Proc. K. Ned. Acad. Wet," , vol. 51 (1948), vol. 51, p. 793. (document)

[40] P. Milonni and C. Eberlein, *The quantum vacuum: an introduction to quantum electrodynamics* (Academic press Boston, 1994). (document), 12

[41] S. Lamoreaux, "Resource letter CF-1: Casimir force," American Journal of Physics **67**, 850 (1999). (document)

[42] M. Bordag, U. Mohideen, and V. Mostepanenko, "New developments in the Casimir effect," Physics reports **353**, 1–205 (2001). (document)

[43] S. Reynaud, A. Lambrecht, C. Genet, and M. Jaekel, "Quantum vacuum fluctuations," Comptes Rendus de l'Académie des Sciences-Series IV-Physics **2**, 1287–1298 (2001). Arxiv preprint arXiv:quant-ph/0105053. (document)

[44] C. Genet, A. Lambrecht, and S. Reynaud, "Casimir effect and vacuum energy," On the nature of dark energy; P. Brax, J. Martin & J.-P. Uzan eds (Frontier Group) pp. 121–130 (2002). Arxiv preprint arXiv:quant-ph/0210173. (document)

[45] K. Milton, "The Casimir effect: recent controversies and progress," Journal of Physics A: Mathematical and General **37**, R209 (2004). (document)

[46] R. Decca, D. López, E. Fischbach, G. Klimchitskaya, D. Krause, and V. Mostepanenko, "Precise comparison of theory and new experiment for the Casimir force leads to stronger constraints on thermal quantum effects and long-range interactions," Annals of Physics **318**, 37–80 (2005). (document)

[47] A. Lambrecht, P. Neto, and S. Reynaud, "The Casimir effect within scattering theory," New Journal of Physics **8**, 243 (2006). (document), 1, 1.1.4, 1.2

[48] R. Barrera and S. Reynaud, "Focus on Casimir forces," New Journal of Physics **8** (2006). (document)

[49] D. Dalvit, P. Milonni, D. Roberts, and F. Rosa, *Casimir Physics*, Lecture Notes in Physics Series (Springer London, Limited, 2011). (document)

[50] M. Jaekel and S. Reynaud, "Movement and fluctuations of the vacuum," Reports on Progress in Physics **60**, 863 (1997). (document)

[51] E. Elizalde, "Quantum vacuum fluctuations and the cosmological constant," Journal of Physics A: Mathematical and Theoretical **40**, 6647 (2007). (document)

[52] M. Jaekel and S. Reynaud, "Mass, Inertia, and Gravitation," Mass and Motion in General Relativity pp. 491–530 (2011). Available at http://www.cnrs-orleans.fr/osuc/conf/files/ecole/Jaekel.pdf. (document)

[53] E. Fischbach and C. Talmadge, *The search for non-Newtonian gravity* (Springer Verlag, 1999). (document)

[54] C. Hoyle, U. Schmidt, B. Heckel, E. Adelberger, J. Gundlach, D. Kapner, and H. Swanson, "Submillimeter test of the gravitational inverse-square law: a search for "large" extra dimensions," Physical Review Letters **86**, 1418–1421 (2001). (document)

[55] A. Lambrecht and S. Reynaud, "Recent experiments on the Casimir effect: description and analysis," Poincaré Seminar on Vacuum Energy and Renormalization **1**, 107 (2002). (document)

[56] J. Long, H. Chan, A. Churnside, E. Gulbis, M. Varney, and J. Price, "Upper limits to submillimetre-range forces from extra space-time dimensions," Nature **421**, 922–925 (2003). (document)

[57] E. Adelberger, B. Heckel, and A. Nelson, "Tests of the gravitational inverse-square law," Annual Review of Nuclear and Particle Science **53**, 77–121 (2003). (document)

[58] C. Hoyle, D. Kapner, B. Heckel, E. Adelberger, J. Gundlach, U. Schmidt, and H. Swanson, "Sub-mm tests of the gravitational inverse-square law," Phys. Rev. D **70**, 042004 (2004). (document)

[59] R. Onofrio, "Casimir forces and non-Newtonian gravitation," New Journal of Physics **8**, 237 (2006). (document)

[60] R. Decca, D. López, E. Fischbach, G. Klimchitskaya, D. Krause, and V. Mostepanenko, "Novel constraints on light elementary particles and extra-dimensional physics from the Casimir effect," The European Physical Journal C-Particles and Fields **51**, 963–975 (2007). (document)

[61] D. Kapner, T. Cook, E. Adelberger, J. Gundlach, B. Heckel, C. Hoyle, and H. Swanson, "Tests of the gravitational inverse-square law below the dark-energy length scale," Physical Review Letters **98**, 21101 (2007). (document)

[62] A. Lambrecht and S. Reynaud, "Casimir and short-range gravity tests," Arxiv preprint arXiv:1106.3848 (2011). (document)

[63] G. Carugno, Z. Fontana, R. Onofrio, and C. Rizzo, "Limits on the existence of scalar interactions in the submillimeter range," Physical Review D **55**, 6591 (1997). (document)

[64] M. Bordag, B. Geyer, G. Klimchitskaya, and V. Mostepanenko, "Stronger constraints for nanometer scale Yukawa-type hypothetical interactions from the new measurement of the Casimir force," Physical Review D **60**, 055004 (1999). (document)

[65] E. Fischbach and D. Krause, "New limits on the couplings of light pseudoscalars from equivalence principle experiments," Physical Review Letters **82**, 4753–4756 (1999). (document)

[66] J. Long, H. Chan, and J. Price, "Experimental status of gravitational-strength forces in the sub-centimeter regime," Nuclear Physics B **539**, 23–34 (1999). (document)

[67] J. Long *et al.*, "New experimental limits on macroscopic forces below 100 microns," Nature **421**, 922–925 (2003). (document)

[68] E. Fischbach, D. Krause, V. Mostepanenko, and M. Novello, "New constraints on ultrashort-ranged Yukawa interactions from atomic force microscopy," Physical Review D **64**, 075010 (2001). (document)

[69] R. Decca, E. Fischbach, G. Klimchitskaya, D. Krause, D. López, and V. Mostepanenko, "Improved tests of extra-dimensional physics and thermal quantum field theory from new Casimir force measurements," Physical Review D **68**, 116003 (2003). (document)

[70] I. Antoniadis, S. Baessler, M. Büchner *et al.*, "," to appear in Compt. Rand. Acad. Sci. (2011). (document)

[71] M. Arndt, O. Nairz, J. Vos-Andreae, C. Keller, G. Van der Zouw, and A. Zeilinger, "Wave-particle duality of C 60 molecules," Nature **401**, 680–682 (1999). (document)

[72] O. Nairz, M. Arndt, and A. Zeilinger, "Experimental verification of the Heisenberg uncertainty principle for fullerene molecules," Physical Review A **65**, 032109 (2002). (document)

[73] O. Nairz, M. Arndt, and A. Zeilinger, "Quantum interference experiments with large molecules," American Journal of Physics **71**, 319 (2003). (document)

[74] B. Brezger, L. Hackermüller, S. Uttenthaler, J. Petschinka, M. Arndt, and A. Zeilinger, "Matter-wave interferometer for large molecules," Physical Review Letters **88**, 100404 (2002). (document)

[75] B. Brezger, M. Arndt, and A. Zeilinger, "Concepts for near-field interferometers with large molecules," Journal of Optics B: Quantum and Semiclassical Optics **5**, S82 (2003). (document)

[76] S. Gerlich, L. Hackermüller, K. Hornberger, A. Stibor, H. Ulbricht, M. Gring, F. Goldfarb, T. Savas, M. Müri, M. Mayor *et al.*, "A Kapitza–Dirac–Talbot–Lau interferometer for highly polarizable molecules," Nature Physics **3**, 711–715 (2007). (document)

[77] R. Grisenti, W. Schöllkopf, J. Toennies, G. Hegerfeldt, and T. Köhler, "Determination of atom-surface van der Waals potentials from transmission-grating diffraction intensities," Physical review letters **83**, 1755–1758 (1999). (document)

[78] K. Hornberger, S. Gerlich, H. Ulbricht, L. Hackermüller, S. Nimmrichter *et al.*, "Theory and experimental verification of Kapitza–Dirac–Talbot–Lau interferometry," New Journal of Physics **11**, 043032 (2009). (document)

[79] O. Nairz, B. Brezger, M. Arndt, and A. Zeilinger, "Diffraction of complex molecules by structures made of light," Physical Review Letters **87**, 160401 (2001). (document)

[80] V. Nesvizhevsky, "Interaction of neutrons with nanoparticles," Physics of Atomic Nuclei **65**, 400–408 (2002). (document), 12

[81] E. Lychagin, D. Kartashov, A. Muzychka, V. Nesvizhevsky, G. Nekhaev, and A. Strelkov, "Mechanism of small variations in energy of ultracold neutrons interacting with a surface," Physics of Atomic Nuclei **65**, 1995–1998 (2002). (document), 12

[82] D. Kartashov, E. Lychagin, A. Muzychka, V. Nesvizhevsky, G. Nekhaev, and A. Strelkov, "An investigation into the origin of small energy changes ($\sim 10^{-7}$ eV) of ultracold neutrons in traps," International Journal of Nanoscience **6**, 501–514 (2007). (document), 12

[83] V. Parsegian, *Van der Waals forces: a handbook for biologists, chemists, engineers, and physicists* (Cambridge Univ Pr, 2006). (document)

[84] E. Buks and M. Roukes, "Stiction, adhesion energy, and the Casimir effect in micromechanical systems," Physical Review B **63**, 033402 (2001). (document)

[85] H. Chan, V. Aksyuk, R. Kleiman, D. Bishop, and F. Capasso, "Quantum mechanical actuation of microelectromechanical systems by the Casimir force," Science **291**, 1941 (2001). (document)

[86] K. Ekinci and M. Roukes, "Nanoelectromechanical systems," Rev. Sci. Instrum **76**, 061101 (2005). (document)

[87] C. Genet, A. Lambrecht, and S. Reynaud, "The Casimir effect in the nanoworld," The European Physical Journal-Special Topics **160**, 183–193 (2008). (document)

[88] M. Sparnaay, "Measurements of attractive forces between flat plates," Physica **24**, 751–764 (1958). (document)

[89] P. van Blokland and J. Overbeek, "Van der Waals forces between objects covered with a chromium layer," J. Chem. Soc., Faraday Trans. 1 **74**, 2637–2651 (1978). (document)

[90] B. Deriagin and I. Abrikosova, "," Soviet Phys. JETP **3**, 819 (1957). (document)

[91] W. Black, J. De Jongh, J. Overbeek, and M. Sparnaay, "Measurements of retarded Van Der Waals' forces," Trans. Faraday Soc. **56**, 1597–1608 (1960). (document)

[92] D. Tabor and R. Winterton, "Surface forces: Direct measurement of normal and retarded van der Waals forces," Nature **219**, 1120–1121 (1968). (document)

[93] E. Sabisky and C. Anderson, "Verification of the Lifshitz theory of the van der Waals potential using liquid-helium films," Physical Review A **7**, 790–806 (1973). (document)

[94] M. Sparnaay, "The historical background of the Casimir effect," Physics in the Making (A. Sarlemijn, M. Sparnaay, Eds) (1989). (document), 2

[95] V. Mostepanenko, N. Trunov, and R. Znajek, *The Casimir effect and its applications* (Oxford University Press, USA, 1997). (document)

[96] S. Lamoreaux, "Demonstration of the Casimir force in the 0.6 to 6 μm range," Physical Review Letters **78**, 5–8 (1997). (document), 2

[97] S. Lamoreaux, "Erratum: Demonstration of the Casimir Force in the 0.6 to 6 μm Range [Phys. Rev. Lett. 78, 5 (1997)]," Physical Review Letters **81**, 5475–5476 (1998). (document)

[98] A. Lambrecht and S. Reynaud, "Comment on "Demonstration of the Casimir Force in the 0.6 to 6 μm Range"," Physical Review Letters **84**, 5672–5672 (2000). (document)

[99] S. Lamoreaux, "Lamoreaux Replies," Physical Review Letters **84**, 5673–5673 (2000). (document)

[100] S. Lamoreaux, "Systematic Correction for" Demonstration of the Casimir Force in the 0.6 to 6 micrometer Range"," Arxiv preprint arXiv:1007.4276 (2010). (document)

[101] U. Mohideen and A. Roy, "Precision measurement of the Casimir force from 0.1 to 0.9 μm," Physical Review Letters **81**, 4549–4552 (1998). (document), 2

[102] A. Roy, C. Lin, and U. Mohideen, "Improved precision measurement of the Casimir force," Physical Review D **60**, 111101 (1999). (document)

[103] B. Harris, F. Chen, and U. Mohideen, "Precision measurement of the Casimir force using gold surfaces," Physical Review A **62**, 052109 (2000). (document), 2

[104] H. Chan, V. Aksyuk, R. Kleiman, D. Bishop, and F. Capasso, "Nonlinear micromechanical Casimir oscillator," Physical Review Letters **87**, 211801 (2001). (document)

[105] R. Decca, D. Lopez, E. Fischbach, and D. Krause, "Measurement of the Casimir force between dissimilar metals," Physical Review Letters **91**, 50402 (2003). (document), 2

[106] G. Klimchitskaya, R. Decca, E. Fischbach, D. Krause, D. López, and V. Mostepanenko, "Casimir effect as a test for thermal corrections and hypothetical long-range interactions," International Journal of Modern Physics A **20**, 2205–2221 (2005). (document)

[107] R. Decca, D. López, E. Fischbach, G. Klimchitskaya, D. Krause, and V. Mostepanenko, "Tests of new physics from precise measurements of the Casimir pressure between two gold-coated plates," Physical Review D **75**, 077101 (2007). (document), 14, 2, 2.3, 3

[108] V. Mostepanenko, R. Decca, E. Fischbach, G. Klimchitskaya, D. Krause, and D. López, "Stronger constraints on non-Newtonian gravity from the Casimir effect," Journal of Physics A: Mathematical and Theoretical **41**, 164054 (2008). (document)

[109] G. Klimchitskaya, U. Mohideen, and V. Mostepanenko, "The Casimir force between real materials: experiment and theory," Reviews of Modern Physics **81**, 1827 (2009). (document), 2, 3

[110] A. Sushkov, W. Kim, D. Dalvit, and S. Lamoreaux, "Observation of the thermal Casimir force," Nature Physics **7**, 230–233 (2011). (document), 3, 15.3

[111] K. Milton, "The Casimir force: Feeling the heat," Nature Physics **7**, 190–191 (2011). (document), 3

[112] T. Ederth, "Template-stripped gold surfaces with 0.4-nm rms roughness suitable for force measurements: application to the Casimir force in the 20–100 nm range," Physical Review A **62**, 062104 (2000). (document), 2

[113] A. Roy and U. Mohideen, "Demonstration of the nontrivial boundary dependence of the Casimir force," Physical review letters **82**, 4380–4383 (1999). (document)

[114] F. Chen, U. Mohideen, G. Klimchitskaya, and V. Mostepanenko, "Demonstration of the lateral Casimir force," Physical review letters **88**, 101801 (2002). (document)

[115] G. Bressi, G. Carugno, A. Galvani, R. Onofrio, and G. Ruoso, "Experimental searches for extra-gravitational forces in the submillimetre range," Classical and Quantum Gravity **17**, 2365 (2000). (document)

[116] G. Bressi, G. Carugno, A. Galvani, R. Onofrio, G. Ruoso, and F. Veronese, "Experimental studies of macroscopic forces in the micrometre range," Classical and Quantum Gravity **18**, 3943 (2001). (document)

[117] G. Bressi, G. Carugno, R. Onofrio, and G. Ruoso, "Measurement of the Casimir force between parallel metallic surfaces," Physical review letters **88**, 041804 (2002). (document), 2

[118] E. Lifshitz, "The Theory of Molecular Attractive Forces between Solids," Soviet Phys. JETP **2**, 73 (1956). (document)

[119] I. Dzyaloshinskii, E. Lifshitz, and L. Pitaevskii, "General theory of van der waals' forces," Physics-Uspekhi **4**, 153–176 (1961). (document)

[120] E. Lifshitz, L. Landau, and L. Pitaevskii, *Statistical Physics; Pt. 2. Theory of the Condensed State; chap VIII: Electromagnetic Fluctuations* (Pergamon Press, 1991). (document)

[121] A. Lambrecht and S. Reynaud, "Casimir force between metallic mirrors," The European Physical Journal D-Atomic, Molecular, Optical and Plasma Physics **8**, 309–318 (2000). (document), 12.2.1

[122] V. Svetovoy, P. Van Zwol, G. Palasantzas, and J. De Hosson, "Optical properties of gold films and the Casimir force," Physical Review B **77**, 035439 (2008). (document)

[123] F. Chen, G. Klimchitskaya, U. Mohideen, and V. Mostepanenko, "Theory confronts experiment in the Casimir force measurements: Quantification of errors and precision," Physical Review A **69**, 022117 (2004). (document), 2

[124] J. Munday and F. Capasso, "Precision measurement of the Casimir-Lifshitz force in a fluid," Physical Review A **75**, 060102 (2007). (document), 2

[125] P. Van Zwol, G. Palasantzas, and J. De Hosson, "Influence of random roughness on the Casimir force at small separations," Physical Review B **77**, 075412 (2008). (document), 2

[126] J. Munday, F. Capasso, and V. Parsegian, "Measured long-range repulsive Casimir–Lifshitz forces," Nature **457**, 170–173 (2009). (document), 2

[127] G. Jourdan, A. Lambrecht, F. Comin, and J. Chevrier, "Quantitative non-contact dynamic Casimir force measurements," EPL (Europhysics Letters) **85**, 31001 (2009). (document), 2

[128] M. Masuda and M. Sasaki, "Limits on nonstandard forces in the submicrometer range," Physical review letters **102**, 171101 (2009). (document), 2

[129] S. De Man, K. Heeck, R. Wijngaarden, and D. Iannuzzi, "Halving the Casimir force with conductive oxides," Physical review letters **103**, 40402 (2009). (document), 2

[130] J. Mehra, "Temperature correction to the Casimir effect," Physica **37**, 145–152 (1967). (document)

[131] L. Brown and G. Maclay, "Vacuum stress between conducting plates: an image solution," Physical Review **184**, 1272 (1969). (document)

[132] J. Schwinger, L. de Raad, and K. Milton, "Casimir Effect in Dielectrics," Ann. Phys **115** (1978). (document)

[133] C. Genet, A. Lambrecht, and S. Reynaud, "Temperature dependence of the Casimir effect between metallic mirrors," Physical Review A **62**, 012110 (2000). (document), 12.2.1

[134] M. Planck, "Zur Theorie des Gesetzes der Energieverteilung im Normalspektrum," Deutsch Phys. Ges **2**, 237 (1900). (document)

[135] M. Planck, *The theory of heat radiation*, History Of Modern Physics (Tomash, 1906). (document)

[136] M. Planck, "Eine neue Strahlungshypothese," Verhandlungen der deutschen physikalischen Gesellschaft **13**, 138–148 (1911). (document), 3

[137] M. Boström and B. Sernelius, "Thermal effects on the Casimir force in the 0.1–5 μm range," Physical Review Letters **84**, 4757–4760 (2000). (document), 3, 3.2.1, V, 14.2

[138] V. Bezerra, G. Klimchitskaya, and V. Mostepanenko, "Correlation of energy and free energy for the thermal Casimir force between real metals," Physical Review A **66**, 062112 (2002). (document)

[139] M. Boström and B. Sernelius, "Entropy of the Casimir effect between real metal plates," Physica A: Statistical Mechanics and its Applications **339**, 53–59 (2004). (document)

[140] G. Ingold, A. Lambrecht, and S. Reynaud, "Quantum dissipative Brownian motion and the Casimir effect," Physical Review E **80**, 041113 (2009). (document), 2.3, 12.1.2, 13.4, 14.1

[141] S. Reynaud, A. Lambrecht, and C. Genet, "The Casimir force between real mirrors at non zero temperature," in "Quantum Field Theory Under the Influence of External Conditions," (Ed. Milton KA, Rinton Press, 2004). ArXiv: quant-ph/0312224. (document), V, 14.2

[142] G. Klimchitskaya and V. Mostepanenko, "Experiment and theory in the Casimir effect," Contemporary Physics **47**, 131–144 (2006). (document), V

[143] I. Brevik, S. Ellingsen, and K. Milton, "Thermal corrections to the Casimir effect," New Journal of Physics **8**, 236 (2006). (document), V

[144] I. Brevik, S. Ellingsen, J. Høye, and K. Milton, "Analytical and numerical demonstration of how the Drude dispersive model satisfies Nernst's theorem for the Casimir entropy," Journal of Physics A: Mathematical and Theoretical **41**, 164017 (2008). (document), V

[145] K. Milton, "Recent developments in the Casimir effect," in "Journal of Physics: Conference Series," , vol. 161 (IOP Publishing, 2009), vol. 161, p. 012001. (document), V

[146] B. Deriaguin, "Friction and adhesion. IV. The theory of adhesion of small particles," Kolloid Zeits **69**, 155–164 (1934). (document), 4

[147] B. Deriagin, I. Abrikosova, and E. Lifshitz, "," Q. Rev **10**, 295 (1968). (document), 4

[148] J. Błocki, J. Randrup, W. Swiatecki, and C. Tsang, "Proximity forces," Annals of Physics **105**, 427–462 (1977). (document), 4

[149] M. Schaden and L. Spruch, "Infinity-free semiclassical evaluation of Casimir effects," Physical Review A **58**, 935–953 (1998). (document), 9, 9.2, 9.2, 9.2

[150] M. Schaden and L. Spruch, "Focusing virtual photons: Casimir energies for some pairs of conductors," Physical Review Letters **84**, 459–462 (2000). (document)

[151] R. Jaffe and A. Scardicchio, "Casimir effect and geometric optics," Physical review letters **92**, 70402 (2004). (document), 9.2, B.1

[152] O. Schröder, A. Scardicchio, and R. Jaffe, "Casimir energy for a hyperboloid facing a plate in the optical approximation," Physical Review A **72**, 012105 (2005). (document)

[153] R. Balian and B. Duplantier, "Electromagnetic waves near perfect conductors. I. Multiple scattering expansions. Distribution of modes," Annals of physics **104**, 300–335 (1977). (document)

[154] R. Balian and B. Duplantier, "Electromagnetic waves near perfect conductors. II. Casimir effect," Annals of Physics **112**, 165–208 (1978). (document)

[155] R. Balian and B. Duplantier, "Geometry of the Casimir effect," in "15th SIGRAV Conference on General Relativity and Gravitation," (2004). Arxiv preprint quant-ph/0408124. (document)

[156] H. Gies, K. Langfeld, and L. Moyaerts, "Casimir effect on the worldline," Journal of High Energy Physics **2003**, 018 (2003). (document), 9.2, 9.2, B.1, B.1.2

[157] H. Gies and K. Klingmüller, "Casimir effect for curved geometries: Proximity-Force-Approximation validity limits," Physical review letters **96**, 220401 (2006). (document), 9.2, 9.2, 9.2, 9.2

[158] H. Gies and K. Klingmüller, "Worldline algorithms for Casimir configurations," Physical Review D **74**, 045002 (2006). (document), 9.2, 9.2, 9.2

[159] K. Klingmüller and H. Gies, "Geothermal Casimir phenomena," Journal of Physics A: Mathematical and Theoretical **41**, 164042 (2008). (document), V

[160] A. Scardicchio and R. Jaffe, "Casimir effects: an optical approach I. Foundations and examples," Nuclear Physics B **704**, 552–582 (2005). (document), 9.2, 9.2, B.1, B.1.1, B.1.2

[161] A. Scardicchio and R. Jaffe, "Casimir effects: an optical approach II. Local observables and thermal corrections," Nuclear Physics B **743**, 249–275 (2006). (document), 9.2, 9.2, 9.2

[162] A. Bulgac, P. Magierski, and A. Wirzba, "Scalar Casimir effect between Dirichlet spheres or a plate and a sphere," Physical Review D **73**, 025007 (2006). (document), 9.2, 9.2, B.1, B.1.1, B.1.2

[163] M. Bordag and V. Nikolaev, "Casimir force for a sphere in front of a plane beyond proximity force approximation," Journal of Physics A: Mathematical and Theoretical **41**, 164002 (2008). (document), 9.2, 9.2, 9.2, 9.3, 47, 10.3

[164] M. Bordag and V. Nikolaev, "First analytic correction beyond PFA for the electromagnetic field in sphere-plane geometry," Arxiv preprint arXiv:0911.0146 (2009). (document), 9.3, 9.4, 47, 10.3, 15.1, 15.1, 15.1

[165] S. Reynaud, P. Neto, and A. Lambrecht, "Casimir energy and geometry: beyond the proximity force approximation," Journal of Physics A: Mathematical and Theoretical **41**, 164004 (2008). (document), 3

[166] T. Emig and R. Jaffe, "Casimir forces between arbitrary compact objects," Journal of Physics A: Mathematical and Theoretical **41**, 164001 (2008). (document)

[167] T. Emig, "Fluctuation-induced quantum interactions between compact objects and a plane mirror," Journal of Statistical Mechanics: Theory and Experiment **2008**, P04007 (2008). (document), 9.2, 9.2, 9.3, 9.3, 9.4, 10.3, 10.3, 14.4

[168] A. Wirzba, "The Casimir effect as a scattering problem," Journal of Physics A: Mathematical and Theoretical **41**, 164003 (2008). (document)

[169] L. Moyaerts, K. Langfeld, and H. Gies, "Worldline approach to the Casimir effect," Quantum Field Theory Under the Influence of External Conditions (QFEXT03) (2003). Arxiv preprint hep-th/0311168. (document)

[170] H. Gies and K. Klingmüller, "Quantum energies with worldline numerics," Journal of Physics A: Mathematical and General **39**, 6415 (2006). (document)

[171] H. Gies and K. Klingmüller, "Casimir edge effects," Physical review letters **97**, 220405 (2006). (document)

[172] A. Weber and H. Gies, "Interplay between geometry and temperature for inclined Casimir plates," Physical Review D **80**, 065033 (2009). (document), V

[173] H. Gies and A. Weber, "Geometry-temperature interplay in the Casimir effect," Quantum Field Theory Under the Influence of External Conditions (QFEXT09): Devoted to the Centenary of HBG Casimir p. 178 (2010). (document), V

[174] A. Weber and H. Gies, "Nonmonotonic thermal Casimir force from geometry-temperature interplay," Physical review letters **105**, 40403 (2010). (document), V, 13

[175] A. Weber and H. Gies, "Geothermal Casimir phenomena for the sphere-plate and cylinder-plate configurations," Physical Review D **82**, 125019 (2010). (document), V, B.1

[176] T. Emig, "Casimir physics: geometry, shape and material," International Journal of Modern Physics A **25**, 2177–2195 (2010). (document), 9.3, 9.3

[177] K. Milton and J. Wagner, "Multiple scattering methods in Casimir calculations," Journal of Physics A: Mathematical and Theoretical **41**, 155402 (2008). (document)

[178] P. Neto, A. Lambrecht, and S. Reynaud, "Roughness correction to the Casimir force: Beyond the proximity force approximation," EPL (Europhysics Letters) **69**, 924 (2005). (document), 15.3

[179] P. Neto, A. Lambrecht, and S. Reynaud, "Casimir effect with rough metallic mirrors," Physical Review A **72**, 012115 (2005). (document), 15.3

[180] R. Rodrigues, P. Neto, A. Lambrecht, and S. Reynaud, "Lateral Casimir force beyond the proximity-force approximation," Physical review letters **96**, 100402 (2006). (document)

[181] R. Rodrigues, P. Neto, A. Lambrecht, and S. Reynaud, "Reply to: Comment on "Lateral Casimir force beyond the proximity-force approximation"," Physical Review Letters **98**, 68902 (2007). (document)

[182] R. Rodrigues, P. Neto, A. Lambrecht, and S. Reynaud, "Lateral Casimir force beyond the proximity force approximation: A nontrivial interplay between geometry and quantum vacuum," Physical Review A **75**, 062108 (2007). (document)

[183] R. Rodrigues, P. Neto, A. Lambrecht, and S. Reynaud, "Vacuum-induced torque between corrugated metallic plates," EPL (Europhysics Letters) **76**, 822 (2006). (document)

[184] S. Reynaud, A. Canaguier-Durand, R. Messina, A. Lambrecht, and P. Neto, "The scattering approach to the Casimir force," International Journal of Modern Physics A **25**, 2201–2211 (2010). (document), 15.3

[185] A. Lambrecht and V. Marachevsky, "Casimir interaction of dielectric gratings," Physical review letters **101**, 160403 (2008). (document), 15.3

[186] A. Lambrecht, "Nanotechnology: Shaping the void," Nature **454**, 836–837 (2008). (document), 15.3

[187] Y. Bao, R. Guérout, J. Lussange, A. Lambrecht, R. Cirelli, F. Klemens, W. Mansfield, C. Pai, and H. Chan, "Casimir force on a surface with shallow nanoscale corrugations: Geometry and finite conductivity effects," Physical review letters **105**, 250402 (2010). (document), 15.3

[188] A. Rodriguez, M. Ibanescu, D. Iannuzzi, F. Capasso, J. Joannopoulos, and S. Johnson, "Computation and visualization of Casimir forces in arbitrary geometries: Nonmonotonic lateral-wall forces and the failure of proximity-force approximations," Physical review letters **99**, 80401 (2007). (document)

[189] A. Rodriguez, M. Ibanescu, D. Iannuzzi, J. Joannopoulos, and S. Johnson, "Virtual photons in imaginary time: Computing exact Casimir forces via standard numerical electromagnetism techniques," Physical Review A **76**, 032106 (2007). (document)

[190] S. Zaheer, A. Rodriguez, S. Johnson, and R. Jaffe, "Optical-approximation analysis of sidewall-spacing effects on the force between two squares with parallel sidewalls," Physical Review A **76**, 063816 (2007). (document)

[191] S. Rahi, A. Rodriguez, T. Emig, R. Jaffe, S. Johnson, and M. Kardar, "Nonmonotonic effects of parallel sidewalls on Casimir forces between cylinders," Physical Review A **77**, 030101 (2008). (document)

[192] A. Rodriguez, J. Joannopoulos, and S. Johnson, "Repulsive and attractive Casimir forces in a glide-symmetric geometry," Physical Review A **77**, 062107 (2008). (document)

[193] A. Rodriguez, J. Munday, J. Joannopoulos, F. Capasso, D. Dalvit, and S. Johnson, "Stable suspension and dispersion-induced transitions from repulsive Casimir forces between fluid-separated eccentric cylinders," Physical review letters **101**, 190404 (2008). (document)

[194] M. Reid, A. Rodriguez, J. White, and S. Johnson, "Efficient computation of Casimir interactions between arbitrary 3D objects," Physical review letters **103**, 40401 (2009). Extension in Arxiv preprint arXiv:1010.5539. (document)

[195] A. Rodriguez, A. McCauley, J. Joannopoulos, and S. Johnson, "Casimir forces in the time domain: Theory," Physical Review A **80**, 012115 (2009). (document)

[196] A. McCauley, A. Rodriguez, J. Joannopoulos, and S. Johnson, "Casimir forces in the time domain: Applications," Physical Review A **81**, 012119 (2010). (document)

[197] A. Rodriguez, A. McCauley, J. Joannopoulos, and S. Johnson, "Theoretical ingredients of a Casimir analog computer," Proceedings of the National Academy of Sciences **107**, 9531 (2010). (document)

[198] A. Rodriguez, A. McCauley, D. Woolf, F. Capasso, J. Joannopoulos, and S. Johnson, "Nontouching Nanoparticle Diclusters Bound by Repulsive and Attractive Casimir Forces," Physical review letters **104**, 160402 (2010). (document)

[199] M. Levin, A. McCauley, A. Rodriguez, M. Reid, and S. Johnson, "Casimir repulsion between metallic objects in vacuum," Physical review letters **105**, 90403 (2010). (document)

[200] A. Rodriguez, D. Woolf, A. McCauley, F. Capasso, J. Joannopoulos, and S. Johnson, "Achieving a strongly temperature-dependent Casimir effect," Physical review letters **105**, 60401 (2010). (document)

[201] A. McCauley, R. Zhao, M. Reid, A. Rodriguez, J. Zhou, F. Rosa, J. Joannopoulos, D. Dalvit, C. Soukoulis, and S. Johnson, "Microstructure effects for Casimir forces in chiral metamaterials," Physical Review B **82**, 165108 (2010). (document)

[202] S. Johnson, "Numerical methods for computing Casimir interactions," Casimir Physics pp. 175–218 (2011). (document)

[203] A. McCauley, F. Rosa, A. Rodriguez, J. Joannopoulos, D. Dalvit, and S. Johnson, "Structural anisotropy and orientation-induced Casimir repulsion in fluids," Physical Review A **83**, 052503 (2011). (document)

[204] K. Pan, A. McCauley, A. Rodriguez, M. Reid, J. White, and S. Johnson, "Calculation of nonzero-temperature Casimir forces in the time domain," Physical Review A **83**, 040503 (2011). (document)

[205] A. Rodriguez, D. Woolf, P. Hui, E. Iwase, A. McCauley, F. Capasso, M. Loncar, and S. Johnson, "Designing evanescent optical interactions to control the expression of Casimir forces in optomechanical structures," Applied Physics Letters **98**, 194105 (2011). (document)

[206] A. McCauley, A. Rodriguez, M. Reid, and S. Johnson, "Casimir repulsion beyond the dipole regime," Arxiv preprint arXiv:1105.0404 (2011). (document)

[207] C. Genet, "La force de Casimir entre deux miroirs métalliques à température non nulle," Ph.D. thesis, Université Paris VI (2002). Available (in french) at http://tel.archives-ouvertes.fr/tel-00001749. I, 3, 1.4, 3.2.3, 3.2.3, 11.3, 14.3.1

[208] C. Genet, A. Lambrecht, and S. Reynaud, "Casimir force and the quantum theory of lossy optical cavities," Physical Review A **67**, 43811 (2003). I, 3, 1.2

[209] C. Cohen-Tannoudji, J. Dupont-Roc, and G. Grynberg, *Photons et atomes: introduction à l'électrodynamique quantique* (L'Editeur: EDP Sciences, 2001). 1.1.2, 2.2, 5.1.1

[210] G. Celep, E. Cottancin, J. Lermé, M. Pellarin, L. Arnaud, J. Huntzinger, J. Vialle, M. Broyer, B. Palpant, O. Boisron *et al.*, "Optical properties of copper clusters embedded in alumina: An experimental and theoretical study of size dependence," Physical Review B **70**, 165409 (2004). 2.2, 12.1

[211] E. Cottancin, G. Celep, J. Lermé, M. Pellarin, J. Huntzinger, J. Vialle, and M. Broyer, "Optical properties of noble metal clusters as a function of the size: comparison between experiments and a semi-quantal theory," Theoretical Chemistry Accounts: Theory, Computation, and Modeling (Theoretica Chimica Acta) **116**, 514–523 (2006). 2.2, 12.1

[212] W. Sellmeier, "Zur erklärung der abnormen farbenfolge im spectrum einiger substanzen," Annalen der Physik und Chemie **219**, 272–282 (1871). 2.4

[213] D. Materials, "The cvd diamond booklet," http://www.diamond-materials.com/EN/cvd_diamond/overview.htm (2008). 2

[214] L. Bergstrom, "Hamaker constants of inorganic materials," Advances in Colloid and Interface Science **70**, 125–169 (1997). 2

[215] A. Milling, P. Mulvaney, and I. Larson, "Direct measurement of repulsive van der Waals interactions using an atomic force microscope," Journal of colloid and interface science **180**, 460–465 (1996). 2

[216] C. Genet, F. Intravaia, A. Lambrecht, and S. Reynaud, "Electromagnetic vacuum fluctuations, Casimir and Van der Waals forces," Ann. Fond. L. de Broglie **29**, 311 (2004). Arxiv preprint quant-ph/0302072. 2.5, 12.3.2

[217] C. Henkel, K. Joulain, J. Mulet, and J. Greffet, "Coupled surface polaritons and the Casimir force," Physical Review A **69**, 023808 (2004). 2.5

[218] A. Gérardin, "Projet de thèse de doctorat," Ph.D. thesis, Université Paris VI (2013). 2.5, 12.2.1

[219] S. Reynaud, A. Lambrecht, and C. Genet, "The Casimir force between real mirrors at non zero temperature," Quantum Field Theory Under the Influence of External Conditions p. 36 (2004). 3

[220] C. Bohren and D. Huffman, "Absorption and scattering of light by small particles," Research supported by the University of Arizona and Institute of Occupational and Environmental Health. New York, Wiley-Interscience, 1983, 541 p. **1** (1983). 5.2.2

[221] D. Varshalovich, A. Moskalev, and V. Khersonskii, *Quantum theory of angular momentum* (World Scientific Pub. Co., Teaneck, NJ, 1987). 5.2.4

[222] H. Nussenzveig, *Diffraction effects in semiclassical scattering* (Cambridge Univ Pr, 1992). 6.1.1

[223] A. Sushkov, W. Kim, D. Dalvit, and S. Lamoreaux, "Observation of the thermal Casimir force," Arxiv preprint arXiv:1011.5219 (2010). 6.1.3

[224] D. Krause, R. Decca, D. López, and E. Fischbach, "Experimental investigation of the Casimir force beyond the proximity-force approximation," Physical Review Letters **98**, 50403 (2007). 6.1.3, 9.4, 10.3, 11.4

[225] N. Temme, "On the numerical evaluation of the modified bessel function of the third kind," Journal of Computational Physics **19**, 324–337 (1975). 6.5

[226] W. Lentz, "Generating Bessel functions in Mie scattering calculations using continued fractions," Applied Optics **15**, 668–671 (1976). 6.5

[227] W. Lentz, "A method of computing spherical Bessel functions of complex argument with tables," Tech. rep., DTIC Document (1973). 6.5

[228] R. Zandi, T. Emig, and U. Mohideen, "Quantum and thermal Casimir interaction between a sphere and a plate: Comparison of Drude and plasma models," Physical Review B **81**, 195423 (2010). 8.2, V

[229] M. Bordag and I. Pirozhenko, "Vacuum energy between a sphere and a plane at finite temperature," Physical Review D **81**, 85023 (2010). 8.2, V

[230] M. Bordag, "Casimir effect for a sphere and a cylinder in front of a plane and corrections to the proximity force theorem," Physical Review D **73**, 125018 (2006). 9.2

[231] O. Schroeder, A. Scardicchio, and R. Jaffe, "Casimir energy for a hyperboloid facing a plate in the optical approximation," Physical Review A **72**, 12105 (2005). 14

[232] L. Datta *et al.*, "Retarded Van der Waals potential between a conducting plane and a polarizable particle," Physics Letters A **83**, 314–316 (1981). 9.2

[233] P. Maia Neto, A. Lambrecht, and S. Reynaud, "Casimir energy between a plane and a sphere in electromagnetic vacuum," Physical Review A **78**, 12115 (2008). 9.3, 9.3, 9.4, 10.3, 10.3, 10.3, 14.4

[234] A. Canaguier-Durand, P. Maia Neto, I. Cavero-Pelaez, A. Lambrecht, and S. Reynaud, "Casimir interaction between plane and spherical metallic surfaces," Physical Review Letters **102**, 230404 (2009). 11.4

[235] A. Canaguier-Durand, A. Gérardin, R. Guérout, P. Maia Neto, V. Nesvizhevsky, A. Voronin, A. Lambrecht, and S. Reynaud, "Casimir interaction between a dielectric nanosphere and a metallic plane," Phys. Rev. A **83**, 032508 (2011). 12, 12.1.2, 12.2.1

[236] H. B. G. Casimir and D. Polder, "The influence of retardation on the London-van der Waals forces," Phys. Rev. **73**, 360–372 (1948). 12, 12.1.1, 12.1.2

[237] E. Lifshitz and L. Pitaevskii, "Statistical Physics Part 2, Landau and Lifshitz Course of Theoretical Physics, vol. 9," (1980). 12

[238] J. Babb, G. Klimchitskaya, and V. Mostepanenko, "Casimir-Polder interaction between an atom and a cavity wall under the influence of real conditions," Physical Review A **70**, 42901 (2004). 12

[239] D. Dalvit, P. Neto, A. Lambrecht, and S. Reynaud, "Probing quantum-vacuum geometrical effects with cold atoms," Physical review letters **100**, 40405 (2008). 12, 12.1.1

[240] R. Messina, D. Dalvit, P. Neto, A. Lambrecht, and S. Reynaud, "Dispersive interactions between atoms and nonplanar surfaces," Physical Review A **80**, 22119 (2009). 12, 12.1.1

[241] K. Case, "Singular potentials," Physical Review **80**, 797–806 (1950). 12.1.4

[242] R. Messina, S. Pelisson, M.-C. Angonin, and P. Wolf, "Atomic states in optical traps near a planar surface," Phys. Rev. A **83**, 052111 (2011). Arxiv preprint arXiv:1103.1581. 12.2.1

[243] A. Canaguier-Durand, P. Neto, A. Lambrecht, and S. Reynaud, "Thermal Casimir effect in the plane-sphere geometry," Physical Review Letters **104**, 40403 (2010). V

[244] L. Pitaevskii, "Casimir-lifshitz forces and entropy," Quantum Field Theory Under the Influence of External Conditions (QFEXT09): Devoted to the Centenary of HBG Casimir p. 227 (2010). 13.4

[245] V. Svetovoy and M. Lokhanin, "Precise calculation of the Casimir force between gold surfaces," Modern Physics Letters A **15**, 1437–1444 (2000). 14.2

[246] V. Svetovoy and M. Lokhanin, "Linear temperature correction to the Casimir force," Physics Letters A **280**, 177–181 (2001). 14.2

[247] S. Lamoreaux, "Comment on "Thermal effects on the Casimir force in the 0.1–5 μm range"," Physical Review Letters **87**, 139101 (2001). 14.2

[248] B. Sernelius, "Sernelius replies," Physical Review Letters **87**, 139102 (2001). 14.2

[249] B. Sernelius and M. Bostr
"om, "Comment on "Casimir force at both nonzero temperature and finite conductivity"," Physical Review Letters **87**, 259101 (2001). 14.2

[250] M. Bordag, B. Geyer, G. Klimchitskaya, and V. Mostepanenko, "Bordag, Geyer, Klimchitskaya, and Mostepanenko reply," Physical Review Letters **87**, 259102 (2001). 14.2

[251] G. Klimchitskaya and V. Mostepanenko, "Investigation of the temperature dependence of the Casimir force between real metals," Physical Review A **63**, 062108 (2001). 14.2

[252] G. Klimchitskaya, "What is the temperature dependence of the Casimir force between real metals?" International Journal of Modern Physics A **17**, 751–760 (2002). 14.2

[253] F. Mazzitelli, F. Lombardo, and P. Villar, "On the accuracy of the PFA: Analogies between Casimir and electrostatic forces," in "Journal of Physics: Conference Series," , vol. 161 (IOP Publishing, 2009), vol. 161, p. 012015. 15.1

[254] C. Genet, A. Lambrecht, P. Neto, and S. Reynaud, "The Casimir force between rough metallic plates," EPL (Europhysics Letters) **62**, 484 (2003). 15.3

[255] P. Van Zwol, V. Svetovoy, and G. Palasantzas, "Distance upon contact: Determination from roughness profile," Physical Review B **80**, 235401 (2009). 15.3

[256] P. van Zwol, V. Svetovoy, and G. Palasantzas, "Characterization of optical properties and surface roughness profiles: The casimir force between real materials," Casimir Physics pp. 311–343 (2011). 15.3

[257] W. Broer, G. Palasantzas, J. Knoester, and V. Svetovoy, "Roughness correction to the casimir force beyond perturbation theory," EPL (Europhysics Letters) **95**, 30001 (2011). 15.3

[258] J. Camp, T. Darling, and R. Brown, "Macroscopic variations of surface potentials of conductors," Journal of applied physics **69**, 7126–7129 (1991). 15.3

[259] N. Robertson, J. Blackwood, S. Buchman, R. Byer, J. Camp, D. Gill, J. Hanson, S. Williams, and P. Zhou, "Kelvin probe measurements: investigations of the patch effect with applications to ST-7 and LISA," Classical and Quantum Gravity **23**, 2665 (2006). 15.3

[260] S. Pollack, S. Schlamminger, and J. Gundlach, "Temporal extent of surface potentials between closely spaced metals," Physical review letters **101**, 71101 (2008). 15.3

[261] E. Adelberger, J. Gundlach, B. Heckel, S. Hoedl, and S. Schlamminger, "Torsion balance experiments: A low-energy frontier of particle physics," Progress in Particle and Nuclear Physics **62**, 102–134 (2009). 15.3

[262] W. Kim, A. Sushkov, D. Dalvit, and S. Lamoreaux, "Surface contact potential patches and Casimir force measurements," Physical Review A **81**, 022505 (2010). 15.3

[263] J. Carter and J. Martin, "Energy shifts of rydberg atoms due to patch fields near metal surfaces," Physical Review A **83**, 032902 (2011). 15.3

[264] B. Guilfoyle, W. Klingenberg, and S. Sen, "The Casimir effect between non-parallel plates by geometric optics," Arxiv preprint math/0406399 (2004). B.1

[265] H. Hamaker, "The london–van der waals attraction between spherical particles," physica **4**, 1058–1072 (1937). B.2.5

Résumé

Nous évaluons l'interaction de Casimir entre un miroir plan et un miroir sphérique, à température arbitraire, en tenant compte de la réflexion imparfaite. Cela nous permet d'étudier la riche dépendance à la géométrie de l'effet Casimir, et d'estimer l'erreur faite par l'approximation de proximité (PFA), communément utilisée pour cette configuration sphère-plan qui est celle des expériences.

Pour cette évaluation nous appliquons la méthode de diffusion, basée sur la théorie des réseaux optiques, à la géométrie sphère-plan. La température est prise en compte par la formule de Matsubara. La réflexion sur le plan est exprimée à l'aide d'ondes planes, celle sur la sphère à l'aide d'ondes sphériques, entraînant un développement multipolaire. Les indices (ℓ, m) de ces dernières sont tronqués à une valeur maximale pour l'évaluation numérique.

Nous étudions d'abord le cas de la température nulle. Les résultats numériques permettent de caractériser l'erreur des différentes méthodes d'approximation, en fonction du modèle utilisé pour les miroirs, et de mettre en évidence des corrélations entre les effets de géométrie et de conductivité finie.

Nous analysons ensuite la dépendance de l'effet Casimir à la température. Pour des miroirs parfaits, nous observons des corrélations entre les effets thermiques et géométriques pouvant entraîner une contribution répulsive des photons thermiques à la force de Casimir. Ce phénomène peut être associé à l'apparition de valeurs négatives pour l'entropie. Enfin, pour des miroirs métalliques à température ambiante nous observons une grande variété de corrélations entre les effets de la géométrie, de la température et de la dissipation dans les métaux.

Mots clés : effet Casimir, fluctuations du vide et thermiques, développement multipolaire, géométrie sphère-plan, approximation de proximité, dépendance géométrique de l'effet Casimir.

Abstract

We evaluate the Casimir interaction between a sphere and a plane, at arbitrary temperature, accounting for imperfect reflection. This enables us to study the rich dependance of the Casimir effect on the geometry, and to estimate the error made by the proximity approximation (PFA) commonly used in this sphere-plane configuration, which is the one of the experiments.

For this evaluation we apply the scattering method, based on the theory of optical networks, to the sphere-plane geometry. The temperature is taken care of through the Matsubara formula. We use planar waves to express the reflection on the plane, and spherical waves for the reflection on the sphere, which leads to a multipolar expansion. The indices (ℓ, m) for the spherical waves are truncated to maximum value for the sake of numerical evaluation.

We first study the zero temperature case. We use the numerical results to characterise the error made the various approximation methods, depending on the model used to describe the mirrors, and to reveal correlations between the effects of geometry and of finite conductivity.

We then analyse the dependence of the Casimir effect on the temperature. For perfect mirrors, we observe correlations between the thermal geometrical effects, that can yield to a repulsive contribution of the thermal photons to the Casimir force. This feature can be associated to the appearance of negative values for the entropy. Finally, we evaluate the Casimir effect for metallic mirrors at ambient temperature. We observe strong correlations between the effects of geometry, temperature, and dissipation in the metals.

Keywords: Casimir effect, quantum vacuum and thermal fluctuations, multipolar expansion, sphere-plane geometry, proximity approximation, dependance of the Casimir effect on the geometry.